

Computational Methods in Applied Sciences 46

Eugenio Oñate
Djordje Peric
Eduardo de Souza Neto
Michele Chiumenti *Editors*

Advances in Computational Plasticity

A Book in Honour of D. Roger J. Owen



 Springer

Computational Methods in Applied Sciences

Volume 46

Series editor

Eugenio Oñate
CIMNE
Edificio C-1, Campus Norte UPC
Gran Capitán, s/n.
08034 Barcelona, Spain
onate@cimne.upc.edu

More information about this series at <http://www.springer.com/series/6899>

Eugenio Oñate · Djordje Peric
Eduardo de Souza Neto
Michele Chiumenti
Editors

Advances in Computational Plasticity

A Book in Honour of D. Roger J. Owen

 Springer

Editors

Eugenio Oñate
CIMNE, Universitat Politècnica de
Catalunya
Barcelona
Spain

Djordje Peric
Swansea University
Swansea
UK

Eduardo de Souza Neto
Swansea University
Swansea
UK

Michele Chiumenti
CIMNE, Universitat Politècnica de
Catalunya
Barcelona
Spain

ISSN 1871-3033

Computational Methods in Applied Sciences

ISBN 978-3-319-60884-6

ISBN 978-3-319-60885-3 (eBook)

DOI 10.1007/978-3-319-60885-3

Library of Congress Control Number: 2017943249

© Springer International Publishing AG 2018

This work is subject to copyright. All rights are reserved by the Publisher, whether the whole or part of the material is concerned, specifically the rights of translation, reprinting, reuse of illustrations, recitation, broadcasting, reproduction on microfilms or in any other physical way, and transmission or information storage and retrieval, electronic adaptation, computer software, or by similar or dissimilar methodology now known or hereafter developed.

The use of general descriptive names, registered names, trademarks, service marks, etc. in this publication does not imply, even in the absence of a specific statement, that such names are exempt from the relevant protective laws and regulations and therefore free for general use.

The publisher, the authors and the editors are safe to assume that the advice and information in this book are believed to be true and accurate at the date of publication. Neither the publisher nor the authors or the editors give a warranty, express or implied, with respect to the material contained herein or for any errors or omissions that may have been made. The publisher remains neutral with regard to jurisdictional claims in published maps and institutional affiliations.

Printed on acid-free paper

This Springer imprint is published by Springer Nature

The registered company is Springer International Publishing AG

The registered company address is: Gewerbestrasse 11, 6330 Cham, Switzerland



D. Roger J. Owen

Preface

This book presents twenty-one invited contributions in the field of computational plasticity and related topics written by distinguished scientists on computational solid mechanics. The book has been conceived to honour Prof. Roger Owen on the occasion of his 75th birthday. The 21 technical chapters in the book are completed with a first chapter highlighting the scientific and technical contributions of Prof. Owen along his career, and, in particular his role in fostering the cooperation between the computational mechanics communities at the University of Swansea in Wales and the Technical University of Catalunya in Barcelona, Spain.

The release of the book has been chosen to be coincident with the 14th edition of the international conference on Computational Plasticity, Fundamentals and Applications (COMPLAS) held in Barcelona on 5–7 September 2017. The objectives of the COMPLAS conferences are to address both the theoretical bases for the solution of plasticity problems, the numerical algorithms necessary for efficient and robust computer implementation and present state-of-the-art applications of the numerical methods for solving practical problems in engineering. The COMPLAS conference series have been jointly organized since its start by the Swansea and Barcelona groups above mentioned.

Previous meetings in the COMPLAS series were held in Barcelona in 1987, 1989, 1992, 1995, 1997, 2000, 2003, 2005, 2007, 2009, 2011, 2013 and 2015. COMPLAS 2017 has been a special occasion as it is the 30th anniversary of the first COMPLAS conference held in 1987. The fourteen conferences in the series have been technically and academically successful, and the COMPLAS meetings have become established events in the field of computational solid mechanics.

The COMPLAS conferences are one of the Thematic Conferences of the European Community on Computational Methods in Applied Sciences (ECCOMAS). They are also Special Interest Conference of the International Association for Computational Mechanics (IACM).

A reason for the success of the COMPLAS conferences is that the ever increasing rate of development of new engineering materials required to meet advanced technological needs poses fresh challenges in the field of constitutive modelling. The complex behaviour of such materials demands a closer

interaction between numerical analysts and material scientists in order to produce thermodynamically consistent models which provide a response, while keeping with fundamental micromechanical principles and experimental observations. This necessity for collaboration is further highlighted by the continuing remarkable developments in computer hardware which makes the numerical simulation of complex deformation responses increasingly possible. Contributing to fostering and disseminating the advances in these challenging fields is the main objective of COMPLAS, and also a motivation for the publication of this book.

The 21 technical chapters in the book cover topics related to the History of Computational Plasticity, Advanced Material Models, Biomechanics, Composites, Contact Problems, Damage, Fracture and Fatigue, Forming Processes, Granulation Processes, High Velocity Impact, Industrial Applications, Innovative Computational Methods (FEM, Discrete Element Methods, Meshless Methods, Particle-based Methods, etc.), Multi-Fracturing Solids, Multi-Scale Material Models and High Performance Computing Techniques.

We would like to thank all authors by their contributions to this book. These contributions have been sent directly by the authors, and the editors cannot accept responsibility for any inaccuracies and opinions contained in the text.

Finally, we thank Prof. Owen for his many contributions to the field of computational mechanics and express our congratulations and best wishes on his 75 birthday.

Barcelona, Spain
Swansea, UK
Swansea, UK
Barcelona, Spain
September 2017

Eugenio Oñate
Djordje Peric
Eduardo de Souza Neto
Michele Chiumenti

Contents

Comparison of Phase-Field Models of Fracture Coupled with Plasticity	1
R. Alessi, M. Ambati, T. Gerasimov, S. Vidoli and L. De Lorenzis	
Bridging the Gap Between Concrete Microstructures and Tunnel Linings	23
E. Binder, H. Wang, T. Schlappal, J.L. Zhang, Y. Yuan, B. Pichler and H.A. Mang	
Phase-Field Formulation for Ductile Fracture	45
Michael J. Borden, Thomas J.R. Hughes, Chad M. Landis, Amin Anvari and Isaac J. Lee	
Computational Strategies for Speeding-Up F.E. Simulations of Metal Forming Processes	71
Lionel Fourment, Koffi K’podzo, Fabien Delalondre, Ugo Ripert, Mohamad Ramadan, Frédéric Vi and Hugues Digonnet	
Discrete Simulation of Cone Penetration in Granular Materials	95
Antonio Gens, Marcos Arroyo, Joanna Butlanska and Catherine O’Sullivan	
A Brief Review on Computational Modeling of Rupture in Soft Biological Tissues	113
Osman Gültekin and Gerhard A. Holzapfel	
Performance Comparison of Nodally Integrated Galerkin Meshfree Methods and Nodally Collocated Strong Form Meshfree Methods	145
M. Hillman and J.S. Chen	
Data-Driven Computing	165
Trenton Kirchdoerfer and Michael Ortiz	

Elasto-Plastic Response of Thick Plates Built in Functionally Graded Material Using the Third Order Plate Theory	185
Michal Kleiber, Maciej Taczala and Ryszard Buczkowski	
Extended-PGD Model Reduction for Nonlinear Solid Mechanics Problems Involving Many Parameters.	201
P. Ladevèze, Ch. Paillet and D. Néron	
Data-Driven Self-consistent Clustering Analysis of Heterogeneous Materials with Crystal Plasticity	221
Zeliang Liu, Orion L. Kafka, Cheng Yu and Wing Kam Liu	
A Viscoelastic-Viscoplastic Combined Constitutive Model for Thermoplastic Resins	243
Seishiro Matsubara and Kenjiro Terada	
Fracturing in Dry and Saturated Porous Media.	265
Enrico Milanese, Toan Duc Cao, Luciano Simoni and Bernhard A. Schrefler	
On Multi-scale Computational Design of Structural Materials Using the Topological Derivative	289
J. Oliver, A. Ferrer, J.C. Cante, S.M. Giusti and O. Lloberas-Valls	
Advances in the DEM and Coupled DEM and FEM Techniques in Non Linear Solid Mechanics	309
Eugenio Oñate, Francisco Zárata, Miguel A. Celigueta, José M. González, Juan Miquel, Josep M. Carbonell, Ferran Arrufat, Salvador Latorre and Miquel Santasusana	
The Influence of the Collagen Architecture on the Mechanical Response of the Human Cornea.	337
Anna Pandolfi	
History of Computational Classical Elasto-Plasticity	357
Erwin Stein	
VEM for Inelastic Solids	381
R.L. Taylor and E. Artioli	
Improved Contact Stress Recovery for Mortar-Based Contact Formulations	395
Christoph Wilking, Manfred Bischoff and Ekkehard Ramm	
Efficient Low Order Virtual Elements for Anisotropic Materials at Finite Strains.	417
P. Wriggers, B. Hudobivnik and J. Korelc	

Professor David Roger Jones Owen

A Tribute to 40 Years of Cooperation Between the Computational Mechanics Communities at Barcelona and Swansea

Professor Roger Owen (Roger to his many friends) was born in Bynea (near Llanelli) in Wales, on 27 May 1942. He is a Research Professor in Civil Engineering at Swansea University, Wales, UK, and an international authority on finite element and discrete element techniques; he is the author of six textbooks and over four hundred scientific publications. In addition to being the editor of forty monographs and conference proceedings, Prof. Owen is also the founding editor of the International Journal for Engineering Computations and is a member of several editorial boards. He is currently the Engineering Editor of the Proceedings of the Royal Society A. His involvement in academic research has led to the supervision of over seventy Ph.D. students.

Professor Owen's research, in the field of solid and structural mechanics, has centred on the development of solution procedures for nonlinear problems encountered in science and engineering. After undertaking his initial degrees at Swansea University, he completed his Ph.D. at Northwestern University, USA, under the guidance of Prof. T. Mura, in the field of Theoretical and Applied Mechanics. This work, and also his early postdoctoral experience as Walter P. Murphy Research Fellow at Northwestern University, involved both the analytical and computational studies of fundamental plastic material deformation described by continuously distributed dislocation mechanisms.

Professor Owen subsequently returned to University of Wales Swansea to take up an academic post in the Department of Civil Engineering, where under the influence of Prof. O.C. Zienkiewicz, he developed an interest in computational methods. From that time, Prof. Owen has contributed prominently to the development of computational strategies for plastic deformation problems, both for fundamental material studies and for application to engineering structures and components.

Over the last three decades, Prof. Owen's work has focused on the development of discrete element methods for particulate modelling and the simulation of multi-fracturing phenomena in materials, where much of his research has been pioneering. This work has extended developments in the continuum modelling of finitely deforming solids by including damage/fracture-based failure and introducing material separation on a local basis to permit simulation of the degradation of a continuum into a multi-fractured particulate state. Based upon this methodology, contributions have been made to fundamental understanding in several key application areas, including explosive simulations which necessitates coupling of the multi-fracturing solid behaviour with the evolving detonation gas distribution, deep-level mining/oil recovery operations, defence problems related to high velocity impact involving penetration of metallic and ceramic materials and structural failure predictions for impact, seismic and blast loading.

With an interest in solving large-scale problems, Prof. Owen has over the last three decades been engaged in the development of parallel processing strategies for the simulation of engineering and scientific problems. Commencing from early work on shared memory machines, his most recent work has involved implementation on distributed memory platforms, where for problems involving multi-fracturing solids or adaptive mesh refinement in which continual changes in mesh topology take place, the development of dynamic domain partitioning schemes and incremental inter-processor data migration is essential.

More recently, Prof. Owen has become involved in research for describing random media fields in stochastic finite element modelling with a view to modelling both uncertainties in the distribution of material properties and the presence of internal fractures in geo-materials and other solids. A further topic of recent research has been the coupling of particulate systems and multi-fracturing solids with other physical fields, involving liquids or gases, through the introduction of a Lattice Boltzmann description.

He has published seminal books in the field of finite element methods and computational solid mechanics. Among these, we note the book *Finite Element Programming* (1979), a reference for all who wanted an introduction to the coding aspects of the finite element method, *An Introduction to Finite Element Computations* and the two editions of his book on *Computational Plasticity*.

Professor Owen plays a leading role in national and international scientific affairs. For example, for many years, he has been a member of the *Executive Council* of IACM (International Association for Computational Mechanics) which is a worldwide organization established to promote and guide research and applications in the field of numerical modelling. He has also been *Board Member* of the European Council for Computational Mechanics (ECCM) of ECCOMAS and is also *Past Chairman* of the UK Association for Computational Mechanics in Engineering, which is the national association affiliated to IACM. A further measure of Prof. Owen's research esteem is his membership of the Research Assessment Exercise panel for Civil Engineering in the UK in 2001. He has been appointed to similar panels for the corresponding exercise in Mechanical Engineering for the Netherlands (QANU—Quality Assurance Netherlands Universities)

in 2000 and 2008 and Deutsche Forschungsgemeinschaft (DFG), Germany, in 2006 and 2007 for its Graduate Schools, Centres of Excellence and Institutional Funding initiatives. He was also a member of the International Advisory Board for the Institute for High Performance Computing in Singapore for a five-year period. Due to his industrial involvement, Prof. Owen served for over ten years as elected *Council Member* of NAFEMS, which is an international organization aimed at establishing standards and quality assurance procedures for the safe use of finite element methods. Professor Owen was also a member of the Civil Engineering Panel for the UK Research Excellence Framework (REF) exercise undertaken in 2014.

Professor Owen's contribution to research has been recognized by the following awards and distinctions:

- Elected Fellow of the Royal Academy of Engineering in 1996.
- Awarded an Honorary D.Sc. by the University of Porto, Portugal, in 1998.
- Engineering Council Award, Institution of Civil Engineers, 2002.
- Received the Computational Mechanics Award of the International Association for Computational Mechanics (IACM) in 2002 for "outstanding contributions in the field of computational mechanics".
- Awarded the Warner T. Koiter Medal of the American Society of Mechanical Engineers (ASME) in 2003 for "contributions to the field of theoretical and computational solid mechanics".
- Awarded the Gauss–Newton Medal of IACM in 2004 for "outstanding contributions in the field of computational mechanics".
- Awarded the Gold Medal of the University of Split, Croatia, in 2004 for "international achievements in the field of computational mechanics".
- Awarded the Premium Medal of the Spanish Society for Computational Mechanics (SEMNI) in 2005 in "recognition of his outstanding scientific work". SEMNI was created in 1989 by initiative of a group of academics in the Universitat Politècnica de Catalunya (UPC).
- Awarded an Honorary D.Sc. by Ecole Normale Supérieure de Cachan, France, in 2007.
- In 2009, he was elected Fellow of the Royal Society, this being one of his greatest scientific achievements.
- Honorary Professor, Welsh Institute for Mathematics and Computational Science, 2009.
- Founding Fellow, Learned Society of Wales, 2009.
- Outstanding Research Activity Award, Swansea University, 2009.
- Awarded the Grand Prize of the Japan Society for Computational Engineering and Science (JSCES), 2010.
- Elected Foreign Member of the United States National Academy of Engineering (NAE) in 2011.
- Elected Foreign member of Chinese Academy of Sciences in 2011.
- Awarded an Honorary D.Sc. by Polytechnic University of Catalunya (UPC), Barcelona, Spain, in 2012.

- Elected Council Member of the Royal Society, 2012.
- Elected Council Member of the Learned Society of Wales, 2012.
- Elected Honorary Professor of China Agricultural University, Beijing, China, in 2014.
- Elected Honorary Professor of Wuhan University, China, in 2015.
- Awarded an Honorary D.Sc. by University of Split, Croatia, 2016.
- Awarded an Honorary Doctor of Engineering by Swansea University, UK, in 2016.
- Awarded the China Friendship Medal, China, 2016.

Named Lectures

Professor Owen is an entertaining lecturer. As a former student of his and colleague in many joint courses, I can say that his lectures are most enjoyable and highly appreciated by students. He has been invited to deliver many named lectures, including the following:

2002 Prestige Lecture of the Institution of Civil Engineers and the Royal Academy of Engineering, Institution of Civil Engineers, November 2002.

2003 Warner T. Koiter Lecture of the American Society of Mechanical Engineers, Washington, D.C., November 2003.

2007 Alan Jennings Memorial Lecture Queen's University Belfast, April 2007.

2011 Higginson Lecture, Durham University, November 2011.

2012 Koiter Lecture, Netherlands Graduate School on Computational Mechanics, November 2012.

2013 Zienkiewicz Memorial Lecture, Livingstone, Zambia, July 2013.

In addition, he has presented a total of over 90 keynote and plenary lectures at leading international conferences in the field of computational mechanics.

Entrepreneurship

In 1985, Prof. Owen formed Rockfield Software Ltd. aimed at disseminating his academic research based on computational modelling procedures to the industrial sector. The company, initially employing two engineers, was based in the Innovation Centre at Swansea University. Over subsequent years, Rockfield Software expanded to over 35 personnel, with over two-thirds of the staff possessing Ph.D. degrees, making the company a leading employer of high technology graduates in the Swansea area.

Rockfield has a wide portfolio of clients and operates in several commercial areas. Principal sectors in which the company is involved include:

- Failure prediction for structures under seismic or blast loading.
- Industrial forming processes for glass, plastics and metals.
- Food technology processes.
- Defence applications involving explosive and impact conditions.
- Deep-level mining and other mineral recovery operations.
- Oil recovery operations and resource prediction.

The success of the company resulted, under Prof. Owen's Chairmanship, to the granting of the Queen's Award for Innovation, the most prestigious industrial accolade in the UK, on two separate occasions:

- In **2002**, Rockfield received the award for the development of finite element/discrete element simulation techniques for the strengthening of masonry bridges and arches. This technology has been utilized within a consortium that includes Cintec International and Gifford & Partners, to provide a complete service from assessing the need for strengthening, determination through the FE/DE approach of the precise location for insertion of retrofitted reinforcement anchors, to the clean and efficient installation of anchors.
- In **2007**, the award was granted for outstanding innovation in the development of the ELFEN computational system for the simulation of multi-fracturing solids. Recognition was given to the versatility and widespread industrial application of the methodology in diverse areas such as blast and impact loading of structures, defence applications, mining and minerals operations and oil recovery processes.

Since founding Rockfield Software in 1985, Prof. Owen was firstly its Managing Director, then becoming Chairman until his retirement from the company in 2010.

Professor Roger Owen and COMPLAS

Professor Owen has had a long-standing relationship with the computational mechanics community at UPC. As early as December 1979, Roger and Prof. Ernie Hinton organized the first Basic Course on the Finite Element Method. This course was attended by some 70 participants from all parts of Spain. Indeed, this course, that was repeated every December for 10 consecutive years up to 1989, can be considered the foundation of the numerical methods community in UPC at the Civil Engineering School of Barcelona. The visits of Roger and Ernie to UPC around December 15th every year soon become a tradition, almost a pre-Christmas event, that brought us many good moments of scientific interchange and friendship with our colleagues from Swansea. The culminating effect of these courses was that they created the seed of the first Spanish conference on Numerical Methods in Engineering, held in Barcelona on 1986. This conference was immediately followed by a series of very successful international conferences organized in cooperation with Roger and his colleagues at Swansea. The first one was the International

Conference on Nonlinear Finite Element Methods (1984) and a series of conferences on Computational Plasticity (COMPLAS) starting in 1987. COMPLAS has subsequently successfully run in Barcelona for 13 editions (<http://congress.cimne.com/complas2017/>).

COMPLAS has established itself as an international reference in the field of computational solid mechanics. Over 4000 delegates from over the world have attended one of the editions of this conference that combines a blend of high scientific level within an informal setting, a friendly atmosphere and a sophisticated and lively social programme. COMPLAS 14, to be held in Barcelona on 5–7 September 2017, celebrates the 30th anniversary of this successful conference series.

Ernie Hinton, with whom Roger published a number of seminal books on the finite element method, unfortunately passed away in November 1999. The cooperation with Roger and his team, however, continued through the COMPLAS conferences and even expanded by creating, jointly with UPC, international conferences in new fields such as the International Conference on Computer Aided Training in Science and Technology held in Barcelona in 1990 and a series of conferences in the field of Particle Methods (www.congress.cimne.com/particles2017/).

Roger Owen has played an important role in supporting the activities of the International Center for Numerical Methods in Engineering (CIMNE). Indeed, CIMNE, which this year celebrates its 30th anniversary, was created in 1987 under the auspices of the many activities in the field of numerical methods at the School of Civil Engineering of UPC.

To name the many interactions of UPC with Professor Owen and his team at Swansea during the last 25 years will be indeed too long. This cooperation was indeed strengthened by the fact that Prof. O.C. Zienkiewicz, one of the founders of our scientific community of computational mechanics and former Director of the Civil Engineering Department at Swansea, spent 20 years in periodic stays at UPC as UNESCO Professor of Numerical Methods in Engineering, this being the first UNESCO chair in the world created in 1989 at the initiative of UPC.

I want to highlight two other important activities at UPC where Roger has had a major role. The first is his participation in the editorial board of the Journal *Revista Internacional de Métodos Numéricos en Ingeniería*. This journal, ranked in JCR, is the only journal in the field of numerical methods in engineering published in Spanish and Portuguese. The journal is published jointly by UPC and CIMNE since 1985.

The second activity is his participation as Associate Editor of two journals: Archives of Computational Methods in Engineering (ACME, www.link.springer.com/journal/11831) and Computational Particle Mechanics (CPM, <http://www.springer.com/engineering/mechanics/journal/40571>). ACME was founded at UPC in 1994 and is currently co-published by Springer and CIMNE. ACME has an impact factor of 4210 (2015) and is the highest ranked international journal in the computational mechanics field. CPM was created in 2014 after a number of successful conferences co-chaired by Roger held at UPC in the field of particle-based

methods and their applications mentioned above. CPM, also published by Springer, is currently the leading journal in its field.

Many European research projects, joint courses, workshops, seminars and scientific meetings have taken place in cooperation with Prof. Owen and his team in that period. All of them have indeed helped UPC to establish a reputation in the field of numerical methods in engineering and computational mechanics. Roger, many thanks for that.

I will not be surprised if due to these interchanges Roger has visited UPC and Barcelona over one hundred times.

Let me also mention the important role that Roger has had in supporting the Spanish Association for Numerical Methods in Engineering (SEMNI). This scientific organization, created in 1989, presented to Roger its highest award in recognition of his scientific merits and also for his contribution to the development of the field in Spain. In 2014, SEMNI organized in cooperation with CIMNE and the School of Civil Engineering of UPC three major events in Barcelona that took place simultaneously: the World Congress on Computational Mechanics, the European Conference on Solid and Structural Mechanics and the European Conference on Fluid Dynamics. This was a landmark event in the field of computational methods in engineering and applied sciences.

Roger has also been very supportive to the Latin American community of numerical methods in Engineering. He was a founder member of the Mexican Association in that field and as such took part in the inaugural conference in Guanajuato in January 2002. He has also taken part in scientific events on computational mechanics in Argentina and Brazil, as well as other Latin American countries.

On the personal side, I consider Roger as a friendly and well-humoured person. He is one of these persons that find it difficult to say no to a request from a colleague or a friend. He is extremely hard working, and among his hobbies, I can say that he is a fine airplane pilot, an activity that took a considerable amount of his time for many years, he is an avid supporter of Welsh rugby and a dedicated expert on international cuisine and fine wines.

At UPC, we all acknowledge that your contribution has been very important in the transformation of our university to become a world reference in the field of computational mechanics.

I would like to end these remarks by congratulating Roger on his 75th birthday and thank him for fostering the cooperation between the computational mechanics communities in Barcelona and Swansea for so many years.

Eugenio Oñate
Professor of Continuum and Structural Mechanics at UPC
Founder and Director of CIMNE
Past President of SEMNI, ECCOMAS and IACM

Comparison of Phase-Field Models of Fracture Coupled with Plasticity

R. Alessi, M. Ambati, T. Gerasimov, S. Vidoli and L. De Lorenzis

Abstract In the last few years, several authors have proposed different phase-field models aimed at describing ductile fracture phenomena. Most of these models fall within the class of variational approaches to fracture proposed by Francfort and Marigo [13]. For the case of brittle materials, the key concept due to Griffith consists in viewing crack growth as the result of a competition between bulk elastic energy and surface energy. For ductile materials, however, an additional contribution to the energy dissipation is present, related to plastic deformations. Of crucial importance, for the performance of the modeling approaches, is the way the coupling is realized between plasticity and phase field evolution. Our aim is a critical revision of the main constitutive choices underlying the available models and a comparative study of the resulting predictive capabilities.

R. Alessi (✉)

Department of Mathematics, SAPIENZA Università di Roma, Piazzale Aldo Moro 5, 00185 Rome, Italy
e-mail: roberto.alessi@uniroma1.it

M. Ambati · T. Gerasimov · L. De Lorenzis

Institute of Applied Mechanics, Technische Universität Braunschweig, Pockelsstrasse 3, 38106 Braunschweig, Germany
e-mail: m.ambati@tu-braunschweig.de

T. Gerasimov

e-mail: t.gerasimov@tu-braunschweig.de

L. De Lorenzis

e-mail: l.delorenzis@tu-braunschweig.de

S. Vidoli

Department of Structural and Geotechnical Engineering, SAPIENZA Università di Roma, Via Eudossiana 18, 00184 Rome, Italy
e-mail: stefano.vidoli@uniroma1.it

© Springer International Publishing AG 2018

E. Oñate et al. (eds.), *Advances in Computational Plasticity*, Computational Methods in Applied Sciences 46, DOI 10.1007/978-3-319-60885-3_1

1 Introduction

Both theoretical and numerical investigations have proved the efficiency of gradient damage models in modeling the nucleation and evolution of cracks in brittle materials. Under suitable choices of the constitutive functions, it is possible to prove that gradient damage models Γ -converge to Griffith's model of brittle fracture in the limit to zero of an internal length parameter. These models are also referred to as phase-field models as they contain one or more internal variables to describe the material degradation.

In brittle materials, since the creation of a crack surface is the main source of dissipation, a scalar field is usually sufficient to represent the material level of degradation and to account for the surface energy of Griffith's theory. Ductile fracture is, instead, associated to more complex processes: a large energy absorption, due to the nucleation and coalescence of micro-voids accompanied by extensive plastic deformations, precedes the actual formation of cracks. Hence, measures of the current and accumulated plastic strains seem natural candidates to complement the scalar damage in the internal material description.

Several authors have recently proposed gradient damage models coupled to plastic effects. The main difficulty is the simultaneous presence and competition of two dissipative terms, due to plastic flow and to crack growth. In particular, we cite the models by [1–5, 9, 12, 14, 17]. Our purpose is to review these recent contributions and to attempt a comparative study of their performance in describing the main aspects of ductile fracture. For the models under consideration, the only rigorous result of Γ -convergence obtained so far concerns the model [1–3], see [11].

Limiting ourselves to infinitesimal deformations, we formulate a common variational setting encompassing all the considered models, in which we are able to highlight the different choices for the main constitutive functions. Then, we perform a numerical comparison of all models for a standard uniaxial tension test. The paper is organised as follows. Section 2 sets the variational framework. Section 3 overviews and comments on the specific choices made in the various models, whereas Sect. 4 reports numerical comparisons. Conclusions are drawn in Sect. 5.

2 A General Framework for Phase-Field Models of Fracture Coupled with Plasticity

In this section, we present a unified variational setting which encompasses several recently proposed phase-field fracture models coupled with plasticity. Assuming that external actions are sufficiently smooth in time and inertial effects are negligible, we consider the *energetic formulation* for rate-independent problems [18]. This relies on three simple energetic principles, namely an *energy balance*, a *dissipation inequality* and a *stability criterion*, from which all the standard governing equations can be easily obtained. In such a context, for each model under consideration, it is sufficient to define the basic state variables and to introduce the total internal energy density, a state function which includes both potential and dissipative contributions.

2.1 State Variables

Let Ω be an open bounded domain in \mathbb{R}^N representing the reference configuration of a body, with Neumann and Dirichlet boundaries $\partial\Omega_N$ and $\partial\Omega_D$, Fig. 1. The state of each point $\mathbf{x} \in \Omega$ is defined by the variables in Table 1.

Only the displacement field $\mathbf{u}(\mathbf{x}, t)$, the plastic strain field $\mathbf{p}(\mathbf{x}, t)$ and the damage field $d(\mathbf{x}, t)$ are independent. The infinitesimal strain is the symmetric gradient of the displacement field, and the hardening variable, identified in this context with the accumulated plastic strain, is given by

$$\alpha(\mathbf{x}, t) := k_N \int_0^t \|\dot{\mathbf{p}}\| \, d\tau, \quad k_N = \begin{cases} 1, & \text{if } N = 1 \\ \frac{N-1}{N}, & \text{otherwise} \end{cases} \quad (1)$$

The scalar damage field is bounded, since we assume $d \in [0, 1]$; $d = 0$ means a sound material and $d = 1$ a fully damaged material. This field must satisfy the following irreversibility condition to prevent healing effects, as first introduced in [7] and [16]

$$\dot{d} \geq 0, \quad \forall t \text{ and } \forall \mathbf{x}. \quad (\text{ir})$$

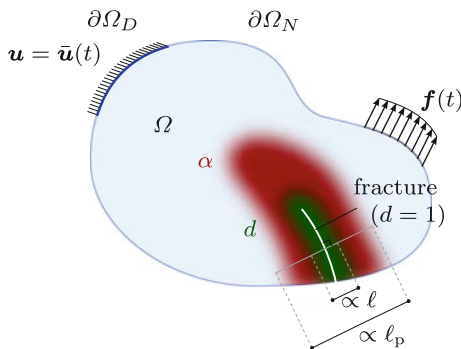


Fig. 1 Schematic representation of the problem

Table 1 State variables

State	Variables	Type
\mathbf{u}	Displacement	Observable
$\boldsymbol{\varepsilon}$	Total strain	
\mathbf{p}	Plastic strain (trace free, $\text{tr } \mathbf{p} = 0$)	Internal
α	Scalar plastic hardening (accumulated plastic strain, <i>irreversible</i>)	
$\nabla\alpha$	Gradient of plastic hardening	
d	Scalar damage (<i>irreversible</i>)	Internal
∇d	Gradient of damage	

In the following subsections, we briefly introduce the *total energy densities* of gradient damage models, traditionally used to describe brittle or quasi-brittle fracture phenomena, and of gradient plasticity models, traditionally used to describe plastic hinges or shear bands. Their combination is discussed in Sect. 2.4, whereas Sect. 2.5 summarises the governing equations and evolution laws.

2.2 Gradient Damage Models

The total internal energy density is the sum of two terms

$$W_D(\boldsymbol{\varepsilon}, d, \nabla d) := \underbrace{\mathfrak{g}(d)\psi_e(\boldsymbol{\varepsilon})}_{\substack{\text{free en.} \\ \text{(elastic pot.)}}} + \underbrace{\Delta_f(d, \nabla d)}_{\text{damage diss.}}, \quad (2)$$

the first representing the *free energy density* and the second the *local dissipated damage work*. Here, $\psi_e(\boldsymbol{\varepsilon})$ is the elastic energy density of a sound material. The scalar degradation function $\mathfrak{g}(d)$ models the material deterioration due to the microcracks nucleation and growth. This function is assumed to satisfy the following conditions

$$\mathfrak{g}(0) = 1, \quad \mathfrak{g}(1) = 0, \quad \mathfrak{g}'(d) \leq 0. \quad (3)$$

In almost all the considered models, this function is assumed in the form

$$\mathfrak{g}(d) := (1 - d)^2. \quad (4)$$

The damage dissipation term accounts for the energy lost during the cracking process. A widely adopted expression¹ is

$$\Delta_f(d, \nabla d) := \frac{G_c}{c_\omega} \left(\frac{\omega(d)}{\ell} + \ell |\nabla d|^2 \right) \quad (7)$$

¹In the gradient damage context, a different expression is often considered instead of (7), namely

$$\Delta_d(d, \nabla d) := w(d) + \frac{1}{2} \ell_d^2 w_1 |\nabla d|^2 \quad (5)$$

The constitutive functions and constants are linked by the following relations

$$\ell_d = \sqrt{2}\ell, \quad w(1) =: w_1 = G_c / (\ell c_\omega), \quad w(d) / w_1 = \omega(d) \quad (6)$$

where the constant G_c represents the fracture toughness of the material, that is the energy dissipated to create a crack of unitary area. As follows, the two most commonly used models will be considered and termed AT-1 and AT-2 (AT refers to the *Ambrosio-Tortorelli* functional [6]):

$$\omega(d) = \begin{cases} d, & \text{AT-1} \\ d^2, & \text{AT-2} \end{cases} \quad \text{and} \quad c_\omega := 4 \int_0^1 \sqrt{\omega(\beta)} \, d\beta = \begin{cases} 8/3, & \text{AT-1} \\ 2, & \text{AT-2} \end{cases} \quad (8)$$

The main difference between these two models is that AT-1, due to the linear term, owns an elastic stage before the onset of damage, while with AT-2 damage starts to evolve as soon as the material is loaded.

Phase-field models characterized by total energies in the form (2) have been rigorously proved to Γ -converge to Griffith's brittle fracture model. As the internal length ℓ tends to zero, the phase-field variable, which can be mechanically interpreted as a damage variable [15], localizes towards the fracture path and the global minima of the phase-field energy functional tend towards those of the energy functional of Griffith's brittle fracture [10].

2.3 Gradient Plasticity Models

The total internal energy density is taken as

$$W_P(\boldsymbol{\varepsilon}, \mathbf{p}, \alpha, \nabla\alpha) := \underbrace{\psi_e(\boldsymbol{\varepsilon} - \mathbf{p})}_{\text{elastic pot.}} + \underbrace{\psi_p(\alpha, \nabla\alpha)}_{\text{plastic hard.}} + \underbrace{\Delta_p(\alpha)}_{\text{plastic diss.}}, \quad (9)$$

Here we consider, for sake of brevity, only the Hencky-Mises plastic model. The first term represents the elastic energy of an undamaged material and depends on the elastic strain $\boldsymbol{\varepsilon} - \mathbf{p}$. The second free energy term represents a non-local isotropic hardening contribution and reads

$$\psi_p(\alpha, \nabla\alpha) := \frac{1}{2} H \alpha^2 + \mathbf{f}(\alpha) + \frac{1}{2} \ell_p^2 |\nabla\alpha|^2, \quad (10)$$

the first two terms being, respectively, the linear and non-linear hardening contributions while the last term is a gradient plasticity energy source. H is the hardening modulus while ℓ_p is an internal material length governing the plastic localisation band width. The last term in (9) represents the plastic dissipated work and is given by

$$\Delta_p(\alpha) := \sigma_p \alpha, \quad (11)$$

with σ_p as the plastic yield stress.

2.4 Gradient Damage Models Coupled with Plasticity

This section presents a gradient damage model coupled with plasticity by merging the two basic models presented in the previous subsections. From total energy densities (2) and (9), the following coupled total internal energy density is postulated

$$\begin{aligned}
 W_{\text{PD}}(\boldsymbol{\varepsilon}, \mathbf{p}, d, \nabla d, \alpha, \nabla \alpha) &:= \underbrace{\psi(\boldsymbol{\varepsilon}, \mathbf{p}, d, \alpha, \nabla \alpha)}_{\text{free energy}} + \underbrace{\Delta(d, \nabla d, \alpha)}_{\text{dissipated work}} = \\
 &= \underbrace{\mathbf{g}(d)\psi_e(\boldsymbol{\varepsilon} - \mathbf{p})}_{\mathbf{E}} + \underbrace{\mathbf{h}(d)\psi_p(\alpha, \nabla \alpha)}_{\mathbf{H}} + \underbrace{\Delta_f(d, \nabla d)}_{\mathbf{F}} + \underbrace{\mathbf{p}(d)\Delta_p(\alpha)}_{\mathbf{P}}. \tag{12}
 \end{aligned}$$

The first term (**E**) represents the elastic potential and its expression is obtained by combining the elastic potential of (2) and (9) with the degradation function $\mathbf{g}(d)$ satisfying (3). The second term (**H**) represents the isotropic plastic hardening contribution supposed to be affected by a damage degradation function $\mathbf{h}(d)$ satisfying the conditions in (3), with $\psi_p(\cdot)$ defined in (10). The third term (**F**) is the fracture energy defined in (7), not directly affected by plasticity. Finally, (**P**) is a damage-plasticity coupled dissipation term which contains not only the entire source of plastic dissipation but also a contribution to the damage dissipation, see also [3]. Its expression is obtained by penalizing the plastic dissipation (11) by another damage-dependent degradation function $\mathbf{p}(d)$ satisfying again (3).

The stress is defined as

$$\boldsymbol{\sigma} := \partial_{\boldsymbol{\varepsilon}} \psi = \mathbf{g}(d) \partial_{\boldsymbol{\varepsilon}} \psi_e(\boldsymbol{\varepsilon} - \mathbf{p}) \tag{13}$$

The assumption (12) for the total energy encompasses all the models under consideration as special cases.

2.5 Governing Equations and Evolution Laws

According to the *energetic formulation*, the evolution of a rate-independent system is simply governed by three energetic principles: an *energy balance*, a *dissipation inequality* and a *stability criterion*. Moreover, some explicit irreversibility conditions may be prescribed, such as here (ir). For the purposes of the present work and thanks

Table 2 Governing equations and evolution laws deduced from the energetic formulation

equilibrium	
Equilibrium equations	$\operatorname{div} \boldsymbol{\sigma} + \mathbf{b} = \mathbf{0}, \quad \forall \mathbf{x} \in \Omega$ (14)
Boundary conditions	$\begin{cases} \boldsymbol{\sigma} \mathbf{n} = \mathbf{f}, & \forall \mathbf{x} \in \partial \Omega_N \\ \boldsymbol{\sigma} \mathbf{n} = \mathbf{f}_r, & \forall \mathbf{x} \in \partial \Omega_D \end{cases}$ (15)
plasticity conditions	
KKT system	$\begin{cases} f_p(\boldsymbol{\sigma}, \alpha, d) \leq 0 \\ \dot{\alpha} \geq 0 \\ f_p(\boldsymbol{\sigma}, \alpha, d) \dot{\alpha} = 0 \end{cases}, \quad \forall \mathbf{x} \in \Omega$ (16)
Flow rule	$\mathbf{p} = \dot{\alpha} \mathbf{n}_{\boldsymbol{\sigma}'}, \quad \forall \mathbf{x} \in \Omega$ (17) ($\mathbf{n}_{\boldsymbol{\sigma}'}$ = deviatoric stress direction)
Yield surface	$f_p(\boldsymbol{\sigma}, \alpha, d) := \boldsymbol{\sigma} - h(d) \left(H\alpha + f'(\alpha) - \ell_p^2 \Delta \alpha \right) - p(d) \sigma_p$ (18)
Boundary condition	$\nabla \alpha \cdot \mathbf{n} = 0, \quad \forall \mathbf{x} \in \partial \Omega$ (19)
damage conditions	
KKT system	$\begin{cases} f_d(\boldsymbol{\varepsilon}, \mathbf{p}, \alpha, d) \leq 0 \\ \dot{d} \geq 0 \\ f_d(\boldsymbol{\varepsilon}, \mathbf{p}, \alpha, d) \dot{d} = 0 \end{cases}, \quad \forall \mathbf{x} \in \Omega$ (20)
Yield surface	$f_d(\boldsymbol{\varepsilon}, \mathbf{p}, \alpha, d) := -g'(d) \psi_c(\boldsymbol{\varepsilon} - \mathbf{p}) - h'(d) \psi_p(\alpha, \nabla \alpha) - \frac{G_c}{c_\omega} \left(\frac{\omega'(d)}{\ell} - \ell \Delta d \right) - p'(d) \Delta_p(\alpha)$ (21)
Boundary condition	$\nabla d \cdot \mathbf{n} = 0, \quad \forall \mathbf{x} \in \partial \Omega$ (22)

to the regularity of the energetic functionals, it is sufficient to consider the first-order energy balance condition and the first-order directional stability condition.

Then, the evolution problem consists in finding a process $(\mathbf{u}, \mathbf{p}, \alpha, d)_t$, satisfying at each instant t the boundary conditions, the energy balance, dissipation inequality and the first-order stability. For a detailed description of these equations see e.g. [2]. For the present model, the derived governing equations are summarised in Table 2.

3 Overview of Existing Models

Table 3 gives an overview of the existing models, presented with a unified notation and with the format induced by (12). Each model is presented in terms of the energy contributions **E**, **H**, **F** and **P**. The next sections are devoted to the discussion of the different constitutive choices the investigated models rely on. However, some preliminary observations are immediately given:

Table 3 Overview of the total internal energy density W_{pp} for the compared models. The labels refer to (12)

model name	E	H	F	P
Alessi et al. [1, 2, 3]	$\mathbf{g}(d)\psi_e(\boldsymbol{\varepsilon} - \mathbf{p})$ $\frac{(1-d)^2}{k - (k-1)(1-d)^2} \psi_e(\boldsymbol{\varepsilon} - \mathbf{p})$ with $k > 0$. For $k = 1$ one recovers (4)	—	$\Delta_{\text{F}}(d, \nabla d)$ $\frac{3G_c}{8} \left(\frac{d}{\ell} + \ell \nabla d ^2 \right)$ AT-1, (7)-(8)	$\mathbf{p}(d)\Delta_{\text{P}}(\alpha)$ $(1-d)^{2n} \sigma_{\text{p}} \alpha$ with $n > 0$
Borden et al. [9]	$\mathbf{g}(d)\psi_e(\boldsymbol{\varepsilon} - \mathbf{p})$ with $\mathbf{g}(d) = (1-d)^2 (1+d(2-k))$ and $k > 0$. For $k = 2$ one recovers (4)	$\mathbf{h}(d) \left(\frac{1}{2} H \alpha^2 \right)$ with $\mathbf{h}(d) \equiv \mathbf{g}(d)$, \mathbf{g} defined in E .	$\frac{C_c}{2} \left(\frac{d^2}{\ell} + \ell \nabla d ^2 \right)$ AT-2, (7)-(8)	$\mathbf{p}(d)\sigma_{\text{p}} \alpha$ with $\mathbf{p}(d) \equiv \mathbf{g}(d)$, \mathbf{g} defined in E .
Duda et al. [12]	$(1-d)^2 \psi_e(\boldsymbol{\varepsilon} - \mathbf{p})$	$\frac{1}{2} H \alpha^2$		$\sigma_{\text{p}} \alpha$
Kuhn et al. [14]		$(1-d)^2 \left(\frac{1}{2} H \alpha^2 \right)$		$(1-d)^2 \sigma_{\text{p}} \alpha$
Miehe et al. [17]		$(1-d)^2 \left(\frac{1}{2} H \alpha^2 + \mathbf{f}(\alpha) + \frac{1}{2} \frac{d^2}{\ell} \nabla \alpha ^2 \right)$ with $\mathbf{f}(\alpha) = (\sigma_{\infty} - \sigma_{\text{p}})(\alpha + \frac{1}{\eta} e^{-\eta \alpha})$ and $\eta > 0$, $\sigma_{\infty} > \sigma_{\text{p}}$	$(1-(1-d)^2) w_c + \frac{w_c}{\xi} \ell \left(\frac{d^2}{\ell} + \ell \nabla d ^2 \right)$ with $w_c > 0$, $\xi > 0$.	
Ambati et al. [5]	$(1-d)^{2b(\alpha)} \psi_e(\boldsymbol{\varepsilon} - \mathbf{p})$ where $b(\alpha) = (\alpha/\alpha_{\text{crit}})^m$, with $\alpha_{\text{crit}} > 0$ and $m > 0$	$\frac{1}{2} H \alpha^2$	$\frac{C_c}{2} \left(\frac{d^2}{\ell} + \ell \nabla d ^2 \right)$ AT-2, (7)-(8)	$\sigma_{\text{p}} \alpha$

1. Concerning **E** in (12), the models differ only for the choice of the degradation function \mathfrak{g} , for which the key properties (3) are always fulfilled. Most models adopt the standard quadratic expression (4). Different parametric non-linear degradation functions are considered by Alessi et al. [1, 2] and Borden et al. [9], both containing, as a limit case, the standard quadratic expression. Finally, a specific quadratic-like \mathfrak{g} , which also depends on the accumulated plastic strain, is considered by Ambati et al. [5]. The motivation behind each particular choice is outlined in Sects. 3.1 and 3.4.
2. Stronger differences concern the plastic isotropic hardening entry **H**. The most general representation for ψ_p is considered by Miehe et al. [17], where the leading linear hardening term $\frac{1}{2}H\alpha^2$ is enriched by adding a non-linear one and a non-local gradient contribution with its own length-scale parameter, as in (10). All other models consider at most linear hardening effects. Only Alessi et al. [1–3] do not consider plastic hardening effects, see Sect. 3.3. However a straightforward extension of their model by Ulloa et al. [20] does. In all models, with the exceptions of Duda et al. [12] and Ambati et al. [5], plastic hardening is coupled with damage and the degradation multiplier h is typically taken identical to the function \mathfrak{g} . Such a coupling has a strong impact on the evolution and interplay of damage and plasticity during the softening stage, as discussed in Sects. 3.1, 3.2 and 4.
3. In contrast to **H**, the fracture energy entry **F** is quite standard for all the examined models. In all but one cases, Δ_f is given by (7) combined with either AT-1 or AT-2, (8). The only exception, discussed in Sect. 3.5, is proposed in Miehe et al. [17], where the fracture energy term can formally be viewed as a two-parametric extension of the AT-2 model.
4. Finally, the fourth term **P** differs between the models only for the presence or not of the degradation function $\mathfrak{p}(d)$ which indicates whether the plastic dissipation (11) is affected or not by the damage evolution. In the case of coupling, the corresponding degradation function \mathfrak{p} is typically chosen identical to \mathfrak{g} . The only exception is in Alessi et al. [1–3], where a simple parametric expression allows to achieve different coupling orders, including the quadratic and uncoupled case, and to describe very different material behaviours. No coupling is assumed in Duda et al. [12] and Ambati et al. [5].

3.1 On the Lack of a Damage-Plastic Coupling

In Duda et al. [12], no coupling between damage and plasticity is prescribed, in the sense that the plastic yield condition (16) does not depend upon the damage variable whereas the damage yield condition (20) does not depend upon the plastic variable. Thus, the damage evolution is driven only by elastic strains and is governed by the classical brittle phase-field law. Therefore, the formulation in [12] is a model for “brittle fracture in elastic-plastic solids”.

The coupling source for the model in Ambati et al. [5] relies only on the special degradation function of the elastic potential energy \mathbf{E} whereas for the remaining models coupling effects originate from \mathbf{H} and/or \mathbf{P} .

3.2 On the Identical Degradation Functions

In the models of Borden et al. [9], Kuhn et al. [14] and Miehe et al. [17], all three degradation functions in \mathbf{E} , \mathbf{H} and \mathbf{P} are assumed identical, *i.e.* $\mathbf{g} \equiv \mathbf{h} \equiv \mathbf{p}$. After factoring them out in the plastic yield function f_p , (18), one arrives at the representation

$$f_p(\boldsymbol{\sigma}, \alpha, d) = \mathbf{g}(d)(|\boldsymbol{\varepsilon}' - \mathbf{p}| - (H\alpha + \sigma_p))$$

with $\boldsymbol{\varepsilon}'$ as the deviatoric part of $\boldsymbol{\varepsilon}$ and where non-linear hardening and gradient plastic terms are omitted. Thus, the evolution of the accumulated plastic strain becomes independent on the phase-field. This allows the straightforward use of standard elasto-plastic algorithms. As a side effect, α will grow approximatively with half the rate of $|\dot{\boldsymbol{\varepsilon}}|$ even in regions where the material is already fully degraded, possibly causing convergence issues since $\boldsymbol{\varepsilon}$ strongly localises and so must \mathbf{p} and α . Such behaviour is illustrated in Sect. 4. Note that $\mathbf{g} \equiv \mathbf{h} \equiv \mathbf{p}$ does not affect the damage yield function f_d in the way it happens for f_p , meaning that the evolution of d will still be affected by α .

3.3 On the Lack of Plastic Hardening

In the original model of Alessi et al. [1–3], no plastic hardening effects are considered. This allows for plastic strains to localise as *Dirac's measures* leading to the formation of shear bands. In such a case, the governing equations of Table 2 are complemented with the equations for the singular parts of displacement and plastic strain fields, leading to a rigorous description of shear bands and therefore displacement jumps. This has been proved to be a key feature in describing different fracture cohesive responses, [3].

3.4 Non-standard Degradation Functions

Referring to (4) as the “standard” quadratic degradation function, non-standard choices for \mathbf{g} (yet fulfilling (3)), have been considered in the models of Alessi et al. [1, 2], Borden et al. [9] and Ambati et al. [5].

Alessi et al. [1, 2] considered the one-parametric non-linear degradation function

$$\mathbf{g}(d) := \frac{(1-d)^2}{k - (k-1)(1-d)^2}, \quad k > 0,$$

which recovers (4) for $k = 1$. The parameter k controls the material response in the post-critical stage. In particular, as shown e.g. in [2], for the stress-strain uniaxial homogeneous response, a larger k leads to a less steep softening curve, i.e. to a slower damage evolution.

The one-parametric cubic degradation function

$$\mathbf{g}(d) = (1-d)^2(1+d(2-k)), \quad k > 0,$$

in [9] is adopted from Borden et al. [8], where its implications are discussed in detail. Unlike for the combination “quadratic \mathbf{g} + AT-2”, where damage starts to evolve as soon as the material is loaded, the combination “quadratic \mathbf{g} + AT-1” has a linearly elastic stage up to the peak stress. However, the boundness of $d \in [0, 1]$, which automatically holds for the “quadratic \mathbf{g} + AT-2” combination, is no longer fulfilled. This leads to the need for constrained minimization algorithms. The cubic function proposed in [8], with an extremely small k , used with AT-2, retains the presence of the elastic limit and the boundedness of d .

Finally, a specific non-linear function

$$\mathbf{g}(d, \alpha) := (1-d)^{2(\alpha/\alpha_{\text{crit.}})^m}, \quad m > 0, \quad (23)$$

is proposed in [5]. Its introduction serves the purpose of realizing the plastic-damage coupling, as already explained in Sect. 3.1. With the above \mathbf{g} , α explicitly appears in the damage evolution equation and fracture is triggered by the accumulation of the ductile damage once the threshold $\alpha_{\text{crit.}}$ is reached. The parameter m provides additional flexibility: the increase of m slows down the accumulation of damage before reaching $\alpha_{\text{crit.}}$ and accelerates it when $\alpha_{\text{crit.}}$ is exceeded, see [5] for a complete numerical assessment.

3.5 Non-standard Fracture Dissipation Term

A feature of the model in [17] is the damage dissipation density function

$$\Delta_f := (1 - \mathbf{g}(d)) w_c + \frac{w_c}{\xi} \ell \left(\frac{d^2}{\ell} + \ell |\nabla d|^2 \right), \quad w_c > 0, \quad \xi > 0, \quad (24)$$

The parameter w_c governs the onset of fracture, whereas ξ controls the slope of softening. The proposed Δ_f can formally be viewed as an extension of the AT-2 model. An interesting question is that of the relation between w_c and G_c . Being

ξ dimensionless, w_c has the dimension of G_c/ℓ . Our idea of deriving the explicit dependency of w_c on G_c is to rescale $\ell = \sqrt{2}\tilde{\ell}$ and collapse the two terms in Δ_f . This yields the representation

$$\Delta_f = 2 \frac{w_c}{\xi} \tilde{\ell} \left(\frac{2\xi d - (\xi - 1)d^2}{2\tilde{\ell}} + \tilde{\ell} |\nabla d|^2 \right).$$

Setting $\xi = 1$, the above Δ_f resembles AT-1 provided $w_c = 3/16 G_c/\tilde{\ell}$.

3.6 On the Damage Irreversibility

The damage irreversibility is imposed by requiring $\dot{d} \geq 0$. Already for *brittle* fracture, this condition is known to lead to a box-constrained optimization problem for the total energy functional \mathcal{W} . To avoid this for the brittle case, the history variable

$$\mathcal{H}_t := \max_{s \leq t} \psi_e(\boldsymbol{\varepsilon}_s),$$

which records the maximal undegraded elastic energy density obtained in a loading process, can be introduced in the evolution equation for d , as originally proposed in [16]. This weak enforcement of irreversibility can only be used with models where d starts to evolve as soon as the material is loaded, as the AT-2 model but not AT-1. Another approach consists on imposing the irreversibility only for totally broken material points, i.e. where $d = 1$, as proposed e.g. in [10].

In ductile phase-field models, the above definition of \mathcal{H}_t appears in the formulations of Duda et al. [12], Ambati et al. [5] and Borden et al. [9]. A more sophisticated expression for \mathcal{H}_t is designed in Miehe et al. [17], see also Sect. 3.7. The formulation of Kuhn et al. [14] uses the irreversibility idea from [10]. The treatment of $\dot{d} \geq 0$ through optimization algorithms is adopted in Alessi et al. [1–3].

3.7 Parameters and Thresholds

The capability to tailor the constitutive response to match experimental data is an important asset of any formulation. The role of some constitutive parameters and thresholds, designed for this purpose, has been already discussed in Sects. 3.4 and 3.5, limited to the formulations of Alessi et al. [1–3], Borden et al. [9], Miehe et al. [17] and Ambati et al. [5]. As follows, we focus on additional quantities introduced in some formulations at a later stage of the model derivation. This holds for the models of Borden et al. [9] and Miehe et al. [17]. In [9], the evolution equation for d (with the identity $\mathbf{h} \equiv \mathbf{p}$) reads

$$\mathbf{g}'(d)\psi_e + \mathbf{h}'(d)(\psi_p + \Delta_p) + \frac{G_c}{\ell}(d - \ell^2\Delta d) = 0.$$

This expression is furthermore modified by introducing (i) the elasticity-based history variable \mathcal{H}_t for irreversibility, (ii) a plastic work threshold W_0 , and (iii) two parameters $\beta_e, \beta_p \in [0, 1]$ to weigh the influence of damage on the elastic strain energy and plastic work. The resulting equation becomes

$$\beta_e \mathbf{g}'(d)\mathcal{H}_t + \beta_p \mathbf{h}'(d)\langle \psi_p + \Delta_p - W_0 \rangle_+ + \frac{G_c}{\ell}(d - \ell^2\Delta d) = 0, \quad (25)$$

where $\langle a \rangle_+ := \max(0, a)$. In [17] the evolution equation for d is equipped with the history variable $\mathcal{H}_c := \max_{s \in [0, t]} \langle \psi_e + \psi_p + \Delta_p - w_c \rangle_+$, yielding

$$-2(1 - d)\mathcal{H}_c + 2\frac{w_c}{\xi}(d - \ell^2\Delta d) = 0.$$

3.8 Variational (In)consistency

Almost all models in Table 3 fit in the variational framework. However, as discussed in the previous sections, the introduction of various indicator and ramp functions, tuning parameters and threshold values into the *strong form equations* to enable a greater flexibility in the model response inevitably leads to the loss of variational consistency. This holds for the works of Duda et al. [12], Ambati et al. [5], Borden et al. [9] and Miehe et al. [17]. Only the formulations of Alessi et al. [1–3] and Kuhn et al. [14] retain a truly variational nature. However, only the former model is rich enough to capture a variety of anticipated ductile and cohesive fracture responses.

3.9 Additive Split of the Elastic Energy Density Function

Our last comment concerns the so-called tension-compression additive split of the elastic energy density function ψ_e , first discussed by [7, 16], which is incorporated in several models but omitted for the sake of brevity in Table 3. In general, the split representation $\mathbf{g}(d)\psi_e^+ + \psi_e^-$ for \mathbf{E} , with ψ_e^+ and ψ_e^- as a “sort of” tensile and compressive parts of ψ_e , respectively, is present in all formulations except for the one by Alessi et al. [1–3] and Kuhn et al. [14].

4 Numerical Comparisons

This section aims at highlighting the salient features of the models by presenting a short numerical comparative survey of a uniaxial tension test, consisting of a bar of length L , clamped on its left end, with a monotonically increasing displacement \bar{u} prescribed on its right end. The adopted material parameters, taken from [9], are the following: $E_0 = 68.8$ GPa, $\sigma_p = 320$ MPa, $H = 688$ MPa, and $G_c = 138$ MPa m. Such parameters correspond to a ductile fracture response with an elastic stage, a linear-hardening plastic stage and a softening/fracturing stage.

Both homogeneous and non-homogeneous responses are investigated. The former, captured with a short bar length, highlights the underlying material response, whereas the latter evidences the localisation/fracture process. For the non-homogeneous response, the value of the bar length $L = L_n$ is chosen sufficiently large to allow the development of a full localisation but not too large in order to avoid snap-back effects. The influence of the bar length on the non-homogeneous global response is discussed, for instance, in [3]. Homogeneous responses are obtained numerically as well by taking $L = 0.1 L_n$.

Since the damage threshold stress for the phase-field model (7) directly depends on the internal length, even for an homogeneous evolution of the damage variable such as, for instance, during the hardening stage, different internal lengths are chosen for the models in order to obtain (except for Duda et al.) approximately the same peak stress and its corresponding limit strain. Setting $\ell = L_n/30$, different bar lengths L_n are considered.

The finite element mesh is uniform with element size $h = L/500$. A staggered numerical solution scheme [5] is adopted. For the present simple test, irreversibility is not taken into account.

As follows, the numerical results for each model are presented. The homogeneous (H) and non-homogeneous (NH) responses of each model are visualised by four plots: (a) stress-mean strain H and NH responses, (b) accumulated plastic strain and damage profiles for the NH response, (c) plastic strain and damage evolutions for the H response, (d) maximum plastic strain and maximum damage evolutions for the NH response.

In the results presented in Figs. 2 and 3, the model by Alessi et al. is enriched by a linear hardening term, not present in the original formulation, according to [20]. Hence, plastic strains cannot localise as a Dirac measure anymore, Sect. 3.3. Nevertheless, they localise in a narrower band than damage. The main difference between Figs. 2 and 3 is the value of the exponent of the degradation function $\mathfrak{p}(d)$, Table 3. During the softening stage, for $n = 1$ the stress approaches asymptotically zero (Barenblatt's cohesive behaviour), whereas for $n = 0.5$ it vanishes at a finite strain value (Dugdale's cohesive behaviour). This different behaviour is due to the fact that in the former case plasticity continues to evolve during the softening stage, whereas in the latter it does not.

Plastic strains evolve in a localised manner during the softening stage also in Miehe et al. (Fig. 8), whose response is very similar to Alessi et al. in Fig. 2, in

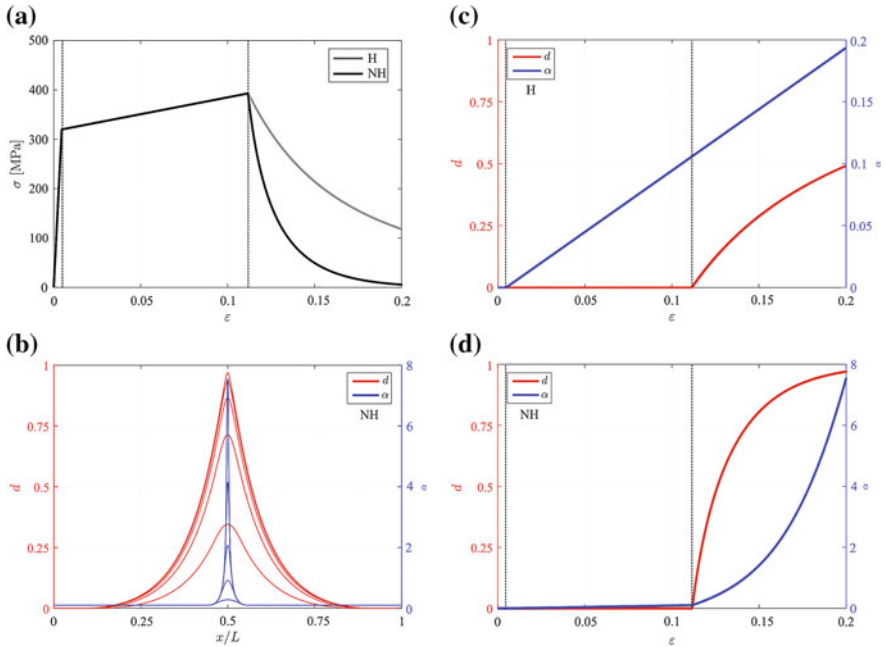


Fig. 2 Alessi et al. Homogeneous and non-homogeneous responses for a bar length $L_n = 10$ mm and $n = 1$

Borden et al. (Fig. 4) and in Kuhn et al. (Fig. 6). Conversely, plastic strains stop their evolution immediately after the peak stress in Duda et al. (Fig. 7) and Ambati et al. (Fig. 10), since here the plastic evolution is associated to a stress-hardening response.

In the global response, an asymptotically vanishing stress in the fracturing stage is observed in Alessi et al. (Fig. 3), Borden et al. (Fig. 4), Kuhn et al. (Fig. 6) and Ambati et al. (Fig. 10). Within the last model no plastic strain localisation is observed while for the remaining models a true fracture with vanishing stress is achieved for a finite strain value (Fig. 5).

The plastic hardening-damaging softening transition is smooth for Borden et al. (Fig. 4) and Kuhn et al. (Fig. 6) and sharp in all other cases. In Kuhn et al. Fig. 6, no stress-hardening effects are observed, which is in contrast with the experimental evidence.

Some models (Duda et al., Kuhn et al. and Ambati et al.) show after the peak stress an homogeneous damage evolution and only successively a damage localisation evolution associated to a steeper global response curve. Such *material bifurcation*, associated to the choice of an “intermediate” bar length, is very well investigated and explained in [19].

Damage increases very fast during the plastic-hardening stage in Kuhn et al. and Ambati et al. while it increases imperceptibly in all other models, except for Alessi et

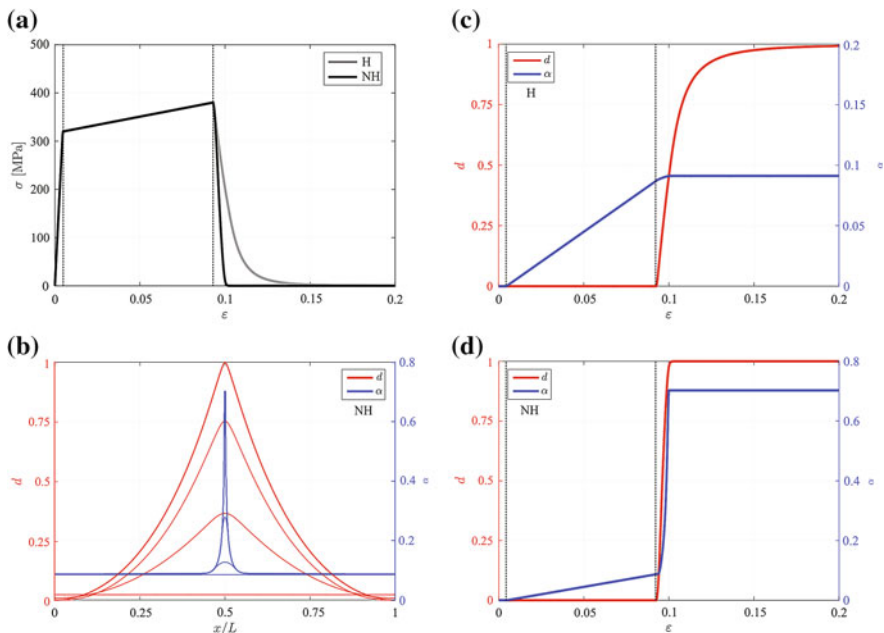


Fig. 3 Alessi et al. Homogeneous and non-homogeneous responses for a bar length $L_n = 22$ mm and $n = 0.5$

al. where it does not evolve at all, even during the elastic stage, Sect. 2.2. In addition, Duda et al. model has a significant damage evolution even during the elastic stage.

Figure 5 highlights the role of W_0 in (25), see Sect. 3.7, which essentially tunes the value of the peak stress. A similar control is performed by the parameter α_{crit} in Ambati et al., see Sect. 3.4 and Fig. 11. In addition, Fig. 9 highlights the role of ξ in (24), see Sect. 3.5, which tunes the concavity of the global response in the softening stage.

5 Concluding Remarks

We reported a critical comparative review of existing phase-field models for fracture in elasto-plastic materials. All models can be cast in the same variational framework and differ mainly by the choices of the damage dissipation term, by the degradation function(s) as well as by the way the coupling between plasticity and damage is realized. The models in “basic” form (i.e. with the minimum possible amount of tailorable parameters, if any) retain a variational nature but are not always able to reproduce an experimental response due to lack of flexibility. More elaborated versions with additional ingredients such as thresholds and indicator functions gain

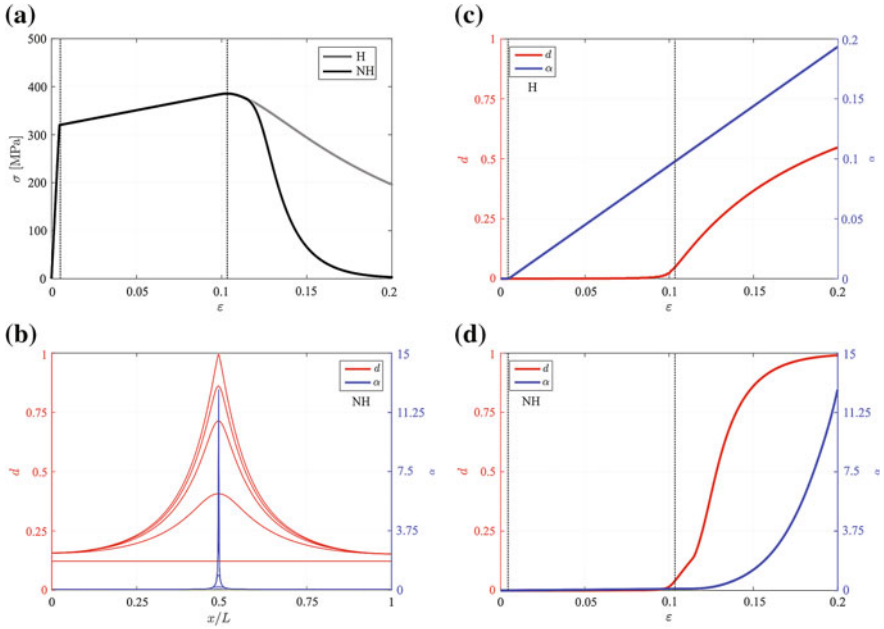


Fig. 4 Borden et al. Homogeneous and non-homogeneous responses for a bar length $L_n = 10$ mm and $W_0 = 0$

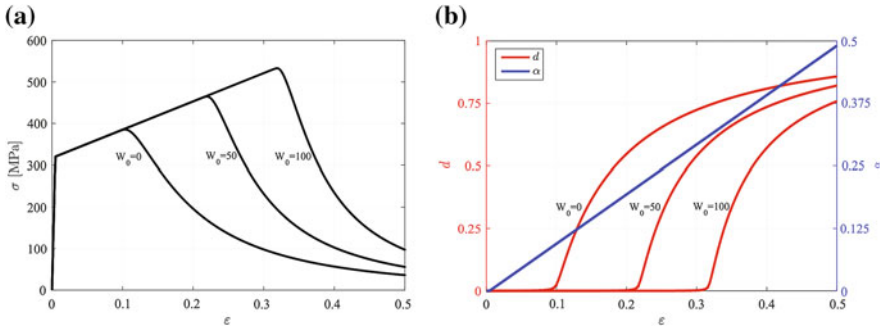


Fig. 5 Borden et al. Effect of W_0 on the homogeneous response

flexibility but may lose the variational nature. Two main categories of models can be identified based on whether the plastic hardening variable stops or continues its evolution once damage is triggered. The behavior of real materials in this respect would be easily identified by analyzing the unloading response in uniaxial stress-strain curves. Finally, more sophisticated aspects of the phenomenology such as those examined in [5] as well as triaxiality effects remained out of the scope of this paper and should be accounted for in future work.

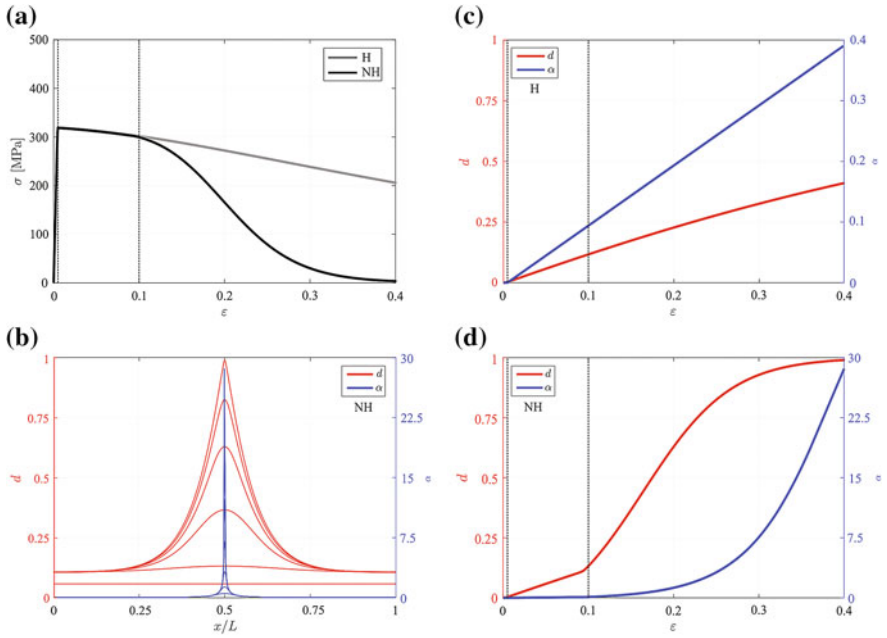


Fig. 6 Kuhn et al. Homogeneous and non-homogeneous responses for a bar length $L_n = 3.5$ mm

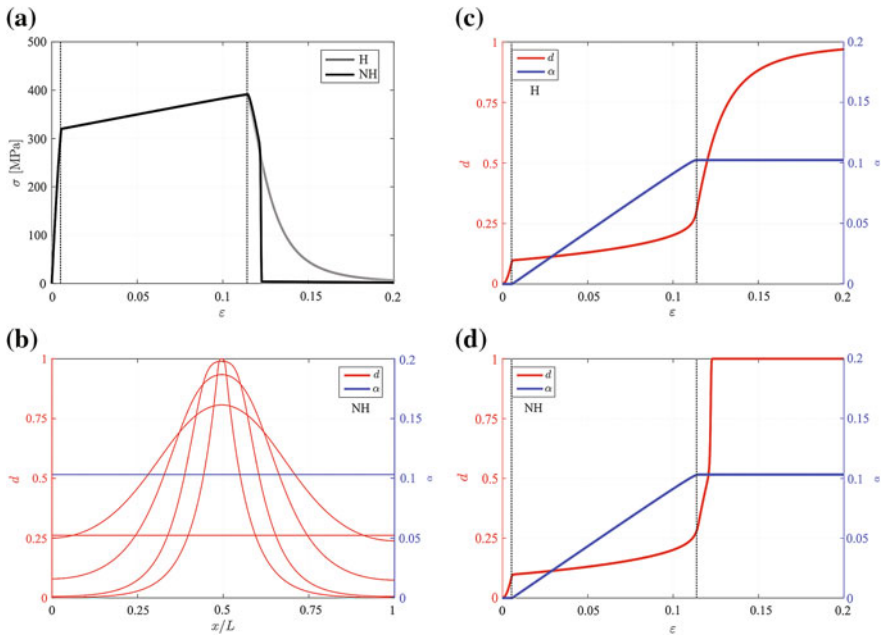


Fig. 7 Duda et al. Homogeneous and non-homogeneous responses for a bar length $L_n = 100$ mm

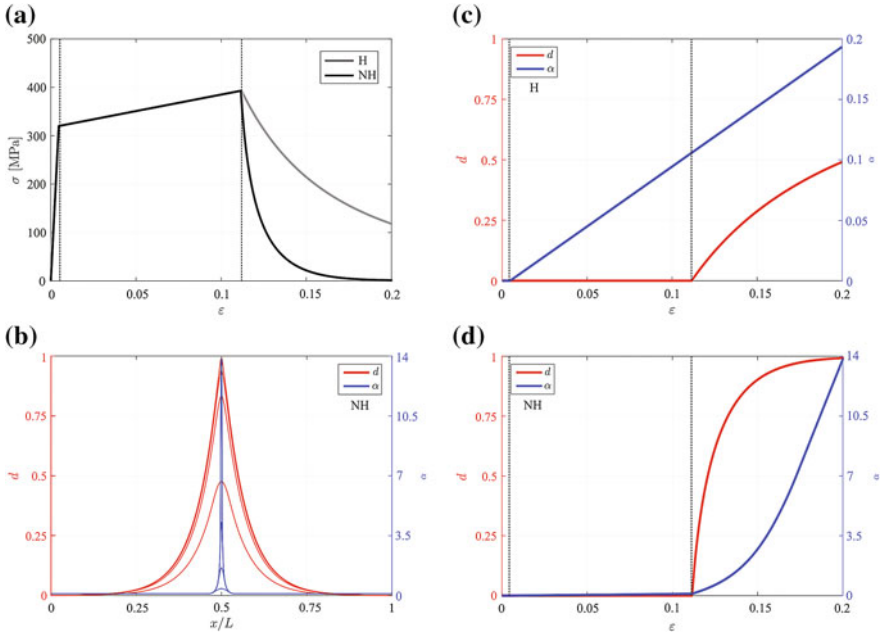


Fig. 8 Miehe et al. homogeneous and non-homogeneous responses for a bar length $L_n = 10$ mm, $w_c = \frac{3G_c}{16l}$ and $\xi = 1$

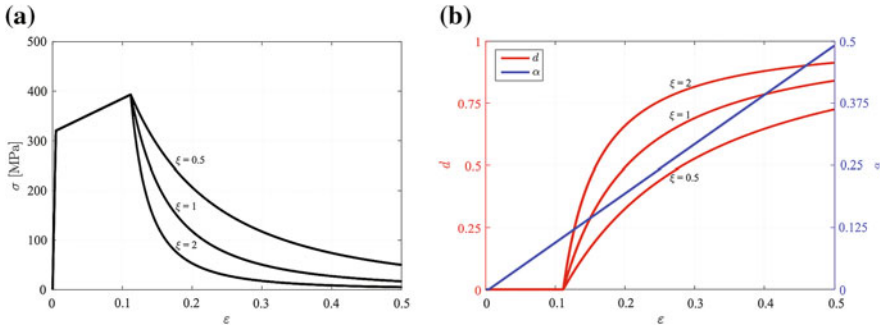


Fig. 9 Miehe et al. Effect of ξ on the homogeneous response

Acknowledgements The authors would like to acknowledge the support of the DAAD through the project “Variational approach to fatigue phenomena with phase-field models”.

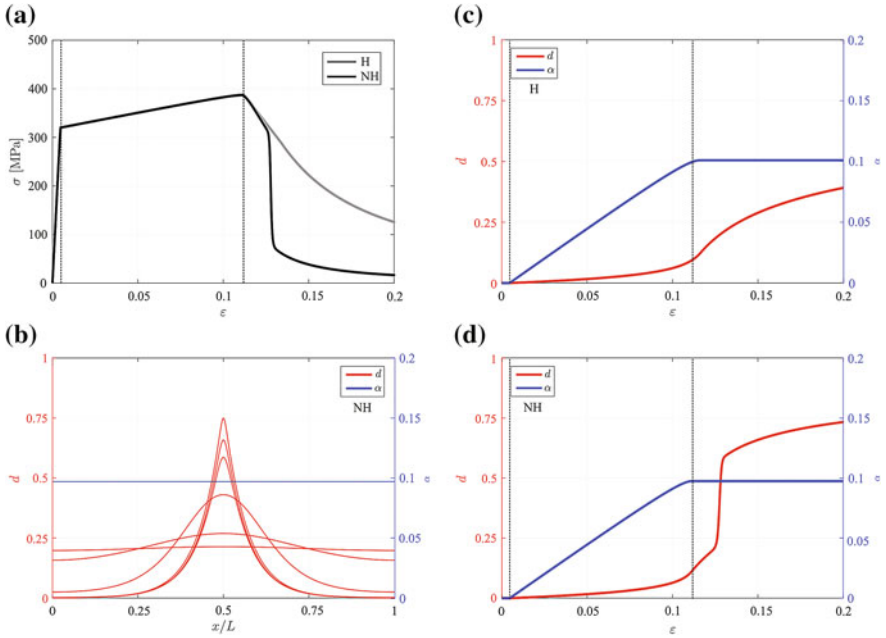


Fig. 10 Ambati et al. homogeneous and non-homogeneous responses for a bar length $L_n = 10$ mm, and $\alpha_{crit} = 0.025$

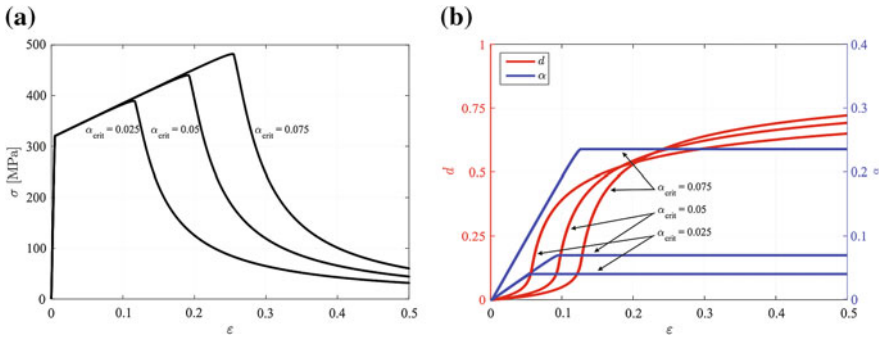


Fig. 11 Ambati et al. Effect of α_{crit} on the homogeneous response

References

1. R. Alessi, J.J. Marigo, S. Vidoli, Gradient damage models coupled with plasticity and nucleation of cohesive cracks. *Arch. Ration. Mech. Anal.* **214**(2), 575–615 (2014)
2. R. Alessi, J.J. Marigo, S. Vidoli, Gradient damage models coupled with plasticity: variational formulation and main properties. *Mech. Mater.* **80**(Part B), 351–367 (2015)
3. R. Alessi, J.J. Marigo, C. Maurini, S. Vidoli, Coupling damage and plasticity for a phase-field regularisation of brittle, cohesive and ductile fracture: one-dimensional examples. *Int. J. Mech.*

- Sci. In press (2017). doi:[10.1016/j.ijmecsci.2017.05.047](https://doi.org/10.1016/j.ijmecsci.2017.05.047)
4. M. Ambati, R. Kruse, L. De Lorenzis, A phase-field model for ductile fracture at finite strains and its experimental verification. *Comput. Mech.* **57**, 149–167 (2016)
 5. M. Ambati, T. Gerasimov, L. De Lorenzis, Phase-field modeling of ductile fracture. *Comput. Mech.* **55**(5), 1017–1040 (2015)
 6. L. Ambrosio, V.M. Tortorelli, Approximation of functional depending on jumps by elliptic functional via Gamma-convergence. *Commun. Pure Appl. Math.* **43**(8), 999–1036 (1990)
 7. H. Amor, J.J. Marigo, C. Maurini, Regularized formulation of the variational brittle fracture with unilateral contact: numerical experiments. *J. Mech. Phys. Solids* **57**(8), 1209–1229 (2009)
 8. M.J. Borden, C.V. Verhoosel, M.A. Scott, T.J.R. Hughes, C.M. Landis, A phase-field description of dynamic brittle fracture. *Comput. Methods Appl. Mech. Eng.* **217**, 77–95 (2012)
 9. M.J. Borden, T.J.R. Hughes, C.M. Landis, A. Anvari, I.J. Lee, A phase-field formulation for fracture in ductile materials: finite deformation balance law derivation, plastic degradation, and stress triaxiality effects. *Comput. Methods Appl. Mech. Eng.* **312**, 130–166 (2016)
 10. B. Bourdin, G.A. Francfort, J.J. Marigo, The variational approach to fracture. *J. Elast.* **91**(1), 5–148 (2008)
 11. G. Dal Maso, G. Orlando, R. Toader, Fracture models for elasto-plastic materials as limits of gradient damage models coupled with plasticity: the antiplane case. *Calc. Var. Partial Differ. Equ.* **55**(3), 45 (2016)
 12. F.P. Duda, A. Ciarbonetti, P.J. Sánchez, A.E. Huespe, A phase-field/gradient damage model for brittle fracture in elastic-plastic solids. *Int. J. Plast.* **65**, 269–296 (2015)
 13. G.A. Francfort, J.J. Marigo, Revisiting brittle fracture as an energy minimization problem. *J. Mech. Phys. Solids* **46**(8), 1319–1342 (1998)
 14. C. Kuhn, T. Noll, R. Müller, On phase field modeling of ductile fracture. *GAMM-Mitteilungen* **39**(1), 35–54 (2016)
 15. J.J. Marigo, C. Maurini, K. Pham, An overview of the modelling of fracture by gradient damage models. *Meccanica* **51**(12), 3107–3128 (2016)
 16. C. Miehe, F. Welschinger, M. Hofacker, Thermodynamically consistent phase-field models of fracture: variational principles and multi-field FE implementations. *Int. J. Numer. Methods Eng.* **83**(10), 1273–1311 (2010)
 17. C. Miehe, S. Teichtmeister, F. Aldakheel, Phase-field modelling of ductile fracture: a variational gradient-extended plasticity-damage theory and its micromorphic regularization. *Philos. Trans. Ser. A, Math. Phys. Eng. Sci.* **374**(2066) (2016)
 18. A. Mielke, T. Roubíček, *Rate-Independent Systems: Theory and Application.* (Springer, 2015)
 19. K. Pham, J.J. Marigo, C. Maurini, The issues of the uniqueness and the stability of the homogeneous response in uniaxial tests with gradient damage models. *J. Mech. Phys. Solids* **59**(6), 1163–1190 (2011)
 20. J. Ulloa, P. Rodríguez, E. Samaniego, On the modeling of dissipative mechanisms in a ductile softening bar. *J. Mech. Mater. Struct.* **11**(4), 463–490 (2016)

Bridging the Gap Between Concrete Microstructures and Tunnel Linings

E. Binder, H. Wang, T. Schlappal, J.L. Zhang, Y. Yuan,
B. Pichler and H.A. Mang

Abstract The title of this work represents a figurative counterpart of bridging the topographical gap between Hongkong and Macao. Presently under construction, the bridge that connects these two cities at opposite sides of the mouth of the Pearl River is interrupted by a submersed tunnel, which is the actual research object of this paper. By means of four different topics in the framework of the general subject of this contribution, reflected by its title, the scientific progress resulting from multiscale structural analyses of tunnel linings is documented. The four topics are: (a) microstructural analysis of impact and blast loading in tunnel linings, (b) multiscale analysis of thermal stresses in concrete linings due to sudden temperature changes, (c) experiments and finite element modeling of concrete hinges in Mechanized Tunneling, and (d) multiscale structural analysis of a segmented tunnel ring.

1 Introduction

The title of this work follows the one of a research project, sponsored by the Austrian Science Fund. It reads as “Bridging the gap by means of multiscale structural analysis” [1]. The ambitious goal of this project, in which the authors of this contribution are involved, is quantification of the added value of multiscale analyses, notwithstanding the explicit acknowledgment of scientific progress that manifests itself in such analyses. The overriding research object is the 35.6 km long Hongkong-Zhuhai-Macao Bridge, presently under construction. For shipping, the bridge is interrupted by a 5.7 km long tunnel below the bottom of the sea, representing the actual research object. Figure 1 shows the course of the bridge. Figure 2 refers to the tunnel, which is located between the West Artificial Island and the East Artificial Island (see Fig. 1). A figurative counterpart of bridging the topographical gap between Hongkong and

E. Binder · H. Wang · T. Schlappal · J.L. Zhang · Y. Yuan ·
B. Pichler · H.A. Mang (✉)
TU Wien – Vienna University of Technology, Karlsplatz 13/202,
1040 Vienna, Austria
e-mail: herbert.mang@tuwien.ac.at

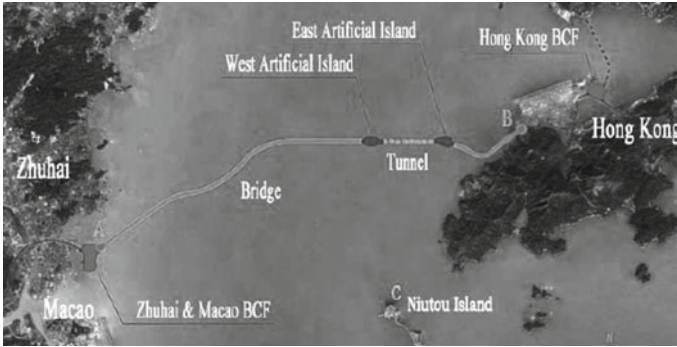


Fig. 1 Course of the Hongkong-Zhuhai-Macao-Bridge [1]

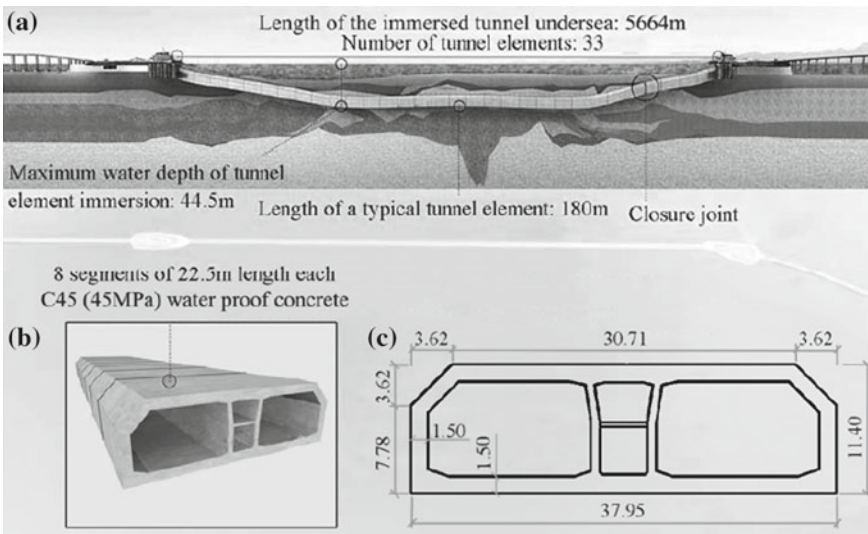
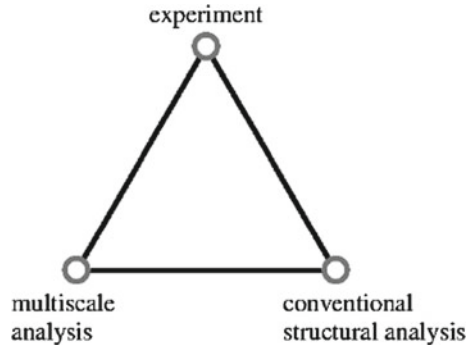


Fig. 2 Tunnel between the West Artificial Island and the East Artificial Island (see Fig. 1). Tunnel: **a** longitudinal section, **b** typical tunnel element, **c** cross-section of a tunnel element [1]

Macao is the bridging of several orders of magnitude in multiscale structural analyses. The intended assessment of the added value of such analyses requires a triad of related results (see Fig. 3). The focus of the scientific work in the first half of the aforementioned research project, which was started in Fall of 2015, has been on multiscale analyses of tunnel linings. Selected results of this research work are presented in this contribution.

Fig. 3 Triad of results, required for assessing the added value of multiscale analyses of tunnel linings [1]



2 Organization of the Paper

In the framework of the general subject of this paper the following four topics are treated: (a) Microstructural analysis of impact and blast loading in tunneling (Sect. 3), (b) Multiscale analysis of thermal stresses in concrete linings due to sudden temperature changes (Sect. 4), (c) Experiments and FE modeling of concrete hinges in Mechanized Tunneling (Sect. 5), (d) Multiscale structural analysis of a segmented tunneling ring (Sect. 6). Section 7 contains a summary of this work, conclusions drawn from the underlying research.

3 Microstructural Analysis of Impact and Blast Loading in Tunneling

Current safety standards require that tunnels withstand exceptional loading events such as e.g. impact and blast loads. Such events may result from traffic accidents, e.g. from cars crashing into a tunnel lining, or from the detonation of Improved Explosive Devices. This has been the motivation to investigate concrete subjected to high-dynamic loading rates. It is well known from the large database of available test results that the strength of cementitious materials increases with increasing loading rate. This strengthening is significant in the high dynamic testing regime, where strain rates are typically larger than 1 s^{-1} . The available experimental database has resulted in several modeling attempts. The CEB-recommendation [2], the model of Tedesco and Ross [3], and the model of Grote et al. [4] provide empirical formulae for the high-dynamic compressive strength of cementitious materials. Mihashi and Wittmann [5] as well as Bažant et al. [6] have developed models, based on the assumption that micro-cracking depends on the strain rate. Cotsovos and Pavlovic [7], Li and Meng [8], and Gary and Bailly [9] have attributed the strength increase with increasing strain rate to inertial confinement, which is a structural effect.

Table 1 Experimental data from high-dynamic strength tests by Kühn et al. [11]

Specimen properties: $f_{sta} = 25.1 \text{ MPa}$ $E = 32 \text{ GPa}$ $\nu = 0.2$					
$h = 80 \text{ mm}$ $\varnothing = 50 \text{ mm}$ $a_{max} = 8 \text{ mm}$ $\rho = 2400 \text{ kg/m}^3$					
$\dot{\varepsilon}$ [s^{-1}]	136.6	150.1	185.5	190.0	202.7
f_{dyn} [MPa]	95.1	104.2	119.2	125.7	142.5

Fischer et al. [10] have explained dynamic strengthening based on the quasi-static strength and the duration of the failure process, lasting from the start of crack propagation to the disintegration of the tested specimen. Herein, the latter model is extended towards consideration of uncertainty regarding the quasi-static strength. It is used to re-analyze a recent high-dynamic test series on concrete, see Table 1 and [11].

3.1 Prediction of High-Dynamic Strength, Based on Quasi-Static Strength Data

3.1.1 Statistical Scatter of Quasi-Static Strength Values

While test repetitions are desirable in experimental mechanics in order to quantify the dispersion of the investigated material properties, many researchers carry out just one test, or they communicate only the mean value of results from several tests. In both cases an estimation of statistical quantiles is impossible. As a remedy, it is proposed herein to follow the Eurocode and to consider compressive strength values of concrete to scatter according to a Gaussian distribution. In addition, the Eurocode defines the characteristic strength for ultimate limit state design as the 5%-quantile of the strength distribution. Concerning the compressive strength of concrete, the 5%-quantile is introduced as by 8 MPa smaller than the mean strength determined in laboratory testing. This approach is related to a standard deviation of the uniaxial compressive strength amounting to $\hat{\sigma} = 4.865 \text{ MPa}$.

Considering the compressive strength as a positive quantity, a lognormal distribution is more appropriate to describe statistical properties. In order to convert the standard deviation of the Eurocode to the one of the envisioned lognormal distribution, it is proposed to set the 5%-quantile of the Gaussian distribution equal to the 5%-quantile of the lognormal distribution. Denoting the mean strength value from the experiments as \hat{f} and the standard deviation of the Eurocode as $\hat{\sigma}$, the proposed approach yields the sought standard deviation of the lognormal distribution as

$$\bar{\sigma}(\hat{\sigma}, \hat{f}) = u(5\%) + \sqrt{u(5\%)^2 - 2 \cdot \ln \left(1 + \frac{u(5\%) \cdot \hat{\sigma}}{\hat{f}} \right)}, \quad (1)$$

where $u(5\%) = -1.645$ is the value that cuts an area of 5% of the standardized normal distribution, exhibiting a vanishing mean value. Based on the standard deviation of the lognormal distribution according to Eq.(1), any p -quantile of the lognormal distribution can be quantified according to the following standard relation:

$$f(p) = \exp \left(\ln(\hat{f}) + u(p) \cdot \bar{s} \right). \quad (2)$$

3.1.2 High-Dynamic Strength Modeling, Considering Uncertainty of the Failure Mode

The present contribution follows Fischer et al. who developed a model for the dynamic increase factor (DIF) of the compressive strength of cementitious materials, see [10]. Herein, the model is extended towards consideration of the experimental dispersion of the quasi-static strength. Furthermore, it is shown that re-analysis of high-dynamic strength tests requires careful consideration of the failure mechanism. Along this line of research, it is assumed that macroscopic cracking starts—also under high-dynamic compressive loading—once the stress level has reached the quasi-static strength, and that the ultimate load of the specimen is reached, once the first crack has propagated through the entire specimen such that it disintegrates into pieces. In this context, it is noteworthy that the speed of cracks, propagating along nanoscopic material interfaces, is equal to the Rayleigh wave speed [12], which is only a little smaller than the shear wave velocity v_s . With the static strength f_{sta} , Young's modulus E , and the strain rate $\dot{\epsilon}$, the DIF (dynamic strength increase factor) is obtained as

$$DIF = \frac{f_{dyn}}{f_{sta}} = 1 + \frac{\dot{\epsilon} \cdot E}{f_{sta}} \cdot \frac{l_c}{v_s}. \quad (3)$$

In Eq. (3), l_c stands for the relevant crack propagation length. It is equal to the length along which the relevant crack must propagate in order to split the sample. Therefore, l_c depends on the geometrical properties of the tested specimen. Considering that axial splitting is the typical failure mode under uniaxial compression, the ultimate load sustained by the specimen is reached, once the crack size is equal to the height h of the specimen. Realistic scenarios are bounded by the following two cases: (a) if the relevant crack starts right at the interface between the specimen and the load plate, the crack will grow along the total height h of the specimen, and (b) if cracking starts at the center of the specimen, two crack edges will propagate simultaneously, and each of them will cover a length equal to $h/2$.

According to the previous explanation, the dispersion of the high-dynamic strength values results from two sources: (a) the uncertainty regarding the quasi-static strength, see f_{sta} in Eq. (3) as well as Sect.3.1.1, and (b) the uncertainty regarding the position from which the relevant crack starts to propagate, see l_c in Eq. (3). These uncertainties result in intervals of possible strength values, which are

quite wide in the quasi-static regime, but form a rather narrow band in the high-dynamic regime. When comparing Eq. (3) with experimental data, the only free parameter is the relevant crack propagation length l_c . It can be optimized such that model-predicted DIF values, DIF_{pred} , agree in the best-possible fashion with their experimental counterparts, DIF_{exp} , according to

$$E_{tot} = \left| \frac{1}{n} \sum_{i=1}^n \frac{DIF_{pred,i} - DIF_{exp,i}}{DIF_{exp}^{mean}} \right| \rightarrow \min. \quad (4)$$

In Eq. (4), n denotes the number of experimentally determined DIF values, and E_{tot} stands for the total prediction error.

3.2 Model Application to High-Dynamic Strength Data

In this contribution the model validation is extended to high-dynamic strength tests performed by Kühn et al. [11] on concrete specimens. In the following, Eq. (3) is used to analyze the experimental data, listed in Table 1. Kühn et al. specify the specimen properties, listed in Table 1, and provided images showing the remaining fragments of specimens after testing, see Fig. 4. Presumably, the remaining cone-shaped fragments, with a height about one half of the specimen height, are caused by a confinement, resulting from friction in the contact area between the specimen and the pressure bar.

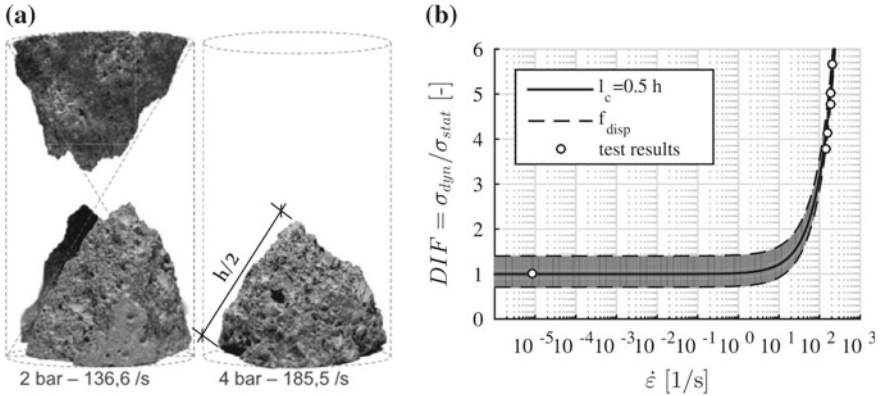


Fig. 4 **a** Illustration of the specimen fragments from [11], **b** validation of the model for high-dynamic strength increase according to Eq. (3): comparison of measured dynamic strength-increase factors from Kühn et al. [11] with corresponding model predictions obtained for the specimen properties listed in Table 1, and for $h = 80$ mm

The remaining fragments of the specimen show that cracks had to propagate along a length $l_c \approx h/2$ in order to split the specimen, see Fig. 4a. Using this length together with properties of the tested specimen (Table 1) as input for Eq. (3) yields model predictions that agree very well with the experimental data, see the solid line in Fig. 4b. The uncertainty regarding the quasi-static strength manifests itself in Fig. 4b in the form of the dashed boundary lines.

3.3 Conclusions

The present study suggests that the propagation length, required for the first crack to split a specimen under high-dynamic compression, has a great influence on the ultimate load of the tested specimen. As for modeling, it was assumed that also for high-dynamic loading, crack propagation starts at the quasi-static strength and that the ultimate load sustained by the tested specimen increases with increasing propagation length, required for the first crack to split the specimen. It is concluded that, no matter how short a stress pulse exceeding the quasi-static strength may be, tunnel linings will be damaged. Therefore, they need to be inspected carefully even after non-catastrophic high-dynamic loading events. Furthermore, the model allows to estimate the depth of the damage zone, provided the duration of the stress pulse is known. It is equal to the period of time, during which the stress is larger than the quasi-static strength, multiplied by the crack propagation speed, i.e. by the shear wave velocity.

4 Multiscale Analysis of Thermal Stresses in Concrete Linings Due to Sudden Temperature Changes

A change of the temperature of a concrete structure induces thermal eigenstrains. In general, they result in thermal stresses which may lead to cracking of the material. Instationary heat conduction, i.e. transient heat conduction, inevitably activates *macroscopic* thermal stresses. Kinematic constraints, preventing temperature-induced deformations, also result in thermal stresses. Furthermore, the mismatch of the thermal expansion coefficients of the concrete constituents (cement paste matrix and aggregate inclusions) [13] gives rise to *microscopic* self-equilibrated stresses, even if the concrete volume is free of macroscopic kinematic constraints.

A model for multiscale thermo-mechanical analysis is presented. Bottom-up homogenization of the concrete allows for upscaling of elastic stiffnesses and of thermal expansion coefficients of the concrete constituents. The resulting homogenized properties of concrete serve as input for macroscopic thermal stress analysis. Top-down stress concentration in turn provides access to microscopic thermal stresses in the cement paste and the aggregates, as functions of both the macroscopic stresses and a mismatch of microscopic thermal expansion coefficients. The proposed model

is applied to stress analysis of a 3-D simply-supported concrete beam, subjected to 1-D heat conduction.

4.1 Multiscale Thermo-Mechanical Model of Concrete

Concrete is a matrix-inclusion composite, consisting of a cement paste matrix and aggregate inclusions. Homogenized material properties of concrete, such as the stiffness and the thermal expansion coefficient, are related to the corresponding properties of the constituents.

As the temperature increases (or decreases), the cement paste and the aggregates expand (or contract) in accordance to their coefficients of thermal expansion, inducing eigenstrains $\boldsymbol{\epsilon}_{cp}^e$ and $\boldsymbol{\epsilon}_{agg}^e$, reading as

$$\boldsymbol{\epsilon}_{cp}^e = \alpha_{cp} \Delta T \mathbf{1}, \quad \boldsymbol{\epsilon}_{agg}^e = \alpha_{agg} \Delta T \mathbf{1}, \quad (5)$$

where α_{cp} and α_{agg} are the thermal expansion coefficients of the cement paste and the aggregates, respectively. Corresponding eigenstresses of the cement paste and the aggregates can be computed as

$$\boldsymbol{\sigma}_{cp}^e = -\mathbb{C}_{cp} : \boldsymbol{\epsilon}_{cp}^e, \quad \boldsymbol{\sigma}_{agg}^e = -\mathbb{C}_{agg} : \boldsymbol{\epsilon}_{agg}^e, \quad (6)$$

where \mathbb{C}_{cp} and \mathbb{C}_{agg} are the elastic stiffness tensors of the cement paste and the aggregates, respectively. The transition to the macroscopic scale of concrete is provided by Levin's theorem [14], containing the macroscopic stress tensor $\boldsymbol{\Sigma}_{con}$, the macroscopic strain tensor \boldsymbol{E}_{con} , and the macroscopic eigenstrain and eigenstress tensors \boldsymbol{E}_{con}^e and $\boldsymbol{\Sigma}_{con}^e$ as

$$\boldsymbol{\Sigma}_{con} = \mathbb{C}_{con} : (\boldsymbol{E}_{con} - \boldsymbol{E}_{con}^e) = \mathbb{C}_{con} : \boldsymbol{E}_{con} + \boldsymbol{\Sigma}_{con}^e, \quad (7)$$

with the homogenized stiffness tensor reading as

$$\mathbb{C}_{con} = f_{cp} \mathbb{C}_{cp} : \mathbb{A}_{cp} + f_{agg} \mathbb{C}_{agg} : \mathbb{A}_{agg}, \quad (8)$$

and with the homogenized eigenstress tensor reading as

$$\boldsymbol{\Sigma}_{con}^e = f_{cp} \boldsymbol{\sigma}_{cp}^e : \mathbb{A}_{cp} + f_{agg} \boldsymbol{\sigma}_{agg}^e : \mathbb{A}_{agg}, \quad (9)$$

where f_{cp} and f_{agg} are the volume fractions of the cement paste and the aggregates in the concrete, and \mathbb{A}_{cp} and \mathbb{A}_{agg} are the strain concentration tensors of the cement paste and the aggregates, which are estimated by means of the Mori-Tanaka method [15].

As for relating the thermal expansion coefficient of concrete, α_{con} , to the thermal expansion coefficients of the constituents, i.e. to α_{cp} and α_{agg} , it is assumed that

concrete can deform freely, such that the macroscopic stress tensor vanishes. For this scenario, Eq. (7) yields

$$\boldsymbol{\Sigma}_{con} = 0 \Rightarrow \mathbf{E}_{con} = \mathbf{E}_{con}^e = -\mathbb{C}_{con}^{-1} : \boldsymbol{\Sigma}_{con}^e. \quad (10)$$

The sought expression for α_{con} is obtained by setting \mathbf{E}_{con} in Eq. (10) equal to $\alpha_{con} \Delta T \mathbf{1}$ and inserting (5) into (6), followed by substituting the resulting expression into (9), and, finally, by substituting the outcome together with (8) into (10). This delivers, after division by ΔT ,

$$\alpha_{con} \mathbf{1} = \left[f_{cp} \mathbb{C}_{cp} : \mathbb{A}_{cp} + f_{agg} \mathbb{C}_{agg} : \mathbb{A}_{agg} \right]^{-1} : \left[\alpha_{cp} f_{cp} (\mathbb{C}_{cp} : \mathbf{1}) : \mathbb{A}_{cp} + \alpha_{agg} f_{agg} (\mathbb{C}_{agg} : \mathbf{1}) : \mathbb{A}_{agg} \right]. \quad (11)$$

The thermal expansion coefficient α_{con} from Eq. (11) intervenes in macroscopic thermal analysis of concrete structures.

After thermal analysis of a concrete structure, the macrostress $\boldsymbol{\Sigma}_{con}$ and the temperature change ΔT are known at every point of the structure. The scale transition to the cement paste and the aggregates at all structural points is carried out as follows: starting from the temperature change ΔT and combining Eqs. (5), (6), and (9), delivers the homogenized eigenstress tensor $\boldsymbol{\Sigma}_{con}^e$. Inserting the latter together with Eq. (8) into Eq. (7) allows for quantifying the macroscopic strains \mathbf{E}_{con} . The auxiliary strain \mathbf{E}_{∞} , representing the remote loading of the Eshelby problems, is given in [15]. Then, the strains $\boldsymbol{\varepsilon}_{cp}$ and $\boldsymbol{\varepsilon}_{agg}$ are quantified as

$$\boldsymbol{\varepsilon}_{cp} = \mathbf{E}_{\infty}, \quad \boldsymbol{\varepsilon}_{agg} = [\mathbb{I} + \mathbb{P} : (\mathbb{C}_{agg} - \mathbb{C}_{cp})] : [\mathbf{E}_{\infty} - \mathbb{P} : (\boldsymbol{\sigma}_{agg}^e - \boldsymbol{\sigma}_{cp}^e)]. \quad (12)$$

The stresses $\boldsymbol{\sigma}_{cp}$ and $\boldsymbol{\sigma}_{agg}$ finally follow from the elasticity laws as

$$\boldsymbol{\sigma}_{cp} = \mathbb{C}_{cp} : (\boldsymbol{\varepsilon}_{cp} - \boldsymbol{\varepsilon}_{cp}^e), \quad \boldsymbol{\sigma}_{agg} = \mathbb{C}_{agg} : (\boldsymbol{\varepsilon}_{agg} - \boldsymbol{\varepsilon}_{agg}^e). \quad (13)$$

4.2 Multiscale Thermo-Mechanical Analysis of a Simply-Supported Concrete Beam Subjected to Sudden Cooling

4.2.1 Analytical Solution of Heat Conduction Problem

Multiscale thermo-mechanical analysis is carried out for a simply-supported concrete beam with a rectangular cross-section. Initially, the beam exhibits a uniform temperature field, denoted as the reference temperature T_{ref} , i.e.

$$T(z, t = 0) = T_{ref}. \quad (14)$$

The structure is loaded by sudden cooling of the top surface, $z = h$, to zero-degree centigrade, while the temperature at the bottom surface, $z = 0$, the beam remains at T_{ref} , i.e.

$$T(z = h, t) = 0^\circ\text{C}, \quad T(z = 0, t) = T_{ref}. \quad (15)$$

Consideration of thermal insulation of the lateral surfaces results in 1-D heat conduction along the height of the beam, i.e. along the z -direction. Therefore, the heat equation reads as

$$\frac{\partial T}{\partial t} - a \frac{\partial^2 T}{\partial z^2} = 0, \quad (16)$$

where a represents the thermal diffusivity of concrete.

The analytical solution of the heat conduction problem, defined in Eqs. (14)–(16), is obtained as follows [16]:

$$T(z, t) = T_{ref} \left[\left(1 - \frac{z}{h}\right) + \sum_{n=1}^{\infty} \frac{2(-1)^{n-1}}{n\pi} \sin\left(\frac{n\pi z}{h}\right) \exp\left(-\frac{n^2\pi^2 a t}{h^2}\right) \right]. \quad (17)$$

4.2.2 Macroscopic and Microscopic Thermal Stress Analysis

A 3-D FE model of a simply-supported beam with the dimensions $l \times b \times h = 2 \text{ m} \times 0.4 \text{ m} \times 0.3 \text{ m}$ is chosen for thermo-mechanical analysis. The stiffness tensor and the thermal expansion coefficient of concrete are predicted by means of the established multiscale model of concrete, see Eqs. (8) and (11).

The beam is loaded by temperature distributions according to Eq. (17), referring to the dimensionless time instants $at/h^2 \in [1, 10^{-1}, 10^{-2}]$, with $a = 4.73 \times 10^{-7} \text{ m}^2/\text{s}$. The distribution of the normal stresses along the height of the cross-section in the middle of the beam, $\Sigma_{xx}(z)$, is shown in Fig. 5a. Large thermal stresses are obtained right after sudden cooling. They gradually decrease and finally vanish, as the temperature profile along the height of the beam approaches the linear distribution. Tensile stresses appear close to the top and bottom surfaces of the beam, while compressive stresses prevail in its middle part. Notably, because of overall equilibrium of the structure, stress resultants in the form of a normal force and a bending moment vanish at all instants of time.

Microscopic stresses in the cement paste and the aggregates are quantified by the established multiscale model, with the macroscopic stress tensor and the temperature distribution along the height of the beam as input. The average stresses in the cement paste matrix and in the aggregate inclusions at the dimensionless time instant $at/h^2=10^{-1}$ are shown in Fig. 5b. Compared to the aggregates, the tensile stresses in the cement paste are larger, which increases the risk of microcracking of the cement paste.

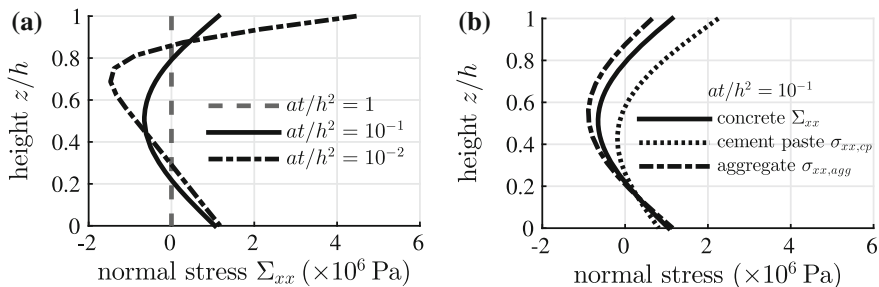


Fig. 5 Evaluation of **a** the macroscopic normal stresses Σ_{xx} for dimensionless time instants $at/h^2 \in [1, 10^{-1}, 10^{-2}]$ and **b** the normal stresses of the homogenized concrete, the cement paste and the aggregates at $at/h^2 = 10^{-1}$, along the height of the cross-section in the middle of the beam

4.3 Conclusions

A model for multiscale thermo-mechanical analysis of concrete structures was proposed and applied to a simply-supported concrete beam, subjected to 1-D heat conduction. Considerable temperature-induced tensile stresses develop right after the time instant of sudden cooling. Thereafter, they gradually decrease and finally vanish, as the heat conduction approaches the steady-state regime. Since the thermal expansion coefficient of the cement paste is typically much larger than the one of the aggregates, the cement paste matrix exhibits tensile stresses which are (a) larger than the ones of the aggregates and (b) larger than the overall macroscopic stresses of concrete. Therefore, the presented mode of multiscale modeling is highly recommended for analysis focusing on the possibility of cracking of concrete tunnel linings under thermal loading.

5 Experiments and FE Modeling of Concrete Linings in Mechanized Tunneling

Primary linings in Mechanized Tunneling are made of precast reinforced concrete segments. Such linings contain both longitudinal and circumferential segment-to-segment interfaces which are referred to as concrete hinges. The linings are subjected to external loads, resulting from the ground pressure and from the tunnel boring machine. The overall safety of segmented linings is strongly related to the integrity of segment-to-segment interfaces, which have to transmit both normal forces and bending moments. The resulting relative rotation angles are of prime interest for designers who typically rely on formulae by Gladwell [17] or Janßen [18]. Notably, Janßen's formulae were derived from older ones by Leonhardt and Reimann [19], who developed design guidelines for concrete hinges used in integral bridge construction. However, these guidelines refer to serviceability conditions, i.e. they do not provide information on the bearing capacity of concrete hinges. This is the motivation for the present contribution.

5.1 Experimental Data from Testing of Concrete Hinges

The structural behavior of concrete hinges under eccentric compression was recently studied by Schlappal et al. [20]. In the following, information is provided on the materials and on the chosen geometric dimensions of the concrete hinges, furthermore, on the test setup and on test results from eccentric compression up to the bearing capacity. Notably, throughout this work compression is considered by a positive sign.

5.1.1 Materials and Test Specimens

The three tested concrete hinges were made of steel-reinforced concrete. Concrete C 35/45 was produced with a commercial cement, Viennese tap water, and with calcite aggregates with a maximum size of 16 mm. The cube compressive strength, $f_{c,cube} = 56.25$ MPa, and Young's modulus, $E = 34.75$ GPa, were determined 28 days after production, following the Austrian standards for testing of concrete. The steel quality of the rebars was chosen as B550 A.

The geometric shape of the tested concrete hinges complied with the design guidelines of Leonhardt and Reimann [19]. The overall width amounted to 25 cm, the height to 35 cm, and the depth to 40 cm, see Fig. 6a. The depth of the lateral and the front-side notches amounted to 8.75 cm and 5 cm, respectively. Therefore, the cross-section of the neck was equal to 7.5×30 cm², see Fig. 6a. At the top and the bottom of the concrete hinges, steel plates of two centimeter thickness were provided. They ensured an effective distribution of the concentrated external line loads. Each steel plate was welded to the neighboring reinforcement cage. The top and bottom reinforcement cages were in turn connected by three pairs of crossed steel rebars with cross-over points right at the center of the neck, see Fig. 6a.

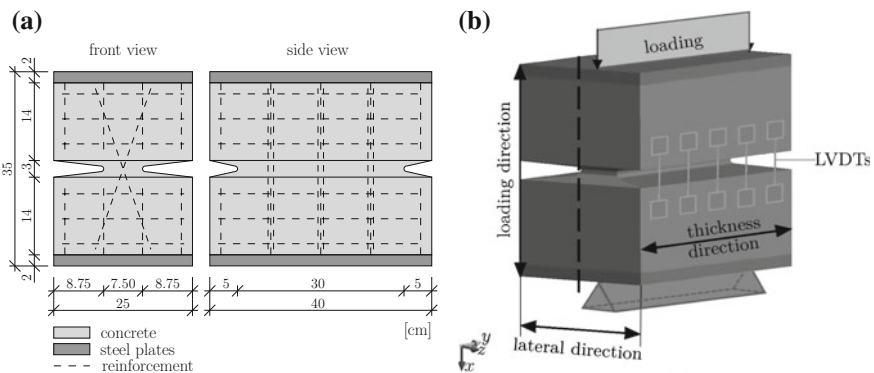


Fig. 6 a Geometric dimensions [20] and b boundary conditions [21] of the tested reinforced concrete hinges

5.1.2 Test Setup

The tests consisted of three nominally identical concrete hinges that were subjected, one after another, to eccentric line loads, see Fig. 6b. This resulted in combined compression and bending, whereby the bending moment M was equal to the applied normal force N , times the eccentricity e :

$$M = N e . \tag{18}$$

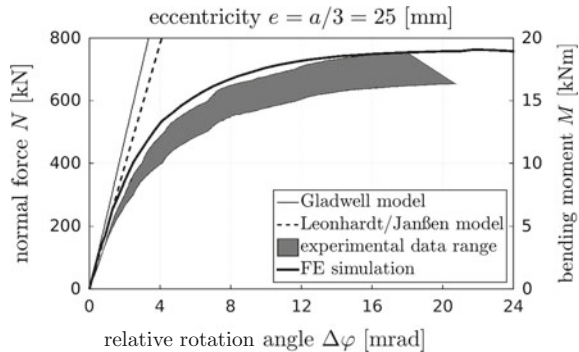
As for quantification of the displacements, inductive displacement sensors (LVDTs) were mounted at the lateral surfaces of the concrete hinges. They permitted measuring changes of the notch mouth opening displacements of the lateral notches.

As for studying the development of tensile cracking as a function of e and N , a reasonable value of e had to be defined. In this context, the design guidelines of Leonhardt and Reimann [19] were followed. They are applicable to eccentricities up to as $a/3 = 25$ mm, where a denotes the width of the neck. The guidelines take into account that for $\max e = a/3$ tensile cracking will extend across half of the neck width, i.e. right to the center of the concrete hinge.

5.1.3 Eccentric Compression up to the Bearing Capacity

The measured relation between the increasing eccentric normal force and the corresponding relative rotation angle of the concrete hinges is shown in Fig. 7. Once the normal force exceeded 200 kN, the relative rotation angle increased superlinearly with increasing loading. When it exceeded 15 mrad, the loading could no longer be increased significantly. The bearing capacity of each one of the three tested concrete hinges was equal to approximately 700 kN. This refers to a bending moment, equal to approximately 17.5 kNm, see Eq. (18), considering $e = 25$ mm.

Fig. 7 Comparison of measurements from eccentric compression tests [20] with numerical results from three-dimensional FE simulations [21] and with relationships by Gladwell [17], Leonhardt and Reimann [19], and Janßen [18]



5.2 FE Simulations of the Tested Concrete Hinges

The experimental observations, described in Sect. 5.1, were analyzed by means of the FEM by Kalliauer et al. [21]. Geometrically linear FE simulations were performed in order to gain insight into the structural behavior of concrete hinges, based on quantification of stress states *inside* their volume, which is typically inaccessible in experimental testing.

5.2.1 2-D FE Simulations for Quantification of the Stress Triaxiality in the Neck Region

In order to gain insight into the triaxiality of the compressive stresses in the neck region, 2-D FE simulations were carried out, considering a plane strain state in the x - z plane containing the center of the concrete hinge (Fig. 6b). The characteristic ratio of the principal stresses in the neck region was 1.00 : 0.45 : 0.30. The characteristic triaxial compressive stress state σ can be formulated as

$$\sigma = \sigma_\ell \cdot \left[1.00 \mathbf{e}_x \otimes \mathbf{e}_x + 0.45 \mathbf{e}_y \otimes \mathbf{e}_y + 0.30 \mathbf{e}_z \otimes \mathbf{e}_z \right], \quad (19)$$

where σ_ℓ denotes the principal compressive normal stress in the loading direction. This confinement results in a significant strengthening of concrete relative to its uniaxial compressive strength.

5.2.2 Micromechanics-Assisted Updating of Input Parameters for 3-D FE Simulations

3-D FE simulations based on default input values do not deliver quantitatively reliable results. In particular, the initial structural stiffness and the bearing capacity are overestimated. This indicates pre-existing damage of the concrete hinges. Model updating consists of identifying suitable values of Young's modulus, the uniaxial tensile strength, the fracture energy, and the triaxial compressive strength. In order to reduce the number of free parameters from four to two, a multiscale model for tensile softening of concrete was used [22]. It establishes quantitative links between the increasing crack density, on the one hand, and the corresponding reductions of the elastic stiffness, the tensile strength, and the fracture energy of concrete, on the other hand. This results in micromechanics-assisted FE simulations of concrete hinges. In addition, pre-existing damage indicates the necessity to reduce the *triaxial* compressive strength of concrete. This can be achieved by increasing the input parameter λ_t , which quantifies the ratio between the *auxiliary* uniaxial tensile strength f'_t of the Men etrey-Willam failure surface and the *actual* uniaxial tensile strength f_t of the Rankine failure surface. Based on the default input parameter $\lambda_t = 2$, the Men etrey-Willam failure surface suggests that the triaxial compressive strength $\sigma_{\ell u}$ is equal

to 5.65 times the uniaxial compressive strength. Increasing the value of the input parameter λ_t in the framework of sensitivity analysis, delivers Men etrey-Willam failure surfaces with decreasing slopes in the $\xi - \rho$ diagrams, where by ξ and ρ are proportional to the first invariant of the stress tensor and to the square-root of the second invariant of the stress deviator, respectively. It is found that $\lambda_t = 8.5$ allows for reproducing the experimentally obtained bearing capacity of the tested concrete hinges in a qualitatively and quantitatively satisfactory fashion, see Fig. 7.

5.3 Conclusions

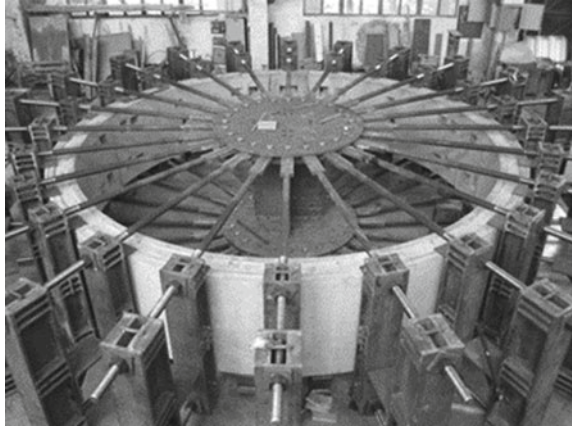
Researchers working in Mechanized Tunneling are interested in relative rotation angles, developing across concrete necks, subjected to compression and bending. Models with predictive capacity are needed in order to develop powerful simulation tools for segmented tunnel linings. To support such a development, a combined experimental-computational study on concrete hinges subjected to eccentric compression was performed. FE simulations allowed for quantifying the *triaxial* compressive stress state prevailing in the neck region and for reproducing the nonlinear structural behavior right up to the bearing capacity. Existing guidelines do not consider the nonlinear behavior of concrete hinges under eccentric compression, see the linear functions in Fig. 7. The presented research results are expected to support the future development of a structural simulation tool for segmented tunnel linings.

6 Multiscale Structural Analysis of a Segmented Tunnel Ring

A real-scale test of a segmented tunnel ring, see Fig. 8, which was carried out at Tongji University [23], is re-analyzed. The tested ring consisted of 6 reinforced concrete segments. The diameter of the ring amounted to 6.2 m. The ring was subjected to anisotropic loading, imposed by 24 hydraulic jacks up to the Ultimate Limit State (ULS). The convergences in both the vertical and the horizontal direction as well as the displacement/rotation discontinuities at the interfaces of the segments were measured. Cracking of concrete was observed during the test.

The test provided valuable insight into the progressive failure and the bearing capacity of segmented tunnel linings. However, real-scale tests on segmented tunnel rings are expensive and time-consuming. This was the motivation for the development of a structural analysis model, reproducing real-scale tests. To this end, a multiscale model for concrete [22] and transfer relations for structural analysis of segmented tunnel rings [24] are combined, resulting in multiscale structural analysis of such rings.

Fig. 8 Setup of a real-scale test of a segmented tunnel ring at Tongji University [23]



6.1 Multiscale Model of Concrete

The microstructure of the concrete is considered to be hierarchically organized in six length scales, i.e. the solid calcium-silicate-hydrates (C-S-H), the hydrate gel, the hydrate foam, the cement paste, the mortar, and the concrete. The elastic stiffness and the fracture energy of the C-S-H, known from molecular dynamics simulations documented in the literature, are upscaled via the hierarchically-organized scales to the material scale of concrete [22]. In this way, Young's modulus, Poisson's ratio, and the tensile strength of the homogenized concrete are obtained as [25]

$$E_c^{hom} = 43.57 \text{ GPa}, \quad (20)$$

$$\nu_c^{hom} = 0.2424, \quad (21)$$

$$f_t = 3.17 \text{ MPa}. \quad (22)$$

6.2 Hybrid Analysis of the Segmented Tunnel Ring, Based on Transfer Relations

The transfer relations express the vector of the state variables at an arbitrary cross-section with the angular coordinate φ as the product of a transfer matrix and the vector of the state variables at the initial cross-section (index "i") $\varphi_i = 0$. They read as [24]

$$\begin{bmatrix} u(\varphi) \\ v(\varphi) \\ \theta(\varphi) \\ M(\varphi) \\ N(\varphi) \\ V(\varphi) \\ 1 \end{bmatrix} = \begin{bmatrix} \cos \varphi & \sin \varphi & T_{13}(\varphi) & T_{14}(\varphi) & T_{15}(\varphi) & T_{16}(\varphi) & \sum u^L(\varphi) \\ -\sin \varphi & \cos \varphi & T_{23}(\varphi) & T_{24}(\varphi) & T_{25}(\varphi) & T_{26}(\varphi) & \sum v^L(\varphi) \\ 0 & 0 & 1 & T_{34}(\varphi) & T_{35}(\varphi) & T_{36}(\varphi) & \sum \theta^L(\varphi) \\ 0 & 0 & 0 & 1 & T_{45}(\varphi) & T_{46}(\varphi) & \sum M^L(\varphi) \\ 0 & 0 & 0 & 0 & \cos \varphi & -\sin \varphi & \sum N^L(\varphi) \\ 0 & 0 & 0 & 0 & \sin \varphi & \cos \varphi & \sum V^L(\varphi) \\ \hline 0 & 0 & 0 & 0 & 0 & 0 & 1 \end{bmatrix} \begin{bmatrix} u_i \\ v_i \\ \theta_i \\ M_i \\ N_i \\ V_i \\ 1 \end{bmatrix}, \quad (23)$$

where u , v , and θ stand for the radial displacement, the tangential displacement, and the cross-sectional rotation, respectively; M , N , and V are the bending moment, the axial force, and the shear force, respectively; EI , EA , and R denote the bending stiffness, the extensional stiffness, and the radius of the neutral axis of the arch, respectively. Notably, the complete list of the nonzero elements of the transfer matrix T_{ij} is available in [24]. The top six elements of the last column of the transfer matrix in Eq. (23) contain so-called load integrals, representing the solutions for the radial point loads and for the interfacial dislocations. As an example, the load integral of the radial displacement for a radial point load P reads as [24]:

$$u^L(\varphi) = \frac{1}{2} \left(\frac{PR}{EA} + \frac{PR^3}{EI} \right) \left[(\varphi - \varphi_p) \cos(\varphi - \varphi_p) - \sin(\varphi - \varphi_p) \right] H(\varphi - \varphi_p), \quad (24)$$

where P and φ_p denote the jack force and its circumferential position, respectively, and $H(\varphi - \varphi_p)$ stands for the Heaviside function. The load integral of the radial displacement for interfacial discontinuities happening at circumferential position ϕ_j reads as [24]:

$$u^L(\varphi) = \left[\Delta u_j \cos(\varphi - \varphi_j) + \Delta v_j \sin(\varphi - \varphi_j) + R \Delta \theta_j \sin(\varphi - \varphi_j) \right] H(\varphi - \varphi_j), \quad (25)$$

where Δu_j , Δv_j and $\Delta \theta_j$, are the interfacial discontinuities of the radial displacement, the circumferential displacement, and the cross-sectional rotation, respectively. The expressions for the remaining five load integrals are also available in [24]. The prescribed point loads, P , the measured interfacial displacement/rotation discontinuities, Δu_j , Δv_j , $\Delta \theta_j$, and φ_j , appearing in the load integrals, e.g. Eqs. (24) and (25), serve as input for the “hybrid analysis”.

The state variables at the initial cross-section are determined as follows: Measuring φ from the middle cross-section of the crown segment and specifying the transfer relations (23) for $\varphi = 2\pi$ provides a relation between the vectors of the state variables at the initial and the final (index “f”) cross-section. The compatibility of the deformations of the *closed* ring requires $u_f = u_i$, $v_f = v_i$, $\theta_f = \theta_i$. These three conditions permit determination of the static variables at the initial cross-section, i.e. of M_i , N_i , and V_i . The kinematic state variables at the initial cross-section, u_i , v_i , and θ_i , refer to rigid body motions. Therefore, they may be set equal to zero or to arbitrary non-zero values.

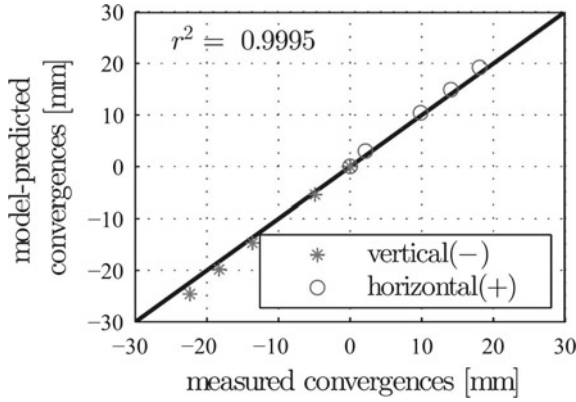


Fig. 9 Comparison of the convergences obtained from the simulation and the measurements [24]

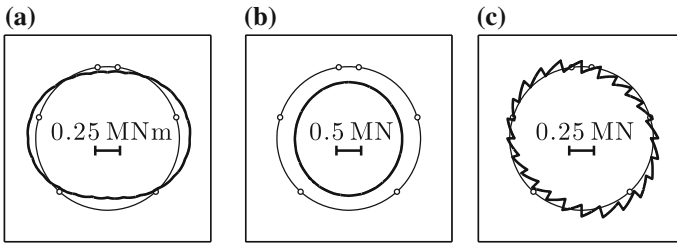


Fig. 10 Analysis results referring to the 4th load step at which cracking of concrete started: **a** bending moment distribution; **b** axial force distribution; **c** shear force distribution [24]

In order to validate the simulation approach, the normal stresses of the concrete and the two orthogonal convergences are computed and compared to the experimental results. The computed stresses exceed the tensile strength of concrete (see Eq. (22)) at the 4th load step, which agrees perfectly well with the corresponding experimental observation that cracking was first observed at this load step [23]. This proves the usefulness of the model. In addition, the model-predicted convergences agree very well with measurements, as follows from the quadratic correlation coefficient, amounting to $r^2 = 0.9995$, see Fig. 9. Notably, this comparison is a non-trivial assessment of the predictive capabilities of the model, (a) since the experimentally measured convergences are independent of the input of the model, and (b) since the model does not involve any fitted parameters.

Figure 10 shows the distributions of the bending moments, the axial forces, and the shear forces along the axis of the ring. Figure 11 illustrates the deformed configuration of the segmented tunnel and the stress-to-strength ratio of concrete [24].

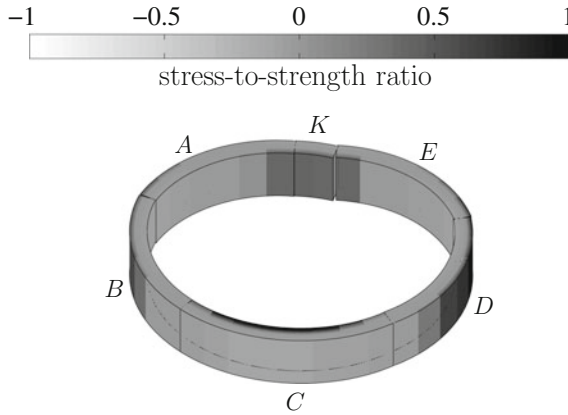


Fig. 11 Deformed configuration and stress-to-strength ratio of concrete at the 4th load step; the magnification factors of the cross-sectional dimensions and the displacements are 1 and 100, respectively [24]

6.3 Conclusions

A multiscale micro-fracture-mechanics model permits upscaling of the elastic stiffness and the tensile strength from the molecular to the material scale. “Hybrid analysis” provides a shortcut to avoid the challenge of conventional structural analysis, involving identification of the constitutive relations of the interfaces between the segments. Up to the stage of concrete cracking, the proposed analysis approach reproduced the experimental observations. It increases the insight into the structural behavior of the tested tunnel ring.

The present work is viewed as the first step towards a multiscale-hybrid method for the design of segmented tunnel linings. In order to consider cracking in a straightforward manner, a softening law of concrete on the basis of micro-fracture-mechanics is desirable. As for design-oriented calculations, the interfacial dislocations are unknown. The development of a reliable model of the interfacial behavior is a topic of ongoing research, see also Sect. 5.

7 Summary and Conclusions

The structural behavior of tunnel linings is strongly influenced by the material behavior of concrete. The latter results etiologically from thermo-hygro-chemo-mechanical processes, occurring at the microstructure of the hierarchically organized material. This is the motivation for multiscale structural analysis, which aims at relating the *causes* at microstructural material scales to the *effects* at macrostructural scales of tunnel linings. It consists of three steps: (a) Identification of the microstructural

processes, influencing the structural behavior. (b) Upscaling of the microstructural processes to the material scale of concrete. (c) Performing structural simulations, based on multiscale models of concrete. The four topics addressed in the present contribution are related to different stages of multiscale structural analysis.

Concrete failure under impact loading refers to crack propagation along nanoscopic material interfaces [10, 26]. Cracking starts, once the static strength is reached. The speed of the crack propagation is equal to the Rayleigh wave speed [12]. During cracking, i.e. during the evolution of concrete failure, the impact load can be further increased, thus resulting in high-dynamic strengthening. In the present contribution, the probabilistic version of the described multiscale model was successfully applied to re-analysis of a series of high-dynamic tests regarding the uniaxial compressive strength of concrete [11].

When concrete is subjected to temperature changes, homogenization techniques for eigenstrains are used for scale transitions [15]. Mismatching thermal expansion coefficients of the cement paste and the aggregates, respectively, are upscaled to the effective thermal expansion coefficient of the concrete. Stresses imposed on the concrete are downscaled to average stresses of the cement paste and the aggregates, respectively. Applying this model in the context of multiscale structural analysis, it was shown that sudden cooling of a concrete structure is particularly harmful, because tensile stresses are concentrated in the cement paste, thus increasing the risk of cracking of concrete.

Multiscale structural analysis may be carried out with standard FE software and the phenomenological material models implemented therein. This became possible by involving a multiscale model for tensile failure of concrete, which uses a crack density parameter as the damage variable. The model establishes relations between the Young's modulus, the tensile strength, and the fracture energy of concrete. This enables a significant reduction of fitting parameters in the typical case that default FE input values do not allow for reproducing the measured structural behavior reliably, thus raising the need for model updating techniques.

Multiscale structural analysis was also applied to a real-scale test on a segmented tunnel ring. Stiffness and strength of the concrete were quantified by means of the aforementioned multiscale material model. As for the structural analysis, the prescribed external loading *and* the measured discontinuities of displacements/rotations at the segment-to-segment interfaces served as input for analytically derived transfer relations for circular segmented tunnel linings. This allowed for a hybrid analysis of the experiment without the need to describe the nontrivial behavior of the segment-to-segment interfaces.

Acknowledgements Financial support by the Austrian Science Fund (FWF), provided within project P 281 31-N32 Bridging the Gap by Means of Multiscale Structural Analyses, is gratefully acknowledged. Interesting discussions with J. Kalliauer and M. Ausweger and support by them are also gratefully acknowledged.

References

1. H.A. Mang, Bridging the gap by means of multiscale structural analyses. Research project supported by the Austrian Science Fund (FWF) P281, 31–N32 (2015)
2. Comité Euro-International du Béton, CEB-FIP Model Code (1993)
3. J.W. Tedesco, C.A. Ross, Strain-rate-dependent constitutive equations for concrete. *J. Press. Vessel Technol.* **120**, 398–405 (1998)
4. D.L. Grote, S.W. Park, M. Zhou, Dynamic behavior of concrete at high strain rates and pressure: I. Experimental characterization. *Int. J. Impact Eng.* **25**(9), 869–886 (2001)
5. H. Mihashi, F.H. Wittmann, Stochastic approach to study the influence of rate of loading on strength of concrete. *Heron* **25** (1980)
6. Z.P. Bazant, F.C. Caner, M.D. Adley, S.A. Akers, Fracturing rate effect and creep in microplane model for dynamics. *J. Eng. Mech.* **126**, 962–970 (2000)
7. D.M. Cotsovos, M.N. Pavlovic, Numerical investigation of concrete subjected to compressive impact loading. Part I: a fundamental explanation for the apparent strength gain at high loading rates. *Comput. Struct.* **86**, 145–163 (2008)
8. Q.M. Li, H. Meng, About the dynamic strength enhancement of concrete-like materials in a split Hopkinson pressure bar test. *Int. J. Solid Struct.* **40**, 343–360 (2003)
9. G. Gary, P. Bailly, Behaviour of quasi-brittle material at high strain rate. experiment and modelling. *Eur. J. Mech. A/Solid* **17**(3), 403–420 (1998)
10. I. Fischer, B. Pichler, E. Lach, C. Terner, E. Barraud, F. Britz, Compressive strength of cement paste as a function of loading rate: experiments and engineering mechanics analysis. *Cem. Concr. Res.* **58**, 186–200 (2014)
11. T. Kühn, C. Steinke, Z. Sile, I. Zreid, M. Kaliske, M. Curbach, Dynamische Eigenschaften von Beton im Experiment und in der Simulation (Dynamic properties of concrete in experiments and simulations). *Beton-und Stahlbeton* **111** (2016)
12. F.F. Abraham, H. Gao, How fast can cracks propagate? *Phys. Rev. Lett.* **84**(14), 3113–3116 (2000)
13. J.K. Emanuel, J.L. Hulsey, Prediction of the thermal coefficient of expansion of concrete. *ACI J.* **74**, 149–155 (1977)
14. V.M. Levin, Coefficients of temperature expansion of heterogeneous materials. *Mekha. Tverd. Tela* **2**, 83–94 (1967)
15. B. Pichler, C. Hellmich, Estimation of influence tensors for eigenstressed multiphase elastic media with nonaligned inclusion phases of arbitrary ellipsoidal shape. *J. Eng. Mech.* **136**, 1043–1053 (2010)
16. M. Ausweger, Spannungen und Verformungen gerader Einzelstäbe zufolge Temperaturbeanspruchung (Stresses and deformation of straight beams resulting from temperature changes). Bachelor thesis, Vienna University of Technology, Austria (2016)
17. G.M. Gladwell, *Contact Problems in the Classical Theory of Elasticity* (Springer Science & Business Media, 1980)
18. P. Janßen, Tragverhalten von Tunnelausbauten mit Gelenktübbings (Structural behavior of segmented tunnel linings) Ph.D. thesis, Technical University of Braunschweig, Germany, 1986
19. F. Leonhardt, H. Reimann, Betongelenke (Concrete hinges). *Dtsch. Ausschuss für Stahlb.* **175**, 1–33 (1965). German
20. T. Schlappal, M. Schweigler, S. Gmainer, M. Peyerl, B. Pichler, Creep and cracking of concrete hinges—Insight from centric and eccentric experiments. *Mat. Struct.* Under Review (2017)
21. J. Kalliauer, T. Schlappal, M. Vill, H.A. Mang, B. Pichler, Bearing capacity of concrete hinges subjected to eccentric compression—Multiscale structural analysis of experiments. *Acta Mech.* Accepted for Publication (2017)
22. M. Hlobil, M. Göstl, J. Burrus, C. Hellmich, B. Pichler, Molecular-to-macro upscaling of concrete fracture: theory and experiments. *J. Mech. Phys. Sol.* Under Revision
23. X. Liu, Y. Bai, Y. Yuan, H.A. Mang, Experimental investigation of the ultimate bearing capacity of continuously-jointed segmental tunnel linings. *Struct. Infrastruct. E* **12**, 1–16 (2016)

24. J.L. Zhang, C. Vida, Y. Yuan, C. Hellmich, H.A. Mang, B. Pichler, A hybrid analysis method for displacement-monitored segmented circular tunnel rings. *Eng. Struct.* Accepted for Publication (2017)
25. J.L. Zhang, H.A. Mang, X. Liu, Y. Yuan, B. Pichler, Hybrid multiscale analysis of the bearing capacity of a segmented tunnel ring
26. B. Pichler, I. Fischer, E. Lach, C. Turner, E. Barraud, F. Britz, The influence of loading rate on the compressive strength of cementitious materials: experiments and separation of time scales-based analysis, in *Computational Modeling of Concrete Structures, Proceedings of Euro-C*, vol 2 (2014), pp. 731–739

Phase-Field Formulation for Ductile Fracture

Michael J. Borden, Thomas J.R. Hughes, Chad M. Landis,
Amin Anvari and Isaac J. Lee

Abstract Phase-field models have been a topic of much research in recent years. Results have shown that these models are able to produce complex crack patterns in both two and three dimensions. A number of extensions from brittle to ductile materials have been proposed and results are promising. To date, however, these extensions have not accurately represented strains after crack initiation or included important aspects of ductile fracture such as stress triaxiality. This work describes a number of contributions to further develop phase-field models for fracture in ductile materials.

1 Introduction

One of the authors (TJRH) has enjoyed the friendship of D.R.J. (“Roger”) Owen for a very long time, measured in many decades rather than years. Roger is a brilliant engineering scientist who has made enormous contributions to computational mechanics, especially in the area of inelasticity and particle methods. His work on this latter topic is some of the most important and impressive in recent decades. What is remarkable about Roger is that despite his strong work ethic resulting in a very long list of outstanding publications, and all the time it has taken to be a successful entrepreneur and founder of a very successful engineering company, he has found time to enjoy life and have fun. In fact, he has found a great deal of time to enjoy life and have fun! That is why he is a great friend. Roger, best wishes on your

M.J. Borden (✉)

Civil, Construction, and Environmental Engineering, North Carolina State University, Box 7908, Raleigh, NC 27695, USA
e-mail: mjborden@ncsu.edu

T.J.R. Hughes · C.M. Landis · I.J. Lee

Institute for Computational Engineering and Science, The University of Texas at Austin, 201 East 24th St. Stop C0200, Austin, TX 78712, USA

T.J.R. Hughes · C.M. Landis · A. Anvari

Aerospace Engineering and Engineering Mechanics, The University of Texas at Austin, 210 East 24th St. Stop C0600, Austin, TX 78712, USA

© Springer International Publishing AG 2018

E. Oñate et al. (eds.), *Advances in Computational Plasticity*, Computational Methods in Applied Sciences 46, DOI 10.1007/978-3-319-60885-3_3

75th birthday, and good health and many more productive years in the future. This paper is dedicated to you with affection.

The development of computational methods that accurately predict complex failure and fracture processes in ductile materials has proven difficult, particularly for full three-dimensional geometries, and many approaches have been proposed with varying success. The phase-field method, also known as the variational approach to fracture, is an approach that has recently received much attention in the literature. It has been shown that this method is able to produce complex crack patterns, including branching and merging, in both two and three dimensions. This approach leads to a system of partial differential equations that fully describe the evolution of crack surfaces without the need for ad hoc additions to the theory. Computations with this method are performed on the original mesh and no crack interface tracking is required. This leads to robust computational implementations. To date, most of the research has focused on brittle material. In this work we introduce additions and modifications to the theory that improve its ability to predict fracture in ductile materials.

The variational approach to brittle fracture, proposed by Francfort and Marigo [16], seeks to find a solution to the fracture problem by minimizing a potential energy based on Griffith's theory of brittle fracture. This approach leads to a Mumford-Shah [34] type energy potential that can be approximated by a phase-field formulation following the work of Ambrosio and Tortorelli [3]. This approximation was adopted by Bourdin et al. [10] to facilitate numerical solutions of the variational formulation. An alternative formulation, based on continuum mechanics and thermodynamic arguments, was presented by Miehe et al. [27, 28]. In addition to an alternative derivation, Miehe et al. [27] also added an important mechanism for distinguishing tensile and compressive effects on crack growth. The works of Larsen [23], Larsen et al. [24], Bourdin et al. [8, 12], and Hofacker and Miehe [21] have shown that this approach can be extended to dynamic fracture and produces results that agree well with several benchmark problems. Other problems of interest that the variational approach to fracture has been applied to include hydraulic fracturing [13, 33], piezoelectric ceramics [42], rubbery polymers [30], and thermo-elastic solids [31].

Initial work to extend the variational approach to ductile materials has been reported in Ambati et al. [1, 2] and Miehe et al. [29, 32]. The approach presented by Ambati et al. [1] augments the degradation function by a term that increases damage based on the accumulation of an equivalent plastic strain measure. Miehe et al. [29] have modified the history functional, \mathcal{H} , which drives the evolution of the phase-field, to include an equivalent plastic strain measure. A similar approach is presented by McAuliffe and Waisman [25] where a model that couples the phase-field with ductile shear band development is described. In this approach shear bands are modeled using an elastic-viscoplastic model and fracture is modeled as the degradation of the volumetric elastic stress terms only (the deviatoric stress is undamaged).

In these previous approaches, however, the accumulation of plastic deformation reduces the elastic strength of the material in some way, but the plastic response is unmodified. This means that the yield surface and hardening modulus are not effected by the evolution of the phase-field. The result of this is that at some point

the plastic strains saturate and the deformation becomes dominated by recoverable elastic strains. However, the experimental results presented in [17] show that ductile failure of an aluminum alloy is preceded by large plastic strains and that void nucleation and growth occurs in a relatively short strain interval just before failure. This behavior is contrary to what is predicted by the existing phase-field models for ductile materials.

In this work we present several contributions for phase-field models of fracture in ductile materials. These contributions include: (1) A microforce derivation of the governing equations in terms of a general energy potential for finite deformation problems. (2) The introduction of a yield surface degradation function that provides a mechanism for plastic softening and corrects the non-physical elastic deformations after crack initiation. (3) A mechanism for including a measure of stress triaxiality as a driving force for crack initiation and propagation. (4) A modification of the elastoplastic return mapping algorithm for J_2 flow theory presented by Simo and Hughes [38] that corrects an error in the update of the elastic configuration, which leads to errors in the calculation of the strain energy.

The paper will proceed as follows: In Sect. 2 we will establish the notation, describe the phase-field approach to fracture, and present a balance law derivation of the governing equations in terms of a general energy potential. In Sect. 3 we will present the hyperelastic-plastic constitutive model that governs the stress response of a body and determines the contributing factors to crack growth. In this section we introduce new developments that couple crack growth with stress triaxiality and plastic softening. A summary of the constitutive model is given in Sect. 3.4. Section 4 presents the return mapping algorithm. Numerical results are presented in Sect. 5 for an explosively loaded plate structure.

2 Formulation

In this section we develop a large deformation phase-field formulation for fracture in ductile materials. In this formulation, we will assume an energetic description of the fracture process and derive the governing equations from an energy balance principle.

2.1 Kinematics

We begin by establishing the notation that we will use to describe the kinematics of the body. We let $\Omega_0 \subset \mathbb{R}^d$ (with $d \in \{2, 3\}$) be the reference configuration of an arbitrary body with external boundary $\partial\Omega_0$ and evolving internal discontinuity boundary $\Gamma_0(t)$ as shown in Fig. 1a. We assume that the internal discontinuity evolves in an irreversible manner such that $\Gamma_0(t) \subset \Gamma_0(t + \Delta t)$ for all $\Delta t > 0$. The motion of the body is described by the time dependent deformation map $\varphi : (\Omega_0 \times \mathbb{R}) \rightarrow \mathbb{R}^d$,

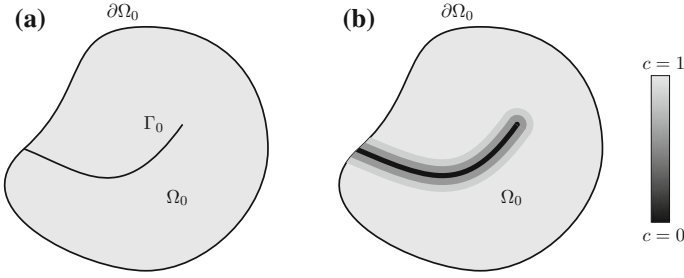


Fig. 1 **a** A sketch of a body, Ω_0 , with an internal discontinuity boundary Γ_0 . **b** The phase-field representation of the internal discontinuity

which maps a point $\mathbf{X} \in \Omega_0$ at time $t \in [0, T]$ to a point $\mathbf{x} = \varphi(\mathbf{X}, t) \in \mathbb{R}^d$. The reference configuration is mapped to the current configuration through the motion as $\Omega_t = \varphi(\Omega_0, t)$ and the boundary of the current configuration is represented as $\partial\Omega_t$. The internal discontinuity is also mapped to the current configuration through the motion as $\Gamma_t = \varphi(\Gamma_0(t), t)$.

The deformation gradient is a second-order tensor defined as

$$\mathbf{F} = \varphi_{,\mathbf{X}}(\mathbf{X}, t) = \frac{\partial \varphi(\mathbf{X}, t)}{\partial \mathbf{X}}, \quad (1)$$

and the displacement of a point \mathbf{X} at time t is denoted by $\mathbf{u}(\mathbf{X}, t) = \varphi(\mathbf{X}, t) - \mathbf{X}$. The displacement field satisfies time-dependent Dirichlet boundary conditions, $u_i(\mathbf{X}, t) = g_i(\mathbf{X}, t)$, on $\partial\Omega_{g_i} \subseteq \partial\Omega_t$, and time-dependent Neumann boundary conditions on $\partial\Omega_{h_i} \subseteq \partial\Omega_t$.

For a ductile response, we assume the existences of a stress-free deformation from which the elastic deformation can be characterized. This assumption leads to a local multiplicative decomposition of the deformation gradient into elastic and plastic parts that takes the form

$$\mathbf{F} = \mathbf{F}^e \mathbf{F}^p \quad (2)$$

where \mathbf{F}^e and \mathbf{F}^p are the elastic and plastic deformations gradients respectively (see Simo and Hughes [38] for details). We denote derivatives with respect to the coordinates in the reference configuration as

$$(\cdot)_{,\mathbf{X}} = \frac{\partial}{\partial \mathbf{X}}(\cdot) \quad \text{DIV}(\cdot) = \frac{\partial}{\partial \mathbf{X}} \cdot (\cdot) \quad \Delta_{\mathbf{X}}(\cdot) = \frac{\partial}{\partial \mathbf{X}} \cdot (\cdot)_{,\mathbf{X}}. \quad (3)$$

2.2 Phase-Field Approximations of Fracture

For energetic descriptions of fractured bodies, e.g. Griffith's theory of brittle fracture, the stored energy of a body can be written in the reference configuration as

$$\Psi(\mathbf{F}, \Gamma_0) = \int_{\Omega_0} W(\mathbf{F}) \, d\Omega_0 + \int_{\Gamma_0} \mathcal{G}_c^0 \, d\Gamma_0 \quad (4)$$

where W is the elastic strain energy per unit volume and \mathcal{G}_c^0 is the critical fracture energy per unit area in the reference configuration. For the case of brittle fracture, Francfort and Marigo [16] have proposed a variational approach that predicts crack evolution by finding a global minimizer of (4). To facilitate the numerical solution of this problem, Bourdin et al. [11] introduced a phase-field approximation of (4) that takes the form

$$\tilde{\Psi}(\mathbf{F}, c, c_{,\mathbf{X}}) = \int_{\Omega_0} g(c)W(\mathbf{F}) \, d\Omega_0 + \int_{\Omega_0} \mathcal{G}_c^0 \Gamma_c(c, c_{,\mathbf{X}}) \, d\Omega_0 \quad (5)$$

where $c \in [0, 1]$ is the phase-field parameter, $g(c)$ is the degradation function that acts to reduce the elastic strength of the material, and

$$\int_{\Omega_0} \mathcal{G}_c^0 \Gamma_c \, d\Omega_0 \approx \int_{\Gamma_0} \mathcal{G}_c^0 \, d\Gamma_0 \quad (6)$$

is a volumetric approximation of the energy contribution from the crack surface. We call Γ_c the crack density functional, which typically takes the form

$$\Gamma_c(c, c_{,\mathbf{X}}) = \frac{1}{4\ell_0} [(c-1)^2 + 4\ell_0^2 |c_{,\mathbf{X}}|^2] \quad (7)$$

where $\ell_0 \in \mathbb{R}^+$ is a length scale parameter that determines the width of the approximation. Other crack density functionals have been proposed, for example those by Burke et al. [15] and also a higher-order functional by Borden et al. [9].

Amor et al. [4], Miehe et al. [27, 28] further refined this approximation by introducing an additive decomposition of the elastic strain energy to distinguish between tensile and compressive contributions. The resulting approximation takes the form

$$\tilde{\Psi}(\mathbf{F}, c, c_{,\mathbf{X}}) = \int_{\Omega_0} \{g(c)W^+(\mathbf{F}) + W^-(\mathbf{F})\} \, d\Omega_0 + \int_{\Omega_0} \mathcal{G}_c^0 \Gamma_c(c, c_{,\mathbf{X}}) \, d\Omega_0 \quad (8)$$

where W^+ represents tensile contributions and W^- represents compressive contributions to the stored elastic strain energy. This modification provides a mechanism for distinguishing states of strain under which cracks will grow. For example, one popular decomposition introduced in [27, 28] is based on a spectral decomposition

of the strain tensor. In this form the sign of the principal strains are used to determine tensile and compressive contributions. Another approach proposed in [4] uses a constitutive model that decouples the volumetric and deviatoric response and defines the tensile contributions as the deviatoric part of the model. We will discuss these approaches in more detail in Sect. 3.1.

For the energy functional presented in (8) crack growth is driven by elastic strain energy. To extend this theory to ductile materials and provide a mechanism for plastic yielding to contribute to crack growth we add an effective plastic work contribution, W_p , to the stored energy. The stored energy functional that we propose is

$$\begin{aligned} \check{\Psi}(\mathbf{F}, c, c_{,\mathbf{x}}, \mathbf{F}^p, \alpha) = & \int_{\Omega_0} \{g(c)W^+(\mathbf{F}, \mathbf{F}^p) + W^-(\mathbf{F}, \mathbf{F}^p) + g_p(c)W_p(\alpha)\} d\Omega_0 \\ & + \int_{\Omega_0} \frac{\mathcal{G}_c^0}{4\ell_0} [(c-1)^2 + 4\ell_0^2 |c_{,\mathbf{x}}|^2] d\Omega_0 \end{aligned} \quad (9)$$

where α is an internal hardening variable and $g_p(c)$ is the plastic degradation function. The plastic degradation function is analogous to the elastic degradation function and provides a mechanism for driving crack growth by the development of plastic strains.

2.3 Balance Law Derivation of the Phase-Field Fracture Model

In this section we postulate the existence of a microforce balance law that describes the kinematics of the phase-field. This balance law supplements the usual linear and angular momentum balance laws and provides a theory that allows a general, thermodynamically consistent derivation of the governing equations for phase-field models of fracture. This derivation separates balance laws from constitutive behavior. It also provides a natural way to introduce dissipation mechanisms through a general analysis of the second law of thermodynamics.

Microforce theories have been applied to other phase-field models. For example, Gurtin [19] has derived the Cahn-Hilliard equation from a microforce balance law. In addition, Stumpf and Hackl [39] introduced a microforce derivation for damage laws that provides a thermodynamically consistent framework for thermo-viscoelastic and quasi-brittle materials. More recently, a phase-field model for fracture in piezoelectric ceramics has been derived by Wilson et al. [42] based on a microforce approach. We follow the developments of this later work to derive a formulation in the large deformation setting restricted to purely mechanical processes.

We begin the derivation of the phase-field model with the usual linear and angular momentum balance laws. In order to localize the balance laws, we assume that the following integral equations hold for all $\mathcal{U} \subset \Omega_0$, where \mathcal{U} is an open set with

Lipshitz boundary $\partial\mathcal{U}$, and we assume all integrands are at least C^0 -continuous functions. The linear and angular momentum balance laws are

Linear momentum:

$$\frac{d}{dt} \int_{\mathcal{V}} \rho_0 \dot{\mathbf{U}} d\mathcal{V} = \int_{\mathcal{V}} \mathbf{B} d\mathcal{V} + \int_{\partial\mathcal{V}} \mathbf{PN} d\partial\mathcal{V} \quad (10)$$

$$\Rightarrow \text{DIV } \mathbf{P} + \mathbf{B} = \rho_0 \ddot{\mathbf{U}} \quad (11)$$

Angular momentum:

$$\frac{d}{dt} \int_{\mathcal{V}} \mathbf{x} \times \rho_0 \dot{\mathbf{U}} d\mathcal{V} = \int_{\mathcal{V}} \mathbf{x} \times \mathbf{B} d\mathcal{V} + \int_{\partial\mathcal{V}} \mathbf{x} \times (\mathbf{PN}) d\partial\mathcal{V} \quad (12)$$

$$\Rightarrow \mathbf{PF}^T = \mathbf{FP}^T \quad (13)$$

where ρ_0 is the mass density in the reference configuration, \mathbf{P} is the first Piola-Kirchhoff stress tensor, \mathbf{N} is the outward unit normal of $\partial\mathcal{U}$, \mathbf{B} is the body force, \mathbf{U} is the displacement, and the superposed dot is the material time derivative.

To derive the microforce balance law, we assume that at each time step the phase-field can be characterized by an internal microforce $\pi(\mathbf{x}, t) \in \mathbb{R}$, an external microforce $l(\mathbf{x}, t) \in \mathbb{R}$ acting on the body, and an external microforce $\lambda(\mathbf{x}, t) \in \mathbb{R}$ acting on the surface of the body. We also assume the existence of a micro force traction vector, $\xi(\mathbf{x}, t) \in \mathbb{R}^d$, such that $\lambda = \xi \cdot \mathbf{N}$ on $\partial\mathcal{U}$. Furthermore, we assume that there are no inertial terms associated with the microforces. Given these assumptions, we postulate the microforce balance law to be

Microforce:

$$\int_{\partial\mathcal{V}} \xi \cdot \mathbf{N} d\partial\mathcal{V} + \int_{\mathcal{V}} l d\mathcal{V} + \int_{\mathcal{V}} \pi d\mathcal{V} = 0 \quad (14)$$

$$\Rightarrow \text{DIV } \xi + \pi + l = 0. \quad (15)$$

Given these balance laws, the thermodynamic analysis of the phase-field fracture model follows:

Energy Balance Letting e denote the internal energy per unit mass density and noting that \dot{c} is rate-of-work conjugate to the microforces, the energy balance is stated as

$$\frac{d}{dt} \int_{\mathcal{V}} \left(\frac{1}{2} \rho_0 |\dot{\mathbf{U}}|^2 + \rho_0 e \right) d\mathcal{V} \quad (16)$$

$$= \int_{\partial\mathcal{V}} (\mathbf{PN}) \cdot \dot{\mathbf{U}} d\partial\mathcal{V} + \int_{\mathcal{V}} \mathbf{B} \cdot \dot{\mathbf{U}} d\mathcal{V} + \int_{\partial\mathcal{V}} (\xi \cdot \mathbf{N}) \dot{c} d\partial\mathcal{V} + \int_{\mathcal{V}} l \dot{c} d\mathcal{V}$$

$$\Rightarrow \rho_0 \dot{e} = \mathbf{P} : \dot{\mathbf{F}} + \xi \cdot \dot{c}_{,X} - \pi \dot{c}. \quad (17)$$

Second law Let s be the entropy per unit mass density. Then the second law of thermodynamics can be stated as

$$\frac{d}{dt} \int_{\mathcal{V}} \rho_0 s \, d\mathcal{V} \geq - \int_{\partial\mathcal{V}} \frac{\mathbf{q} \cdot \mathbf{N}}{\Theta} \, d\partial\mathcal{V} + \int_{\mathcal{V}} \frac{\rho_0 r}{\Theta} \, d\mathcal{V} \quad (18)$$

$$\Rightarrow \Theta \rho_0 \dot{s} \geq \frac{1}{\Theta} \mathbf{q} \cdot \Theta_{,X} - \text{DIV } \mathbf{q} + \rho_0 r \quad (19)$$

where Θ is absolute temperature, \mathbf{q} is the heat flux, and r is a heat source. For the formulation presented here we assuming $r = 0$, $\text{DIV } \mathbf{q} = 0$, and $\Theta_{,X} = \mathbf{0}$. Under these assumptions, the second law inequality simplifies to

$$\Theta \rho_0 \dot{s} \geq 0. \quad (20)$$

Dissipation inequality Using the Legendre transformation we write the internal energy in terms of the Helmholtz free energy and entropy as

$$\rho_0 e = \rho_0 \psi + \Theta \rho_0 s. \quad (21)$$

The dissipation inequality follows from this equation and is given by

$$\rho_0 \dot{\psi} \leq \rho_0 \dot{e}. \quad (22)$$

Substituting (17) into (22), the dissipation inequality is written in terms of the Piola-Kirchhoff stress tensors and microforces as

$$\rho_0 \dot{\psi} \leq \mathbf{P} : \dot{\mathbf{F}} + \boldsymbol{\xi} \cdot \dot{c}_{,X} - \pi \dot{c} \quad (23)$$

or

$$\rho_0 \dot{\psi} \leq \frac{1}{2} \mathbf{S} : \dot{\mathbf{C}} + \boldsymbol{\xi} \cdot \dot{c}_{,X} - \pi \dot{c} \quad (24)$$

where $\mathbf{C} = \mathbf{F}^T \mathbf{F}$ is the right Cauchy-Green deformation tensor and $\mathbf{S} = \mathbf{F}^{-1} \mathbf{P}$ is the second Piola-Kirchhoff stress tensor.

This derivation provides a general formulation for phase-field fracture models. As long as the free energy, ψ , is defined such that (23) and (24) hold the model will be thermodynamically consistent.

2.3.1 Governing Equations

To derive the governing equations we assume the Helmholtz free energy function takes the general form $\psi = \psi(\mathbf{C}, \mathbf{C}^p, \mathbf{Q}, c, c_{,X}, \dot{c})$, where \mathbf{Q} is a set of internal plastic variables and

$$\mathbf{C}^p = \mathbf{F}^{pT} \mathbf{F}^p \quad (25)$$

is the plastic right Cauchy-Green deformation tensor. Substituting this into (24) and integrating over the reference domain we get

$$\begin{aligned} & \int_{\Omega_0} \left(\rho_0 \frac{\partial \psi}{\partial \mathbf{C}} : \dot{\mathbf{C}} + \rho_0 \frac{\partial \psi}{\partial \mathbf{C}^p} : \dot{\mathbf{C}}^p + \rho_0 \frac{\partial \psi}{\partial \mathbf{Q}} \cdot \dot{\mathbf{Q}} + \rho_0 \frac{\partial \psi}{\partial c} \dot{c} + \rho_0 \frac{\partial \psi}{\partial c_{,X}} \cdot \dot{c}_{,X} + \rho_0 \frac{\partial \psi}{\partial \dot{c}} \ddot{c} \right) d\Omega_0 \\ & \leq \int_{\Omega_0} \left(\frac{1}{2} \mathbf{S} : \dot{\mathbf{C}} + \xi \cdot \dot{c}_{,X} - \pi \dot{c} \right) d\Omega_0. \end{aligned} \quad (26)$$

We now wish to relate terms on the left hand side of the inequality with terms on the right hand side. We begin by noting that for purely elastic deformations, we can assume that the plastic dissipation, defined as

$$\mathbb{D}^p(\mathbf{C}, \mathbf{C}^p, \mathbf{Q}; \dot{\mathbf{C}}^p, \dot{\mathbf{Q}}) = -\rho_0 \frac{\partial \psi}{\partial \mathbf{C}^p} : \dot{\mathbf{C}}^p - \rho_0 \frac{\partial \psi}{\partial \mathbf{Q}} \cdot \dot{\mathbf{Q}}, \quad (27)$$

is zero. The remaining terms on the left hand side are linear in $\dot{\mathbf{C}}$, \dot{c} , $\dot{c}_{,X}$, and \ddot{c} and we assume that the inequality must hold for arbitrary time histories of these variables. This leads to the following relations:

$$\rho_0 \frac{\partial \psi}{\partial \dot{c}} = 0 \quad (28)$$

$$\rho_0 \frac{\partial \psi}{\partial c_{,X}} = \xi \quad (29)$$

$$2\rho_0 \frac{\partial \psi}{\partial \mathbf{C}} = \mathbf{S} \quad (30)$$

$$\left(\pi + \rho_0 \frac{\partial \psi}{\partial c} \right) \dot{c} \leq 0 \Rightarrow \pi = -\rho_0 \frac{\partial \psi}{\partial c} - \beta \dot{c} \quad (31)$$

$$\mathbb{D}^p = -\rho_0 \frac{\partial \psi}{\partial \mathbf{C}^p} : \dot{\mathbf{C}}^p - \rho_0 \frac{\partial \psi}{\partial \mathbf{Q}} \cdot \dot{\mathbf{Q}} \geq 0 \quad (32)$$

where $\beta = \beta(\mathbf{C}, \mathbf{C}^p, c, c_{,X}) \geq 0$ a function that can be used to account for other dissipation mechanisms. Substituting these equations into the balance laws using $\mathbf{P} = \mathbf{F}\mathbf{S}$ we get:

Linear momentum:

$$\text{DIV} \left(2\mathbf{F}\rho_0 \frac{\partial \psi}{\partial \mathbf{C}} \right) + \mathbf{B} = \rho_0 \ddot{\mathbf{U}} \quad (33)$$

Microforce:

$$\text{DIV} \left(\rho_0 \frac{\partial \psi}{\partial \mathbf{c}, \mathbf{x}} \right) + l - \rho_0 \frac{\partial \psi}{\partial c} = \beta \dot{c} \quad (34)$$

With the governing equations of motion and the second-order approximation from Sect. 2.2 in hand, we can derive the strong form of the phase-field model for ductile fracture. It follows from (9) that the Helmholtz free-energy is given by

$$\rho_0 \psi(\mathbf{C}, \mathbf{C}^p, \mathbf{Q}, c, c, \mathbf{x}) = g(c)W^+(\mathbf{C}, \mathbf{C}^p) + W^-(\mathbf{C}, \mathbf{C}^p) + g_p(c)W_p(\mathbf{Q}) + \mathcal{G}_c^0 \left[\frac{(1-c)^2}{4\ell_0} + \ell_0 c, \mathbf{x} \cdot c, \mathbf{x} \right] \quad (35)$$

where we have left the energy density functions W^+ , W^- , and W_p to be defined later. Then

$$\text{DIV} \left(2\mathbf{F} \rho_0 \frac{\partial \psi}{\partial \mathbf{C}} \right) = \text{DIV} \left(2\mathbf{F} \left(g(c) \frac{\partial W^+}{\partial \mathbf{C}} + \frac{\partial W^-}{\partial \mathbf{C}} \right) \right) \quad (36)$$

$$\text{DIV} \left(\rho_0 \frac{\partial \psi}{\partial c, \mathbf{x}} \right) = 2\mathcal{G}_c^0 \ell_0 \Delta_{\mathbf{x}} c \quad (37)$$

$$\rho_0 \frac{\partial \psi}{\partial c} = g'W^+ + g'_p W_p - \mathcal{G}_c^0 \frac{1-c}{2\ell_0}. \quad (38)$$

substituting these back into (33) and (34) and taking $l = 0$ and $\beta = 0$ we get the following governing equations

$$\text{DIV} \left(2\mathbf{F} \left(g(c) \frac{\partial W^+}{\partial \mathbf{C}} + \frac{\partial W^-}{\partial \mathbf{C}} \right) \right) + \mathbf{B} = \rho_0 \ddot{\mathbf{U}} \quad (39)$$

$$\frac{2\ell_0}{\mathcal{G}_c^0} \left(g'W^+ + g'_p W_p \right) + c - 4\ell_0^2 \Delta_{\mathbf{x}} c = 1. \quad (40)$$

Irreversibility of crack growth due to elastic deformation will be enforced through the history functional introduced by Miehe et al. [27], i.e.

$$\mathcal{H}(\mathbf{C}, \mathbf{C}^p) = \max_{\hat{t} \leq t} W^+(\mathbf{C}(\hat{t}), \mathbf{C}^p(\hat{t})). \quad (41)$$

Since it is assumed that the effective plastic work, W_p , is monotonically increasing no constraints are needed to enforce irreversible crack growth due to plastic deformation. However, in order to have more control of the contribution of plastic deformation to crack growth we introduce a plastic work threshold, W_0 , to the formulation and replace W_p in (40) with $\langle W_p - W_0 \rangle$ where the angle bracket operator is defined as

$$\langle x \rangle = \begin{cases} 0 & x < 0 \\ x & x \geq 0 \end{cases}. \quad (42)$$

This modification provides a mechanism to control the point at which plastic deformation begins to contribute to crack growth. We also introduce two parameters $\beta_e \in [0, 1]$ and $\beta_p \in [0, 1]$ that may be used to weight the contribution to crack growth from elastic strain energy and plastic work. Substituting these modifications into (40) the updated phase-field equation becomes

$$\frac{2\ell_0}{\mathcal{G}_c^0} \left(\beta_e g' \mathcal{H} + \beta_p g'_p \langle W_p - W_0 \rangle \right) + c - 4\ell_0^2 \Delta_{\mathbf{x}} c = 1. \quad (43)$$

The governing equations are summarized in Sect. 3.4.1.

3 Large Deformation Constitutive Response

In Sect. 2 we have derived the strong form equations in terms of the general energy functionals W^+ , W^- , and W_p . In this section we describe the constitutive relations we use to complete the formulation. This will include a finite deformation hyperelastic constitutive model, an elastoplastic constitutive model based on J_2 flow theory with isotropic hardening, and the effective plastic work driving energy term that takes into account the state of stress triaxiality.

3.1 Finite Deformation Hyperelastic Model

The constitutive model governing the elastic response will be based on the assumption that the strain energy can be decomposed into volumetric and deviatoric contributions. We follow the strain energy decomposition introduced by Amor et al. [4] and define the tensile and compressive contributions to be

$$W^+ = \begin{cases} U(J^e) + \bar{W}(\bar{\mathbf{C}}, \mathbf{C}^p) & J^e \geq 1 \\ \bar{W}(\bar{\mathbf{C}}, \mathbf{C}^p) & J^e < 1 \end{cases} \quad (44)$$

$$W^- = \begin{cases} 0 & J^e \geq 1 \\ U(J^e) & J^e < 1 \end{cases} \quad (45)$$

respectively, where

$$J^e = \det \mathbf{F}^e \quad (46)$$

and

$$\bar{\mathbf{C}} = J^{e-2/3} \mathbf{C}. \quad (47)$$

The damaged elastic strain energy is then given by

$$W(J^e, \bar{\mathbf{C}}, \mathbf{C}^p, c) = g(c)W^+(J^e, \bar{\mathbf{C}}, \mathbf{C}^p) + W^-(J^e). \quad (48)$$

For the formulation presented here, we use the specific forms

$$U(J^e) = \frac{1}{2} \kappa \left[\frac{1}{2}(J^{e2} - 1) - \ln J^e \right], \quad (49)$$

$$\bar{W}(\bar{\mathbf{C}}, \mathbf{C}^p) = \frac{1}{2} \mu (\bar{\mathbf{C}} : \mathbf{C}^{p-1} - 3) \quad (50)$$

where κ and μ are the bulk and shear modulus respectively. The resulting constitutive model for the elastic response is summarized in Sect. 3.4.2.

3.2 Elastoplastic Constitutive Model

In this section we describe an associative elastoplastic constitutive model based on J_2 flow theory with isotropic hardening. We assume an isotropic stress response governed by the damage elastic constitutive model given in Sect. 3.4.2. We also assume the plastic flow to be isochoric, i.e.,

$$\det \mathbf{F}^p = 1 \quad \Rightarrow \quad J = \det \mathbf{F}^e. \quad (51)$$

The standard yield function for J_2 plasticity is given by

$$f(\boldsymbol{\tau}, \alpha) = \|\mathbf{s}\| - \sqrt{\frac{2}{3}} k(\alpha), \quad \mathbf{s} = \text{dev } \boldsymbol{\tau} \quad (52)$$

where α is the hardening parameter and $k(\alpha)$ the isotropic hardening modulus. The hardening law is determined by the choice of $k(\alpha)$ as, for example,

$$k(\alpha) = \begin{cases} \sigma_y & \text{(Perfect plasticity)} \\ \sigma_y + K\alpha & \text{(Linear hardening)} \end{cases} \quad (53)$$

where $\boldsymbol{\tau} = J^e \boldsymbol{\sigma}$ is the Kirchhoff stress, σ_y is the yield stress, and K is the linear hardening coefficient.

The standard yield function shown in (52) does not produce the correct physical response when coupled with the phase-field model for crack growth. As the material fails the damaged elastic response pulls the stress back within the yield surface

and any further deformation up to complete failure is purely elastic (i.e. recoverable). This is contrary to what is observed physically for ductile materials where the deformation is dominated by plastic strain. To compensate for this behavior we multiply the yield surface by the plastic degradation function, $g_p(c)$. The modified yield function that we propose is

$$f(\boldsymbol{\tau}, \alpha) = \|\mathbf{s}\| - g_p(c) \sqrt{\frac{2}{3}} k(\alpha). \quad (54)$$

The elastoplastic constitutive model is completed by the associative flow rule, which is derived assuming maximum plastic dissipation. Under this assumption, and given the constitutive model summarized in Sect. 3.4.2 and yield function (54), the flow rule is

$$\text{dev} [L_v \mathbf{b}^e] = -\frac{2}{3} \dot{\gamma} \text{tr} [\mathbf{b}^e] \mathbf{n} \quad (55)$$

$$\mathbf{n} = \frac{\mathbf{s}}{\|\mathbf{s}\|} \quad (56)$$

where $\mathbf{b}^e = \mathbf{F}^e \mathbf{F}^{eT}$, $L_v \mathbf{b}^e$ is the Lie derivative of \mathbf{b}^e (see Simo and Hughes [38] for details), and $\dot{\gamma}$ is the plastic multiplier from the constrained minimization problem that follows from the principle of maximum plastic dissipation. We note that the principle of maximum plastic dissipation determines only the deviatoric part of $L_v \mathbf{b}^e$. The evolution of the spherical part of \mathbf{b}^e must be determined by the isochoric assumption, i.e. $\det [\mathbf{b}^e] = J^2$. A brief summary of the elastic/plastic constitutive model is given in Sect. 3.4.3.

3.3 *Effective Plastic Work Driving Energy and Stress Triaxiality*

We take two approaches for computing the effective plastic work contribution to (43). In the first approach the effective plastic work is defined by the rate equation

$$\dot{W}_p = \dot{\gamma} \|\mathbf{s}\|. \quad (57)$$

This approach provides a simple measure of the effective plastic work but provides no information about the state of stress.

In the second approach we modify the rate equation (57) to include information about stress triaxiality. It has long been established that the failure of ductile materials can be characterized by a combination of the effective plastic strain and the level of stress triaxiality. Material ductility as quantified by the equivalent strain to failure is higher for stress states when the ratio of the mean stress to the effective stress

is low than when this measure of triaxiality is high. The microscopic mechanism of void growth responsible for this behavior was modeled in the seminal works of Bridgman [14], Rice and Tracey [35], and McClintock [26]. Thereafter, the Gurson-Tvergaard-Needleman (GTN) plasticity model [18, 40], which includes the volume fraction of voids as an internal variable, was established and has been used extensively to model ductile failure of metals. It is of note that the failure behavior at low triaxiality levels has received renewed interest due to the fact that the GTN model does not perform well in this regime [5–7, 20]. In this work it is recognized that the effects of triaxiality play a key role in the failure of ductile metals and must be incorporated into any phenomenological model that attempts to capture the physics of ductile failure. The recent works referenced above indicate that a full phenomenological description should incorporate triaxiality as well as the third invariant of the deviatoric stress tensor, however for the sake of simplicity the present modeling approach will implement the simpler failure criterion due to Johnson and Cook [22]. We note that the present framework allows for a more detailed failure criterion once established.

In this work stress triaxiality is measured in terms of the Kirchhoff stress as

$$\frac{\tau_m}{\|\mathbf{s}\|} \quad (58)$$

where

$$\tau_m = \frac{\text{tr} [\boldsymbol{\tau}]}{3}. \quad (59)$$

This measure of stress triaxiality is then incorporated into the measure of effective plastic work by modifying the rate equation for \dot{W}_p such that

$$\dot{W}_p = \dot{\gamma} \frac{\|\mathbf{s}\|}{\varphi} \quad (60)$$

$$\varphi = d_1 + d_2 \exp \left[d_3 \frac{\tau_m}{\|\mathbf{s}\|} \right] \quad (61)$$

where d_1 , d_2 , and d_3 are dimensionless model parameters.

3.4 Summary

In this section we summarize the initial/boundary-value problem and constitutive relations that have been described in the previous sections.

3.4.1 Strong Form Initial/Boundary-Value Problem

The strong form of the initial/boundary-value problem can be stated as

$$(S) \left\{ \begin{array}{ll} \text{DIV} \left(2\mathbf{F} \left(g(c) \frac{\partial W^+}{\partial \mathbf{C}} + \frac{\partial W^-}{\partial \mathbf{C}} \right) \right) + \mathbf{B} = \rho_0 \ddot{\mathbf{U}} & \text{on } \Omega_0 \times]0, T[\\ \frac{2\ell_0}{\mathcal{G}_c^0} \left(\beta_e g' \mathcal{H} + \beta_p g_p' \langle W_p - W_0 \rangle \right) + c - 4\ell_0^2 \Delta_{\mathbf{X}} c = 1 & \text{on } \Omega_0 \times]0, T[\\ U_i = G_i & \text{on } \partial\Omega_{0,G_i} \times]0, T[\\ T_i = H_i & \text{on } \partial\Omega_{0,H_i} \times]0, T[\\ c_{,\mathbf{X}} \cdot \mathbf{N} = 0 & \text{on } \partial\Omega_0 \times]0, T[\\ \mathbf{U}(\mathbf{X}, 0) = \mathbf{U}_0(\mathbf{X}) \quad \mathbf{X} \in \Omega_0 \\ \dot{\mathbf{U}}(\mathbf{X}, 0) = \mathbf{V}_0(\mathbf{X}) \quad \mathbf{X} \in \Omega_0 \end{array} \right. \quad (62)$$

where $G_i(\mathbf{X}, t)$ are prescribe displacement boundary conditions on $\partial\Omega_{0,G_i}$, $H_i(\mathbf{X}, t)$ are prescribed traction boundary conditions on $\partial\Omega_{0,H_i}$, $\mathbf{T} = \mathbf{P} \cdot \mathbf{N}$ is the Piola-Kirchhoff traction vector, \mathbf{U}_0 is an initial displacement, and \mathbf{V}_0 is an initial velocity. These equations of motion can be solved to find both the displacement field $\mathbf{U}(\mathbf{X}, t)$ and phase-field $c(\mathbf{X}, t)$.

3.4.2 Damaged Hyperelastic Constitutive Model

The damaged elastic constitutive model in the reference configuration.

Positive, negative and damaged elastic strain energy density functions

$$\begin{aligned} U(J^e) &= \frac{1}{2} \kappa \left[\frac{1}{2} (J^{e2} - 1) - \ln J^e \right] \\ \bar{W}(\bar{\mathbf{C}}, \mathbf{C}^p) &= \frac{1}{2} \mu \left(\bar{\mathbf{C}} : \mathbf{C}^{p-1} - 3 \right) \\ W^+(J^e, \bar{\mathbf{C}}, \mathbf{C}^p) &= \begin{cases} U(J^e) + \bar{W}(\bar{\mathbf{C}}, \mathbf{C}^p) & J^e \geq 1 \\ \bar{W}(\bar{\mathbf{C}}, \mathbf{C}^p) & J^e < 1 \end{cases} \\ W^-(J^e) &= \begin{cases} 0 & J^e \geq 1 \\ U(J^e) & J^e < 1 \end{cases} \\ W(J^e, \bar{\mathbf{C}}, \mathbf{C}^p) &= g(c) W^+(J^e, \bar{\mathbf{C}}, \mathbf{C}^p) + W^-(J^e) \end{aligned}$$

Positive, negative and damaged second Piola-Kirchhoff stress tensors

$$\mathbf{S}^+ = \begin{cases} J^e U'(J^e) \mathbf{C}^{-1} + \mu J^{e-2/3} \left[\mathbf{C}^{p-1} - \frac{1}{3} (\mathbf{C} : \mathbf{C}^{p-1}) \mathbf{C}^{-1} \right] & J^e \geq 1 \\ \mu J^{e-2/3} \left[\mathbf{C}^{p-1} - \frac{1}{3} (\mathbf{C} : \mathbf{C}^{p-1}) \mathbf{C}^{-1} \right] & J^e < 1 \end{cases}$$

$$\mathbf{S}^- = \begin{cases} \mathbf{0} & J^e \geq 1 \\ J^e U'(J^e) \mathbf{C}^{-1} & J^e < 1 \end{cases}$$

$$\mathbf{S} = g(c) \mathbf{S}^+ + \mathbf{S}^-$$

The Cauchy stress obtained by a standard push-forward of the second Piola-Kirchhoff stress

$$\boldsymbol{\sigma}^+ = \begin{cases} U'(J^e) \mathbf{I} + J^{e-1} \mu \operatorname{dev} [\bar{\mathbf{b}}^e] & J^e \geq 1 \\ J^{e-1} \mu \operatorname{dev} [\bar{\mathbf{b}}^e] & J^e < 1 \end{cases}$$

$$\boldsymbol{\sigma}^- = \begin{cases} \mathbf{0} & J^e \geq 1 \\ U'(J^e) \mathbf{I} & J^e < 1 \end{cases}$$

$$\boldsymbol{\sigma} = g(c) \boldsymbol{\sigma}^+ + \boldsymbol{\sigma}^-$$

3.4.3 Elastoplastic Constitutive Model

A finite deformation rate-independent elastoplastic constitutive model based on J_2 flow theory with an associative flow rule is considered. The stress response is governed by the damage elastic constitutive model from Sect. 3.4.2.

Elastic-plastic strain decomposition:	$\mathbf{F} = \mathbf{F}^e \mathbf{F}^p$
Isochoric assumption:	$\det [\mathbf{F}^p] = 1$ $J^e = J = \det [\mathbf{F}]$
Constitutive model (see Sect. 3.4.2):	$\boldsymbol{\sigma} = g(c) \boldsymbol{\sigma}^+ + \boldsymbol{\sigma}^-$, $\boldsymbol{\tau} = J^e \boldsymbol{\sigma}$
Mises-Huber yield function:	$f = \ \mathbf{s}\ - g_p(c) \sqrt{\frac{2}{3}} k(\alpha)$, $\mathbf{s} = \operatorname{dev} \boldsymbol{\tau}$
Flow rule:	$\operatorname{dev} [L_v \mathbf{b}^e] = -\frac{2}{3} \dot{\gamma} \operatorname{tr} [\mathbf{b}^e] \mathbf{n}$, $\mathbf{n} = \frac{\mathbf{s}}{\ \mathbf{s}\ }$ $\det [\mathbf{b}^e] = J^2$
Hardening law:	$\dot{\alpha} = \sqrt{\frac{2}{3}} \dot{\gamma}$
Kuhn-Tucker loading/unloading conditions:	$f \leq 0$, $\dot{\gamma} \geq 0$, $f \dot{\gamma} = 0$

3.4.4 Effective Plastic Work

The effective plastic work is calculated from the following rate equations:

$$\begin{aligned}
 \text{No triaxiality:} \quad & \dot{W}_p = \dot{\gamma} \|s\| \\
 & \dot{W}_p = \dot{\gamma} \frac{\|s\|}{\varphi} \\
 \text{With triaxiality:} \quad & \varphi = d_1 + d_2 \exp \left[d_3 \frac{\tau_m}{\|s\|} \right] \\
 & \tau_m = \frac{\text{tr}[\boldsymbol{\tau}]}{3}
 \end{aligned}$$

4 Return-Mapping

During plastic flow the configuration is updated based on the elastoplastic constitutive theory summarized in Sect. 3.4.3. The updated configuration at time t_{n+1} must satisfy the discrete form of the Karush-Kuhn-Tucker conditions

$$f(\boldsymbol{\tau}_{n+1}, \alpha_{n+1}) \leq 0, \quad \Delta\gamma \geq 0, \quad \Delta\gamma f(\boldsymbol{\tau}_{n+1}, \alpha_{n+1}) = 0 \quad (63)$$

where $\boldsymbol{\tau}_{n+1} = \text{tr}[\boldsymbol{\tau}_n] \mathbf{I} + g(c)\mu \text{ dev}[\bar{\mathbf{b}}_{n+1}^e]$ and $\Delta\gamma$ is the algorithmic counterpart to $\dot{\gamma}$. For each time increment $[t_n, t_{n+1}]$ we assume a trial state based on a purely elastic deformation, i.e.

$$\bar{\mathbf{f}}_{n+1} = \det[\mathbf{f}_{n+1}]^{-1/3} \mathbf{f}_{n+1} \quad (64)$$

$$\bar{\mathbf{b}}_{n+1}^{e \text{ trial}} = \bar{\mathbf{f}}_{n+1} \bar{\mathbf{b}}_n^e \bar{\mathbf{f}}_{n+1}^T \quad (65)$$

$$\alpha_{n+1}^{\text{trial}} = \alpha_n \quad (66)$$

where

$$\mathbf{f}_{n+1} = \mathbf{I} + \nabla_{x_n} \mathbf{u}_n. \quad (67)$$

is the relative deformation gradient between the configurations at time t_n and t_{n+1} . If the trial state satisfies the discrete KKT conditions then it is accepted as the updated configuration. If the discrete KKT conditions are not satisfied then the trial state is inadmissible and the configuration must be updated according to the discrete form of the flow rule and hardening law

$$\text{dev}[\bar{\mathbf{b}}_{n+1}^e] = \text{dev}[\bar{\mathbf{b}}_{n+1}^{e \text{ trial}}] - \frac{2}{3} \Delta\gamma \text{tr}[\bar{\mathbf{b}}_{n+1}^e] \mathbf{n}_{n+1} \quad (68)$$

$$\alpha_{n+1} = \alpha_n + \sqrt{\frac{2}{3}} \Delta\gamma. \quad (69)$$

This update leads to the return-mapping algorithm summarized in the following section.

We point out that this algorithm deviates from the algorithm presented in [38] in two ways. First, we have included the elastic and plastic degradation functions from the theory presented in Sect. 3. Second, we have modified the update of the intermediate configuration (Step 6) to maintain the correct determinant of $\bar{\mathbf{b}}^e$. This update affects only the trace of $\bar{\mathbf{b}}^e$ and has no effect on the stress computations but is necessary to compute the correct strain energy.

4.1 The Return-Mapping Algorithm

The steps of the return-mapping algorithm are summarized in this section. This algorithm follows the algorithm presented by Simo and Hughes [38] with modifications to include the degradation functions and correct the update of the intermediate configuration. The modifications are indicated by the boxed lines.

1. Update the current configuration

$$\begin{aligned}\phi_{n+1}(\mathbf{X}) &= \phi_n(\mathbf{X}) + \mathbf{u}_n(\phi_n(\mathbf{X})) \\ \mathbf{f}_{n+1} &= \mathbf{I} + \nabla_{x_n} \mathbf{u}_n \\ \mathbf{F}_{n+1} &= \mathbf{f}_{n+1} \mathbf{F}_n\end{aligned}$$

2. Compute the damage/elastic predictor

$$\begin{aligned}\bar{\mathbf{f}}_{n+1} &= \det[\mathbf{f}_{n+1}]^{-1/3} \mathbf{f}_{n+1} \\ \bar{\mathbf{b}}_{n+1}^{e \text{ trial}} &= \bar{\mathbf{f}}_{n+1} \bar{\mathbf{b}}_n^e \bar{\mathbf{f}}_{n+1}^T\end{aligned}$$

$$\boxed{\mathbf{s}_{n+1}^{\text{trial}} = g(c) \mu \operatorname{dev} [\bar{\mathbf{b}}_{n+1}^{e \text{ trial}}]}$$

3. Check for plastic loading

$$\boxed{f_{n+1}^{\text{trial}} = \|\mathbf{s}_{n+1}^{\text{trial}}\| - g_p(c_n) \sqrt{\frac{2}{3}} k(\alpha_n)}$$

IF $f_{n+1}^{\text{trial}} \leq 0$ THEN

Set $(\cdot)_{n+1} = (\cdot)_{n+1}^{\text{trial}}$, and EXIT

ELSE

Go to 4 (return-mapping)

ENDIF

4. Return-mapping

$$\bar{J}_{n+1}^e \text{ trial} = \frac{1}{3} \text{tr} [\bar{\mathbf{b}}_{n+1}^e \text{ trial}]$$

$$\bar{\mu} = g(c)\mu \bar{J}_{n+1}^e \text{ trial}$$

$$\text{Solve: } \hat{f}(\Delta\gamma) = \|\mathbf{s}_{n+1}^{\text{trial}}\| - g_p(c_n)\sqrt{\frac{2}{3}}k(\alpha_n + \sqrt{\frac{2}{3}}\Delta\gamma) - 2\bar{\mu}\Delta\gamma = 0$$

$$\mathbf{s}_{n+1} = \mathbf{s}_{n+1}^{\text{trial}} - 2\bar{\mu}\Delta\gamma\mathbf{n}$$

$$\alpha_{n+1} = \alpha_n + \sqrt{\frac{2}{3}}\Delta\gamma$$

5. Update the Kirchhoff stress

$$J_{n+1} = \det [\mathbf{F}_{n+1}]$$

$$p_{n+1} = \begin{cases} g(c)U'(J_{n+1}) & J_{n+1} \geq 1 \\ U'(J_{n+1}) & J_{n+1} < 1 \end{cases}$$

$$\boldsymbol{\tau}_{n+1} = J_{n+1}p_{n+1}\mathbf{I} + \mathbf{s}_{n+1}$$

6. Update the intermediate configuration (corrects error in algorithm presented in [38])

$$\text{dev} [\bar{\mathbf{b}}_{n+1}^e] = \frac{\mathbf{s}_{n+1}}{g(c)\mu}$$

$$\text{Solve (to find } \bar{J}_{n+1}^e \text{): } \det [\text{dev} [\bar{\mathbf{b}}_{n+1}^e] + \bar{J}_{n+1}^e \mathbf{I}] = 1$$

$$\bar{\mathbf{b}}_{n+1}^e = \text{dev} [\bar{\mathbf{b}}_{n+1}^e] + \bar{J}_{n+1}^e \mathbf{I}$$

5 Bolted Plate

In this example we present numerical results of simulations of a circular steel plate subjected to a blast load. These simulations are based on an underwater explosion experiment performed on a steel plate that was bolted to a reaction frame. A simplified model has been used for the analysis as shown in Fig. 2a. In this model, the reaction frame has been replaced by a penalty term. Details of the bolted connections between the plate and reaction frame, however, have been included in the analysis model. A detailed cross-section view of the bolted connection is shown in Fig. 2b. The discretization is continuous between the bolt head and washer and between the

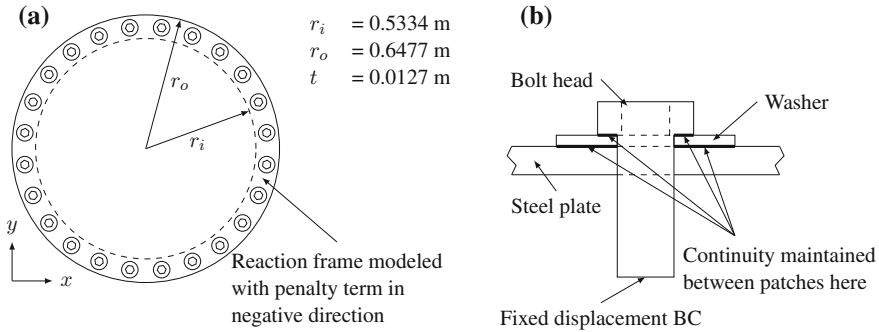


Fig. 2 **a** Plan view of the simplified analysis model with dimensions of the steel plate. The reaction frame is modeled by penalizing displacements in the negative-z direction on the back side of the plate in the outer annulus between r_i and r_o . **b** Detailed cross-section of a bolt connection. To simplify the computation, the bolt head is connected to the washer and the washer is connected to the steel plate in the discretization. The barrel of the bolt passes freely through the hole in the washer and plate and contact between the bolt and the washer or plate is not considered during the simulation. A fixed displacement boundary condition is applied to the end of the bolt. The length of the barrel of the bolt in the analysis model is 2.5 in. The other dimensions of the bolt are based on a standard 1 in. diameter bolt

washer and steel plate. Furthermore, the barrel of the bolt passes freely through the hole in the washer and plate and contact here is ignored, i.e., the barrel of the bolt is allowed to penetrate the washer and plate. These simplifications remove the need to include contact and reduces the computation complexity. Fixed displacement boundary conditions are applied to the end of the bolt.

The geometry of the analysis model is constructed as a quadratic multi-patch NURBS as shown in Fig. 3. This allows the geometry to be represented exactly in the analysis model. A detailed view of the Bézier representation of the multi-patch NURBS description of a bolt is shown in Fig. 3. We note that the number of degrees-of-freedom for this problem can be greatly reduced by the use of hierarchical refinement schemes as described by Schillinger et al. [36] and Scott et al. [37], but this has not been considered in our calculations.

The material properties used in the analysis model are given in Table 1, and the quadratic degradation function is used in all computations for this problem. The blast load is approximated as a radially distributed pressure impulse that is applied to the front surface of the plate in the current configuration. The non-dimensional radial distribution of the pressure, g , is defined as a function of the distance r (in meters) measured from the center of the plate as

$$g(r) = \exp\left(\frac{-r^2}{2 \times 0.3^2}\right). \quad (70)$$

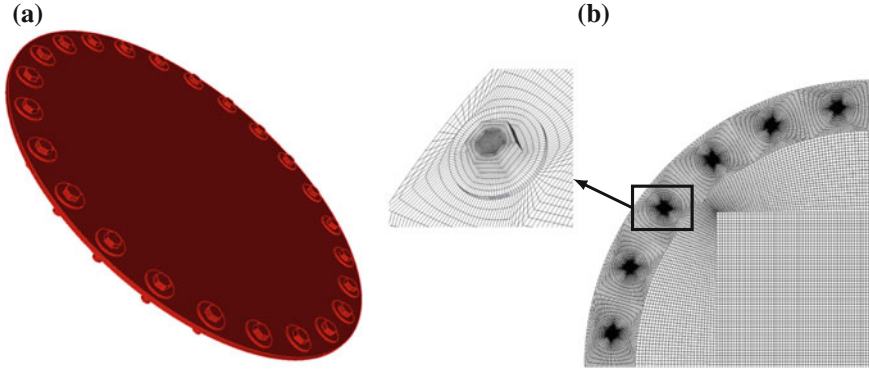


Fig. 3 **a** Shows an oblique angle of the geometry used for the analysis. **b** shows details of the Bézier representation of the multi-patch quadratic NURBS that describes the geometry with a close-up view of one of the bolt heads. C^0 continuity is maintained between the patches

Table 1 Material properties

Young's modulus	206 GPa
Poisson's ratio	0.281
Mass density	7780 kg/m ³
Yield stress	355 MPa
Critical fracture energy	10 ⁶ J/m ²
ℓ_0	1.27×10^{-2} m

The temporal distribution of the impulsive blast load is

$$\tilde{p}_0(t) = t \cdot \exp\left(1 - t \cdot 50 \times 10^3 / s\right) \cdot 2.25 \times 10^6 \text{ MPa/s} \quad (71)$$

$$p_0(t) = \tilde{p}_0(t) + \begin{cases} 0 & 0 \leq t < 20 \mu\text{s} \\ \left(1.0 + \sin\left(\frac{\pi(t-2 \times 10^{-5} \text{s})}{10^{-4} \text{s} - 2 \times 10^{-5} \text{s}} - \frac{\pi}{2}\right)\right) \cdot 1 \text{ MPa} & 20 \mu\text{s} \leq t < 100 \mu\text{s} \\ 2 \text{ MPa} & t \geq 100 \mu\text{s} \end{cases} \quad (72)$$

The pressure is given by

$$p(t, r) = p_0(t) * g(r) \quad (73)$$

and results in a peak of 45 MPa at the center of the plate at $t = 20 \mu\text{s}$.

The results for a number of simulations are shown in Fig. 4. This figure compares the crack progression at three time intervals using both of the effective plastic work equations for a number of different plastic work threshold values. The $W_0 = 0$ case provides a good comparison that shows how introducing the triaxiality modification to the effective plastic work term effects the crack behavior. For the “No triaxiality”

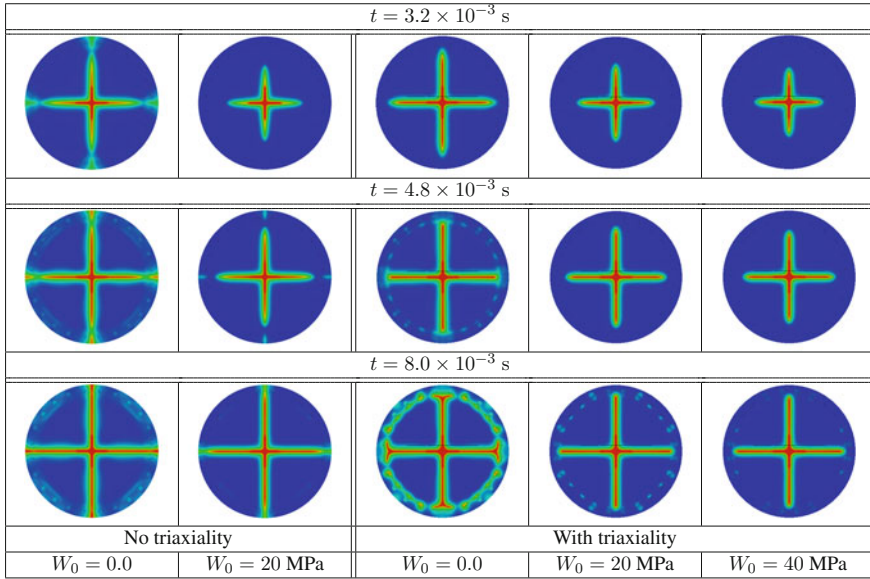


Fig. 4 A comparison of crack progression at three time steps for different values of W_0 with and without the triaxiality modification to the effective plastic work term

case a secondary crack begins to develop at the edge of the plate and propagates back towards the main crack as it approaches the edge. For the “With triaxiality” case this secondary crack does not develop and instead the crack branches when it reaches the area of the plate supported by the reaction frame. The “With triaxiality” case also has more damage around the perimeter of the plate. For the $W_0 = 20 \text{ MPa}$ case the crack begins to propagate sooner for the “With triaxiality” case, which agrees with the behavior seen in the previous sections. Setting $W_0 = 40 \text{ MPa}$ for the “With triaxiality” case results in a crack progression that more closely matches the “No triaxiality” case with $W_0 = 20 \text{ MPa}$.

A detailed view of the deformed configuration of the “No triaxiality” case with $W_0 = 20 \text{ MPa}$ is shown in Fig. 5. This figure shows that the phase-field model we are using is able to capture localized ductile behavior, which qualitatively compares well with experimental results (see for example Webster [41]).

Figure 6 shows that in the computational results the bolts immediately adjacent to the cracks fractured in tension. In Fig. 7, depicting the experiment, it may be noted that several of the bolts immediately adjacent to the cracks are still present in the plate after its separation from the test frame. Our interpretation is that these bolts also fractured in tension and did not need to be pulled out in order to separate the plate from the test frame. In the experiment, all the other bolts are gone, indicating they had to be removed in order to separate the plate from the test frame.

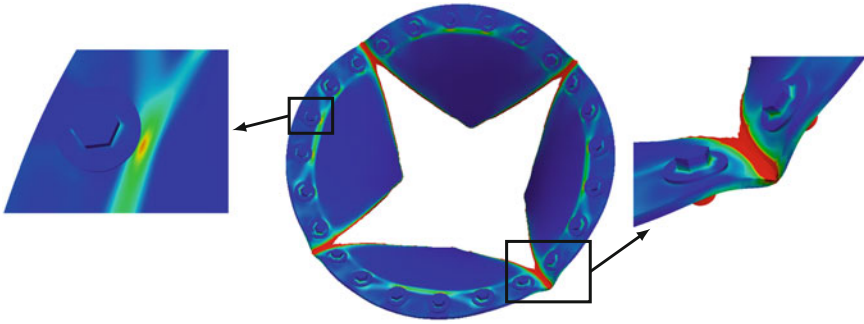


Fig. 5 Details of the deformed plate for computations with $W_0 = 20$ MPa. The color plots indicate the level of plastic yielding. On the *left*, we see the effect of a bolt hole on the distribution of plastic yielding. On the *right* we see that the plate begins to fold as the crack nears the edge. This behavior matches well qualitatively with experimental results

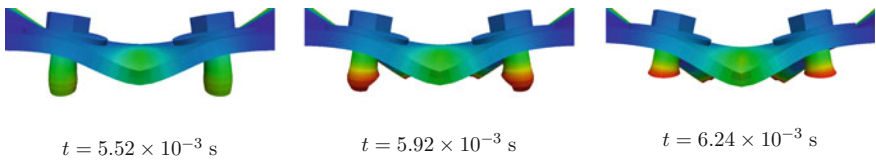


Fig. 6 A detailed view showing the progression of the failure of the bolts for the computational with $W_0 = 20$ MPa. The color scale indicates the value of the phase-field



Fig. 7 Figures showing the experimental results from [41]

6 Conclusion

In this work we have presented several innovations to the phase-field modeling of fracture that improve upon its representation of fracture in ductile material behavior. Our theoretical framework is based on a microforce balance and a general energy potential accounting for large deformation elastic-plastic response and plastic softening. We have introduced a plastic yield surface degradation function that accounts for plastic softening as cracks develop, eliminates non-physical elastic deformations after crack initiation, and leads to better representation of the physical processes that occur during failure. We have also provided a mechanism that allows for stress triaxiality to influence crack initiation and growth. Finally, we have also identified and corrected a shortcoming in a widely used return-mapping implementation of a hyperelastic-plastic large deformation constitutive model that can lead to non-physical behavior.

Acknowledgements This work was partially supported by Grants from the Office of Naval Research under contract number N00014-08-1-0992 and the Army Research Office under contract number W911NF-10-1-0216. T.J.R. Hughes, A. Anvari, and C.M. Landis were also supported by ARO grant number W911NF-13-1-0220. This support is gratefully acknowledged. The authors also acknowledge the Texas Advanced Computing Center (TACC) at The University of Texas at Austin for providing HPC and visualization resources that have contributed to the research results reported within this paper. URL: <http://www.tacc.utexas.edu>.

References

1. M. Ambati, T. Gerasimov, L. De Lorenzis, Phase-field modeling of ductile fracture. *Comput. Mech.* **55**(5), 1017–1040 (2015)
2. M. Ambati, R. Kruse, L. De Lorenzis, A phase-field model for ductile fracture at finite strains and its experimental verification. *Comput. Mech.* **57**(1), 149–167 (2016)
3. L. Ambrosio, V.M. Tortorelli, Approximation of functional depending on jumps by elliptic functional via Γ -convergence. *Commun. Pure Appl. Math.* **43**(8), 999–1036 (1990)
4. H. Amor, J.J. Marigo, C. Maurini, Regularized formulation of the variational brittle fracture with unilateral contact: numerical experiments. *J. Mech. Phys. Solids* **57**(8), 1209–1229 (2009)
5. Y.-L. Bai, T. Wierzbicki, A new model of metal plasticity and fracture with pressure and Lode dependence. *Int. J. Plast.* **24**, 1071–1096 (2008)
6. Y.-L. Bai, T. Wierzbicki, Application of extended mohr-coulomb criterion to ductile fracture. *Int. J. Fract.* **161**, 1–20 (2010)
7. Y.-B. Bao, T. Wierzbicki, On fracture locus in the equivalent strain and stress triaxiality space. *Int. J. Mech. Sci.* **46**, 81–98 (2004)
8. M.J. Borden, C.V. Verhoosel, M.A. Scott, T.J.R. Hughes, C.M. Landis, A phase-field description of dynamic brittle fracture. *Comput. Methods Appl. Mech. Eng.* **217–220**, 77–95 (2012)
9. M.J. Borden, T.J.R. Hughes, C.M. Landis, C.V. Verhoosel, A higher-order phase-field model for brittle fracture: formulation and analysis within the isogeometric analysis framework. *Comput. Methods Appl. Mech. Eng.* **273**, 100–118 (2014)
10. B. Bourdin, G.A. Francfort, J.-J. Marigo, Numerical experiments in revisited brittle fracture. *J. Mech. Phys. Solids* **48**(4), 797–826 (2000)
11. B. Bourdin, G.A. Francfort, J.-J. Marigo, The variational approach to fracture. *J. Elast.* **91**(1–3), 5–148 (2008)

12. B. Bourdin, C. Larsen, C. Richardson, A time-discrete model for dynamic fracture based on crack regularization. *Int. J. Fract.* **168**(2), 133–143 (2011)
13. B. Bourdin, C.P. Chukwudozie, K. Yoshioka, A variational approach to the numerical simulation of hydraulic fracturing, in *Proceedings of the 2012 SPE Annual Technical Conference and Exhibition*, volume SPE 159154 (Society of Petroleum Engineers, 2012)
14. P. Bridgman, *Studies in Large Plastic Flow and Fracture* (McGraw-Hill Book Company, London, 1952)
15. S. Burke, C. Ortner, E. Süli, An adaptive finite element approximation of a generalized Ambrosio-Tortorelli functional. *Math. Models Methods Appl. Sci.* **23**(9), 1663–1697 (2013)
16. G.A. Francfort, J.-J. Marigo, Revisiting brittle fracture as an energy minimization problem. *J. Mech. Phys. Solids* **46**(8), 1319–1342 (1998)
17. A. Ghahremaninezhad, K. Ravi-Chandar, Ductile failure behavior of polycrystalline al 6061–t6. *Int. J. Fract.* **174**(2), 177–202 (2012)
18. A.L. Gurson, Continuum theory of ductile rupture by void nucleation and growth—Part I. Yield criteria and flow rules for porous ductile media. *J. Eng. Mater. Technol.* **99**, 2–15 (1977)
19. M.E. Gurtin, Generalized Ginzburg-Landau and Cahn-Hilliard equations based on a microforce balance. *Phys. D: Nonlinear Phenom.* **92**(3–4), 178–192 (1996)
20. S.S. Halton, S. Kyriakides, K. Ravi-Chandar, Ductile failure under combined shear and tension. *Int. J. Solids Struct.* **50**, 1507–1522 (2013)
21. M. Hofacker, C. Miehe, A phase field model of dynamic fracture: robust field updates for the analysis of complex crack patterns. *Int. J. Numer. Methods Eng.* **93**(3), 276–301 (2013)
22. G.R. Johnson, W.H. Cook, Fracture characteristics of three metals subjected to various strains, strain rates, temperatures and pressures. *Eng. Fract. Mech.* **21**, 31–48 (1985)
23. C.J. Larsen, Models for dynamic fracture based on Griffith’s criterion, in *IUTAM Symposium on Variational Concepts with Applications to the Mechanics of Materials*, vol. 21, ed. by K. Hackl (Springer, Netherlands, 2010), pp. 131–140
24. C.J. Larsen, C. Ortner, E. Süli, Existence of solutions to a regularized model of dynamic fracture. *Math. Methods Models Appl. Sci.* **20**(7), 1021–1048 (2010)
25. C. McAuliffe, H. Waisman, A unified model for metal failure capturing shear banding and fracture. *Int. J. Plast.* **65**, 131–151 (2015)
26. F.A. McClintock, A criterion for ductile fracture by the growth of holes. *J. Appl. Mech.* **35**, 363–371 (1968)
27. C. Miehe, M. Hofacker, F. Welschinger, A phase field model for rate-independent crack propagation: robust algorithmic implementation based on operator splits. *Comput. Methods Appl. Mech. Eng.* **199**(45–48), 2765–2778 (2010a)
28. C. Miehe, F. Welschinger, M. Hofacker, Thermodynamically consistent phase-field models of fracture: variational principles and multi-field FE implementations. *Int. J. Numer. Methods Eng.* **83**(10), 1273–1311 (2010b)
29. C. Miehe, M. Hofacker, L.-M. Schänzel, F. Aldakheel, Phase field modeling of fracture in multi-physics problems. Part II. Coupled brittle-to-ductile failure criteria and crack propagation in thermo-elastic-plastic solids. *Comput. Methods Appl. Mech. Eng.* **294**, 486–522 (2015a)
30. C. Miehe, L.-M. Schänzel, Phase field modeling of fracture in rubbery polymers. Part I. *J. Mech. Phys. Solids* **65**, 93–113 (2014)
31. C. Miehe, L.-M. Schänzel, H. Ulmer, Phase field modeling of fracture in multi-physics problems. Part I. Balance of crack surface and failure criteria for brittle crack propagation in thermo-elastic solids. *Comput. Methods Appl. Mech. Eng.* **294**, 449–485 (2015b)
32. C. Miehe, F. Aldakheel, A. Raina, Phase field modeling of ductile fracture at finite strains. a variational gradient-extended plasticity-damage theory. *Int. J. Plast.* (in press) (2016). doi:[10.1016/j.ijplas.2016.04.011](https://doi.org/10.1016/j.ijplas.2016.04.011)
33. A. Mikelic, M.F. Wheeler, T. Wick, A phase-field method for propagating fluid-filled fractures coupled to a surrounding porous medium. *Multiscale Model. Simul.* **13**, 367–398 (2015)
34. D. Mumford, J. Shah, Optimal approximations by piecewise smooth functions and associated variational problems. *Commun. Pure Appl. Math.* **42**(5), 577–685 (1989)

35. J.R. Rice, D.M. Tracey, On the ductile enlargement of voids in triaxial stress fields. *J. Mech. Phys. Solids* **17**, 201–217 (1966)
36. D. Schillinger, L. Dedè, M.A. Scott, J.A. Evans, M.J. Borden, E. Rank, T.J.R. Hughes, An isogeometric design-through-analysis methodology based on adaptive hierarchical refinement of NURBS, immersed boundary methods, and T-spline CAD surfaces. *Comput. Methods Appl. Mech. Eng.* **249–252**, 116–150 (2012)
37. M.A. Scott, D.C. Thomas, E.J. Evans, Isogeometric spline forests. *Comput. Methods Appl. Mech. Eng.* **269**(0), 222–264 (2014)
38. J.C. Simo, T.J.R. Hughes, *Computational Inelasticity* (Springer, New York, 1998)
39. H. Stumpf, K. Hackl, Micromechanical concept for the analysis of damage evolution in thermo-viscoelastic and quasi-brittle materials. *Int. J. Solids Struct.* **40**(6), 1567–1584 (2003)
40. V. Tvergaard, A. Needleman, Analysis of the cup-cone fracture in a round tensile bar. *Acta Metallurgica* **32**, 157–169 (1984)
41. K.G. Webster, Investigation of close proximity underwater explosion effects on a ship-like structure using the multi-material arbitrary Lagrangian Eulerian finite element method. Master's thesis, Virginia Polytechnic Institute and State University, Jan 2007
42. Z.A. Wilson, M.J. Borden, C.M. Landis, A phase-field model for fracture in piezoelectric ceramics. *Int. J. Fract.* **183**(2), 135–153 (2013)

Computational Strategies for Speeding-Up F.E. Simulations of Metal Forming Processes

Lionel Fourment, Koffi K'podzo, Fabien Delalondre, Ugo Ripert, Mohamad Ramadan, Frédéric Vi and Hugues Digonnet

Abstract An overview of various numerical methods developed for speeding-up computations is presented in the field of the bulk material forming under solid state, which is characterized by complex and evolving geometries requiring frequent remeshings and numerous time increments. These methods are oriented around the axis that constitutes the meshing problem. The *multi-mesh* method allows to optimally solve several physics involved on the same domain, according to its finite element discretization with several different meshes, for example in the cogging or cold pilgering processes. For quasi steady-state problems and problems with quite pronounced localization of deformation, such as Friction Stir Welding (FSW) or High Speed Machining, an Arbitrary Lagrangian or Eulerian formulation (ALE) with mesh adaptation shows to be imperative. When the problem is perfectly steady, as for the rolling of long products, the direct search for the stationary state allows huge accelerations. In the general case, where no process specificity can be used to solve the implicit equations, the multigrid method makes it possible to construct a much more efficient iterative solver, which is especially characterized by an almost linear asymptotic cost.

L. Fourment (✉) · K. K'podzo · F. Vi
MINES ParisTech, PSL Research University, CEMEF, CNRS UMR 7635,
CS 10207 rue Claude Daunesse, 06904 Sophia Antipolis Cedex, France
e-mail: lionel.fourment@mines-paristech.fr

F. Delalondre
EPFL, Biotech Campus, Bâtiment B1, Chemin des Mines, 9 1211,
Geneva, Switzerland

U. Ripert
Transvalor, Parc de haute technologie de Sophia Antipolis, 06255
Mougins Cedex, France

M. Ramadan
School of Engineering, Lebanese International University, PO Box 146404,
Beirut, Lebanon

H. Digonnet
Ecole Centrale de Nantes, ICI - Institut du Calcul Intensif, 44321 Nantes, France

1 Introduction

The reduction of computing time remains one of the obsessions of numerical simulation, especially in the field of material forming where the end-users generally do not have access to large clusters of parallel computers. In addition, the parallelization of the code is not the only key to reduce computation times, in particular for incremental processes that require a very large number of time steps. In fact, simulation of forming processes such as the cogging of a bar or the multi-cage rolling of a slab may require several days or weeks of calculations [1] even with large parallel calculation resources, which is of course inconsistent with the time assigned to the design processes in the industry. In recent years, a number of specific numerical methods have been developed in the field of material forming, whether it is the extension of methods originally developed in the field of fluid or structure mechanics, or whether it is specific methods using some of the particularities of forming processes. All these numerical methods aim to take into account the specificities of bulk forming process simulations, which consist of complex and evolving geometries requiring frequent remeshings and numerous time increments, under the constraint of being robust with a wide spectrum of applications and not requiring to appeal to a number of processors incompatible with industrial reality.

The axis around which all presented methods are oriented, are the problems of meshing and remeshing, and that of remapping between incompatible meshes. Thus, after introducing the basic equations for a bulk material forming problem in Sects. 2 and 3 describes how the multi-mesh method can be applied to problems requiring the resolution of several physics on the same domain and how it thus greatly reduces calculation times. For quasi-stationary problems with very pronounced localizations, the Arbitrary Lagrangian or Eulerian (ALE) formulation based on the operator decoupling and mesh adaptation proves to be essential (Sect. 4), but if the problem is perfectly stationary, then the direct search for this steady-state provides huge acceleration (Sect. 5). In the general case, where no particularity can be used, the multigrid method presented in Sect. 6 makes it possible to construct a more efficient iterative solver, which is especially characterized by an almost linear asymptotic cost.

2 Basic Equations

The equations solved in the various addressed forming problems can be summarized as those of a viscous flow [2]. The material is therefore incompressible (1) and obeys the Norton-Hoff law (1):

$$\operatorname{div}(\mathbf{v}) = 0 \quad ; \quad \mathbf{s}(\mathbf{v}) = \boldsymbol{\sigma} + p\mathbf{1} = 2K(T) \left(\sqrt{3} \dot{\boldsymbol{\varepsilon}}(\mathbf{v}) \right)^{m-1} \dot{\boldsymbol{\varepsilon}}(\mathbf{v}) \quad (1)$$

where \mathbf{v} is the velocity, p the pressure, $\boldsymbol{\sigma}$ the stress tensor, s the deviatoric one and $\dot{\boldsymbol{\varepsilon}}(\mathbf{v})$ that of the strain rates, T is the temperature on which the consistence K of the material depends. In the absence of a significant role played by inertia and gravity forces, the equilibrium equation consists of:

$$\operatorname{div}(\boldsymbol{\sigma}) = 0 \quad ; \quad \boldsymbol{\sigma} \mathbf{n} = 0 \quad (2)$$

with free surface boundary conditions (2), contact Eq. (3) (where δ is the contact distance at the beginning of increment, \mathbf{u}_{tool} is the displacement vector and \mathbf{n}_{tool} is the tool normal) and friction modeled by a Norton law (3) (where α and q are the friction coefficients and $\Delta \mathbf{v}_t$ is the relative tangential velocity at the interface):

$$(\mathbf{u}(\mathbf{v}) - \mathbf{u}_{tool}) \cdot \mathbf{n}_{tool} \leq \delta \quad ; \quad \boldsymbol{\tau}(\mathbf{v}) = \boldsymbol{\sigma} \mathbf{n} - (\boldsymbol{\sigma} \mathbf{n} \cdot \mathbf{n}) \mathbf{n} = -\alpha K (\Delta \mathbf{v}_t)^{q-1} \Delta \mathbf{v}_t \quad (3)$$

The weak form of the mixed velocity/pressure problem is written as:

$$\begin{cases} \forall \mathbf{v}^*, \int_{\Omega} s(\mathbf{v}): \boldsymbol{\varepsilon}(\mathbf{v}^*) d\omega - \int_{\Omega} p \operatorname{div}(\mathbf{v}^*) d\omega - \int_{\partial\Omega_{contact}} \boldsymbol{\tau}(\mathbf{v}) \cdot \mathbf{v}^* ds = 0 \\ \forall p^*, - \int_{\Omega} p^* \operatorname{div}(\mathbf{v}) d\omega = 0 \end{cases} \quad (4)$$

which is discretized using mixed P1 + / P1 tetrahedral elements, a linear velocity and pressure interpolation with the addition of a bubble function for the velocity [3]. The contact condition is written at the nodes of the mesh (node-to-facet contact) before being imposed by penalization in the mixed formulation [4]. After condensation of velocity bubble degrees of freedom, the resulting nonlinear system is solved by a Newton algorithm (5) leading to the resolution of the following linear system (5):

$$\begin{cases} R_v(\mathbf{v}_h, p_h) = 0 \\ R_p(\mathbf{v}_h) = 0 \end{cases} \quad ; \quad H(\mathbf{v}_h^{(i)}, p_h^{(i)}) \begin{pmatrix} \delta \mathbf{v}_h^{(i+1)} \\ \delta p_h^{(i+1)} \end{pmatrix} = - \begin{pmatrix} R_v(\mathbf{v}_h^{(i)}, p_h^{(i)}) \\ R_p(\mathbf{v}_h^{(i)}) \end{pmatrix} \quad (5)$$

which is solved by the PRC-ILU1 iterative solver, the Preconditioned Conjugate Residual (PCR) preconditioned by an Incomplete Choleski factorization with an additional fill-in level (ILU1).

The evolution of the material temperature is given by the heat equation:

$$\rho_m C_p \frac{dT}{dt} + k \Delta T = -f_p \boldsymbol{\sigma} : \dot{\boldsymbol{\varepsilon}} \quad (6)$$

where ρ_m is the material density, C_p its specific heat, k its conductivity and f_p is the fraction of the deformation power transformed into heat. It is complemented by boundary conditions of conduction (with h_c coefficient), of convection and radiation

(with h_{cr} coefficient), and of imposed thermal flux resulting from friction interface. The weak form of this equation is:

$$\begin{aligned} \forall T^*, \int_{\Omega} T^* \rho_m C_p \frac{dT}{dt} d\omega - \int_{\Omega} k \nabla T \cdot \nabla T^* d\omega - \int_{\Omega} T^* f_p \boldsymbol{\sigma} : \dot{\boldsymbol{\epsilon}} d\omega \\ = - \int_{\partial\Omega_{air}} T^* h_{cr} (T - T_{air}) ds - \int_{\partial\Omega_{contact}} T^* h_c (T - T_{tool}) ds - \int_{\partial\Omega_{contact}} T^* b_r (\boldsymbol{\tau}(v) \cdot \Delta v_g) ds \end{aligned} \quad (7)$$

where h_{cr} is the conduction coefficient with the T_{tool} tool at temperature, h_{cr} is the convection and radiation coefficient with air at temperature T_{air} and b_r is the relative effusivity of materials in contact. After time discretization, using an implicit scheme, and spatial discretization with P1 elements, Eq. (7) takes the form (8). Taking into account the thermal dependency of velocity equations (5), and the velocity dependency of the heat equation (8), the equations to be solved are rewritten as (8):

$$Q(T_h) = 0 \quad ; \quad \begin{cases} R(T_h, v_h, p_h) = 0 \\ Q(v_h, T_h) = 0 \end{cases} \quad (8)$$

According to the time steps size used in the time integration scheme within an Updated Lagrangian formulation (9), and to the nature of the thermo-mechanical coupling, an incremental coupling method of the equations is sufficient. It allows reducing the number of unknowns per node, through separate resolutions of mechanical and thermal equations (9):

$$\forall inc = 1, NBinc, \quad X_h^{inc+1} = X_h^{inc} + V_h^{inc+1} \Delta t \quad ; \quad \begin{cases} R(T_h^{inc}, v_h^{inc+1}, p_h^{inc+1}) = 0 \\ Q(v_h^{inc+1}, T_h^{inc+1}) = 0 \end{cases} \quad (9)$$

The domain evolution induced by the material large deformations during the forming process requires frequent remeshings. They are based on a topological mesh generator operating by topological mesh improvement [5, 6]. For parallel computations, the domain is partitioned into as many parts as processors, so that each processor has access only to the mesh of its domain and to the interface information. Since the equations of the problem are solved by an iterative method, consisting of matrix/vector and scalar products, its parallelization is simple and efficient [3]. The remeshing and repartitioning operations are also carried out in parallel, using an iterative approach [7].

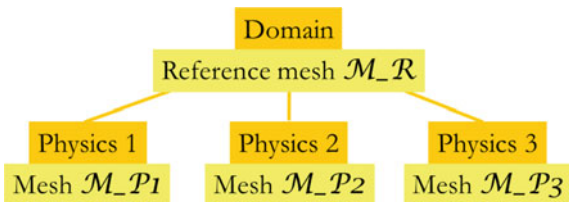
3 Multi-mesh Method

3.1 Principle of Multi-mesh Method

A first way to reduce computing time is provided by the *multi-mesh* method. It applies to problems requiring to solve equations from several physics on the same domain, as for example to solve mechanical and thermal equations. It is then customary to use a mesh adapted to the different physics, in other words which is sufficiently fine for each of them, but which can consequently be too refined for one or the other of the physics and therefore exaggeratedly expensive. In material forming, this situation is encountered for the simulation of cogging [8] and cold pilgering (see Fig. 2) [9] processes which involve very elongated parts and very localized deformation under the tool gap. While it is necessary to use a uniformly refined mesh over the entire domain to correctly calculate the temperature and to keep memory of the deformation gradients undergone during the process, a mesh only refined under the tool gap is sufficient to accurately compute the velocity field. In this framework, the multi-physics multi-mesh method allows to use an optimal mesh for each physic and thus optimize the calculation times. It is based on the construction of a specific mesh M_{P_i} for each physical P_i and on the use of a reference mesh M_R , finer than all the others, to assemble and archive the results (see Fig. 1). The key point of this approach lies in the construction of transfer operators between the different meshes, in their accuracy and their compatibility with parallel computations.

In [8], the precision of the remapping operator is ensured at the mesh nodes by building meshes that are nested by nodes. Having constructed the reference mesh M_R , which is the finest over the entire domain, the other meshes M_{P_i} are deduced from it by derefinement while respecting the node nesting constraint [10]. Thus, any nodal field backed up on the reference mesh M_R is perfectly restricted on the mesh M_{P_i} associated with a particular physic, and any physical field calculated on its dedicated mesh M_{P_i} is accurately projected at the nodes of the reference mesh M_R and is interpolated to the other nodes without introducing any significant error, considering that the reference mesh is over-discretized.

Fig. 1 Scheme of the multi-mesh method



3.2 Super-Convergent Remapping Method

For the values known at integration points, such as the stresses or the strains of the mechanical problem, the nesting condition is not realized. It is then necessary to use a more precise remapping operator than the simple projection or interpolation which leads to diffusion errors making the method inefficient. Using a P1 interpolation for the velocity, the fields at the integration points are P0, constant by element. Their remapping is so achieved by a super-convergent recovery method [9, 11] inspired from the works of Zienkiewicz and Zhu in error estimation [12].

From a P0 discontinuous field φ^{dep} defined on the departure mesh, the method consists in constructing a P1 continuous field $\tilde{\varphi}^{dep}$ (10) on the same mesh, using the Super-convergent Patch Recovery (SPR) method, and then in interpolating this field $\tilde{\varphi}^{dep}$ at the center of the elements of the arrival mesh (11).

$$\tilde{\varphi}^{dep}(\xi) = \sum_k \tilde{\varphi}_k^{dep} N_k^{dep}(\xi) \quad (10)$$

$$\forall e' \in \Omega^{arr}, \exists e \in \Omega^{dep}, \exists \xi' \in [0, 1]^3, \quad \begin{cases} \sum_k x_k^{dep} N_k^{dep}(\xi') = x_{e'}^{arr} \\ \varphi_{e'}^{arr} = \tilde{\varphi}^{dep}(x_{e'}^{arr}) = \sum_k \tilde{\varphi}_k^{dep} N_k^{dep}(\xi') \end{cases} \quad (11)$$

where $\tilde{\varphi}_k^{dep}$ is computed according to the SPR method [12] from a local linear recovery $\tilde{\varphi}_k^{dep}$ (12) of φ constructed on the patch of elements centered in k through the minimization of (13). Utilized weighting factors (13) are however slightly different from the original ones (equal to 1), as suggested in [13–15], to minimize the least squares functional (13):

$$\forall x = [x_1, x_2, x_3]^t, \quad \tilde{\varphi}_k^{dep}(x) = [a_0^k, a_1^k, a_2^k, a_3^k]^t \cdot \left[1, (x_1 - x_{1k}^{dep}), (x_2 - x_{2k}^{dep}), (x_3 - x_{3k}^{dep}) \right] \quad (12)$$

$$\Pi\left((a_i^k)_{i=0,3}\right) = \frac{1}{2} \sum_{e \ni k} \omega_{ek} \left(\tilde{\varphi}_k^{dep}(x_e^{dep}) - \varphi_e^{dep} \right)^2 \quad ; \quad \omega_{ek} = \left\| x_e^{dep} - x_k^{dep} \right\|^{-4} \quad (13)$$

which minimization result provides: $a_0^k = \tilde{\varphi}_k^{dep}(x_k^{dep}) = \tilde{\varphi}_k^{dep}$. It is shown in [11] that this method is actually of better accuracy and a higher convergence order than the usual P0 remapping methods, whether by interpolation or global least square. However, in forming, most phenomena and field gradients arise at the surface so that it is fundamental to preserve these properties of accuracy and “super-convergence” on the surface. This necessitates enriching the information available on a surface patch from the neighboring patches, for example by using the super-convergent nodal values that can be computed at the volume nodes of the surface patch through the same SPR method [11]. This iterative approach is quite

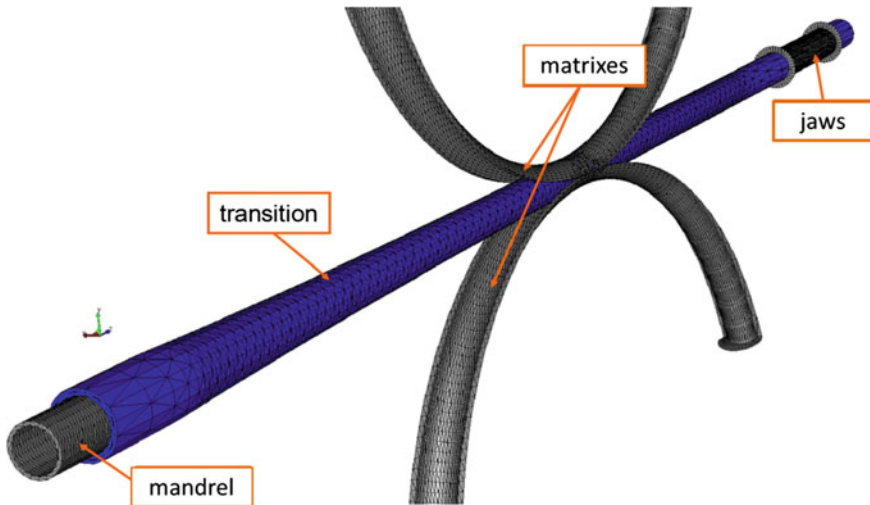


Fig. 2 Cold pilgering process

compatible with parallel computations and makes it possible to recover the higher convergence order at surface nodes. In [9], it is verified that the resulting remapping operator is accurate enough to properly transfer the stress tensor involved in elastoplasticity problems, and to consequently use the multi-mesh method with such constitutive models. It is thus applied to the cold pilgering rolling problem (Fig. 2) where the two physics are the mechanic and the thermic.

3.3 Application to the Cold Pilgering and Cogging Processes

The mesh dedicated to the resolution of the heat equation being uniformly refined, it is merged to the reference mesh. The mechanical mesh is constructed by derefining this thermal-reference mesh outside the roll gap (Fig. 3).

The results obtained with the multi-mesh method are perfectly superimposable to those obtained with the reference mesh (Fig. 4), but the computation times are considerably reduced by thus solving the mechanical problem (by far the most expensive) on the reduced mechanical mesh. On this problem characterized by strongly anisotropic meshes (see Figs. 2 and 4) and an elastoplastic behavior, the accelerations are between 2.8 and 6.5 (Table 1) according to the size of the utilized reference mesh. For a more massive forging problem (cogging) and a viscoplastic material, the accelerations obtained with this method can be much greater; they range between 50 and 100 [8].

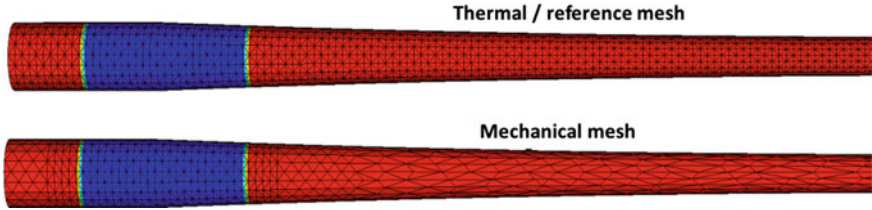


Fig. 3 Thermal/reference mesh with 33,000 nodes (*top*) and mechanical mesh with 5800 nodes (*bottom*)

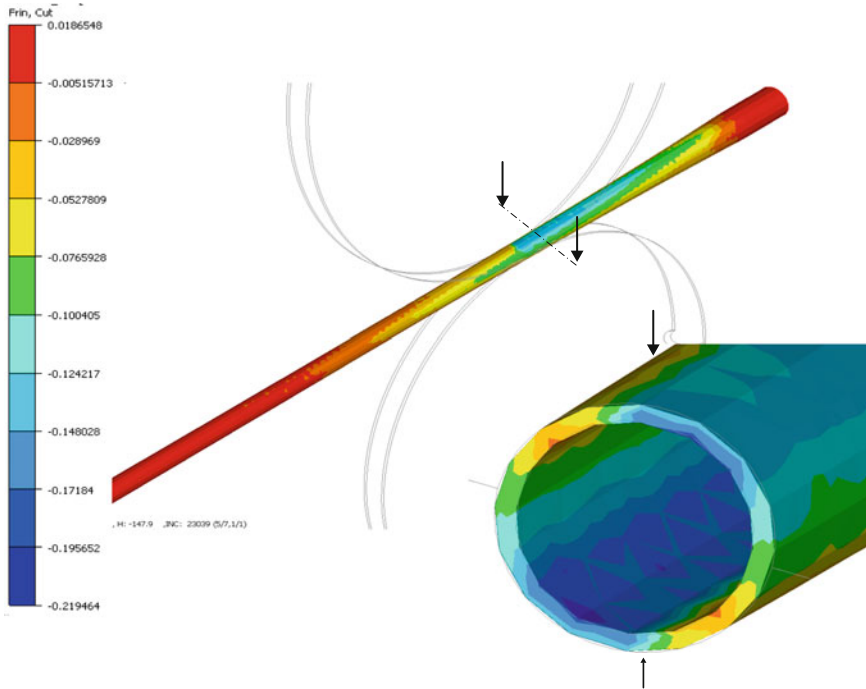


Fig. 4 Isovalues of the radial deformation after 0.20 s of process

Table 1 Multi-mesh speed-up according to the mesh size

Reference/thermal mesh	Mechanical mesh	Speed-up
8640	1800	2.8
33,696	5800	5.1
75,780	12,796	6.5

For computations on several processors based on domain partitioning, the construction of the different meshes adapted to each of the physics through mesh derefinement is carried out in parallel, on each domain, using the same iterative

algorithm as for the remeshing operations of Sect. 2 [7] but in the frame of a node nested approach [10]. After the final domain repartitioning that allows balancing the loads among all the processors, the partitions of the different meshes of the multi-mesh method are not located on the same processor (Fig. 5). The remapping operators are then adapted to take this constraint into account in the most efficient way, by minimizing the communications between the processors. An octree-based hierarchical search algorithm is used in an iterative way. If no node of the departure mesh (reference mesh, M_R) coincides with the node of the arrival mesh (physical mesh, M_{P_i}), then this node will be searched onto another processor in the next iteration. This algorithm is extended to the remapping between meshes without nesting condition, which requires to search for the element of the departure mesh containing a node of the arrival mesh, and will be also used in Sect. 5 to construct the transfer operators between the meshes of the multigrid method.

Although the multi-mesh method is perfectly parallelized, its effectiveness decreases with the number of processors, as shown in Table 2 for the cold pilgering problem. The lower the number of nodes, the faster is this decrease. It originates in the specificity of this method which is to use meshes of very different sizes. For the studied problems, the main part of the computation time is devoted to solving the mechanical problem. As a result, the parallel efficiency of the multi-mesh method is that of the resolution on the mechanical mesh, which contains far fewer nodes (see Table 2) than the reference mesh. But the larger the number of nodes, the larger is the parallel efficiency. Thus, on the mesh with 33,000 nodes, parallel computing with 16 processors on a single mesh consists of assigning approximately 2000 nodes to each processor. Since the mechanical mesh has only 5800 nodes, its partitioning into 16 produces sub-domains with only 360 nodes, which is too little, so that the communication times between the processors become

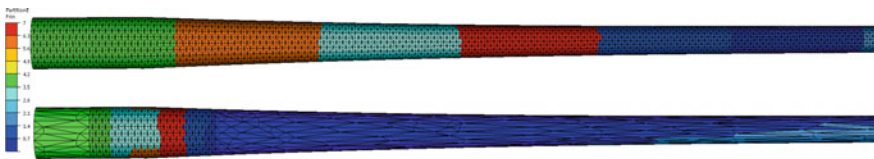
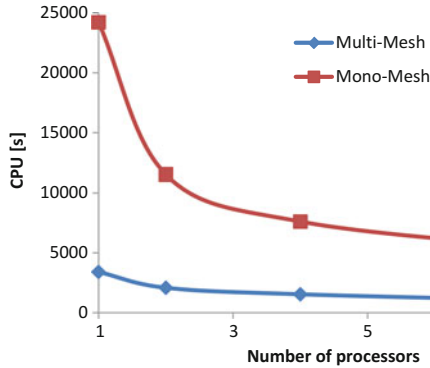


Fig. 5 Mesh partitioning on 8 processors for the reference/thermal mesh (*top*) and for the mechanical mesh (*bottom*)

Table 2 Multi-mesh speed-up according to number of processors and to mesh size

No procs	33,000 nodes mesh	76,000 nodes mesh
1	5.1	6.5
2	3.9	5.4
4	3.4	4.8
8	2.5	3.2
16	1.8	2.9

Fig. 6 Evolution of computational time with the multi-mesh and usual (mono-mesh) resolution method according to the number of processors for the cogging problem [8]



significant. It is numerically verified that the parallel efficiency of the multi-mesh method is in fact that of its mechanical mesh.

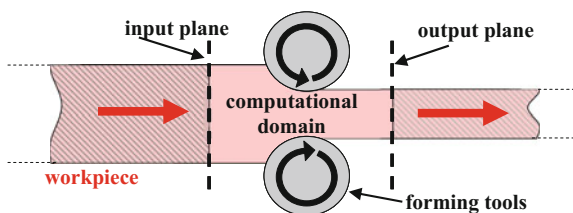
For the viscoplastic cogging problem presented in [8], the same observations are made (Fig. 6). The speed-up similarly decreases with the number of processors. It is equal to 7.1 on 1 processor, reduces to 5.5 on 2 processors, to 4.9 on 4 processors and to 5.3 on 8 processors, which is however very interesting and very appreciable for calculations that may require several days.

4 Adaptive ALE Formulation

4.1 Decoupled ALE Formulation

Another characteristic of certain forming methods that can be used to reduce computation times is their almost stationary nature, over the entire domain or more particularly in the deformation zone that is then highly localized. This occurs in rolling, extrusion, machining or friction stir welding (FSW) ... On the one hand, the Arbitrary Lagrangian or Eulerian (ALE) formulation makes it possible to significantly reduce the size of the computational domain by considering only the part of the domain that actually undergoes the deformation (Fig. 7) or by limiting mesh refinement to the gradient zone (Fig. 8). On the other hand, it allows to considerably reduce the number of time-consuming remeshing operations while providing a more accurate finite element discretization in the highly deformed zones.

Fig. 7 Reduction of the computational domain through using an ALE formulation



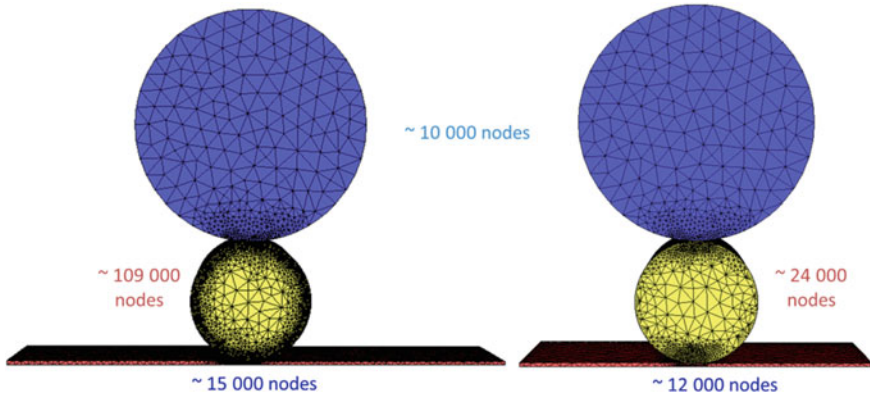


Fig. 8 Reduction of both the computational domain (metal sheet) and of the number of elements (in the intermediate roll) through using an ALE formulation: lagrangian (*left*) and ALE (*right*) models

The retained approach is based on the decoupling of the operators in three steps: (1) the problem equations are solved according to an Updated Lagrangian formulation at time t , then (2) the meshing velocity v_{mesh} is calculated to establish the new geometry of the domain at time $t + \Delta t$ and (3) the state variables are evaluated on this new domain at time $t + \Delta t$. The first step is identical to the resolution performed in a Lagrangian formulation (see Sect. 2). The transfer of fields of the third step, between the Updated Lagrangian mesh and the ALE mesh, uses the super-convergent remapping presented in Sect. 3.2 for the constant P0 fields, and an upstream convection method for the P1 continuous fields:

$$\frac{d_{grid}\varphi}{dt} = \frac{\partial_{mat}\varphi}{\partial t} + (v_{mesh} - v) \cdot \nabla\varphi \quad (14)$$

where $\nabla\varphi$ is calculated in the upstream element [16]. In material forming, the main difficulties are concentrated in the second step, the calculation of the meshing velocity v_{mesh} , in other words in the adaptive regularization of the mesh at $t + \Delta t$. The accuracy of the computations requires an adaptive approach based on an estimation of the discretization error, for example that of Zienkiwicz and Zhu [12]. For a viscoplastic problem, the discretization error is then estimated by:

$$\theta = \left(\int_{\Omega} (\tilde{s}_h - s_h) : (\tilde{\epsilon}_h - \dot{\epsilon}_h) d\omega \right)^{1/2} \quad (15)$$

where the recovered deviatoric stress tensor \tilde{s}_h and strain rate tensors $\tilde{\epsilon}$ are either calculated by the SPR technique presented in Sect. 3.2, or by using the Recovery by Equilibrium in Patches (REP) approach [17]. The mesh regularization so results

into a compromise between respecting the optimal mesh size h_e^{opt} provided by the error estimator and obtaining elements of the best possible quality [15, 18]. A weighted centering algorithm is used:

$$\forall k, \quad x_k^{(it+1)} = \frac{1}{|\Gamma_k|} \sum_{e \in \Gamma_k} \omega_e^{tot} x_e^{(it)} \quad (16)$$

$$\omega_e^{adapt} = \left(\frac{h_e^{opt}}{h_e^{act}} \right) ; \quad \omega_e^{qual} = \chi \frac{[V_e^{act}]^+}{(p_e^{act})^3} ; \quad \omega_e^{tot} = (1 - \zeta) \omega_e^{qual} + \zeta \omega_e^{adapt} \quad (17)$$

where Γ_k is the set of element containing node k , $x_e^{(it)}$ is the coordinate of the center of element e at the centering iteration i , h_e^{act} its size, V_e^{act} its volume and p_e^{act} its perimeter. ζ is a weighting coefficient between the two objectives.

4.2 Surface Regularization

The regularized mesh is then projected onto the surface of the domain updated at time $t + \Delta t$ by the Updated Lagrangian formulation. This involves a new transport equation which now applies to the surface of the domain. It has the same characteristics of showing strong diffusion if the scheme is not of a sufficient order. Therefore, a similar approach to that of Sect. 3.2 is used by first constructing a surface C_{arr}^1 that is almost C^1 (continuous with continuous derivative), starting from the updated surface C_{arr}^0 that is only C^0 (continuous with discontinuous derivative), and then projecting the regularized surface C_{dep}^0 onto C_{arr}^1 . C_{arr}^1 is constructed according to the approach proposed in [19] for the smoothing of tools surface for contact treatment. It is inspired by the technique proposed in [20], itself derived from works in computer vision for surface smoothing [21]. The surface C_{arr}^0 being described by linear triangles (P1), it is sufficient to construct a surface C_{arr}^1 which is discretized by quadratic (P2) facets (Fig. 9). It amounts to transforming the linear segments of the mesh into quadratic segments (Fig. 10).

Normal vectors are generally unknown at mesh vertices. It is observed that the quality of surface smoothing is closely related to the quality of the normals. The *normal voting* strategy proposed in [22] is shown to provide best results [19]. It also

Fig. 9 From linear to quadratic interpolation of the surface based on node normals

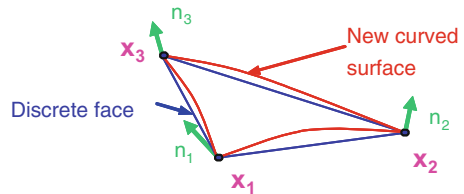
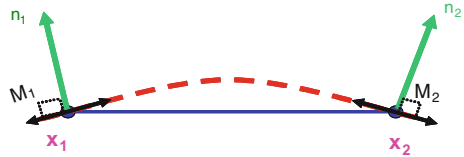


Fig. 10 From linear to quadratic interpolation of surface edges based on node normals



allows detecting surface singularities, such as edges and corners, from the eigenvalues of the *voting* (or covariance) matrix [19, 22, 23].

4.3 Application to Simulation of Adiabatic Shear Band

The ALE formulation can thus be used to reduce computation times by allowing meshes with fewer degrees of freedom to be used, such as, for example, the problem of sheet rolling with deformable rolls of Fig. 8. Lagrangian calculation requires 290 h whereas the ALE calculation is limited to 40 h, so providing acceleration by a factor of 7. The ALE formulation can also be used to calculate very complex flows with large material deformations that require too many remeshings within a Lagrangian formulation. It was thus used with great success for the simulation of the FSW, allowing to accurately model the formation of the tool print on the welded sheet, and to predict the formation of defects such as tunnel holes or flash formation [18, 24]. Here, it is applied to the simulation of an equally complex phenomenon, the formation of Adiabatic Shear Bands (ASB) during the machining of titanium alloys at very high speed where it does not require introducing any unsound physical model such as damage or any specifically dedicated numerical technique such as in [25]. The studied problem is extracted from [25] and consists of the 3D high speed orthogonal cutting of a micrometric component described in Fig. 11.

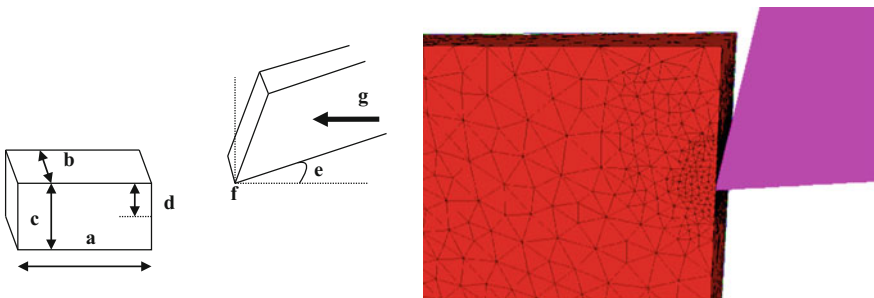


Fig. 11 Scheme speed orthogonal cutting process and initial mesh with 4800 nodes

Figure 12 shows how the adaptive ALE formulation not only allows to refine the mesh at the tool tip, but also provides elements of excellent quality in this zone where all studied phenomena originate. The simulation of a shear band formation (see Fig. 13) could not be carried out to completion without the use of the ALE formulation.

Figure 13 shows how the mesh refinement procedure conforms to the primary shear zone and allows to model the adiabatic localization phenomena which are at the origin of chip fragmentation. In Fig. 15 and Table 3, by using different mesh refinements, it is verified that the width of the adiabatic shear band is independent on the mesh size, so showing the finite element convergence of the model and the advantage of such plain thermo-mechanical approach with respect to the introduction of a damage model sensitive to mesh size (Fig. 14).

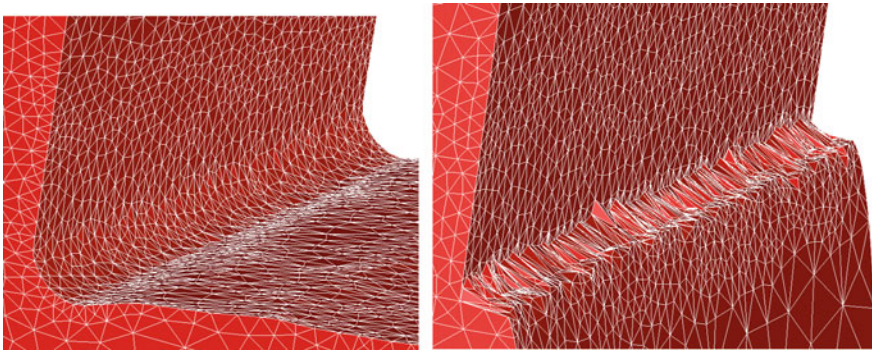


Fig. 12 Mesh at the tool edge with (left) and without (right) using ALE algorithm

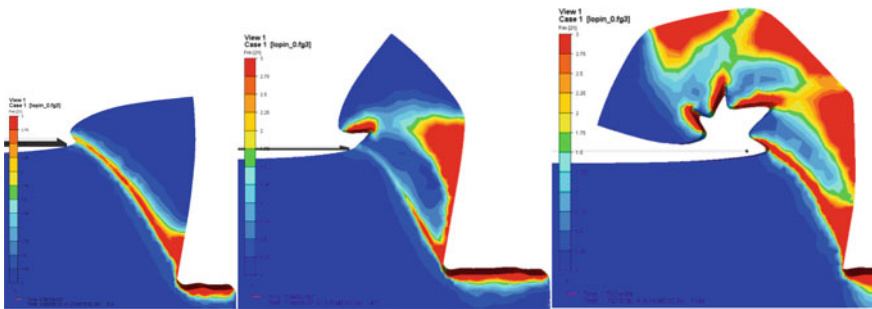


Fig. 13 Distributions of deformation (scale cut off at 3.0)

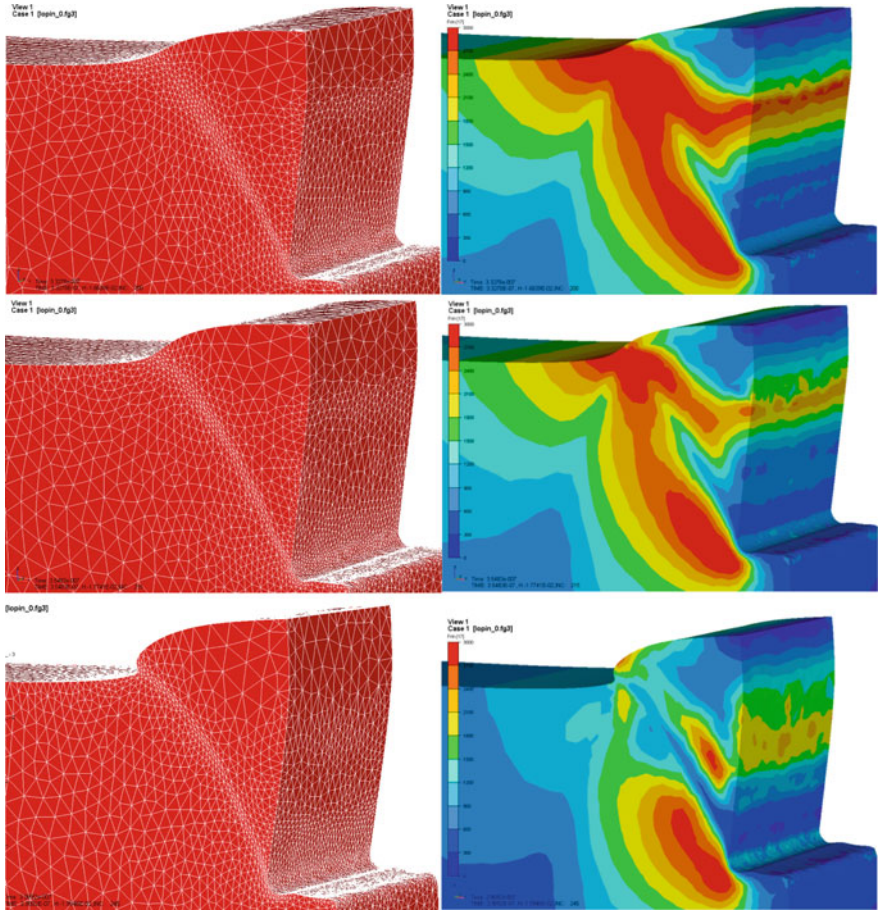


Fig. 14 Evolution of mesh adaptation guided by isotropic error estimator (*left*) and Von Mises stress (MPa) at different times of the ASB formation

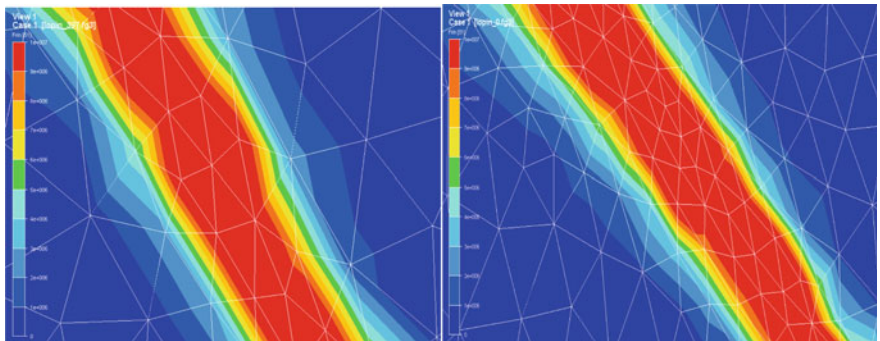


Fig. 15 ASB bandwidth for several meshes based on distribution of strain rate. Mesh of the whole model are respectively made of 54,000 (*left*) and 260,000 (*right*) elements

Table 3 Bandwidths for different mesh sizes in ASB formation

No of elements of the whole model	No of elements throughout ASB	Band width (μm)
54,000	4–5	3.49
65,000	6	3.43
130,000	8	3.40
260,000	10	3.38

5 Steady-State Formulation

When the problem is clearly stationary, it is much more efficient to directly calculate the steady state rather than to approach it incrementally either with a Lagrangian formulation requiring to model the entire domain in both space as in time or with an ALE formulation allowing to only reduce the space domain, as previously suggested. A steady-state formulation makes it possible to eliminate time and to reduce the spatial domain as much as an ALE formulation. On the other hand, it requires solving a multi-field problem [26, 27] consisting at least of the variables of the thermo-mechanical problem and of the domain surface geometry, which is also unknown. The literature is divided between fixed-point iterative approaches [28–30] and the direct resolution of the coupled multi-field problem [26, 27]. The first approach allows preserving the initial solver by easily coupling it to a fixed-point iterative method of free surface correction. The resolution of the thermo-mechanical problem on a given domain is so alternatively solved with the correction of the domain surface according to a given velocity [30]. The key point of the steady-state formulation therefore regards the resolution of this free surface problem for a known velocity field \mathbf{v} . \mathbf{X} defining the domain coordinates at the current iteration, \mathbf{x} the coordinates of the corrected domain and \mathbf{t} the correction, the stationarity condition is written:

$$\mathbf{v}(\mathbf{X}) \cdot \mathbf{n}(\mathbf{x}) = \mathbf{v}(\mathbf{X}) \cdot \mathbf{n}(\mathbf{X} + \mathbf{t}) = 0 \quad ; \quad \mathbf{t} = \bar{t}_1 \mathbf{d}_1 + \bar{t}_2 \mathbf{d}_2 \quad (18)$$

where \mathbf{d}_1 and \mathbf{d}_2 are two vectors perpendicular to the flow direction, \bar{t}_1 and \bar{t}_2 the domain corrections in each of these directions. The stationarity Eq. (18) allowing the computation of (\bar{t}_1, \bar{t}_2) is shown to be a convection equation. It so requires to be solved by an upstream scheme. Having introduced two degrees of freedom for \mathbf{t} makes it possible to correct the surface along its edges but requires a Least Squares type formulation. In [30], a SUPG type Least Squares formulation is then proposed. For the points belonging to the non-singular parts of the surface, it leads to an indefinite system, so the problem is stabilized by introducing a Laplacian allowing to regularize the surface mesh. This approach amounts to minimizing a multi-objective problem consisting of antagonistic objectives which compromise solutions prove difficult to calculate. This results into a rather large number of iterations of the fixed point algorithm [30].

Using the normal voting method [19, 21, 22] discussed in Sect. 4.2, it is possible to automatically identify the edges of the surface and to calculate the two normals d_1 and d_2 which characterize them (Fig. 16). On the non-singular parts of the surface, the normal voting method provides the normal d_1 to the surface. According to its degree of singularity, a mesh node will thus be assigned a single degree of freedom \bar{t}_1 , or two (\bar{t}_1, \bar{t}_2). For a node with a single degree of freedom, the weak form of the problem is given by a rather conventional SUPG formulation [28]:

$$\forall k, \int_{\partial\Omega} N_k^{SUPG}(v(X) \cdot n(X + \bar{t}_1 d_1)) ds = 0 \quad (19)$$

Whereas with two degrees of freedom, this equation is written both for correction directions d_1 and d_2 respectively on the patches of elements $\partial\Omega_1$ and $\partial\Omega_2$ that are perpendicular to each of them (see Fig. 16):

$$\forall k, \forall i = 1, 2, \int_{\partial\Omega_i} N_k^{SUPG}(v(X) \cdot n(X + \bar{t}_i d_i)) ds = 0 \quad (20)$$

This steady-state formulation is applied to the multi-stand Kocks rolling shown in Fig. 17. The computation times obtained with the incremental formulation and with the two stationary formulations—from [30] and from Eqs. (19) and (20)—are given in Table 4. They show an acceleration factor of 5 provided by the first approach [30], despite a much finer mesh. However, the number of iterations of fixed-point algorithm remains relatively high, as also observed in [30], seeking a compromise between surface correction and mesh regularization. The second formulation derived from Eqs. (19) and (20) makes it possible to overcome this difficulty, reducing by almost three the number of iterations, and bringing the acceleration to 30 with respect to the incremental approach.

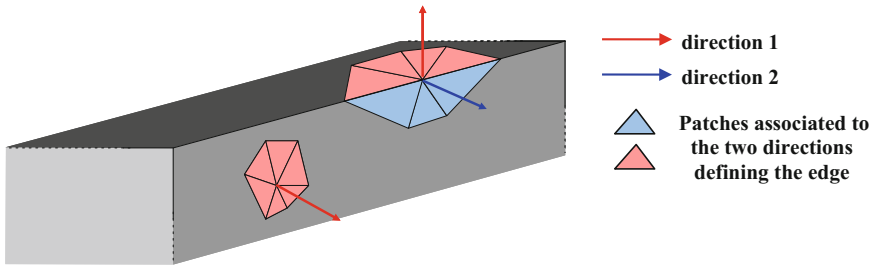


Fig. 16 Normals (d_1 and d_2) and associated patches of elements on surface and edges

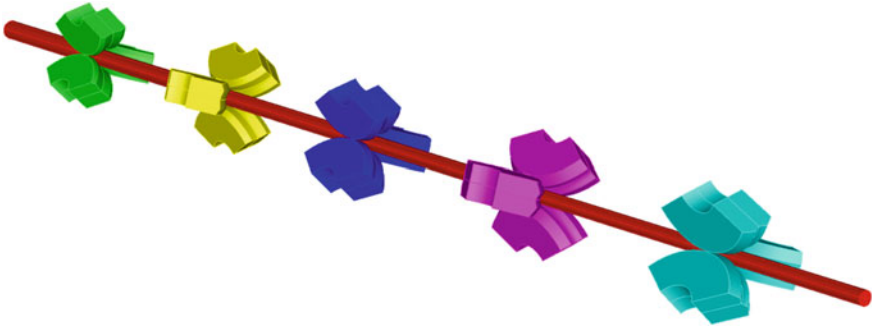


Fig. 17 Multi-stand Kocks rolling with 5 stands

Table 4 Computing time for the multi-stand (2 stands) rolling

	No of nodes	No of increments/iterations	Computing time
Lagrangian formulation	10,000 → 15,500	1280	15 h 49 min
First formulation	50,500	40	2 h 54 min
Second formulation	27,600	15	28 min



Fig. 18 Bar of the multi-stand Kocks rolling partitioned on 12 processors

Handling problems of larger dimensions, here considering 5 rolling stands, justifies using the parallel calculation. The mesh is thus partitioned into 12 sub-domains in Fig. 18, and Fig. 19 shows the excellent parallel efficiency of the steady-state formulation. It consequently shows to be an excellent alternative to incremental computation when the problem allows it.

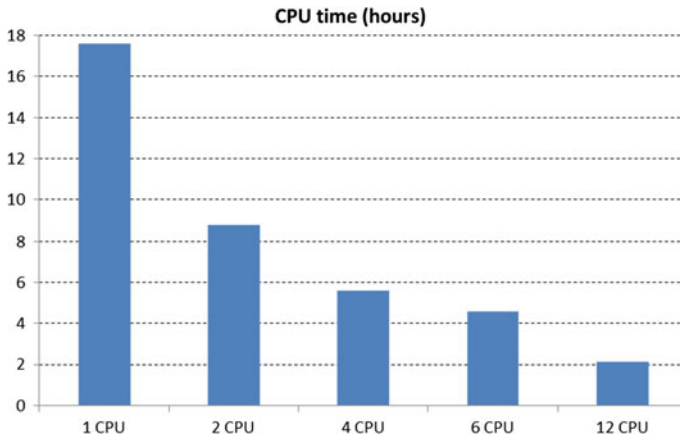


Fig. 19 Computational time for the multi-stand Kocks rolling according to the number of processors

6 Multigrid Preconditioner

In the most general case where no specificity of the problem or of its geometry can be considered to speed-up the calculations, it is still possible to try to improve the performances of the resolution method. With the utilized implicit formulation, and for large-scale problems, 80% of the computation time is devoted to the resolution of linear systems. Its algorithmic complexity, using the conjugate residual method preconditioned by an incomplete Choleski resolution (PCR-ILU1, see Sect. 2) is proportional to $N^{1.5}$, N being the number of degrees of freedom. As a result, the mesh refinement by a factor 2 in each space direction results in a multiplication of the number of degrees of freedom by a factor 8 and of the computation time by a factor 22. Using additional parallel resources makes it possible to compensate for the increase in the number of degrees of freedom (the factor 8). However, the increase in the number of solver iterations (factor $N^{0.5}$ or 2.8) cannot be reduced in this manner. It is therefore of the greatest interest, for the resolution of very large systems, to use solvers which complexity is close to N . The multigrid (MG) methods present such property through using several hierarchical levels of “grids” on the same domain. The coarser grids make it possible to very efficiently compute the low frequencies of the solution, those that an iterative solver find it difficult to obtain, and which are at the origin of the complexity in N^α with $\alpha > 1$. Following [31, 32], a hybrid MG approach is retained. The different levels of grids are obtained by hierarchical derefinement of the computational mesh; in the applications, only 3 grids are considered (Fig. 20). The transfer operators between the grids are then constructed from the interpolation operators between the meshes, which provides the “geometrical” character to the approach. If the linear system is written as (21) where the index h represents the fine grid and the index H the coarse

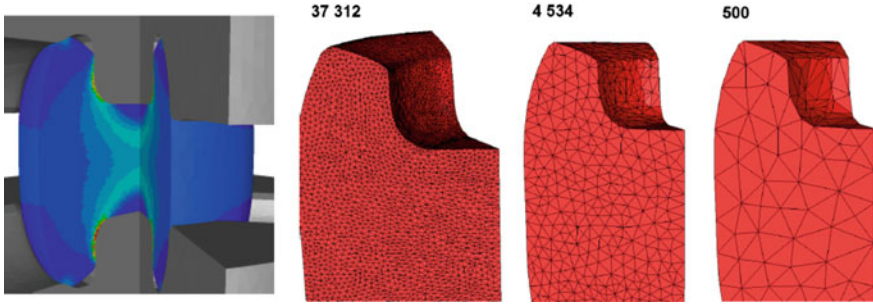


Fig. 20 Forged spindle near the end of the process (*left*). Three mesh levels utilized at an intermediate stage of forging (*right*)

grid, assuming that there are only two grids, the problem to be solved on the coarse grid is given by (21) where δX_H is the correction calculated on the coarse grid, R_h^H is the restriction operator and R_H^h the interpolation operator:

$$A_h X_h = b_h \quad ; \quad A_H \delta X_H = r_H \quad ; \quad r_H = R_h^H r_h = R_h^H (A_h X_h - b_h) \quad (21)$$

The linear systems constructed on the intermediate and coarse grid are also obtained by projection, according to the Ritz-Galerkin method, which provides the “algebraic” character to the approach. With 2 grids, the A_H matrix of the linear system on the coarse grid is given by (22):

$$\delta x_h = R_H^h \delta X_H \quad ; \quad A_H = R_H^h A_h R_h^H \quad ; \quad R_h^H = (R_H^h)^t \quad (22)$$

This algebraic approach is essential to preserve on the different grid levels both the incompressibility condition and the contact conditions [31, 32]. The different operators necessary for the construction of a parallel multigrid method are therefore quite the same as those developed for the multi-mesh approach of Sect. 3. For the considered mixed problem, a multigrid cycle is used as a preconditioner for the conjugated residual (PCR). At the intermediate and higher levels, it uses pre and post smoothing iterations by incomplete Choleski decomposition (ILU0). On the coarser grid, the linear system is directly solved in parallel using MUMPS library [33].

For the linear system derived from an upsetting between flat dies, the multigrid preconditioner is numerically shown to provide an asymptotical behavior of $N^{1.08}$ close to the optimal linear complexity. Its parallel efficiency is also quite satisfying, being the same as those of the reference solver [34]. The robustness with respect to frequent remeshings and efficiency of the algorithm is evaluated for the complete forging of a spindle component (Fig. 20). Figure 21 shows the evolution of the total computational time compared to the reference PCR-ILU1 solver. A global speed-up

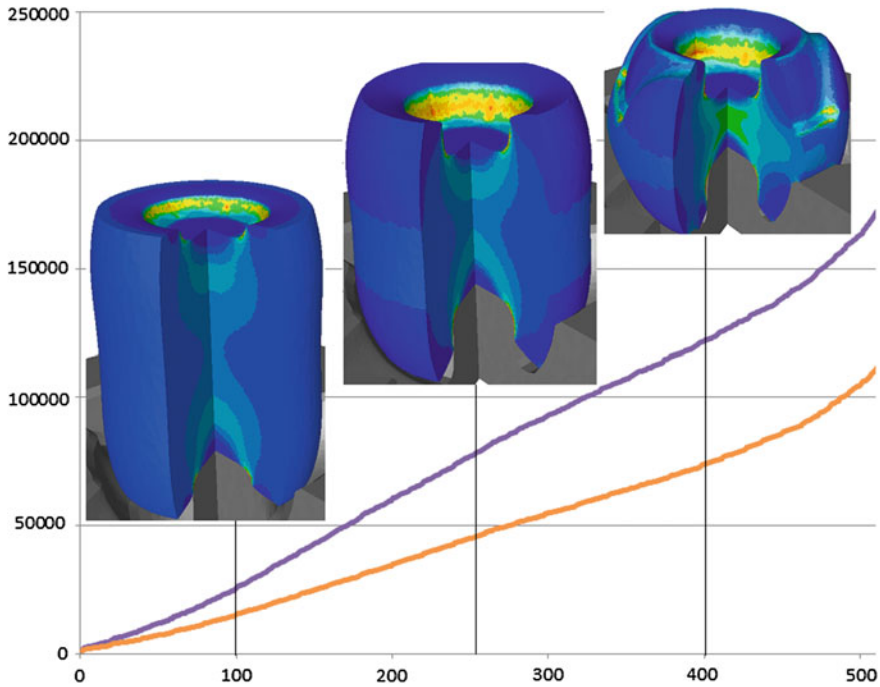


Fig. 21 Time evolution (increments) of the total computation time for the spindle forging with the reference solver (PCR-ILU1) (*purple*) and with PCR-3G multigrid preconditioner (*yellow-orange*), along with the cumulated strain isovalues

of 1.61 is obtained. For other problems, speed-ups up to 2.7 can be observed [34], but the most interesting results of the MG approach regards the almost linear asymptotic complexity.

7 Conclusion

When the problem involves several physics requiring different spatial discretization, then the multi-mesh method offers the possibility of using optimal meshes for each of the physics and thus of significantly reducing the computation time. Depending on the type of problem studied, the speed-ups are between 3 and 7, or between 50 and 100. However, in parallel calculations, these speed-ups decrease with the number of processors. The multi-mesh method has the parallel efficiency of the resolution on its coarsest mesh. More generally, its use requires to control the precision of the remapping operators between the meshes. Whereas the node nesting condition is sufficient to achieve this accuracy with simple viscoplasticity problems, the extension to elastoplasticity requires the development of more

efficient remapping operators at integrating points. They are obtained from super-convergent recovery (SPR) techniques, improved to preserve the superconvergence properties on the surface of the domain as well as in parallel computations.

When the problem is almost stationary, then the ALE formulation allows to significantly reduce the size of the computational domain. In some cases such as the rolling with deformable cylinders, this is sufficient to speed-up the calculations by a factor of 7. The ALE formulation also makes it possible to simulate especially complex problems that cannot be addressed with a Lagrangian formulation, such as the formation of adiabatic shear bands during machining at very high speed. These bands can be simulated without using any damage model or numerical artefact, and their size (width) is independent of mesh size, thanks to the adaptive formulation used. A method similar to that of the superconvergence recovery makes it possible to smooth the mesh surface and so to preserve with accuracy the domain geometry during the regularization steps.

When the problem is perfectly stationary, then the direct calculation of this state allows the calculations to be significantly speeded-up by more than 30. In part, this result is based on the use of a new formulation of the steady-state equation, of SUPG type, differently written according to whether the node belongs to the surface or to an edge, thanks to a prior recognition of these edges by the normal voting method. The fixed point iterative algorithm then converges faster, and the calculations are up to 6 times faster than with the previous formulation, a least squares method with an upstream shift of SUPG type. For parallel calculations, this speed-up factor is correctly preserved.

Finally, when no particular strategy can be proposed, the multi-grid method can still accelerate the calculations by a factor of 2.7 or more. It is based on a hybrid, algebraic and geometric approach, and on the use of mesh derefinement and field transfer operators working in parallel on complex geometries. The more specific potential offered by this multigrid method, with the aim of handling problems with more degrees of freedom, is its almost linear complexity observed on an upsetting problem.

References

1. M. Péréme et al., Benefits of high performance computing applied to the numerical simulation of forged parts, in *20th International Forging Congress* (2011)
2. N. Soyris et al., Forging of a connecting rod: 3D finite element calculation. *Eng. Comput.* **9**(1), 63–80 (1992)
3. T. Coupez, S. Marie, From a direct solver to a parallel iterative solver in 3-D forming simulation. *Int. J. Supercomput. Appl. High Perform. Comput.* **11**(4), 277–285 (1997)
4. J.L. Chenot, L. Fourment, K. Mocellin, Numerical treatment of contact and friction in FE simulation of forming processes. *J. Mater. Process. Technol.* **125–126**, 45–52 (2002)
5. T. Coupez, N. Soyris, J.-L. Chenot, 3-D finite element modelling of the forging process with automatic remeshing. *J. Mater. Process. Technol.* **27**(1–3), 119–133 (1991)
6. T. Coupez, A mesh improvement method for 3D automatic remeshing, in *Numerical Grid Generation in Computational Fluid Dynamics and Related Fields* (Pineridge Press, 1994)

7. T. Coupez, H. Dignonnet, R. Ducloux, Parallel meshing and remeshing. *Appl. Math. Model.* **25**(2), 153–175 (2000)
8. M. Ramadan, L. Fourment, H. Dignonnet, A parallel two mesh method for speeding-up processes with localized deformations: application to cogging. *Int.J. Mater. Form.* **2**, 581–584 (2009)
9. K.W. Kpodzo, Accélération des calculs pour la simulation du laminage à pas de pèlerin en utilisant la méthode multimallages. Ecole Nationale Supérieure des Mines de Paris (2014)
10. G. Carte et al., Coarsening techniques in multigrid applications on unstructured meshes, in *European Congress on Computational Methods in Applied Sciences and Engineering, ECCOMAS* (2000)
11. S. Kumar, L. Fourment, S. Guerdoux, Parallel, second-order and consistent remeshing transfer operators for evolving meshes with superconvergence property on surface and volume. *Finite Elem. Anal. Des.* **93**, 70–84 (2015)
12. O.C. Zienkiewicz, J.Z. Zhu, The superconvergent patch recovery (SPR) and adaptive finite element refinement. *Comput. Methods Appl. Mech. Eng.* **101**(1–3), 207–224 (1992)
13. L. Fourment, J.L. Chenot, Error estimators for viscoplastic materials—application to forming processes. *Eng. Comput.* **12**(5), 469–490 (1995)
14. R. Boussetta, T. Coupez, L. Fourment, Adaptive remeshing based on a posteriori error estimation for forging simulation. *Comput. Methods Appl. Mech. Eng.* **195**(48–49), 6626–6645 (2006)
15. S. Guerdoux, L. Fourment, Error estimation and accurate mapping based ALE formulation for 3D simulation of friction stir welding, in *NUMIFORM '07: Materials Processing and Design: Modeling, Simulation and Applications, Pts I and II* (2007), pp. 185–190
16. C. Stoker et al., A velocity approach for the ALE-method applied to 2D and 3D problems. *Simul. Mater. Process.: Theory Methods Appl.* (1998), pp. 95–101
17. B. Boroomand, O.C. Zienkiewicz, Recovery by equilibrium in patches (REP). *Int. J. Numer. Meth. Eng.* **40**, 137–164 (1997)
18. S. Guerdoux, L. Fourment, A 3D numerical simulation of different phases of friction stir welding. *Model. Simul. Mater. Sci. Eng.* **17**(7) (2009)
19. M. Hachani, L. Fourment, A smoothing procedure based on quasi-C 1 interpolation for 3D contact mechanics with applications to metal forming. *Comput. Struct.* **128**, 1–13 (2013)
20. T. Hama et al., Finite-element simulation of springback in sheet metal forming using local interpolation for tool surfaces. *Int. J. Mech. Sci.* **50**(2), 175–192 (2008)
21. T. Nagata, Simple local interpolation of surfaces using normal vectors. *Comput. Aided Geom. Des.* **22**, 327–347 (2005)
22. D.L. Page et al., Normal vector voting: crease detection and curvature estimation on large, noisy meshes. *Graph. Models* **64**(3–4), 199–229 (2002)
23. G. Medioni, M.-S. Lee, C.-K. Tang, *A Computational Framework for Segmentation and Grouping* (Elsevier, 2000)
24. M. Assidi et al., Friction model for friction stir welding process simulation: calibrations from welding experiments. *Int. J. Mach. Tools Manuf.* **50**(2), 143–155 (2010)
25. M. Bäker, J. Rösler, C. Siemers, A finite model of high speed metal cutting with adiabatic shearing. *Comput. Struct.* **80**, 495–513 (2002)
26. D. Balagangadhar, D.A. Tortorelli, A displacement based reference frame formulation for the analysis of steady manufacturing processes, in *Simulation of Materials Processing: Theory, Methods and Applications* (1998), pp. 77–83
27. X. Qin, P. Michaleris, Thermo-elasto-viscoplastic modelling of friction stir welding. *Sci. Technol. Weld. Joining* **14**(7), 640–649 (2009)
28. Y.S. Lee, P.R. Dawson, T.B. Dewhurst, Bulge predictions in steady-state bar rolling processes. *Int. J. Numer. Meth. Eng.* **30**(8), 1403–1413 (1990)
29. A. Hacquin, P. Montmitonnet, J.P. Guillerault, A steady state thermo-elastoviscoplastic finite element model of rolling with coupled thermo-elastic roll deformation. *J. Mater. Process. Technol.* **60**(1–4), 109–116 (1996)

30. U. Ripert, L. Fourment, J.-L. Chenot, An upwind least square formulation for free surfaces calculation of viscoplastic steady-state metal forming problems. *Adv. Model. Simul. Eng. Sci.* **2**(1), 15 (2015)
31. K. Mocellin et al., Toward large scale F.E. computation of hot forging process using iterative solvers, parallel computation and multigrid algorithms (English). *Int. J. Numer. Methods Eng.* **52**(5–6), 473–488 (2001)
32. B. Rey, K. Mocellin, L. Fourment, A node-nested Galerkin multigrid method for metal forging simulation. *Comput. Vis. Sci.* **11**(1), 17–25 (2008)
33. P.R. Amestoy et al., A fully asynchronous multifrontal solver using distributed dynamic scheduling. *SIAM J. Matrix Anal. Appl.* **23**(1), 15–41 (2001)
34. F. Vi et al., Hybrid parallel multigrid preconditioner based on automatic mesh coarsening for 3D metal forming simulations (submitted)

Discrete Simulation of Cone Penetration in Granular Materials

Antonio Gens, Marcos Arroyo, Joanna Butlanska
and Catherine O’Sullivan

Abstract The simulation of penetration problems into granular materials is a challenging problem as it involves large deformations and displacements as well as strong non-linearities affecting material behaviour, geometry and contact surfaces. In this contribution, the Discrete Element Method (DEM) has been adopted as the modelling formulation. Attention is focused on the simulation of cone penetration, a basic reconnaissance tool in geotechnical engineering, although the approach can be readily extended to other penetration problems. It is shown that DEM analysis results in a very close quantitative representation of the cone resistance obtained in calibration chambers under a wide range of conditions. DEM analyses also provides, using appropriate averaging techniques, relevant information concerning mesoscale continuum variables (stresses and strains) that appear to be in agreement with physical calibration chamber observations. The examination of microstructural variables contributes to a better understanding of the mechanisms underlying the observed effects of a number of experimental and analysis features of the cone penetration test.

1 Introduction

Penetration problems are ubiquitous in geotechnical engineering and other geomechanical applications. Notable examples are the use of tube samplers to recover soil specimens, the installation of driven piles in the ground or a variety of

A. Gens (✉) · M. Arroyo · J. Butlanska
Universitat Politècnica de Catalunya, Barcelona, Spain
e-mail: antonio.gens@upc.edu

M. Arroyo
e-mail: marcos.arroyo@upc.edu

J. Butlanska
e-mail: joanna.butlanska@upc.edu

C. O’Sullivan
Imperial College, London, UK
e-mail: cath.osullivan@imperial.ac.uk

penetration probes for site investigation purposes. A realistic numerical simulation of those type of problems would yield important advantages concerning the understanding of the processes involved during penetration and its effects on the state of the soil possibly leading to a more rational approach for, among others, in situ test interpretation, assessment of sampling disturbance and pile design. A variety of computational techniques are available to tackle this kind of problems [1].

Here attention is focused on the use of the Discrete-Element Method (DEM) to simulate the penetration of a cone into a granular material although the same approach can be readily extended to other penetration problems. The cone penetration test (CPT) is a widely used site investigation tool for geomechanical applications. The tests consists in introducing the cone, of standard dimensions, into the granular material at a constant rate of penetration. The unit cone resistance is measured in a quasi-continuous manner during penetration. Normally, lateral friction and pore pressures are also measured but those parameters are not considered herein.

Cone penetration tests are invariably interpreted based on empirical correlations derived either from calibrated observations in the field or, often, from calibration chambers. The latter provide more consistent information as the material is homogenous and installed at a specified density. Also, the boundary conditions (stresses or displacements) are directly controlled. However, calibration chambers cannot incorporate the effects of aging (except in a very limited manner) and they often require a size correction because of the necessarily restricted dimensions of the facility.

A successful simulation of cone penetration would be able to complement and partially replace the performance of tests in calibration chambers that are generally expensive and time-consuming. In this contribution, 3D DEM simulations of cone penetration tests are performed and compared with experimental results from calibration chambers, both at the macroscale and at the continuum mesoscale. A number of microstructural variables are then examined in order to enhance the understanding of the mechanisms underlying the penetration process.

2 Features of the Analysis

DEM has been used for the modelling of the cone penetration [2]. The granular medium is represented by a number of finite size particles that interact through their contacts. The method tracks the motion of those particles subjected to a series of forces transmitted by the adjacent particles through the contacts [3]. A number of 2D DEM analyses of cone penetration have been reported (e.g. [4–6]). However, it is clear that a proper description of the kinematics of the penetration requires 3D analyses (see, for instance, [7–10]).

Table 1 Parameters of the contact law

Parameter	Value
K_{coeff} (MN/m)	300
Stiffness ratio, α	0.25
Friction coefficient $\tan(\Phi_\mu)$	0.35
Damping	0.05

In this study, code PFC3D [11] has been employed. Particles are assumed to be spherical to ensure a more efficient computational procedure. Particle rotation was prevented (except in one case to be discussed later) to mimic roughly the particle entanglement caused by the non-spherical shape of real particles [12]. The simulations employed numerical non-viscous damping [13]; this is equivalent to suppressing mechanical wave propagation in the system and it is particularly useful to achieve rapid convergence in quasi-static problems.

An elasto-plastic constitutive law has been adopted. The elastic part is linear and the normal and tangential stiffness at any contact, k_N and k_S , are described by the following expressions:

$$k_N = 2K_{coeff} \frac{D_1 D_2}{D_1 + D_2} \quad ; \quad k_S = \alpha k_N$$

where D_1 and D_2 are the diameters of the two contacting particles and K_{coeff} is the normal modulus. A constant ratio, α , between normal and shear stiffness has been selected. The plastic part of the contact law is defined by the interparticle friction angle, Φ_μ . No cohesion has been included in the contact model. A further non-linearity involves a no-tension constraint in the normal direction. The contact model parameters have been calibrated by simulating a triaxial compression test on Ticino sand [7]. They are listed in Table 1.

3 Model Construction and Data Treatment

The cone shaft has been modelled using four rigid cylindrical walls, one frictionless and three frictional as illustrated in Fig. 1. The cone tip angle is 60° . Perfect roughness was assumed in the contact between cone and particles, and the cone-particle friction coefficient was set equal to the interparticle friction. The calibration chamber walls are frictionless. In most tests described here the cone diameter, d_c , was 72 mm and the calibration chamber diameter D_c was 1200 mm. The ratio of these two quantities is 16.5; this is a value for which radial boundary effects are known to influence the results in physical chambers [14]. Procedures to correct scale effects on cone resistance are discussed in [15].

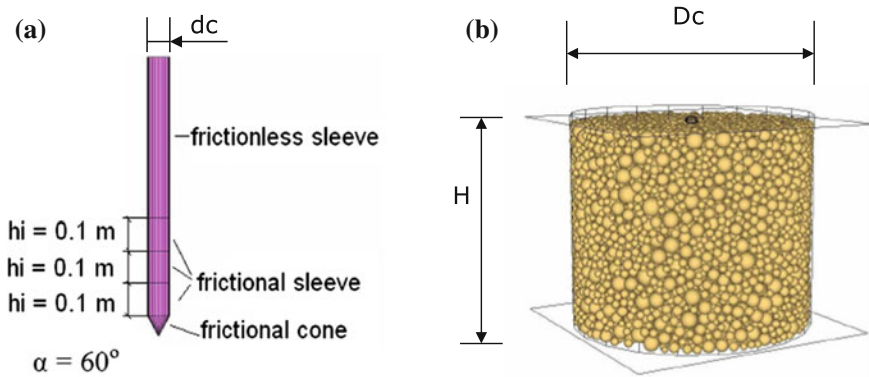


Fig. 1 DEM model of cone penetration in a calibration chamber. **a** Cone **b** calibration chamber

To achieve a manageable particle number, a uniform scaling factor of 50 was applied to the grain size distribution of Ticino sand, the material used in the comparison physical tests. This resulted in a model of about 65,000 particles in the densest specimens. Now the mean particle diameter is 26.5 mm compared to 0.53 mm of the real Ticino sand. Specimens were created to a relative density slightly above the target value using the radial expansion method. Velocities were then reset to zero. Isotropic compression to 10 kPa in which the interparticle friction might be reduced, by trial and error, was used to obtain a close fit to the required relative density. Interparticle friction was then reset to the calibrated value and isotropic stress ramped up to the target value. After equilibration, cone penetration proceeded. Two different boundary conditions have been used: constant lateral stress (BC1) and zero lateral displacements (BC3).

A typical example of the results obtained can be seen in Fig. 2 where the cone tip resistance, q_c , is plotted against depth of penetration. It can be observed that the response is quite noisy due to the large size of the particles relative to the size of the cone. The effect of this relative size on the results can be readily verified by reference to Fig. 3 where the results obtained using different cone sizes have been plotted. It can be noted that as the size of the cone increases, the fluctuations drastically reduce. Since the oscillations are an artefact of the scaled discrete material, it is desirable to filter out the raw results. An exponential filter has proved useful in this regard, based on the following expression:

$$q_c(h) = a(1 - e^{-bh})$$

where h is the penetration depth and a and b are fitting parameters. As a matter of fact, a represents the asymptotic value of the cone resistance. The resulting filtered data is shown in Fig. 2.

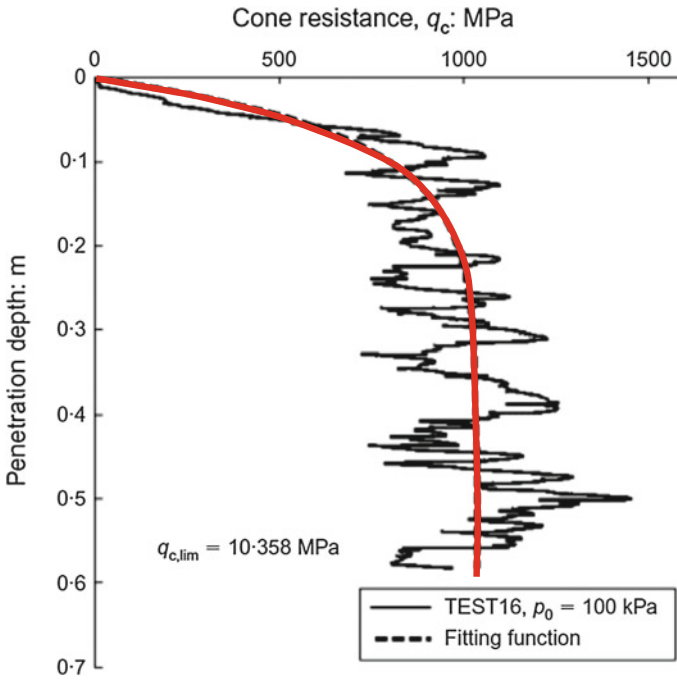


Fig. 2 Typical result of a penetration test simulation and filtered penetration curve. BC1 boundary condition. Confining stress: 100 kPa, relative density, D_R : 75%

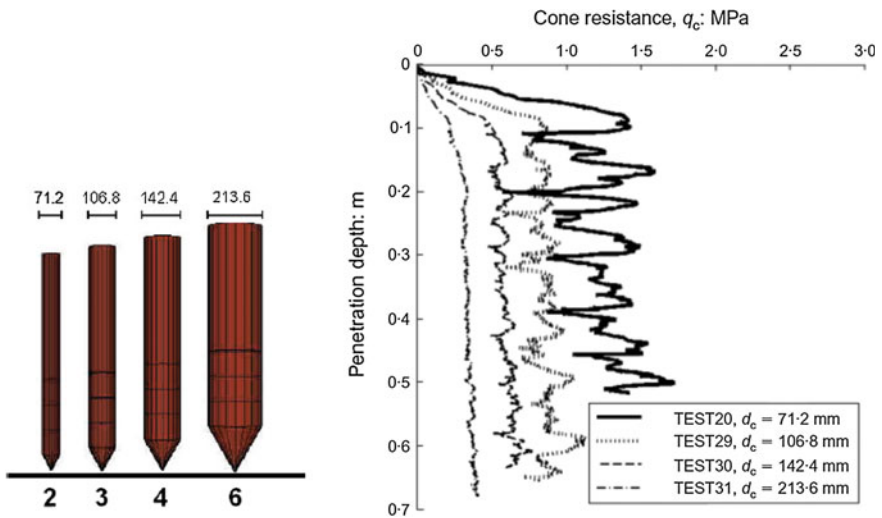


Fig. 3 Results of the simulations of the penetration tests using different cone sizes

4 Macroscale

In this section, the macroscale results are reviewed; that is the observations that are obtained from the usual performance of the CPT. Only the tip cone resistance, q_c , is considered here. The reference database for comparison with the simulation results are an extensive series of CPT tests on Ticino sand performed in calibration chambers and reported by Jamiolkowski et al. [16]. In order to perform a relevant comparison, it is necessary to correct for the chamber size effect. The correction is based on the same correction factor obtained in the physical tests. The results of the physical tests were plotted as the relationships between cone resistance, q_c , and mean stress, p_o (Fig. 4). The results obtained from the numerical simulations have been superposed. It can be noted that a very good correspondence is achieved.

A more global comparison is offered in Fig. 5, where the corrected cone resistance from the DEM calculations and the corrected cone resistance value from the physical tests are collected. The simulations cover tests spanning relative densities from 60 to 90% and confining stresses from 40–400 kPa. The mean error is below 7%. It appears, therefore, that the DEM analysis is capable of reproducing adequately the physical tests, at least at a macroscopic scale, in spite of the scaling differences forced by current computational limitations.

Fig. 4 Relationships between cone resistance, q_c , and mean stress, p_o obtained from calibration chamber tests on Ticino sand [16]. The results of the DEM analyses have been superposed

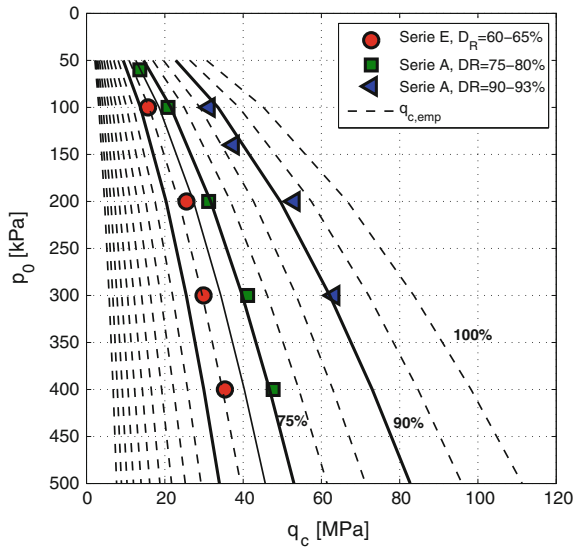
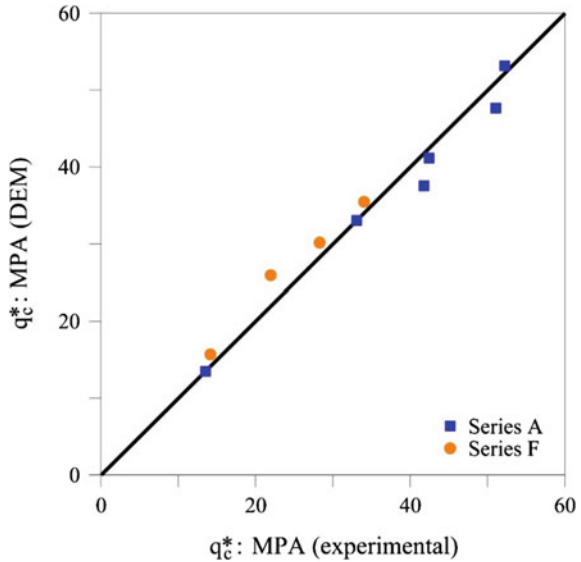


Fig. 5 Comparison between corrected cone resistance values from physical tests on Ticino sand [16] and corrected cone resistance from DEM analyses



5 Mesoscale

Mesoscale parameters refer to those variables that are significant in the context of continuum analysis, notably stresses and strains. Only stresses are discussed here. The calculation of the stresses arising from the DEM analyses has been based on the well-established method proposed by Potyondy and Cundall [17]. It involves a two-step procedure: the average grain stresses are computed first; those stresses are subsequently averaged over the selected reference volume to yield the continuum stresses.

Figure 6 shows the distribution of the radial stress (normalized by a , the tip cone resistance) at three different radial distances for two boundary conditions (BC1 and BC3). It can be observed that a large radial stress peak appears close to the cone tip but the magnitude of radial stress reduces quickly both above and below the peak location. Also, radial stresses drop very rapidly as the distance to the cone axis increases. A similar pattern of radial stress variation is widely accepted for the case of driven piles and has in fact been incorporated into design [18].

Naturally, the standard performance of CPT test does not give information on those variables but some recent research work has provided information on stresses around a penetrating cone-tipped object [19] thus allowing some quantitative comparisons. Figure 7 shows the observed value of the normalised peak stress at two radial distances in a physical chamber test on dense Fontainebleau sand. The peak values derived from DEM analysis show a similar quantitative trend. It appears therefore that the successful replication of CPT tests by DEM analyses may well extend to mesoscale variables as well.

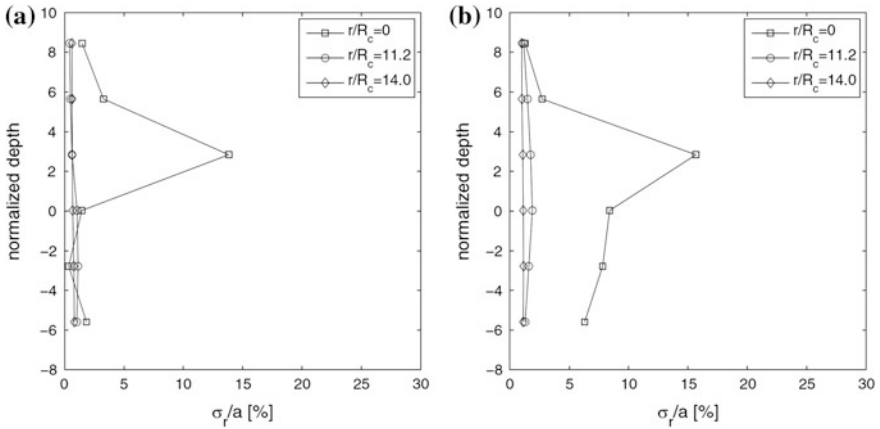
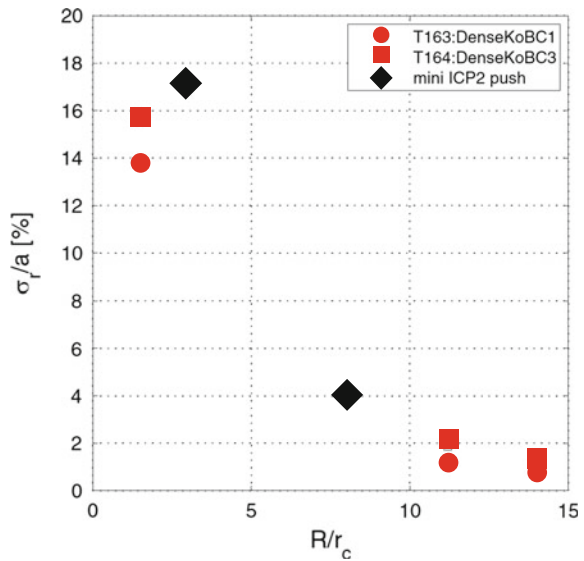


Fig. 6 Distribution of radial stresses at different radial distances, r , normalized by cone radius, R_c . Stresses are normalized by cone resistance, a . Normalized depth 0 corresponds to the cone tip position. **a** No lateral displacement condition (BC3). **b** Constant lateral stress condition (BC1)

Fig. 7 Peak values of normalized radial stress versus normalized radial distance (see caption of Fig. 6). Physical chamber observations from [19] and DEM results



6 Microscale

The results of the DEM analysis have identified a number of parameters with a potential influence on the results such as the lateral boundary condition, the stress system, granular material density and the prevention of particle rotation in the calculations. Observations at the microscale may shed light on the mechanisms that

underlie those potential effects. For this purpose, a number of analyses have been selected for examination; they all share the same particle size, the same cone and chamber dimensions and, approximately, the same lateral stresses (around 100 kPa). The selected cases are:

- T16 (MedIsoBC1). Relative density 75%, isotropic stress system, BC1 lateral boundary condition (stress controlled).
- T20 (DenseIsoBC1). Relative density 90%, isotropic stress system, BC1 lateral boundary condition (stress controlled).
- T163 (DenseKoBC1). Relative density 96.8%, Ko stress system, BC1 lateral boundary condition (stress controlled).
- T164 (DenseKoBC3). Relative density 96.8%, Ko stress system, BC3 lateral boundary condition (no lateral displacement).
- T16Rot (MedIsoRotBC1). Relative density 75%, isotropic stress system, BC1 lateral boundary condition (stress controlled). Free particle rotation allowed.

The final case, T16Rot, is the only analysis where free rotation of the particles has been allowed.

The issues related to the boundary conditions used will be examined first. Figure 8a shows the smoothed penetration curves for T163 and T164; their only difference is the lateral boundary condition: constant stress (BC1) for T163 and no lateral displacement (BC3) for T164. It can be observed that the lateral boundary condition has a very strong effect on the computed cone resistance; a similar effect has been observed in physical tests [14].

Microstructural results for these two cases are collected side-by-side in Fig. 9 to facilitate comparison. Figure 9a and b illustrate the magnitude of the normal forces between particles; for clarity, only the forces exceeding the average normal force are shown. The lines join the centre of contacting spheres and their thickness is

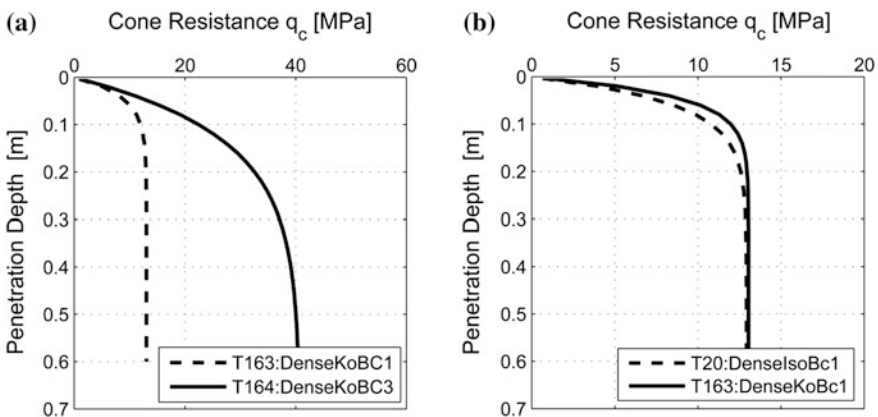


Fig. 8 **a** Penetration curves for analyses T163 and T164 showing the effect of the lateral boundary condition. **b** Penetration curves for analyses T163 and TC20 showing the effect of the applied stress system

proportional to the value of the normal force. Figure 9c and d show the displacement vectors projected on a vertical plane passing through the axis of the chamber. A magnification factor of 30 has been used.

Comparing Fig. 9a and b, it is apparent that the network of normal contact forces is quite different reflecting the influence of the different lateral boundary conditions.

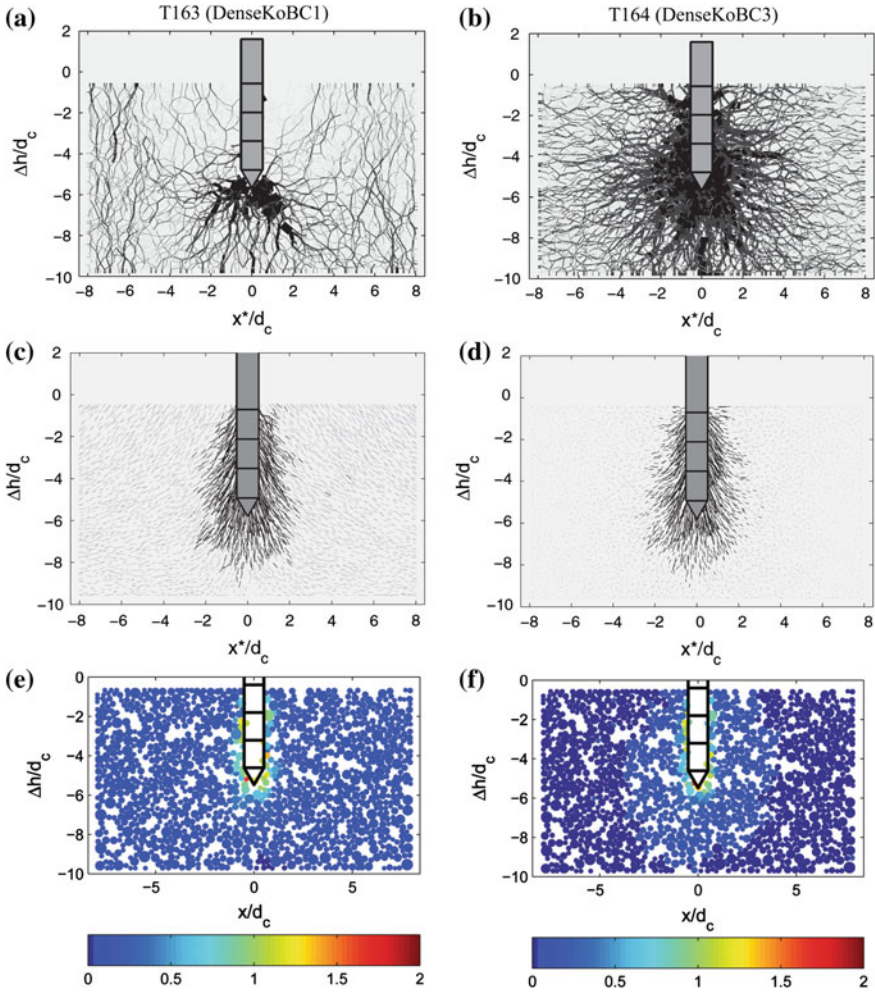


Fig. 9 Microstructural results for analyses T163 (DenseKoBC1) and T164 (DenseKoBC3) differing in their lateral boundary condition. **a** and **b** Contact normal forces for particles lying within a vertical section of the chamber. Only forces exceeding average normal forces are plotted. Line thickness is proportional to the magnitude of the normal force. **c** and **d** Particle displacement vectors (magnified by a factor of 30) projected on a vertical section of the chamber. **e** and **f** Total displacement magnitude (normalized by cone diameter) for particles contained in a vertical chamber section

Whereas for BC1 (stress controlled) the normal force network extends mainly from the cone tip downwards and sideways, for BC3 (zero lateral displacement) the strong normal force network occupies also the region around the shaft. This quite different force distribution underlies the very different cone penetration resistances obtained for those two cases.

Examining the pattern of displacements (Fig. 9c, d, e and f), it can be noted that a small number of particles close to the cone shaft are entrapped by the cone movement and exhibit large displacements. This entrapped material forms a kind of coating around the shaft, not always continuous, with a thickness of about two particles. In fact, this feature can be observed in all the tests and it therefore appears independent of the conditions of the analysis. It is probably kinematically-controlled by the cone penetration itself. Similar observations have been made in 2D DEM analyses [6] and in physical laboratory tests of pile penetration [20].

It is also noticeable that analysis T164 (BC3 boundary condition) has a more gradual radial reduction of displacements away from the cone whereas in analysis T163 (BC1 boundary condition) absolute movements are more concentrated around the cone and shaft. The zero lateral displacement condition also implies that the vertical movement away from the penetration is upwards to compensate the downward penetration into the granular material. In contrast, in the analysis with stress control, T163, penetration is accommodated by the lateral displacements of the outer material.

Analyses T163 and T20 differ in the stress system applied. Analysis T20 is performed under isotropic boundary stress conditions with a value of 100 kPa. Instead, analysis T163 is performed under approximately K_0 conditions with a boundary vertical stress of 313 kPa and a boundary lateral stress of 109 kPa. Note that the lateral stresses are very similar in both cases. The penetration curves for those two cases are compared in Fig. 8b. It can be seen that they practically coincide in spite of the difference between the two stress systems. This is consistent with the work reported by Houlsby and Hitchman [21] that showed that the boundary vertical stress has very little influence on the cone resistance measured in calibration chambers using BC1 conditions.

Figure 10 allows the comparison between the two analyses in terms of contact normal forces, projected displacement vectors and displacement magnitudes. Because of the common BC1 conditions, the network of normal contact forces emerges from the cone tip and it does not involve the trailing shaft. Overall, the pattern of contact forces and displacement distributions turns out to be quite similar for both analyses confirming, from a microstructural perspective, the scarce effect of the boundary vertical stress on the penetration mechanism.

The effect of the initial density of the specimen can be examined comparing analysis T16, with a relative density of 75.2%, and T20 with a relative density of 90%. All other parameters of the analyses are the same; the boundary conditions are stress-controlled and isotropic. The penetration curves of the two tests are plotted in Fig. 11a. As expected, a larger cone resistance is associated with the higher density.

The comparison of microstructural variables for these two analyses is offered in Fig. 12. The main difference lies in the pattern of contact forces; they are larger and

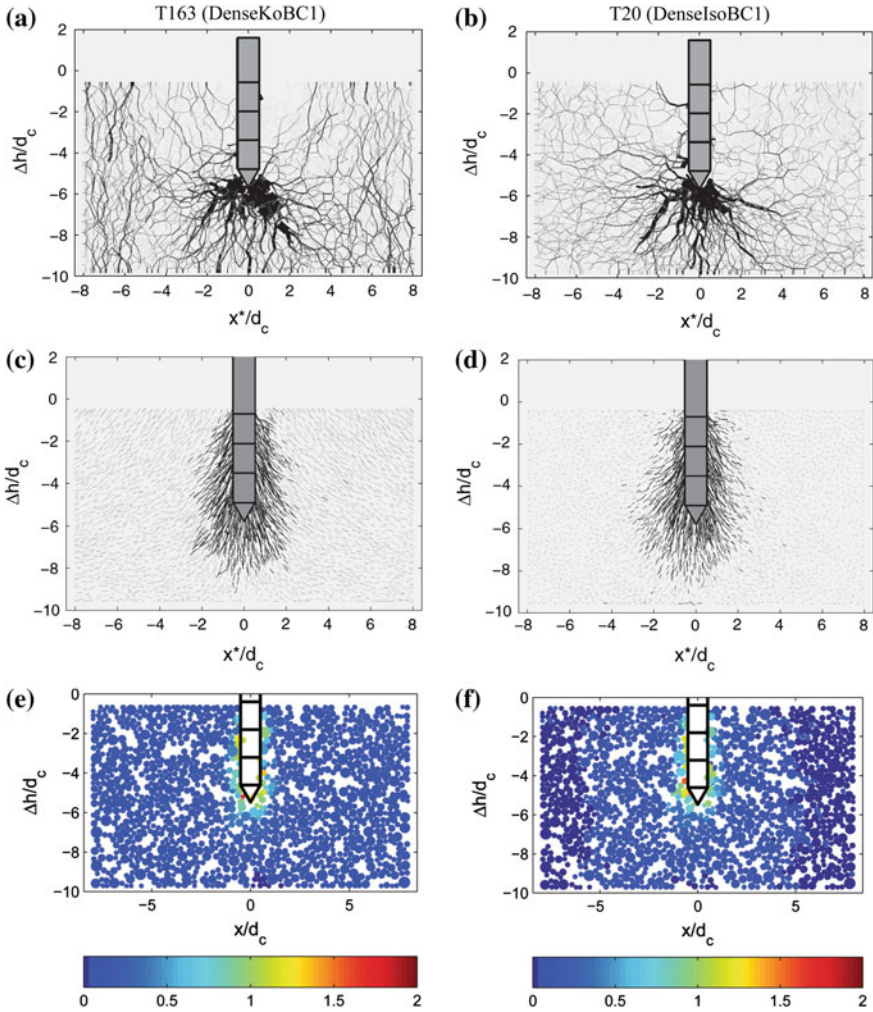


Fig. 10 Microstructural results for analyses T163 (DenseKoBC1) and T20 (DenseIsoBC1) differing in their boundary stress systems. **a** and **b** Contact normal forces for particles lying within a vertical section of the chamber. Only forces exceeding average normal forces are plotted. Line thickness is proportional to the magnitude of the normal force. **c** and **d** Particle displacement vectors (magnified by a factor of 30) projected on a vertical section of the chamber. **e** and **f** Total displacement magnitude (normalized by cone diameter) for particles contained in a vertical chamber section

more extended in the dense case (T20) reflecting the higher resistance of the denser material to penetration. In addition, although in both cases the network of strong normal contact forces sharply decays towards the shaft, the reduction is much more noticeable in the case of the looser material (T16).

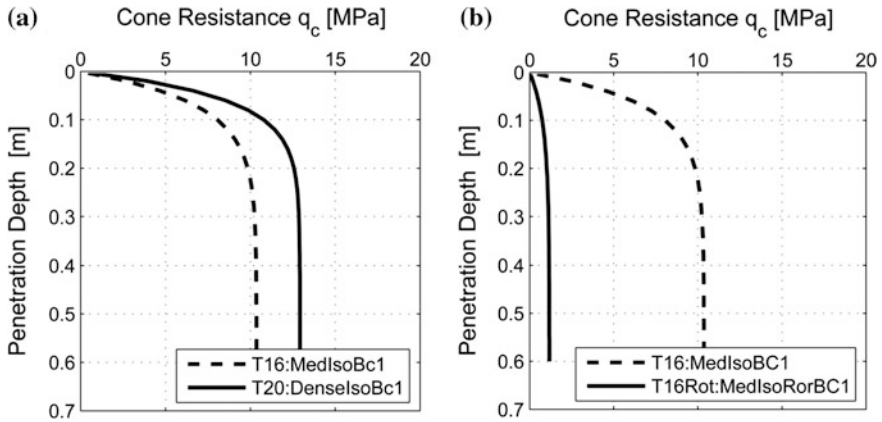


Fig. 11 **a** Penetration curves for analyses T16 and T20 showing the effect of the initial density of the granular material. **b** Penetration curves for analyses T163 and TC20 showing the effect of allowing free rotation to the particles

So far, all the analyses have been performed preventing any rotation of the spherical particles. This hypothesis is likely to be reasonable for materials with angular particles but it may be less acceptable when the grains have a more spherical shape. It is of interest, therefore, to check on the effects produced by the zero-rotation feature of the analyses. To this end, an analysis has been performed in which the particles could rotate freely. This is obviously a limit case, unlikely to be representative of real materials apart from some cases that are specifically engineered in this way.

The comparison of the penetration curves of the analysis with free rotation, T16Rot, with the equivalent one with zero rotation (T16) is presented in Fig. 11b. All other analysis' conditions are the same: relative density 75.2%, the boundary conditions are stress-controlled and isotropic. It is clear that the effect of allowing rotation is drastic, the cone resistance drops by nearly an order of magnitude.

It is immediately apparent that there are important differences in the microstructural variables in the two analyses (Fig. 13). Thus, when there is no rolling resistance, the normal contact force network is more diffused and uniform with no evidence of chains supporting large contact forces. This difference arises from the known observation that rotational resistance is required to stabilize strong force chains that disappear if the rolling resistance is reduced to zero. It is not surprising therefore that the penetration resistance is much lower in this case. Displacement patterns are also different; in the case of free rotation, large displacements do not penetrate so much below the tip of the cone but they are more uniformly distributed around the penetration body.

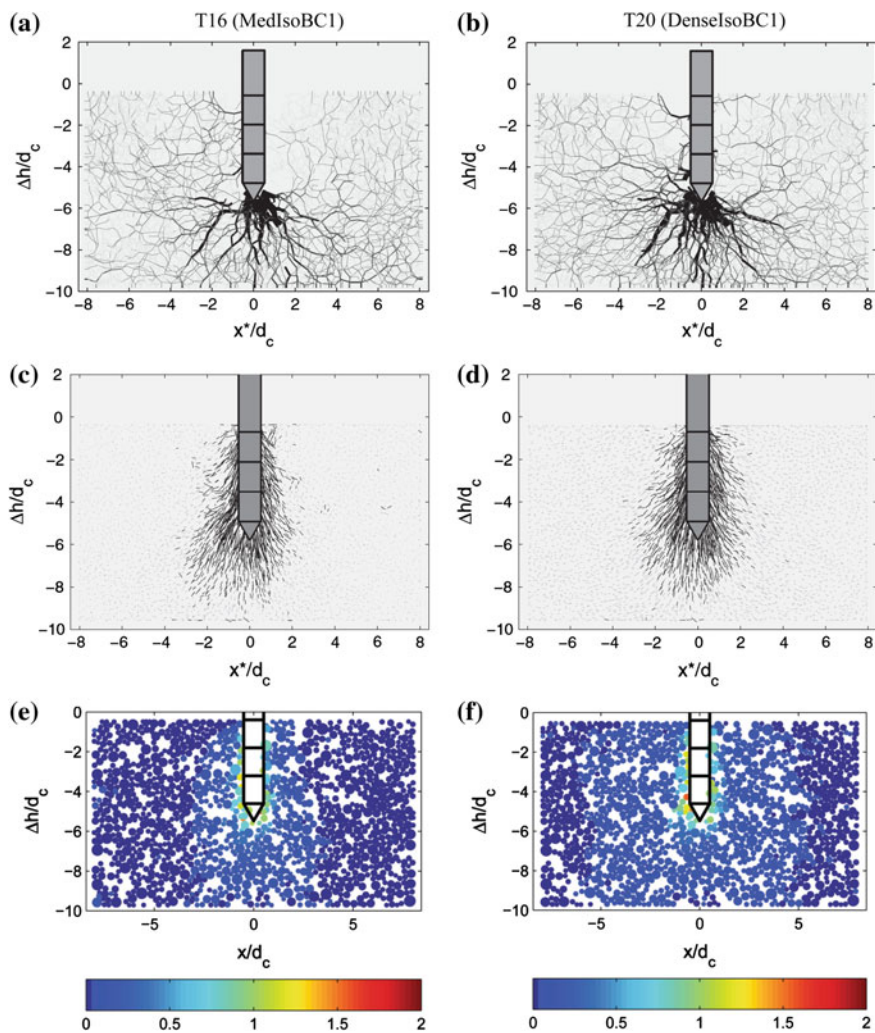


Fig. 12 Microstructural results for analyses T16 (MedIsoBC1) and T20 (DenseIsoBC1) differing in the initial density of the granular material. **a** and **b** Contact normal forces for particles lying within a vertical section of the chamber. Only forces exceeding average normal forces are plotted. Line thickness is proportional to the magnitude of the normal force. **c** and **d** Particle displacement vectors (magnified by a factor of 30) projected on a vertical section of the chamber. **e** and **f** Total displacement magnitude (normalized by cone diameter) for particles contained in a vertical chamber section

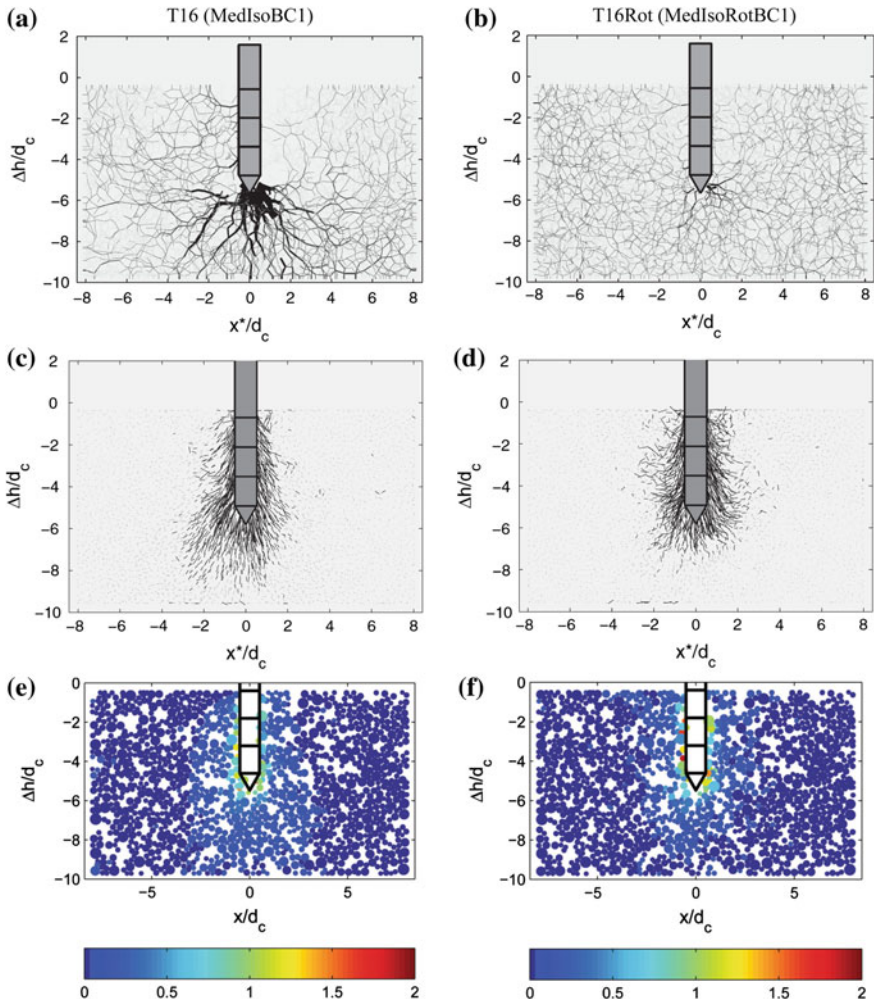


Fig. 13 Microstructural results for analyses T16 (MedIsoBC1) with no particle rotation and T16Rot (MedIsoRotBC1) where particle rotation is freely allowed. **a** and **b** Contact normal forces for particles lying within a vertical section of the chamber. Only forces exceeding average normal forces are plotted. Line thickness is proportional to the magnitude of the normal force. **c** and **d** Particle displacement vectors (magnified by a factor of 30) projected on a vertical section of the chamber. **e** and **f** Total displacement magnitude (normalized by cone diameter) for particles contained in a vertical chamber section

7 Concluding Remarks

Penetration problems are widespread in geomechanics. However, their numerical simulation is especially challenging because it involves large deformations and displacements as well as strong non-linearities affecting material behaviour,

geometry and contact surfaces. In this contribution, the cone penetration test (CPT) has been analysed numerically using the Discrete Element Method (DEM). Although a number of simplifications and scale changes have been introduced to reduce the computational effort to a manageable level, the results obtained indicate that DEM is a useful technique to tackle this type of problems. An advantage of DEM is that the complexity of material behaviour can be derived from simple contact laws using very limited number of parameters. Moreover, large strains and displacements are naturally accommodated by the procedure.

It has been proved that the DEM analysis is able to provide a very close quantitative representation of the cone resistances obtained in a large study performed in calibration chambers on Ticino sand. This material is a hard siliceous sand and therefore not prone to grain crushing in a significant way. Material with weaker grains (e.g. calcareous sand) would undergo significant particle crushing and additional developments of the formulation would be required [22].

DEM analysis also yields, by appropriate averaging techniques, relevant information concerning mesoscale continuum variables (stresses and strains). Experimental evidence is more scarce in this case but the results of a quantitative comparison made with calibration chamber observations are again quite encouraging.

A benefit of DEM analysis is that microstructural variables can be readily obtained from the computed results. It has been shown that this microstructural information sheds light on the mechanisms underlying the observed effects of a number of experimental and analysis features of the penetration tests.

The use of spherical particles in DEM is very favourable computationally but it requires the incorporation of some rolling resistance in order to obtain realistic results from the analyses. In the calculations performed, satisfactory results have been obtained by preventing completely particle rotation, a probably reasonable assumption for sand with angular particles. However, an analysis allowing free rotation has shown that the impact of the zero rotation hypothesis is very strong indeed. Analyses of penetration problems in materials with more rounded particles will probably require a more nuanced approach to this question.

Acknowledgements The support of the Ministerio de Economía y Competividad of Spain through research grants BIA2008-06537, BIA2011-27217 and BIA2014-59467-R is gratefully acknowledged.

References

1. A. Gens, M. Arroyo, J. Butlanska, J.M. Carbonell, M. Ciantia, L. Monforte, C. O'Sullivan, Simulation of the cone penetration test: discrete and continuum approaches. *Aust. Geomech.* **51**(4), 169–182 (2016)
2. C. O'Sullivan, *Particle-Based Discrete Element Modeling: A Geomechanics Perspective* (Taylor & Francis, Hoboken, NJ, 2011)
3. P.A. Cundall, O.D.L. Strack, Discrete numerical model for granular assemblies. *Géotechnique* **29**(1), 47–65 (1979)

4. F. Calvetti, R. Nova, Micro-macro relationships from DEM simulated element and in-situ tests, in *Proceedings of 5th International Conference of Micromechanics of Granular Media: Powders and Grains 2005*, (Stuttgart, 2005), pp. 245–250
5. A.-B. Huang, M.Y. Ma, An analytical study of cone penetration tests in granular material. *Can. Geotech. J.* **31**, 91–103 (1994)
6. M.J. Jiang, H.-S. Yu, D. Harris, Discrete element modelling of deep penetration in granular soils. *Int. J. Numer. Anal. Meth. Geomech.* **30**, 335–361 (2006)
7. M. Arroyo, J. Butlanska, A. Gens, F. Calvetti, M. Jamiolkowski, Cone penetration tests in a virtual calibration chamber. *Géotechnique* **61**, 525–531 (2011)
8. J. Butlanska, M. Arroyo, A. Gens, C. O’Sullivan, Multi-scale analysis of cone penetration test (CPT) in a virtual calibration chamber. *Can. Geotech. J.* **51**(1), 51–66 (2014)
9. J. Lin, W. Wu, Numerical study of miniature penetrometer in granular material by discrete element method. *Phil. Mag.* **92**(28–30), 3474–3482 (2012)
10. G.R. McDowell, O. Falagush, H.-S. Yu, A particle re-firerem method for simulating DEM of cone penetration testing in granular materials. *Géotechnique Lett.* **2**, 141–147 (2012)
11. Itasca, Particle flow code in three dimensions: software manual. (Minnesota, USA, 2010)
12. J.M. Ting, B.T. Corkum, C.R. Kauffman, Discrete numerical model for soil mechanics. *ASCE J. Geotech. Eng.* **115**(3), 379–398 (1989)
13. P.A. Cundall, Distinct element models of rock and soil structure, in *Analytical and Computational Methods in Engineering Rock Mechanics*, ed. by E.T. Brown (Allen & Unwin, London, 1987), pp. 129–163
14. A.K. Parkin, T. Lunne, Boundary effect in the laboratory calibration of a cone penetrometer in sand, in *Proceedings of the 2nd European Symposium on Penetration Testing*, (Amsterdam, 1982) pp. 761–768
15. J. Butlanska, M. Arroyo, A. Gens, Size effects on a virtual calibration chamber, in *Numerical Methods in Geotechnical Engineering*, ed. by T. Benz, S. Nordal (CRC Press, Balkema, 2010), pp. 225–230
16. M. Jamiolkowski, D.C.F. Lo Presti, M. Manassero, Evaluation of relative density and shear strength of sands from CPT and DMT. *Soil behavior and soft ground construction*. *Am. Soc. Civ Eng.* 201–238 (2003)
17. D.O. Potyondy, P.A. Cundall, A bonded-particle model for rock. *Int. J. Rock Mech. Min. Sci.* **41**(8), 1329–1364 (2004)
18. R.J. Jardine, F. Chow, Some recent developments in offshore pile design, in *Proceedings of 6th International Offshore Site Investigation and Geotechnics*, (London, UK, 2007)
19. R.J. Jardine, B.T. Zhu, P. Foray, Z.X. Yang, Measurement of stresses around closed-ended displacement piles in sand. *Géotechnique* **63**, 1–17 (2013)
20. P. van den Berg, Analysis of soil penetration. Ph.D. thesis, Delft University of Technology (1994)
21. G.T. Houlsby, R. Hitchman, Calibration chamber tests of a cone penetrometer in sand. *Géotechnique* **38**(1), 39–44 (1988)
22. M.O. Ciantia, M. Arroyo, F. Calvetti, A. Gens, An approach to enhance efficiency of DEM modelling of soils with crushable grains. *Geotechnique* **65**(2), 91–110 (2015)

A Brief Review on Computational Modeling of Rupture in Soft Biological Tissues

Osman Gültekin and Gerhard A. Holzapfel

Abstract Physiological and pathological aspects of soft biological tissues in terms of, e.g., aortic dissection, aneurysmatic and atherosclerotic rupture, tears in tendons and ligaments are of significant concern in medical science. The past few decades have witnessed noticeable advances in the fundamental understanding of the mechanics of soft biological tissues. Furthermore, computational biomechanics, with an ever-increasing number of publications, has now become a third pillar of investigation, next to theory and experiment. In the present chapter we provide a brief review of some constitutive frameworks and related computational models with the potential to predict the clinically relevant phenomena of rupture of soft biological tissues. Accordingly, Euler-Lagrange equations are presented in regard to a recently developed crack phase-field method (CPFM) for soft tissues. The theoretical framework is supplemented by some recently documented numerical results, with a focus on evolving failure surfaces that are predicted by a range of different failure criteria. A peel test of arterial tissue is analyzed using the crack phase-field approach. Subsequently, discontinuous models of tissue rupture are described, namely the cohesive zone model (CZM) and the extended finite element method (XFEM). Traction-separation laws used to determine the crack growth are described, together with the kinematic and numerical foundations. Simulation of a peel test of arterial tissue is then presented for both the CZM and the XFEM. Finally we provide a critical discussion and overview of some open problems and possible improvements of the computational modeling concepts for soft tissue rupture.

Submitted as a **Book chapter dedicated to Prof. D.R.J. Owen.**

O. Gültekin · G.A. Holzapfel (✉)
Institute of Biomechanics, Graz University of Technology,
Stremayrgasse 16/II, 8010 Graz, Austria
e-mail: holzapfel@tugraz.at

G.A. Holzapfel
Faculty of Engineering Science and Technology, Norwegian University of Science
and Technology (NTNU), 7491 Trondheim, Norway

1 Introduction

Physiological and pathological aspects of soft biological tissues in terms of rupture are of fundamental interest in medical science. In fact, aortic dissection, aneurysms, atherosclerosis, tears in tendons and ligaments and interventional treatments such as balloon angioplasty are common cases where rupture phenomena, mainly driven by changes in the biomechanical environment, are encountered (Lee et al. [40], Holzapfel et al. [32], Sharma and Maffulli [61], Katayama et al. [38], Criado [12], Humphrey and Holzapfel [33] and Kim et al. [39]). This has rendered computational mechanics very important to guide and improve medical monitoring and preoperative planning. Although a relatively large number of fracture models have hitherto been proposed in a diverse range of fields in mechanics, the current review article focuses on those which have been implemented to predict the rupture of soft biological tissues, including the cohesive zone model (CZM), the extended finite element method (XFEM) and the crack phase-field model (CPFM).

Fracture mechanics was pioneered by the works of Griffith [22], Westergaard [70] and Irwin [36]. That happened in the first half of the last century when the concepts of energy release rate and the stress-intensity factor were established as representations of crack growth in solids within the context of linear elastic fracture mechanics (LEFM). In the 1960s, however, researchers turned their attention to crack-tip plasticity wherein significant plastic deformations precede failure. During this time, Dugdale [15] and Barenblatt [4], among others, studied yielding of materials at the crack tip. Later, Rice [59] used a line integral, which became known as the J -integral, to express crack initiation and growth which is basically evaluated along an arbitrary contour near the crack tip. Subsequently, Hutchinson [35] and Rice and Rosengren [60] managed to relate the J -integral to the crack-tip stress fields which indicates that the J -integral can be perceived as a nonlinear stress-intensity parameter as well as an energy release rate. Much of the theoretical foundations of fracture mechanics was formulated by 1980. A more elaborate historical account and details of the concepts can be found in the book by Anderson [1]. With the recent advances in computer technology, computational mechanics has assumed an increasingly significant role in the modeling of material fracture.

CZMs, introduced by Barenblatt [3] and Dugdale [15], consider fracture as a separation of two bulk materials which takes place on a cohesive surface placed in between the bulk element boundaries. The resistance to separation is specified through a cohesive law (traction-separation law). In fact, tractions vanish when the separation (opening displacement) reaches a critical value. This method became particularly appealing for problems where the extent of crack growth or the size of the yielding zone are unknown/not predetermined. Later on, Needleman [55], Xu and Needleman [72] and Camacho and Ortiz [11], among several others, modeled cohesive zones pertaining to the irreversible cohesive laws, adaptive insertion of surface elements, and the dynamic fracture, respectively. The CZM was applied to the fracture of a stenotic artery by Ferrara and Pandolfi [16] using an anisotropic extension of the irreversible cohesive law, as proposed by Ortiz and Pandolfi [56].

Later on, Ferrara and Pandolfi [17] simulated a peel test of a dissected aortic medial strip based on the experimental work of Sommer et al. [66]. The main problems regarding CZMs are the mesh dependency of the results, which can only be resolved through an increase in the finite element size, and the necessity of remeshing in cases when the crack path is not known a priori.

XFEM, developed by Belytschko and co-workers [5, 54], is a technique to deal with fracture without (or with minimal) remeshing. The hallmark of XFEM relies on the local enrichment functions with additional degrees of freedom on the basis of partition of unity finite elements (PUFEM), which resorts to Melenk and Babuška [45]. Moës et al. [54] also incorporated discontinuous displacement fields by using Heaviside functions. Later, Moës and Belytschko [53] combined the CZM and XFEM approaches, whereby the previously employed stress intensity factors and the J -integral methods were replaced by the cohesive laws. The latter modality was then adopted by Gasser and Holzapfel [21] to simulate dissections in a strip of an aorta. The main problem associated with XFEM is that it is rather difficult to predict complex crack patterns, e.g., a crack subject to branching.

In contrast to CZMs and XFEM, CPFEM utterly bypasses the modeling of discontinuities as the 2D crack surface smears out in a volume domain in 3D, as determined by a specific field equation alongside the balance of linear momentum describing the elastic mechanical problem in solids. The well-known limitations, e.g. curvilinear crack paths, crack kinking and branching angles, emanating from the classical theory of fracture mechanics are alleviated through a variational principal of the minimum energy (see Francfort and Marigo [19]), which was followed by a numerical study (Bourdin et al. [8]) using the Γ -convergence, see Braides [10] and Bourdin et al. [9]. In addition, a Ginzburg-Landau type of phase-field evolution was used by Hakim and Karma [26]. The thermodynamically consistent and algorithmically robust formulations of CPFEM were introduced by the seminal works of Miehe and co-workers, [49, 52], and were successfully applied to several coupled multi-field problems ranging from thermo-elastic-plastic fracture to chemo-mechanical fracture (Miehe et al. [47, 48, 51]). The application of CPFEM in biomechanics dates back to Gültekin [23] which was later applied by Gültekin et al. [24, 25] and Raina and Miehe [57] using anisotropic failure criteria. The numerical aspects of aortic dissections in regard to the experimental study of Sommer et al. [66] were also investigated by Raina and Miehe [57] and Gültekin et al. [25].

This book chapter is organized as follows. Section 2 outlines the basics of the variational setup of the coupled mechanical-fracture problem in the sense of CPFEM, featuring the Euler-Lagrange equations, from which emerge the quasi-static force balance of momentum and the evolution of the phase-field. Therein, both rate-independent and rate-dependent formulations are presented. Subsequently, a brief account of anisotropic failure criteria is provided. Next, an overview of numerical examination of the phenomena of aortic dissection using CPFEM is presented. Section 3 is concerned with models that introduce a discontinuous domain due to fracture, namely CZMs and XFEM. A short summary of the traction-separation laws used to determine the crack growth is provided together with the key aspects of the kinematic and numerical foundations. A numerical example of a dissecting aorta

is demonstrated for both the CZM and the XFEM. Finally, Sect. 4 provides a critical discussion and overview of some open problems and possible improvements in modeling concepts for soft tissue rupture.

2 Crack Phase-Field Modeling of Failure in Soft Tissues

This section deals with the CPFEM to model fracture of solids at finite strains featuring the primary field variables, namely the crack phase-field d and the deformation map φ in relation to the evolution of the crack and the balance of linear momentum, respectively. An anisotropic arterial tissue comprised of two families of collagen fibers is used as the material. A mixed saddle point principle of the global power balance then yields the Euler-Lagrange equations of the multi-field problem.

2.1 Primary Field Variables of the Multi-Field Problem

Let us consider a continuum body $\mathcal{B} \subset \mathbb{R}^3$ at time $t_0 \in \mathcal{T} \subset \mathbb{R}$ and $\mathcal{S} \subset \mathbb{R}^3$ at time $t \in \mathcal{T} \subset \mathbb{R}$ in the Euclidean space. The finite macroscopic motion of the body is characterized by the bijective deformation map, i.e.

$$\varphi_t(\mathbf{X}) : \begin{cases} \mathcal{B} \times \mathcal{T} & \rightarrow \mathcal{S}, \\ (\mathbf{X}, t) & \mapsto \mathbf{x} = \varphi(\mathbf{X}, t), \end{cases} \quad (1)$$

that transforms a material point $\mathbf{X} \in \mathcal{B}$ onto a spatial point $\mathbf{x} \in \mathcal{S}$ at time $t \in \mathbb{R}^+$, see Fig. 1. As a second primary field variable we introduce the basic geometric mapping for the time-dependent auxiliary crack phase-field d such that

$$d : \begin{cases} \mathcal{B} \times \mathcal{T} & \rightarrow [0, 1], \\ (\mathbf{X}, t) & \mapsto d(\mathbf{X}, t), \end{cases} \quad (2)$$

which interpolates between the intact ($d = 0$) and the ruptured ($d = 1$) state of the material.

2.2 Kinematics

We start with the description of the deformation gradient, i.e.

$$\mathbf{F} = \nabla \varphi, \quad (3)$$

transforming the unit Lagrangian line element $d\mathbf{X}$ onto its Eulerian counterpart $d\mathbf{x} = \mathbf{F}d\mathbf{X}$ (for the relevant nonlinear continuum mechanics used in this chapter see, e.g., the books by Holzapfel [29] and de Souza Neto et al. [14]). Note that $\nabla[\bullet]$ and $\nabla_x[\bullet]$ denote the gradient operators with respect to the reference configuration and the spatial configuration, respectively. The determinant of \mathbf{F} , the Jacobian $J = \det\mathbf{F} > 0$, characterizes the map of an infinitesimal reference volume element to the associated spatial volume element. Furthermore, in this chapter we adopt the formalism in the sense of Marsden and Hughes [44] and equip the two manifolds \mathcal{B} and \mathcal{S} with the covariant reference metric tensor \mathbf{G} and the spatial metric tensor \mathbf{g} transforming the co- and contravariant objects in the Lagrangian and Eulerian manifolds. As a next step, we exploit the multiplicative split of \mathbf{F} into volumetric \mathbf{F}_{vol} and isochoric $\bar{\mathbf{F}}$ parts, as introduced by Flory [18], and write

$$\mathbf{F} = \mathbf{F}_{\text{vol}}\bar{\mathbf{F}} \quad \text{with} \quad \mathbf{F}_{\text{vol}} = J^{1/3}\mathbf{I} \quad \text{and} \quad \bar{\mathbf{F}} = J^{-1/3}\mathbf{F}, \quad (4)$$

where \mathbf{I} is the second-order identity tensor. Subsequently we define the unimodular part of the left Cauchy-Green tensor $\bar{\mathbf{b}}$ as

$$\bar{\mathbf{b}} = \bar{\mathbf{F}}\mathbf{G}^{-1}\bar{\mathbf{F}}^T, \quad (5)$$

which is a strain measure in terms of spatial coordinates. The energy stored in a hyperelastic isotropic material is characterized by the three modified invariants

$$\bar{I}_1 = \text{tr}\bar{\mathbf{b}}, \quad \bar{I}_2 = \frac{1}{2} \left[\bar{I}_1^2 - \text{tr}(\bar{\mathbf{b}}^2) \right], \quad \bar{I}_3 = \det \bar{\mathbf{b}}. \quad (6)$$

The anisotropic structure of biological tissues makes it necessary to consider additional invariants. Therefore, we introduce two reference unit vectors \mathbf{M} and \mathbf{M}' representing the mean fiber orientations, see Fig. 1, and their spatial counterparts as

$$\mathbf{m} = \mathbf{F}\mathbf{M}, \quad \mathbf{m}' = \mathbf{F}\mathbf{M}', \quad (7)$$

which idealizes the micro-structure of the tissue. Subsequently, we can express the related Eulerian form of the structure tensors $\mathbf{A}_{\mathbf{m}}$ and $\mathbf{A}_{\mathbf{m}'}$ as

$$\mathbf{A}_{\mathbf{m}} = \mathbf{m} \otimes \mathbf{m}, \quad \mathbf{A}_{\mathbf{m}'} = \mathbf{m}' \otimes \mathbf{m}'. \quad (8)$$

Finally, we introduce the (physically meaningful) additional invariants

$$I_4 = \mathbf{g} : (\mathbf{m} \otimes \mathbf{m}), \quad I_6 = \mathbf{g} : (\mathbf{m}' \otimes \mathbf{m}'), \quad (9)$$

which measure the squares of stretches along each fiber direction.

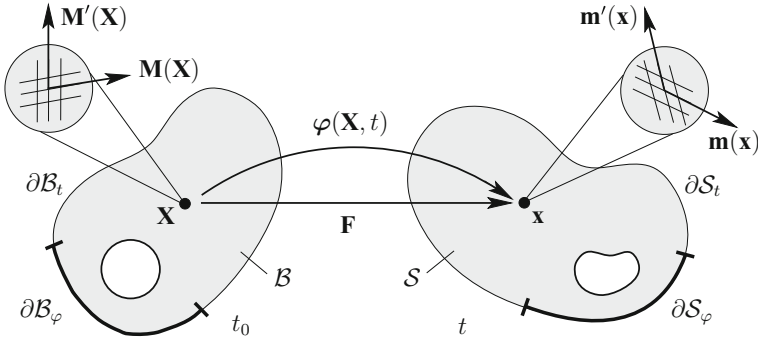


Fig. 1 Nonlinear deformation of an anisotropic solid with the reference configuration $B \in \mathbb{R}^3$ and the spatial configuration $S \in \mathbb{R}^3$. The nonlinear deformation map is $\varphi : B \times \mathbb{R} \mapsto \mathbb{R}^3$, which transforms a material point $\mathbf{X} \in B$ onto a spatial point $\mathbf{x} = \varphi(\mathbf{X}, t) \in S$ at time t . The anisotropic micro-structure of the material point \mathbf{X} is rendered by two families of fibers with unit vectors \mathbf{M} and \mathbf{M}' . Likewise, the anisotropic micro-structure of the spatial point \mathbf{x} is described by \mathbf{m} and \mathbf{m}' , as the spatial counterparts of \mathbf{M} and \mathbf{M}' (adopted from Gültekin et al. [25])

2.3 Field Equation for Crack Phase-Field in a Three-Dimensional Setting

The multi-dimensional problem of fracture consists of a deformable mechanical domain and a non-deformable domain of the phase-field, as depicted in the Fig. 2a and b, respectively. A sharp crack surface topology at time t can be denoted by $\Gamma(t) \subset \mathbb{R}^2$ in the solid body B , with the definition $\Gamma(d) = \int_{\Gamma} dA$. In contrast, a diffusive crack simply approximates the sharp crack surface by a volume integral in the form of a regularized crack surface functional as

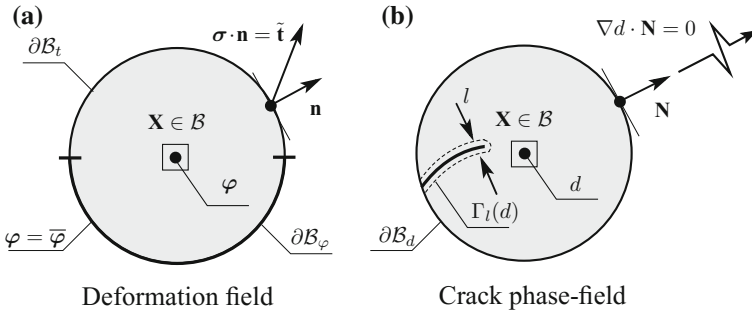


Fig. 2 Multi-field problem: **a** mechanical problem of deformation; **b** evolution of the crack phase-field problem (adopted from Gültekin et al. [25])

$$\Gamma_l(d) = \int_{\mathcal{B}} \gamma(d, \nabla d) dV, \quad \text{where} \quad \gamma(d, \nabla d) = \frac{1}{2l} (d^2 + l^2 |\nabla d|^2), \quad (10)$$

denotes the isotropic volume-specific crack surface while l stands for the length-scale parameter. This can be extended to a class of anisotropic materials via the introduction of an anisotropic volume-specific crack surface γ up to first order, i.e.

$$\gamma(d, \mathbf{Q} \star \nabla d) = \gamma(d, \nabla d), \quad \forall \mathbf{Q} \in \mathcal{G} \subset \mathcal{O}(3), \quad (11)$$

where \mathbf{Q} denotes the rotations in the symmetry group \mathcal{G} , a subset of the orthogonal group $\mathcal{O}(3)$ containing rotations and reflections, and \star denotes an operator. The anisotropic structure is then considered by a second-order structure tensor \mathcal{L} such that

$$\mathcal{L} = l^2 [\mathbf{I} + \omega_{\mathbf{M}} (\mathbf{M} \otimes \mathbf{M}) + \omega_{\mathbf{M}'} (\mathbf{M}' \otimes \mathbf{M}')], \quad (12)$$

which aligns the evolution of the crack according to the orientation of fibers in the continuum using the anisotropy parameters $\omega_{\mathbf{M}}$ and $\omega_{\mathbf{M}'}$, which regulate the transition from weak to strong anisotropy. The anisotropic volume-specific crack surface can now be represented by the alternative form

$$\gamma(d, \nabla d; \mathcal{L}) = \frac{1}{2l} (d^2 + \nabla d \cdot \mathcal{L} \nabla d). \quad (13)$$

We can now state the minimization principle

$$d(\mathbf{X}, t) = \text{Arg} \left\{ \inf_{d \in \mathcal{W}_{\Gamma(t)}} \Gamma_l(d) \right\}, \quad (14)$$

subject to the Dirichlet-type boundary constraint $\mathcal{W}_{\Gamma(t)} = \{d | d(\mathbf{X}, t) = 1 \text{ at } \mathbf{X} \in \Gamma(t)\}$. The Euler-Lagrange equations of the above stated variational principle are then

$$d - \nabla \cdot (\mathcal{L} \nabla d) = 0 \quad \text{in } \mathcal{B} \quad \text{and} \quad \mathcal{L} \nabla d \cdot \mathbf{N} = 0 \quad \text{on } \partial \mathcal{B}, \quad (15)$$

where the non-local effects are considered by the divergence term. In (15)₂ \mathbf{N} is the unit surface normal oriented outward in the reference configuration (for a derivation of the Euler-Lagrange equation see Gültekin [23]).

2.4 Constitutive Modeling of Artery Walls

The effective Helmholtz free-energy function describing the local anisotropic mechanical response of the intact solid assumes a specific form comprising the effective volumetric $U_0(J)$, the isotropic Ψ_0^{iso} and anisotropic Ψ_0^{ani} parts, i.e. (Dal [13])

$$\Psi_0(\mathbf{g}, \mathbf{F}, \mathbf{A}_m, \mathbf{A}_{m'}) = U_0(J) + \Psi_0^{\text{iso}}(\mathbf{g}, \bar{\mathbf{F}}) + \Psi_0^{\text{ani}}(\mathbf{g}, \mathbf{F}, \mathbf{A}_m, \mathbf{A}_{m'}). \quad (16)$$

It needs to be emphasized that in (16) the multiplicative decomposition of the deformation gradient \mathbf{F} is only used for the description of the ground matrix of the artery wall; in other words, we dispense with the multiplicative decomposition for the fiber response. The effective volumetric part in (16) is defined as

$$U_0(J) = \kappa(J - \ln J - 1), \quad (17)$$

while the effective isotropic Ψ_0^{iso} and the effective anisotropic Ψ_0^{ani} parts are functions of the invariant arguments. Thus,

$$\Psi_0^{\text{iso}}(\mathbf{g}, \bar{\mathbf{F}}) = \hat{\Psi}_0^{\text{iso}}(\bar{I}_1), \quad \Psi_0^{\text{ani}}(\mathbf{g}, \mathbf{F}, \mathbf{A}_m, \mathbf{A}_{m'}) = \hat{\Psi}_0^{\text{ani}}(I_4, I_6), \quad (18)$$

which takes on the neo-Hookean and the exponential forms according to Holzapfel et al. [30],

$$\hat{\Psi}_0^{\text{iso}}(\bar{I}_1) = \frac{\mu}{2}(\bar{I}_1 - 3), \quad \hat{\Psi}_0^{\text{ani}}(I_4, I_6) = \frac{k_1}{2k_2} \sum_{i=4,6} \{\exp[k_2(I_i - 1)^2] - 1\}, \quad (19)$$

representing the elastic (and isotropic) response of the ground matrix and the two (distinct) families of collagen fibers, respectively. To give an account of the parameters, κ denotes the penalty parameter enforcing the quasi-incompressible material behavior in (17), while μ indicates the shear modulus in (19)₁. The parameters k_1 and k_2 in (19)₂ denote a stress-like material parameter and a dimensionless parameter, respectively. The anisotropic part contributes to the mechanical response only when a family of fibers is under extension, that is when the invariants $I_4 > 1$ (and $I_6 > 1$). Otherwise the relevant part of the anisotropic function should be excluded from (19)₂. For the derivations of the corresponding constitutive response, i.e. the effective Kirchhoff stress tensor $\boldsymbol{\tau}_0$ and the effective elastic moduli \mathbb{C}_0 see Gültekin et al. [25].

2.5 Variational Formulation Based on Power Balance

We hereby establish the theoretical edifice based on the mixed saddle point principle of the global power balance engendering the coupled Euler-Lagrange equations governing the evolution of the crack phase-field in (i) a rate-dependent and (ii) a rate-independent setting, in addition to the balance of linear momentum and the volumetric constraints. For a degrading continuum the Helmholtz free-energy function becomes

$$\Psi(\mathbf{g}, \mathbf{F}, \mathbf{A}_m, \mathbf{A}_{m'}; d) = g(d)\Psi_0(\mathbf{g}, \mathbf{F}, \mathbf{A}_m, \mathbf{A}_{m'}), \quad (20)$$

where Ψ_0 is the effective Helmholtz free-energy function of the hypothetically intact solid according to (16). The explicit form of the monotonically decreasing quadratic degradation function $g(d)$ is given by

$$g(d) = (1 - d)^2. \quad (21)$$

The function (21) describes the degradation of the tissue as the crack phase-field parameter d evolves, with the following growth conditions:

$$g'(d) \leq 0 \quad \text{with} \quad g(0) = 1, \quad g(1) = 0, \quad g'(1) = 0. \quad (22)$$

Degradation is ensured by the first condition, whereas the second and third conditions set the limits for the intact and the ruptured state of the material. The final condition indicates a saturation as $d \rightarrow 1$. Hence, the volumetric, isotropic and the anisotropic parts of the free-energy function $\Psi = U + \hat{\Psi}^{\text{iso}} + \hat{\Psi}^{\text{ani}}$ for a degenerating material become

$$\begin{aligned} U(J, d) &= g(d)U_0(J), \quad \hat{\Psi}^{\text{iso}}(\bar{I}_1; d) = g(d)\hat{\Psi}_0^{\text{iso}}(\bar{I}_1), \\ \hat{\Psi}^{\text{ani}}(I_4, I_6; d) &= g(d)\hat{\Psi}_0^{\text{ani}}(I_4, I_6), \end{aligned} \quad (23)$$

respectively. In the subsequent treatment, we write the rate of the energy storage functional by considering the time derivative of the isotropic and the anisotropic contributions of (23)_{2,3}, which integrated over the domain gives

$$\mathcal{E}(\dot{\varphi}, \dot{d}; \varphi, d) = \int_{\mathcal{B}} (\boldsymbol{\tau} : \mathbf{g}\nabla_x \dot{\varphi} - f\dot{d}) dV. \quad (24)$$

Therein, we have defined the Kirchhoff stress tensor $\boldsymbol{\tau}$ and the energetic force f such that

$$\boldsymbol{\tau} = g(d)(\boldsymbol{\tau}_0^{\text{iso}} + \boldsymbol{\tau}_0^{\text{ani}}), \quad f = -\partial_d[U(J; d) + \hat{\Psi}^{\text{iso}}(\bar{I}_1; d) + \hat{\Psi}^{\text{ani}}(I_4, I_6; d)]. \quad (25)$$

The Kirchhoff stress tensor $\boldsymbol{\tau}$ is essentially obtained via the effective isotropic and anisotropic Kirchhoff stress tensors $\boldsymbol{\tau}_0^{\text{iso}}$ and $\boldsymbol{\tau}_0^{\text{ani}}$, respectively. Meanwhile, f can be interpreted as the work conjugate of \dot{d} . The external action on the body leads to the external power functional described by

$$\mathcal{P}(\dot{\varphi}) = \int_{\mathcal{B}} \rho_0 \tilde{\gamma} \cdot \dot{\varphi} dV + \int_{\partial \mathcal{B}_i} \tilde{\mathbf{t}} \cdot \dot{\varphi} da, \quad (26)$$

where ρ_0 , $\tilde{\gamma}$ and $\tilde{\mathbf{t}}$ represent the material density, the prescribed body force and the spatial surface traction, respectively. In what follows, the crack dissipation functional \mathcal{D} accounting for the anisotropic dissipated energy in the body is introduced as

$$\mathcal{D}(\dot{d}) = \int_{\mathcal{B}} g_c[\delta_d \gamma(d, \nabla d; \mathcal{L})] \dot{d} dV, \quad (27)$$

where $\delta_d \gamma$ defines the variational derivative of the anisotropic volume-specific crack surface γ according to (Gültekin et al. [24])

$$\delta_d \gamma = \frac{1}{l} [d - \nabla \cdot (\mathcal{L} \nabla d)], \quad (28)$$

and g_c indicates the critical fracture energy (Griffith-type critical energy release rate), see Miehe et al. [49, 52] and Gültekin et al. [24, 25]. Concerning thermodynamics, the dissipation functional has to be non-negative for all admissible deformation processes ($\mathcal{D} \geq 0$), a primary demand of the second law of thermodynamics. This inequality is a priori fulfilled by the local form of the dissipation functional (27) featuring a positive and convex propensity (Miehe et al. [52] and Miehe and Schänzel [50]). The local form of (27) can readily be stated by the principle of maximum dissipation via the following constrained optimization problem

$$g_c[\delta_d \gamma(d, \nabla d; \mathcal{L})] \dot{d} = \sup_{\beta \in \mathbb{E}} \beta \dot{d}, \quad (29)$$

which can be solved by a Lagrange method yielding

$$g_c[\delta_d \gamma(d, \nabla d; \mathcal{L})] \dot{d} = \sup_{\beta, \lambda \geq 0} [\beta \dot{d} - \lambda t_c(\beta; d, \nabla d)], \quad (30)$$

where β is the local driving force, dual to \dot{d} , and λ is the Lagrange multiplier that enforces the constraint. In addition, the threshold function t_c delineating a reversible domain \mathbb{E} is given by

$$\mathbb{E}(\beta) = \{\beta \in \mathbb{R} | t_c(\beta; d, \nabla d) = \beta - g_c[\delta_d \gamma(d, \nabla d; \mathcal{L})] \leq 0\}. \quad (31)$$

Finally, the extended dissipation functional reads

$$\mathcal{D}_\lambda(\dot{d}, \beta, \lambda; d) = \int_{\mathcal{B}} [\beta \dot{d} - \lambda t_c(\beta; d, \nabla d)] dV. \quad (32)$$

2.5.1 Mixed Rate-Independent Variational Formulation Based on Power Balance

The functionals (24), (26), and (32) are brought together for the description of a rate-type potential Π_λ giving rise to the power balance, i.e.

$$\Pi_\lambda = \mathcal{E} + \mathcal{D}_\lambda - \mathcal{P}. \quad (33)$$

On the basis of the rate-type potential (33), the mixed saddle point principle for the quasi-static process states that

$$\{\dot{\varphi}, \dot{d}, \beta, \lambda\} = \text{Arg} \left\{ \inf_{\varphi \in \mathcal{W}_{\dot{\varphi}}} \inf_{\dot{d} \in \mathcal{W}_{\dot{d}}} \sup_{\beta, \lambda \geq 0} \Pi_{\lambda} \right\}, \quad (34)$$

with the admissible domains for the primary variables

$$\mathcal{W}_{\dot{\varphi}} = \{\dot{\varphi} \mid \dot{\varphi} = \mathbf{0} \text{ on } \partial\mathcal{B}_{\varphi}\}, \quad \mathcal{W}_{\dot{d}} = \{\dot{d} \mid \dot{d} = 0 \text{ on } \partial\mathcal{B}_d\}. \quad (35)$$

By considering the variation of Π_{λ} we obtain Euler-Lagrange equations describing the mixed multi-field problem for the rate-independent fracture of an anisotropic hyperelastic solid, i.e.

<ol style="list-style-type: none"> 1: $J \operatorname{div}(J^{-1}\boldsymbol{\tau}) + \rho_0 \tilde{\gamma} = \mathbf{0}$, 2: $\beta - f = 0$, 3: $\dot{d} - \lambda = 0$, 	(36)
---	------

along with the Karush-Kuhn-Tucker-type loading-unloading conditions ensuring the principal of maximum dissipation for the case of an evolution of the crack phase-field parameter d , i.e.

$$\lambda \geq 0, \quad t_c \leq 0, \quad \lambda t_c = 0. \quad (37)$$

The elimination of β and λ through (36)_{2,3} and the explicit form of the threshold function t_c results in

$$\dot{d} \geq 0, \quad f - g_c \delta_d \gamma(d, \nabla d; \mathcal{L}) \leq 0, \quad [f - g_c \delta_d \gamma(d, \nabla d; \mathcal{L})] \dot{d} = 0. \quad (38)$$

The first condition ensures the irreversibility of the evolution of the crack phase-field parameter. The second condition is an equality for an evolving crack, which is negative for a stable crack. The third condition is the balance law for the evolution of the crack phase-field subjected to the former conditions.

2.5.2 Mixed Rate-Dependent Variational Formulation Based on Power Balance

In this section we deal with the viscous extension of the variational approach. To this end, we introduce a Perzyna-type viscous extension of the dissipation functional, i.e.

$$\mathcal{D}_{\eta}(\dot{d}, \beta; d) = \int_{\mathcal{B}} [\beta \dot{d} - \frac{1}{2\eta} \langle t_c(\beta; d, \nabla d) \rangle^2] dV, \quad (39)$$

where the viscosity η determines the viscous over-force governing the evolution of \dot{d} . In (39) the positive values for the threshold function t_c are always filtered out owing to the ramp function $\langle x \rangle = (x + |x|)/2$. The corresponding viscous rate-type potential reads

$$\Pi_{\eta} = \mathcal{E} + \mathcal{D}_{\eta} - \mathcal{P}. \quad (40)$$

On the basis of (40), we establish a mixed saddle point principle for the quasi-static process, i.e.

$$\{\dot{\varphi}, \dot{d}, \beta\} = \text{Arg} \left\{ \inf_{\varphi \in \mathcal{W}_{\dot{\varphi}}} \inf_{\dot{d} \in \mathcal{W}_{\dot{d}}} \sup_{\beta \geq 0} \Pi_{\eta} \right\}, \quad (41)$$

with the admissible domains for the primary state variables as given in (35). One can retrieve the coupled set of Euler-Lagrange equations for the rate-dependent fracture by simply taking the variation of Π_{η} , which gives

$$\begin{array}{l} 1: J \operatorname{div}(J^{-1} \boldsymbol{\tau}) + \rho_0 \tilde{\gamma} = \mathbf{0}, \\ 2: \beta - f = 0, \\ 3: \dot{d} - \frac{1}{\eta} \langle t_c(\beta; d, \nabla d) \rangle = 0. \end{array} \quad (42)$$

The explicit form of the threshold function t_c recasts the equality (42)₃ in the form

$$f = \eta \dot{d} + g_c \delta_d \gamma(d, \nabla d; \mathcal{L}). \quad (43)$$

The rate-independent setting is recovered for $\eta \rightarrow 0$.

2.6 Crack Driving Function and Failure Ansatz

Focusing on the rate-independent case in (43), for $\eta \rightarrow 0$, we elaborate on the energetic force (25)₂. Accordingly, we substitute the Eqs. (21) and (23) into (25)₂ to arrive at

$$f = 2(1-d)(U_0 + \hat{\Psi}_0^{\text{iso}} + \hat{\Psi}_0^{\text{ani}}) = 2(1-d)\Psi_0. \quad (44)$$

Combining (43) and (44), and considering the rate-independent case together with (28), the following relation holds

$$2(1-d) \frac{\Psi_0}{g_c/l} = d - \nabla \cdot (\mathcal{L} \nabla d). \quad (45)$$

With this notion at hand, one can define the dimensionless crack driving function

$$\bar{\mathcal{H}} = \frac{\Psi_0}{g_c/l}. \quad (46)$$

As discussed by Miehe et al. [51] the dimensionless characteristics of $\bar{\mathcal{H}}$ allows the incorporation of different failure criteria. Subsequently, we postulate that a particular form of the failure Ansatz in accordance with two conditions, i.e. (i) irreversibility of the crack and (ii) positiveness of the crack driving function ensuring that the crack growth solely takes place upon loading. Thus,

$$\mathcal{H}(t) = \max_{s \in [0, t]} [\langle \overline{\mathcal{H}}(s) - 1 \rangle]. \quad (47)$$

The above ramp-type function reckons on the positive values for $\overline{\mathcal{H}}(s) - 1$ and keeps the solid intact below a threshold value, i.e. until the failure surface is reached; therefore, the crack phase-field does not evolve for $\overline{\mathcal{H}}(s) < 1$. We also note that (47) always considers the maximum value of $\overline{\mathcal{H}}(s) - 1$ in the deformation history thereby ensuring the irreversibility of cracking. With these adjustments, (45) now takes on the form

$$2(1 - d)\mathcal{H} = d - \nabla \cdot (\mathcal{L}\nabla d), \quad (48)$$

where the right-hand side of (48) is the geometric resistance to crack whereas the left-hand side is the local source term for the crack growth (Miehe et al. [51]). Bearing this in mind, we recall the rate-dependent case for $\eta \neq 0$, i.e.

$$\boxed{2(1 - d)\mathcal{H} = d - \nabla \cdot (\mathcal{L}\nabla d) + \eta \dot{d}}, \quad (49)$$

which compares to (43) with the replacement of the dimensional energetic force by the dimensionless failure Ansatz, the cornerstone of the crack phase-field model. It needs to be highlighted that the use of a free energy is intrinsic in the phase-field model; therefore the variational formulation does not apply to cases apart from an energy-based criterion. Hence, a stress-based criterion can only be incorporated into (48) or (49) on a rather ad hoc basis.

2.7 Anisotropic Failure Criteria

The dimensionless crack driving function stated in (46) already reflects an energy-based criterion for a general isotropic material. However, it is well known that most soft biological tissues exhibit an anisotropic morphology thereby an anisotropic mechanical response to loading. We herein give a short description of the anisotropic failure criteria which may manifest the rupture phenomena in coherence with clinical observations. For simplicity the ensuing formulations are established according to the assumption that the principal axes of anisotropy lie on the axes of reference. Nonetheless, transformation of stress components can be achieved without much effort. For more details the reader is encouraged to look at Gültekin et al. [25].

2.7.1 Energy-Based Anisotropic Failure Criterion

Two distinct failure processes are assumed to govern the cracking of the ground matrix and the fibers, as suggested by Gültekin et al. [24]. Accordingly, the energetic force in (44) can be additively decomposed into an isotropic part f_{iso} and an

anisotropic part f_{ani} such that

$$f_{\text{iso}} = 2(1-d)(U_0 + \hat{\Psi}_0^{\text{iso}}), \quad f_{\text{ani}} = 2(1-d)\hat{\Psi}_0^{\text{ani}}, \quad (50)$$

which, in their turn, modify (45) into two distinct fracture processes which are superposed to give the following relation

$$(1-d)\bar{\mathcal{H}} = d - \frac{1}{2}\nabla \cdot (\mathcal{L}\nabla d), \quad \text{with} \quad \bar{\mathcal{H}} = \bar{\mathcal{H}}^{\text{iso}} + \bar{\mathcal{H}}^{\text{ani}}, \quad (51)$$

where the dimensionless crack driving functions are defined as

$$\bar{\mathcal{H}}^{\text{iso}} = \frac{U_0 + \hat{\Psi}_0^{\text{iso}}}{g_c^{\text{iso}}/l}, \quad \bar{\mathcal{H}}^{\text{ani}} = \frac{\hat{\Psi}_0^{\text{ani}}}{g_c^{\text{ani}}/l}. \quad (52)$$

Therein, g_c^{iso}/l and g_c^{ani}/l are the critical fracture energies over the length scale for the ground matrix and for the fibers, respectively. Finally, we mention here the modified forms of the rate-dependent and rate-independent cases of the crack evolution, i.e.

$$(1-d)\mathcal{H} = d - \frac{1}{2}\nabla \cdot (\mathcal{L}\nabla d), \quad (1-d)\mathcal{H} = d - \frac{1}{2}\nabla \cdot (\mathcal{L}\nabla d) + \eta\dot{d}. \quad (53)$$

2.7.2 Stress-Based Anisotropic Tsai-Wu Failure Criterion

Composed of a scalar function of two strength tensors, i.e. linear and quadratic forms, the Tsai-Wu criterion (Tsai and Wu [68]) recasts the dimensionless crack driving function $\bar{\mathcal{H}}$ in (46) in regard to the effective Cauchy stress tensor σ_0 in the following form

$$\bar{\mathcal{H}} = \mathbf{T} : \sigma_0 + \sigma_0 : \mathbb{T} : \sigma_0, \quad (54)$$

where \mathbf{T} and \mathbb{T} denote the second- and fourth-order strength tensors, respectively. Through a series of assumptions and simplifications introduced by symmetry relations we end up with the following expression

$$T_{ii} = \frac{1}{(\sigma_i^u)^2} \quad (55)$$

for the diagonal terms of the fourth-order strength tensor related to ultimate normal and shear stresses, where $i \in \{1, \dots, 6\}$. For a comprehensive analysis of the simplifications and assumptions the reader is referred to Tsai and Wu [68] and Tsai and Hahn [67].

2.7.3 Stress-Based Anisotropic Hill Failure Criterion

Considered as an anisotropic extension of the von Mises-Huber criterion, the Hill criterion (Hill [28]) is based on a quadratic form of the dimensionless crack driving function $\overline{\mathcal{H}}$ in (46) such that

$$\overline{\mathcal{H}} = \boldsymbol{\sigma}_0^{\text{vm}} : \mathbb{T} : \boldsymbol{\sigma}_0^{\text{vm}}, \quad (56)$$

where $\boldsymbol{\sigma}_0^{\text{vm}}$ represents the effective von Mises stress tensor. The components of $\boldsymbol{\sigma}_0^{\text{vm}}$ can be defined in terms of

$$\begin{aligned} \sigma_{0_1}^{\text{vm}} &= \sigma_{0_1} - \sigma_{0_2}, & \sigma_{0_2}^{\text{vm}} &= \sigma_{0_2} - \sigma_{0_3}, & \sigma_{0_3}^{\text{vm}} &= \sigma_{0_3} - \sigma_{0_1}, \\ \sigma_{0_4}^{\text{vm}} &= \sigma_{0_4}, & \sigma_{0_5}^{\text{vm}} &= \sigma_{0_5}, & \sigma_{0_6}^{\text{vm}} &= \sigma_{0_6}. \end{aligned} \quad (57)$$

The fourth-order strength tensor \mathbb{T} pertains to the effective normal stresses and shear stresses, as described in Gültekin et al. [25]. The Hill criterion essentially admits a surface of von Mises-Huber-type along the isotropic directions.

2.7.4 Principal Stress Criterion

Developed on the basis of principal stresses the criterion of Raina and Miehe [57] reports on the spectral decomposition of the effective Cauchy stress tensor and takes the positive principal stresses into account, i.e.

$$\boldsymbol{\sigma}_0^+ = \sum_{i=1}^3 \langle \sigma_{0_i} \rangle \mathbf{n}_i \otimes \mathbf{n}_i, \quad (58)$$

where σ_{0_i} denote the effective principal stresses, and \mathbf{n}_i are the corresponding eigenvectors for $i \in \{1, 2, 3\}$. Accordingly, the dimensionless crack driving function $\overline{\mathcal{H}}$ in (46) is rewritten in the following format

$$\overline{\mathcal{H}} = \boldsymbol{\sigma}_0^+ : \mathbb{T} : \boldsymbol{\sigma}_0^+, \quad (59)$$

where the fourth-order strength tensor \mathbb{T} is presented as

$$(\mathbb{T})_{ijkl} = \frac{1}{4\sigma_{\text{crit}}^2} (A_{ik}A_{jl} + A_{il}A_{jk}). \quad (60)$$

Therein, σ_{crit} denotes the reference critical stress associated with uniaxial loading in a certain axis that can be conceptually replaced by an ultimate stress. The second-order anisotropy tensor \mathbf{A} is expressed in index notation for $i, j, k, l \in \{1, 2, 3\}$. Details can be found in Raina and Miehe [57].

2.8 Finite Element Formulation

By considering a discrete time increment $\tau = t_{n+1} - t_n$, where t_{n+1} and t_n stand for the current and previous time steps respectively, we carry out a decoupling of the sub-problems, namely the mechanical and the crack phase-field by appealing to a one-pass operator-splitting algorithm, i.e.

$$\text{ALGO}_{\text{CM}} = \text{ALGO}_{\text{C}} \circ \text{ALGO}_{\text{M}}. \quad (61)$$

Here, such an algorithm yields a decoupling within the time interval and results in partitioned symmetric structures for the two sub-problems. Accordingly, the algorithm for each sub-problem is obtained as

$$(\text{M}) : \begin{cases} J \operatorname{div}(J^{-1}\boldsymbol{\tau}) + \rho_0 \tilde{\boldsymbol{\gamma}} = \mathbf{0}, \\ \dot{d} = 0, \end{cases} \quad (\text{C}) : \begin{cases} \dot{\boldsymbol{\varphi}} = \mathbf{0}, \\ d - \nabla \cdot (\mathcal{L} \nabla d) - 2(1-d)\mathcal{H} + \eta \dot{d} = 0. \end{cases} \quad (62)$$

The algorithm (M) is the mechanical predictor step which is solved for the frozen crack phase-field parameter $d = d_n$, while the algorithm (C) is the crack evolution step for the frozen deformation map $\boldsymbol{\varphi} = \boldsymbol{\varphi}_n$. The remainder of the formulation is summarized in Table 1. A staggered solution procedure is implemented based on a one-pass operator-splitting of the coupled Euler-Lagrange equations on the temporal side whereas a Galerkin-type weak formulation on the spatial side furnishes the finite element formulation along with the rate-dependent setting of the phase-field. Such a solution algorithm successively updates the crack phase-field and the deformation map in a typical time step by means of a Newton-Raphson scheme. For an elaborate treatment of discretization methods and a staggered solution procedure based on a one-pass operator-splitting, the reader is referred to, e.g., Miehe [46], Wriggers [71], Miehe et al. [49] and Gültekin et al. [24, 25].

Table 1 General algorithm for the multi-field problem in $[t_n, t_{n+1}]$

1. Initialization	– At time t_n given: deformation map, phase-field, history field $\boldsymbol{\varphi}_n, d_n, \mathcal{H}_n$
2. Update	– Update the prescribed loads $\tilde{\boldsymbol{\gamma}}, \tilde{\boldsymbol{\varphi}}$ and $\tilde{\mathbf{t}}$ at current time t_{n+1}
3. Compute $\boldsymbol{\varphi}_{n+1}$	– Determine $\boldsymbol{\varphi}_{n+1}$ from the minimization problem of elasticity
ALGO _M	• $G^\varphi = \int_{\mathcal{B}} [\mathbf{g} \nabla_x (\delta \boldsymbol{\varphi}) : \boldsymbol{\tau}] dV - \int_{\mathcal{B}} \delta \boldsymbol{\varphi} \cdot \rho_0 \tilde{\boldsymbol{\gamma}} dV - \int_{\partial \mathcal{B}} \delta \boldsymbol{\varphi} \cdot \tilde{\mathbf{t}} da = 0$
4. Compute history	– Check crack initiation/propagation condition, update history
	• $\mathcal{H}(t_{n+1}) \leftarrow \begin{cases} \mathcal{H}(t_n) & \text{if } \mathcal{H}(t_{n+1}) < \mathcal{H}(t_n) \\ \mathcal{H}(t_{n+1}) & \text{else} \end{cases}$
5. Compute d_{n+1}	– Determine d_{n+1} from the minimization problem of crack topology
ALGO _C	• $G^d = \int_{\mathcal{B}} \delta d [d - 2(1-d)\mathcal{H} + \eta \frac{(d-d_n)}{\tau}] dV + \int_{\mathcal{B}} \nabla(\delta d) \cdot \mathcal{L} \nabla d dV = 0$

2.9 Representative Numerical Examples

We now demonstrate the performance of the proposed model applied to rupture of soft biological tissues. The other aim is to investigate the failure criteria introduced in Sect. 2.7 from a numerical point of view. In particular, the failure surface and the crack propagation associated with distinct failure criteria are compared with each other for rather simple numerical examples.

2.9.1 Numerical Investigation of the Failure Surfaces

We provide an insight to the initiation of the crack with regard to different failure criteria. The example, taken from Gültekin et al. [25], deals with a homogeneous problem with a unit cube discretized by one hexahedral element resolving the analytical solution for the deformation and stress via discarding all non-local effects due to the gradient of the crack phase-field ∇d , see Fig. 3a. As a loading protocol, we first consider uniaxial extension tests along the x -, y - and z -directions with a stretch ratio $\lambda_x = \lambda_y = \lambda_z = 2$ which is followed by a series of planar biaxial deformations in the xy -plane with stretch ratios $\lambda_x : \lambda_y = 2 : 1.1, 2 : 1.25, 2 : 1.5, 2 : 1.75, 2 : 2, 1.75 : 2, 1.5 : 2, 1.25 : 2, 1.1 : 2$. Stretch ratios in the xz - and yz -planes for $\lambda_x : \lambda_z$ and $\lambda_y : \lambda_z$ are applied in an analogous manner as for $\lambda_x : \lambda_y$, see Fig. 3b–d. The tissue is regarded as transversely isotropic consisting of one family of fibers with orientation \mathbf{M} along the x -direction, and it is embedded in the ground matrix. The elastic material parameters and the crack phase-field parameters are listed for each failure criterion in Table 2 (for more details see Gültekin et al. [25]).

Figure 4a–c illustrate the resulting failure surfaces at the instance when $d \neq 0$ for the energy-based criterion, the Tsai-Wu criterion and the principal stress criterion, respectively. The results conspicuously retrieve ellipsoidal failure surfaces. It needs to be emphasized that one can envisage a zone between the macroscopic onset ($d \neq 0$) and the completion ($d = 1$) of the crack in the context of diffusive crack modeling

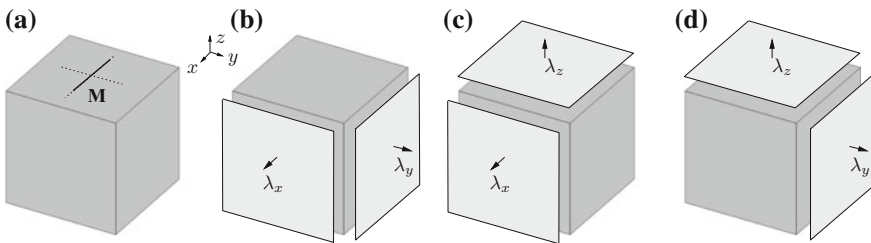


Fig. 3 a Unit cube of a transversely isotropic tissue consisting of one family of fibers with orientation \mathbf{M} parallel to the x -direction, initially subjected to uniaxial deformations in the x -, y -, and z -directions followed by a series of planar biaxial deformations **b** in the xy -plane; **c** in the xz -plane; **d** in the yz -plane (adopted from Gültekin et al. [25])

Table 2 Elastic material parameters and crack phase-field parameters for a transversely isotropic material studied in Sect. 2.9.1

Elastic		$\mu = 10 \text{ kPa}$	$g_c^{\text{ani}} = 15 \text{ kPa mm}$	$\alpha_2 = \alpha_3 = 7$
		$k_1 = 20 \text{ kPa}$		
		$k_2 = 1$		
Crack phase-field	Energy-based criterion	$g_c^{\text{iso}} = 5 \text{ kPa mm}$		
	Tsai-Wu criterion	$\sigma_x^u = 140 \text{ kPa}$	$\sigma_y^u = \sigma_z^u = 20 \text{ kPa}$	
	Principal stress criterion	$\sigma_{\text{crit}} = 140 \text{ kPa}$	$\alpha_1 = 1$	
	Hill criterion	$\sigma_x^u = 30 \text{ kPa}$	$\sigma_y^u = \sigma_z^u = 20 \text{ kPa}$	

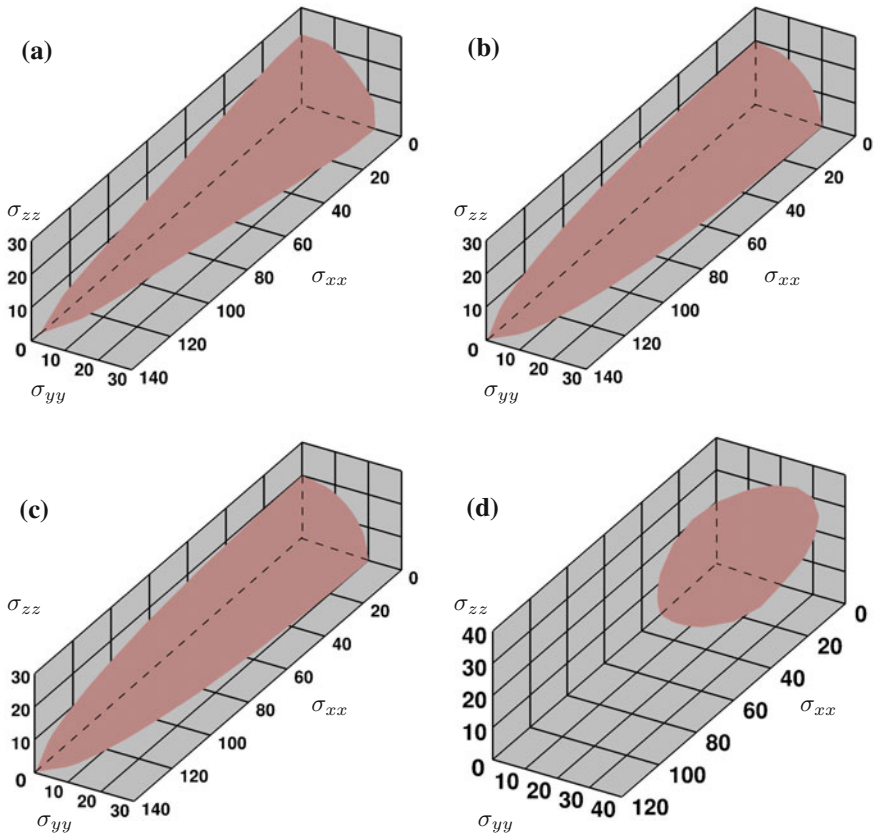


Fig. 4 Failure surfaces in regard to Cauchy stresses σ_{xx} , σ_{yy} and σ_{zz} in kPa at which the failure conditions are satisfied, leading to $d > 0$ for **a** the energy-based; **b** the Tsai-Wu; **c** the maximum principal stress; **d** the Hill failure criterion (adopted from Gültekin et al. [25])

such as the crack phase-field. This example points out the associated macroscopic onset of the crack. Figure 4d shows the failure surfaces obtained at $d \neq 0$ for the Hill criterion (Sect. 2.7.3). In fact, these criteria induce surfaces diverging from being ellipsoidal. In particular, the isotropic failure envelope on the yz -plane eventually becomes discernable, see Fig. 4d, which recovers the von Mises-Huber criterion, as expected.

2.9.2 Peel Test Numerically Analyzed with Different Failure Criteria

Peel tests bear an immense resemblance to the physical phenomena of, e.g., aortic dissections and allow a numerical investigation of the dissection propagation in terms of various failure criteria mentioned in Sect. 2.7. The benchmark with an initial tear models a hypothetical artery comprised of a single family of fibers with orientation \mathbf{M} . The geometric and discrete descriptions of the problem are illustrated in Fig. 5a and b, respectively. The strip was discretized with 2 640 mixed Q1P0 eight-node hexahedral elements. Nodes on the plane at $y = 0$ are fixed in all directions and a horizontal displacement $u_x = 4\text{ mm}$ is incrementally applied at the arms on the top plane in the x -direction. Plain strain conditions are considered in the z -direction. The elastic material parameters are according to Gasser and Holzapfel [21]. The penalty parameter and the length-scale parameter are chosen as $\kappa = 1\,000\text{ kPa}$ and $l = 0.05\text{ mm}$, respectively. The viscosity parameter is adjusted to be $\eta = 1\text{ kPa s}$ for the energy-based criterion and $\eta = 10\text{ kPa s}$ for the stress-based criterion while the anisotropy parameters are selected as $\omega_M = 1.0$ and $\omega_{M'} = 0$ fulfilling weak anisotropy. The other phase-field parameters are taken from Gültekin et al. [25].

The analyses are performed according to the energy-based, the Tsai-Wu, the principal stress and the Hill criterion while the two arms of the strip separated by an initial tear are being pulled in opposite directions, see Fig. 6. It has been observed that the use of stress-based criteria, in general, leads to a crack propagation susceptible to boundary effects not observed in the case of the energy-based criterion.

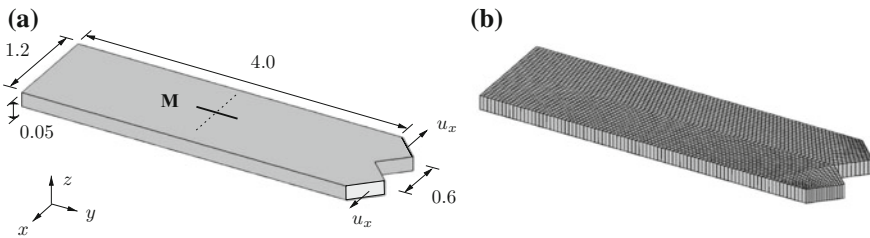


Fig. 5 **a** Geometry of the strip with a single family of fibers with orientation \mathbf{M} in the y -direction, corresponding to the collagenous component of the material. The strip is torn apart by means of a displacement u_x applied at the two arms in the positive and negative x -direction; **b** finite element mesh of the corresponding geometry. Dimensions are provided in millimeters (adopted from Gültekin et al. [25])

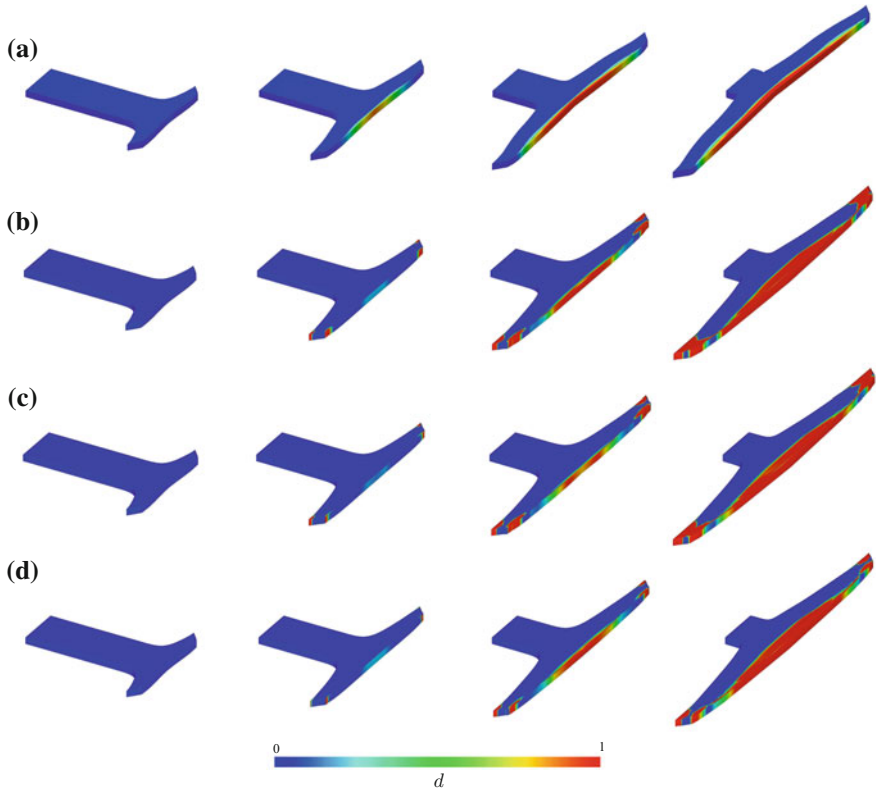


Fig. 6 Evolution of the crack phase-field d for **a** the energy-based; **b** the Tsai-Wu; **c** the principal stress criterion; **d** the Hill criterion, as the arterial tissue with an initial tear is being pulled in two opposite directions (adopted from Gültekin et al. [25])

We close this section by providing a short discussion on the study by Raina and Miehe [57] in which the phase-field of fracture is used to simulate the delamination of the aortic media with the principal stress criterion imparted in Sect. 2.7.4. Although the overall problem setup is akin to the one explained in this section, the finite element mesh comprises of 7 000 displacement-based four-noded quadrilateral elements in 2D. The selected material parameters agree favorably with the parameters identified by Gasser and Holzapfel [21]. Figure 7 shows the contours of the phase-field parameter d at different stages of the deformation, while Fig. 8 provides the load per unit width on one side of the pre-crack at the top line versus the displacement. A good agreement of the plot with the average experimental curve identified by Sommer et al. [66] is discernable.

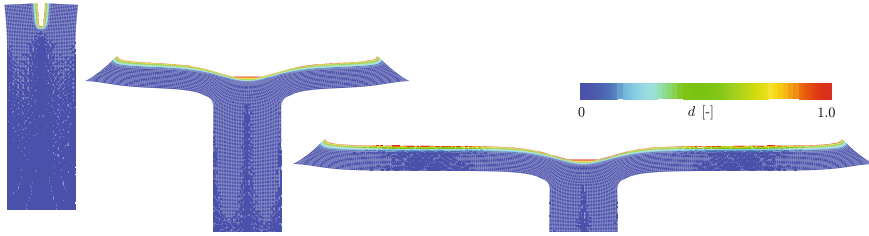
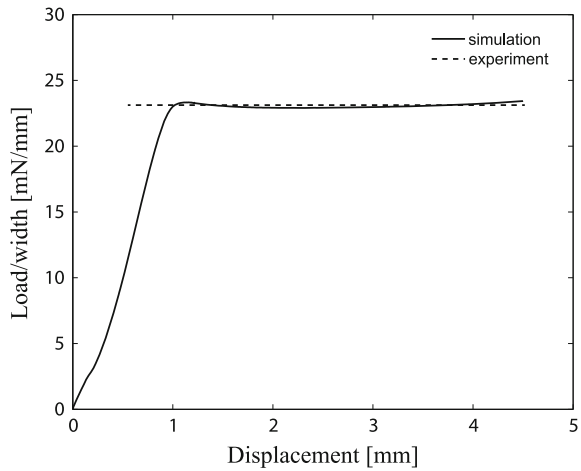


Fig. 7 Contours of the crack phase-field d illustrate the crack propagation in the deformed configuration (adopted from Raina and Miehe [57])

Fig. 8 Plot of load per unit width on one side of the pre-crack at the *top line* against the applied displacement, which is compared with the average experimental data from Sommer et al. [66] (adopted from Raina and Miehe [57])



3 Discontinuous Models of Rupture in Soft Biological Tissues

Endeavors were made to obtain a variational framework for the XFEM and the CZM. In the XFEM, cracks are represented by the enriched nodes enabling asymptotic and discontinuous fields through additional degrees of freedom. CZMs are, however, described by (surface-like) interface elements compatible with general finite element discretization. The concept of cohesive law and XFEM are combined in Moës and Belytschko [53] so that tractions on the crack surface are governed by a traction-separation law. This mixed concept was implemented to model the dissection of an aorta in Gasser and Holzapfel [21] along with the PUFEM. In the forthcoming sections we describe this approach and exploit the mixed saddle point principle. Model implementations are verified by finite element analyses of an abdominal aortic media subject to delamination (mode-I), in accordance to Gasser and Holzapfel [21] and Ferrara and Pandolfi [17].

3.1 Discontinuous Kinematics

Let us assume a continuum body $\mathcal{B} \subset \mathbb{R}^3$ at time $t_0 \in \mathcal{T} \subset \mathbb{R}$ and $\mathcal{S} \subset \mathbb{R}^3$ at time $t \in \mathcal{T} \subset \mathbb{R}$ in the Euclidean space. In view of the entire domain, we assume a strong discontinuity surface $\partial\mathcal{B}_d$ and $\partial\mathcal{S}_d$ in the reference and the spatial configuration, see Fig. 9. The discontinuity separates \mathcal{B} into two subdomains \mathcal{B}_+ and \mathcal{B}_- located in the reference configuration rendering the features $\partial\mathcal{B}_d \cap \mathcal{B}_+ = \emptyset$, $\partial\mathcal{B}_d \cap \mathcal{B}_- = \emptyset$ and $\partial\mathcal{B}_d \cup \mathcal{B}_+ \cup \mathcal{B}_- = \mathcal{B}$. Their spatial counterparts are delineated by $\partial\mathcal{S}_d$, \mathcal{S}_- and \mathcal{S}_+ . The orientations of a material point \mathbf{X}_d and the related spatial point \mathbf{x}_d located on the discontinuous surfaces are characterized by their normal vector \mathbf{N}_d and \mathbf{n}_d , respectively. The essential and the neutral boundary conditions with respect to the reference and spatial configurations are shown in Fig. 9.

Next, we rephrase the deformation map and introduce an additive split of φ into a compatible part φ_c and an enhanced part φ_e , see Simo et al. [65] and Armero and Garikipati [2]. Thus,

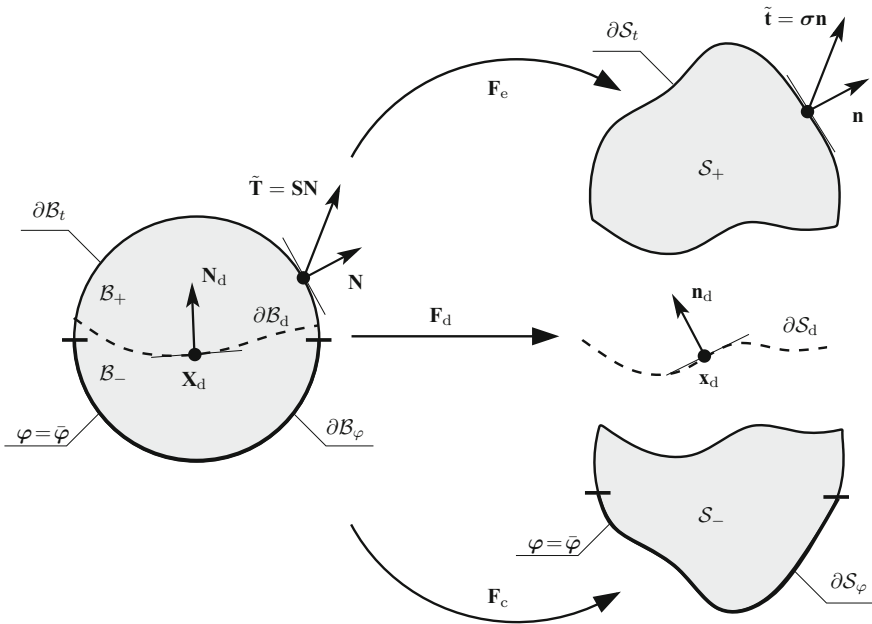


Fig. 9 Discontinuous kinematics representing the reference configuration $\partial\mathcal{B}_d \cup \mathcal{B}_+ \cup \mathcal{B}_- = \mathcal{B}$ and the spatial configuration $\partial\mathcal{S}_d \cup \mathcal{S}_+ \cup \mathcal{S}_- = \mathcal{S}$ of a body subject to the essential and the neutral boundary constraints with the associated deformation gradients \mathbf{F}_d , \mathbf{F}_e and \mathbf{F}_c . Surface tractions on the body surface are denoted by $\tilde{\mathbf{t}}$ (spatial) and $\tilde{\mathbf{T}}$ (referential) with respect to the Cauchy stress tensor $\boldsymbol{\sigma}$ and the second Piola–Kirchhoff stress tensor \mathbf{S} along with the unit normal vectors \mathbf{n} (spatial) and \mathbf{N} (referential). The cohesive tractions on the cohesive surfaces are related to \mathbf{n}_d , the unit spatial normal on $\partial\mathcal{S}_d$

$$\varphi = \varphi_c + \mathcal{H}\varphi_e, \quad (63)$$

where \mathcal{H} denotes the Heaviside function, with values 0 and 1 associated with $\mathbf{X} \in \mathcal{B}_-$ and $\mathbf{X} \in \mathcal{B}_+$, respectively. The assumption that $\partial\mathcal{S}_d$ is the map of $\partial\mathcal{B}_d$ enables the introduction of an average deformation gradient \mathbf{F}_d which resorts to Wells [69], i.e.

$$\mathbf{F}_d = \nabla\varphi_c + \frac{1}{2}\varphi_e \otimes \mathbf{N}_d, \quad (64)$$

where the spatial discontinuity normal \mathbf{n}_d is defined by a contravariant push-forward of the normal vector \mathbf{N}_d such that

$$\mathbf{n}_d = \frac{\mathbf{F}_d^{\text{T}-1}\mathbf{N}_d}{|\mathbf{F}_d^{\text{T}-1}\mathbf{N}_d|}, \quad (65)$$

which gives the preferred direction for anisotropic traction-separation laws. Additionally, we define the compatible deformation gradient \mathbf{F}_c as

$$\mathbf{F}_c = \nabla\varphi_c \quad \text{from } \mathcal{B}_- \text{ to } \mathcal{S}_-, \quad (66)$$

and the enhanced deformation gradient \mathbf{F}_e as

$$\mathbf{F}_e = \nabla\varphi_c + \nabla\varphi_e \quad \text{from } \mathcal{B}_+ \text{ to } \mathcal{S}_+. \quad (67)$$

3.2 Traction-Separation Law

The theory of standard dissipative solids treated via potential-based models are well-established by Biot [7] and Halphen and Nguyen [27], among others. Accordingly, Ortiz and Pandolfi [56] postulated the general form of an objective free-energy density per unit undeformed area $\partial\mathcal{B}_d$ which can be interpreted as a cohesive potential or elastic energy stored in the cohesive surfaces, see, e.g., Xu and Needleman [72]. The constitutive law for the cohesive surface is conjectured to be a phenomenological relation between the traction and the displacement jump across the surface. The general form reads

$$\phi = \hat{\phi}(\mathbf{u}_d, d), \quad (68)$$

where \mathbf{u}_d is referred to as the discontinuous displacement representing the displacement jumps, while d is an internal scalar variable accounting for damage. Now, we give an account for two particular forms of this cohesive potential.

3.2.1 Isotropic Cohesive Law

Gasser and Holzapfel [21] uses an isotropic particularization of the cohesive potential according to

$$\phi = \hat{\phi}(i_1, d) = \frac{t_0}{2d} \exp(-ad^b) i_1, \quad (69)$$

where $i_1 = \mathbf{u}_d \cdot \mathbf{u}_d$ defines the first invariant, t_0 denotes the cohesive tensile strength whereas a and b are non-negative parameters which retrieve the softening response of the material based on mode I fracture. Then the cohesive traction \mathbf{t}_d is defined by

$$\mathbf{t}_d = \partial_{\mathbf{u}_d} \phi = \frac{t_0}{2d} \exp(-ad^b) \mathbf{u}_d. \quad (70)$$

Details about the calculation of the cohesive traction and how to extend it to the anisotropic case can be found in Gasser and Holzapfel [20, 21].

3.2.2 Anisotropic Cohesive Law

Ferrara and Pandolfi [16] implement cohesive laws by postulating specific forms of the cohesive potential as, e.g.,

$$\phi = \hat{\phi}(u_{d,1}, u_{d,2}, u_{d,n}, d), \quad (71)$$

where the opening displacements are introduced as

$$u_{d,1} = \mathbf{u}_d \cdot \mathbf{m}, \quad u_{d,2} = \mathbf{u}_d \cdot \mathbf{m}', \quad u_{d,n} = \mathbf{u}_d \cdot \mathbf{m}_n. \quad (72)$$

Therein, \mathbf{m} and \mathbf{m}' designate the unit vectors representing the mean fiber orientations on $\partial\mathcal{S}_d$ (compare with (7)), with their normal component $\mathbf{m}_n = \mathbf{m} \times \mathbf{m}'$. Then, the cohesive traction \mathbf{t}_d is given by

$$\mathbf{t}_d = \partial_{\mathbf{u}_d} \phi = \partial_{u_{d,1}} \hat{\phi} \mathbf{m} + \partial_{u_{d,2}} \hat{\phi} \mathbf{m}' + \partial_{u_{d,n}} \hat{\phi} \mathbf{m}_n. \quad (73)$$

For further simplifications on the cohesive tractions the interested reader is encouraged to see the papers by Ortiz and Pandolfi [56] and Ferrara and Pandolfi [16].

3.3 Finite Element Formulation

The above elucidated mixed modeling (XFEM/PUFEM and CZM for cohesive crack growth) requires that the discontinuities at the crack tip are adequately described by enriching functions such as \mathcal{H} . The displacement field \mathbf{u} is, e.g., interpolated as

$$\mathbf{u} = \sum_{I=1}^{n_{\text{elem}}} N^I \mathbf{u}_c^I + \mathcal{H} \sum_{I=1}^{n_{\text{elem}}} N^I \mathbf{u}_e^I, \quad (74)$$

where N^I denotes the standard (polynomial) interpolation functions with the index I running from 1 to n_{elem} , the number of nodes per element. Therein, \mathbf{u}_c and \mathbf{u}_e indicate the matrix notation of the associated *compatible* and *enhanced* nodal displacement vectors. An important aspect is that the sum of the shape functions must be unity, see Melenk and Babuška [45]. What follows is a standard Galerkin procedure of the problem at hand and the corresponding linearization. It should be noted that as the element stiffness matrix generally becomes non-symmetric, the application of appropriate solvers are indispensable if a quadratic rate of convergence is sought. Details in regard to finite element formulations and their implementations can be found in Gasser and Holzapfel [20, 21].

3.4 Representative Numerical Examples

For the sake of comparison, numerical examples handling the peel test, based on the experimental data of Sommer et al. [66], are presented.

3.4.1 Analysis of a Peel Test According to Gasser and Holzapfel [21]

The contribution [21] uses both XFEM and CZM in order to model a 3D medial aortic strip with geometry and boundary conditions by analogy with Fig. 5. Two families of collagen fibers oriented by an angle of $\pm 5^\circ$ with respect to the circumferential direction manifests the morphology of the tissue. The finite element mesh consists of 9 993 standard tetrahedral elements and involves a refinement around the regions where the crack growth is expected.

The required elastic parameters are accommodated from Holzapfel et al. [31], whereas the cohesive materials are identified according to the experimental data by Sommer et al. [66]. Therein, the dissection failure response of the media, albeit subject to a rather large standard deviation, is found to be anisotropic as the load required to dissect a strip in the longitudinal direction is higher than that in the circumferential direction (35.0 ± 16.0 vs. 23.0 ± 3.0 mN/mm). The cohesive law used here, see Sect. 3.2.1, delineates an isotropic failure where only the tensile strength normal to the cohesive surface is taken into account.

Computations are performed by using approximately 200 displacement increments and the non-symmetric system of algebraic equations are monolithically handled by a direct solver. The distribution of the radial component $\sigma_r = \mathbf{r} \cdot \boldsymbol{\sigma} \cdot \mathbf{r}$ of the Cauchy stress, with r being the spatial radial direction vector, is demonstrated in Fig. 10. Thereby five different stress states are illustrated which are labeled as (a)–(e). The corresponding load-displacement response is provided via Fig. 11. Upon

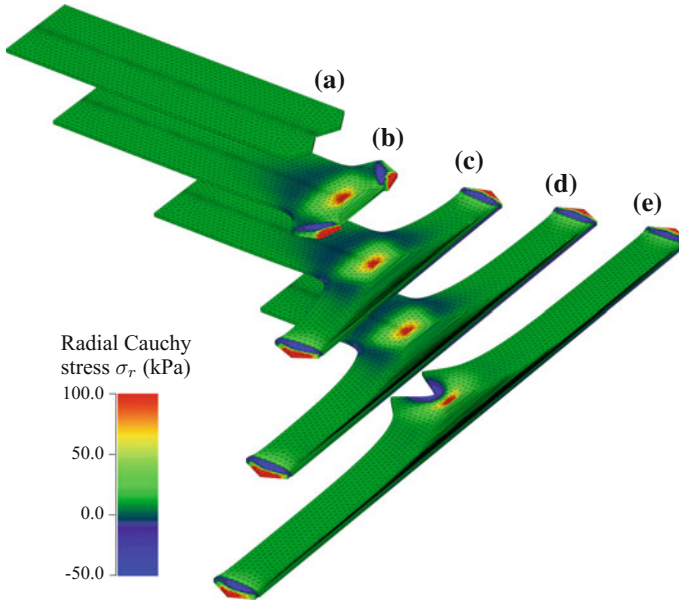
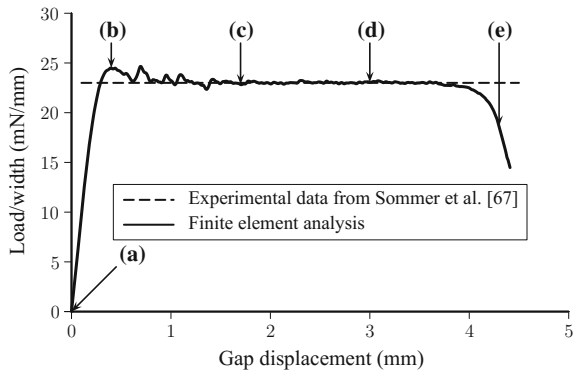


Fig. 10 Spatial distribution and evolution of the radial Cauchy stress σ_r during the propagation of a dissection within a strip of an aortic media (adopted from Gasser and Holzapfel [21])

Fig. 11 Comparison of the (average) experimental load/width with the computed load/width required to propagate a dissection in an aortic human media (adopted from Gasser and Holzapfel [21])



exceeding a threshold value of the load, the response starts to exhibit an oscillatory behavior followed by a gradual degradation after a gap displacement of 4 mm. The plateau region obtained through numerical analysis is in accordance with the experimental data.

3.4.2 Analysis of a Peel Test According to Ferrara and Pandolfi [17]

The study [17] applies the cohesive zone approach to handle a 3D medial aortic strip with geometry and boundary conditions by analogy with Fig. 5. The strip represents a specimen cut out in the circumferential direction with two families of fibers defined by an angle $\pm 5^\circ$ with respect to the circumferential axis. In order to study the effect of the mesh size, the geometry is discretized by a coarse, a medium, and a fine mesh with 10-node standard tetrahedral elements, respectively. The material parameters for the hyperelastic model and the anisotropic cohesive law can be found in Ferrara and Pandolfi [17]. Although the anisotropic cohesive law is employed according to Sect. 3.2.2, problems related to a higher degree of anisotropy occurred which resulted to a breakage of the arms due to bending. This undesired behavior can only be evaded by restricting the crack path along the middle surface of the 3D model.

Figure 12 shows the deformed configurations of three snapshots as the two arms are stretched apart, and the contour levels indicate (a) the first and (b) the second principal Cauchy stress, respectively. As a matter of fact, the second principal Cauchy stress represents the normal component of the stress to the dissecting plane. Figure 13 shows the relationship between the force/width and the total separation of the two arms. The asymptotic behavior of the numerical results is verified through the implementation of three simulations with three different mesh sizes. It is found that the remarkable decrease in the amplitude of the oscillations upon reaching the plateau region is achieved with the finer mesh which resolves the characteristic length scale. Besides, the average pulling force per unit width of 28 mN/mm falls in the range described by experimental data.

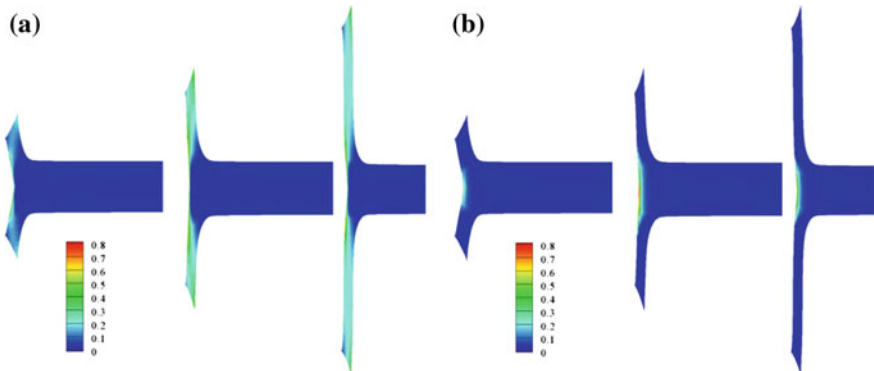
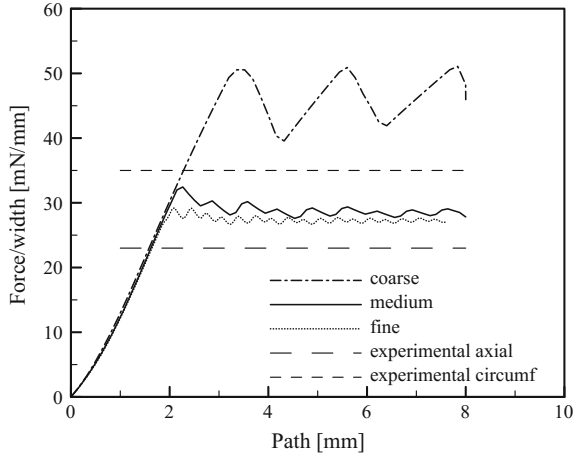


Fig. 12 Evolution of the dissection at three different stages: onset of the dissection, 2 and 4 mm of imposed displacement. Contour levels in MPa refer to **a** the first and **b** the second principal Cauchy stress. With reference to the arterial geometry, the second principal stress corresponds to the radial component (adopted from Ferrara and Pandolfi [17])

Fig. 13 Effects of the mesh size on the numerical simulation of the artery dissection, and comparison with the experimental data from Sommer et al. [66] (adopted from Ferrara and Pandolfi [17])



4 Discussion

Apart from the traditional finite element method relying on mesh-based discretization of the spatial domain, other methods that do not rely on finite element discretization such as meshfree methods based on peridynamic models (Silling [63] and Silling and Askarib [64]), the element-free Galerkin method (Belytschko et al. [6]), and smoothed particle hydrodynamics (Libersky and Petschek [42]), have recently been applied to soft tissue mechanics, see, e.g., Jin et al. [37] and Rausch et al. [58]. The study of Rausch et al. [58] simulated the delamination of an aortic strip according to the experiments performed by Sommer et al. [66], and demonstrated a qualitative agreement of the numerical results with experimental data. Nonetheless, it is also worth mentioning that meshless methods, when utilized in the finite strain context, may require several expedients to suppress non-physical results, e.g., local viscosity augmented to hyperelasticity models to help stabilize the solution, or tracking of free surface particles in order to impose traction-free responses.

Ferrara and Pandolfi [17] adjusted the cohesive law in order to prevent the breakage of the arms and to capture a physically relevant peeling which occurs at the middle of the pre-cracked region. It is worth mentioning that such interventions are not required for the CPFEM when an energy-based failure criterion is used. Apart from that, in both CZM and XFEM, due to their discontinuous setting, the allowed crack paths are prescribed to be along the middle surface of the geometry which render these approaches impractical for complex geometrical and morphological situations as, e.g., a 3D model of dissection propagating through an ascending aorta. It also needs to be emphasized that the presented approaches focus only on the mechanical fracture of solids/tissues, and they completely ignore the intricate feed-back mechanism between the mechanical and the biochemical environment of tissues which may evoke bio-chemo-mechanical fracture.

The mechanical behavior of arterial walls before and after crack initiation is very much dependent on the local variability of collagen, and on the presence of micro-defects and micro-calcifications, see, e.g., Marino and Vairo [43] and Hutchesson et al. [34]. On the top of that, the hierarchical structure of collagen fibers, the main contributor of the mechanical response of soft tissues, is evident from morphological investigations (Sherman et al. [62]). Hence, multi-scale approaches to rupture of soft tissues may provide more physically relevant and holistic approximations than the above-stated macro models.

There is a pressing need for more advanced computational models that can predict the propagation of cracks and the ultimate rupture of soft biological tissues resulting from atherosclerotic plaques, aneurysms, aortic dissection etc. based on clinically available patient-specific data. Such models should also be informed by the underlying mechanobiology of, e.g., the lipid absorbing leukocytes (Libby et al. [41]), matrix-metalloproteinases, Marfan's syndrome, to name but a few (Humphrey and Holzapfel [33]). Growth and remodeling of lesions triggered by mechanobiology should also be taken into account. The focus of modeling and simulation should be more on the tissue structure rather than on a phenomenological description, and should move towards personalized data, ultimately leading to the establishment of soft tissue rupture simulation as a key tool in medical monitoring and planning of surgical intervention.

References

1. T.L. Anderson, *Fracture Mechanics: Fundamentals and Applications*, 3rd edn. (CRC Press, Taylor & Francis Group, Boca Raton, FL, 2005)
2. F. Armero, K. Garikipati, An analysis of strong discontinuities in multiplicative finite strain plasticity and their relation with the numerical simulation of strain localization in solids. *Int. J. Solids Struct.* **33**, 2863–2885 (1996)
3. G.I. Barenblatt, The formation of equilibrium cracks during brittle fracture. General ideas and hypothesis. Axially symmetric cracks. *J. Appl. Math. Mech.* **23**, 622–636 (1959)
4. G.I. Barenblatt, The mathematical theory of equilibrium cracks in brittle fracture. *Adv. Appl. Mech.* **7**, 55–129 (1962)
5. T. Belytschko, T. Black, Elastic crack growth in finite elements with minimal remeshing. *Int. J. Numer. Meth. Eng.* **45**, 601–620 (1999)
6. T. Belytschko, Y.Y. Lu, L. Gu, Element-free Galerkin methods. *Int. J. Numer. Meth. Eng.* **37**, 229–256 (1994)
7. M.A. Biot, *Mechanics of Incremental Deformations* (Wiley, New York, 1965)
8. B. Bourdin, G.A. Francfort, J.-J. Marigo, Numerical experiments in revisited brittle fracture. *J. Mech. Phys. Solids* **48**, 797–826 (2000)
9. B. Bourdin, G.A. Francfort, J.-J. Marigo, *The Variational Approach to Fracture* (Springer, Berlin, 2008)
10. A. Braides, *Gamma-Convergence for Beginners* (Oxford University Press, New York, 2002)
11. G.T. Camacho, M. Ortiz, Computational modelling of impact damage in brittle materials. *Int. J. Solids Struct.* **33**, 2899–2938 (1996)
12. F.J. Criado, Aortic dissection: a 250-year perspective. *Tex. Heart Inst. J.* **38**, 694–700 (2011)
13. H. Dal, Quasi-incompressible and quasi-inextensible element formulation for transversely anisotropic materials. *Int. J. Numer. Meth. Eng.* (2017). Submitted

14. E.A. de Souza Neto, D. Perić, D.R.J. Owen, *Computational Methods for Plasticity: Theory and Applications* (Wiley, Chichester, 2008)
15. D.S. Dugdale, Yielding of steel sheets containing slits. *J. Mech. Phys. Solids* **8**, 100–104 (1960)
16. A. Ferrara, A. Pandolfi, Numerical modeling of fracture in human arteries. *Comput. Methods Biomech. Biomed. Eng.* **11**, 553–567 (2008)
17. A. Ferrara, A. Pandolfi, A numerical study of arterial media dissection processes. *Int. J. Fract.* **166**, 21–33 (2010)
18. P.J. Flory, Thermodynamic relations for highly elastic materials. *Trans. Faraday Soc.* **57**, 829–838 (1961)
19. G.A. Francfort, J.-J. Marigo, Revisiting brittle fracture as an energy minimization problem. *J. Mech. Phys. Solids* **46**, 1319–1342 (1998)
20. T.C. Gasser, G.A. Holzapfel, Modeling 3D crack propagation in unreinforced concrete using PUFEM. *Comput. Meth. Appl. Mech. Eng.* **194**, 2859–2896 (2005)
21. T.C. Gasser, G.A. Holzapfel, Modeling the propagation of arterial dissection. *Eur. J. Mech. A/Solids* **25**, 617–633 (2006)
22. A.A. Griffith, The phenomena of rupture and flow in solids. *Phil. Trans. R. Soc. Lond. A* **221**, 163–197 (1921)
23. O. Gültekin, A Phase Field Approach to the Fracture of Anisotropic Medium. Master's thesis, University of Stuttgart, Institute of Applied Mechanics (CE), Pfaffenwaldring 7, Stuttgart, 2014
24. O. Gültekin, H. Dal, G.A. Holzapfel, A phase-field approach to model fracture of arterial walls: theory and finite element analysis. *Comput. Meth. Appl. Mech. Eng.* **312**, 542–566 (2016)
25. O. Gültekin, H. Dal, G.A. Holzapfel, Numerical aspects of anisotropic failure in soft biological tissues favor energy-based criteria: a rate-dependent anisotropic crack phase-field model. *Comput. Meth. Appl. Mech. Eng.* (2017). Submitted
26. V. Hakim, A. Karma, Laws of crack motion and phase-field models of fracture. *J. Mech. Phys. Solids* **57**, 342–368 (2009)
27. B. Halphen, Q.S. Nguyen, Sur les matériaux standard généralisés. *J. de Mécanique* **14**, 39–63 (1975)
28. R. Hill, A theory of the yielding and plastic flow of anisotropic metals. *Proc. R. Soc. Lond. A* **193**, 281–297 (1948)
29. G.A. Holzapfel, *Nonlinear Solid Mechanics A Continuum Approach for Engineering* (Wiley, Chichester, 2000)
30. G.A. Holzapfel, T.C. Gasser, R.W. Ogden, A new constitutive framework for arterial wall mechanics and a comparative study of material models. *J. Elasticity* **61**, 1–48 (2000)
31. G.A. Holzapfel, C.A.J. Schulze-Bauer, M. Stadler, Mechanics of angioplasty: wall, balloon and stent, in *Mechanics in Biology*, ed. by J. Casey, G. Bao, New York, AMD-Vol. 242/BED-Vol. 46 (The American Society of Mechanical Engineers (ASME), 2000), pp. 141–156
32. G.A. Holzapfel, G. Sommer, P. Regitnig, Anisotropic mechanical properties of tissue components in human atherosclerotic plaques. *J. Biomech. Eng.* **126**, 657–665 (2004)
33. J.D. Humphrey, G.A. Holzapfel, Mechanics, mechanobiology, and modeling of human abdominal aorta and aneurysms. *J. Biomech.* **45**, 805–814 (2012)
34. J.D. Hutcheson, C. Goettsch, S. Bertazzo, N. Maldonado, J.L. Ruiz, W. Goh, K. Yabusaki, T. Faits, C. Bouten, G. Franck, T. Quillard, P. Libby, M. Aikawa, S. Weinbaum, E. Aikawa, Genesis and growth of extracellular-vesicle-derived microcalcification in atherosclerotic plaques. *Nat. Mater.* **15**, 335–343 (2016)
35. J.W. Hutchinson, Singular behaviour at the end of a tensile crack in a hardening material. *J. Mech. Phys. Solids* **16**, 13–31 (1968)
36. G.R. Irwin, Fracture dynamics, in *Fracturing of Metals*, pp. 147–166, Cleveland, OH (American Society for Metals, 1948)
37. X. Jin, G.R. Joldes, K. Miller, K.H. Yang, A. Wittek, Meshless algorithm for soft tissue cutting in surgical simulation. *Comput. Methods Biomech. Biomed. Eng.* **17**, 800–811 (2014)
38. T. Katayama, N. Sakoda, F. Yamamoto, M. Ishizaki, Y. Iwasaki, Balloon rupture during coronary angioplasty causing dissection and intramural hematoma of the coronary artery; a case report. *J. Cardio. Cases* **1**, e17–e20 (2010)

39. J.H. Kim, S. Avril, A. Duprey, J.P. Favre, Experimental characterization of rupture in human aortic aneurysms using a full-field measurement technique. *Biomech. Model. Mechanobiol.* **11**, 841–853 (2012)
40. J.K. Lee, L. Yao, C.T. Phelps, C.R. Wirth, J. Czajka, J. Lozman, Anterior cruciate ligament tears: MR imaging compared with arthroscopy and clinical tests. *Radiology* **166**, 861–864 (1988)
41. P. Libby, P.M. Ridker, G.K. Hansson, Progress and challenges in translating the biology of atherosclerosis. *Nature* **473**, 317–325 (2011)
42. L.D. Libersky, A.G. Petschek, Smooth particle hydrodynamics with strength of materials, in *Advances in the Free-Lagrange Method Including Contributions on Adaptive Gridding and the Smooth Particle Hydrodynamics Method, Proceedings of the Next Free-Lagrange Conference*, ed. by H.E. Trease, M.F. Fritts, W.P. Crowley (Springer, 1990), pp. 248–257
43. M. Marino, G. Vairo, Influence of inter-molecular interactions on the elasto-damage mechanics of collagen fibrils: A bottom-up approach towards macroscopic tissue modeling. *J. Mech. Phys. Solids* **73**, 38–54 (2014)
44. J.E. Marsden, T.J.R. Hughes, *Mathematical Foundations of Elasticity* (Dover, New York, 1994)
45. J.M. Melenk, I. Babuška, The partition of unity finite element method: Basic theory and applications. *Comput. Meth. Appl. Mech. Eng.* **139**, 289–314 (1996)
46. C. Miehe, Aspects of the formulation and finite element implementation of large strain isotropic elasticity. *Int. J. Numer. Meth. Eng.* **37**, 1981–2004 (1994)
47. C. Miehe, H. Dal, L.-M. Schänzel, A. Raina, A phase-field model for chemo-mechanical induced fracture in lithium-ion battery electrode particles. *Int. J. Numer. Meth. Eng.* **106**, 683–711 (2016)
48. C. Miehe, M. Hofacker, L.-M. Schänzel, F. Aldakheel, Phase field modeling of fracture in multi-physics problems. Part II. Coupled brittle-to-ductile failure criteria and crack propagation in thermo-elastic-plastic solids. *Comput. Meth. Appl. Mech. Eng.* **294**, 486–522 (2015)
49. C. Miehe, M. Hofacker, F. Welschinger, A phase field model for rate-independent crack propagation: Robust algorithmic implementation based on operator splits. *Comput. Meth. Appl. Mech. Eng.* **199**, 2765–2778 (2010)
50. C. Miehe, L.-M. Schänzel, Phase field modeling of fracture in rubbery polymers. Part I. Finite elasticity coupled with brittle fracture. *J. Mech. Phys. Solids* **65**, 93–113 (2014)
51. C. Miehe, L.-M. Schänzel, H. Ulmer, Phase field modeling of fracture in multi-physics problems. Part I. Balance of crack surface and failure criteria for brittle crack propagation in thermo-elastic solids. *Comput. Meth. Appl. Mech. Eng.* **294**, 449–485 (2015)
52. C. Miehe, F. Welschinger, M. Hofacker, Thermodynamically consistent phase-field models of fracture: Variational principles and multi-field FE implementations. *Int. J. Numer. Meth. Eng.* **83**, 1273–1311 (2010)
53. N. Moës, T. Belytschko, Extended finite element method for cohesive crack growth. *Engr. Fract. Mech.* **69**, 813–833 (2002)
54. N. Moës, J. Dolbow, T. Belytschko, A finite element method for crack growth without remeshing. *Int. J. Numer. Meth. Eng.* **46**, 131–150 (1999)
55. A. Needleman, Micromechanical modeling of interfacial decohesion. *Ultramicroscopy* **40**, 203–214 (1992)
56. M. Ortiz, A. Pandolfi, Finite-deformation irreversible cohesive elements for three-dimensional crack-propagation analysis. *Int. J. Numer. Meth. Eng.* **44**, 1267–1282 (1999)
57. A. Raina, C. Miehe, A phase-field model for fracture in biological tissues. *Biomech. Model. Mechanobiol.* **15**, 479–496 (2016)
58. M.K. Rausch, G.E. Karniadakis, J.D. Humphrey, Modeling soft tissue damage and failure using a combined particle/continuum approach. *Biomech. Model. Mechanobiol.* **16**, 249–261 (2017)
59. J.R. Rice, A path independent integral and approximate analysis of strain concentration by notches and cracks. *J. Appl. Mech.* **35**, 379–386 (1968)
60. J.R. Rice, G.F. Rosengren, Plane strain deformation near a crack tip in a power-law hardening material. *J. Mech. Phys. Solids* **16**, 1–12 (1968)

61. P. Sharma, N. Maffulli, Tendon injury and tendinopathy: healing and repair. *J. Bone Joint Surg.* **87**, 187–202 (2005)
62. V.R. Sherman, W. Yang, M.A. Meyers, The material science of collagen. *J. Mech. Behav. Biomed. Mater.* **52**, 22–50 (2015)
63. S.A. Silling, Reformulation of elasticity theory for discontinuities and long-range forces. *J. Mech. Phys. Solids* **48**, 175–209 (2000)
64. S.A. Silling, E. Askarib, A meshfree method based on the peridynamic model of solid mechanics. *Comput. Struct.* **83**, 1526–1535 (2005)
65. J.C. Simo, J. Oliver, F. Amero, An analysis of strong discontinuities induced by strain softening in rate-independent inelastic solids. *Comput. Mech.* **12**, 277–296 (1993)
66. G. Sommer, T.C. Gasser, P. Regitnig, M. Auer, G.A. Holzapfel, Dissection properties of the human aortic media: an experimental study. *J. Biomech. Eng.* **130**, 021007-1–12 (2008)
67. S.W. Tsai, H.T. Hahn, *Introduction to Composite Materials* (Technomic Publishing Company, Lancaster, 1980)
68. S.W. Tsai, E.M. Wu, A general theory of strength of anisotropic materials. *J. Compos. Mater.* **5**, 58–80 (1971)
69. G.N. Wells, Discontinuous Modelling of Strain Localization and Failure. PhD thesis, Delft University of Technology, Netherlands, 2001
70. H.M. Westergaard, Bearing pressures and cracks. *J. Appl. Mech.* **6**, 49–53 (1939)
71. P. Wriggers, *Nonlinear Finite Element Methods* (Springer-Verlag, Berlin Heidelberg, 2008)
72. X.-P. Xu, A. Needleman, Numerical simulations of fast crack growth in brittle solids. *J. Mech. Phys. Solids* **42**, 1397–1434 (1994)

Performance Comparison of Nodally Integrated Galerkin Meshfree Methods and Nodally Collocated Strong Form Meshfree Methods

M. Hillman and J.S. Chen

Abstract For a truly meshfree technique, Galerkin meshfree methods rely chiefly on nodal integration of the weak form. In the case of Strong Form Collocation meshfree methods, direct collocation at the nodes can be employed. In this paper, performance of these node-based Galerkin and collocation meshfree methods is compared in terms of accuracy, efficiency, and stability. Considering both accuracy and efficiency, the overall effectiveness in terms of CPU time versus error is also assessed. Based on the numerical experiments, nodally integrated Galerkin meshfree methods with smoothed gradients and variationally consistent integration yield the most effective solution technique, while direct collocation of the strong form at nodal locations has comparable effectiveness.

1 Introduction

There are several attractive features of both Galerkin- and Strong Form Collocation-based meshfree methods, each with their own drawbacks as well. In Galerkin-based methods, their implementation is similar to the finite element method (FEM). They have been shown to be effective for solving problems which are difficult for traditional FEMs [1–5], provide straight-forward h -adaptivity [6, 7], arbitrary order of smoothness, among many other unique properties that can be leveraged in solving PDEs [8]. On the other hand, special techniques are required to obtain optimal convergence without the employment of high-order quadrature [9]. If nodal integration is used, stabilization must also be employed [10]. Essential

M. Hillman

Department of Civil and Environmental Engineering,
The Pennsylvania State University, University Park, PA 16802-1408, USA

J.S. Chen (✉)

Department of Structural Engineering, University of California,
San Diego 9500 Gilman Drive, La Jolla, CA 92093-0085, USA
e-mail: js-chen@ucsd.edu

boundary conditions also need special treatment as well since meshfree methods do not in general possess the Kronecker delta property [11].

Nodal integration has been employed for quadrature in Galerkin meshfree methods for several reasons. Foremost, it maintains the meshfree characteristic of the method as opposed to using background meshes for integration. It also offers simplicity, efficiency, and ease of implementation. As such, the properties of solutions obtained by the Galerkin method with nodal integration have been thoroughly examined, and it is now well known that poor convergence and solution instability can be encountered when left untreated [9, 12–14]. The poor convergence is attributed to the inaccuracy in integrating the weak form [15], while the instability is due to the choice of quadrature locations which yield zero strain energy associated with sawtooth modes [10]. Several nodal integration methods have been developed to circumvent either of these problems, or both [12–14, 16–19]. Many methods are available which circumvent the stability issue such as residual-based methods [12, 13], stress points [10, 20, 21], Taylor expansion of strains [19, 22, 23], gradient-based approaches [24], or strain smoothing with divergence operation of the averaged integral [14]. The strain smoothing method can achieve both optimal convergence and solution stability. This technique was based on satisfaction of the so-called integration constraint [14], which was later generalized to the variational consistency conditions [9]. A method has been developed to satisfy these conditions by employing a Petrov-Galerkin formulation [9]. Recently, a two-level smoothing technique was developed to satisfy the quadratic constraints [25]. Several strategies exist to address other issues with domain integration, but are beyond the scope of discussion in this chapter.

The strong-form based collocation meshfree methods [26–28] are generally very simple to implement. They do not suffer from quadrature issues, nor do they require special techniques for enforcement of essential boundary conditions other than applying weights for optimal accuracy in the solution [29]. They also offer several of the attractive features of their Galerkin counterpart such as straightforward adaptive refinement. To the authors' knowledge, they do not suffer from spatial instability when nodal locations are employed as collocation points.

In the linearization of second order PDEs however, the implementation of collocation methods is not as straightforward as the Galerkin technique, since it requires third order derivatives of the approximation functions, which also increases computational cost. While collocation circumvents quadrature issues, a sufficient number of collocation points is still required for optimal convergence [28, 30]. The solution of second order PDEs in general requires second order derivatives which is not a negligible cost in local meshfree approximations such as the reproducing kernel [28], and quadratic accuracy is also required for convergence [28]. It should be noted that the former issue can be overcome by the employment of implicit gradient approximations [31].

Considering the benefits of each method along with their associated costs, a tradeoff exists and warrants examination. In this work, focus is on the class of nodally collocated strong form and nodally integrated weak form based meshfree methods. These two methods are of interest in that they both offer truly meshfree

solutions to PDEs. The Galerkin version requires quadrature treatment, so variationally consistent integration is employed. The tradeoff between efficiency and accuracy is examined, as well as the stability of the numerical solution. To present a unified analysis, we focus on the reproducing kernel approximation as a basis for these two methods.

This chapter is organized as follows. Section 2 gives an overview of the construction of the reproducing kernel approximation. A model problem and discussion of the solution by Strong Form Collocation and the Galerkin method are presented in Sect. 3, and techniques employed to obtain stable and convergent solutions in nodal integration of the Galerkin method are also given. Section 4 presents several numerical examples, and compares the convergence rates, effectiveness (CPU time versus error), and stability of the two methods. The several conclusions that can be drawn from the study are given in Sect. 5.

2 Reproducing Kernel Approximation

Let a domain $\overline{\Omega} = \Omega \cup \partial\Omega$ be discretized by a set of N_p nodes $\mathcal{N} = \{\mathbf{x}_1, \dots, \mathbf{x}_{N_p} | \mathbf{x}_I \in \overline{\Omega}\}$ with corresponding node numbers $\mathcal{Z} = \{I | \mathbf{x}_I \in \mathcal{N}\}$. The n th order reproducing kernel (RK) approximation $u^h(\mathbf{x})$ of a function $u(\mathbf{x})$ is [1, 32]:

$$u^h(\mathbf{x}) = \sum_{I \in \mathcal{Z}} \Psi_I^{[n]}(\mathbf{x}) u_I \quad (1)$$

where $\{\Psi_I^{[n]}(\mathbf{x})\}_{I \in \mathcal{Z}}$ is the set of RK shape functions, and $\{u_I\}_{I \in \mathcal{Z}}$ are the associated coefficients. The shape functions $\Psi_I^{[n]}(\mathbf{x})$ are constructed by the product of a kernel function $\Phi_a(\mathbf{x} - \mathbf{x}_I)$ and a correction function $C^{[n]}(\mathbf{x}; \mathbf{x} - \mathbf{x}_I)$:

$$\Psi_I^{[n]}(\mathbf{x}) = \Phi_a(\mathbf{x} - \mathbf{x}_I) C^{[n]}(\mathbf{x}; \mathbf{x} - \mathbf{x}_I) \quad (2)$$

where

$$C^{[n]}(\mathbf{x}; \mathbf{x} - \mathbf{x}_I) = \{\mathbf{H}^{[n]}(\mathbf{x} - \mathbf{x}_I)\}^T \mathbf{b}^{[n]}(\mathbf{x}). \quad (3)$$

In the above, $\mathbf{b}^{[n]}(\mathbf{x})$ and $\mathbf{H}^{[n]}(\mathbf{x} - \mathbf{x}_I)$ are column vectors of coefficients and n th order complete monomials, respectively. For example, for quadratic basis ($n=2$) in two dimensions we have

$$\begin{aligned} \mathbf{b}^{[n]}(\mathbf{x}) &= [b_{00}(\mathbf{x}) \quad b_{10}(\mathbf{x}) \quad b_{01}(\mathbf{x}) \quad b_{20}(\mathbf{x}) \quad b_{11}(\mathbf{x}) \quad b_{02}(\mathbf{x})]^T, \\ \mathbf{H}^{[n]}(\mathbf{x} - \mathbf{x}_I) &= [1 \quad x \quad y \quad x^2 \quad xy \quad y^2]^T. \end{aligned} \quad (4)$$

The kernel function $\Phi_a(\mathbf{x} - \mathbf{x}_I)$ has compact support with measure a , and the smoothness of the kernel is inherited by the approximation. For example, a kernel with C^2 continuity gives C^2 continuity of the approximation.

The coefficients $\mathbf{b}^{[n]}(\mathbf{x})$ are determined by enforcing the following reproducing conditions [3]:

$$\sum_{I \in \mathcal{Z}} \mathbf{H}^{[n]}(\mathbf{x}_I) \Psi_I^{[n]}(\mathbf{x}) = \mathbf{H}^{[n]}(\mathbf{x}). \quad (5)$$

With $\mathbf{b}^{[n]}(\mathbf{x})$ obtained from (5), the RK shape functions are constructed as

$$\Psi_I^{[n]}(\mathbf{x}) = \mathbf{H}^{[n]}(\mathbf{0})^T \{ \mathbf{M}^{[n]}(\mathbf{x}) \}^{-1} \mathbf{H}^{[n]}(\mathbf{x} - \mathbf{x}_I) \Phi_a(\mathbf{x} - \mathbf{x}_I), \quad (6)$$

$$\mathbf{M}^{[n]}(\mathbf{x}) = \sum_{I \in \mathcal{Z}} \mathbf{H}^{[n]}(\mathbf{x} - \mathbf{x}_I) \{ \mathbf{H}^{[n]} \}^T(\mathbf{x} - \mathbf{x}_I) \Phi_a(\mathbf{x} - \mathbf{x}_I), \quad (7)$$

where $\mathbf{M}^{[n]}(\mathbf{x})$ is termed the *moment matrix*. The reproducing conditions (5) are met provided the moment matrix is invertible, which requires a sufficient number of nodes with non-zero cover over \mathbf{x} that are not co-linear (in 2D), or co-planar (in 3-D) [33].

3 Solution to Boundary Value Problems by Galerkin and Strong Form Collocation Methods

3.1 Model Problem

Poisson's equation is considered for evaluating the relative performance of mesh-free Galerkin and Strong Form Collocation methods for the approximate solution of boundary value problems:

$$\begin{aligned} \nabla^2 u + s &= 0 & \text{in } \Omega \\ \nabla u \cdot \mathbf{n} &= h & \text{on } \partial\Omega_h \\ u &= g & \text{on } \partial\Omega_g \end{aligned} \quad (8)$$

where s , h and g are given values on the domain Ω , the natural boundary $\partial\Omega_h$, and essential boundary $\partial\Omega_g$, respectively, with $\partial\Omega_h \cap \partial\Omega_g = \emptyset$ and $\partial\Omega_h \cup \partial\Omega_g = \partial\Omega$.

3.2 Solutions Using the Strong Form Collocation Method

The basic approach of the Strong Form Collocation method is to approximate the solution of a boundary value problem by a finite dimensional space and strongly enforce zero residual of the PDE and boundary conditions at a number of points (called collocation points) in the domain and on the boundary of the domain.

Let the set of nodes \mathcal{N} be decomposed into the sets $\mathcal{N}_d = \{\mathbf{x}_I | \mathbf{x}_I \in \Omega\}$, $\mathcal{N}_h = \{\mathbf{x}_I | \mathbf{x}_I \in \partial\Omega_h\}$, and $\mathcal{N}_g = \{\mathbf{x}_I | \mathbf{x}_I \in \partial\Omega_g\}$, with point numbers $\mathcal{Z}_h = \{I | \mathbf{x}_I \in \mathcal{N}_h\}$, $\mathcal{Z}_g = \{I | \mathbf{x}_I \in \mathcal{N}_g\}$, and $\mathcal{Z}_d = \{I | \mathbf{x}_I \in \mathcal{N}_d\}$, respectively. The enforcement of (8) at the set of nodes \mathcal{N} using (1) as an approximation of u yields:

$$\begin{aligned} \sum_{I \in \mathcal{Z}} \nabla^2 \Psi_I(\mathbf{x}_L) u_I &= -s(\mathbf{x}_L), & L \in \mathcal{Z}_d, \\ \sum_{I \in \mathcal{Z}} \nabla \Psi_I(\mathbf{x}_L) u_I \cdot \mathbf{n}(\mathbf{x}_L) &= h(\mathbf{x}_L), & L \in \mathcal{Z}_h, \\ \sum_{I \in \mathcal{Z}} \Psi_I(\mathbf{x}_L) u_I &= g(\mathbf{x}_L), & L \in \mathcal{Z}_g. \end{aligned} \tag{9}$$

Figure 1 shows an example of the three sets of collocation points for the conditions in (9).

For implementation, a matrix version of (9) can be written as

$$\begin{aligned} \mathbf{A} \mathbf{u} &= \mathbf{b} \\ \mathbf{A} &= \{\mathbf{A}_d, \mathbf{A}_h, \mathbf{A}_g\}^T \\ \mathbf{b} &= \{\mathbf{b}_d, \mathbf{b}_h, \mathbf{b}_g\}^T \end{aligned} \tag{10}$$

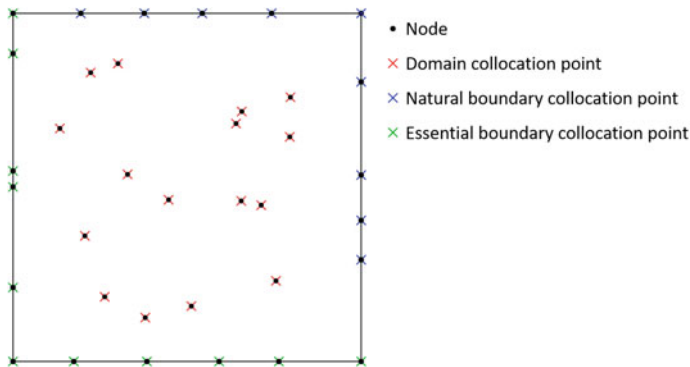


Fig. 1 Sets of collocation points for nodal collocation

where

$$\begin{aligned} [\mathbf{A}_d]_{IJ} &= \nabla^2 \Psi_J(\mathbf{x}_I), & [\mathbf{b}_d]_I &= s(\mathbf{x}_I), & I \in \mathcal{Z}_d, \\ [\mathbf{A}_h]_{IJ} &= \nabla \Psi_J(\mathbf{x}_I) \cdot \mathbf{n}(\mathbf{x}_I), & [\mathbf{b}_h]_I &= h(\mathbf{x}_I), & I \in \mathcal{Z}_h, \\ [\mathbf{A}_g]_{IJ} &= \Psi_J(\mathbf{x}_I), & [\mathbf{b}_g]_I &= g(\mathbf{x}_I), & I \in \mathcal{Z}_g. \end{aligned} \quad (11)$$

The nodes used in the approximation of $u^h(\mathbf{x}_L)$ are termed *source points*. Typically, more collocation points are chosen than source points, and least-square methods are employed to solve the over-determined system. However, when the solution is collocated at the nodes themselves such as in (9), the number of collocation points and source points are equal and the system can be solved directly.

3.3 Solutions Using the Galerkin Method with Nodal Integration

The Galerkin method is based on solving the weak form of (8), which asks to find $u \in U$ such that for all $v \in V$ the following holds:

$$a(v, u) = L(v) \quad (12)$$

where $U = \{u | u \in H^1(\overline{\Omega}), u = g \text{ on } \partial\Omega_g\}$, $V = \{v | v \in H^1(\overline{\Omega}), v = 0 \text{ on } \partial\Omega_g\}$, and the bilinear and linear forms in (12) are

$$\begin{aligned} a(v, u) &\equiv \int_{\Omega} \nabla v(\mathbf{x}) \cdot \nabla u(\mathbf{x}) d\Omega \\ L(v) &= (v, s)_{\Omega} + (v, h)_{\partial\Omega_h} \equiv \int_{\Omega} v(\mathbf{x}) s(\mathbf{x}) d\Omega + \int_{\partial\Omega_h} v(\mathbf{x}) h(\mathbf{x}) d\Gamma. \end{aligned} \quad (13)$$

The Galerkin method introduces finite dimensional approximations $U^h \subset U$, and $V^h \subset V$, and seeks $u^h \in U^h$ for all $v^h \in V^h$ such that

$$a(v^h, u^h) = L(v^h). \quad (14)$$

Utilizing the RK approximation (1) for u^h and v^h :

$$\begin{aligned} u^h(\mathbf{x}) &= \sum_{I \in \mathcal{Z}} \Psi_I^{[n]}(\mathbf{x}) u_I, \\ v^h(\mathbf{x}) &= \sum_{I \in \mathcal{Z}} \Psi_I^{[n]}(\mathbf{x}) v_I, \end{aligned} \quad (15)$$

and the arbitrariness of $\{v_I\}_{I \in \mathcal{Z}}$, the matrix form of (14) is

$$\mathbf{K}\mathbf{u} = \mathbf{f} \tag{16}$$

where \mathbf{u} is the column vector of coefficients $\{u_I\}_{I \in \mathcal{Z}}$, and \mathbf{K} and \mathbf{f} are the stiffness matrix and force column vector defined as

$$\begin{aligned} \mathbf{K} &= \int_{\Omega} \mathbf{B}^T(\mathbf{x})\mathbf{B}(\mathbf{x})d\Omega \\ \mathbf{f} &= \mathbf{f}_s + \mathbf{f}_h \equiv \int_{\Omega} \mathbf{N}^T(\mathbf{x})s(\mathbf{x})d\Gamma + \int_{\partial\Omega_h} \mathbf{N}^T(\mathbf{x})h(\mathbf{x})d\Gamma \end{aligned} \tag{17}$$

where

$$\begin{aligned} \mathbf{B}(\mathbf{x}) &= \begin{bmatrix} \Psi_{1,1}(\mathbf{x}) & \Psi_{2,1}(\mathbf{x}) & \dots & \Psi_{N_p,1}(\mathbf{x}) \\ \vdots & & & \\ \Psi_{1,d}(\mathbf{x}) & \Psi_{2,d}(\mathbf{x}) & \dots & \Psi_{N_p,d}(\mathbf{x}) \end{bmatrix}, \\ \mathbf{N}(\mathbf{x}) &= [\Psi_1(\mathbf{x}) \quad \Psi_2(\mathbf{x}) \quad \dots \quad \Psi_{N_p}(\mathbf{x})], \end{aligned} \tag{18}$$

and $(\cdot)_{,i} \equiv \partial(\cdot)/\partial x_i$.

Domain integration performed using the nodes as integration points is shown in Fig. 2a, where integration points coincide with the nodes has been termed *direct nodal integration* (DNI) in the literature. The nodal integration of the Galerkin equation (16) yields a stiffness matrix and force vector evaluated as

$$\begin{aligned} \mathbf{K} &= \sum_{L \in \mathcal{Z}} \mathbf{B}^T(\mathbf{x}_L)\mathbf{B}(\mathbf{x}_L)W_L \\ \mathbf{f} &= \sum_{L \in \mathcal{Z}} \mathbf{N}^T(\mathbf{x}_L)s(\mathbf{x}_L)W_L + \sum_{L \in \mathcal{Q}} \mathbf{N}^T(\mathbf{x}_L)h(\mathbf{x}_L)S_L \end{aligned} \tag{19}$$

where $\{W_L\}_{L \in \mathcal{Z}}$ are nodal quadrature weights, \mathcal{Q} is the set of indices of quadrature points on the natural boundary, and $\{S_L\}_{L \in \mathcal{Q}}$ is the set of associated quadrature weights.

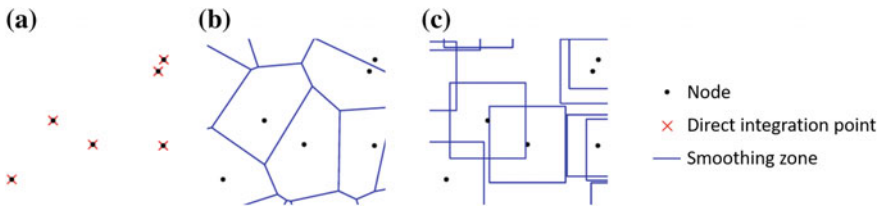


Fig. 2 Integration methods for (a) direct nodal integration, (b) SCNI integration, and (c) SNNI integration

This method does not attain optimal convergence rates in most situations due to the inherent low-order quadrature of this scheme. In addition, the choice of nodes as integration points severely underestimates the strain energy of low energy modes and the solution is subject to rank instability. Because of this, stabilized and corrected methods are usually employed with nodal integration.

To improve the accuracy of nodal integration, the work in [14] derived the following requirement on the approximation space and numerical integration at hand to attain linear exactness (passing the linear patch test) in the Galerkin solution of second order PDEs:

$$\int_{\Omega_L}^{\wedge} \nabla \Psi_I(\mathbf{x}) d\Omega = \int_{\partial\Omega_L}^{\wedge} \Psi_I(\mathbf{x}) \mathbf{n}(\mathbf{x}) d\Gamma \quad \forall I \quad (20)$$

where “ \wedge ” denotes numerical integration and $\{\Psi_I(\mathbf{x})\}_{I \in \mathcal{Z}}$ are shape functions with linear completeness. A stabilized conforming nodal integration (SCNI) has been proposed [14] which employs a smoothed gradient $\tilde{\nabla}$ of the RK approximation (1), calculated in each nodal representative domain Ω_L by

$$\tilde{\nabla} u^h(\mathbf{x}_L) = \frac{1}{W_L} \int_{\Omega_L} \nabla u^h(\mathbf{x}) d\Omega = \frac{1}{W_L} \int_{\partial\Omega_L} u^h(\mathbf{x}) \mathbf{n}(\mathbf{x}) d\Gamma \quad (21)$$

where $W_L = |\Omega_L|$. The nodal domains partition the total domain in a conforming fashion, as shown in Fig. 2b, which yields a method that satisfies (20). Because of the fact first order derivatives are not directly evaluated at the nodes, the zero energy modes in direct nodal integration do not appear in the solution by SCNI, thus addressing both issues with direct nodal integration. When linear bases are employed in (21), the method attains the optimal convergence rate consistent with the linear completeness in the approximation.

Employing the smoothed gradients in (21), the SCNI method can be phrased as

$$\tilde{\mathbf{K}} \mathbf{u} = \mathbf{f} \quad (22)$$

where

$$\tilde{\mathbf{K}} = \sum_{L \in \mathcal{Z}} \tilde{\mathbf{B}}^T(\mathbf{x}_L) \tilde{\mathbf{B}}(\mathbf{x}_L) W_L, \quad \tilde{\mathbf{B}}(\mathbf{x}_L) = \begin{bmatrix} \tilde{b}_{11}(\mathbf{x}_L) & \tilde{b}_{21}(\mathbf{x}_L) & \dots & \tilde{b}_{N_{px}}(\mathbf{x}_L) \\ \vdots & \vdots & \vdots & \vdots \\ \tilde{b}_{1d}(\mathbf{x}_L) & \tilde{b}_{2d}(\mathbf{x}_L) & \dots & \tilde{b}_{N_{pd}}(\mathbf{x}_L) \end{bmatrix}, \quad \tilde{b}_{ii}(\mathbf{x}_L) = \frac{1}{W_L} \int_{\partial\Omega_L} \Psi_I(\mathbf{x}) n_i(\mathbf{x}) d\Gamma. \quad (23)$$

A stabilized non-conforming nodal integration (SNNI) has also been proposed [24] where the smoothing domains do not conform:

$$\tilde{\nabla} u^h(\mathbf{x}_L) = \frac{1}{\overline{W}_L} \int_{\overline{\Omega}_L} \nabla u^h(\mathbf{x}) d\Omega = \frac{1}{\overline{W}_L} \int_{\partial \overline{\Omega}_L} u^h(\mathbf{x}) \mathbf{n}(\mathbf{x}) d\Gamma \quad (24)$$

where $\overline{\Omega}_L$ is a non-conforming smoothing domain, and $\overline{W}_L = |\overline{\Omega}_L|$. The set of nodal domains can be constructed by using boxes for example, as shown in Fig. 2c. This method fails to pass the patch test because of the simplification, but can be corrected with the methods discussed below.

Recently, the conditions in (20) were extended to n th order constraints, with the general framework termed variational consistency [9]. Assuming n th order completeness of the trial functions, the divergence criteria in (20) can be cast in a more general fashion that reduces to the integration constraints for linear solutions:

$$\int_{\Omega} \widehat{\Psi}_{I,i}^{[n]}(\mathbf{x}) \{\mathbf{H}^{[n-1]}\}^T(\mathbf{x}) d\Omega = \int_{\partial \Omega} \widehat{\Psi}_I^{[n]}(\mathbf{x}) \mathbf{H}^{[n-1]}(\mathbf{x}) n_i(\mathbf{x}) d\Gamma - \int_{\Omega} \widehat{\Psi}_I^{[n]}(\mathbf{x}) \mathbf{H}_{,i}^{[n-1]}(\mathbf{x}) d\Omega \quad \forall I \quad (25)$$

where $\{\widehat{\Psi}_I^{[n]}(\mathbf{x})\}_{I \in \mathcal{Z}}$ are shape functions associated with the test function space. The reduction in the order of complete monomials to $n-1$ that appear in the above equation is a result of solving the weak form of a second order PDE with integration by parts.

Leveraging the fact that n th order completeness by the trial space and satisfaction of the n th order integration constraints (25) by the test space are needed to satisfy n th order variational consistency, a Petrov-Galerkin method can be employed where test and trial functions are constructed to play different roles in the Galerkin solution of PDEs. In [9], an assumed test function gradient was introduced in order to satisfy the variational consistency conditions:

$$\begin{aligned} u_{,i}^h(\mathbf{x}) &= \sum_{I=1}^{N_p} \Psi_{I,i}^{[n]}(\mathbf{x}) u_I, \\ v_{,i}^h(\mathbf{x}) &= \sum_{I=1}^{N_p} \widehat{\Psi}_{I,i}^{[n]}(\mathbf{x}) v_I. \end{aligned} \quad (26)$$

The test function gradient can be constructed using the trial shape functions with an additional set of bases $\mathbf{H}^{[n-1]}(\mathbf{x})$ with constant coefficients ξ_{Ii} [9]:

$$\widehat{\Psi}_{I,i}^{[n]}(\mathbf{x}) = \Psi_{I,i}^{[n]}(\mathbf{x}) + \mathbf{H}^{[n-1]}(\mathbf{x}) \xi_{Ii} \Theta_I(\mathbf{x}) \quad (27)$$

where

$$\Theta_I(\mathbf{x}) = \begin{cases} 1 & \text{if } \mathbf{x} \in \text{supp}(\Psi_I^{[n]}(\mathbf{x})) \\ 0 & \text{if } \mathbf{x} \notin \text{supp}(\Psi_I^{[n]}(\mathbf{x})) \end{cases}. \quad (28)$$

Inserting the test functions (27) into (25) yields the linear systems of equations

$$\begin{aligned} \mathbf{A}_I \xi_{I1} &= \mathbf{r}_{I1} \\ &\vdots \\ \mathbf{A}_I \xi_{Id} &= \mathbf{r}_{Id} \end{aligned} \quad (29)$$

where

$$\begin{aligned} \mathbf{A}_I &= \int_{\Omega}^{\wedge} \mathbf{H}^{[n-1]}(\mathbf{x}) \{\mathbf{H}^{[n-1]}\}^T(\mathbf{x}) \Theta_I(\mathbf{x} - \mathbf{x}_I) d\Omega, \\ \mathbf{r}_{li} &= \int_{\partial\Omega}^{\wedge} \Psi_I^{[n]}(\mathbf{x}) \mathbf{H}^{[n-1]}(\mathbf{x}) n_i(\mathbf{x}) d\Gamma - \int_{\Omega}^{\wedge} \Psi_I^{[n]}(\mathbf{x}) \mathbf{H}_{,i}^{[n-1]}(\mathbf{x}) d\Omega \\ &\quad - \int_{\Omega}^{\wedge} \Psi_{I,i}^{[n]}(\mathbf{x}) \{\mathbf{H}^{[n-1]}\}^T(\mathbf{x}) d\Omega. \end{aligned} \quad (30)$$

The type of numerical integration is unspecified, and the framework allows construction of test functions variationally consistent with, for example, direct nodal integration, SCNI (for higher order exactness) and SNNI.

The nodal integration of the weak form with variationally consistent integration can be written as:

$$\widehat{\mathbf{K}} \mathbf{u} = \mathbf{f} \quad (31)$$

where

$$\begin{aligned} \widehat{\mathbf{K}} &= \sum_{L \in \mathcal{Z}} \widehat{\mathbf{B}}^T(\mathbf{x}_L) \mathbf{B}(\mathbf{x}_L) W_L, \\ \widehat{\mathbf{B}}(\mathbf{x}_L) &= \begin{bmatrix} \widehat{\Psi}_{1,1}^{[n]}(\mathbf{x}_L) & \widehat{\Psi}_{2,1}^{[n]}(\mathbf{x}_L) & \dots & \widehat{\Psi}_{N_p,1}^{[n]}(\mathbf{x}_L) \\ \vdots & \vdots & & \vdots \\ \widehat{\Psi}_{1,d}^{[n]}(\mathbf{x}_L) & \widehat{\Psi}_{2,d}^{[n]}(\mathbf{x}_L) & \dots & \widehat{\Psi}_{N_p,d}^{[n]}(\mathbf{x}_L) \end{bmatrix}. \end{aligned} \quad (32)$$

4 Numerical Examples

In this section the relative performance of the meshfree Galerkin and Strong Form Collocation methods discussed in Sect. 3 is examined numerically. The minimum order of approximation required for convergence is employed for each method: for Galerkin methods the minimum is linear, while for Strong Form Collocation the order is quadratic [28]. The studies show that due to the reduced performance of Strong Form Collocation under collocation at nodes (versus using more collocation points), and the superconvergence observed in the gradient smoothing Galerkin methods, both are competitive in terms of rates of convergence and accuracy and yield a “fare” comparison. In Galerkin methods, the uniformity of the domain influences the solution accuracy and rate of convergence, so both cases of uniform and non-uniform discretizations are tested. The nodal integration methods in Sect. 3.3 are employed for the Galerkin method, while direct collocation at the nodes is employed for collocation of the strong form as described in Sect. 3.2. Table 1 summarizes the nomenclature and abbreviations used in the numerical examples.

4.1 Performance of Galerkin and Collocation Methods: Uniform Discretization

Consider the Poisson equation (8) with $\Omega: (-1, 1) \times (-1, 1)$, $\partial\Omega^g = \partial\Omega$ and the prescribed conditions $s = \sin(\pi x) \sin(\pi y)$ and $g = 0$. The exact solution of this problem is

$$u = -\frac{1}{2\pi^2} \sin(\pi x) \sin(\pi y). \tag{33}$$

The problem is solved using linear RK approximations in the Galerkin method and quadratic RK approximations in the Strong Form Collocation method, with cubic B-spline kernels employed with normalized dilations of 1.75 and 2.75,

Table 1 Method nomenclature used in numerical examples

Formulation	Method	Abbreviation	
		Standard	Variationally consistent
Galerkin weak form	Direct nodal integration	DNI	VC-DNI
	Stabilized conforming nodal integration	SCNI	SCNI (no correction needed)
	Stabilized non-conforming nodal integration	SNNI	VC-SNNI
Strong Form Collocation	Direct collocation	DC	DC (passes patch test)

respectively. The domain is discretized uniformly by 36, 121, 441, and 1681 nodes for a convergence study.

The methods discussed in Sect. 3 are employed for the solution of the problem. However, in uniform discretizations the VC methods perform just as well as the non-corrected counterparts in most situations [9], so only the latter are considered in this example. Figure 3 shows the error plotted against the nodal spacing h for each of the methods. It can be seen that all Galerkin methods yield optimal convergence rates of 2.0 in the L^2 norm and 1.0 in the H^1 semi-norm, with the gradient smoothing methods SCNI and SNNI achieving superconvergent rates in derivatives. The direct collocation (DC) in the Strong Form Collocation method exhibits rates in the L^2 norm lower than optimal of 3.0 for the quadratic basis employed. This can be attributed to the low accuracy of using very few collocation points which can be explained by the equivalent least-squares residual of the Strong Form Collocation method [29]. Because of these two observed trends, the rates of convergence in nodal integration of the Galerkin method with linear basis and collocation of the strong form at nodes with quadratic basis seem comparable.

Now comparing the Galerkin methods and the Strong Form Collocation methods in terms of effectiveness (CPU time versus error), it can be seen in Fig. 4 that the Galerkin methods are the most effective in the L_2 norm, although for the solution derivatives, DC and SNNI perform similarly while others are less effective, with DNI the least effective. Overall, considering both norms, the Galerkin method with SCNI and SNNI are the most effective methods in uniform discretizations, with collation using DC a close competitor.

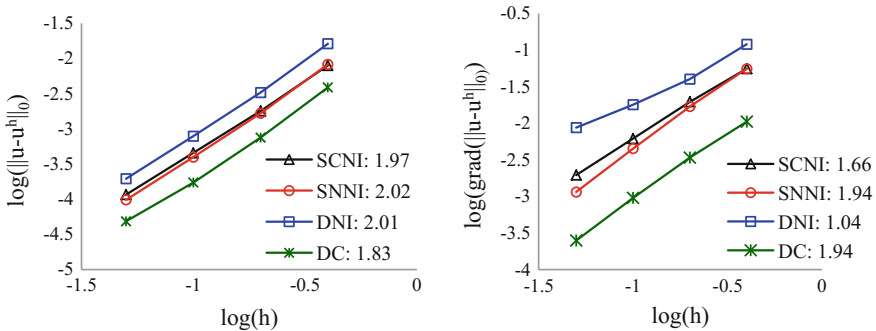


Fig. 3 Convergence of nodal Galerkin method with linear bases (SCNI, SNNI, DNI) and Strong Form Collocation with quadratic bases with direct collocation (DC) under a uniform discretization

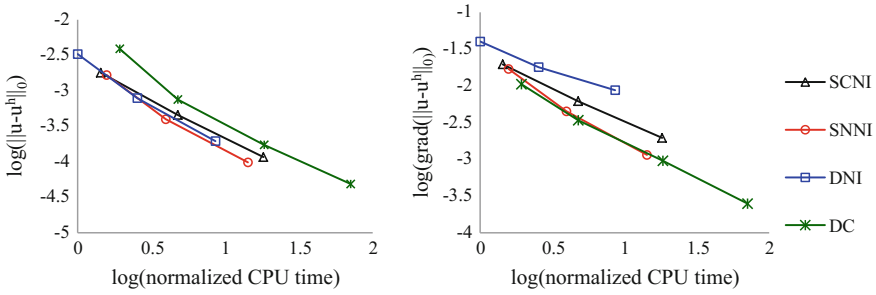


Fig. 4 Relative performances of nodal Galerkin and collocation methods under uniform discretizations

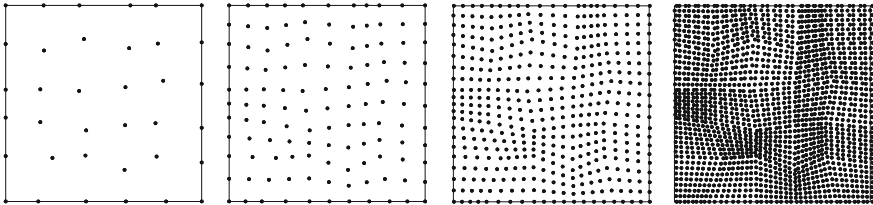


Fig. 5 Refinements for convergence test in non-uniform discretizations

4.2 Performance of Galerkin and Collocation Methods: Non-uniform Discretization

The solutions by meshfree Galerkin methods are particularly sensitive to the uniformity of the discretization. Thus, to truly evaluate the performance of the methods discussed, non-uniform discretizations must also be considered in a convergence study. The boundary value problem and discretization described in the previous example are again employed, except the non-uniform node distributions shown in Fig. 5 are used in place of the uniform discretizations.

As expected, the convergence rates of the VC methods are far superior to their un-corrected counterparts, yielding optimal rates as shown in Fig. 6. Comparing Figs. 3 and 6, it can be seen that the solution by direct collocation at nodes for Strong Form is not severely affected by the uniformity of the discretization, with only slightly lower rates obtained in both norms. As a result of the lower rate of convergence in DC for Strong Form Collocation with quadratic bases and super-convergence in VC Galerkin Methods with linear bases occurring in this example as well, the rates are again comparable as in the case of uniform discretizations.

When comparing the effectiveness of the methods in terms of error and CPU time, it can be seen in Fig. 7 that the Galerkin VC methods and the Strong Form DC method have similar effectiveness in the L^2 norm. However, due to the lower accuracy in derivatives in VC-DNI, only SCNI, VC-SNNI and DC have

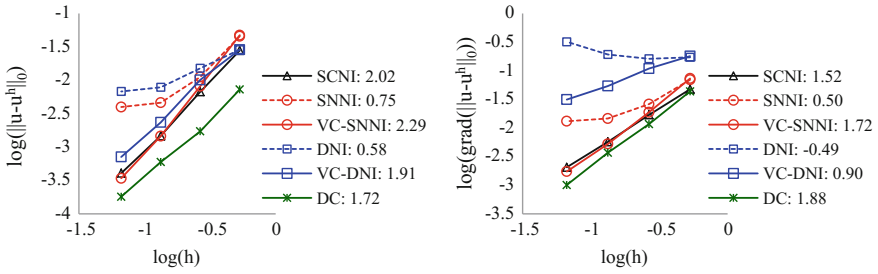


Fig. 6 Convergence of nodal Galerkin method with linear bases (SCNI, SNNI, DNI) and Strong Form Collocation with quadratic bases with direct collocation (DC) under non-uniform discretizations

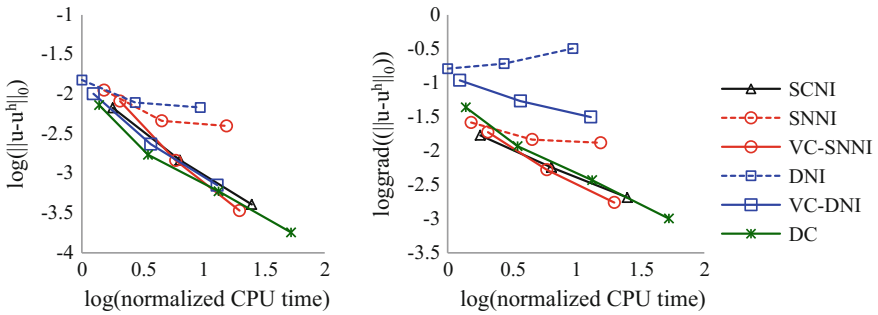


Fig. 7 Relative performances of nodal Galerkin and collocation methods under a non-uniform discretization

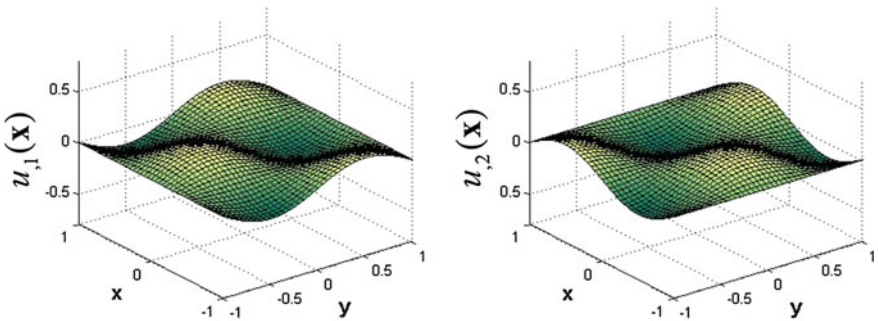


Fig. 8 Derivatives of exact solution

comparable effectiveness in the H^1 semi-norm. The similarity in the performance of these three methods is notable considering the vastly different approaches, including (expensive) higher order derivatives, higher order bases and thus also

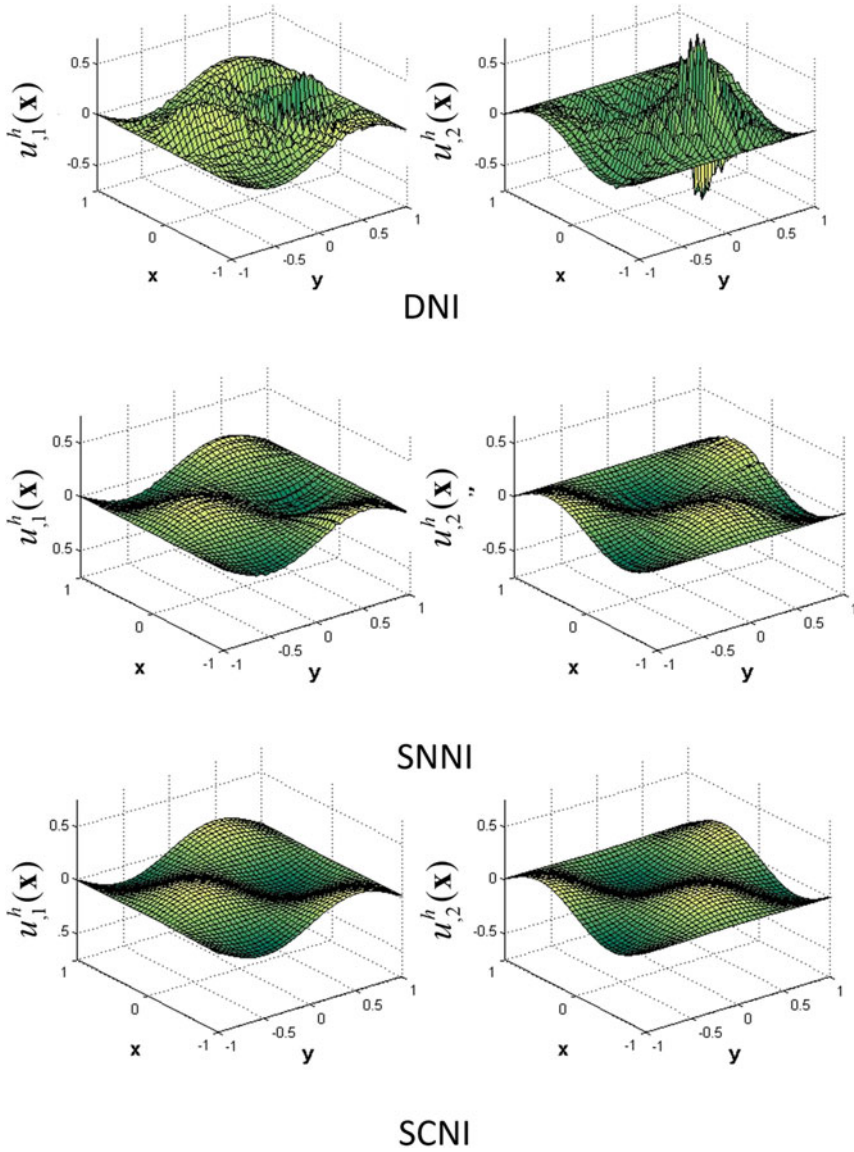


Fig. 9 Solution derivatives obtained by node-based Galerkin and collocation methods

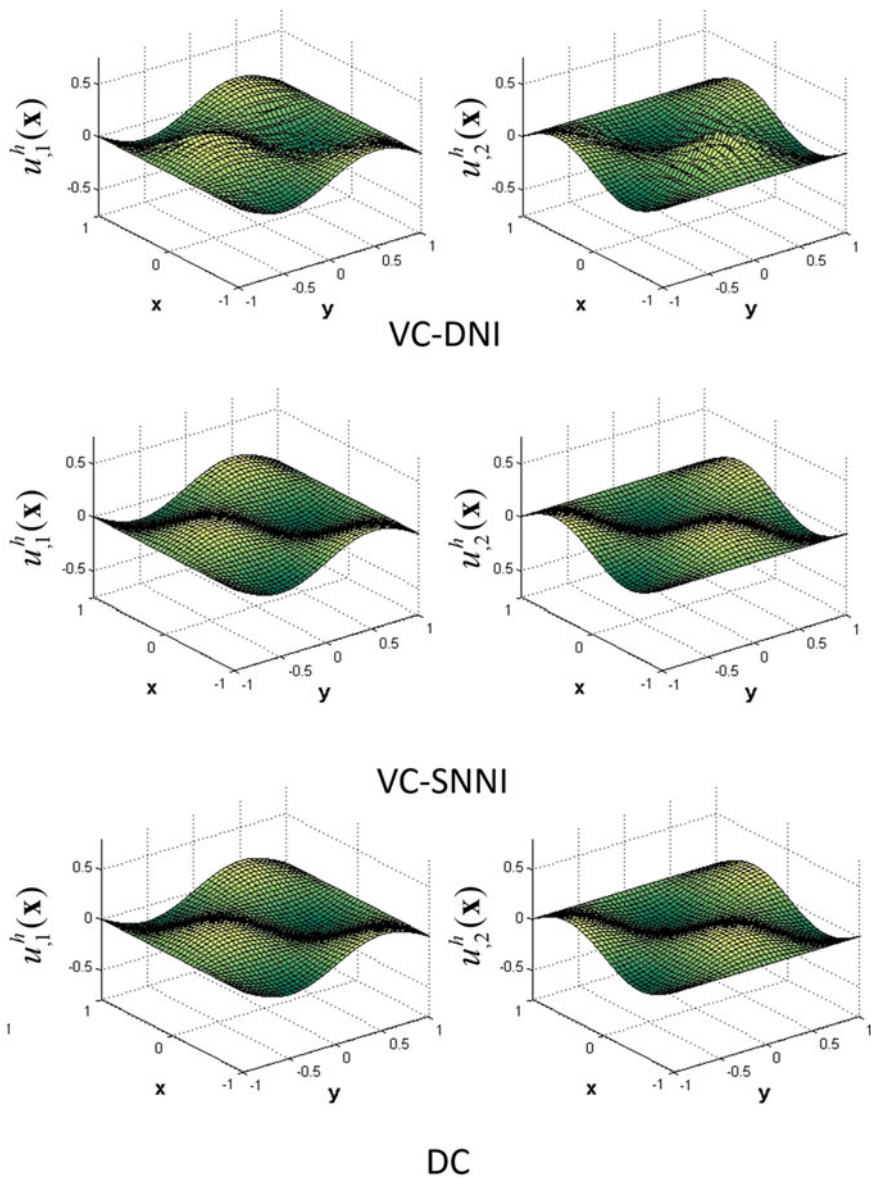


Fig. 9 (continued)

larger dilations employed for Strong Form Collocation. Finally, comparing Figs. 4 and 7, it can be seen that SCNI and VC-SNNI perform the best across both norms of error and both types of discretization, with DC a close competitor.

4.3 *Stability of Node-Based Galerkin and Collocation Methods*

To assess the stability of the methods, we examine the solution derivatives for the last refinement in the previous example. For reference, the derivatives of the exact solution (33) are shown in Fig. 8.

The solution derivatives are shown in Fig. 9 for all the methods considered herein. Several conclusions can be drawn from the Figures. First, it can be seen that the VC correction remarkably stabilizes the solution of the nodally integrated Galerkin method, which has been observed in other contexts as well [17]. However, it is apparent that unstable modes exist in direct nodal integration, which could explain the poorer rates of convergence and poorer levels of error versus the other nodally integrated Galerkin methods. It can also be seen that the VC correction is sufficient to stabilize SNNI, which could explain its apparently good performance in terms of convergence rates and error, yielding solutions similar to SCNI. Finally, the only stable nodally integrated Galerkin methods tested are VC-SNNI and SCNI, while the DC Strong Form Collocation method also gives a stable solution.

5 Conclusions

Several nodal integrations for Galerkin meshfree methods were tested against the purely node-based Strong Form Collocation method. The variationally consistent integration for Galerkin methods yielded optimal convergence rates associated with the linear approximations employed as expected, correcting their counterparts' deficiencies in convergence. However for direct nodal integration, even with the variationally consistent correction, the error in several cases was larger than all other methods indicating it is not a "competitive" method for nodal integration, at least without additional treatment for the stabilization which was not investigated here. In the case of the smoothed gradient VC methods (SCNI, VC-SNNI), superconvergent rates above those associated with linear bases were observed in the numerical examples. For the Strong Form Collocation method with collocation at nodes and quadratic basis, suboptimal convergence rates were observed. As a result, the convergence rates of the direct collocation method for Strong Form with quadratic bases and the smoothed, variationally consistent nodally integrated Galerkin methods with linear bases were similar in all examples. On the other hand, the error was in general always lower for the direct collocation method in the Strong Form method.

In terms of effectiveness, the first conclusion that can be drawn is that VC Galerkin methods are always more effective in the general setting when considering the possibility of non-uniform discretizations. Direct nodal integration for the Galerkin method in general performed more poorly than other methods even with a correction for variational consistency, and again can be considered not “competitive” with the other methods tested. Despite yielding lower error, the Strong Form with direct collocation did not always perform as well as the Galerkin method with SNNI and SCNI in terms of efficiency in uniform discretizations. In the case of non-uniform discretizations, Galerkin methods with VC-SNNI and SCNI performed closely to direct collocation of the strong form at nodes. Considering both uniform and non-uniform discretizations, VC-SNNI and SCNI seem to be the most effective methods tested. That is, for a given level of error, they yield the least CPU time, and for a given CPU time, these methods will yield the least amount of error.

The stability of the solutions obtained by the Galerkin and Strong Form Collocation method was also investigated. First, variationally consistent integration corrected instabilities observed in DNI and SNNI. It could not however, completely remove the unstable modes in DNI, which is possibly why it was not competitive compared to other methods as the error in the derivatives was large due to the instability. Comparison of stabilized direct nodal integration, such as naturally stabilized nodal integration [19] was beyond the scope of this study but warrants investigation, particularly since SCNI and SNNI also require additional treatments to remain stable in certain special situations. As a result of the stabilizing effect of the VC corrections, VC-SNNI yielded stable solutions, and SCNI and VC-SNNI were the only Galerkin methods that did not exhibit instability.

Direct collocation of the strong form also did not yield an instability. It would appear that in contrast to Galerkin methods, collocation methods do not suffer from instability when evaluating the 2nd order derivatives at nodal locations, and do not require special treatment in this case.

Overall, the numerical examples showed that the smoothed gradient, variationally consistent nodal integration for the Galerkin method performed very similar to direct collocation of the strong form at the nodes. Both yielded similar rates of convergence and effectiveness, and all three methods did not show instability in the numerical solution. However, direct collocation in some cases was not as effective, and therefore, although all competitive, the smoothed Galerkin methods with variational consistency yielded the most effective solution techniques.

There is also a striking similarity between the behavior of variationally consistent smoothed gradient Galerkin methods, SCNI and VC-SNNI. However, as a non-conforming method, VC-SNNI has the advantage of dispensing of conforming cells which has several implications, such as using VC-SNNI for ease of implementation, or for solving extremely large deformation problems where non-conforming smoothing is more effective. On the other hand, SCNI has the advantage of yielding a symmetric system of equations, and this feature can also be leveraged in the choice of solver. Future work will investigate the effectiveness of other stabilized nodal integrations, as well as background collocation and background integration, comparing them to the methods discussed in this work.

References

1. J.S. Chen, C. Pan, C.-T. Wu, W.K. Liu, Reproducing Kernel particle methods for large deformation analysis of non-linear structures. *Comput. Methods Appl. Mech. Eng.* **139**(1–4), 195–227 (1996)
2. J.-S. Chen, C. Pan, C.-T. Wu, Large deformation analysis of rubber based on a reproducing kernel particle method. *Comput. Mech.* **19**(3), 211–227 (1997)
3. J.-S. Chen, C. Pan, C.M.O.L. Roque, H.-P. Wang, A Lagrangian reproducing kernel particle method for metal forming analysis. *Comput. Mech.* **22**(3), 289–307 (1998)
4. P.C. Guan, J.S. Chen, Y. Wu, H. Teng, J. Gaidos, K. Hofstetter, M. Alsaleh, Semi-Lagrangian reproducing kernel formulation and application to modeling earth moving operations. *Mech. Mater.* **41**(6), 670–683 (2009)
5. S.-W. Chi, C.-H. Lee, J.-S. Chen, P.-C. Guan, A level set enhanced natural kernel contact algorithm for impact and penetration modeling. *Int. J. Numer. Methods Eng.* **102**(3–4), 839–866 (2015)
6. Y. You, J.-S. Chen, H. Lu, Filters, reproducing kernel, and adaptive meshfree method. *Comput. Mech.* **31**(3), 316–326 (2003)
7. T. Rabczuk, T. Belytschko, Adaptivity for structured meshfree particle methods in 2D and 3D. *Int. J. Numer. Methods Eng.* **63**(11), 1559–1582 (2005)
8. S. Li, W.K. Liu, Meshfree and particle methods and their applications. *Appl. Mech. Rev.* **55**(1), 1–34 (2002)
9. J.S. Chen, M. Hillman, M. Rüter, An arbitrary order variationally consistent integration for Galerkin meshfree methods. *Int. J. Numer. Methods Eng.* **95**(5), 387–418 (2013)
10. T. Belytschko, Y. Guo, W.K. Liu, S.P. Xiao, A unified stability analysis of meshless particle methods. *Int. J. Numer. Methods Eng.* **48**(9), 1359–1400 (2000)
11. T. Belytschko, Y.Y. Lu, L. Gu, Element-free Galerkin methods, *Int. J. Numer. Methods Eng.* **37**, April 1993, 229–256, (1994)
12. S.R. Beissel, T. Belytschko, Nodal integration of the element-free Galerkin method. *Comput. Methods Appl. Mech. Eng.* **139**, 49–74 (1996)
13. J. Bonet, S. Kulasegaram, Correction and stabilization of smooth particle hydrodynamics methods with applications in metal forming simulations. *Int. J. Numer. Methods Eng.* July 1998, 1189–1214, (2000)
14. J.-S. Chen, C.-T. Wu, S. Yoon, A stabilized conforming nodal integration for Galerkin mesh-free methods, *Int. J. Numer. Methods Eng.* **207**, February 2000, 435–466 (2001)
15. I. Babuška, U. Banerjee, J.E. Osborn, Q. Li, Quadrature for meshless methods. *Int. J. Numer. Methods Eng.* **76**(9), 1434–1470 (2008)
16. S.N. Atluri, T.L. Zhu, A new meshless local Petrov-Galerkin (MLPG) approach to nonlinear problems in computer modeling and simulation. *Comput. Model. Simul. Eng.* **3**(3), 187–196 (1998)
17. M. Hillman, J.-S. Chen, S.-W. Chi, Stabilized and variationally consistent nodal integration for meshfree modeling of impact problems. *Comp. Part. Mech.* **1**, 245–256 (2014)
18. C.-T. Wu, M. Koishi, W. Hu, A displacement smoothing induced strain gradient stabilization for the meshfree Galerkin nodal integration method, *Comput. Mech.* (2015)
19. M. Hillman, J.S. Chen, An accelerated, convergent, and stable nodal integration in Galerkin meshfree methods for linear and nonlinear mechanics. *Int. J. Numer. Methods Eng.* **107**, 603–630 (2016)
20. P.W. Randles, L.D. Libersky, Normalized SPH with stress points, *Int. J. Numer. Methods Eng.* **48**, May 1999, 1445–1462 (2000)
21. T. Rabczuk, T. Belytschko, S.P. Xiao, Stable particle methods based on Lagrangian kernels. *Comput. Methods Appl. Mech. Eng.* **193**(12–14), 1035–1063 (2004)
22. T. Nagashima, Node-By-Node Meshless Approach and Its Applications to Structural Analyses, vol. 385, April 1997, pp. 2–3, (1999)

23. G.-R. Liu, G.Y. Zhang, Y.Y. Wang, Z.H. Zhong, G.Y. Li, X. Han, A nodal integration technique for meshfree radial point interpolation method (NI-RPIM). *Int. J. Solids Struct.* **44** (11–12), 3840–3860 (2007)
24. J.-S. Chen, W. Hu, M.A. Puso, Y. Wu, X. Zhang, Strain smoothing for stabilization and regularization of galerkin meshfree methods. *Lect. Notes Comput. Sci. Eng.* **57**, 57–75 (2007)
25. D. Wang, J. Wu, An efficient nesting sub-domain gradient smoothing integration algorithm with quadratic exactness for Galerkin meshfree methods. *Comput. Methods Appl. Mech. Eng.* **298**, 485–519 (2016)
26. E.J. Kansa, Multiquadrics—a scattered data approximation scheme with applications to computational fluid-dynamics—I surface approximations and partial derivative estimates. *Comput. Math. with Appl.* **19**(8), 127–145 (1990)
27. E. Oñate, S.R. Idelsohn, O.C. Zienkiewicz, R.L. Taylor, A finite point method in computational mechanics. Applications to convective transport and fluid flow, *Int. J. Numer. Methods Eng.* **39**, December 1995, 3839–3866 (1996)
28. H.-Y. Hu, C.-K. Lai, J.-S. Chen, A study on convergence and complexity of reproducing kernel collocation method. *Interact. Multiscale Mech.* **2**(3), 295–319 (2009)
29. H.-Y. Hu, J.-S. Chen, W. Hu, Weighted radial basis collocation method for boundary value problems. *Int. J. Numer. Methods Eng.* **69**(13), 2736–2757 (2007)
30. H.-Y. Hu, J.-S. Chen, W. Hu, Error analysis of collocation method based on reproducing kernel approximation. *Numer. Methods Partial Differ. Equ.* **27**(3), 554–580 (2011)
31. S.-W. Chi, J.-S. Chen, H.-Y. Hu, J.P. Yang, A gradient reproducing kernel collocation method for boundary value problems. *Int. J. Numer. Methods Eng.* **93**(13), 1381–1402 (2013)
32. W.K. Liu, S. Jun, Y.F. Zhang, Reproducing kernel particle methods. *Int. J. Numer. Methods Fluids.* **20**(8–9), 1081–1106 (1995)
33. W.K. Liu, S. Li, T. Belytschko, Moving least-square reproducing kernel methods (I) Methodology and convergence. *Comput. Methods Appl. Mech. Eng.* **143**(1–2), 113–154 (1997)

Data-Driven Computing

Trenton Kirchdoerfer and Michael Ortiz

Abstract Data-Driven Computing is a new field of computational analysis which uses provided data to directly produce predictive outcomes. Recent works in this developing field have established important properties of Data-Driven solvers, accommodated noisy data sets and demonstrated both quasi-static and dynamic solutions within mechanics. This work reviews this initial progress and advances some of the many possible improvements and applications that might best advance the field. Possible method improvements discuss incorporation of data quality metrics, and adaptive data additions while new applications focus on multi-scale analysis and the need for public databases to support constitutive data collaboration.

1 Introduction

The computational sciences, as applied to physics and engineering problems, has always been about using data inputs to provide solution results. Most of the methodologies that have been developed since the dawn of modern numerical analysis in the 1950s has been preoccupied with discretizing space and time. Finite differences, finite elements, finite volumes, molecular dynamics and mesh free methods are all examples of different ways of calculating solution fields. The constitutive data that gives rise to these methods predictive validity is used to create models which are then embedded into the various solution methods. These models are designed to act as succinct summaries for, at times, complicated material responses for which summarization is a difficult task. Machine learning has been applied to automate this summarization process, but there remain real difficulties in using reduced forms to accurately reproduce complex phenomena. Primary among issues that restrict model quality is the need to characterize responses across regimes that are *data sparse*. In cases such as this, the foundation of the model lies upon summarization and various amounts of inference and intuition.

T. Kirchdoerfer · M. Ortiz (✉)
California Institute of Technology, 1200 E California Blvd, Pasadena,
CA 91125, USA
e-mail: ortiz@caltech.edu

As we transition into an era of data generation and collection, constitutive relations will come to be characterized by information sets that are *data rich* throughout the regimes of interest. In this new environment, where inference is no longer required, empirical summaries will be necessarily less rich than the data upon which they were based. In these circumstances, modeling then finds itself unable to take full advantage of the increasingly large data sets. Ultimately, the assumed properties of a model become a restriction on the ability of a calculation to converge to measured behavior. This lack of convergence then leads to unresolvable modeling errors which ultimately influence the quality of the solution field. The question then becomes how to move scientific computing beyond the modeling paradigm and have it operate directly on the supplied data sets. In its most general form, *Data Science* is the extraction of *knowledge* from large volumes of unstructured data [1–4]. It uses analytics, data management, statistics and machine learning to derive mathematical models for subsequent use in decision making. Data Science already provides classification methods capable of processing source data directly into query answers in non-STEM problems, but no analogous method exists to perform scientific calculations.

The present discussion is focused on recent [5, 6] and ongoing work in the development of a new scientific computational paradigm for Data Science known as *Data Driven Computing*. Previous works making use of Data Science in the service of scientific computing have focused on making use of traditional machine learning techniques to develop models for predicting new material properties, or generally automating the modeling process. Public materials databases also exist, but at present the contained data are themselves the parameterized outcomes of modeling processes. Data Driven Computing instead reformulates initial-boundary-value problems around data associations defined at integration points within the discretized domain. As a result, constitutive relations are explicitly defined by the source data associations. Material modelling empiricism, error and uncertainty are then eliminated entirely with no loss of constitutive information. Initial work on the subject [5] developed a distance-minimizing scheme which converges for sequences of uniformly convergent data sets. Quasistatic simulations then acted as the primary demonstration case for Data-Driven material distance minimization. Subsequent work on the subject [6] has made use of a max-ent based clustering argument to thermalize the method within the context of an annealing schedule making it more robust to outliers. Beyond the improvement of quasistatic response for noisy data sets, this thermalized extension proves especially valuable in the multi-step evolution of dynamics calculations.

These beginning stages of development for Data Driven Computing demonstrate new possibilities for a young paradigm of computational science. Within mechanics these new methods offer not just the potential to provide powerful scale-linking capacity to multi-scale analysis. Data Driven solvers move constitutive data away from being a loose substrate upon which analysis resides, into becoming a core constituent of the analytical process. This process provides the techniques new forms of causality and convergence that will make their use foundational to any number of new strategies and foci of modeling.

2 State-of-the-art and Difference with Previous Work

It is important to frame Data-Driven Computing within the context of past and present efforts to automate and strengthen the connection between data and science. It is also particularly important to recognize the unique aspects of Data-Driven Computing and how it differs from other efforts.

2.1 Material Informatics

There has been extensive previous work focusing on the application of Data Science and Analytics to material data sets. The field of Material Informatics [7–24] uses data searching and sorting techniques to survey large material data sets. It also uses machine-learning regression [25, 26] and other techniques to identify patterns and correlations in the data for purposes of combinatorial materials design and selection. These approaches represent, at best, an application of standard sorting and statistical methods to material data sets, and, at worst, little more than numerology. While efficient at looking up and sifting through large data sets, it is questionable that any real epistemic knowledge is generated by these methods. What is missing in Material Informatics is a direct use—and solution of—the field equations of physics as a means of constraining and ascertaining material behaviour. By way of contrast, such field equations play a prominent role in Data-Driven Computing and make the approach *predictive*, and not just *postdictive*.

2.2 Material Identification

There has also been extensive previous work concerned with the use of empirical data for parameter identification in prespecified material models, or for automating the calibration of the models. For instance, the Error-in-Constitutive-Equations (ECE) method is an inverse method for the identification of material parameters such as the Young’s modulus of an elastic material [27–38]. While such approaches are efficient and reliable for their intended application, namely, the identification of material parameters, they are radically different from Data-Driven Computing: Material identification schemes aim to determine the parameters of a prespecified material law from experimental data; Data-Driven Computing dispenses with material models altogether and uses material data directly in the formulation of initial-boundary-value problems and attendant calculations thereof. In particular, in Data-Driven Computing no a priori assumptions are made regarding material behaviour and the material data that is generated and used is *fundamental, unbiased and model-independent*.

2.3 Data Repositories

A number of repositories are presently in existence aimed at data-basing and disseminating material property data, e.g., [39–42]. Some of these repositories receive extensive support from governmental agencies and other sources. However, it is important to note that the existing material data repositories archive parametric data that are specific to prespecified material models, which considerably limits their value and usefulness and puts them at variance with Data-Driven Computing. For instance, OpenKIM [42] provides parametrizations of standard interatomic potentials, such as the embedded-atom method (EAM), for a wide range of materials systems. Evidently, such data is strongly biased by the assumption of a specific form of the interatomic potential. By way of sharp contrast, Data-Driven Computing supports the development of data repositories that store fundamental, unbiased, model-independent material data only. Thus, suppose that the field equations of interest are the equations of molecular dynamics. In this case, the fundamental fields are the particle position and force fields, and the local states consist of atomic positions and corresponding forces over local clusters of atoms. It thus follows that, in this case, model-free unbiased data takes the form of local atomic positions and forces, determined, e.g., by means of first-principles quantum-mechanical calculations. For more complex mesoscopic systems, the role of mathematical analysis in determining what constitutes fundamental and unbiased material data—and what unit-cell problem determines the data—is of the essence.

In summary, the Data-Driven Computing paradigm is unique in that it entirely bypasses any reference to preconceived empirical material models, i. e., it is *strictly model-free*, and incorporates directly—and without bias—into initial-boundary-value problems data that is *fundamental*, i. e., that ‘lives’ in the natural phase space of the governing field equations.

3 Data-Driven Computing and Distance Minimizing Solutions

A main task of scientific calculations is to resolve coupled field responses to boundary conditions. Constitutive relationships then define the nature of coupling between the related fields. The language here restricts itself to mechanics, but mechanics is itself a special case of potential field theory through which electrostatics, diffusion and others present a similar need for constitutive definitions. Continuing within mechanics, the relations of interest are the extensive kinematic and kinetic work conjugate fields, e.g. ε and σ . Individually these fields must satisfy *material independent* properties with strong constraints. Kinematic fields must satisfy compatibility, while kinetic fields conserve momentum to be consistent with known physical laws. The certainty with which such field constraints can be asserted stands in stark contrast to the *material dependent* constitutive model which typically relates the two fields.

Such models must be informed by supplied data, whose summarization into a model is typically performed using ad-hoc empirical fits. These fits, while providing speed and the opportunity for the introduction of intuition and inference, simultaneously introduce a modeling error that influences computational conclusions in way which are hard to characterize.

To move beyond modeling, we now focus on the material data sets upon which such a models are based. This data E exists as a finite point set in phase space Z , where an example from small deformation mechanics would express the set as

$$E = ((\varepsilon_i, \sigma_i), i = 1, \dots, N).$$

The discrete nature of the set would naturally confound constitutive strategies which rely upon making use of a characterized function form. If compatibility, equilibrium, and boundary conditions are represented by the constraint set C , a problem arises in the likely case where the combined constraints cannot be satisfied by couplings defined by the discrete data set, thus $E \cap C$ returns an empty set. What is sought then is a relaxation which continues to satisfy all the members of C while minimizing deviations from E through direct data references.

In exploring the need for a constitutive relaxation, it is helpful to first recall how constitutive relationships are affected in spacial discretization schemes. For any fixed domain, the fields are directly sampled for enforcement at the integration points X . This sampling, later written as $z \in C$, is more fully expressed as

$$z(x_i) = (\varepsilon(x_i), \sigma(x_i)),$$

where

$$X = (x_i, i = 1, \dots, m),$$

$z \in Z$, and the constraint set C is satisfied, can imply that each of the fields is free to vary away from these points. As a result, since direct data associations $y \in E$ are discrete, it then suggests associations must be specific to integration points. This separation of the field values and data associations provides an elegant basis from which to formulate relaxed constitutive data methodologies.

Moving beyond the generalities of relaxation, the question becomes how to relate $z \in C$ and $y \in E$ to best reflect E as a constitutive description. The simplest demonstration of Data Driven Computing (DDC) [5] identifies its measure of deviation as the distance between z and y in a defined metric space, $d(z, y)$. Thus is defined the equivalent minimization problems

$$\min_{z \in C} \min_{y \in E} d(z, y) = \min_{y \in E} \min_{z \in C} d(z, y).$$

This formulation then defines an optimal solution which would provide the field values z satisfying constraints C , and the data associations y in the material set E .

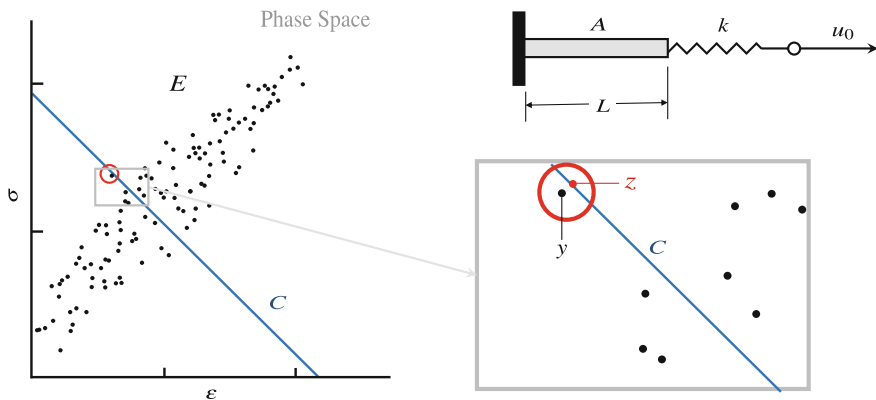


Fig. 1 Bar loaded by soft device. The line C is the constraint set consistent the applied displacement u_0 . The material data set is the point set E . The distance minimizing, Data-Driven solution is the red-encircled point y and projection z which generate the smallest distance in the phase space

The Data-Driven Computing scheme just outlined is illustrated in Fig. 1 by means of the elementary example of a uniformly-deformed bar deforming under the action of a loading device of known behavior. As discussed, the constraint set C and the material data set E have an empty intersection. Through the selection of a relaxed minimization criteria, an ideal solution can be identified without the crutch of an assumed constitutive form. Beyond the need for solution results to be processed directly from a material data set, a Data-Driven method needs to also be capable of exhibiting data-convergence. Such convergence is shown for a sequence of data sets E_i with corresponding size n_i , where $n_{i-1} > n_i$ if the solution converges as $i \rightarrow \infty$. For example, the constraint set and data set shown in Fig. 1 make it apparent that under a distance minimizing scheme, data-convergence would be achieved if the data sets converge to a graph in phase space. Data-convergence demonstrations are required for the verification of a given method, arising out of the need for a given solution to reflect intrinsic features of the data, *should they exist*. The set of sequence properties for which a Data-Driven method data-converges then defines an important characteristic of the given method. Depending on the data set to be analyzed, understanding these method properties could aid in the selection of the proper Data-Driven solution methodology.

4 Quasistatic Problems

As a way to demonstrate the viability of distance minimizing Data-Driven computation, initial work focused on quasistatic test cases [5]. Among the two explored test cases, the most thorough of these initial explorations targeted a small deformation, hyperelastic truss with 1048 degrees of freedom and a mix of specified boundary

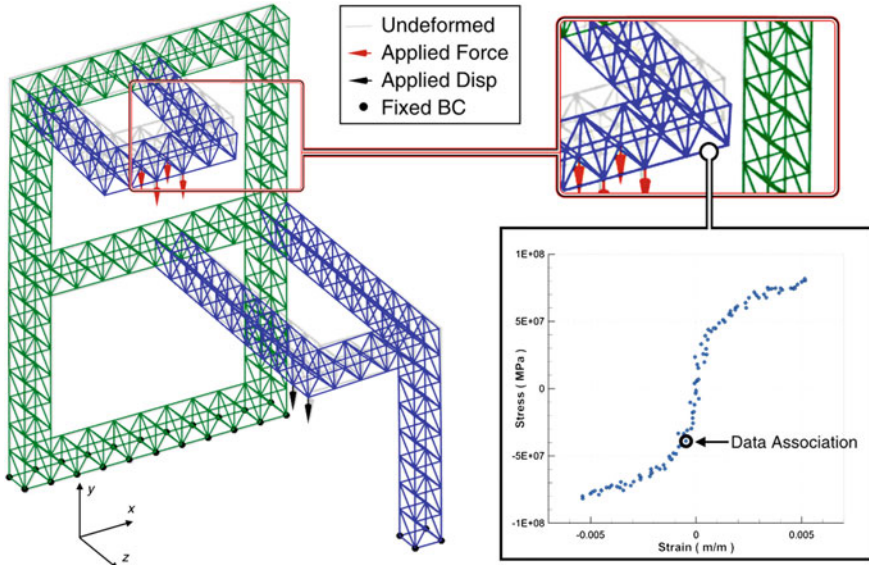


Fig. 2 Static equilibrium of a three-dimensional truss in which the behavior of the material is known only through the data set shown

conditions. Figure 2 shows the structure with magnified deformation effects generated from the material data shown on the right. The diagram illustrates both how the constitutive relation of the bar is defined by a data set, and the specific nature of a data association. The distance function that defines the metric space for a stress-strain (σ, ϵ) phase space can be expressed as

$$d^2(z_1, z_2) = \frac{E}{2}(\epsilon_2 - \epsilon_1)^2 + \frac{1}{2E}(\sigma_2 - \sigma_1)^2$$

where $z = (\epsilon, \sigma)$ and E is a selected weighting modulus. The full optimization problem then becomes

$$\min_{z^{dat} \in E} \min \left(\sum_{e=1}^n w_e \left(\frac{E}{2} (B_e u - \epsilon_e^{dat})^2 + \frac{1}{2E} (\sigma_e - \sigma_e^{dat})^2 \right) - \mu^T \left(\sum_{e=1}^n w_e B_e^T \sigma_e - f \right) \right)$$

where substitution is used to enforce compatibility $(\epsilon = Bu)$ and equilibrium is imposed using Lagrange multipliers (μ) in the final term. This ordering of the function minimums represents the solution as one that minimizes the distance between the data association set and its projection onto the constraint set. Since the expression of all possible data associations includes all permutations of the bar-wise data assignments, the method cannot rigorously explore the entire material data space. Instead a

fixed point iteration scheme is formulated to create a series of reductions in the minimizing function. This scheme, starting with an arbitrary assignment, projects the association set onto the constraint set. The projected solution is then used to perform a nearest neighbor search for new data associations. This scheme then terminates when all the data selections represent the closest point to their own projection.

Implementations of this method [5] include demonstrations with sufficient size and complexity (e.g., Fig. 2) to show the viability of the method beyond the confines of simple examples. Numerical demonstrations of distance minimizing Data-Driven calculations are seen to exhibit data-convergence when the data sets uniformly converge to a graph in the metric space. Solution costs are reasonable regarding both speed and complexity, while the material data set size most strongly impacts the computational expense of the described method. These initial demonstrations of efficacy opened the door to the development of other Data-Driven solvers as well as application of the method to new mechanics problems.

5 Extensions to Data Sets with Persistent Noise

Initial work on Data-Driven computing focused primarily on establishing and demonstrating of a new class of Data-Driven solvers [5]. The distance-minimizing data solver discussed previously stands as an excellent vehicle for the exposition of this new class of methods, due in large part to the elegant simplicity of the distance-minimizing form. However, such solvers exhibit data-convergence for noisy sets only if the sequence of data sets converges to a graph in the phase space. The problem is adequately described by imagining what would happen to the data scenario pictured in Fig. 1 if the data, instead of collapsing to a line, sees additions to the visualized set which are consistent with the pictured scatter. The points which best satisfy the constraint C would “hop” to a new point whenever one of the newly added points more closely approximates the constraint. Leaving aside the possibility of some distance ideal solution, $E \cap C$, this process would continue indefinitely, thus preventing the convergence to a final solution. The need to accommodate a finite band of data obviates the need for a *probabilistic* solution strategy which arbitrates on the relevance and importance of different data points based on proximity. Distance-minimizing Data-Driven solvers are incapable of data-convergence for banded data sets because they seek a single data member of E which most closely approximates the constraint set C . *Cluster analysis* provides a means of incorporating the influence of data neighborhoods to allow data-convergence in the presence of deeper samplings of fixed distributions.

Data-Driven solvers for noisy data have been developed which employ cluster analysis so as to make a new kind of data driven solvers robust to outliers and is well suited to data sources with finite data bands [6]. The foundations of cluster analysis have their roots in concepts provided by Information Theory, such as *maximum-entropy* estimation [43]. Specifically, we wish to quantify how well a point z in phase space is represented by a point z_i in a material data set $E = (z_1, \dots, z_n)$. Equivalently,

we wish to quantify the *relevance* of a point z_i in the material data set to a given point z in phase space. We measure the relevance of points z_i in the material data set by means of *weights* $p_i \in [0, 1]$ with the property: $\sum_{i=1}^n p_i = 1$. We wish the ranking by relevance of the material data points to be *unbiased*. It is known from Information Theory that the most unbiased distribution of weights is that which maximizes *Shannon's information entropy* [44–46]. In addition, we wish to accord points distant from z less weight than nearby points. These competing objectives can be combined by introducing a Pareto weight $\beta \geq 0$. The optimal and least-biased distribution is given by the Boltzmann distribution [46, 47]:

$$p_i = \frac{1}{Z} \exp(-\beta d^2(z, z_i)), \quad Z = \sum_{i=1}^n \exp(-d^2(z, z_i))$$

where the corresponding *max-ent* Data-Driven solver now consists of minimizing the free energy $F(z) = -\log Z/\beta$ over the constraint set C . Making use of fixed point iteration, the method uses a field solution z to weight the summed data associations, which are then projected onto C to generate an updated field solution for z . We note that because both methods use the same projection, the distance-minimizing Data-Driven scheme is recovered in the limit of $\beta \rightarrow \infty$. For finite β , all points in the material data set influence the solution, but their corresponding weights diminish with distance to the trial solution z . The clustering scheme just described is in analogy to information-theoretical methods for reconstructing geometrical objects and functions from point data sets [47, 48].

Since the Pareto weight β is not based on any physical or data parameter, an annealing schedule is used to remove any direct solution dependency. The schedule is initialized with β chosen to provide a convex free energy after which the method proceeds to raise β via a sequence of contracting local convexity estimates. A free parameter λ is introduced to control the speed of annealing, where solutions for a fixed data set converge under reductions to the annealing rate at significant increases to computational cost. Figure 3a shows the data selections made by the distance-minimizing method to solve the truss shown in Fig. 2 from the pictured data set. In comparison, Fig. 3b presents how the process of annealed data clustering produces selections along the center of the distribution for the same data set. Demonstrations of maximum entropy methods on the pictured static truss showed the method to data-converge faster than the equivalent distance-minimizing solver for banded data converging to a graph. Additionally, the entropy maximizing method was also numerically shown to data-converge for material data sets sampled from a fixed, finitely banded, probability distribution in the phase space [6]. While the demonstrations were computationally expensive, little effort was invested in computational efficiency and there exist several simple strategies that would greatly improve the algorithm performance. The new solver represents a significant extension of Data-Driven Computing to a much broader class of possible data problems.

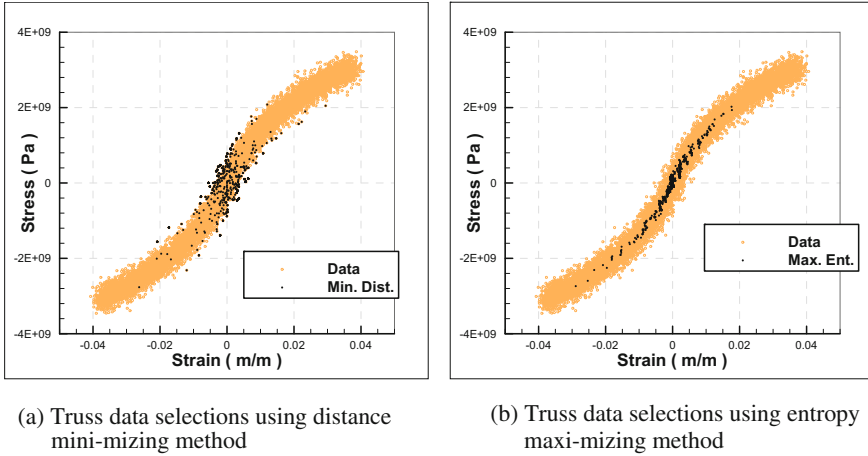
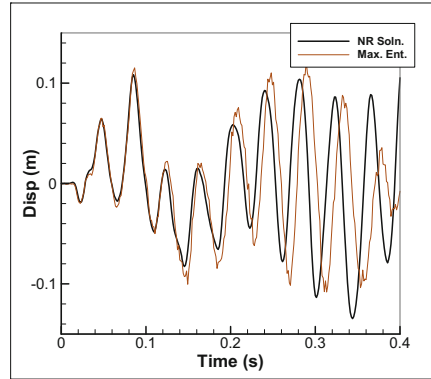


Fig. 3 Minimum-distance and maximum-entropy Data-Driven solvers point selections for a noisy 10,000 point data set

6 Dynamic Problems

The dynamic extension of the static Data-Driven solvers only requires substituting a discretized momentum balance for the static equilibrium equation used previously. Stationarity, instead of providing two uncoupled linear systems for u and μ , provides two linear systems which are coupled in both variables. It has been found that, with limited modification, both discussed methods admit the dynamic equilibrium constraints without issue. Numerical tests to date have shown convergence metrics which are consistent with previous [5, 6] performance assessments. Entropy-maximizing solvers provide better results in the presence of noisy data sets, the compounding error of multi-step solutions drives their solutions to dynamics calculations to be essential in the presence of a finitely banded data. To create a dynamics test case, the quasi-static case from Fig. 2 was modified to include an oscillating base with no external force or displacement conditions. Making use of the data sets shown in Fig. 3, the deflection u_x at one of the former force application points was recorded. Figure 4 plots that deflection over 10 base oscillations compared to the results of a traditional non-linear implicit dynamics solver solution which made direct use of the model about which the pictured data was centered. Given the significant scatter of the input data, results show a remarkable correlation between the Data-Driven and reference solutions.

Fig. 4 Dynamic x displacement response of top of a base-excited truss based on noisy constitutive data



7 Method Extensions to Data-Driven Computing

A number of extensions to Data-Driven solvers can be devised with a view to incorporating new kinds of data and data sources. The most direct addition is to handle data with descriptive confidence metrics, here these act as a natural outgrowth of clustered annealing solvers. The other interesting improvement would be to incorporate intermediate Data-Driven results to drive improved material response sampling.

7.1 Data Quality, Error Bounds, Confidence

In general, it is important to keep careful record of the pedigree, or ancestry, of each data point and to devise metrics for quantifying the level of confidence that can be placed on the data [49]. The confidence level in a material data point z_i can be quantified by means of a confidence factor $c_i \in [0, 1]$, with $c_i = 0$ denoting no confidence and $c_i = 1$ denoting full confidence. The weighting of the data points can then be modified to

$$p_i = \frac{c_i}{Z} \exp(-d^2(z, z_i)), \quad Z = \sum_{i=1}^n c_i \exp(-d^2(z, z_i)),$$

which effectively factors the confidence factors into the calculations. In addition, material data obtained through experimental measurements often comes with error bounds attached. The standard error of a measurement of mean z_i is normally identified with its standard deviation s_i . In such cases, assuming the distribution of measurements to be Gaussian we obtain the distribution of weights:

$$p_i = \frac{1}{Z} \exp\left(\frac{-d^2(z, z_i)}{2s_i^2 + 1/\beta}\right), \quad Z = \sum_{i=1}^n \exp\left(\frac{-d^2(z, z_i)}{2s_i^2 + 1/\beta}\right).$$

These simple analytical devices effectively factors the experimental error bounds and quality estimates directly into Data-Driven solvers.

7.2 Data Coverage, Sampling Quality, Adaptivity

Data-Driven solvers have the capacity, not just to make use of supplied data, but also suggest what additional data would be most useful in improving a characterized response. Recall that in general $z \in C$ represents a sampling of the Data-Driven field value and $y \in E$ corresponds to data associations specific to the integration points. Solutions to Data-Driven problems then naturally supply solutions z_e and y_e at each of the integration points e . The distance $d_e(z_e, E_e)$ then supplies a natural measure of how well the local state z_e is represented within the local material data set E_e . For any given material data set, a certain spread in the values of $d_e(z_e, E_e)$ may be expected, indicating that certain local states in a solution are better sampled than others. Specifically, local states with no nearby data points result in high values of $d_e(z_e, E_e)$, indicative of poor coverage by the material data set. Thus, the analysis of the local values $d_e(z_e, E_e)$ of the distance function provides a means of improving material data sets adaptively for particular applications. Evidently, the optimal strategy is to target for further sampling the regions of phase space corresponding to the local states with highest values of $d_e(z_e, E_e)$. Local states lying far from the material data set become targets for further testing. In this manner, the material data set may be adaptively expanded to provide the best possible coverage for a particular application.

Some care in exercising the use of additional sampling in the presence of data clustering arguments would be required to prevent a targeting bias. More specifically, it is expected that the introduction of additional data would suggest a strategy of “reheating” a solution and resuming an annealing process. Since clustering arguments cause regions of the phase space with denser data sampling to be favored, any additional material sampling then needs to populate a region broader than the effective diameter of the reheated clustering argument. Despite these additional complications, the ability of a solver to provide specific suggestions for improving simulation accuracy is a fascinating outcome of Data-Driven computational strategies.

8 Data Mining and Multiscale Data-Driven Analysis

So far, we have assumed that a material data set is somehow available and provides a suitable basis for Data-Driven analysis. In general, the material data may origi-

nate from a variety of sources, including experimental sources, theoretical sources, first-principles calculations, and others. A particularly appealing possibility, which is highly synergistic with the Data-Driven Computing paradigm, is the use of *multiscale analysis* to generate material data, i.e., for purposes of *Data Mining*. Data-Driven Computing provides a unique foundation from which to couple the simulation scales due to its ability to directly link calculations through the determined material data associations. In effect, it lets the analysis zoom in directly on the subgrid phenomena that are causing local responses at a higher scale. Multiscale metal plasticity supplies a representative example of application of Data-Driven Computing, including the Data-Driven model-free formulation of molecular dynamics, dislocation dynamics, and crystal and polycrystal plasticity.

8.1 From Density Functional Theory to Molecular Dynamics

For metals, the foundational, or first-principles, theory is Quantum Mechanics, which characterizes the electronic structure at the subatomic level. At present, the prevailing quantum-mechanical theory is Density-Functional Theory (DFT), which relies on models of exchange-correlation and pseudopotentials to reduce the dimensionality of the problem. Force-field data mined from DFT calculations provides a suitable basis for Data-Driven Molecular-Dynamics (DDMD). The force-field space can be covered by means of *importance-sampling*, specifically by focusing on low-energy atomic configurations. Thus, whether from extensive observational evidence or from mathematical analysis [50–53], it is known that such low-energy configurations consist of: (i) affine deformations of a perfect lattice; (ii) short-range defects of dimension zero, such as vacancies and interstitials; (iii) short-range defects of dimension one, such as dislocations; and (iv) short-range defects of dimension two, including free surfaces and interfaces. The aim of the DFT-based Data Mining may thus be focused on the characterization of force fields representative of said low-energy configurations in specific metals such as Al (FCC), Fe (BCC) and Mg (HCP).

8.2 Data-Driven Molecular Dynamics

In using the force-field data for Data-Driven Molecular Dynamics, it becomes necessary to define a distance in the phase space of atomic clusters and forces. A convenient choice of distance is supplied by ‘lattice matching’ [54, 55]. This distance provides a means of matching local atomic configurations against the closest configuration in the data repository and retrieving the most relevant local force field. Again we emphasize that, whereas DFT calculations have been extensively used to ‘train’ specific interatomic potentials [56–62], the distinguishing characteristic of Data-Driven Molecular Dynamics is that the DFT data are used directly in mole-

cular dynamics calculations, without the intermediary of an empirical interatomic potential.

8.3 *From Molecular Dynamics to Dislocation Dynamics and Plasticity*

The passage from discrete-to-continuum descriptions can be effected in a number of ways, including the Quasicontinuum Method [63–66], phase-field models [51, 52, 67–74], and others. The resulting coarse-grained theory is Dislocation Dynamics (DD) in otherwise elastic crystals. In this coarse-grained theory, the relevant material laws are: (i) the dislocation mobility law, which relates the Peach-Koehler force to dislocation velocity; (ii) the core energy or line tension, which gives the core energy per unit length as a function of dislocation direction; and (iii) the elastic interaction forces between dislocation segments and between dislocation segments and applied stresses. Conveniently, these laws are accessible to Data-Driven Molecular Dynamics. In the case of the segment-segment elastic interaction law, the relevant phase spaces are too large to allow for uniform sampling and importance sampling must be performed instead. The interaction between distant segments can be characterized by recourse to linear elasticity [75], which restricts sampling requirements to dislocation interactions at close range. The important configurations to be sampled are low-energy configurations, specifically close-range dipoles, nodes, junctions, networks and walls [73, 76–80]. Finally, polycrystal plasticity data can be generated from Data-Driven single-crystal plasticity by means of standard and mathematically well-understood periodic representative-volume problems [81].

9 Publicly-Editable, Open Access Material Data Repository

As already emphasized, Data-Driven Computing makes use of fundamental, unbiased, model-independent data ‘living’ in phase spaces set forth directly by the field equations of the problem. Thus, for instance, Data-Driven Molecular Dynamics is formulated from data consisting of local atomic coordinates and corresponding forces, without reference to any particular interatomic potential and without any a priori assumptions on material behavior. This strict adherence to fundamental, unbiased and model-free data not only represents a novel and significant conceptual advance but also greatly facilitates material data sharing, collection and dissemination within the community.

Specifically, *publicly-editable repository* model accessible for use by—and to contributions from—the entire scientific community become an attractive possibility. Publicly-editable repositories have demonstrated a remarkable ability for organic decentralized growth and collaborative development. Perhaps the most notable of

all publicly-editable repositories is *Wikipedia* [82], the self-styled *free encyclopedia*, launched on January 15, 2001 by Jimmy Wales and Larry Sanger, which currently features over 38 million articles in more than 250 languages. As of February of 2014, *Wikipedia* had 18 billion views and 500 million unique visitors per month. *Wikipedia* forever changed the field of reference and displaced well-established and capitalized encyclopedias. What is truly remarkable about *Wikipedia*, and similar publicly-supported enterprises, is that it is free of cost, had no governmental support and grew collaboratively from anonymous contributions. *Wikipedia* was made possible by key technological advances, most notably, the internet and the development of mark-up languages, such as *Wiki*, specially designed for collaborative content modification; but it was also the result of a radically new way of thinking.

Data-Driven Computing has the potential for enabling—and ushering in—a similar paradigm shift and new thinking in science and engineering, a shift towards *collaborative development of material data repositories*. Thus, by insisting on fundamental, unbiased and model-free data, material data becomes *homogeneous* and *fungible*, and data sets of different extractions can be readily *integrated* and *fused* [83]. Data-Driven Computing also makes material data repositories relevant and useful by providing the analytical and algorithmic means of integrating material data sets directly into scientific analysis or computation.

10 Concluding Remarks

Data-Driven computation represents a new direction in computational analysis that seeds new growth in the fields of predictive science. Traditional modeling techniques have acted as a barrier between solutions and the data that provides them validity and accuracy. Removing this barrier means that detailed flows of causality can exist between data sources and computational solutions. Continuing to improve the ability to link data properties and simulation outcomes represents some of the most likely extensions of developed methods. With such flows being processed with improved strategies, the number of possible new applications for Data-Driven computation seem to be beyond summary.

Even restricting the domain to mechanics, the potential reach of these solution strategies touches on a common problem in a modern analysis, the need to resolve response at multiple scales. Here, we have discussed how materials science could see a revolution in predictive capacity, but also: structural analysis could directly integrate extremely localized phenomena and fluids simulations would have better ways of relating different flow scales. These capacities arise from our new abilities of numerical science to generate data, and once such data are created, there are few restrictions on their potential use. Thus, public databases might allow for new forms of collaboration and quicker advances within the communities that study diverse arrays of phenomena. The works summarized and suggested in this writing stand as features of a new landscape still largely unseen and unexperienced. As storage costs continue to fall and computational capacity becomes ever more ubiquitous, Data-

Driven Computing offers an expanding world of analytical capacity to science and engineering.

References

1. D. Agarwal, Y.W. Cheah, D. Fay, J. Fay, D. Guo, T. Hey, M. Humphrey, K. Jackson, J. Li, C. Poulain, Y. Ryu, C. van Ingen, Data-intensive science: the terapixel and modisazure projects. *Int. J. High Perform. Comput. Appl.* **25**(3), 304–316 (2011)
2. D.A. Agarwal, B. Faybishenko, V.L. Freedman, H. Krishnan, G. Kushner, C. Lansing, E. Porter, A. Romosan, A. Shoshani, H. Wainwright, A. Weidmer, K.S. Wu, A science data gateway for environmental management. *Concur. Comput. Pract. Exp.* **28**(7), 1994–2004 (2016)
3. R. Agarwal, V. Dhar, Big data, data science, and analytics: the opportunity and challenge for is research. *Inf. Syst. Res.* **25**(3), 443–448 (2014)
4. B. Baesens, *Analytics in a Big Data World : The Essential Guide to Data Science and its Applications* (Wiley & SAS business series. John Wiley & Sons Inc, Hoboken, New Jersey, 2014)
5. T. Kirchdoerfer, M. Ortiz, Data-driven computational mechanics. *Comput. Method Appl. Mech. Eng.* **304**, 81–101 (2016)
6. T. Kirchdoerfer, M. Ortiz, Data driven computing with noisy material data sets. Submitted for publication, Feb. 2017 ([arXiv:1702.01574](https://arxiv.org/abs/1702.01574) [physics.comp-ph])
7. C.M. Breneman, L.C. Brinson, L.S. Schadler, B. Natarajan, M. Krein, K. Wu, L. Morkowchuk, Y. Li, H. Deng, H.Y. Xu, Stalking the materials genome: a data-driven approach to the virtual design of nanostructured polymers. *Adv. Funct. Mat.* **23**(46), 5746–5752 (2013)
8. S. Broderick, K. Rajan, Informatics derived materials databases for multifunctional properties. *Sci. Technol. Adv. Mat.* **16**(1) (2015)
9. S. Broderick, C. Suh, J. Nowers, B. Vogel, S. Mallapragada, B. Narasimhan, K. Rajan, Informatics for combinatorial materials science. *Jom* **60**(3), 56–59 (2008)
10. G. Ceder, D. Morgan, C. Fischer, K. Tibbetts, S. Curtarolo, Data-mining-driven quantum mechanics for the prediction of structure. *Mrs Bulletin* **31**(12), 981–985 (2006)
11. S. Curtarolo, D. Morgan, K. Persson, J. Rodgers, G. Ceder, Predicting crystal structures with data mining of quantum calculations. *Phys. Rev. Lett.* **91**(13) (2003)
12. A. Gupta, A. Cecen, S. Goyal, A.K. Singh, S.R. Kalidindi, Structure-property linkages using a data science approach: application to a non-metallic inclusion/steel composite system. *Acta Materialia* **91**, 239–254 (2015)
13. S.R. Kalidindi, Data science and cyberinfrastructure: critical enablers for accelerated development of hierarchical materials. *Int. Mater. Rev.* **60**(3), 150–168 (2015)
14. S.R. Kalidindi, M. De Graef, Materials data science: current status and future outlook. *Annu. Rev. Mater. Res.* **45**(45), 171–193 (2015)
15. S.R. Kalidindi, J.A. Gombert, Z.T. Trautt, C.A. Becker, Application of data science tools to quantify and distinguish between structures and models in molecular dynamics datasets. *Nanotechnology* **26**(34) (2015)
16. S.R. Kalidindi, S.R. Niezgodza, A.A. Salem, Microstructure informatics using higher-order statistics and efficient data-mining protocols. *Jom* **63**(4), 34–41 (2011)
17. Z.K. Liu, L.Q. Chen, K. Rajan, Linking length scales via materials informatics. *Jom* **58**(11), 42–50 (2006)
18. D. Morgan, G. Ceder, S. Curtarolo, High-throughput and data mining with ab initio methods. *Meas. Sci. Technol.* **16**(1), 296–301 (2005)
19. K. Rajan, Materials informatics. *Mater. Today* **8**(10), 38–45 (2005)
20. K. Rajan, Materials informatics part i: a diversity of issues. *Jom* **60**(3), 50–50 (2008)
21. K. Rajan, Informatics and integrated computational materials engineering: part ii. *Jom* **61**(1), 47–47 (2009)

22. K. Rajan, Materials informatics how do we go about harnessing the “big data” paradigm? *Mater. Today* **15**(11), 470–470 (2012)
23. K. Rajan, Materials informatics: the materials “gene” and big data. *Annual Rev. Mater. Res.* **45**(45), 153–169 (2015)
24. K. Rajan, M. Zaki, K. Bennett, Informatics based design of materials. *Abstr. Pap. Am. Chem. Soc.* **221**, U464–U464 (2001)
25. C.M. Bishop, *Pattern Recognition and Machine Learning* (Information science and statistics. Springer, New York, 2006)
26. I. Steinwart, A. Christmann, *Support Vector Machines*, 1st edn. (Information science and statistics. Springer, New York, 2008)
27. M.A. Aguilo, L. Swiler, A. Urbina, An overview of inverse material identification within the frameworks of deterministic and stochastic parameter estimation. *Int. J. Uncertain. Quantif.* **3**(4), 289–319 (2013)
28. B. Banerjee, T.F. Walsh, W. Aquino, M. Bonnet, Large scale parameter estimation problems in frequency-domain elastodynamics using an error in constitutive equation functional. *Comput. Method. Appl. Mech. Eng.* **253**, 60–72 (2013)
29. M. Ben Azzouna, P. Feissel, P. Villon, Robust identification of elastic properties using the modified constitutive relation error. *Comput. Method. Appl. Mech. Eng.* **295**, 196–218 (2015)
30. M. Bonnet, W. Aquino, Three-dimensional transient elastodynamic inversion using the modified error in constitutive relation, in *4th International Workshop on New Computational Methods for Inverse Problems (NCMIP2014)* **542** (2014)
31. L. Chamoin, P. Ladeveze, J. Waeys, Goal-oriented updating of mechanical models using the adjoint framework. *Comput. Mech.* **54**(6), 1415–1430 (2014)
32. P. Feissel, O. Allix, Modified constitutive relation error identification strategy for transient dynamics with corrupted data: the elastic case. *Comput. Method. Appl. Mech. Eng.* **196**(13–16), 1968–1983 (2007)
33. S. Guchhait, B. Banerjee, Constitutive error based material parameter estimation procedure for hyperelastic material. *Comput. Method. Appl. Mech. Eng.* **297**, 455–475 (2015)
34. F. Latourte, A. Chrysochoos, S. Pagano, B. Wattrisse, Elastoplastic behavior identification for heterogeneous loadings and materials. *Exp. Mech.* **48**(4), 435–449 (2008)
35. T. Merzouki, H. Nouri, F. Roger, Direct identification of nonlinear damage behavior of composite materials using the constitutive equation gap method. *Int. J. Mech. Sci.* **89**, 487–499 (2014)
36. H.M. Nguyen, O. Allix, P. Feissel, A robust identification strategy for rate-dependent models in dynamics. *Inverse Probl.* **24**(6) (2008)
37. N. Promma, B. Raka, M. Grediac, E. Toussaint, J.B. Le Cam, X. Balandraud, F. Hild, Application of the virtual fields method to mechanical characterization of elastomeric materials. *Int. J. Solid Struct.* **46**(3–4), 698–715 (2009)
38. J.E. Warner, M.I. Diaz, W. Aquino, M. Bonnet, Inverse material identification in coupled acoustic-structure interaction using a modified error in constitutive equation functional. *Comput. Mech.* **54**(3), 645–659 (2014)
39. The materials project. <https://materialsproject.org/>
40. The NIST materials genome initiative. <https://mgi.nist.gov/materials-data-repository/>
41. The NoMaD repository. <http://nomad-repository.eu/cms/>
42. The knowledgebase of interatomic models. <https://openkim.org/>
43. A.I. Khinchin, *Mathematical Foundations of Information Theory*, New dover edn. (Dover Publications, New York, 1957)
44. C.E. Shannon, A mathematical theory of communication. *Bell Syst. Tech. J.* **27**(3), 379–423 (1948)
45. C.E. Shannon, A mathematical theory of communication. *Bell Syst. Tech. J.* **27**(4), 623–656 (1948)
46. C.E. Shannon, Communication theory of secrecy systems. *Bell Syst. Tech. J.* **28**(4), 656–715 (1949)

47. M. Arroyo, M. Ortiz, Local maximum-entropy approximation schemes: a seamless bridge between finite elements and meshfree methods. *Int. J. Num. Method Eng.* **65**(13), 2167–2202 (2006)
48. C.J. Cyron, M. Arroyo, M. Ortiz, Smooth, second order, non-negative meshfree approximants selected by maximum entropy. *Int. J. Num. Method Eng.* **79**(13), 1605–1632 (2009)
49. A.R. Newman, Confidence, pedigree, and security classification for improved data fusion, in *Proceedings of the Fifth International Conference on Information Fusion*, vol. II (2002), pp. 1408–1415
50. S. Conti, G. Dolzmann, B. Kirchheim, S. Muller, Sufficient conditions for the validity of the cauchy-born rule close to $so(n)$. *J. Eur. Math. Soc.* **8**(3), 515–530 (2006)
51. M. Flucher, A. Garroni, S. Muller, Concentration of low energy extremals: identification of concentration points. *Calc. Var. Partial Diff. Equ.* **14**(4), 483–516 (2002)
52. A. Garroni, S. Muller, Concentration phenomena for the volume functional in unbounded domains: identification of concentration points. *J. Func. Anal.* **199**(2), 386–410 (2003)
53. S. Luckhaus, L. Mugnai, On a mesoscopic many-body hamiltonian describing elastic shears and dislocations. *Continuum Mech. Thermodyn.* **22**(4), 251–290 (2010)
54. B. Runnels, I.J. Beyerlein, S. Conti, M. Ortiz, An analytical model of interfacial energy based on a lattice-matching interatomic energy. *J. Mech. Phys. Solid* **89**, 174–193 (2016)
55. B. Runnels, I.J. Beyerlein, S. Conti, M. Ortiz, A relaxation method for the energy and morphology of grain boundaries and interfaces. *J. Mech. Phys. Solid* **94**, 388–408 (2016)
56. S.Y. Kim, N. Kumar, P. Persson, J. Sofo, A.C.T. van Duin, J.D. Kubicki, Development of a reaxff reactive force field for titanium dioxide/water systems. *Langmuir* **29**(25), 7838–7846 (2013)
57. J.P. Larentzos, B.M. Rice, E.F.C. Byrd, N.S. Weingarten, J.V. Lill, Parameterizing complex reactive force fields using multiple objective evolutionary strategies (moes). part 1: Reaxff models for cyclotrimethylene trinitramine (rdx) and 1,1-diamino-2,2-dinitroethene (fox-7). *J. Chem. Theory Comput.* **11**(2), 381–391 (2015)
58. J. Ludwig, D.G. Vlachos, A.C.T. van Duin, W.A. Goddard, Dynamics of the dissociation of hydrogen on stepped platinum surfaces using the reaxff reactive force field. *J. Phys. Chem. B* **110**(9), 4274–4282 (2006)
59. G. Psofogiannakis, A.C.T. van Duin, Development of a reaxff reactive force field for si/ge/h systems and application to atomic hydrogen bombardment of si, ge, and sige (100) surfaces. *Surf. Sci.* **646**, 253–260 (2016)
60. O. Rahaman, A.C.T. van Duin, V.S. Bryantsev, J.E. Mueller, S.D. Solares, W.A. Goddard, D.J. Doren, Development of a reaxff reactive force field for aqueous chloride and copper chloride. *J. Phys. Chem. A* **114**(10), 3556–3568 (2010)
61. W.X. Song, S.J. Zhao, Development of the reaxff reactive force field for aluminum-molybdenum alloy. *J. Mater. Res.* **28**(9), 1155–1164 (2013)
62. B. Zhang, A.C.T. van Duin, J.K. Johnson, Development of a reaxff reactive force field for tetrabutylphosphonium glycinate/ CO_2 mixtures. *J. Phys. Chem. B* **118**(41), 12008–12016 (2014)
63. M.I. Espanol, D.M. Kochmann, S. Conti, M. Ortiz, A gamma-convergence analysis of the quasicontinuum method. *Multiscale Model. Simul.* **11**(3), 766–794 (2013)
64. J. Knap, M. Ortiz, An analysis of the quasicontinuum method. *J. Mech. Phys. Solid* **49**(9), 1899–1923 (2001)
65. E.B. Tadmor, M. Ortiz, R. Phillips, Quasicontinuum analysis of defects in solids. *Philos. Mag. A* **73**(6), 1529–1563 (1996) (Physics of Condensed Matter Structure Defects and Mechanical Properties)
66. E.B. Tadmor, R. Phillips, M. Ortiz, Mixed atomistic and continuum models of deformation in solids. *Langmuir* **12**(19), 4529–4534 (1996)
67. A.S. Argon, G. Xu, M. Ortiz, Kinetics of dislocation emission from crack tips and the brittle to ductile transition of cleavage fracture. *Fract. Instab. Dyn. Scaling Ductile/Brittle Beh.* **409**, 29–44
68. A.S. Argon, G. Xu, M. Ortiz, Kinetics of the crack-tip-governed brittle to ductile transitions in intrinsically brittle solids. *Cleavage Fract.* 125–135

69. S. Conti, A. Garroni, S. Muller, Singular kernels, multiscale decomposition of microstructure, and dislocation models. *Arch. Ration. Mech. Anal.* **199**(3), 779–819 (2011)
70. A. Garroni, S. Muller, Gamma-limit of a phase-field model of dislocations. *Siam J. Math. Anal.* **36**(6), 1943–1964 (2005)
71. A. Garroni, S. Muller, A variational model for dislocations in the line tension limit. *Arch. Ration. Mech. Anal.* **181**(3), 535–578 (2006)
72. M. Koslowski, A.M. Cuitino, M. Ortiz, A phase-field theory of dislocation dynamics, strain hardening and hysteresis in ductile single crystals. *J. Mech. Phys. Solid* **50**(12), 2597–2635 (2002)
73. M. Koslowski, M. Ortiz, A multi-phase field model of planar dislocation networks. *Model. Simul. Mater. Sci. Eng.* **12**(6), 1087–1097 (2004)
74. G. Xu, A.S. Argon, M. Ortiz, Nucleation of dislocations from crack tips under mixed-modes of loading—implications for brittle against ductile behavior of crystals. *Philos. Mag. A* **72**(2), 415–451 (1995) (*Physics of Condensed Matter Structure Defects and Mechanical Properties*)
75. J.P. Hirth, J. Lothe, *Theory of Dislocations*, 2nd edn. (Wiley, New York, 1982)
76. V.V. Bulatov, W. Cai, Nodal effects in dislocation mobility. *Phys. Rev. Lett.* **89**(11) (2002)
77. V.V. Bulatov, L.L. Hsiung, M. Tang, A. Arsenlis, M.C. Bartelt, W. Cai, J.N. Florando, M. Hiratani, M. Rhee, G. Hommes, T.G. Pierce, T.D. de la Rubia, Dislocation multi-junctions and strain hardening. *Nature* **440**(7088), 1174–1178 (2006)
78. S. Conti, M. Ortiz, Dislocation microstructures and the effective behavior of single crystals. *Arch. Ration. Mech. Anal.* **176**(1), 103–147 (2005)
79. T. Hochrainer, S. Sandfeld, M. Zaiser, P. Gumbsch, Continuum dislocation dynamics: towards a physical theory of crystal plasticity. *J. Mech. Phys. Solid* **63**, 167–178 (2014)
80. D. Weygand, J. Senger, C. Motz, W. Augustin, V. Heuveline, P. Gumbsch, High performance computing and discrete dislocation dynamics: Plasticity of micrometer sized specimens. *High Perform. Comput. Sci. Eng.* '08 507–523 (2009)
81. G. Dal Maso, An Introduction to Γ -convergence, in *Progress in nonlinear differential equations and their applications* (Birkhauser, Boston, MA, 1993)
82. Wikipedia. <https://en.wikipedia.org/wiki/Wikipedia>
83. A. Azevedo, M.F. Santos, *Integration of Data Mining in Business Intelligence Systems* (Business Science Reference, Hershey, 2015)

Elasto-Plastic Response of Thick Plates Built in Functionally Graded Material Using the Third Order Plate Theory

Michał Kleiber, Maciej Taczała and Ryszard Buczkowski

Abstract We present an application of the third-order plate theory for investigation of the elasto-plastic response of thick plates made of functionally graded material. The theory was originally developed by Reddy and Kim [1]. In their formulation they expanded the in-plane displacements up to the cubic term and the transverse displacement up to the quadratic term with respect to the coordinate perpendicular to the plate surface, obtaining a quadratic variation of the transverse shear strains through the plate thickness. FGM properties are modelled following the power law distribution of constituent ratio across the thickness. The plates are modelled using a 16-noded lagrangian elements using Lobatto integration rules. The problem is solved using Newton-Raphson method applying modified Crisfield constant arc-length procedure. Numerical examples are provided to illustrate the advantages of the method proposed.

1 Introduction

Functionally graded materials (FGMs) are a new class of composite materials known for over two decades and receiving a well-deserved attention [2–4]. FGMs are composed of ceramics and metals, with components distributed so that external ceramic layers, exposed to high temperatures, protect internal metallic functions. The most important problem here is the reduction of thermal stresses due to very

M. Kleiber (✉)

Institute of Fundamental Technological Research, Polish Academy of Sciences,
Pawinskiego 5B, 02-106 Warsaw, Poland
e-mail: mkleiber@ippt.pan.pl

M. Taczała · R. Buczkowski

Faculty of Maritime Technology and Transport, West Pomeranian University
of Technology, Szczecin, Piastow 41, 71-065 Szczecin, Poland
e-mail: maciej.taczała@zut.edu.pl

R. Buczkowski

e-mail: rbuczkowski@ps.pl

high temperatures and substantial differences of component thermal expansion coefficients. Numerous FGM applications include medicine (orthopedic resorption controllable implants with highly useful mechanical properties, lens, bioceramic materials, porous ceramics, bioactive ceramics, resorptive ceramics, biostable bonding materials), machine industry (cutting tools, toothed wheels or turbine blades) and power industry (jet engine chambers, functionally graded components of fuel cells, thermonuclear power generation—thermal barrier protection), electronics industry (heat sensors, piezoelectric activators, optical fibres).

In relation to the analytical and numerical calculations of the FGM beams, plates and shells the interested readers are referred to the works of Reddy and his co-workers, see for example [5–7].

Here, we present an application of the third-order plate theory for investigation of the elasto-plastic response of thick plates made of functionally graded material. We based our analysis on a theory originally developed by Reddy and Kim [1]. A 16-node isoparametric Mindlin plate finite element of the Lagrange family using Lobatto integration scheme which does not exhibit shear locking phenomena, was used as developed by the authors [8].

2 Mathematical Formulation

Nonlinear finite element equations in the incremental formulation will be derived using the principle of virtual work. The virtual work of internal forces $\delta^{t+\Delta t} W_{ext}$ for increment $t + \Delta t$ and iteration $i + 1$ equals the virtual work of internal forces $\delta^{t+\Delta t} W_{int}$:

$$\delta^{t+\Delta t} W_{int} = \delta^{t+\Delta t} W_{ext} \quad (1)$$

The virtual work of external forces is the sum of body forces $\{^{t+\Delta t} b_i\}$ and distributed loading $\{^{t+\Delta t} p_i\}$ acting on virtual displacements $\{\delta^{t+\Delta t} u_i\}$:

$$\delta^{t+\Delta t} W_{ext} = \int_V ^{t+\Delta t} b_i \delta^{t+\Delta t} u_i dV + \int_\Omega ^{t+\Delta t} p_i \delta^{t+\Delta t} u_i d\Omega \quad (2)$$

Virtual work of internal forces (2nd Piola-Kirchhoff stresses) $\delta^{t+\Delta t} W_{int}$ is:

$$\delta^{t+\Delta t} W_{int} = \int_V ^{t+\Delta t} S_i \delta^{t+\Delta t} \Delta E_i dV \quad (3)$$

Assuming large displacements, increments of Green-Lagrange strains $\{\delta^{t+\Delta t} \Delta E_i\}$ in the present formulation are derived using equations defining displacements of arbitrary point of the plate according to the third-order shear

deformation theory proposed by Reddy and Kim, referred here as “A general third-order theory with tangential traction free surfaces” [1, 9, 10]:

$$\begin{aligned}
 {}^{t+\Delta t}_i u &= {}^{t+\Delta t}_i u_m + z {}^{t+\Delta t}_i v_x + z^2 {}^{t+\Delta t}_i \varphi_x + z^3 {}^{t+\Delta t}_i \psi_x \\
 {}^{t+\Delta t}_i v &= {}^{t+\Delta t}_i v_m + z {}^{t+\Delta t}_i v_y + z^2 {}^{t+\Delta t}_i \varphi_y + z^3 {}^{t+\Delta t}_i \psi_y \\
 {}^{t+\Delta t}_i w &= {}^{t+\Delta t}_i w_m + z {}^{t+\Delta t}_i v_z + z^2 {}^{t+\Delta t}_i \varphi_z
 \end{aligned} \tag{4}$$

The assumed displacement field allows for quadratic variation of transverse shear strains and inextensibility of the transverse normal lines. Displacement functions are then modified in a way which makes the transverse shear stresses be equal to zero on the top and bottom of the plate for $z = \pm t/2$, similarly as in the formulation of the Reddy third-order theory. This conditions, expressed in terms of the strains, takes the form

$$\begin{aligned}
 {}^{t+\Delta t}_i w_{m,x} + {}^{t+\Delta t}_i v_x + z({}^{t+\Delta t}_i v_{z,x} + 2 {}^{t+\Delta t}_i \varphi_x) + z^2({}^{t+\Delta t}_i \varphi_{z,x} + 3 {}^{t+\Delta t}_i \psi_x) &= 0 \\
 {}^{t+\Delta t}_i w_{m,y} + {}^{t+\Delta t}_i v_y + z({}^{t+\Delta t}_i v_{z,y} + 2 {}^{t+\Delta t}_i \varphi_y) + z^2({}^{t+\Delta t}_i \varphi_{z,y} + 3 {}^{t+\Delta t}_i \psi_y) &= 0
 \end{aligned} \tag{5}$$

We note that in Eq. 5 it is only the linear part of the shear strain which is taken to derive the equation relating some displacement functions and their derivatives

$$\begin{aligned}
 {}^{t+\Delta t}_i w_{m,x} + {}^{t+\Delta t}_i v_x + \frac{1}{2} t {}^{t+\Delta t}_i v_{z,x} + t {}^{t+\Delta t}_i \varphi_x + \frac{1}{4} t^2 {}^{t+\Delta t}_i \varphi_{z,x} + \frac{3}{4} t^2 {}^{t+\Delta t}_i \psi_x &= 0 \\
 {}^{t+\Delta t}_i w_{m,x} + {}^{t+\Delta t}_i v_x - \frac{1}{2} t {}^{t+\Delta t}_i v_{z,x} - t {}^{t+\Delta t}_i \varphi_x + \frac{1}{4} t^2 {}^{t+\Delta t}_i \varphi_{z,x} + \frac{3}{4} t^2 {}^{t+\Delta t}_i \psi_x &= 0 \\
 {}^{t+\Delta t}_i w_{m,y} + {}^{t+\Delta t}_i v_y + \frac{1}{2} t {}^{t+\Delta t}_i v_{z,y} + t {}^{t+\Delta t}_i \varphi_y + \frac{1}{4} t^2 {}^{t+\Delta t}_i \varphi_{z,y} + \frac{3}{4} t^2 {}^{t+\Delta t}_i \psi_y &= 0 \\
 {}^{t+\Delta t}_i w_{m,y} + {}^{t+\Delta t}_i v_y - \frac{1}{2} t {}^{t+\Delta t}_i v_{z,y} - t {}^{t+\Delta t}_i \varphi_y + \frac{1}{4} t^2 {}^{t+\Delta t}_i \varphi_{z,y} + \frac{3}{4} t^2 {}^{t+\Delta t}_i \psi_y &= 0
 \end{aligned} \tag{6}$$

From these equations we obtain the following relationships relating some of the displacement functions and their derivatives:

$$\begin{aligned}
 {}^{t+\Delta t}_i \psi_x &= -\frac{4}{3t^2} {}^{t+\Delta t}_i v_x - \frac{4}{3t^2} {}^{t+\Delta t}_i w_{m,x} - \frac{1}{3} {}^{t+\Delta t}_i \varphi_{z,x} \\
 {}^{t+\Delta t}_i \varphi_x &= -\frac{1}{2} {}^{t+\Delta t}_i v_{z,x} \\
 {}^{t+\Delta t}_i \psi_y &= -\frac{4}{3t^2} {}^{t+\Delta t}_i v_y - \frac{4}{3t^2} {}^{t+\Delta t}_i w_{m,y} - \frac{1}{3} {}^{t+\Delta t}_i \varphi_{z,y} \\
 {}^{t+\Delta t}_i \varphi_y &= -\frac{1}{2} {}^{t+\Delta t}_i v_{z,y}
 \end{aligned} \tag{7}$$

These are in turn used in equations defining the displacement functions as

$$\begin{aligned}
 {}^{t+\Delta t}u_i &= {}^{t+\Delta t}u_m + z {}^{t+\Delta t}v_x - \frac{1}{2}z^2 {}^{t+\Delta t}v_{z,x} - \frac{4}{3t^2}z^3 \left({}^{t+\Delta t}w_{m,x} + {}^{t+\Delta t}v_x + \frac{1}{4}t^2 {}^{t+\Delta t}\varphi_{z,x} \right) \\
 {}^{t+\Delta t}v_i &= {}^{t+\Delta t}v_m + z {}^{t+\Delta t}v_y - \frac{1}{2}z^2 {}^{t+\Delta t}v_{z,y} - \frac{4}{3t^2}z^3 \left({}^{t+\Delta t}w_{m,y} + {}^{t+\Delta t}v_y + \frac{1}{4}t^2 {}^{t+\Delta t}\varphi_{z,y} \right) \\
 {}^{t+\Delta t}w_i &= {}^{t+\Delta t}w_m + z {}^{t+\Delta t}v_z + z^2 {}^{t+\Delta t}\varphi_z
 \end{aligned} \tag{8}$$

which reduces the number of displacement functions from original eleven to seven functions governing the structural response of the plate in Eq. 8, i.e. $u_m, v_m, w_m, v_x, v_y, v_z, \varphi_z$.

Employing von Karman theory of plates for geometrically nonlinear analysis the components of the strain tensor are

$$\begin{aligned}
 {}^{t+\Delta t}E_{xx} &= {}^{t+\Delta t}u_{,x} + \frac{1}{2} \left({}^{t+\Delta t}u_{,x}^2 + {}^{t+\Delta t}v_{,x}^2 + {}^{t+\Delta t}w_{,x}^2 \right) \\
 {}^{t+\Delta t}E_{yy} &= {}^{t+\Delta t}v_{,y} + \frac{1}{2} \left({}^{t+\Delta t}u_{,y}^2 + {}^{t+\Delta t}v_{,y}^2 + {}^{t+\Delta t}w_{,y}^2 \right) \\
 {}^{t+\Delta t}E_{zz} &= {}^{t+\Delta t}w_{,z} + \frac{1}{2} \left({}^{t+\Delta t}u_{,z}^2 + {}^{t+\Delta t}v_{,z}^2 + {}^{t+\Delta t}w_{,z}^2 \right) \\
 {}^{t+\Delta t}E_{xy} &= \frac{1}{2} \left({}^{t+\Delta t}u_{,y} + {}^{t+\Delta t}v_{,x} + {}^{t+\Delta t}u_{,x} {}^{t+\Delta t}u_{,y} + {}^{t+\Delta t}v_{,x} {}^{t+\Delta t}v_{,y} + {}^{t+\Delta t}w_{,x} {}^{t+\Delta t}w_{,y} \right) \\
 {}^{t+\Delta t}E_{xz} &= \frac{1}{2} \left({}^{t+\Delta t}u_{,z} + {}^{t+\Delta t}w_{,x} + {}^{t+\Delta t}u_{,x} {}^{t+\Delta t}u_{,z} + {}^{t+\Delta t}v_{,x} {}^{t+\Delta t}v_{,z} + {}^{t+\Delta t}w_{,x} {}^{t+\Delta t}w_{,z} \right) \\
 {}^{t+\Delta t}E_{yz} &= \frac{1}{2} \left({}^{t+\Delta t}v_{,z} + {}^{t+\Delta t}w_{,y} + {}^{t+\Delta t}u_{,y} {}^{t+\Delta t}u_{,z} + {}^{t+\Delta t}v_{,y} {}^{t+\Delta t}v_{,z} + {}^{t+\Delta t}w_{,y} {}^{t+\Delta t}w_{,z} \right)
 \end{aligned} \tag{9}$$

where

$$\begin{aligned}
 {}^{t+\Delta t}u_{,x} &= {}^{t+\Delta t}u_{m,x} + z {}^{t+\Delta t}v_{x,x} - \frac{1}{2}z^2 {}^{t+\Delta t}v_{z,xx} - \frac{4}{3t^2}z^3 \left({}^{t+\Delta t}w_{m,xx} + {}^{t+\Delta t}v_{x,x} + \frac{1}{4}t^2 {}^{t+\Delta t}\varphi_{z,xx} \right) \\
 {}^{t+\Delta t}u_{,y} &= {}^{t+\Delta t}u_{m,y} + z {}^{t+\Delta t}v_{x,y} - \frac{1}{2}z^2 {}^{t+\Delta t}v_{z,xy} - \frac{4}{3t^2}z^3 \left({}^{t+\Delta t}w_{m,xy} + {}^{t+\Delta t}v_{x,y} + \frac{1}{4}t^2 {}^{t+\Delta t}\varphi_{z,xy} \right) \\
 {}^{t+\Delta t}u_{,z} &= {}^{t+\Delta t}v_x - z {}^{t+\Delta t}v_{z,x} - \frac{4}{t^2}z^2 \left({}^{t+\Delta t}w_{m,x} + {}^{t+\Delta t}v_x + \frac{1}{4}t^2 {}^{t+\Delta t}\varphi_{z,x} \right) \\
 {}^{t+\Delta t}v_{,x} &= {}^{t+\Delta t}v_{m,x} + z {}^{t+\Delta t}v_{y,x} - \frac{1}{2}z^2 {}^{t+\Delta t}v_{z,xy} - \frac{4}{3t^2}z^3 \left({}^{t+\Delta t}w_{m,xy} + {}^{t+\Delta t}v_{y,x} + \frac{1}{4}t^2 {}^{t+\Delta t}\varphi_{z,xy} \right) \\
 {}^{t+\Delta t}v_{,y} &= {}^{t+\Delta t}v_{m,y} + z {}^{t+\Delta t}v_{y,y} - \frac{1}{2}z^2 {}^{t+\Delta t}v_{z,yy} - \frac{4}{3t^2}z^3 \left({}^{t+\Delta t}w_{m,yy} + {}^{t+\Delta t}v_{y,y} + \frac{1}{4}t^2 {}^{t+\Delta t}\varphi_{z,yy} \right) \\
 {}^{t+\Delta t}v_{,z} &= {}^{t+\Delta t}v_y - z {}^{t+\Delta t}v_{z,y} - \frac{4}{t^2}z^2 \left({}^{t+\Delta t}w_{m,y} + {}^{t+\Delta t}v_y + \frac{1}{4}t^2 {}^{t+\Delta t}\varphi_{z,y} \right) \\
 {}^{t+\Delta t}w_{,x} &= {}^{t+\Delta t}w_{m,x} + z {}^{t+\Delta t}v_{z,x} + z^2 {}^{t+\Delta t}\varphi_{z,x} \\
 {}^{t+\Delta t}w_{,y} &= {}^{t+\Delta t}w_{m,y} + z {}^{t+\Delta t}v_{z,y} + z^2 {}^{t+\Delta t}\varphi_{z,y} \\
 {}^{t+\Delta t}w_{,z} &= {}^{t+\Delta t}v_z + 2z {}^{t+\Delta t}\varphi_z
 \end{aligned} \tag{10}$$

Employing the finite element approximation

$$\begin{aligned} {}^{t+\Delta t}_i u &= N_{1j} {}^{t+\Delta t}_i d_j; \quad {}^{t+\Delta t}_i v = N_{2j} {}^{t+\Delta t}_i d_j; \quad {}^{t+\Delta t}_i w = N_{3j} {}^{t+\Delta t}_i d_j; \quad \dots \\ {}^{t+\Delta t}_i v_x &= N_{4j} {}^{t+\Delta t}_i d_j; \quad {}^{t+\Delta t}_i \varphi_z = N_{11,j} {}^{t+\Delta t}_i d_j \end{aligned} \quad (11)$$

we obtain the strain increments given by

$${}^{t+\Delta t}_i \Delta E_{mn} = \frac{1}{2} \left[B_{mnj}^{(1)} {}^{t+\Delta t}_i \Delta d_j + B_{mnjk}^{(2)} {}^{t+\Delta t}_i \Delta d_k {}^{t+\Delta t}_i \Delta d_j \right] \quad (12)$$

where ${}^{t+\Delta t}_i B_{mj}^{(1)}$, $B_{mjk}^{(2)}$ are the strain-displacement matrices.

The stress increment is expressed via a constitutive relationship as

$${}^{t+\Delta t}_{i+1} \Delta S_{ij} = {}^{t+\Delta t}_i C_{ijkl} {}^{t+\Delta t}_{i+1} \Delta E_{kl} \quad (13)$$

where $[{}^{t+\Delta t}_i C_{ijkl}]$ is the constitutive matrix for elastic-plastic behaviour. The linear elastic response of FGMs obeys Hooke's law. Furthermore, it is assumed that the metallic constituent in the FG plate exhibits the elasto-plastic behaviour whereas the ceramic constituent is elastic. Mixture of both fractions is locally isotropic and the von-Mises criterion governs the plastic behaviour. Several models have been proposed to describe the nonlinear response of FGM composites [11–14]. According to the modified rule of mixtures for composites [15, 16], elastoplastic material properties of the metal-ceramic composite in terms of the volume fraction of its constituents can be expressed as follows:

$${}^{t+\Delta t}_i S_Y = {}^{t+\Delta t}_1 S_{Ym} \left(V_m + \frac{q + E_m}{q + E_c} \frac{E_c}{E_m} (1 - V_m) \right) \quad (14)$$

and

$$H_f = \frac{\left(E_c V_c + \frac{q + E_c}{q + H_m} H_m V_m \right)}{V_c + \frac{q + E_c}{q + H_m} V_m} \quad (15)$$

where ${}^{t+\Delta t}_i S_{Yf}$, ${}^{t+\Delta t}_1 S_{Ym}$ are yield stresses for composite and steel, respectively, H_f and H_m are tangent moduli for composite and steel, E_m and E_c are moduli of elasticity of metal and ceramic, V_m and V_c are the volume fractions of the metal and ceramic and q is the ratio of stress to strain transfer between two phases assumed equal to 4.5 GPa as an approximation to experimental values for dual-phase steels. The constitutive tensor in the elastic part is consistent with the one used in the theory of elasticity

$${}^{t+\Delta t}_i C_{ijkl} = 2G_f \left[\delta_{ik} \delta_{jl} + \frac{\nu_f}{(1 - 2\nu_f)} \delta_{ij} \delta_{kl} \right] \quad (16)$$

Using the Prandtl-Reuss plastic flow theory the constitutive tensor takes the form

$${}^{t+\Delta t}_i C_{ijkl} = 2G_f \left[\delta_{ik}\delta_{jl} + \frac{\nu_f}{(1-2\nu_f)} \delta_{ij}\delta_{kl} - \frac{9}{2} G_f \frac{{}^{t+\Delta t}_i \widehat{S}_{ij} {}^{t+\Delta t}_i \widehat{S}_{kl}}{(3G_f + {}^{t+\Delta t}_i H) {}^{t+\Delta t}_i S_{eq}^2} \right] \quad (17)$$

where the Kirchhoff modulus is evaluated based on elasticity modulus and Poisson ratio obtained by considering combinations of material constants and volumetric fractions of both components in the FGM as

$$E_f = \frac{\left(E_c V_c + \frac{q+E_c}{q+H_m} H_m V_m \right)}{V_c + \frac{q+E_c}{q+H_m} V_m} \quad (18)$$

$$\nu_f = \nu_m V_m + \nu_c V_c$$

The volume fraction of ceramics is

$$V_c = \left(\frac{1}{2} + \frac{z}{t} \right)^n \quad (n \geq 0) \quad (19)$$

where n is the volume fraction exponent.

The principle of virtual work takes the form:

$$\left({}^{t+\Delta t}_i K_{pk}^{(d)} + {}^{t+\Delta t}_i K_{pk}^{(S)} \right) {}^{t+\Delta t}_{i+1} \Delta d_k = \left({}^{t+\Delta t}_i \lambda^{(P)} + {}^{t+\Delta t}_{i+1} \Delta \lambda^{(P)} \right) P_p - {}^{t+\Delta t}_i F_p \quad (20)$$

where:

$${}^{t+\Delta t}_i K_{pq}^{(d)} = \int_V {}^{t+\Delta t}_i C_{ijkl} {}^{t+\Delta t}_i B_{ijp}^{(1)} {}^{t+\Delta t}_i B_{klq}^{(1)} dV \quad (21)$$

is the stiffness matrix dependent on displacements (including also the linear term)

$${}^{t+\Delta t}_i K_{pq}^{(S)} = \int_V \left({}^{t+\Delta t}_i B_{ijpq}^{(2)} + {}^{t+\Delta t}_i B_{ijqp}^{(2)} \right) {}^{t+\Delta t}_i S_{ij} dV \quad (22)$$

is the stiffness matrix dependent on stresses

$$P_p = \int_V b_i N_{ip} dV + \int_{\Omega} p_i N_{ip} d\Omega \quad (23)$$

is the reference load vector and

$${}^{t+\Delta t}F_p = \int_V {}^{t+\Delta t}B_{ij}^{(1)} {}^{t+\Delta t}S_{ij} dV \quad (24)$$

is the internal force vector.

A typical loading scheme for the analysis of isolated plates and panels is a displacement loading corresponding to the interaction of individual components. Partitioning the stiffness matrix as well as the displacement and force vectors into the part associated with unknown displacement increments ⁽¹⁾ and imposed boundary ⁽²⁾ conditions leads to

$$\begin{bmatrix} {}^{t+\Delta t}\mathbf{K}^{(11)} & {}^{t+\Delta t}\mathbf{K}^{(12)} \\ {}^{t+\Delta t}\mathbf{K}^{(21)} & {}^{t+\Delta t}\mathbf{K}^{(22)} \end{bmatrix} \begin{Bmatrix} {}^{t+\Delta t}\Delta\mathbf{d}^{(1)} \\ {}^{t+\Delta t}\Delta\mathbf{d}^{(2)} \end{Bmatrix} = ({}^{t+\Delta t}\lambda + {}^{t+\Delta t}\Delta\lambda) \begin{Bmatrix} \mathbf{P}^{(1)} \\ \mathbf{P}^{(2)} \end{Bmatrix} - \begin{Bmatrix} {}^{t+\Delta t}\mathbf{F}^{(1)} \\ {}^{t+\Delta t}\mathbf{F}^{(2)} \end{Bmatrix} \quad (25)$$

Now the increment displacement vector in each iteration can be calculated as

$$\begin{aligned} {}^{t+\Delta t}\Delta\mathbf{d}_{iter}^{(1)} = & \left({}^{t+\Delta t}\mathbf{K}^{(11)} \right)^{-1} \left[({}^{t+\Delta t}\lambda + {}^{t+\Delta t}\Delta\lambda) \mathbf{P}^{(1)} \right. \\ & \left. - {}^{t+\Delta t}\mathbf{K}^{(12)} {}^{t+\Delta t}\Delta\mathbf{d}^{(2)} - {}^{t+\Delta t}\mathbf{F}^{(1)} \right] \end{aligned} \quad (26)$$

As a the path-following technique we employ the well-known Crisfield constant arc-length method which consists in formulating a constraint condition in addition to Eq. 25. The constraint limits for the displacement increment in each load step ${}^{t+\Delta t}\Delta\mathbf{d}_{incr}$ is expressed by

$$\left({}^{t+\Delta t}\Delta\mathbf{d}_{incr} \right)^T {}^{t+\Delta t}\Delta\mathbf{d}_{incr} = \Delta l^2 \quad (27)$$

The step increment in the actual iteration is the sum of the previous value and iterative correction of displacements, given by Eq. 26, as

$${}^{t+\Delta t}\Delta\mathbf{d}_{incr} = {}^{t+\Delta t}\Delta\mathbf{d}_{incr} + {}^{t+\Delta t}\Delta\mathbf{d}_{iter}^{(1)} \quad (28)$$

Dividing the load factor into the part resulting from applying load increment ${}^{t+\Delta t}\Delta\lambda_{app}$ and iterative correction ${}^{t+\Delta t}\Delta\lambda_{iter}$, we substitute to the constraint given by Eq. 27 to get a quadratic equation with respect to iterative change of the loading factor

$$\begin{aligned} & \left({}^{t+\Delta t}\Delta\mathbf{d}_{incr}^{(1)T} + {}^{t+\Delta t}\Delta\mathbf{d}_{app}^{(1)T} \right) \left({}^{t+\Delta t}\Delta\mathbf{d}_{incr}^{(1)} + {}^{t+\Delta t}\Delta\mathbf{d}_{app}^{(1)} \right) - \Delta l^2 + \\ & 2\mathbf{d}_{ref}^{(1)T} \left({}^{t+\Delta t}\Delta\mathbf{d}_{incr}^{(1)} + {}^{t+\Delta t}\Delta\mathbf{d}_{app}^{(1)} \right) {}^{t+\Delta t}\Delta\lambda_{iter} + \mathbf{d}_{ref}^{(1)T} \mathbf{d}_{ref}^{(1)} {}^{t+\Delta t}\Delta\lambda_{iter}^2 \end{aligned} \quad (29)$$

where

$$\begin{aligned} \Delta \mathbf{d}_{app}^{(1)} = & \left({}^{t+\Delta t}_i \mathbf{K}^{(11)} \right)^{-1} \left[\left({}^{t+\Delta t}_i \lambda + {}^{t+\Delta t}_{i+1} \Delta \lambda_{app} \right) \mathbf{P}^{(1)} \right. \\ & \left. - {}^{t+\Delta t}_{i+1} \Delta \lambda_{app} {}^{t+\Delta t}_i \mathbf{K}^{(12)} \mathbf{d}^{(2)} + {}^{t+\Delta t}_{i+1} \Delta \lambda_{app} {}^{t+\Delta t}_i \mathbf{Q}^{(1)} - {}^{t+\Delta t}_i \mathbf{F}^{(1)} \right] \end{aligned} \quad (30)$$

and

$$\mathbf{d}_{ref}^{(1)} = \left({}^{t+\Delta t}_i \mathbf{K}^{(11)} \right)^{-1} \left[\mathbf{P}^{(1)} - {}^{t+\Delta t}_i \mathbf{K}^{(12)} \mathbf{d}^{(2)} + {}^{t+\Delta t}_i \mathbf{Q}^{(1)} \right] \quad (31)$$

Parameter Δl^2 is determined using the initial value of applied loading.

3 Numerical Examples

3.1 Verification of the Formulation

The formulation has been verified by comparing the results obtained with those presented in [17] for the isotropic plate. In that paper plasticity was treated in an approximate manner according to the method originally developed by Ilyushin (based on the von Mises yield function) with some modifications introduced by Crisfield.

An example of rectangular plate with aspect ratio length to breadth $a/b = 0.875$ and thickness 3.175 mm was analysed with the Young modulus $E_m = 206,000$ MPa, Poisson ratio $\nu_m = 0.3$ and yield stress $S_{Ym} = 250$ MPa. Three cases were analysed for $b/t = 40, 55$ and 80 , respectively. Boundary conditions were taken to model simple support of the plate and unrestrained (free to move) mid-surface. Loading was applied in the form of kinematic excitation of the compressed edge. A quarter of the plate was modelled in each case using the 4×4 mesh. In each case initial deflection was assumed in the sinusoidal form as a single half-wave in both directions with amplitude $w_{11}^{(0)} = 0.001 b$ (Eq. 32 and Fig. 1).

$$w = w_{11}^{(0)} \sin \frac{\pi x}{a_1} \sin \frac{\pi y}{b} \quad (32)$$

Results in the form of the average stress ratio vs. average strain ratio, where the average stress ratio is the average compressive stress at the loaded edge related to the nominal metal yield stress and the average strain ratio is the average compressive strain at the loaded edge related to the yield strain (yield stress divided by Young modulus of the metallic constituent), are presented in Fig. 2.

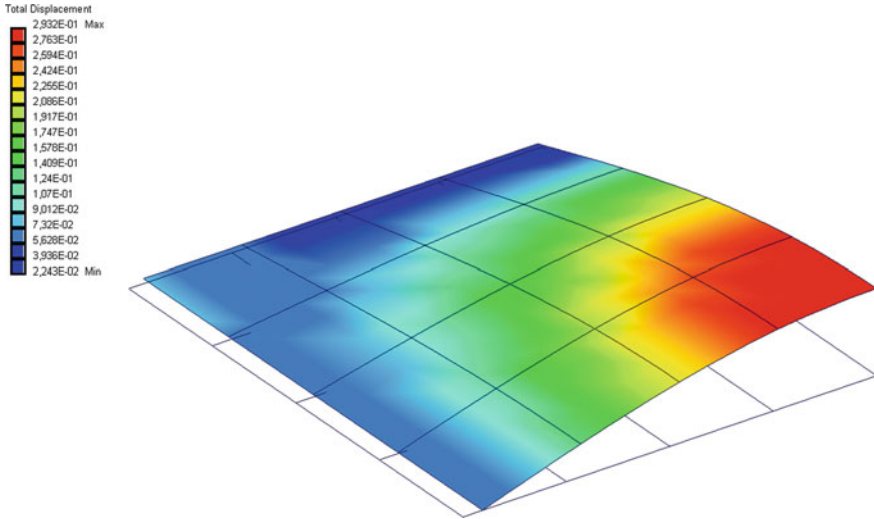
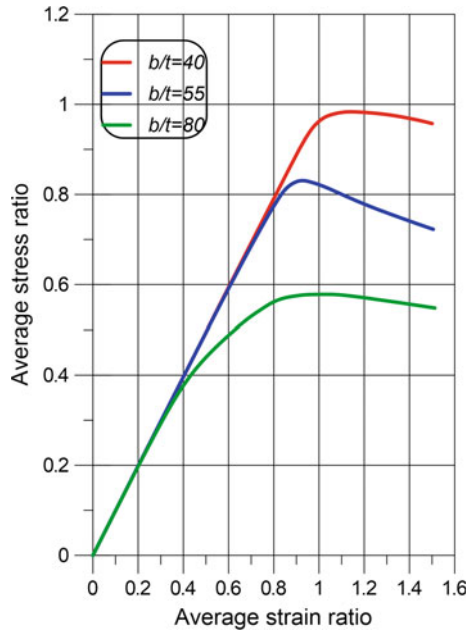


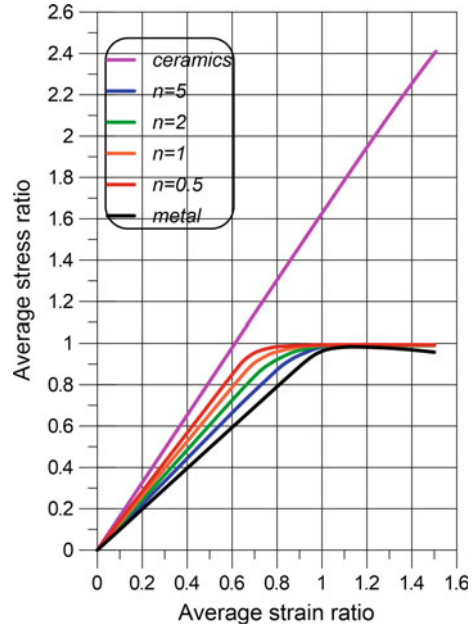
Fig. 1 Initial deflection of plate $a/b=0.875$

Fig. 2 Load-shortening curves for simply supported plate $a/b=0.875$ — comparison against results of [17]



The ultimate capacity for plate $b/t=40$ resulted as $S_{ult}/S_Y=0.9835$, for $b/t=55$ as $S_{ult}/S_Y=0.8307$ and for $b/t=80$ as $S_{ult}/S_Y=0.5782$. These results, and the curves presented in Fig. 2, agree well with the results given in [17].

Fig. 3 Load-shortening curves for simply supported plate $a/b = 0.875$, $b/t = 40$



In the next step FGM hypothetical plates were analysed assuming metal properties as in the Crisfield model while for the ceramic fraction $E_c = 340,000$ MPa and Poisson ratio $\nu_c = 0.25$. The aspect ratio of the plates was the same as for the metal plate. The influence of the exponent n (Eq. 19) on structural response of the plate was analyzed. The results, for plates $b/t = 40, 55$ and 80 are presented in

Fig. 4 Load-shortening curves for simply supported plate $a/b = 0.875$, $b/t = 55$

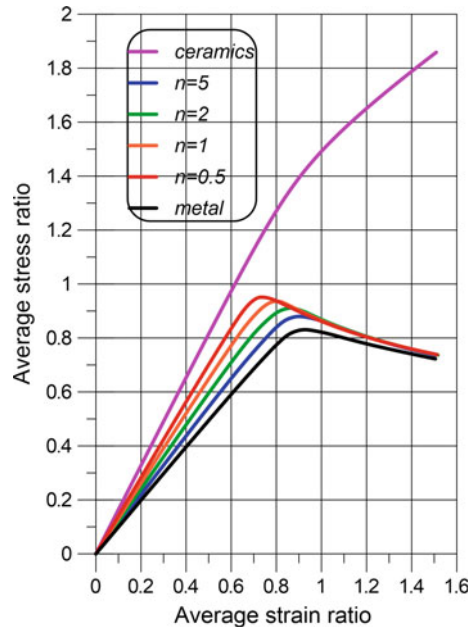
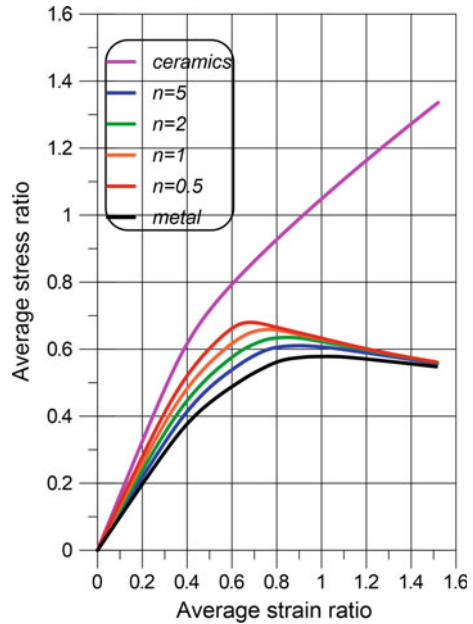


Fig. 5 Load-shortening curves for simply supported plate $a/b = 0.875$, $b/t = 80$



Figs. 3, 4 and 5, respectively. For plates $b/t = 40$ the geometrical effect is practically negligible; it is yielding which governs the structural response for all plates, both isotropic and FGM. For the plates with greater slender ratio we can observe decrease of the ultimate capacity with growing value of n which means increasing content of the metallic constituent what results in decreasing yield stress according to Eq. 14. According to our formulation the purely ceramic plate does not exhibit yielding; however, elastic buckling can be observed. Failure modes for all analysed plates were consistent with the initial deflection mode—in the form of one half-sine wave in both loading and perpendicular direction.

More complex behaviour can be observed for the plates having greater aspect ratio. The length of the plate was taken 3 times greater, thus the aspect ratio was $a/b = 2.625$. The initial deflection is again taken in the form of the one half-sine wave along the length.

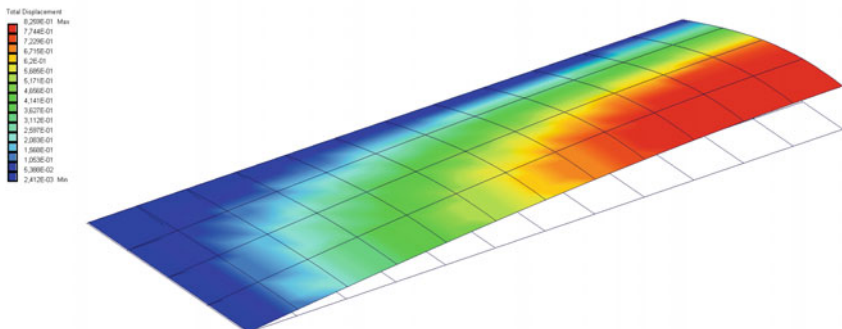
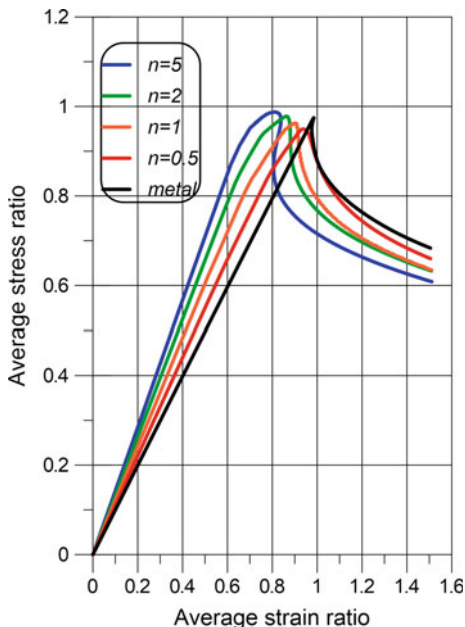


Fig. 6 Load-shortening curves for simply supported plate $a/b = 2.625$, $b/t = 55$



For plates $a/b = 2.625$ such an initial deflection is inconsistent with the failure mode, therefore the values of the ultimate capacity are greater than for the plate $a/b = 0.875$. For plates $b/t = 55$ we receive practically the same values of the ultimate capacity for all exponents n as shown in Fig. 6. However, we observe a different behaviour of the plates represented by the failure modes; the mode is typical for elastic behaviour in the case of ceramic plate—analysis without plasticity (Fig. 7), while the influence of plastic yielding can be observed for the FGM (Fig. 8) and metallic plates (Fig. 9).

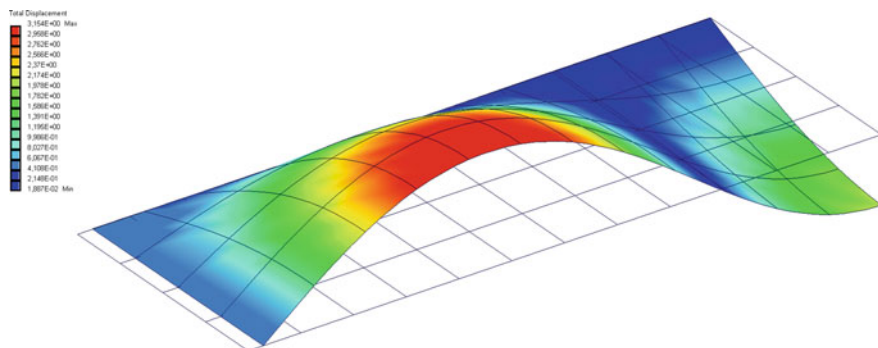


Fig. 7 Failure mode for simply supported ceramic plate $a/b = 2.625$, $b/t = 55$

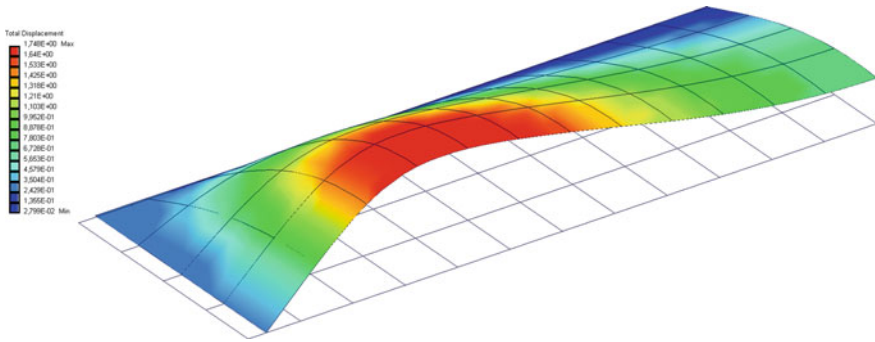


Fig. 8 Failure mode for simply supported metallic plate $a/b = 2.625$, $b/t = 55$

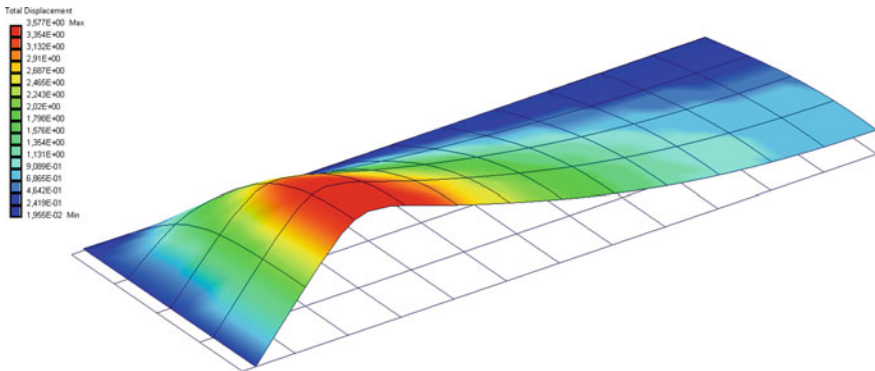
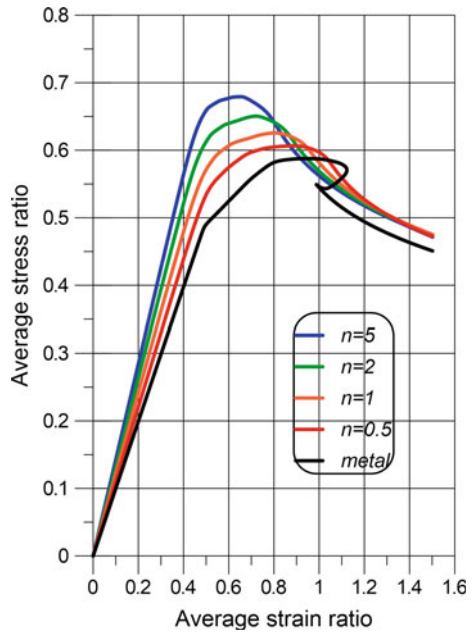


Fig. 9 Failure mode for simply supported FGM ($n = 5$) plate, $a/b = 2.625$, $b/t = 55$

Fig. 10 Load-shortening curves for simply supported plate $a/b = 2.625$, $b/t = 80$



In the case of plates with $b/t = 80$ we can observe elastic buckling followed by a complex behaviour in the elastic-plastic region, cf. Fig. 10.

4 Conclusions

Efficiency of the third order plate theory in the elastic-plastic analysis of FGM plates has been presented. The results prove a complex behaviour of axially compressed rectangular FGM plates. Further investigation is necessary to find the correctness of the assumed displacement functions and their final form, after application of the boundary conditions, to analyse the structural response of thick plates including the plates made of FGM. It appears that further developments are necessary employing the 3D solution for both isotropic and FGM plates in the form of 2D plate theories.

Acknowledgements The figures presenting deformations of plates have been created using the computer code (graphic post-processing) developed by Dr. Bartek Żyliński (Bartłomiej.Zyliński@rolls-royce.com, Rolls-Royce Marine AS, Ålesund, Norway).

References

1. J.N. Reddy, J. Kim, A nonlinear modified couple stress-based third-order theory of functionally graded plates. *Compos. Struct.* **94**(3), 1128–1153 (2012)
2. A.M.A. Neves, A.J.M. Ferreira, E. Carrera, M. Cinefra, C.M.C. Roque, R.M.N. Jorge, C.M. M. Soares, Static, free vibration and buckling analysis of isotropic and sandwich functionally graded plates using a quasi-3D higher-order shear deformation theory and a meshless technique. *Compos. B* **44**, 657–674 (2013)
3. K. Swaminathan, D.T. Naveenkumar, A.M. Zenkour, E. Carrera, Stress, vibration and buckling analyses of FGM plates—a state-of-art review. *Compos. Struct.* **120**, 10–31 (2015)
4. K.M. Liew, Z.X. Lei, L.W. Zhang, Mechanical analysis of functionally graded carbon nanotube reinforced composites: a review. *Compos. Struct.* **120**, 90–97 (2015)
5. B.R. Goncalves, A. Karttunen, J. Romanoff, J.N. Reddy, Buckling and free vibration of shear-flexible sandwich beams using a couple-stress-based finite element. *Compos. Struct.* **165**, 233–241 (2017)
6. A.T. Karttunen, R. von Herten, J.N. Reddy, J. Romanoff, Bridging plate theories and elasticity solutions. *Int. J. Solid Struct.* **106–107**, 251–262 (2017)
7. A.T. Karttunen, R. von Herten, J.N. Reddy, J. Romanoff, Exact elasticity-based finite element for circular plates. *Comput. Struct.* **182**, 219–226 (2017)
8. R. Buczkowski, M. Taczała, M. Kleiber, A 16-noded locking-free Mindlin plate resting on two-parameter elastic foundation—static and eigenvalue analysis. *Comput. Assist. Mech. Eng. Sci.* **22**, 99–114 (2015)
9. J. Kim, J.N. Reddy, A general third-order theory of functionally graded plates with modified couple stress effect and the von Kármán nonlinearity: theory and finite element analysis. *Acta Mech.* **226**, 2973–2998 (2015)
10. J.N. Reddy, A simple higher-order theory for laminated composite plates. *J. Appl. Mech. ASME* **51**, 745–752 (1984)

11. J.L. Chaboche, P. Kanoute, A. Roos, On the capabilities of mean-field approaches for the description of plasticity in metal matrix composites. *Int. J. Plast.* **21**, 1409–1434 (2005)
12. B.M. Love, R.C. Batra, Determination of effective thermomechanical parameters of a mixture of two elasto-thermo-viscoplastic constituents. *Int. J. Plast.* **22**, 1026–1061 (2006)
13. T. Mori, K. Tanaka, Average stress in matrix and average elastic energy of materials with misfitting inclusions. *Acta Metall.* **21**, 571–574 (1973)
14. P. Vena, R. Gastaldi, Determination of the effective elastic–plastic response of metal-ceramic composites. *Int. J. Plast.* **24**, 483–508 (2008)
15. S.-H. Shen, *Functionally Graded Materials: Nonlinear Analysis of Plates and Shells* (CRC Press, Boca-Raton, 2009)
16. R. Vaghefi, M.R. Hematiyan, A. Nayebi, Three-dimensional thermo-elastoplastic analysis of thick functionally graded plates using the meshless local Petrov-Galerkin method. *Eng. Anal. Boundary Elem.* **71**, 34–49 (2016)
17. M.A. Crisfield, Full-range analysis of steel plates and stiffened plating under uniaxial compression. *Proc. Inst. Civ. Eng. Part 2*, **59**, 595–624 (1975)

Extended-PGD Model Reduction for Nonlinear Solid Mechanics Problems Involving Many Parameters

P. Ladevèze, Ch. Paillet and D. Néron

Abstract Reduced models and especially those based on Proper Generalized Decomposition (PGD) are decision-making tools which are about to revolutionize many domains. Unfortunately, their calculation remains problematic for problems involving many parameters, for which one can invoke the “curse of dimensionality”. The paper starts with the state-of-the-art for nonlinear problems involving stochastic parameters. Then, an answer to the challenge of many parameters is given in solid mechanics with the so-called “parameter-multiscale PGD”, which is based on the Saint-Venant principle.

1 Introduction

Numerical simulation has made a forceful entry into design and analysis offices. This revolution, which is anything but complete, has entered in a new stage, called simulation-driven “robust” design. It leads to a major scientific challenge: simulations should be performed in quasi real-time. The key is a new generation of reduced-order methods which comprises essentially the Proper Orthogonal Decomposition (POD), the Proper Generalized Decomposition (PGD) and the Reduced Basis Method (RB), the basis and recent developments of which are given in [6]. These are problems in which uncertainties or variations in parameters are to be taken into account, or problems with very high number of degrees of freedom, with multiple scales or interactions between several physics. These methods, together with the notions of offline and online calculations, also open the way to new approaches where simulation and analysis of structures can be carried out almost in real time.

The object of this work is the PGD, that was introduced in [13, 14] for the treatment of nonlinear time-dependent problems of solid mechanics. Many developments have been made over the last thirty years: multi-scale, multiphysics, stochastic or non-stochastic parameters, acoustics, large displacements and deformations ...

P. Ladevèze (✉) · Ch. Paillet · D. Néron
LMT (ENS Paris-Saclay, CNRS, Université Paris-Saclay), 61 Avenue du Président
Wilson, 94235 Cachan Cedex, France
e-mail: ladeveze@lmt.ens-cachan.fr

In [18], one can find a synthesis of most of the developments in Cachan, where the method LATIN plays a central role. Currently, a number of tools have become mature and have been applied to industrial cases and then are competitors of classical computational methods (see book [7]). This is the case for the calculation of (visco)-plastic structures with less than ten parameters. The PGD not only makes it possible to construct reduced models that can be used in real time, but it also makes it possible to reduce drastically the calculation time in many situations. However, a major limitation is still the number of the parameters that can be involved (no more than 10). The paper starts with the state-of-the-art for nonlinear problems involving parameters which could be stochastic. It appears that the key to extend the PGD to a large number of parameters and then to cancel the “curse of dimensionality” is the same for linear and nonlinear problems.

Several attempts have been introduced for problems with a large number of parameters: Tucker tensors, Tensor Train tensors, Hierarchical Tucker tensors or more general tree-based Hierarchical Tucker tensors [3, 8, 9, 12, 24]. As they are generic a priori approximations, we believe that their improvement which is real, is limited. Here, in this paper we are following quite a different way. The idea is to notice that the operator underlying the problem treated is a binder between the parameters. Thus, at the level of the solution, the “curse of dimensionality” is no longer relevant. More, we go further with the parameter-multiscale PGD which takes its source in a fine analysis of the solution according to parameters, analysis built on the Principle of Saint-Venant. The basic idea is to introduce a two-level description of each parameter, the “macro” scale and the “micro” scale as one considers two scales for the space or the time. Also, to implement this vision, we have been led to use completely discontinuous approximations [18]. To carry out these idea, we use the Weak-Trefftz Discontinuous Method introduced in [16] and applied in [20] for the calculation of “medium frequency” phenomena. This paper is limited to fundamental aspects and the first numerical experiments for linear problems. More details can be founded in [25].

2 Nonlinear Problems with Parameters: The State-of-the-art

We have been working on ROM computation for 30 years with the so-called LATIN-PGD and what we are doing at the present time is the result of many works. PGD means Proper Generalized Decomposition and LATIN denotes the computational method which is nonincremental. The LATIN-PGD method was introduced in [13] for viscoplastic materials whose constitutive relations are described using a functional approach. Its extension to modern material descriptions involving internal variables, still for viscoplastic materials, was proposed in [14]. A number of mathematical properties regarding convergence and error indicators were proved in the book [15]. Overview could be found in [15, 18]. Originally, PGD was called radial

loading approximation, which, to us, meant a “mechanics” approximation in solid mechanics. LATIN-PGD leads today to a general and robust PGD computation technique which is based on an “abstract” reformulation of parametric nonlinear solid mechanics problems defined over a time-space-parameter domain. This work is the follow-up to [11, 19, 22, 27]. Today, there are few other works except the works of Ryckelynck and its group done with POD [28]. However, things are changing and today there are more and more POD-approaches developed in relation with the homogenization technique FE2 [10, 21, 26]. Additional reduction or interpolation are then introduced to reduce their computation cost. This is done offline with the PGD computation. Our answer is the so-called Reference Point Method (RPM) [4].

2.1 The Reference Problem and Its Reformulation

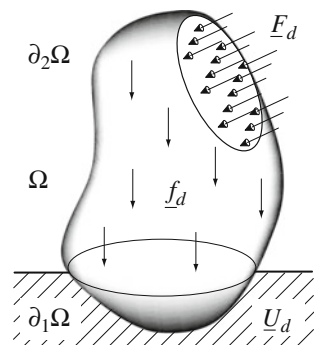
2.1.1 Notations

With the assumption of small perturbations, let us consider the quasi-static and isothermal evolution of a structure defined over the time-space domain $[0, T] \times \Omega$ and depending of the parameters $\underline{\mu} \in \Sigma_\mu$. This structure is subjected to prescribed body forces \underline{f}_d , traction forces \underline{F}_d over a part $\partial_2\Omega$ of the boundary, and displacements \underline{u}_d over the complementary part $\partial_1\Omega$ (see Fig. 1). All the data and the material characteristics depend on the parameters $\underline{\mu} \in \Sigma_\mu$.

The state of the structure is defined by the set of the fields $\mathbf{s} = (\dot{\epsilon}_p, \dot{X}, \sigma, Y)$ (where the dot notation $\dot{\square}$ denotes the time derivative), in which:

- ϵ_p designates the inelastic part of the strain field ϵ which corresponds to the displacement field \underline{u} , uncoupled into an elastic part ϵ_e such that $\epsilon_p = \epsilon - \epsilon_e$; X designates the remaining internal variables;
- σ designates the Cauchy stress field and Y the set of variables conjugate of X (and X have the same dimension). X could be hardening variables, damage variables, chemical variables, ...

Fig. 1 The reference problem



- generalized quantities over the parameter-time-space domain.

All these quantities are defined over the parameter-time-space domain $\Sigma_\mu \times [0, T] \times \Omega$ and assumed to be sufficiently regular. For the sake of simplicity, the displacement \underline{u} alone is assumed to have a nonzero initial value, denoted \underline{u}_0 . Introducing the following notations for the primal fields:

$$\mathbf{e}_p = \begin{bmatrix} \boldsymbol{\varepsilon}_p \\ -\dot{\mathbf{X}} \end{bmatrix}, \quad \mathbf{e} = \begin{bmatrix} \boldsymbol{\varepsilon} \\ 0 \end{bmatrix} \quad \text{and} \quad \mathbf{e}_e = \begin{bmatrix} \boldsymbol{\varepsilon}_e \\ \dot{\mathbf{X}} \end{bmatrix} \quad \text{so that} \quad \mathbf{e}_p = \mathbf{e} - \mathbf{e}_e \quad (1)$$

and for the dual fields:

$$\mathbf{f} = \begin{bmatrix} \boldsymbol{\sigma} \\ \mathbf{Y} \end{bmatrix} \quad (2)$$

The mechanical dissipation rate for the entire structure Ω is:

$$\int_{\Omega} (\dot{\boldsymbol{\varepsilon}}_p : \boldsymbol{\sigma} - \dot{\mathbf{X}} \cdot \mathbf{Y}) d\Omega = \int_{\Omega} (\dot{\mathbf{e}}_p \circ \mathbf{f}) d\Omega \quad (3)$$

where \cdot denotes the contraction adapted to the tensorial nature of \mathbf{X} and \mathbf{Y} . Notation \circ denotes the contraction operator for generalized quantities. Let us introduce the following fundamental bilinear ‘‘dissipation’’ form:

$$\langle \mathbf{s}, \mathbf{s}' \rangle = \int_{\Sigma_\mu \times [0, T] \times \Omega} \left(1 - \frac{t}{T}\right) (\dot{\mathbf{e}}_p \circ \mathbf{f}' + \dot{\mathbf{e}}_p' \circ \mathbf{f}) d\Omega dt d\mu \quad (4)$$

along with \mathbf{E} and \mathbf{F} , the spaces of the fields $\dot{\mathbf{e}}_p$ and \mathbf{f} which are compatible with (4). These spaces enable us to define $\mathbf{S} = \mathbf{E} \times \mathbf{F}$, the space in which the state $\mathbf{s} = (\dot{\mathbf{e}}_p, \mathbf{f})$ of the structure is being sought.

2.1.2 The State Equations over $\Sigma_\mu \times [0, T] \times \Omega$

Following [15], a normal formulation with internal state variables is used to represent the behavior of the material. If ρ denotes the mass density of the material, from the free energy $\rho\Psi(\boldsymbol{\varepsilon}_e, \mathbf{X})$ with the usual uncoupling assumptions, the state law yields:

$$\begin{aligned} \boldsymbol{\sigma} &= \rho \frac{\partial \Psi}{\partial \boldsymbol{\varepsilon}_e} = \mathbf{K} \boldsymbol{\varepsilon}_e \\ \mathbf{Y} &= \rho \frac{\partial \Psi}{\partial \mathbf{X}} = \boldsymbol{\Lambda} \mathbf{X} \end{aligned} \quad (5)$$

where the Hooke’s tensor \mathbf{K} and the constant, symmetric and positive definite tensor $\boldsymbol{\Lambda}$ are material characteristics.

2.1.3 The State Evolution Laws over $\Sigma_\mu \times [0, T] \times \Omega$

The state evolution laws can be written:

$$\dot{\mathbf{e}}_p = \mathbf{B}(\mathbf{f}) \quad \text{with} \quad \mathbf{e}_p|_{t=0} = 0 \quad (6)$$

where \mathbf{B} is a positive operator which is also for most viscoplastic models maximal monotone [15]. Let us introduce now the space $\mathcal{U}_{\mu,ad}^{[0,T]}$ of admissible displacement fields \underline{u} defined over $\Sigma_\mu \times [0, T] \times \Omega$ and $\mathcal{U}_{\mu,0}^{[0,T]}$ the associated vectorial space. The compatibility equation can be written as:

$$\begin{aligned} \text{Find } \underline{u} \in \mathcal{U}_{\mu,ad}^{[0,T]} \text{ such that } \forall \mu \in \Sigma_\mu, \forall \underline{u}^* \in \mathcal{U}_{\mu,0}^{[0,T]}, \\ \int_{[0,T] \times \Omega} \text{Tr}[\boldsymbol{\varepsilon}(\underline{u}) \mathbf{K} \boldsymbol{\varepsilon}(\underline{u}^*)] d\Omega dt = \int_{[0,T] \times \Omega} \text{Tr}[\boldsymbol{\varepsilon}_p \mathbf{K} \boldsymbol{\varepsilon}(\underline{u}^*)] d\Omega dt + \\ \int_{[0,T] \times \Omega} \underline{f}_d \cdot \underline{u}^* d\Omega dt + \int_{[0,T] \times \partial_2 \Omega} \underline{F}_d \cdot \underline{u}^* dS dt \quad (7) \end{aligned}$$

It follows that the stress $\boldsymbol{\sigma} = \mathbf{K}(\boldsymbol{\varepsilon}(\underline{u}) - \boldsymbol{\varepsilon}_p)$ can be written:

$$\boldsymbol{\sigma} = \boldsymbol{\Omega} \boldsymbol{\varepsilon}_p + \mathbf{r}_d \quad (8)$$

where $\boldsymbol{\Omega}$ is a linear given operator and \mathbf{r}_d is a prestress depending on the data. Introducing the generalized stress, the admissibility conditions can be written as:

$$\mathbf{f} = \mathbf{Q} \boldsymbol{\varepsilon}_p + \mathbf{r}_d \quad (9)$$

with

$$\mathbf{Q} = \begin{bmatrix} \boldsymbol{\Omega} & \mathbf{0} \\ \mathbf{0} & \boldsymbol{\Lambda} \end{bmatrix} \quad \text{and} \quad \mathbf{r}_d = \begin{bmatrix} \mathbf{r}_d \\ \mathbf{0} \end{bmatrix} \quad (10)$$

where \mathbf{Q} is a linear symmetric positive operator. Finally, the problem to solve, which is defined over $\Sigma_\mu \times [0, T] \times \Omega$, is:

$$\begin{aligned} \text{Find } \mathbf{s} = (\dot{\mathbf{e}}_p, \mathbf{f}) \in \mathbf{S} \text{ such that:} \\ \mathbf{f} = \mathbf{Q} \boldsymbol{\varepsilon}_p + \mathbf{r}_d \quad \text{and} \quad \dot{\mathbf{e}}_p = \mathbf{B}(\mathbf{f}) \quad \text{with} \quad \mathbf{e}_p|_{t=0} = 0 \quad (11) \end{aligned}$$

Consequently, one has to solve a first order differential equation with an initial condition; The operators \mathbf{Q} and \mathbf{B} as well as the right-hand-side member \mathbf{r}_d depends on the parameter $\underline{\mu}$ belonging to the parameter set Σ_μ .

2.2 The LATIN Solver for PGD Computation

2.2.1 The LATIN Solver

The LATIN method is an iterative strategy which differs from classical incremental or step-by-step techniques in that, at each iteration, it produces an approximation of the complete structural response over the whole loading history being considered. A review of the state-of-the-art and more recent extensions could be found in [18]. The LATIN method is designed as a mechanics-based computational strategy whose aim is to achieve the best possible performance level for solid mechanics problems. Consequently, this alternative approach is rooted in some remarkable properties which are verified by most of the models encountered in structural mechanics.

The LATIN method operates here over the parameter-time-space domain $\Sigma_\mu \times [0, T] \times \Omega$, and its first principle (P1) consists in separating the difficulties. Thus, the equations are divided into:

- a set of linear equations which can be global in the space variables: the equilibrium and compatibility equations, the state equations;
- a set of equations which are local in the space variables but can be nonlinear: the state evolution laws.

The reformulation (11) of the reference problem enters into this framework because:

- \mathbf{Q} is a linear operator;
- \mathbf{B} is at least local in space variables.

In the geometric representation given Fig. 2, \mathbf{A}_d and Γ represent the solutions of the first and second set respectively, \mathbf{A}_d being associated to the free energy and Γ with the dissipation. The LATIN second principle (P2) is also very natural. It consists in solving the two sets of equations alternatively until practical convergence. In order to do that, one uses search directions given as parameters of the LATIN method. One possible choice (Newton search direction) consists of the tangent direction and its conjugate direction (see Fig. 3).

Local stage principle at iteration $n + 1$ —Find $\hat{\mathbf{s}}_{n+1/2} = (\hat{\boldsymbol{\varepsilon}}_{p,n+1/2}, \hat{\mathbf{f}}_{n+1/2}) \in \mathbf{S}$ such that:

Fig. 2 The geometric representation associated to the reformulation of the reference problem

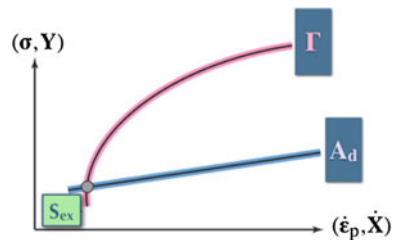
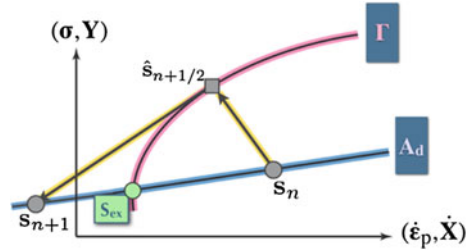


Fig. 3 Iteration $n + 1$ of the LATIN method over $[0, T] \times \Omega$



$$\begin{aligned} \hat{\mathbf{e}}_{p,n+1/2} &= \mathbf{B}(\hat{\mathbf{f}}_{n+1/2}) \quad \text{with} \quad \hat{\mathbf{e}}_{p,n+1/2} = 0 \text{ at } t = 0 \\ \hat{\mathbf{e}}_{p,n+1/2} - \hat{\mathbf{e}}_{p,n} + \mathbf{H}^+(\hat{\mathbf{f}}_{n+1/2} - \mathbf{f}_n) &= 0 \end{aligned} \quad (12)$$

The search direction \mathbf{H}^+ is a LATIN parameter. Practically, one takes a linear positive operator which is local both on time and space variables. This local stage is very suitable for parallel computing.

Linear stage principle at iteration $n + 1$ —Find $\mathbf{s}_{n+1} = (\hat{\mathbf{e}}_{p,n+1}, \mathbf{f}_{n+1}) \in \mathbf{S}$ such that:

$$\begin{aligned} \mathbf{f}_{n+1} &= \mathbf{Q}\mathbf{e}_{p,n+1} + \mathbf{r}_d \\ \hat{\mathbf{e}}_{p,n+1} - \hat{\mathbf{e}}_{p,n+1/2} - \mathbf{H}^-(\mathbf{f}_{n+1} - \hat{\mathbf{f}}_{n+1/2}) &= 0 \quad \text{with} \quad \mathbf{e}_{p,n+1} = 0 \text{ at } t = 0 \end{aligned} \quad (13)$$

The search direction \mathbf{H}^- is a LATIN parameter. This is a linear positive operator which is local both on time and space variables. It is associated to the material operator \mathbf{B} . One has to solve a first order linear differential equation with an initial condition, the operator \mathbf{Q} being non-explicit.

Remark In practice, \mathbf{H}^- is chosen close to the tangent to the manifold Γ at the point $\hat{\mathbf{s}}_{n+1/2} = (\hat{\mathbf{e}}_{p,n+1/2}, \hat{\mathbf{f}}_{n+1/2})$. For \mathbf{H}^+ , one takes $\mathbf{0}$ or \mathbf{H}^- . The convergence of the iterative process has been proved in the case of non-softening materials and contacts without friction [15]. The distance between two successive approximations gives a good and easily computed error indicator. Let us also note that one often uses an additional relaxation with a coefficient equal to 0.8.

2.2.2 PGD Computation

Let us recall that the problem is defined over the parameter-time-space domain $\Sigma_\mu \times [0, T] \times \Omega$.

Linear stage at iteration $n + 1$ —Let us introduce corrections:

$$\begin{aligned} \Delta \hat{\mathbf{e}}_p &= \hat{\mathbf{e}}_{p,n+1} - \hat{\mathbf{e}}_{p,n} \\ \Delta \mathbf{f} &= \mathbf{f}_{n+1} - \mathbf{f}_n \end{aligned} \quad (14)$$

where $\mathbf{s}_{n+1} = (\dot{\mathbf{e}}_{p,n}, \mathbf{f}_n)$ has been computed at iteration n . The problem to solve over $\Sigma_\mu \times [0, T] \times \Omega$ at iteration $n + 1$ is then:

$$\begin{aligned} &\text{Find } \Delta \mathbf{s} = (\Delta \dot{\mathbf{e}}_p, \Delta \mathbf{f}) \in \mathbf{S} \text{ such that} \\ &\Delta \mathbf{f} = \mathbf{Q} \Delta \dot{\mathbf{e}}_p \\ &\Delta \dot{\mathbf{e}}_p - \mathbf{H}^- \Delta \mathbf{f} = \mathbf{R}_d \quad \text{with} \quad \Delta \mathbf{e}_p = 0 \text{ at } t = 0 \end{aligned} \quad (15)$$

The main idea is to interpret the search direction as a linear constitutive relation, the operator \mathbf{H}^- being local both on time and space variables and positive definite as the Hooke tensor. Consequently, one introduces the associated constitutive relation error which will be minimized:

$$r(\Delta \mathbf{s}, t) = \frac{1}{2} \int_{\Omega} [\Delta \dot{\mathbf{e}}_p - \mathbf{H}^- \Delta \mathbf{f} - \mathbf{R}_d] (\mathbf{H}^-)^{-1} [\Delta \dot{\mathbf{e}}_p - \mathbf{H}^- \Delta \mathbf{f} - \mathbf{R}_d] d\Omega \quad (16)$$

and

$$R(\Delta \mathbf{s}) = \int_{\Sigma_\mu \times [0, T]} \left(1 - \frac{t}{T}\right) r(\Delta \mathbf{s}, t) dt d\mu \quad (17)$$

with $\Delta \mathbf{s} = (\Delta \dot{\mathbf{e}}_p, \Delta \mathbf{f}) \in \mathbf{S}$. The problem (15) becomes:

$$\begin{aligned} &\text{Find } \Delta \mathbf{s} \in \mathbf{S} \text{ minimizing} \\ &\Delta \mathbf{s} \in \mathbf{S} \mapsto R(\mathbf{s}) \in \mathbb{R} \\ &\text{with the constrains } \Delta \mathbf{f} = \mathbf{Q} \Delta \dot{\mathbf{e}}_p \text{ and } \Delta \mathbf{e}_p = 0 \text{ at } t = 0 \end{aligned} \quad (18)$$

One only prescribes that:

$$\Delta \mathbf{e}_p = \sum_{i=1}^m \lambda_i(t) \gamma_i(\underline{\mu}) \mathbf{g}_i(\underline{x}) \quad (19)$$

with $\lambda_i(0) = 0$ (initial condition), $\mathbf{g}_i \in L^2(\Omega)$, $\lambda_i(t) \in L^2[0, T]$ and $\gamma_i(\underline{\mu}) \in L^2(\Sigma_\mu)$. It follows, using admissibility conditions, that:

$$\Delta \mathbf{f} = \sum_{i=1}^m \lambda_i(t) \gamma_i(\underline{\mu}) \mathbf{Q} \mathbf{g}_i(\underline{x}) \quad (20)$$

where $\mathbf{Q} \mathbf{g}_i(\underline{x})$ are computed solving several elasticity problems. For the sake of simplicity, let us consider now that \mathbf{Q} does not depend on t and $\underline{\mu}$ belonging to $\Omega \times [0, T] \times \Sigma_\mu$. The general case does not involve serious difficulties, the \mathbf{Q} -constraint being satisfied in a mean sense.

A greedy algorithm with updating is used to solve the minimization problem. More details can be founded in [17, 18]. For few parameters, it could be advantageous to describe point-by-point the parameter space using the remarkable property

of the LATIN method: the initialization of the iterative process can be any function defined over $[0, T] \times \Sigma_\mu$ [27].

Local stage at iteration $n + 1$ —One has to solve a problem which is local over the parameter-time-space domain for which “hyper-reduction” techniques are also welcome. A very popular technique is the Empirical Interpolation Method (EIM) [2] and its discrete version named DEIM [5]. The Hyperreduction method [28] makes the most of a restricted subdomain of the space domain. Here we use the Reference Point Method (RPM) developed in [4]. Let us note that such method can be also used for solving the linear stage.

2.3 An Engineering Illustration

To illustrate the use of the technique to deal with parametrized problems, we consider an example issued from [22] and which is freely inspired from a blade of the Vulcain engine of the Ariane 5 launcher. The geometry, boundary conditions and mesh are presented on Fig. 4. A four-sinusoidal-cycles displacement with is prescribed on the lower part. The total number of DOFs is 141,500 and the time interval is discretized using 120 time steps. The material coefficients used for the Marquis-Chaboche elastic-viscoplastic material are typical of a Titanium TA6V material at 500° K. The parametric study is defined by Table 1. It concerns the influence of the loading amplitude, of the limit stress and the power coefficient in the evolution law. The range of variation of each parameter was discretized into 10 values, leading to 1000 different problems. Figure 5 shows the total agreement of the results obtained with the LATIN-PGD compared to the one obtained with ABAQUS.

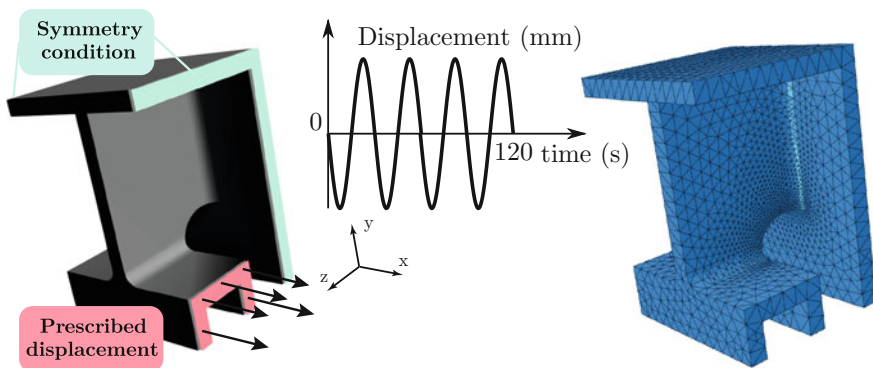
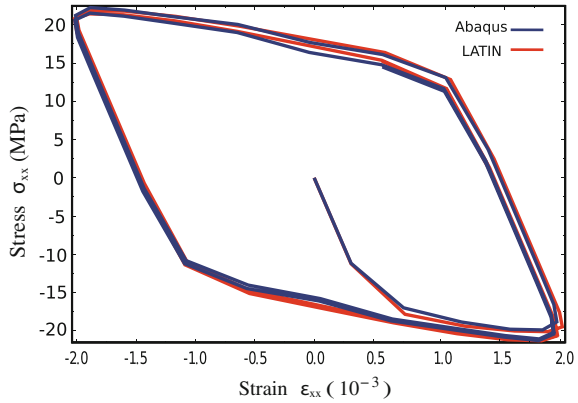


Fig. 4 Geometry, boundary conditions and mesh of the blade test-case

Table 1 Range of variation of loading amplitude, R_0 and γ

Parameter	Min. value	Max. value	Step	Range of variation (%)
\pm loading amplitude	0.1 mm	0.19 mm	0.01 mm	± 31
Limit stress R_0	20 MPa	29 MPa	1 MPa	± 18
Power γ	285	330	5	± 7

Fig. 5 Stress versus strain curves at the most loaded gauss point

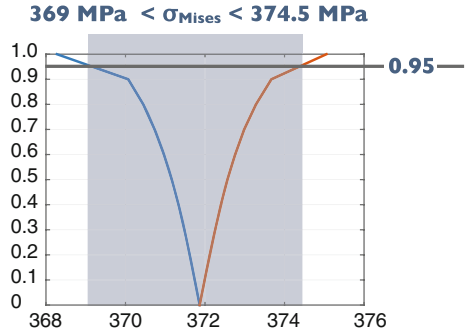


To illustrate the performances of LATIN-PGD, we compare compare the CPU times:

- about 50 days (estimated time) are necessary to complete the 1000 resolution with ABAQUS;
- less than 17 h are necessary to complete the 1000 resolution with the multiple runs algorithm.

The gain is a about 70 using the multiple runs algorithm, but can achieve more than 700 when using also the RPM strategy. The important point is that, once this parametric study has been performed, a reduced-model of the nonlinear problem is built. For example, some stochastic studies can be performed very easily. Assuming a probabilistic distribution of the three parameters, a probabilistic distribution of the quantity of interest can be computed in quasi-real time. Let us consider now that the first parameter is fuzzy and the two others follow a normal law. Then, it is easy to compute the probability law related to the maximum Mises stress over $[0, T] \times \Sigma_\mu$ (see Fig. 6).

Fig. 6 Probability of the maximum Mises stress



3 The Parameter-Multiscale PGD

3.1 Model Problem

The basic principles of parameters-multiscale-PGD are given in [17]. One considers an elastic media which occupies the domain Ω divided into sub-domains or elements $\Omega_E, E \in \mathbf{E}$. The parameters $\mu_E \in \mathbb{R}^{q_E}$ are associated to the rigidity of the volume Ω_E . For the sake of simplicity, we consider that μ_E is a scalar; it belongs to $[-1/2; 1/2]$. Let us introduce $\underline{\mu} \equiv \{\mu_E \mid E \in \mathbf{E}\}$, the corresponding space being Σ_μ . The problem to solve can be written as:

$$\begin{aligned} &\text{Find } \underline{X}(\underline{\mu}) \in U^\mu \text{ where } U = \mathbf{R}^N \text{ such that:} \\ &\forall \underline{\mu} \in \Sigma_\mu \quad \mathbf{A}\underline{X}(\underline{\mu}) = \underline{F}_d \end{aligned}$$

where \mathbf{A} is a linear positive definite operator depending on $\underline{\mu}$. \underline{F}_d is a given loading which could also depend on $\underline{\mu}$.

Numerical illustration with the standard PGD—The standard parameter-PGD has been introduced by [1]. Stochastic framework has been considered by [23]. An overview is given in [6]. Figure 7 shows an illustration of the model problem. This is a cube submitted to a uniaxial traction displacement, the opposite face being clamped. The parameters $\underline{\mu}$ could be interpreted as damage intensity.

Convergence curves for the classical PGD are given Fig. 8 for 8, 27 and 64 parameters; they show that convergence cannot be obtained when the number of parameters is more than 30.

3.2 The Key Idea

One has to solve:

$$\mathbf{A}(\underline{\mu})\underline{X}(\underline{\mu}) = \underline{F}_d$$

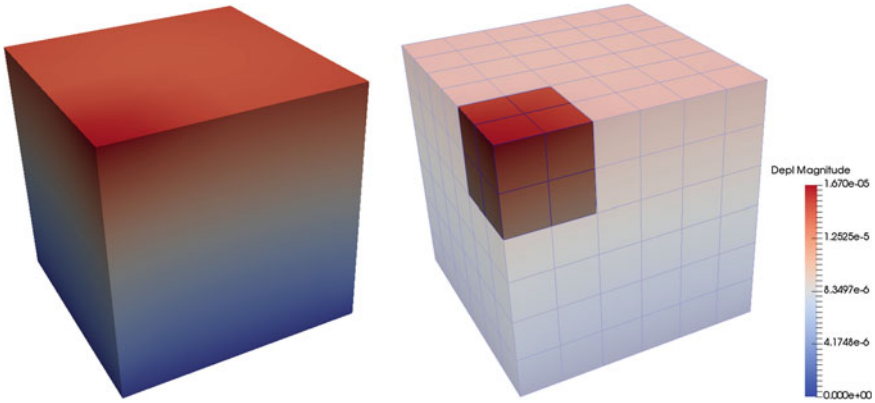


Fig. 7 Model problem with 27 parameters: particular solution and highlighting of a subdomain

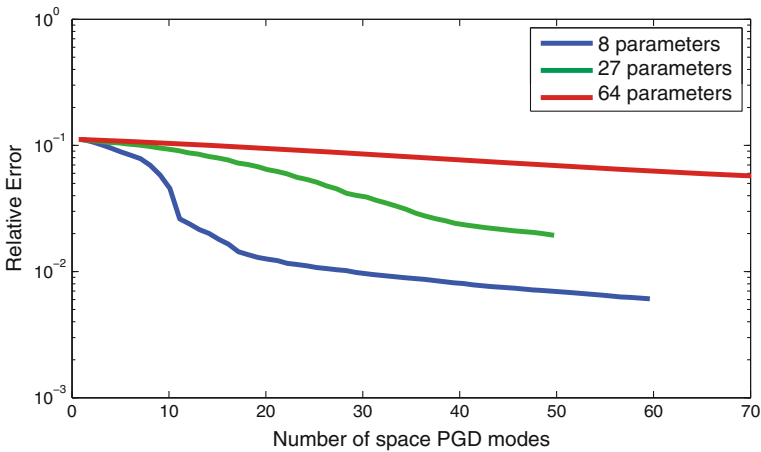


Fig. 8 Convergence curve of the classical PGD

Let us introduce $\mathbf{A}^0 = \mathbf{A}(0)$ and let us suppose for the sake of simplicity that \underline{F}_d does not depend on $\underline{\mu}$. One has:

$$\mathbf{A} = \mathbf{A}^0 [\mathbf{1} - \underbrace{(\mathbf{1} - \mathbf{A}^{0^{-1}} \mathbf{A})}_{\Delta}]$$

Let be $\underline{X}_0 = \mathbf{A}^{0^{-1}} \underline{F}_d$; the solution can be written as:

$$\underline{X}(\underline{\mu}) : \underline{X}_0 + \underbrace{\Delta \underline{X}_0}_{\underline{X}_1(\underline{\mu})} + \underbrace{\Delta^2 \underline{X}_0}_{\underline{X}_2(\underline{\mu})} + \dots \tag{21}$$

where \underline{X}_1 is $\underline{\mu}$ -linear and \underline{X}_2 $\underline{\mu}$ -quadratic. It follows that with only few terms, one gets a good approximation and then, the curse of dimensionality disappears; the operator \mathbf{A} links the parameters. Let us go further: on each element, one has:

$$\mathbf{A}_E = \mathbf{A}_E^0 + \mu_E \bar{\mathbf{A}}_E$$

and then

$$\mathbf{A} = \mathbf{A}_{E \in \mathbb{E}} \mathbf{A}_E$$

where $\mathbf{A}_{E \in \mathbb{E}}$ is the finite element assembly operator. Introducing the operator \mathbf{I}_E , giving the restriction \underline{V}_E of a spatial vector \underline{V} on the subdomain Ω_E through the relation $\underline{V} = \mathbf{I}_E \underline{V}_E$, one can write: $\mathbf{A} = \mathbf{A}_{E \in \mathbb{E}} \mathbf{A}_E = \sum_{E \in \mathbb{E}} \mathbf{I}_E \mathbf{A}_E \mathbf{I}_E^T$. It follows:

$$\underline{X}_1(\underline{\mu}) = -\mathbf{A}^{0^{-1}} \left[\sum_{E \in \mathbb{E}} \mu_E \mathbf{I}_E \bar{\mathbf{A}}_E \mathbf{I}_E \underline{X}_{0,E} \right] = \sum_{E \in \mathbb{E}} -\mu_E \mathbf{A}^{0^{-1}} \mathbf{I}_E \underbrace{\left[\bar{\mathbf{A}}_E \underline{X}_{0,E} \right]}_{\underline{Z}_E}$$

The term $\mathbf{I}_E \underline{Z}_E$ is associated to a self-equilibrated loading. Therefore, from the Principle of Saint-Venant, the solution is localized in the neighborhood of the element E , essentially over the elements sharing a common point with E noted C_E . Let be:

$$\underline{Z}_{1,E} = \mathbf{A}^{0^{-1}} \mathbf{I}_E \underline{Z}_E$$

which can be seen as negligible over the complement of C_E . One has:

$$\underline{Z}_{1,E} \equiv \mathbf{A}^{0^{-1}} \mathbf{I}_E \underline{Z}_E \simeq \mathbf{I}_{E'} \underline{Z}_{1,E'E} \quad E' \in C_E$$

and $\underline{X}_1(\underline{\mu}) = -\sum_{E \in \mathbb{E}} \mu_E \underline{Z}_{1,E}$; \underline{X}_1 is then $\underline{\mu}$ -linear and $\underline{Z}_{1,E}$ is localized over the neighborhood C_E of E . A similar property holds for \underline{X}_2 :

$$\begin{aligned} \underline{X}_2(\underline{\mu}) &= \sum_{E' \in \mathbb{E}} \sum_{E \in \mathbb{E}} \mu_{E'} \mu_E \mathbf{A}^{0^{-1}} \mathbf{I}_{E'} \bar{\mathbf{A}}_{E'} \mathbf{I}_{E'} \underline{Z}_{1,E} \\ &\simeq \sum_{E' \in \mathbb{E}} \sum_{E \in \mathbb{E}} \mu_{E'} \mu_E \mathbf{A}^{0^{-1}} \mathbf{I}_{E'} \bar{\mathbf{A}}_{E'} \mathbf{I}_{E'} \mathbf{I}_{E''} \underline{Z}_{1,E''} \quad E'' \in C_E \\ &\simeq \sum_{E' \in C_E} \sum_{E \in \mathbb{E}} \mu_{E'} \mu_E \mathbf{A}^{0^{-1}} \mathbf{I}_{E'} \bar{\mathbf{A}}_{E'} \underline{Z}_{1,E'E} \end{aligned}$$

$$\begin{aligned} &\simeq \sum_{E \in \mathbf{E}} \mu_E^2 \mathbf{A}^{0^{-1}} \mathbf{I}_E \bar{\mathbf{A}}_E \underline{Z}_{1,EE} + \sum_{E \in \mathbf{E}} \sum_{\substack{E' \in C_E \\ E \neq E'}} \mu_E \mu_{E'} \mathbf{A}^{0^{-1}} \mathbf{I}_{E'} \bar{\mathbf{A}}_{E'} \underline{Z}_{1,E'E} \\ &\simeq \sum_{E \in \mathbf{E}} \mu_E^2 \underline{Z}_{2,E} + \sum_{E \in \mathbf{E}} \sum_{\substack{E' \in C_E \\ E \neq E'}} \mu_E \mu_{E'} \underline{Z}_{2,EE'} \end{aligned}$$

It follows from the Saint-Venant principle that the quadratic term of $\underline{X}_2(\mu)$ is such that $\underline{Z}_{2,EE'}$ is in practice localized over a close neighborhood of C_E . The second term is linear with respect to each parameter; more, the μ_E -contribution concerns essentially the neighborhood of C_E .

The parameter-multiscale PGD that we propose is based on these remarks. Thus we introduce two scales, micro and macro, to describe the parameter space Σ_μ . In this way, we propose as approximation:

$$\underline{X}_E(\underline{\mu}) = \sum_{i=1}^m \tilde{\underline{X}}_E^{(i)} \prod_{E'' \notin \bar{C}_E} f_{E''}^{M(i)}(\mu_{E''}) \prod_{E' \in \bar{C}_E} g_{EE'}^{m(i)}(\mu_{E'}) \tag{22}$$

where f^M and g^m are respectively “macro” and “micro” functions. \bar{C}_E denotes a chosen neighborhood of E defining the “micro” impact in space of the parameter μ_E . One can take the elements having a common point with E . Here, we will choose a linear discretization of the “macro” functions $f_{E''}^M$ and thus consider only their value on two points, $\mu_{E''} = \{\pm 1/2\}$.

However, there is a difficulty: $\underline{X}(\mu)$ is discontinuous from an element to another. It is removed using the so-called Weak-Trefftz Discontinuous Galerkin method (WTDG) proposed in [19] and extended to the quasistatic loadings in [18]. This approach is introduced in the next paragraph.

3.3 The WTDG Method

The domain is still split into elements or subdomains $\Omega_E, E \in \mathbf{E}$ on which the Hooke tensor \mathbf{K}_E is constant but depends on μ_E , belonging to $[-1/2, 1/2]$. The classical WTDG is modified here by adding a regularization term which assure the positivity of the operator, even if the rigidity vanishes over one or several subdomains.

The admissible space associated to $E \in \mathbf{E}$ is denoted: $\mathcal{W}_{E,ad}^{h,\mu}$ and the associated vectorial space: $\mathcal{W}_{E,0}^{h,\mu}$.

The problem to solve is then:

Find $\underline{U}_E \in \mathcal{U}_{E,ad}^{h,\mu}$, $E \in \mathbf{E}$ such that $\forall \underline{U}_E^* \in \mathcal{U}_{E,0}^{h,\mu}$ one has:

$$\begin{aligned} \forall \underline{\mu} \in \Sigma_\mu \sum_{E \in \mathbf{E}} \left[\sum_{E' \in \bar{C}_E} \left[\int_{\Gamma_{EE'}} dS \left[(\underline{\sigma}_n + \underline{\sigma}'_n) \cdot \frac{(\underline{U}^* + \underline{U}'^*)}{2} + (\underline{U} - \underline{U}') \cdot \frac{(\underline{\sigma}^*_n - \underline{\sigma}'^*_n)}{2} \right. \right. \right. \\ \left. \left. \left. + k(\underline{U} - \underline{U}') \cdot (\underline{U}^* - \underline{U}'^*) \right] \right] - \frac{1}{2} \int_{\Omega_E} \left[(\underline{\text{div}}(\underline{\sigma}) + \underline{f}_d) \cdot \underline{U}^* + \underline{\text{div}}(\underline{\sigma}^*) \cdot \underline{U} \right] d\Omega \\ + \sum_{\Gamma_{EE} \subset \partial_1 \Omega} \int_{\Gamma_{EE}} \left[(\underline{U} - \underline{U}_d) \cdot \underline{\sigma}^*_n + k(\underline{U} - \underline{U}_d) \cdot \underline{U}^* \right] dS \\ + \sum_{\Gamma_{EE} \subset \partial_2 \Omega} \int_{\Gamma_{EE}} \left[(\underline{\sigma}_n - \underline{F}_d) \cdot \underline{U}^* \right] dS \right] = 0 \end{aligned} \quad (23)$$

with $\underline{\sigma} = \mathbf{K}\varepsilon(\underline{U})$. $\Gamma_{EE'}$ is the common boundary of two adjacent subdomain E and E' ; Γ_{EE} is the common boundary of Ω_E and $\partial\Omega$. One consider here approximations such that the interior equation

$$\underline{\text{div}}(\underline{\sigma}) + \underline{f}_d = 0$$

is satisfied in an average sense, i.e. in resultant and moment over Ω_E . Two elements WP1 and WP2 can be easily associated to the classical elements P1 and P2. With these elements, one gets a coercivity property leading to the unicity of the solution [17].

On each element E , the WTDG leads to a contribution:

$$\sum_{E' \in \bar{C}^E} \mathbf{A}_{EE'} \underline{X}^{E'}$$

The symmetric part is \mathbf{A}_E and its value for $\underline{\mu} = \underline{0}$ is \mathbf{A}_E^0 . The generalized force given by the WTDG is then:

$$\mathbf{A} \sum_{E' \in \bar{C}^E} \mathbf{A}_{EE'} \underline{X}^{E'}$$

3.4 Computational Method

3.4.1 Basic Operators

- Computation of $\mathbf{I}_E(\underline{R}^E) \equiv \underline{\tilde{Z}}^E \in \mathbb{R}^n$

\underline{R} is a known residual, the contribution to the subdomains $E \in \mathbf{E}$ being \underline{R}^E . One computes here a search direction in space using as conditioner the symmetric operator \mathbf{A}_E^0 .

Let be $(\gamma^E(\underline{\mu}), \underline{\tilde{Z}}^E) \in \mathbb{R} \times \mathbb{R}^n$; the corresponding space is $\mathbf{I} \times \mathbb{R}^n$. One defines:

$$(\gamma^E(\underline{\mu}), \tilde{\underline{Z}}^E) = \arg \left[\min_{\gamma' \in \Gamma, \tilde{\underline{Z}}' \in \mathbb{R}^n} \left\langle (\underline{R}^E - \gamma' \mathbf{A}_E^0 \tilde{\underline{Z}}') \mathbf{A}_E^{0-1} (\underline{R}^E - \gamma' \mathbf{A}_E^0 \tilde{\underline{Z}}') \right\rangle \right]$$

where $\langle \bullet \rangle = \int_{\Sigma_\mu} \bullet d\mu$

It follows:

$$\tilde{\underline{Z}}^E = \arg \max_{\tilde{\underline{Z}}' \in \mathbb{R}^n, \tilde{\underline{Z}}'^T \mathbf{A}_E^0 \tilde{\underline{Z}}' = 1} \tilde{\underline{Z}}'^T \left\langle \underline{R}^{ET} \underline{R}^E \right\rangle \tilde{\underline{Z}}'$$

The $\underline{\mu}$ -integration can be done using the macro description.

- Computation of the extension $\tilde{\underline{X}} = \mathbf{A} \underline{a}_E \tilde{\underline{Z}}^E$ with $\underline{a} = \mathbf{J}(\underline{R}, \tilde{\underline{Z}})$

From $\tilde{\underline{Z}}^E$, $E \in \mathbf{E}$, ones defines a space search direction over Ω . One has:

$$(a_E, E \in \mathbf{E}) = \arg \left[\min_{\gamma' \in \Gamma, a'_E \in \mathbb{R}} \sum_{E \in \mathbf{E}} \left\langle (\underline{R}^E - \gamma' a'_E \mathbf{A}_E^0 \tilde{\underline{Z}}^E) \mathbf{A}_E^{0-1} (\underline{R}^E - \gamma' a'_E \mathbf{A}_E^0 \tilde{\underline{Z}}^E) \right\rangle \right]$$

which is equivalent to find the maximum of the Rayleigh quotient:

$$\frac{\underline{a}^T \mathbf{M} \underline{a}}{\underline{a}^T \underline{a}}$$

which is relatively easy to compute.

- Computation of the “macro” functions $f^M = \mathbf{K}(\underline{R}, \tilde{\underline{X}})$
- One minimize the residual:

$$f^M = \arg \left[\min_{f' \in \Gamma^M} \sum_{E \in \mathbf{E}} \left\langle (\underline{R}^E - [\mathbf{A}(f' \tilde{\underline{X}})]_{|E})^T \mathbf{A}_E^{0-1} (\underline{R}^E - [\mathbf{A}(f' \tilde{\underline{X}})]_{|E}) \right\rangle \right]$$

and then

$$f^M = \arg \left[\max_{f' \in \Gamma} \mathcal{R}(f') \right]$$

where

$$\mathcal{R}(f) \equiv \frac{\left\langle f \sum_{E \in \mathbf{E}} \underline{R}^{ET} \mathbf{A}_E^{0-1} \tilde{\underline{X}}^E \right\rangle}{\left\langle f^2 [\mathbf{A}(\tilde{\underline{X}})]_{|E}^T \mathbf{A}_E^{0-1} [\mathbf{A}(\tilde{\underline{X}})]_{|E} \right\rangle}$$

The classical PGD technique is used with for example two complete iterations over the parameter space.

- Computation of the “micro” functions $\{g^{EE'}, E' \in \overline{C}_E\} = \mathbf{L}_E(\underline{R}, \underline{\tilde{X}}, f^M)$

Let us consider that the initial residual is:

$$\underline{R}^0 = \underline{R} - \mathbf{A}(f^M \underline{\tilde{X}})$$

One introduces a new approximation which is equal to $f^M \underline{\tilde{X}}$ over the complementary part of \overline{C}_E :

$$\gamma^E(\underline{\mu}) = f^M(\underline{\mu}) \prod_{E' \in C_E} \frac{g^{EE'}(\mu_{E'})}{f_{E'}^M(\mu_{E'})}$$

This residual minimization problem which is here a small problem is solved classically.

3.4.2 Computational Strategy

The computational strategy uses error indicators as:

- Global error: $\epsilon_n = \frac{|||(\underline{F}_d - \mathbf{A}\underline{X}^n)|||}{|||\underline{F}_d|||}$
- Norm of the residual $\underline{R}^{E,n}$: $r_{E,n} = \frac{|||\underline{R}^{E,n}|||_E}{\sup_{E \in \mathbb{E}} |||\underline{F}_d|||_E}$

where $|||\bullet|||_E^2 = \langle \bullet, {}^T \mathbf{A}_E^{0-1} \bullet \rangle$

The optimal computational strategy is under study. More details can be found in [17, 25].

3.5 A First Illustration

The parameter-multiscale PGD has been implemented on a monodimensional example. A displacement is imposed at the extremity of a cantilever beam and each element has an independent Young modulus. A solution for a random set of parameters can be seen Fig. 9. This one-dimension example respects the Saint-Venant principle in stress, but not in displacement, requiring the addition of a rigid-body displacement associated to each micro function. This specificity will disappear in a two or three dimensional space.

First, we have computed the errors associated to the different approximations following the development (21) in the case where the variations of E are $\pm 50\%$. Let us introduce the following norms and errors which are E -independent for the studied problem:

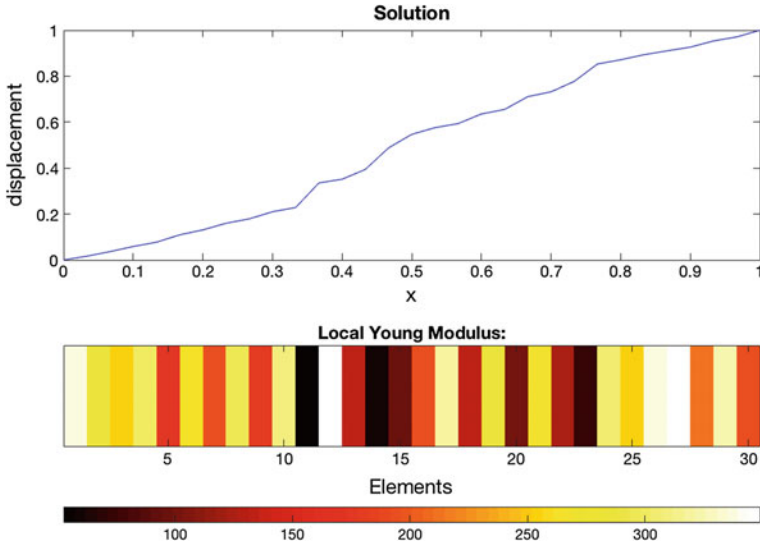


Fig. 9 Displacement in a beam, each element has an independent and random Young Modulus

$$\begin{aligned} \bullet \quad \varepsilon^2 &= \frac{\sup_{E \in \mathbb{E}} \int_{\Sigma_\mu} \|\sigma_{ex} - \sigma\|_E^2 d\mu}{\sup_{E \in \mathbb{E}} \int_{\Sigma_\mu} \|\sigma_{ex}\|_E^2 d\mu} \\ \bullet \quad \bar{\varepsilon}^2 &= \frac{\sup_{\mu \in \Sigma_\mu, E \in \mathbb{E}} \|\sigma_{ex} - \sigma\|_E^2}{\sup_{\mu \in \Sigma_\mu, E \in \mathbb{E}} \|\sigma_{ex}\|_E^2} \end{aligned}$$

with $\|\sigma\|_E^2 = \int_E \frac{1}{E_0} \sigma(\underline{U})^2 dx$

One gets:

- 0-order approximation: $\bar{\varepsilon} = 0.5 \quad \varepsilon = 0.29$
- 1-order approximation: $\bar{\varepsilon} = 0.25 \quad \varepsilon = 0.10$
- 2-order approximation: $\bar{\varepsilon} = 0.11 \quad \varepsilon = 0.042$

Then, the parameter-multiscale PGD has been implemented with the following strategy on a problem involving 64 parameters. For each element, one starts the computation with a micro-function corrected by a macro-one. The error at this stage is already small:

- $\bar{\varepsilon} = 0.12 \quad \varepsilon = 0.07$

Let us note that such an approximation gives the same error for any number of parameters. After introducing macro-functions, the error continues to decrease but slowly.

4 Conclusion

The parameter-multiscale PGD seems to be a very promising way to built reduced order model for problems involving a large number of parameters. Further work will be devoted to the derivation of verification tools and to the extension to nonlinear problems such as viscoplastic ones.

References

1. A. Ammar, B. Mokdad, F. Chinesta, R. Keunings, A new family of solvers for some classes of multidimensional partial differential equations encountered in kinetic theory modelling of complex fluids. Part II: Transient simulation using space-time separated representations. *J. Non-Newton. Fluid Mech.* **144**(2–3), 98–121 (2007)
2. M. Barrault, Y. Maday, N.C. Nguyen, A.T. Patera, An ‘empirical interpolation’ method: application to efficient reduced-basis discretization of partial differential equations. *C. R. Math.* **339**(9), 667–672 (2004)
3. M. Billaud-Friess, A. Nouy, O. Zahm, A tensor approximation method based on ideal minimal residual formulations for the solution of high-dimensional problems. *ESAIM. Math. Mode. Numer. Anal.* **48**(6), 1777–1806 (2014)
4. M. Capaldo, P.-A. Guidault, D. Néron, P. Ladevèze, The Reference Point Method, a "hyper-reduction" technique: application to PGD-based nonlinear model reduction. *Comput. Method. Appl. Mech. Eng.* **322**, 483–514 (2017)
5. S. Chaturantabut, D.C. Sorensen, Nonlinear model reduction via discrete empirical interpolation. *SIAM J. Sci. Comput.* **32**(5), 2737–2764 (2010)
6. F. Chinesta, P. Ladevèze, (eds.) *Separated Representations and PGD-Based Model Reduction: Fundamentals and Applications*, vol. CISM 554 (Springer, 2014)
7. E. de Souza Neto, D. Peric, D.R.J. Owen, *Computational Methods for Plasticity*, vol. 55 (2008)
8. A. Falco, W. Hackbusch, A. Nouy, *Geometric Structures in Tensor Representations* (2015) pp. 1–50 (Work document)
9. W. Hackbusch, *Tensor Spaces and Numerical Tensor Calculus* (Springer, 2012)
10. J.A. Hernandez, J. Oliver, A.E. Huespe, M.A. Caicedo, J.C. Cante, High-performance model reduction techniques in computational multiscale homogenization. *Comput. Methods Appl. Mech. Eng.* **276**, 149–189 (2014)
11. C. Heyberger, P.A. Boucard, D. Néron, A rational strategy for the resolution of parametrized problems in the PGD framework. *Comput. Methods Appl. Mech. Eng.* **259**, 40–49 (2013)
12. S. Holtz, T. Rohwedder, R. Schneider, On manifolds of tensors of fixed TT-rank. *Numer. Math.* **120**(4), 701–731 (2012)
13. P. Ladevèze, On Algorithm Family in Structural Mechanics. *Comptes rendus des séances de l’Academie des sciences. Série 2*, **300**(2) (1985)
14. P. Ladevèze, The large time increment method for the analyse of structures with nonlinear constitutive relation described by internal variables. *Comptes rendus des séances de l’Academie des sciences. Série 2*, **309**(2), 1095–1099 (1989) (in french)
15. P. Ladevèze, *Nonlinear Computational Structural Mechanics: New Approaches and Non-incremental Methods of Calculation* (Springer, New York, 1999)
16. P. Ladevèze, New variational formulations for discontinuous approximations. Technical Report, LMT Cachan, 2011, (in french)
17. P. Ladevèze, A new method for the ROM computation: the parameter-multiscale PGD, Technical report, LMT Cachan, 2016a, (in french)
18. P. Ladevèze, On reduced models in nonlinear solid mechanics. *Eur. J. Mech. A/Solids* **60**, 227–237 (2016b)

19. P. Ladevèze, J.C. Passieux, D. Néron, The LATIN multiscale computational method and the proper generalized decomposition. *Comput. Methods Appl. Mech. Eng.* **199**(21–22), 1287–1296 (2010)
20. P. Ladevèze, H. Riou, On Trefftz and weak Trefftz discontinuous Galerkin approaches for medium-frequency acoustics. *Comput. Methods Appl. Mech. Eng.* **278**, 729–743 (2014)
21. E. Monteiro, J. Yvonnet, Q.C. He, Computational homogenization for nonlinear conduction in heterogeneous materials using model reduction. *Comput. Mater. Sci.* **42**(4), 704–712 (2008)
22. D. Néron, P.A. Boucard, N. Relun, Time-space PGD for the rapid solution of 3D nonlinear parametrized problems in the many-query context. *Int. J. Numer. Methods Eng.* **103**(4), 275–292 (2015)
23. A. Nouy, A priori model reduction through proper generalized decomposition for solving time-dependent partial differential equations. *Comput. Methods Appl. Mech. Eng.* **199**(23–24), 1603–1626 (2010)
24. I.V. Oseledets, Tensor-train decomposition. *SIAM J. Sci. Comput.* **33**(5), 2295–2317 (2011)
25. C. Paillet, P. Ladevèze, D. Néron, A Parametric-multiscale PGD for problems with a large number of parameters (2017) (In preparation)
26. A. Radermacher, S. Reese, POD-based model reduction with empirical interpolation applied to nonlinear elasticity. *Int. J. Numer. Methods Eng.* **107**(6), 477–495 (2016)
27. N. Relun, D. Néron, P.A. Boucard, A model reduction technique based on the PGD for elastic-viscoplastic computational analysis. *Comput. Mech.* **51**(1), 83–92 (2013)
28. D. Ryckelynck, Hyper-reduction of mechanical models involving internal variables. *Int. J. Numer. Methods Eng.* **77**(1), 75–89 (2009)

Data-Driven Self-consistent Clustering Analysis of Heterogeneous Materials with Crystal Plasticity

Zeliang Liu, Orion L. Kafka, Cheng Yu and Wing Kam Liu

1 Introduction

To analyze complex, heterogeneous materials, a fast and accurate method is needed. This means going beyond the classical finite element method, in a search for the ability to compute, with modest computational resources, solutions previously infeasible even with large cluster computers. In particular, this advance is motivated by composites design. Here, we apply similar principle to another complex, heterogeneous system: additively manufactured metals.

The complexities and potential benefits of metal additive manufacturing (AM) provide a rich basis for development of mechanistic material models (e.g. [21]). These models are typically based on finite element modeling of metal plasticity, where Owen has made fundamental contributions. Powder-bed AM uses a high-power laser or electron beam to melt powder layer-by-layer to produce freeform geometries specified by 3D model files [7]. This approach removes the need for special tooling, allowing for rapid and customized part and product realization. It introduces new possibilities for topological and material optimization, but these tasks require a high degree of knowledge and ability to apply that knowledge, viz. control the build conditions sufficiently. The process involves intense and repeated

Z. Liu

Theoretical and Applied Mechanics, Northwestern University, Evanston, USA
e-mail: zeliangliu2017@u.northwestern.edu

O.L. Kafka · C. Yu · W.K. Liu (✉)

Department of Mechanical Engineering, Northwestern University, Evanston, USA
e-mail: w-liu@northwestern.edu

O.L. Kafka

e-mail: olkafka@u.northwestern.edu

C. Yu

e-mail: chengyu2015@u.northwestern.edu

localized energy input, which results in inhomogeneous, anisotropic, location-dependent material properties with complex microstructures.

This work will present a grain-level crystal plasticity model to capture local microstructures such as those that occur in AM—e.g. voids and columnar grains; however, a recently introduced material modeling approach, based on the theories of data mining and originally developed for composites, will be used to vastly increase the speed of these simulations. This will allow for higher detail or larger regions of interest, both of which are desirable for predicting damage and fatigue initiation within a part.

The perpetual challenge in multiscale modeling is predicting macroscopic behavior from microstructure conformation and properties in both an efficient and accurate manner. Analytical approaches such as the rule of mixtures and other micromechanics methods [4–6, 11, 13] are very efficient but lose accuracy particularly when dealing with irregular morphologies and nonlinear properties. In contrast, direct numerical simulations (DNS) [1], offer high accuracy at the expense of prohibitive computational costs to the point where they are inapplicable to concurrent simulations for material design. Recently, data mining has been introduced into the mechanics community to address the limitations of DNS and analytical methods.

In general, data mining is a computational process of discovering patterns in large data sets. Once extracted, these patterns can be used to predict future events. Machine learning methods are the technical basis for data mining, such as clustering and regression methods [9, 24]. Recently, data mining has also been applied to the modeling of heterogeneous materials. As a start, a raw dataset for learning is usually generated from a priori numerical simulations or informed by experiments. Depending on the type of the raw dataset, current data-driven modeling methods can be mainly divided into macroscopic and microscopic approaches.

In *macroscopic approaches*, the input data are usually material properties of each constituent, loading conditions and statistical descriptors that represent the geometry of the microstructures, while the output data are macroscopic mechanical properties from direct numerical simulations (DNS). For instance, Yvonnet et al. use tensor decomposition and neural networks to interpolate the macroscopic effective strain energy density function in [9, 24]. Bessa et al. integrate design of experiment (DoE) and machine learning tools, such as kriging and neural networks, to find the structure-property relationship for hyperelastic and plastic materials [2]. However, the accuracy and smoothness of the prediction of macroscopic approaches is limited by a lack of microscopic information. For example, the localized plastic strain fields, critical for plasticity and damage prediction theories, cannot be well represented by their field averages.

To address this problem, *microscopic approaches* collect data at each discretization point in the DNS. Two methods for making predictions based on gathered local data are worth highlighting: (1) non-uniform transformation field analysis (NTFA) [16, 17, 20, 23] and (2) variants of the proper orthogonal decomposition (POD) [8, 23] method. For both approaches, the predictions under a loading condition are obtained by linear combinations of a finite number of RVE modes from previously completed simulations under various load conditions. Linear combination of eigen-

modes is well established, but extra effort is required for the interpolation for non-linear materials. For NTFA, specific evolution laws of internal variables have to be assumed for each mode of the inelastic field. For POD-based methods, extensive simulations a priori are needed in order to guarantee the robustness of the interpolation under arbitrary loading conditions. However, this still results in an overall decrease in computational cost.

The current work is based on a two-stage approach that uses clustering and subsequent analysis of deformation and can account for heterogeneous material behavior with high accuracy and speed [13]. This method is called self-consistent cluster analysis (SCA). It is a data-driven method designed to reduce the computational degrees of freedom (DOFs) required for predicting macroscopic behaviors of heterogeneous materials, while local information is retained based in part on clustering near features that induce large stress gradients. The basic idea is to solve the equilibrium equation, not at every material point, but on clusters of material points with similar mechanical responses by assuming that local variables of interest (e.g. elastic strain, plastic strain and stress) are uniform in each of these clusters. The two stages of the method are: offline (training or cluster) and online (prediction).

During the offline stage, material points were grouped into clusters using data mining techniques (such as k-means clustering) based on mechanical similarity. To conduct the online computation, the equilibrium equation was written in an integral form using the Green's function, known as the Lippmann-Schwinger equation. This equation was solved for each cluster using a self-consistent scheme to ensure the accuracy, where the reference stiffness was updated iteratively to be consistent with the macroscopic effective stiffness. The major advantage of SCA is that the DOFs are greatly reduced compared to DNS while retaining both local and global response information.

Here we extend this method to be applicable to crystal plasticity (CP), a class of computational plasticity problems specifically formulated to capture the deformation mechanics of crystalline solids, based on the material microstructure. Anisotropic material models such as CP have been derived for both macroscale problems, such as predicting earing during deep drawing, and microscale problems, such as the deformation of nanowires [19].

2 SCA Framework

2.1 Offline Stage: Mechanistic Material Characterization

Grouping material points with similar mechanical behavior into a single cluster is performed by domain decomposition of material points using clustering methods [14]. First, the similarity between two material points is measured by the strain concentration tensor $\mathbf{A}(\mathbf{x})$, which is defined as

$$\boldsymbol{\epsilon}^{\text{micro}}(\mathbf{x}) = \mathbf{A}(\mathbf{x}) : \boldsymbol{\epsilon}^{\text{macro}} \quad \text{in } \Omega, \quad (1)$$

where $\boldsymbol{\epsilon}^{\text{macro}}$ is the elastic macroscopic strain corresponding to the boundary conditions of the Representative Volume Element (RVE), and $\boldsymbol{\epsilon}^{\text{micro}}(\mathbf{x})$ is the elastic local strain at point \mathbf{x} in the microscale RVE domain Ω . For a 2-dimensional (2D) model, $\mathbf{A}(\mathbf{x})$ has nine independent components, requiring a set of elastic direct numerical simulations (DNS) under three orthogonal loading conditions to uniquely define. For a 3-dimensional (3D) model, $\mathbf{A}(\mathbf{x})$ has 36 independent components which are determined by DNS under six orthogonal loading conditions. Once the strain concentration tensor is computed, it is independent of the loading conditions for a linear elastic material, and its Frobenius norm is an invariant under coordinate transformation.

For overall responses of nonlinear plastic materials, we have demonstrated that the elastic strain concentration tensor is a good offline database [12]. However, if the local response is of more interest, the elastic strain concentration tensor often does not provide high enough cluster density near the high strain concentration region. In polycrystalline material with crystal plasticity, all the crystals deform uniformly in the elastic regime, providing no effective data for computing the strain concentration tensor. In these cases, one can choose other types of material responses to construct the offline data, and thus achieve adequate resolution at the region of interest. For example, we choose the plastic strain tensor from DNS calculations for clustering when local plasticity information is required, such as for predicting fatigue initiation. In Sect. 4, we will show how the choice of different material responses affect overall response prediction.

The k-means clustering method [22] is used to group data points based on a grouping metric. For present, let us consider this to be the strain concentration tensor $\mathbf{A}(\mathbf{x})$. Since all the material points in a cluster are assumed to have the same mechanical response, the number of the degrees of freedom is reduced from, e.g., the number of elements in a FEM simulation to the number of clusters. Note that clusters are formed based on the strain concentration tensor and thus do not need to be spatially adjacent to each other.

A primary assumption associated with the domain decomposition is that any local variable $\boldsymbol{\beta}(\mathbf{x})$ is uniform within each cluster. Globally, this is equivalent to having a piece-wise uniform profile of the variable in the RVE:

$$\boldsymbol{\beta}(\mathbf{x}) = \sum_{l=1}^k \boldsymbol{\beta}^l \chi^l(\mathbf{x}), \quad (2)$$

where $\boldsymbol{\beta}^l$ is the homogeneous variable in the l th cluster, and k is the total number of clusters in the RVE. The domain of the l th cluster Ω^l is distinguished by its characteristic function $\chi^l(\mathbf{x})$, which is defined as

$$\chi^l(\mathbf{x}) = \begin{cases} 1 & \text{if } \mathbf{x} \in \Omega^l \\ 0 & \text{otherwise} \end{cases}. \quad (3)$$

This piecewise uniform approximation in Eq. (2) enables us to reduce the number of degrees of freedom for the Lippmann-Schwinger equation, which is solved in the following online stage (see Sect. 2.2). After the domain decomposition based on a prior DNS, the remaining task in the offline stage is to pre-compute the interaction tensors between all the clusters.

In the discretized/reduced Lippmann-Schwinger equation, we can utilize the piecewise uniform assumption to extract the interaction tensor \mathbf{D}^J , which represents the influence of the stress in the J th cluster on the strain in the I th cluster [12]. In an RVE domain Ω with periodic boundary conditions, the interaction tensor can be written as a convolution of the Green's function and the characteristic functions defined in Eq. (3):

$$\mathbf{D}^J = \frac{1}{c^J |\Omega|} \int_{\Omega} \int_{\Omega} \chi^J(\mathbf{x}) \chi^J(\mathbf{x}') \Phi^0(\mathbf{x}, \mathbf{x}') d\mathbf{x}' d\mathbf{x}, \quad (4)$$

where c^J is the volume fraction of the I th cluster and $|\Omega|$ is the volume of the RVE domain. $\Phi^0(\mathbf{x}, \mathbf{x}')$ is the fourth-order periodic Green's function associated with an isotropic linear elastic reference material and its stiffness tensor is \mathbf{C}^0 . Specifically, this reference material is introduced in the online stage as a homogeneous media to formulate the Lippmann-Schwinger integral equation. With the periodicity of the RVE, $\Phi^0(\mathbf{x}, \mathbf{x}')$ takes the following form in the Fourier space,

$$\hat{\Phi}^0(\xi) = \frac{1}{4\mu^0} \hat{\Phi}^1(\xi) + \frac{\lambda^0 + \mu^0}{\mu^0(\lambda^0 + 2\mu^0)} \hat{\Phi}^2(\xi), \quad (5)$$

with

$$\hat{\Phi}_{ijkl}^1(\xi) = \frac{1}{|\xi|^2} (\delta_{ik}\xi_j\xi_l + \delta_{il}\xi_j\xi_k + \delta_{jl}\xi_i\xi_k + \delta_{jk}\xi_i\xi_l) \quad (6)$$

$$\hat{\Phi}_{ijkl}^2(\xi) = -\frac{\xi_i\xi_j\xi_k\xi_l}{|\xi|^4}, \quad (7)$$

where ξ is the coordinate in Fourier space corresponding to \mathbf{x} in real space, and δ_{ij} is the Kronecker delta function. λ^0 and μ^0 are Lamé constants of the reference material. The expression of $\hat{\Phi}_{ijkl}^0(\xi)$ is not well defined at frequency point $\xi = \mathbf{0}$. However, by imposing the boundary conditions for deriving the Green's function, a uniformly distributed polarization stress field will not induce any strain field inside the RVE. As a result, we have

$$\hat{\Phi}_{ijkl}^0(\xi = \mathbf{0}) = \mathbf{0}. \quad (8)$$

Based on Eq. (5), the convolution term in the spatial domain in Eq. (4) can be translated into a direct multiplication at each point ξ in the frequency domain using a Fourier transformation,

$$\bar{\Phi}_j^0(\mathbf{x}) = \int_{\Omega} \chi^j(\mathbf{x}') \Phi^0(\mathbf{x}, \mathbf{x}') d\mathbf{x}' = \mathcal{F}^{-1} \left(\hat{\chi}^j(\xi) \hat{\Phi}^0(\xi) \right). \quad (9)$$

As we can see from Eq. (6), $\hat{\Phi}^1(\xi)$ and $\hat{\Phi}^2(\xi)$ are independent of the material properties, so that they can be computed once, in the offline stage. If the reference material is changed in the self-consistent scheme during the online stage only the coefficients relating to the reference Lamé constants in Eq. (5) need to be updated. For RVEs with microstructure size close to the RVE size or even with a connected microstructure network, such as a woven composite, a correction of \mathbf{D}^J is needed to satisfy the boundary conditions on the RVE.

Currently, we have applied the SCA offline stage to 2D and 3D materials with uniform (regular hexahedral or “voxel”) meshes, so that the Fast Fourier transformation (FFT) method can be used for efficiently computing Eq. (9). Although the domain decomposition is based on a specific selection of properties for each material phase in the offline stage, the same database can be used for predicting responses for new combinations of material constituents in the online stage.

2.2 Online Stage: Self-consistent Lippmann-Schwinger Equation

As discussed in [12], the equilibrium condition in the RVE can be rewritten as a continuous Lippmann-Schwinger integral equation by introducing a homogeneous reference material,

$$\Delta\epsilon(\mathbf{x}) + \int_{\Omega} \Phi^0(\mathbf{x}, \mathbf{x}') : [\Delta\sigma(\mathbf{x}') - \mathbf{C}^0 : \Delta\epsilon(\mathbf{x}')] d\mathbf{x}' - \Delta\epsilon^0 = \mathbf{0}, \quad (10)$$

where $\Delta\epsilon^0$ is the far-field strain increment controlling the evolution of the local strain. It is uniform in the RVE. The reference material is isotropic and linear elastic. Its stiffness tensor \mathbf{C}^0 can be determined by the two independent Lamé parameters λ^0 and μ^0 ,

$$\mathbf{C}^0 = \mathbf{f}(\lambda^0, \mu^0) = \lambda^0 \mathbf{I} \otimes \mathbf{I} + \mu^0 \mathbf{II}. \quad (11)$$

where \mathbf{I} is the second-rank identity tensor, and \mathbf{II} is the symmetric part of the fourth-rank identity tensor. The strain and stress increments are $\Delta\epsilon(\mathbf{x})$ and $\Delta\sigma(\mathbf{x})$. By averaging the incremental integral equation, Eq. (10), in the RVE domain Ω , we have

$$\frac{1}{|\Omega|} \int_{\Omega} \Delta\epsilon(\mathbf{x}) d\mathbf{x} + \frac{1}{|\Omega|} \int_{\Omega} \left[\int_{\Omega} \Phi^0(\mathbf{x}, \mathbf{x}') d\mathbf{x} \right] : [\Delta\sigma(\mathbf{x}') - \mathbf{C}^0 : \Delta\epsilon(\mathbf{x}')] d\mathbf{x}' - \Delta\epsilon^0 = \mathbf{0}. \quad (12)$$

Imposing by the boundary conditions for deriving the Green’s function, Eq. (8) can be equivalently written as

$$\int_{\Omega} \Phi^0(\mathbf{x}, \mathbf{x}') d\mathbf{x} = \mathbf{0}. \quad (13)$$

Substituting Eq. (13) into (12) gives

$$\Delta\epsilon^0 = \frac{1}{|\Omega|} \int_{\Omega} \Delta\epsilon(\mathbf{x}) d\mathbf{x}, \quad (14)$$

which indicates that the far-field strain increment is always equal to the ensemble averaged strain increment in the RVE. In order to solve $\Delta\epsilon(\mathbf{x})$ in the integral equation, Eq. (10), constraints are needed from the macroscopic boundary conditions. The macro-strain constraint can be written as

$$\frac{1}{|\Omega|} \int_{\Omega} \Delta\epsilon(\mathbf{x}) d\mathbf{x} = \Delta\bar{\epsilon}^{\text{macro}} \quad \text{or} \quad \Delta\epsilon^0 = \Delta\bar{\epsilon}^{\text{macro}}, \quad (15)$$

where $\Delta\bar{\epsilon}^{\text{macro}}$ is the macroscopic strain increment applied on the RVE. Similarly, the macro-stress constraint can be related to the macroscopic stress $\bar{\sigma}^{\text{macro}}$,

$$\frac{1}{|\Omega|} \int_{\Omega} \sigma(\mathbf{x}) d\mathbf{x} = \bar{\sigma}^{\text{macro}} \quad (16)$$

For more general cases, mixed constraints (e.g. strain constraint in the 11-direction and stress constraints for the rest) can also be formulated [12].

As the full-field calculations (e.g. FFT-based method) of the continuous Lippmann-Schwinger equation may require excessive computational resources, we will perform the discretization of the integral equation based on the domain decomposition in the offline stage. With the piecewise uniform assumption in Eq. (2), the number of degrees of freedom and the number of internal variables in the new system can be reduced. After decomposition, the discretized integral equation of the l th cluster is:

$$\Delta\epsilon^l + \sum_{J=1}^k \mathbf{D}^{lJ} : [\Delta\sigma^J - \mathbf{C}^0 : \Delta\epsilon^J] - \Delta\epsilon^0 = \mathbf{0}, \quad (17)$$

where $\Delta\epsilon^J$ and $\Delta\sigma^J$ are the strain and stress increment in the J th cluster. The interaction tensor \mathbf{D}^{lJ} is defined in Eq. (4), which is related to the Green's function of the reference material. After discretization, the far field strain is still equal to the average strain in the RVE,

$$\Delta\epsilon^0 = \sum_{l=1}^k c^l \Delta\epsilon^l. \quad (18)$$

The macroscopic boundary conditions also require discretization. For instance, the discrete form of the macro-strain constraint can be written as

$$\sum_{I=1}^k c^I \Delta \epsilon^I = \Delta \bar{\epsilon}^{\text{macro}} \quad \text{or} \quad \Delta \epsilon^0 = \Delta \bar{\epsilon}^{\text{macro}} \quad (19)$$

In the new reduced system, the unknown variables are the strain increments in each cluster $\Delta \epsilon^I$. Significantly fewer clusters than FE nodes means that the ROM is much faster to solve. In a general case such as plasticity, the stress increment $\Delta \sigma^I$ is a nonlinear function of its strain increment $\Delta \epsilon^I$, and Newton's method is used to solve the nonlinear system iteratively for each increment.

The solution of the continuous Lippmann-Schwinger equation (10) is independent of the choice of the reference material \mathbf{C}^0 . This is because the physical problem is fully described by the equilibrium condition and the prescribed macroscopic boundary conditions. However, the equilibrium condition is not strictly satisfied at every point in the RVE for the discretized equations because of the piecewise uniform assumption, and the solution of the reduced system depends on the choices of \mathbf{C}^0 . This discrepancy can be reduced by increasing the number of clusters used, at the cost of increased computational cost due to the increased degrees of freedom.

To achieve both efficiency and accuracy, we propose a self-consistent scheme in the online stage, which retains accuracy with fewer clusters. In the self-consistent scheme, the stiffness tensor of the reference material, \mathbf{C}^0 is approximately the same as the homogenized stiffness tensor $\bar{\mathbf{C}}$,

$$\mathbf{C}^0 \rightarrow \bar{\mathbf{C}}. \quad (20)$$

Material non-linearity generally makes it impossible to determine an isotropic \mathbf{C}^0 exactly matching $\bar{\mathbf{C}}$. Here we propose two types of self-consistent schemes to approximate Eq. (20): (1) linear regression of average strain increment $\Delta \bar{\epsilon}$ and stress increment $\Delta \bar{\sigma}$ (or regression-based scheme) and (2) isotropic projection of the effective stiffness tensor $\bar{\mathbf{C}}$ (or projection-based scheme).

2.2.1 Regression-Based Self-consistent Scheme

In the regression-based scheme [12], the self-consistent scheme is formulated as an optimization problem: the goal is to find an isotropic \mathbf{C}^0 that minimizes the error between the predicted average stress increments. The inputs of the regression algorithm are the average strain increment $\Delta \bar{\epsilon}$ and stress increment $\Delta \bar{\sigma}$, which are computed as

$$\Delta \bar{\epsilon} = \sum_{I=1}^k c^I \Delta \epsilon^I \quad \text{and} \quad \Delta \bar{\sigma} = \sum_{I=1}^k c^I \Delta \sigma^I \quad (21)$$

The objective of the regression-based scheme is to find the λ^0 and μ^0 of the reference material by computing

$$\{\lambda^0, \mu^0\} = \underset{\{\lambda', \mu'\}}{\operatorname{argmin}} \|\Delta\bar{\sigma} - \mathbf{f}(\lambda', \mu') : \Delta\bar{\epsilon}\|^2, \quad (22)$$

where $\|\mathbf{Z}\|^2 = \mathbf{Z} : \mathbf{Z}$ for an arbitrary second-order tensor \mathbf{Z} . The function $\mathbf{f}(\lambda', \mu')$ can be expressed as

$$\mathbf{f}(\lambda', \mu') = \lambda' \mathbf{I} \otimes \mathbf{I} + \mu' \mathbf{II}. \quad (23)$$

where \mathbf{I} is the second-rank identity tensor, and \mathbf{II} is the symmetric part of the fourth-rank identity tensor. Equivalently, the cost function $g(\lambda', \mu')$ of the optimization problem can be written as

$$g(\lambda', \mu') = \|\Delta\bar{\sigma} - \mathbf{f}(\lambda', \mu') : \Delta\bar{\epsilon}\|^2. \quad (24)$$

The optimum point is found via the respective partial derivatives of the cost function,

$$\left. \frac{\partial g}{\partial \lambda'} \right|_{\lambda^0, \mu^0} = 0 \quad \text{and} \quad \left. \frac{\partial g}{\partial \mu'} \right|_{\lambda^0, \mu^0} = 0, \quad (25)$$

which forms a system of two linear equations in terms of the Lamé constants. The system always has a unique solution except under a pure-shear loading condition, where λ^0 is under-determined. In this case, the value of λ^0 is not updated. Additionally, $g(\lambda^0, \mu^0)$ vanishes when the effective macroscopic homogeneous material is also isotropic linear elastic.

Although this scheme does not require computing $\bar{\mathbf{C}}$ explicitly, it has two main drawbacks. First, the optimization problem is under-determined for hydrostatic and pure shear loading conditions, forcing one of the two independent elastic constants to be assumed. Second and more important, the modulus of the optimum reference material may be negative for complex loading histories within a concurrent simulation, which is deleterious to the convergence of the fixed-point method. Fortunately, the regression-based scheme does not encounter any convergence problems for the examples presented in Sect. 4, which have simple loading histories.

2.2.2 Projection-Based Self-consistent Scheme

To avoid the difficulties of the regression-based scheme, we present another self-consistent scheme based on isotropic projection of the effective stiffness tensor $\bar{\mathbf{C}}$, as in [3]. Through the homogenization, the effective stiffness tensor $\bar{\mathbf{C}}$ of the RVE can be expressed as

$$\bar{\mathbf{C}} = \sum_{I=1}^k c^I \mathbf{C}_{\text{alg}}^I : \mathbf{A}^I, \quad (26)$$

where $\mathbf{C}_{\text{alg}}^I$ is the algorithm stiffness tensor of the material in the I th cluster and is an output of the local constitutive law for the current strain increment in the cluster,

$$\mathbf{C}_{\text{alg}}^I = \frac{\partial \Delta \boldsymbol{\sigma}^I}{\partial \Delta \boldsymbol{\varepsilon}^I} \quad (27)$$

The strain concentration tensor of the I th cluster \mathbf{A}^I relates the local strain increment in the I th cluster $\Delta \boldsymbol{\varepsilon}^I$ to the far-field strain increment $\Delta \boldsymbol{\varepsilon}^0$,

$$\Delta \boldsymbol{\varepsilon}^I = \mathbf{A}^I : \Delta \boldsymbol{\varepsilon}^0, \quad (28)$$

which can be determined by first linearizing the discretized integral equation (17) using $\mathbf{C}_{\text{alg}}^I$ and then inverting the Jacobian matrix. Since $\bar{\mathbf{C}}$ is only required for the self-consistent scheme, the calculation of $\bar{\mathbf{C}}$ can be performed once, after the Newton iterations have converged, to save computational cost.

For a 3D problem, the stiffness tensor of the isotropic reference material \mathbf{C}^0 can be decomposed as

$$\mathbf{C}^0 = (3\lambda^0 + 2\mu^0)\mathbf{J} + 2\mu^0\mathbf{K}, \quad (29)$$

where the forth-rank tensors \mathbf{J} and \mathbf{K} are defined as

$$\mathbf{J} = \frac{1}{3}(\mathbf{I} \otimes \mathbf{I}) \quad \text{and} \quad \mathbf{K} = \mathbf{\Pi} - \mathbf{J}. \quad (30)$$

Since the two tensors are still orthogonal, we have

$$\mathbf{J} : \mathbf{K} = 0, \quad \mathbf{J} : \mathbf{J} = 1, \quad \mathbf{K} : \mathbf{K} = 5. \quad (31)$$

Based on Eq. (31), the projection from the homogenized stiffness tensor $\bar{\mathbf{C}}$ to \mathbf{C}^0 can be expressed as

$$\mathbf{C}^0 = \bar{\mathbf{C}}^{iso} = (\mathbf{J} : \bar{\mathbf{C}})\mathbf{J} + \frac{1}{5}(\mathbf{K} : \bar{\mathbf{C}})\mathbf{K}. \quad (32)$$

Meanwhile, the Lamé parameters λ^0 and μ^0 of the reference material can also be determined from the isotropic projection. Since \mathbf{C}^0 is approximated based on $\bar{\mathbf{C}}$ directly, it is guaranteed to be positive definite the condition of $\bar{\mathbf{C}}$. Overall, the projection-based scheme can be considered a relaxation of the regression-based scheme.

2.2.3 Summary of the Online Stage

In both schemes, the optimum reference material must be determined iteratively since the values of $\bar{\mathbf{C}}$ in Eq. (26) are obtained by solving the reduced system with a previous \mathbf{C}^0 . A fix-point method is employed here. For this method, the convergence of the reference material parameters can be reached in only a few iterations in our experience (i.e. less than five reaches a tolerance of 0.001).

The general algorithm for the self-consistent schemes is shown in Box I. The relative iterative error criterion to the L2 norm of the residual is used. Detailed definitions of the residual $\{\mathbf{r}\}$ and system Jacobian $\{\mathbf{M}\}$ can be found in [12]. If all the phases of the material are linear elastic, the Newton iteration will converge in one step. Note that if the self-consistent scheme is not utilized for in the calculation, a constant stiffness tensor \mathbf{C}^0 will be used, which can be chosen to be same as the matrix material. In this case, \mathbf{C}^0 is not updated, which implies that the interaction tensors \mathbf{D}^{IJ} do not need to be updated, and steps 4–5 in Box I can also be skipped. Although the algorithm with a constant \mathbf{C}^0 can save time in terms of finding the optimum \mathbf{C}^0 , the accuracy in predict nonlinear material behavior cannot be guaranteed with a small number of clusters.

**Box I General algorithm for solving the self-consistent
Lippmann-Schwinger equation**

1. Initial conditions and initialization: set (λ^0, μ^0) ; $\{\boldsymbol{\varepsilon}\}_0 = \mathbf{0}$; $n=0$; $\{\Delta\boldsymbol{\varepsilon}\}_{\text{new}} = \mathbf{0}$
2. For loading increment $n + 1$, update the coefficients in the interaction tensor \mathbf{D}^{IJ} and the stiffness tensor of the reference material \mathbf{C}^0
3. Start Newton iterations:
 - a. compute the stress difference $\{\Delta\boldsymbol{\sigma}\}_{\text{new}}$ based on the local constitutive law
 - b. use that compute the residual of the discretized integral equation (17):
 $\{\mathbf{r}\} = \mathbf{f}(\{\Delta\boldsymbol{\varepsilon}\}_{\text{new}}, \{\Delta\boldsymbol{\sigma}\}_{\text{new}})$
 - c. compute the system Jacobian $\{\mathbf{M}\}$
 - d. solve the linear equation $\{d\boldsymbol{\varepsilon}\} = -\{\mathbf{M}\}^{-1}\{\mathbf{r}\}$
 - e. $\{\Delta\boldsymbol{\varepsilon}\}_{\text{new}} \leftarrow \{\Delta\boldsymbol{\varepsilon}\}_{\text{new}} + \{d\boldsymbol{\varepsilon}\}$
 - f. check error criterion; if not met, go to 3a.
4. Calculate (λ^0, μ^0) using the regression-based scheme (22) or the projection-based scheme (32)
5. Check error criterion; if not met, go to 2
6. Update the incremental strain and stress: $\{\Delta\boldsymbol{\varepsilon}\}_{n+1} = \{\Delta\boldsymbol{\varepsilon}\}_{\text{new}}$, $\{\Delta\boldsymbol{\sigma}\}_{n+1} = \{\Delta\boldsymbol{\sigma}\}_{\text{new}}$; Update the index of loading increment $n \leftarrow n + 1$
7. If simulation not complete, go to 2.

3 Crystal Plasticity Model

In this work we present an elasto-plastic, anisotropic, heterogeneous plasticity model of the mechanical response of crystalline materials, to be solved in the SCA framework described in Sect. 2 above. The mechanical model is an implementation of so-called crystal plasticity (CP) constitutive laws, such as outlined in the overview of Roters et al. [19]. The finite element scheme used therein to solve the variational form of the equilibrium equations is replaced with the SCA scheme and its

FFT-basis. Thus, in some regards this begins to resemble recent CP-FFT formulations (e.g. [10]), with the addition of an the offline/online decomposition outlined above.

3.1 A Brief Overview

Crystal plasticity in conjunction with the finite element method (termed CPFEM) has been applied to solve both microscopic and macroscopic problems, following from the early combinations of classical plasticity and the finite element method [18]. It has two primary variants: polycrystal and single crystal plasticity. In the polycrystal formulation, each material point is assumed to represent a collection of crystals such that the overall response of the point is homogeneous. In single crystal plasticity, each material point is assumed to represent a single crystal, or a point in a single crystal, the deformation of which is governed by the particularities of single crystal deformation mechanics (e.g. active slip systems and/or dislocation motion). The former approach is more commonly used for macroscopic problems, where a relatively large solution volume is desired. The later shall be the focus of this chapter, and has been used to solve microscopic problems, e.g. those related to void mechanics within metals. There are many versions of crystal plasticity laws in both forms. Here the basic kinematics and constitutive law of the version of McGinty and McDowell [15] are applied, and are discussed below.

3.2 Kinematics

The deformation gradient \mathbf{F} can be multiplicatively decomposed as:

$$\mathbf{F} = \mathbf{F}^e \mathbf{F}^p \quad (33)$$

where the plastic part \mathbf{F}^p maps points in the reference configuration onto an intermediate configuration which is then mapped to a current configuration through the elastic part \mathbf{F}^e . Note that physically \mathbf{F}^p is associated with the dislocation motion and \mathbf{F}^e is a combination of the elastic stretch and rigid body rotation.

The effect of dislocation motion is modeled by relating the plastic velocity gradient $\tilde{\mathbf{L}}^p$ in the intermediate configuration (usually denoted by $\tilde{\square}$) to simple shear deformation $\dot{\gamma}^{(\alpha)}$:

$$\tilde{\mathbf{L}}^p = \sum_{\alpha=1}^{N_{\text{slip}}} \dot{\gamma}^{(\alpha)} (\tilde{\mathbf{s}}^{(\alpha)} \otimes \tilde{\mathbf{n}}^{(\alpha)}) \quad (34)$$

where \otimes is the dyadic product, N_{slip} is the number of slip systems, $\dot{\gamma}^{(\alpha)}$ is a shear rate, $\tilde{\mathbf{s}}^{(\alpha)}$ is the slip direction, and $\tilde{\mathbf{n}}^{(\alpha)}$ is the slip plane normal, all for a crystal slip

systems (α) in the intermediate configuration. The relationship between $\tilde{\mathbf{L}}^p$ and \mathbf{F}^p is given by

$$\tilde{\mathbf{L}}^p = \dot{\mathbf{F}}^p \cdot (\mathbf{F}^p)^{-1}. \quad (35)$$

3.3 Constitutive Law

The final task in constructing the crystal plasticity framework is defining the constitutive laws of elasto-plasticity. We choose a basis of the Green-Lagrange strain \mathbf{E}^e and Second Piola-Kirchhoff stress \mathbf{S}^e , from the many conjugate pairs available, which are related by:

$$\mathbf{S}^e = \tilde{\mathbf{C}} \cdot \mathbf{E}^e = \frac{1}{2} \tilde{\mathbf{C}} \cdot [(\mathbf{F}^e)^T \mathbf{F}^e - \mathbf{I}], \quad (36)$$

where the elastic stiffness tensor $\tilde{\mathbf{C}}$ is defined in the intermediate configuration.

A phenomenological power law for the plastic shear rate in each slip system given by

$$\dot{\gamma}^{(\alpha)} = \dot{\gamma}_0 \left| \frac{\tau^{(\alpha)} - a^{(\alpha)}}{\tau_0^{(\alpha)}} \right|^{(m-1)} \left(\frac{\tau^{(\alpha)} - a^{(\alpha)}}{\tau_0^{(\alpha)}} \right) \quad (37)$$

is used, where $\tau^{(\alpha)}$ is the resolved shear stress, $a^{(\alpha)}$ is a backstress that describes kinematic hardening, $\dot{\gamma}_0$ is a reference shear rate, $\tau_0^{(\alpha)}$ is a reference shear stress that accounts for isotropic hardening, and m is the material strain rate sensitivity. Shear stress is resolved onto the slip directions with:

$$\tau^{(\alpha)} = \boldsymbol{\sigma} : (\mathbf{s}^{(\alpha)} \otimes \mathbf{n}^{(\alpha)}), \quad (38)$$

where $\boldsymbol{\sigma}$, $\mathbf{s}^{(\alpha)}$ and $\mathbf{n}^{(\alpha)}$ are the Cauchy stress, slip direction and slip plane normal respectively, all of which are in the current configuration. The Cauchy stress is given by:

$$\boldsymbol{\sigma} = \frac{1}{J_e} [\mathbf{F}^e \cdot \mathbf{S}^e \cdot (\mathbf{F}^e)^T], \quad (39)$$

where J_e is the determinant of \mathbf{F}^e . The relationship between $\mathbf{s}^{(\alpha)}$ and $\tilde{\mathbf{s}}^{(\alpha)}$ is given by

$$\mathbf{s}^{(\alpha)} = \mathbf{F}^e \cdot \tilde{\mathbf{s}}^{(\alpha)}, \quad (40)$$

and the relationship between $\mathbf{n}^{(\alpha)}$ and $\tilde{\mathbf{n}}^{(\alpha)}$ is given by

$$\mathbf{n}^{(\alpha)} = \tilde{\mathbf{n}}^{(\alpha)} \cdot (\mathbf{F}^e)^{-1}, \quad (41)$$

which ensures that the slip plane normal vector remains orthogonal to the slip direction in the current configuration.

The reference shear stress $\tau_0^{(\alpha)}$ evolves based on the expression:

$$\dot{\tau}_0^{(\alpha)} = H \sum_{\beta=1}^{N_{\text{slip}}} q^{\alpha\beta} \dot{\gamma}^{(\beta)} - R \tau_0^{(\alpha)} \sum_{\beta=1}^{N_{\text{slip}}} |\dot{\gamma}^{(\beta)}|, \quad (42)$$

where H is a direct hardening coefficient and R is a dynamic recovery coefficient and $q^{\alpha\beta}$ is the latent hardening ratio given by:

$$q^{\alpha\beta} = \chi + (1 - \chi) \delta_{\alpha\beta} \quad (43)$$

where χ is a latent hardening parameter. The backstress $a^{(\alpha)}$ evolves based on the expression:

$$\dot{a}^{(\alpha)} = h \dot{\gamma}^{(\alpha)} - r a^{(\alpha)} |\dot{\gamma}^{(\alpha)}|, \quad (44)$$

where h and r are direct and dynamic hardening factors respectively.

A computational crystal plasticity algorithm needs to solve a set of non-linear equations from Eqs. (33) to (44). Different numerical methods can be used to solve these equations. McGinty and McDowell [15] gave an implicit time integration algorithm for the material law with the finite element method. However, the SCA method uses Fast Fourier Transformation method, CP algorithms have been shown to be effective in this framework as well. For example Lebensohn et al. [10] reformulated a crystal plasticity law for a Fast Fourier Transformation framework to solve micro-mechanics problems with periodic microstructures. Here we simply implement the same crystal plasticity model in our SCA and FEM calculations, albeit with a slight variation in how the deformation gradient, \mathbf{F} , is computed.

4 Examples

In this section, three example cases probing the capabilities of SCA are implemented with the CP routine described in Sect. 3. First, the SCA method is validated for a multi-inclusion system with J_2 plasticity. Second, a simple case of a spherical inclusion in a single-crystal matrix is shown. Finally, the complexity of the system is increased by simulating a polycrystalline cube with equiaxed, randomly oriented grains.

4.1 Multi-inclusion System with J_2 plasticity

The SCA method is firstly validated for a multi-inclusion system using a much simpler material law: J_2 plasticity. The inclusion phase is elastic with Young’s modulus $E_i = 500$ MPa and Poisson’s ratio $\nu_i = 0.19$. The matrix phase is elasto-plastic with $E_m = 100$ MPa and $\nu_m = 0.3$ in the elastic regime, and it has a von Mises yield surface (J_2 plasticity) and a piece-wise hardening law depending on the effective plastic strain ϵ_p :

$$\sigma_Y(\epsilon_p) = \begin{cases} 0.5 + 5\epsilon_p & \epsilon_p \in [0, 0.04) \\ 0.7 + 2\epsilon_p & \epsilon_p \in [0.04, \infty) \end{cases} \text{ MPa.} \tag{45}$$

The inclusions are identical to each other and the volume fraction of the inclusion phase is equal to 20%. The mesh size for the high-fidelity finite element model is $80 \times 80 \times 80$. The clustering results based on the strain concentration tensor $\mathbf{A}(\mathbf{x})$ are shown in Fig. 1. Note that $\mathbf{A}(\mathbf{x})$ has 36 independent components which need to be determined by elastic simulations under 6 orthogonal loadings. Since the volume fraction of the inclusion phase is 20%, we choose $k_i = \lceil k_m/4 \rceil$, where $\lceil \square \rceil$ denotes the nearest integer greater than or equal to \square .

The stress-strain curves predicted by the regression-based and projection-based self-consistent schemes are given in Fig. 2 for uniaxial tension and pure shear

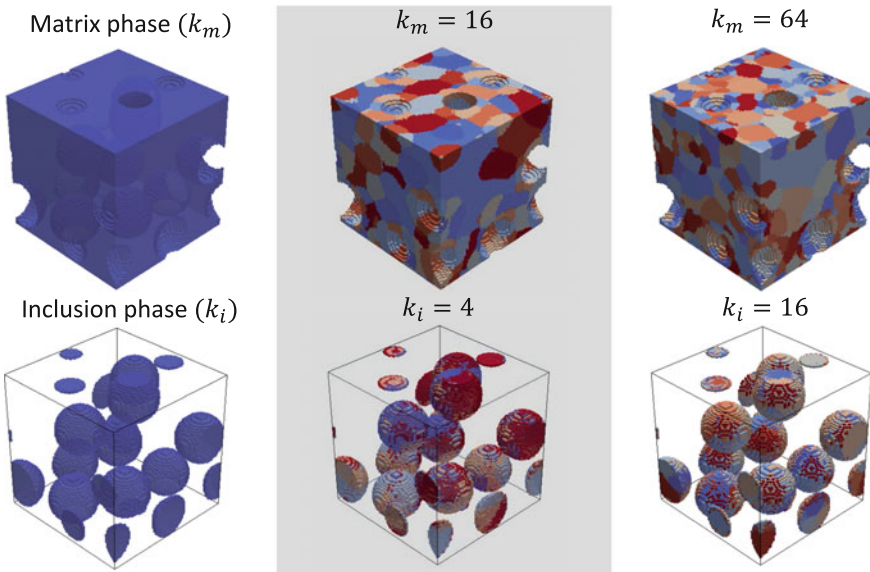


Fig. 1 Clustering results of the multi-inclusion system based on the elastic strain concentration tensor $\mathbf{A}(\mathbf{x})$. The numbers of clusters in the matrix and inclusion are denoted by k_m and k_i , respectively

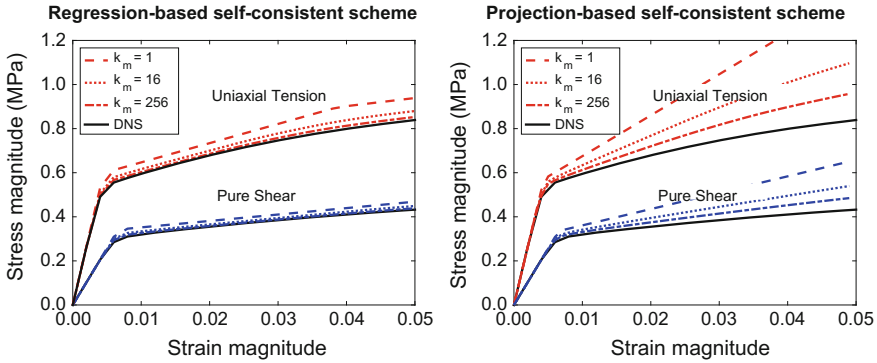


Fig. 2 Stress-strain curves under uniaxial tension and pure shear loading conditions predicted by the regression-based and projection based self-consistent scheme. The solid lines represent the DNS results for comparison

loading conditions. The DNS results are plotted as solid lines for comparison. For both schemes, the predictions converge to the DNS results by increasing the number of clusters in the system, but the regression-based scheme has a better accuracy than the one based on isotropic projection of the effective stiffness tensor. However, the accuracy of the projection-based scheme can be greatly improved through weighted projection, which will be presented in a forthcoming paper. For robustness, we will use the projection-based scheme for crystal plasticity in the following sections.

For this $80 \times 80 \times 80$ mesh, the DNS based on FEM typically takes 25 h on 24 cores (in a state-of-the-art high performance computing cluster with two 12-core/processor Intel Haswell E5-2680v3 2.5 GHz processors per compute node). With the same number of loading increments, the SCA reduced order method (in MATLAB) only takes 0.1 s, 2 s and 50 s on one Intel i7-3632 processor for $k_m = 1, 16$ and 256, respectively.

4.2 Spherical Inclusion with Crystal Plasticity

The crystal plasticity law is introduced for the simplest geometric case here, that approximating the 3D Eshelby problem: a spherical inclusion/void embedded in an infinite (periodic boundary) single-crystal matrix. A schematic of the geometry is given in Fig. 3. In the context of AM, provided in the introduction, this could be thought of as a spherical void occurring in the interior of a part. Such voids, between 1–2 microns and 50 microns diameter are often attributed to boiling and material vaporization during the build process. To model this, an nearly infinitely compressible, very low modulus material law is applied within the sphere, while the CP model is used for the matrix material. A set of crystal plasticity parameters are listed in Table 1; the Young's modulus and Poisson's ratio of the soft inclusion are 500 MPa

Fig. 3 Schematic of the simple 3D void geometry

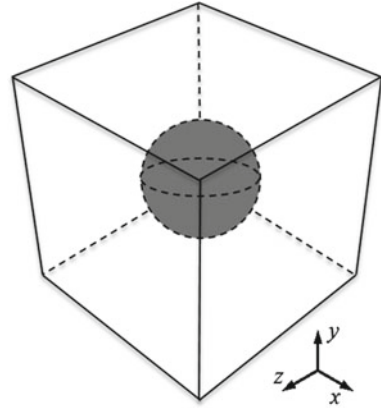


Table 1 Crystal plasticity parameters for a FCC metal

C_{1111} , MPa	C_{1122} , MPa	C_{2323} , MPa
80869	40356	20257
$\dot{\gamma}_0$, s^{-1}	m	Initial τ_0 , MPa
0.002	10	320
H , MPa	R , MPa	χ
0	0	1
Initial a_0 , MPa	h , MPa	r , MPa
0.0	500	0

and 0.19, respectively. These parameters match reasonably well with a FCC metal, though are not yet calibrated for AM materials specifically.

To solve for the overall and local response of this geometry, an appropriate choice of data for the domain decomposition stage must be made. Using the strain concentration tensor and the elastic response provides a reasonable overall match in load history to the DNS solution, but the local solution (near the inclusion) does not match well. As noted above, different variables may be used to conduct the clustering. Figure 4a shows the elastic DNS solution, and Fig. 4b shows the clusters built from the strain concentration tensor. Choosing the plastic part of the strain tensor at the onset of plasticity, contours plotted in Fig. 4c, results in the decomposition shown in Fig. 4d. This gives much higher cluster density near the inclusion, and we will show in our future work that this allows for much more accurate local solutions. Using the fully developed plastic solution, Fig. 4e, gives the clustering shown in Fig. 4d. Uniaxial tension in z direction is applied until the whole system has fully yielded. The crystal is orientated with Euler angles $\psi = 0^\circ$, $\theta = 45^\circ$, $\phi = 0^\circ$ (using the Roe convention) with respect to a coordinate system aligned with the global axes.

Once the clusters are determined, total and local solutions for stress and strain can be computed with the SCA reduced order method with crystal plasticity, denoted

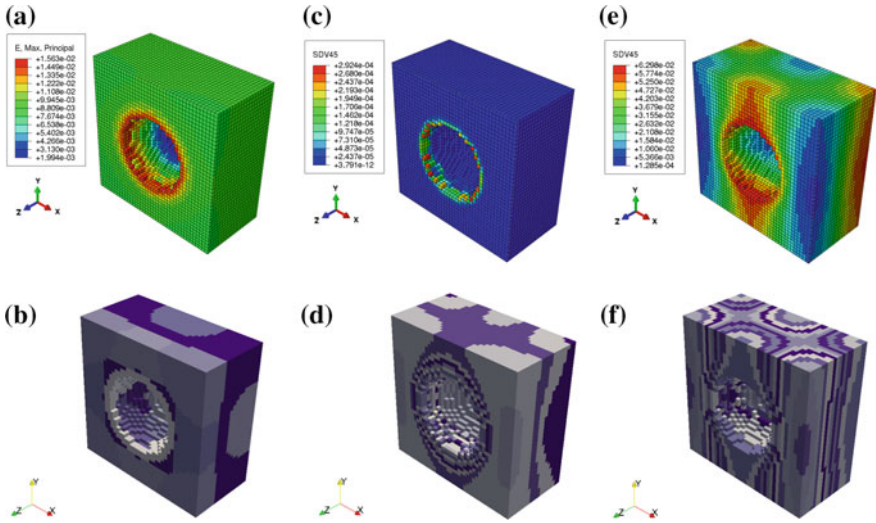


Fig. 4 RVE cut in half to show the **a** elastic region solution and **b** resulting clusters around the inclusion; **c** the solution at the onset of plasticity and **d** the resulting clusters; **e** after plasticity fully develops, **f** the resulting clusters

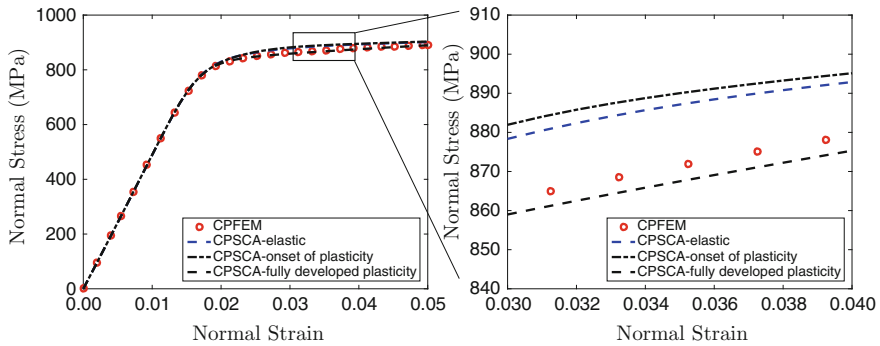


Fig. 5 Overall stress-strain response of the single inclusion, based on different choices of cluster

as CPSCA, in the online stage. The overall solution corresponding to the clustering in Fig. 4 is shown in Fig. 5. The first set of solutions match very well in the elastic region, and begins to develop a slight difference at the onset of plasticity. CPSCA based on elasticity clustering and onset plasticity clustering gives harder response while that based on fully developed plasticity has softer response compared to CPFEM results.

For this $40 \times 40 \times 40$ mesh, the DNS CPFEM implemented as a user material in Abaqus typically takes 4600 s on 24 cores. With the same number of loading increments, CPSCA (in FORTRAN) only takes 5 s on one Intel i7-3632 processor using 16 clusters in the matrix.

4.3 Polycrystalline RVE

In this section, CPSCA is used to predict the overall response of a RVE consisting of equiaxed, randomly oriented grains with the fully developed plastic strain tensor calculated a priori as offline database. An example of such a RVE is shown in Fig. 6. Figure 7 shows the comparison of overall stress strain curve predicted by CPFEM and CPSCA respectively. We see that the overall response for the coarser cases converge to very similar solutions when element or clusters are added. CPSCA results in harder response than the CPFEM solutions when very coarse clustering (e.g. 1 cluster/grain) is used. This is not an exceptional result, because SCA uses a FFT solution based on the Lippmann-Schwinger equation.

The full 3D solution state for S_{33} at 5% averaged strain is shown in the opacity and color contour plots shown in Fig. 8. With this visualization, some differences in the interior can be observed: in the CPSCA method, stress is generally more concentrated, and lower outside of the concentration region, when compared to the CPFEM solutions with more distributed and generally higher levels of overall stress. In both solution methods and with all mesh sizes and number of clusters, stress concentrates in grains with high Schmid factor. The peak values for the FEM and SCA solutions are generally within 10%, while the minimum values differ by more.

Again, the DNS CPFEM implemented as a user material in Abaqus typically takes 587, 5177, and 31446 s for the $20 \times 20 \times 20$, $30 \times 30 \times 30$ and $40 \times 40 \times 40$ mesh respectively, on 24 cores. With the same number of loading increments, CPSCA (in FORTRAN) only takes 18, 96 and 793 s using 1 cluster/grain, 2 clusters/grain and 4 clusters/grain respectively on one Intel i7-3632 processor.

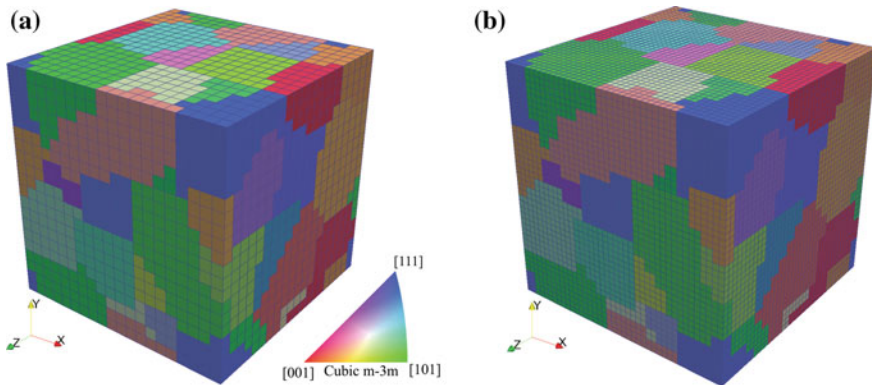


Fig. 6 RVE consisting of 35 equiaxed, randomly oriented grains (as shown by the inverse pole figure color map) with **a** $20 \times 20 \times 20$ and **b** $40 \times 40 \times 40$ voxel mesh

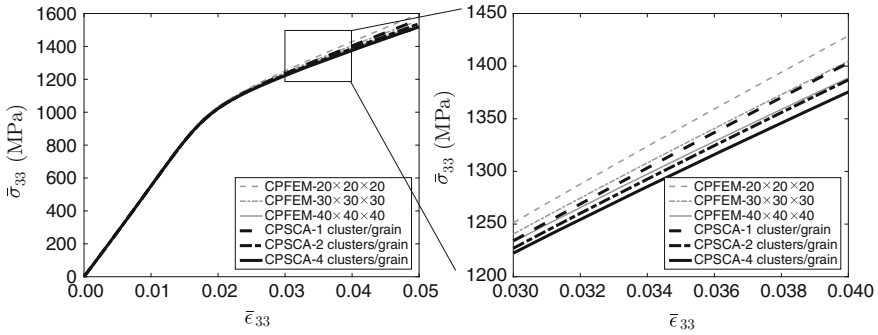


Fig. 7 $\bar{\sigma}_{33}$ versus $\bar{\epsilon}_{33}$ using CPFEM and CPSCA respectively, showing convergence with mesh size and number of clusters

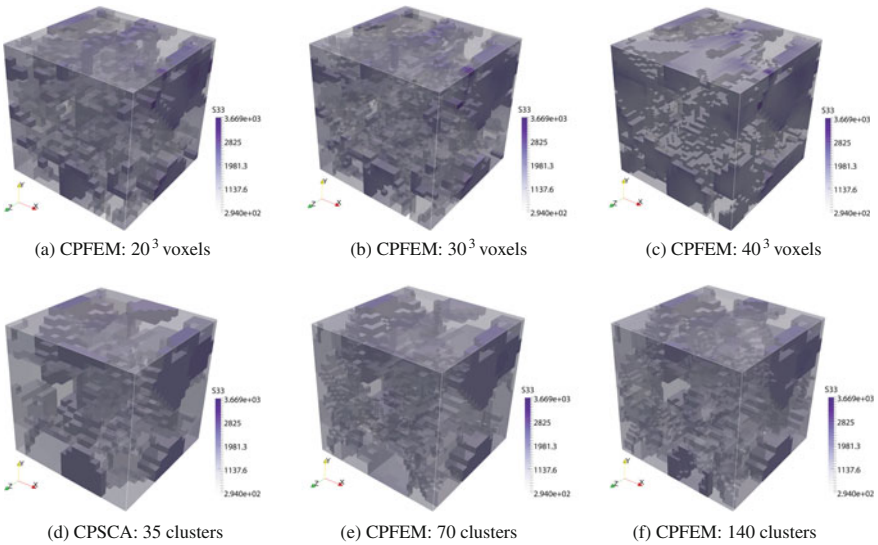


Fig. 8 Volume plots of S33 for six different cases: **a** the 20^3 mesh with CPFEM, **b** the 30^3 mesh with CPFEM, **c** the 40^3 mesh with CPFEM clusters, **d** the 40^3 mesh with 35 clusters, **e** the 40^3 with 70 clusters, and **f** the 40^3 mesh with 140 clusters. The 35 cluster case has one cluster per grain, whereas the 140 cluster case has four clusters per grain. Opacity scales with stress level

5 Conclusion

We have presented herein a method to dramatically decrease the computational cost associated with conducting microscopic crystal plasticity simulations, of the type that can be used to calibrate homogenization models, or to investigate the mechanics of processes pertaining to damage or localization within metals. This was motivated by a desire to predict the mechanical response of material resulting from the

additive manufacturing process—a challenge of great interest recently. In these materials, microscale and mesoscale factors (e.g. voids of different sizes, grains sizes dependent on physical location) are of interest, necessitating a fast method to predict micromechanical solutions over a relatively large volume. The method was demonstrated with three examples: J_2 plasticity in a multi-inclusion system, a simple void-like inclusion embedded within a single-crystal matrix, and a polycrystalline RVE of equiaxed grains.

Acknowledgements Z.L., O.L.K., C.Y. and W.K.L. warmly thank the support from AFOSR grant No. FA9550-14-1-0032, National Institute of Standards and Technology and Center for Hierarchical Materials Design (CHiMaD) under grant No. 70NANB13HI94 and 70NANB14H012, and DOE CF-ICME project under grant No. DE-EE0006867. O.L.K. thanks United States National Science Foundation (NSF) for their support through the NSF Graduate Research Fellowship Program (GRFP) under financial award number DGE-1324585.

References

1. T. Belytschko, S. Loehnert, J.H. Song, Multiscale aggregating discontinuities: a method for circumventing loss of material stability. *Int. J. Numer. Methods Eng.* **73**(6), 869–894 (2008)
2. M.A. Bessa et al., A framework for data-driven analysis of materials under uncertainty: countering the curse of dimensionality. *Comput. Methods Appl. Mech. Eng.* **320**, 633–667 (2017)
3. I. Doghri, A. Ouair, Homogenization of two-phase elasto-plastic composite materials and structures: study of tangent operators, cyclic plasticity and numerical algorithms. *Int. J. Solid. Struct.* **40**(7), 1681–1712 (2003)
4. J.D. Eshelby, The determination of the elastic field of an ellipsoidal inclusion, and related problems, in *Proceedings of the Royal Society of London A: Mathematical, Physical and Engineering Sciences*, vol. 241 (The Royal Society, 1957) pp. 376–396
5. Z. Hashin, S. Shtrikman, A variational approach to the theory of the elastic behaviour of multiphase materials. *J. Mech. Phys. Solid.* **11**(2), 127–140 (1963)
6. R. Hill, A self-consistent mechanics of composite materials. *J. Mech. Phys. Solid.* **13**(4), 213–222 (1965)
7. International A, *Standard Terminology for Additive Manufacturing Technologies*, F2792-12a edn (2015)
8. P. Krysl, S. Lall, J. Marsden, Dimensional model reduction in non linear finite element dynamics of solids and structures. *Int. J. Numer. Methods Eng.* **51**, 479–504 (2001)
9. B. Le, J. Yvonnet, Q.C. He, Computational homogenization of nonlinear elastic materials using neural networks. *Int. J. Numer. Methods Eng.* (2015)
10. R.A. Lebensohn, A.K. Kanjarla, P. Eisenlohr, An elasto-viscoplastic formulation based on fast fourier transforms for the prediction of micromechanical fields in polycrystalline materials. *Int. J. Plast.* **32**, 59–69 (2012)
11. Z. Liu, J.A. Moore, S. M. Aldousari, H.S. Hedia, S.A. Asiri, W.K. Liu, A statistical descriptor based volume-integral micromechanics model of heterogeneous material with arbitrary inclusion shape. *Comput. Mech.* 1–19 (2015)
12. Z. Liu, M. Bessa, W. Liu, Self-consistent clustering analysis: an efficient multi-scale scheme for inelastic heterogeneous materials. *Comput. Methods Appl. Mech. Eng.* **306**, 319–341 (2016a)
13. Z. Liu, J. Moore, W. Liu, An extended micromechanics method for probing interphase properties in polymer nanocomposites. *J. Mech. Phys. Solid.* (2016). doi:[10.1016/j.jmps.2016.05.002](https://doi.org/10.1016/j.jmps.2016.05.002)

14. J. MacQueen et al., Some methods for classification and analysis of multivariate observations, in *Proceedings Of The Fifth Berkeley Symposium On Mathematical Statistics And Probability*, vol. 14, Oakland, CA, USA, pp. 281–297 (1967)
15. R.D. McGinty, Multiscale representation of polycrystalline inelasticity. PhD thesis, Georgia Tech, 2001
16. J.C. Michel, P. Suquet, Computational analysis of nonlinear composite structures using the nonuniform transformation field analysis. *Comput. Methods Appl. Mech. Eng.* **193**, 5477–5502 (2004)
17. C. Oskay, J. Fish, Eigendeformation-based reduced order homogenization for failure analysis of heterogeneous materials. *Comput. Methods Appl. Mech. Eng.* **196**, 1216–1243 (2007)
18. D.R. Owen, E. Hinton, *Finite Elements in Plasticity* (Pineridge Press, 1980)
19. F. Roters, P. Eisenlohr, L. Hantcherli, D. Tjahjanto, T. Bieler, D. Raabe, Overview of constitutive laws, kinematics, homogenization and multiscale methods in crystal plasticity finite-element modeling: theory, experiments, applications. *Acta Mater.* **58**, 1152–1211 (2010)
20. S. Roussette, J.C. Michel, P. Suquet, Nonuniform transformation field analysis of elastic viscoplastic composites. *Compos. Sci. Technol.* **69**, 22–27 (2009)
21. C. Ventola, Medical applications for 3d printing: current and projected uses. *Pharm. Ther.* **39**, 704–711 (2014)
22. I.H. Witten, E. Frank, *Data Mining: Practical machine learning tools and techniques* (Morgan Kaufmann, 2005)
23. J. Yvonnet, Q.C. He, The reduced model multiscale method (r3m) for the non-linear homogenization of hyperelastic media at finite strains. *J. Comput. Phys.* **223**, 341–368 (2007)
24. J. Yvonnet, E. Monteiro, Q.C. He, Computational homogenization method and reduced database model for hyperelastic heterogeneous structures. *Int. J. Multiscale Comput. Eng.* **11** (2013)

A Viscoelastic-Viscoplastic Combined Constitutive Model for Thermoplastic Resins

Seishiro Matsubara and Kenjiro Terada

Abstract A viscoelastic-viscoplastic combined constitutive model is presented to represent large deformations of amorphous thermoplastic resins. The model is endowed with viscoelastic and viscoplastic rheology elements connected in series. The standard generalized Maxwell model is used to determine the stress and characterize the viscoelastic material behavior at small or moderate strain regime. To realize the transient creep deformations along with kinematic hardening due to frictional resistance and orientation of molecular chains, a proven finite strain viscoplastic model is employed. After identifying the material parameters with reference to experimental data, we verify and demonstrate the fundamental performances of the proposed model in reproducing typical material behavior of resin.

1 Introduction

Thermoplastic resins are known to exhibit peculiar material behavior. Early researches were inspired by the work done by Eyring [10] who studied it physicochemically based on reaction kinetics of molecular chains. Among them, Argon's double kink hypothesis [5, 6], which is based on disclination loop theory Li and Gilman [21], has been widely used for the viscoplastic multiplier in various constitutive models for thermoplastic resins to represent the initial yielding at a moderate deformation regime; see also Liu and Li [22] in this context. With the help of high-performance of computational resource, these early theoretical developments enjoys the fruits of computational plasticity [26] in representing complex material behavior and accelerates further elaboration of material models for thermoplastic resins.

S. Matsubara

Department of Civil Engineering, Tohoku University, Sendai, Japan

e-mail: seishiro.matsubara.t4@dc.tohoku.ac.jp

K. Terada (✉)

International Research Institute of Disaster Science, Tohoku University,
Sendai, Japan

e-mail: tei@irides.tohoku.ac.jp

Boyce et al. [8] proposed a phenomenological constitutive model that can successfully represent the stress-softening behavior after initial yielding by introducing pressure dependency and evolution of shear yield strength into the Argon's model [6]. This model is extended by Wu and Giessen [31, 32] to reproduce shear bands and necking phenomena at a moderate deformation regime. Also, based on the Boyce's theory, Anand and Gurtin [4] provide a model within the thermodynamics framework that represents smooth transition from the initial yielding to stress-softening in consideration of the evolution of free volume in the viscoplastic deformations. Moreover, Fleischhauer et al. [11] extend the models developed by Mulliken et al. [23] and Dupaix and Boyce [9] and propose a rheology model involving a viscoplastic element connected with a Langevin element in parallel to represent compressive material behavior of both thermosetting and thermoplastic resins.

Apart from the Argon's framework [5, 6], the cooperative model, which is developed by Richeton et al. [27–29] based on the model introduced by Fotheringham and Cherry [13], is worthy of attention. By extending the cooperative model, Anand et al. [3] and Ames et al. [2] propose phenomenological models within the thermodynamics framework, which incorporate the viscoplastic defect energy to represent the dynamic recovery behavior during unloading. The extension of these models, which is proposed by Srivastava et al. [30], is a rheology model composed of multiple viscoplastic elements to adjust for the material behavior above a glass-transition temperature. This model enables us to work with the change of physical properties around the glass-transition temperature, but entails a bunch of parameters and seems to be remotely related to physical ground. In the meantime, according to Aleksy et al. [1] and Kermouche et al. [18], glassy thermoplastic resins behave as a viscoelastic material in small and moderately large deformation regimes, whereas the viscoplastic behavior tends to be dominant in a large deformation regime. Surprisingly few studies have so far been made at the constitutive modeling in this context, though there seem to be some models representing the coupling between viscoelastic and viscoplastic material responses; see, e.g., Nedjar [24, 25].

To encompass various material responses depending on different amounts of deformation, the article presents a new rheology-based constitutive model for glassy amorphous thermoplastic resins that is composed of viscoelastic and viscoplastic elements in series. The distinct feature of the proposed model is that the elastic elements are installed in the viscoelastic part only so that the viscoplastic part is not directly related to the stress. Also, thanks to the series combination, three types of rheology elements are introduced in the model to represent different characteristic features of the material behavior according to the amount of deformation. Specifically, the uniform creep behavior in a small deformation regime is represented by the standard generalized Maxwell model [15, 16]. Two sets of rheology elements are connected in parallel to construct the viscoplastic part of the model. One of them is composed of serially connected frictional slider-dumper element to represent non-uniform creep deformation along with the initial yielding followed by stress-softening in a moderately large deformation regime. In this study, the model proposed by Boyce et al. [8] is employed for this part. The other is a special type of spring elements introduced by Ames et al. [2] to represent the orientation hardening

in a large deformation regime. As a ground for the argument of such a viscoelastic and viscoplastic combination in series, we start the formulation with the first and second laws of thermodynamics. The experimental data for polymethylmethacrylate (PMMA) available in the literature are used to identify the material parameters and the fundamental performances of the proposed model in reproducing typical material behavior of resin are verified and demonstrated with simple numerical examples.

2 A Viscoelastic-Viscoplastic Combined Constitutive Law

This section is devoted to the formulation of the viscoelastic-viscoplastic combined constitutive law within the finite strain framework. Thermomechanical deformation is also considered without loss of generality, but isotropy is assumed for both the thermal and mechanical deformations in this study.

2.1 Kinematic Variables

Figure 1 shows the rheology model corresponding to the constitutive law proposed in this study. The model is composed of viscoelastic and viscoplastic parts connected in series, each of which corresponds to viscoelastic and viscoplastic components, F^{ve} and F^{vp} , obtained as a result of the following multiplicative decomposition of the mechanical deformation gradient \tilde{F} with reference to the initial, thermally dilated, viscoplastic (intermediate) and current configurations depicted in Fig. 2 along the line of Kröner [19] and Lee [20]:

$$\tilde{F} = F^{ve} F^{vp} \tag{1}$$

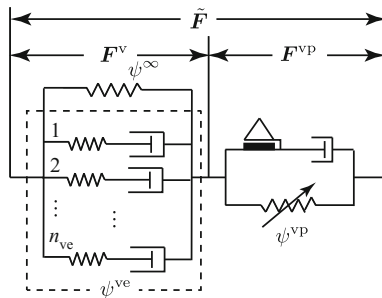


Fig. 1 Rheology model of coupled viscoelasticity with viscoplasticity. The model combines a viscoplastic element with a generalized Maxwell model in series and necessitates the multiplicative decomposition of the deformation gradient into viscoelastic and viscoplastic ones. The total stress is determined only with the generalized Maxwell model

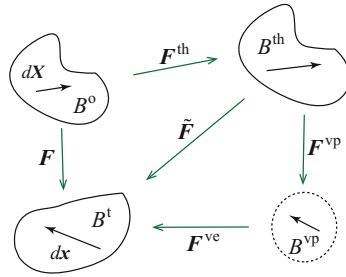


Fig. 2 Configurations associated with multiplicative decomposition of deformation gradient; B^{vp} : viscoelastically unloaded configuration with viscoplastic deformation gradient F^{vp} ; thermally dilated configuration B^{th} ; current configuration B^t with viscoelastic deformation gradient F^{ve}

Here, the total deformation gradient is expressed as

$$F = \tilde{F}F^{th} \tag{2}$$

with F^{th} being the thermal deformation gradient, which, due to isotropy, can be expressed as

$$F^{th} = (1 + \alpha_t \theta)\mathbf{1} \tag{3}$$

where $\mathbf{1}$ is the second-order identify tensor, θ is the change in temperature and α_t is the coefficient of thermal expansion (CTE).

The viscoelastic part of this rheology model corresponds to a finite strain version of the generalized Maxwell elements, whereas the viscoplastic part covers a lot of ground for corresponding constitutive models. However, the spring element set in parallel with the serially connected frictional slider-dumper element is worthy of attention, as the back stress due to orientation hardening is developed in it after the expansion according to the viscoplastic deformation. In what follows, kinematic variables necessary in the formulation are defined based on the multiplicative decomposition introduced above.

The mechanical deformation gradient \tilde{F} can be decomposed into the volumetric and isochoric components, $J^{\frac{1}{3}}$ and \bar{F} , as

$$\tilde{F} = J^{\frac{1}{3}}\bar{F} \tag{4}$$

where $J := \det(\tilde{F})$ [12]. These volumetric and isochoric components can also be decomposed into viscoelastic and viscoplastic parts as

$$J = J^{ve}J^{vp}, \quad \text{and} \quad \bar{F} = \bar{F}^{ve}\bar{F}^{vp} \tag{5}$$

where we have defined $J^{\text{ve}} := \det(\mathbf{F}^{\text{ve}})$ and $J^{\text{vp}} := \det(\mathbf{F}^{\text{vp}})$. In this study, incompressibility is assumed for the viscoplastic deformation so that $J^{\text{vp}} = 1$, from which (5)₁ and (1) yields $J = J^{\text{ve}}$ and $\tilde{\mathbf{F}} = \mathbf{F}^{\text{ve}}\bar{\mathbf{F}}^{\text{vp}}$, respectively.

The right Cauchy-Green and left Cauchy-Green tensors associated with the mechanical deformation are given as $\tilde{\mathbf{C}} = (\bar{\mathbf{F}}^{\text{vp}})^{\text{T}} \mathbf{C}^{\text{ve}} \bar{\mathbf{F}}^{\text{vp}}$ and $\tilde{\mathbf{b}} = \mathbf{F}^{\text{ve}} \bar{\mathbf{b}}^{\text{vp}} (\mathbf{F}^{\text{ve}})^{\text{T}}$. Here, \mathbf{C}^{ve} and $\bar{\mathbf{b}}^{\text{vp}}$ are the viscoelastic right Cauchy-Green and viscoplastic left Cauchy-Green tensors that have respectively been defined as

$$\mathbf{C}^{\text{ve}} = (\mathbf{F}^{\text{ve}})^{\text{T}} \mathbf{F}^{\text{ve}} \quad \text{and} \quad \bar{\mathbf{b}}^{\text{vp}} = \bar{\mathbf{F}}^{\text{vp}} (\bar{\mathbf{F}}^{\text{vp}})^{\text{T}} \quad (6)$$

Also, the mechanical velocity gradient can be additively decomposed as

$$\tilde{\mathbf{l}} = \dot{\tilde{\mathbf{F}}}\tilde{\mathbf{F}}^{-1} = \mathbf{l}^{\text{ve}} + \mathbf{F}^{\text{ve}}\bar{\mathbf{l}}^{\text{vp}}(\mathbf{F}^{\text{ve}})^{-1} \quad (7)$$

where we have respectively defined the viscoelastic and viscoplastic velocity gradients referring to the viscoelastically unloaded configuration B^{vp} as $\mathbf{l}^{\text{ve}} = \dot{\mathbf{F}}^{\text{ve}} (\mathbf{F}^{\text{ve}})^{-1}$ and $\bar{\mathbf{l}}^{\text{vp}} = \dot{\bar{\mathbf{F}}}^{\text{vp}} (\bar{\mathbf{F}}^{\text{vp}})^{-1}$. Each of these velocity gradients can be decomposed into the symmetric and anti-symmetric parts as

$$\tilde{\mathbf{l}} = \text{sym} [\tilde{\mathbf{l}}] + \text{skew} [\tilde{\mathbf{l}}] = \tilde{\mathbf{d}} + \tilde{\mathbf{w}}, \quad (8)$$

$$\bar{\mathbf{l}}^{\text{vp}} = \text{sym} [\bar{\mathbf{l}}^{\text{vp}}] + \text{skew} [\bar{\mathbf{l}}^{\text{vp}}] = \bar{\mathbf{d}}^{\text{vp}} + \bar{\mathbf{w}}^{\text{vp}}, \quad (9)$$

$$\mathbf{l}^{\text{ve}} = \text{sym} [\mathbf{l}^{\text{ve}}] + \text{skew} [\mathbf{l}^{\text{ve}}] = \mathbf{d}^{\text{ve}} + \mathbf{w}^{\text{ve}} \quad (10)$$

where $\text{sym}[\bullet]$ and $\text{skew}[\bullet]$ are the symmetric and anti-symmetric parts of a second-order tensor \bullet .

We assume that the viscoplastic deformation of thermoplastic resins is affine so that the mapping between viscoelastically unloaded configuration B^{vp} and current configuration B^{t} is irrotational (as suggest by Boyce et al. [8]) as $\mathbf{R}^{\text{ve}} = \mathbf{1}$ and $\mathbf{w}^{\text{ve}} = \mathbf{0}$. This assumption postulates that the flow direction of the viscoplastic permanent deformation in current configuration B^{t} be coincident with the slip direction of molecular chains. In this case, the second term of the right-hand side of (7) becomes $\mathbf{F}^{\text{ve}}\bar{\mathbf{l}}^{\text{vp}}(\mathbf{F}^{\text{ve}})^{-1} = \mathbf{V}^{\text{ve}}\bar{\mathbf{l}}^{\text{vp}}(\mathbf{V}^{\text{ve}})^{-1} = \bar{\mathbf{l}}^{\text{vp}}$ so that $\tilde{\mathbf{l}} = \mathbf{l}^{\text{ve}} + \bar{\mathbf{l}}^{\text{vp}}$. Therefore, with (10), we have $\tilde{\mathbf{d}} = \mathbf{d}^{\text{ve}} + \bar{\mathbf{d}}^{\text{vp}}$ and $\tilde{\mathbf{w}} = \bar{\mathbf{w}}^{\text{vp}}$.

2.2 Free Energy

The total free energy ψ for the material under consideration is defined as

$$\psi = \psi^{\text{th}}(\mathbf{F}^{\text{th}}, \theta) + \psi^{\text{ve}}(\tilde{\mathbf{C}}, \bar{\mathbf{F}}^{\text{vp}}, \mathbf{I}^{\alpha}, \theta) + \psi^{\text{vp}}(\bar{\mathbf{b}}^{\text{vp}}, \theta) \quad (11)$$

where ψ^{th} and ψ^{ve} are the free energies for thermal, viscoelastic-viscoplastic deformations [15, 16], respectively, and ψ^{vp} is the defect energy associated with viscoplastic deformation [4]. Here, $\mathbf{\Gamma}^\alpha$ ($\alpha = 1, \dots, n_{\text{ve}}$) are thermodynamic strains of rheology elements referring to viscoelastically unloaded configuration B^{vp} .

In consideration of stress-free dilation volume $\mathbf{p}^{\text{th}} = -\frac{\partial\psi^{\text{th}}}{\partial\mathbf{F}^{\text{th}}} = \mathbf{0}$, the material time derivative of the total free energy ψ becomes

$$\dot{\psi} = \frac{\partial\psi^{\text{ve}}}{\partial\tilde{\mathbf{C}}} : \dot{\tilde{\mathbf{C}}} + \frac{\partial\psi^{\text{ve}}}{\partial\bar{\mathbf{F}}^{\text{vp}}} : \dot{\bar{\mathbf{F}}^{\text{vp}}} + \frac{\partial\psi^{\text{vp}}}{\partial\bar{\mathbf{F}}^{\text{vp}}} : \dot{\bar{\mathbf{F}}^{\text{vp}}} + \sum_{\alpha=1}^{n_{\text{ve}}} \frac{\partial\psi^{\text{ve}}}{\partial\mathbf{\Gamma}^\alpha} : \dot{\mathbf{\Gamma}}^\alpha + \frac{\partial\psi}{\partial\theta} \dot{\theta} \quad (12)$$

in which the 2nd Piola-Kirchhoff stress and the entropy density can be identified as

$$\mathbf{S} = 2\rho_0 \frac{\partial\psi^{\text{ve}}}{\partial\tilde{\mathbf{C}}} \quad \text{and} \quad \eta = -\frac{\partial\psi}{\partial\theta}. \quad (13)$$

Here, ρ_0 is the initial mass density. Then, applying the 1st and 2nd laws of thermodynamics along with (12), we have the internal or intrinsic dissipation energy referring to the thermally dilated configuration B^{th} , as

$$\begin{aligned} \phi_{\text{internal}} &= \frac{1}{2} \mathbf{S} : \dot{\tilde{\mathbf{C}}} - \rho_0 (\dot{\psi} + \dot{\theta}\eta) \\ &= -\rho_0 \frac{\partial\psi^{\text{ve}}}{\partial\bar{\mathbf{F}}^{\text{vp}}} : \dot{\bar{\mathbf{F}}^{\text{vp}}} - \rho_0 \frac{\partial\psi^{\text{vp}}}{\partial\bar{\mathbf{F}}^{\text{vp}}} : \dot{\bar{\mathbf{F}}^{\text{vp}}} - \sum_{\alpha=1}^{n_{\text{ve}}} \rho_0 \frac{\partial\psi^{\text{ve}}}{\partial\mathbf{\Gamma}^\alpha} : \dot{\mathbf{\Gamma}}^\alpha \end{aligned} \quad (14)$$

where the sum of the first and second terms of the right-hand side is the viscoplastic dissipation energy density and the third term represents the viscoelastic dissipation energy density.

2.3 Viscoelastic Rheology Element

The viscoelastic part of the rheology element is formulated based on the theory presented by Holzapfel et al. [15, 16]. First, we introduce the following form of the viscoelastic-viscoplastic coupled free energy density:

$$\rho_0\psi^{\text{ve}} = \rho_0\psi^\infty + \sum_{\alpha=1}^{n_{\text{ve}}} \left[\mathbf{\Gamma}^\alpha : \mathbb{C}^\alpha : \mathbf{\Gamma}^\alpha - 2\rho_0 \frac{\partial\psi^\alpha}{\partial\mathbf{C}^{\text{ve}}} : \mathbf{\Gamma}^\alpha + \rho_0\psi^\alpha \right] \quad (15)$$

where $\psi^\infty = \psi^\infty(\tilde{\mathbf{C}}, \bar{\mathbf{F}}^{\text{vp}}, \theta)$ is the free energy density of the purely elastic element. Also, $\psi^\alpha = \psi^\alpha(\tilde{\mathbf{C}}, \bar{\mathbf{F}}^{\text{vp}}, \theta)$ is the ideally elastic energy density of Maxwell elements, each which is virtually defined as the elastic stored energy during the relaxation process. Furthermore, $\mathbb{C}^\alpha = \mathbb{C}^\alpha(\tilde{\mathbf{C}}, \bar{\mathbf{F}}^{\text{vp}}, \theta)$ is a positive definite fourth-order tensor introduced for each Maxwell element, which has the same unit with that of the elastic moduli tensor.

With this definition of the free energy density ψ^{ve} , Eq. (13) becomes

$$\mathbf{S} = 2\rho_0 \frac{\partial \psi^{ve}}{\partial \tilde{\mathbf{C}}} = (\mathbf{F}^{vp})^{-1} \left[2\rho_0 \frac{\partial \psi^{ve}}{\partial \mathbf{C}^{ve}} \right] (\mathbf{F}^{vp})^{-T} = (\mathbf{F}^{vp})^{-1} \mathbf{H} (\mathbf{F}^{vp})^{-T} \quad (16)$$

which defines the 2nd Piola-Kirchhoff stress referring thermally dilated configuration B^{th} . Here, we have defined the thermodynamic non-equilibrated stress that refers to viscoelastically unloaded configuration B^{vp} as

$$\begin{aligned} \mathbf{H} &= 2\rho_0 \frac{\partial \psi^{ve}}{\partial \mathbf{C}^{ve}} \\ &= 2\rho_0 \frac{\partial \psi^\infty}{\partial \mathbf{C}^{ve}} + \sum_{\alpha=1}^{n_{ve}} \left[\boldsymbol{\Gamma}^\alpha : 2 \frac{\partial \mathbf{C}^\alpha}{\partial \mathbf{C}^{ve}} : \boldsymbol{\Gamma}^\alpha - 2 \frac{\partial \mathbf{H}^\alpha}{\partial \mathbf{C}^{ve}} : \boldsymbol{\Gamma}^\alpha + 2\rho_0 \frac{\partial \psi^\alpha}{\partial \mathbf{C}^{ve}} \right] \\ &= \mathbf{H}^\infty + \sum_{\alpha=1}^{n_{ve}} \left[\boldsymbol{\Gamma}^\alpha : 2 \frac{\partial \mathbf{C}^\alpha}{\partial \mathbf{C}^{ve}} : \boldsymbol{\Gamma}^\alpha - 4\rho_0 \frac{\partial^2 \psi^\alpha}{\partial \mathbf{C}^{ve} \partial \mathbf{C}^{ve}} : \boldsymbol{\Gamma}^\alpha + \mathbf{H}^\alpha \right] \end{aligned} \quad (17)$$

along with the viscoelastic thermodynamic strain $\boldsymbol{\Gamma}^\alpha$. Here, \mathbf{H}^∞ and \mathbf{H}^α have been defined as

$$\mathbf{H}^\infty = 2\rho_0 \frac{\partial \psi^\infty}{\partial \mathbf{C}^{ve}} \quad \text{and} \quad \mathbf{H}^\alpha = 2\rho_0 \frac{\partial \psi^\alpha}{\partial \mathbf{C}^{ve}}. \quad (18)$$

In this study, we employ the following St. Venant-Kirchhoff hyperelastic strain energy for the free energy of the purely elastic element in the generalized Maxwell model:

$$\rho_0 \psi^\infty = \frac{1}{2} K^\infty [\text{tr}(\mathbf{E}^{ve})]^2 + G^\infty [\text{dev}(\mathbf{E}^{ve}) : \text{dev}(\mathbf{E}^{ve})] \quad (19)$$

so that the stress in the purely elastic element referring to the viscoelastically unloaded configuration B^{vp} yields

$$\mathbf{H}^\infty = K^\infty \text{tr}(\mathbf{E}^{ve}) \mathbf{1} + 2G^\infty \text{dev}(\mathbf{E}^{ve}) \quad (20)$$

where viscoelastic Green strain \mathbf{E}^{ve} is expressed as $\mathbf{E}^{ve} = \frac{1}{2} (\mathbf{C}^{ve} - \mathbf{1})$ using the right-Cauchy-Green viscoelastic deformation tensor \mathbf{C}^{ve} in (6). Also, K^∞ and G^∞ are equivalent to the bulk and shear moduli.

We postulate that the ideal elastic free energy of each Maxwell element (15) be proportional to the purely elastic free energy as $\psi^\alpha = \gamma^\alpha \psi^\infty$ so that the stress referring to viscoelastically unloaded configuration B^{vp} becomes

$$\mathbf{H}^\alpha = 2\rho_0 \frac{\partial \psi^\alpha}{\partial \mathbf{C}^{ve}} = \gamma^\alpha \mathbf{H}^\infty \quad (21)$$

where $\gamma^\alpha \in (0, 1]$ is the relative elastic modulus defined as $\gamma^\alpha = \frac{E^\alpha}{E^\infty}$. Here, E^α and E^∞ are Young's moduli of each Maxwell element and of the purely elastic element.

Also, by defining the tangent modulus of each Maxwell element as

$$\mathbb{D}^\alpha = 4\rho_0 \frac{\partial^2 \psi^\alpha}{\partial \mathbf{C}^{\text{ve}} \partial \mathbf{C}^{\text{ve}}} = \gamma^\alpha (K^\infty \mathbf{I}^{\text{sym}} + 2G^\infty \mathbf{I}^{\text{dev}}) \quad (22)$$

we assume that the fourth-order modulus tensor \mathbb{C}^α is proportional to the tangent modulus tensor \mathbb{D}^α such that $2\mathbb{C}^\alpha = \mathbb{D}^\alpha$ so that

$$2 \frac{\partial \mathbb{C}^\alpha}{\partial \mathbf{C}^{\text{ve}}} = \frac{\partial \mathbb{D}^\alpha}{\partial \mathbf{C}^{\text{ve}}} = \mathbf{0} \quad (23)$$

This assumption is valid, since the St. Venant-Kirchhoff model is convex with respect to \mathbf{C}^{ve} . It should be noted, however, that some elastic energies that may not have convexity do not advocate this assumption [7]. Finally, with (18), (21) and (23), Eq. (17) can be written as

$$\mathbf{H} = \mathbf{H}^\infty + \sum_{\alpha=1}^{n_{\text{ve}}} [\gamma^\alpha \mathbf{H}^\infty - \mathbb{D}^\alpha : \boldsymbol{\Gamma}^\alpha] \quad (24)$$

The thermodynamic non-equilibrated stress that drives thermodynamic strain $\boldsymbol{\Gamma}^\alpha$ is defined as $\mathbf{R}^\alpha = -\rho_0 \frac{\partial \psi^{\text{ve}}}{\partial \boldsymbol{\Gamma}^\alpha}$ and its evolution equation can be derived with the internal dissipation energy (14) along the line of Holzapfel et al. [15, 16] as

$$\dot{\mathbf{R}}^\alpha + \frac{1}{\tau^\alpha} \mathbf{R}^\alpha = \frac{d}{dt} [\gamma^\alpha \mathbf{H}^\infty] - \mathbf{R}_{\text{cpl}} \quad (25)$$

where τ^α is the relaxation time of each Maxwell element, which is defined as a coefficient of the following relationship:

$$\mathbb{D}^\alpha : \dot{\boldsymbol{\Gamma}}^\alpha = \frac{1}{\tau^\alpha} \mathbf{R}^\alpha \quad (26)$$

Also, \mathbf{R}_{cpl} is the relaxation stress defined as

$$\mathbf{R}_{\text{cpl}} = \frac{D\mathbb{D}^\alpha}{Dt} : \boldsymbol{\Gamma}^\alpha \quad (27)$$

Here, since the components of \mathbb{D}^α are constants, the relaxation stress in (27) is zero in this study. Thus, the thermodynamic non-equilibrated stress can be expressed as

$$\mathbf{R}^\alpha = \int_0^t \gamma^\alpha \frac{d\mathbf{H}^\infty}{ds} \exp\left[-\frac{s-t}{\tau^\alpha}\right] ds \quad (28)$$

Also, the thermodynamic strain $\mathbf{\Gamma}^\alpha$ can be represented as

$$\mathbb{D}^\alpha : \mathbf{\Gamma}^\alpha = \gamma^\alpha \mathbf{H}^\infty - \mathbf{R}^\alpha \quad (29)$$

Finally, the substitution of (29) into (24) provides the non-equilibrated stress \mathbf{H} referring to B^{vp} as the sum of \mathbf{H}^∞ and \mathbf{R}^α as

$$\mathbf{H} = \mathbf{H}^\infty + \sum_{\alpha=1}^{n_{\text{ve}}} \mathbf{R}^\alpha \quad (30)$$

2.4 Viscoplastic Rheology Element

The viscoplastic constitutive laws for amorphous thermoplastic resins must be capable of representing pseudo yielding followed by stress-softening in a small deformation regime and orientation hardening behavior in a large deformation regime.

2.4.1 Pseudo Yielding and Stress-Softening

The stress is exclusively determined in the viscoelastic rheology element described above and is applied to the viscoplastic rheology element, which is composed of viscoplastic slider and back-stress elements. Thus, the driving force acting on the viscoplastic slider element is the following effective stress referring to viscoelastically unloaded configuration B^{vp} :

$$\mathbf{M}^{\text{eff}} = \text{dev} (\mathbf{C}^{\text{ve}} \mathbf{H}(t) - \mathbf{M}^{\text{back}}) \quad (31)$$

Here, \mathbf{M}^{back} is the back stress. Defining the viscoplastic potential by $\phi = \phi(\mathbf{M}^{\text{eff}}, \theta) = (\mathbf{M}^{\text{eff}} : \mathbf{M}^{\text{eff}})^{\frac{1}{2}}$, we postulate the viscoplastic flow rule of the form

$$\bar{\mathbf{d}}^{\text{vp}} = \dot{\gamma}^{\text{vp}}(\theta) \mathbf{N}(\theta) \quad (32)$$

where $\dot{\gamma}^{\text{vp}}$ is the viscoplastic multiplier, which is non-negative, and the flow vector has been defined as

$$\mathbf{N}(\theta) = \frac{\partial \phi}{\partial \mathbf{M}^{\text{eff}}} = \frac{1}{\sqrt{2}} \frac{\mathbf{M}^{\text{eff}}}{\tau} \quad (33)$$

Here, τ is recognized as the equivalent stress of \mathbf{M}^{eff} defined as

$$\tau = \frac{1}{\sqrt{2}} \|\mathbf{M}^{\text{eff}}\| \quad (34)$$

As for the evolution equation of the viscoplastic multiplier, we employ the following phenomenological model, which was proposed by Boyce et al. [8] along the line of Argon [5] to represent pseudo yielding followed by stress softening in a relatively small deformation regime:

$$\dot{\gamma}^{\text{vp}}(\theta) = \dot{\gamma}_0^{\text{vp}} \exp \left[-\frac{As^*}{\theta} \left\{ 1 - \left(\frac{\tau}{s^*} \right)^n \right\} \right] \quad (35)$$

where $\dot{\gamma}_0^{\text{vp}}$ is the initial viscoplastic multiplier. Here, along with n , A is the material parameter determined from the activation energy of Argon [5, 6] and is referred to as the activation volume. Also, s^* is a sort of yield strength representing the deformation resistance and has the following function form that depends on both the shear yield strength s and the hydrostatic pressure $p = -\frac{1}{3} \text{tr}(\mathbf{C}^{\text{ve}} \mathbf{H})$:

$$s^* = s + \alpha_v p \quad (36)$$

Here, α_v is the pressure coefficient and the evolution law for s is postulated as

$$\dot{s} = h \left(1 - \frac{s}{s_{\text{ss}}} \right) \dot{\gamma}^{\text{vp}} \quad (37)$$

where h is the inclination of the stress-softening response with respect to plastic strain after the initial yielding and s_{ss} is the shear yield strength in the steady state. Also, the athermal initial shear yield strength is introduced as $s_0 = mG/(1-\nu)$, where m is the material parameter associated with the activation energy. Here, we have used the shear modulus of elasticity defined as $G = (1 + \sum_{\alpha}^{n_{\text{ve}}} \gamma^{\alpha}) G^{\infty}$ and Poisson's ratio ν of the purely elastic element in the viscoelastic rheology element.

2.4.2 Back Stress to Represent Orientation Hardening

When the conformation motion of a molecular chain transitions to the configuration motion due to its extension, the amorphous thermoplastic resin tends to exhibit an orientation hardening phenomenon, which has an analogy with the elastic behavior of rubber materials. Along the line of Ames et al. [2], we employ the following Gent's hyperelastic energy function [14] to represent the orientation hardening.

$$\rho_0 \psi^{\text{vp}} = -\frac{1}{2} \mu J_m \ln \left(1 - \frac{I_1 - 3}{J_m} \right) \quad (38)$$

Here, $I_1 = \text{tr}(\bar{\mathbf{b}}^{\text{vp}})$ is the first invariant of the viscoelastic left-Cauchy-Green deformation tensor $\bar{\mathbf{b}}^{\text{vp}}$, J_m is the characteristic length of extended molecular chains, which is supposed to satisfy $J_m > I_1 - 3$. Also, μ is the shear modulus-like material parameter associated with the back stress. Then, it can be derived as

$$\mathbf{M}^{\text{back}} = 2\rho_0 \frac{\partial \Psi^{\text{vp}}}{\partial \bar{\mathbf{b}}^{\text{vp}}} \bar{\mathbf{b}}^{\text{vp}} = \mu \left(1 - \frac{I_1 - 3}{J_m} \right)^{-1} \bar{\mathbf{b}}^{\text{vp}} \quad (39)$$

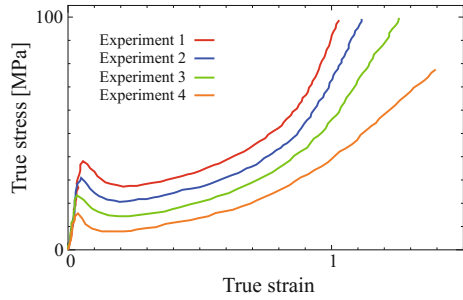
3 Identification of Material Parameters

The set of constitutive equations proposed in this study is summarized in Fig. 3. This section is devoted to the identification of the material parameters used in these equations. The experimental data are borrowed from Hope et al. [17] who conducted a series of uniaxial tension tests for PMMA with different deformation rates. The tests were carried out with four levels of true strain rates 0.1, 0.01, 0.001 and 0.0001 s at ambient temperature of 90 °C . The obtained empirical relationships between true stresses and true strains are shown in Fig. 4. Although the maximum tensile strain attains 1.5, the parameter identification in this study is made for the data up to true strain of 1.0.

[1] Kinematic variables			
(1) Multiplicative decomposition of total deformation gradient	$\mathbf{F} = \bar{\mathbf{F}}\mathbf{F}^{\text{th}}$	(4) Thermomechanical non-equilibrium stress	$\mathbf{R}^\alpha = \int_0^t \dot{\gamma}^\alpha \frac{\partial \mathbf{H}^\infty}{\partial s} \exp\left(\frac{s-t}{\tau_\alpha}\right) ds$
(2) Thermal dilatation deformation gradient	$\mathbf{F}^{\text{th}} = (1 + \alpha_t \theta)\mathbf{1}$	(5) Tangent modulus of ideal elasticity tensor of Maxwell element	$\mathbb{D} = \dot{\gamma}^\alpha (K^\infty \mathbf{I}^{\text{sym}} + 2G\mathbf{I}^{\text{dev}})$
(3) Multiplicative decomposition of mechanical deformation gradient	$\bar{\mathbf{F}} = \mathbf{F}^{\text{ve}}\bar{\mathbf{F}}^{\text{vp}}$	[3] Viscoplasticity	
(4) Viscoelastic right Cauchy-Green tensor	$\mathbf{C}^{\text{ve}} = (\mathbf{F}^{\text{ve}})^\top \mathbf{F}^{\text{ve}}$	(1) Viscoplastic hardening law	$\bar{\mathbf{d}}^{\text{vp}} = \dot{\gamma}^{\text{vp}} \frac{\mathbf{M}^{\text{eff}}}{\ \mathbf{M}^{\text{eff}}\ }$
(5) Viscoplastic left Cauchy-Green tensor	$\bar{\mathbf{b}}^{\text{vp}} = \bar{\mathbf{F}}^{\text{vp}}(\bar{\mathbf{F}}^{\text{vp}})^\top$	(2) Effective deviatoric stress	$\mathbf{M}^{\text{eff}} = \text{dev}(\mathbf{C}^{\text{ve}}\mathbf{H} - \mathbf{M}^{\text{back}})$
(6) Viscoelastic Green-Lagrange strain tensor	$\mathbf{E}^{\text{ve}} = \frac{1}{2}(\mathbf{C}^{\text{ve}} - \mathbf{1})$	(3) Back stress	$\mathbf{M}^{\text{back}} = \mu \left(1 - \frac{I_1^{\text{vp}}}{J_m} \right)^{-1} \bar{\mathbf{b}}^{\text{vp}}$
(7) Viscoplastic velocity Gradient tensor	$\bar{\mathbf{T}}^{\text{vp}} = \bar{\mathbf{d}}^{\text{vp}} + \dot{\bar{\mathbf{w}}}$	(4) Evolution law of viscoplastic multiplier	$\dot{\gamma}^{\text{vp}} = \dot{\gamma}_\sigma^{\text{vp}} \exp\left[-\frac{\Delta S^*}{\theta} \left(1 - \frac{\ \mathbf{M}^{\text{eff}}\ ^2}{\sqrt{2} s^*} \right) \right]$
(8) Mechanical spin tensor	$\dot{\bar{\mathbf{w}}} = \text{skew}(\dot{\bar{\mathbf{F}}}\bar{\mathbf{F}}^{-1})$	(5) Yield strength	$s^* = s - \frac{\alpha_s}{3} \text{tr}(\mathbf{C}^{\text{ve}}\mathbf{H})$
[2] Viscoelasticity		(6) Evolution law of shear yield strength	$\dot{s} = h \left(1 - \frac{s}{s_s} \right) \dot{\gamma}^{\text{vp}}$
(1) 2nd Piola-Kirchhoff real stress	$\mathbf{S} = (\bar{\mathbf{F}}^{\text{vp}})^{-1} \mathbf{H}(\bar{\mathbf{F}}^{\text{vp}})^{-\top}$	(7) Athermal initial shear yield strength	$s_0 = m \frac{G}{1-\nu}$
(2) Real stress	$\mathbf{H} = \mathbf{H}^\infty + \sum_{\alpha=1}^{n_{\text{bc}}} \mathbf{R}^\alpha$		
(3) Pure elastic stress	$\mathbf{H}^\infty = K^\infty \text{tr}(\mathbf{E}^{\text{ve}})\mathbf{1} + 2G\text{dev}(\mathbf{E}^{\text{ve}})$		

Fig. 3 Summary of the proposed constitutive model

Fig. 4 Experimental data of the uniaxial tensile test in Hope et al. [17]. The data shows the relationship between the true stress and true strain for 4 levels of deformation rates; “0.1, 0.01, 0.001, 0.0001 (1/s)” under temperature 90°



It should be noted that the relaxation times and CTE can hardly be identified with the referential experimental data. Therefore, these parameters are assumed as in Table 1, where the number of Maxwell elements are presumably set at 18. Thus, the number of unknown parameters to be identified is 27, which counts eighteen relative elastic moduli in the generalized Maxwell model.

The method of differential evolution (DE) is used for meta-heuristic optimization of the material parameters. Displacement is imposed on the end nodes of a cubic single eight-node hexahedral element with dimension of $1.0 \times 1.0 \times 1.0 \text{ mm}^3$ for each tensile test with a specified strain rate. The boundary condition is set to realize the uniform uniaxial stress state. Then all the calculated relationships between true stresses and true strains are compared with experimental ones provided in Fig. 4.

The material parameters thus determined are presented in Tables 2 and 3. Figure 5 shows the corresponding curves representing relationships between true stresses and true strains. As can be seen from the figure, the stress softening behavior after the initial yielding can be captured, as the viscoelastic model of Boyce et al. [8] employed

Table 1 Fixed parameters

Maxwell elements	CTE (1/°C)	Relaxation time (s)
18	5.0×10^{-5}	10^x (x are integers from 1 to 18)

Table 2 Identified parameters

Parameter	Value
E (MPa)	2061
ν	0.3772
$\dot{\gamma}_0^{vp}$ (1/s)	1.145×10^{11}
A (K/MPa)	166
α	0.2289
h (MPa)	844.6
s_{ss} (MPa)	81.55
J_m	22.28
μ (MPa)	4.651

Table 3 Identified relative elastic moduli

α	Value	α	Value
1	1.328×10^{-3}	10	2.818×10^{-2}
2	2.174×10^{-3}	11	1.930×10^{-2}
3	2.974×10^{-3}	12	7.350×10^{-2}
4	1.674×10^{-3}	13	3.400×10^{-2}
5	1.106×10^{-4}	14	2.642×10^{-2}
6	5.612×10^{-3}	15	2.707×10^{-2}
7	3.951×10^{-4}	16	4.294×10^{-2}
8	1.139×10^{-2}	17	8.415×10^{-3}
9	2.290×10^{-2}	18	9.351×10^{-2}

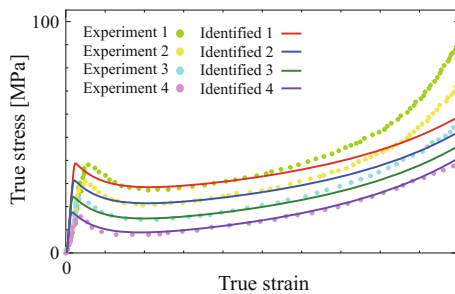


Fig. 5 Identification results. The result successfully captures the stress softening after quasi-yielding and followed by the orientation-hardening phenomenon. However, in all the cases, the initial elastic regime deviate from the experimental one and the hardening progresses in a large deformation regime are almost in parallel. These discrepancies must be due to the lack of the data of dynamic viscoelastic behavior

in the proposed model takes into account the variation of the shear yield strength. However, since the time-variation of the free volume caused by molecular chain slippage is not considered, the calculated curves lack the smoothness of the softening behavior around the upper yielding points. Also, the orientation hardening can be represented thanks to the introduction of the back stress, though the representation of the effect of extended chains are insufficient. This discrepancy is probably due to the fact that the viscoplastic deformation rates of all the rate levels are almost the same in a large strain regimes and so are the evolutions of the back stresses that depends on the viscoplastic deformation. The improvement of these performances are future subjects of study.

Finally, in order to reflect the temperature-dependent behavior and viscoelastic characteristics in the proposed model, we need more tensile test results with different temperature levels, dynamic viscoelastic measurements and strain recovery tests. It is therefore to be noted that the material behavior presented in this study with the assumed material parameters are not relevant to these properties and cannot be representative of actual thermoplastic materials.

4 Numerical Examples

Using the proposed constitutive laws with the material parameters determined in the previous section, we demonstrate the fundamental material behavior that can be represented by the proposed constitutive model.

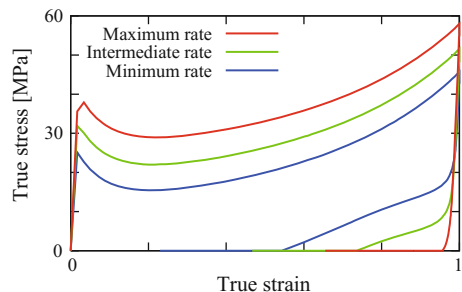
4.1 Behavior Under Loading, Unloading and Uncontrolled States

With the same single element model used for the parameter identification in the previous section, consecutive uniaxial responses under loading, unloading and uncontrolled conditions are demonstrated. Three levels of deformation rates at ambient temperature of 90 °C are considered in this example. The corresponding analysis cases are labelled as Maximum, Intermediate and Minimum Cases in the order of the rates. For Maximum Case, the single element is subjected to loading in the first 10 s, unloading in the next 10 s and then uncontrolled for the last 30 s. For Intermediate and Minimum Cases, the time intervals are 10 and 100 times longer than the maximum case, respectively. In each of these analysis cases, the maximum tensile true strain is set to be 1.0.

Figure 6 shows the calculated relationships between true stresses and true strains. As can be recognized from this figure, the yielding behavior depends on the deformation rates; that is, the higher the initial yield stress, the higher the deformation rate. Also, after the stress softening, all the stress responses evolve in the same manner. Specifically, the stresses are increased at the same rate so that the curves are almost parallel. This is probably due to the fact that the evolution rates of the viscoplastic multiplier are the same for all the cases, implying that the evolution rates of the shear yielding strength s^* are the same regardless of deformation rates.

In the unloading process, the higher the deformation rate, the larger the inclination. More specifically, the stress in Maximum Case is almost linearly decreased and only a small amount of strain is recovered by the stress-free state. This is due the fact that, as the deformation rate becomes lower, the inelastic deformation becomes

Fig. 6 Relationships between true stresses and true strains obtained under tensile loading, unloading and uncontrolled conditions



more prominent during the unloading process. On the other hand, as the deformation rate becomes lower in the unloading process, the curves are more gently inclined. In fact, almost half of the total true strain is recovered in Minimum Case. This is due to the viscoplastic deformation in the unloading process caused by the residual stress. These responses in the unloading process are not consistent with the experimental evidence reported in the literature (see, for example, Srivastava et al. [30]) and the discrepancy must be due to the assumed values of viscoelastic material parameters such as elastic moduli and relaxation times.

In the uncontrolled process with the external loading being zero, the amount of strain recovery is the same for all the cases, implying that the corresponding residual stresses due to viscoelastic deformation are comparable. Although this kind of strain recovery is always observed in experiments with cyclic loading, few existing constitutive models for amorphous thermoplastic resins direct attention towards the representation of strain recovery along with viscoplastic characteristics.

To study the underlining mechanisms of the above-mentioned apparent behavior, we provide the variations of viscoelastic non-equilibrated stresses in some Maxwell elements in Fig. 7 Here, we have chosen elements No. 12, 16, 17 and 18, as they exhibit relatively large viscoelastic stresses. First, in the loading process, the dominant stress responses in each of the subfigures are similar to those of the total

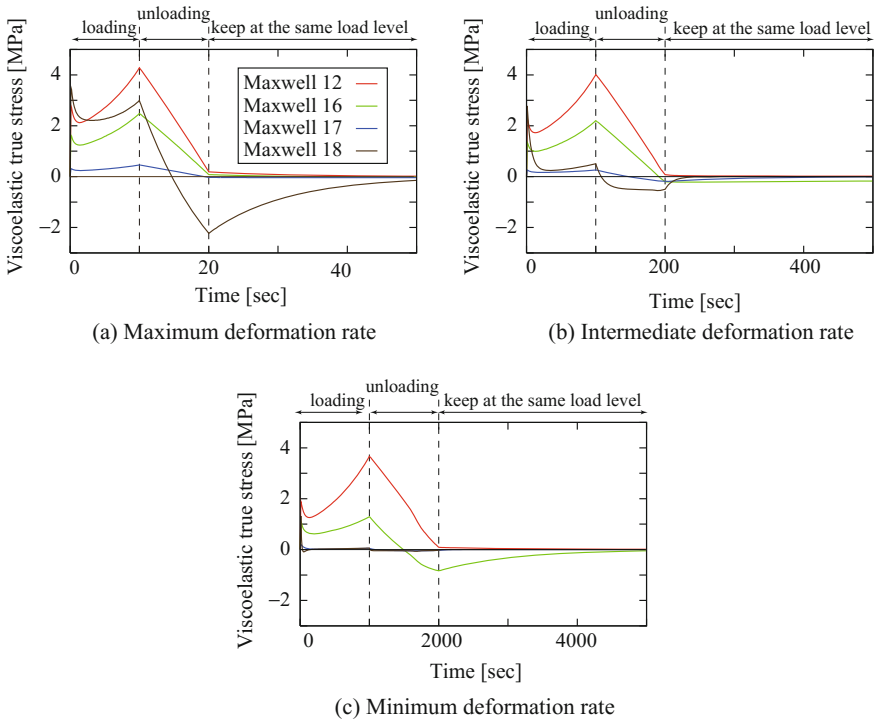


Fig. 7 Thermomechanical viscoelastic stresses of Maxwell elements

true stresses depicted in Fig. 6. This must be due to the fact that the stress in the proposed constitutive model is realized only in the set of viscoelastic rheology elements and directly affected by viscoplastic flow and back stress. Also, in the unloading process, most of the viscoelastic stresses are decreased in an almost linear manner, but some of them exhibit negative or compressive values, even though the total stress are positive. Then, these negative stresses remain when the external loading becomes zero and gradually relaxed in the uncontrolled process. Thus, the main sources of the residual stress that plays a driving force for the strain recovery mentioned above must be these negative viscoelastic stresses.

In addition, element No. 12 and 16 are active in all the cases. However, element No. 17 and 18 contribute the total stress in Maximum Case, while the effect of element No. 18 disappears in Intermediate Case. Moreover, both the effects of element No. 17 and 18 are not negligible in Minimum Case. These viscoelastic responses that depend on deformation rate are relevant to the relationship between relaxation time and time rate of change of deformation. In fact, the time spent in the loading process of Maximum Case is 10 s, which is comparable with the relaxation time of element No. 18. It is reasonable for Maxwell's elements with short relaxation times to respond to higher rates of deformation.

4.2 Stress Relaxation and Strain Recovery in a Standard Specimen

Using the same material parameters determined above, we carry out two simulations of uni-axial tests for a standard specimen shown in Fig. 8 to demonstrate the capability of the proposed constitutive model. One of them is a stress relaxation test and the other is a strain recovery test. The finite element (FE) model used here is composed of 2160 eight-node hexahedral elements with 3597 nodes and one-quarter of the specimen. The maximum elongation in the loading process is set at 60 mm for both of the simulations and the ambient temperature of 50 °C is kept constant during the entire process.

For both cases of numerical simulations, the specimen is loaded in 10 s. Then the elongation of 60 mm is kept for 10 s in the stress relaxation case. In the strain recovery case, the reaction force at the end section is reduced to zero in 10 s and the specimen is left untouched for 10 s. Figures 9 and 10 show the time-variations of the apparent stress and the relationships between true stress and strain for the stress relaxation and strain recovery cases, respectively. Here, the apparent stress is defined as the reaction force divided by the end section area of the specimen, which is referred to as nominal stress in this study. On the other hand, the true stress and strain are measured at the center of element A indicated in Fig. 8. In these figure, State (F) corresponds to the end of the loading, while (L) in Fig. 9 and (J) in Fig. 10 correspond the ends of the processes of stress relaxation and strain recovery, respectively.

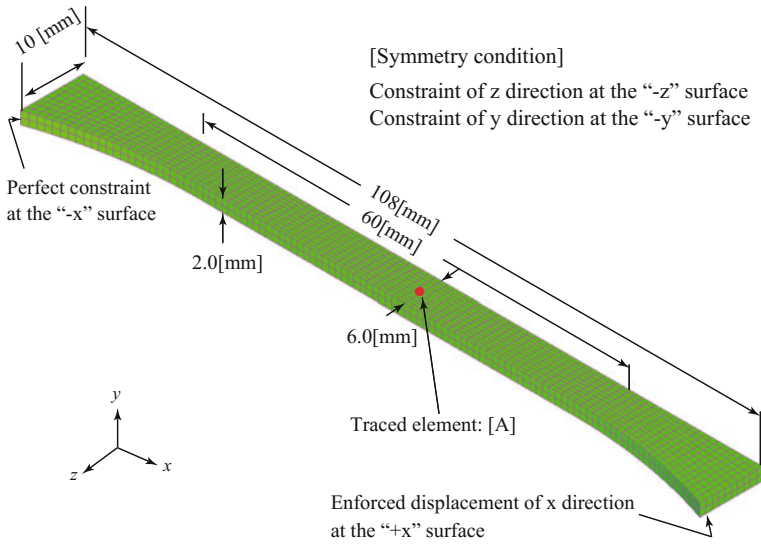


Fig. 8 Tensile specimen model with spatial dimension and boundary conditions

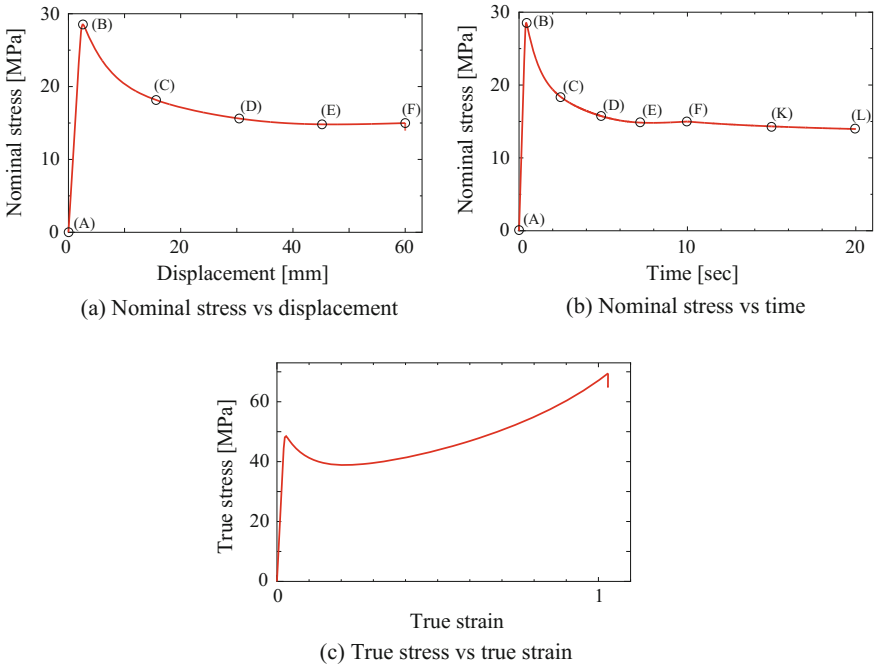


Fig. 9 Analysis results of stress relaxation test: **a** Relationship between nominal stress and enforced displacement; **b** Relationship between nominal stress and time; **c** Relationship between true stress and true strain

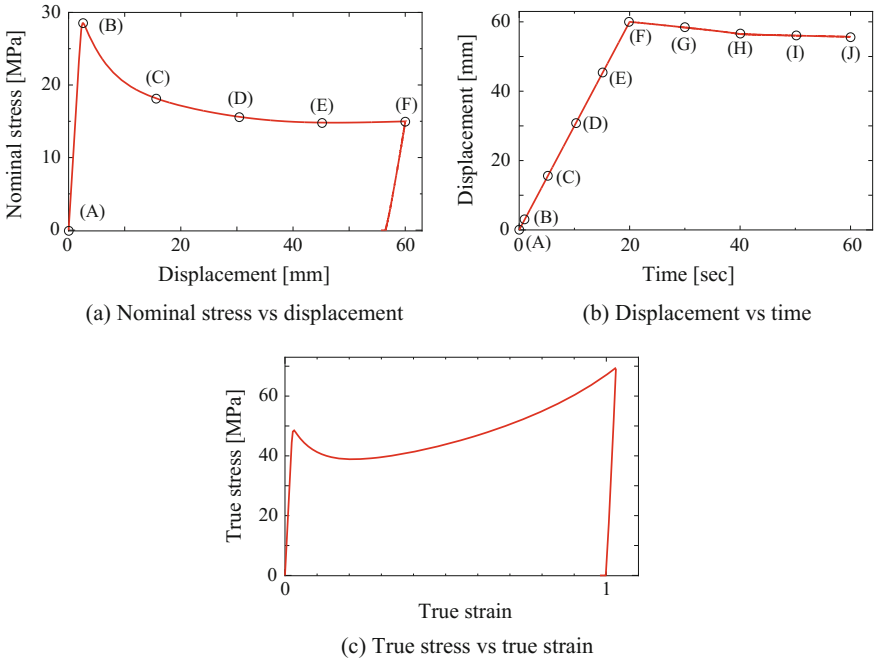


Fig. 10 Analysis results of strain recovery test: **a** Relationship between nominal stress and enforced displacement; **b** Relationship between enforced displacement and time; **c** Relationship between true stress and true strain

Fig. 11 Deformed configurations with von-Mises equivalent stress distributions in the tensile specimen of during loading process

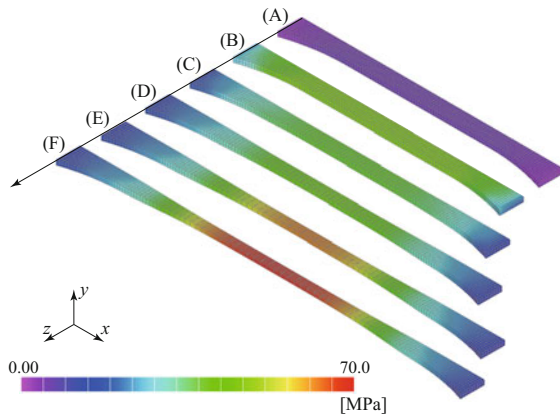


Figure 11 shows the deformed configurations with the distributions of von-Mises stresses at six deformation states calculated in the loading process. As can be seen in the figure, when the specimen reaches a moderate deformation level, the necking phenomenon becomes visible around the central part of the specimen, which is

followed by the stress concentration due to large deformation. The subsequent deformed configurations with the von-Mises stress distributions are shown in Fig. 12 for the stress relaxation case and Fig. 13 for the strain recovery case, in which each of the deformed configurations corresponds to the state indicated in Figs. 9 and 10.

The deformation process from States (A)–(F) depicted in Fig. 11 is common to both the stress relaxation and strain recovery cases. In State (B) at the beginning of tensile deformation, both the apparent and true stresses attain their maximum values and then decrease towards State (C). Although the decrease in the apparent stress here is also typical in standard specimens of metals, the decrease in the true stress is unique to the mechanical behavior of amorphous thermoplastic resins. It is, however, known that, in actual experiments, the specimen exhibits the localization of viscoplastic strain due to necking at the central part of the specimen and its region expands towards the end section during the stress softening behavior after the initial yielding. The proposed model is capable of representing stress softening, but not such localization phenomena. In fact, the necking starts after State (D) of moderate deformation in our numerical simulation. As can be seen in (E) and (F) of (c) in Figs. 9 and 10, the orientation hardening is observed in the true stress at the last stage of the loading process. This has also been demonstrated in the previous subsection. In these states of deformation, the stress is concentrated around the central part of

Fig. 12 Deformed configurations with the von-Mises equivalent stress distributions in tensile specimen during sustained tensile process in stress relaxation case

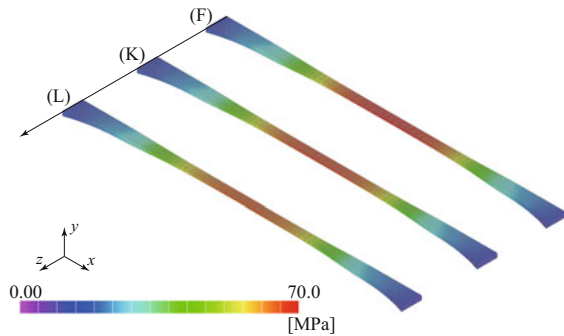
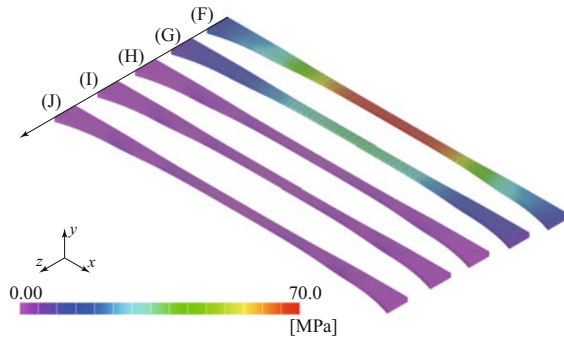


Fig. 13 Deformed configurations with von-Mises equivalent stresses distributions in the tensile specimen of during unloading and sustaining processes in strain recovery case



the specimen. On the contrary, the apparent stress is not affected by such hardening behavior and provides almost constant level reflecting only the resistance against the viscoplastic flow.

The deformed configurations with stress distributions from States (F)–(L) for the stress relaxation case, which is illustrated in Fig. 12, show that the stress relaxation is observed in the whole part of the specimen, but predominant around the central part of the specimen. However, the amount of stress relaxation is small, because the sustained period of constant elongation was set short.

For the strain recovery case, the whose deformation states during unloading and sustaining processes are illustrated in Fig. 13. In the unloading process, which corresponds to States (G) and (H), the nominal and true stresses significantly decrease due to the rapid recovery of elastic springs of each Maxwell element. As can be seen from Fig. 10, some of the Maxwell elements are supposed to be non-equilibrated in State (I) in Fig. 13 and then equilibrated in State (J) so that a small strain is recovered in the sustaining process.

Both the stress transitions and deformation states have been obtain as we originally intended. It should be noted that the stress relaxation and strain recovery responses simulated here are attributed to the coupling between viscoelasticity and viscoplasticity whose rheology elements are aligned in series. However, mainly due to inadequate parameter setting, the extents of stress relaxation and strain recovery are scarce. Also, there must be some room for improvement in function forms of the constitutive laws.

5 Conclusion

We have proposed a viscoelastic-viscoplastic combined constitutive model for amorphous thermoplastic resins within the finite strain framework. The simple rheology model introduced consisted of viscoelastic and viscoplastic elements connected in series. The standard generalized Maxwell model was used to determine the stress and characterize the viscoelastic material behavior at small or moderate strain regimes. On the other hand, we employed a proven finite strain viscoplastic model to realize the creep deformations along with the kinematic hardening behavior due to orientation of molecular chains. After the material parameters were identified with reference to experimental data, the fundamental performances of the proposed model were verified in representative numerical examples. In particular, it has been confirmed that the proposed model is capable of reproducing stress softening and strain recovery simultaneously.

However, due to the lack of experimental data that consistently represent both viscoelastic and viscoplastic responses, the quantitative agreement with the actual material behavior could not be confirmed. Indeed, a simple viscoplastic model seems not to have adequate performance in reflecting the limiting extensibility of polymer chains. Also, the identification accuracy of the viscoelastic spectral characteristics was not satisfactory and accordingly the strain recovery phenomenon were unreal-

istic. Nonetheless, it was our original contribution that the elastic characteristics of thermoplastic resins were totally taken by the set of viscoelastic rheology elements because of the connection of these two separate rheology elements in series.

Of course, various improvements must be introduced to our model. For example, the present model neglects the dependencies of the elastic and orientation hardening responses on temperature. It is also known that viscoelastic properties of amorphous thermoplastic resins become prominent when microscopic Brownian motions of molecular chains become active around the glass transition temperature and when pseudo chemical crosslink is constructed by the change in molecular chain orientation caused by crystallization. Thus, the rubber-like material behavior must appear above the glass-transition temperature. It remains a challenge for future research to incorporate these temperature dependencies.

References

1. N. Aleksy, G. Kermouche, A. Vautrin, J.M. Bergheau, Numerical study of scratch velocity effect on recovery of viscoelastic-viscoplastic solids. *Int. J. Mech. Sci.* **52**, 455–463 (2010)
2. N.M. Ames, V. Srivastava, S.A. Chester, L. Anand, A thermo-mechanically coupled theory for large deformations of amorphous polymers. part II: applications. *Int. J. Plast.* **25**, 1495–1539 (2009)
3. L. Anand, N.M. Ames, V. Srivastava, S.A. Chester, A thermo-mechanically coupled theory for large deformations of amorphous polymers. part I: formulation. *Int. J. Plast.* **25**, 1474–1494 (2009)
4. L. Anand, M.E. Gurtin, A theory of amorphous solids undergoing large deformations with application to polymeric glasses. *Int. J. Solids Struct.* **40**, 1465–1487 (2003)
5. A.S. Argon, A theory for the low-temperature plastic deformation of glassy polymers. *Philos. Mag.* **28**, 839–865 (1973)
6. A.S. Argon, *The Physics of Deformation and Fracture of Polymers* (Cambridge University Press, Cambridge, New York, USA, 2013)
7. J.M. Ball, Convexity conditions and existence theorems in nonlinear elasticity. *Arch. Ration. Mech. Anal.* **63**, 337–403 (1976)
8. M.C. Boyce, D.M. Parks, A.S. Argon, Large inelastic deformation of glassy polymers. part I: rate dependent constitutive model. *Mech. Mater.* **7**, 15–33 (1988)
9. R.B. Dupaix, M.C. Boyce, Constitutive modeling of the finite strain behaviour of amorphous in and above the glass transition. *Mech. Mater.* **39**, 39–52 (2007)
10. H. Eyring, Viscosity, plasticity, and diffusion as examples of absolute reaction rates. *J. Chem. Phys.* **4**, 283 (1936)
11. R. Fleischhauer, H. Dal, M. Kaliske, K. Schneider, A constitutive model for finite deformation of amorphous polymers. *Int. J. Mech. Sci.* **65**, 48–63 (2012)
12. P.J. Flory, Thermodynamic relations for high elastic materials. *Trans. Faraday Soc.* **57**, 829–838 (1961)
13. D.G. Fotheringham, B.W. Cherry, The role of recovery forces in the deformation of linear polyethylene. *J. Mater. Sci.* **13**, 951–964 (1978)
14. A.N. Gent, A new constitutive relation for rubber. *Rubber Chem. Technol.* **69**, 59–61 (1996)
15. G.A. Holzapfel, J.C. Simo, A new viscoelastic constitutive model for continuous media at finite thermomechanical changes. *Int. J. Solids Struct.* **33**, 3019–3034 (1996)
16. G.A. Holzapfel, *Nonlinear Solid Mechanics a Continuum Approach for Engineering* (Wiley) (2000)

17. P.S. Hope, I.M. Ward, A.G. Gibson, The hydrostatic extrusion of polymethylmethacrylate. *J. Mater. Sci.* **15**, 2207–2220 (1980)
18. G. Kermouche, N. Aleksey, J.M. Bergheau, Viscoelastic-viscoplastic modelling of the scratch response of PMMA. *Adv. Mater. Sci. Eng.* **2013** (2013), Article ID 289698
19. E. Kröner, Allgemeine kontinuumstheorie der versetzungen und eigenspannungen. *Arch. Ration. Mech. Anal.* **4**, 273–334 (1960)
20. E.H. Lee, Elastic plastic deformation at finite strain. *J. Appl. Mech.* **36**, 16 (1969)
21. J.C.M. Li, J.J. Gilman, Disclination loops in polymers. *J. Appl. Phys.* **41**, 4248–4256 (1970)
22. G.C.T. Liu, J.C.M. Li, Strain energies of disclination loops. *J. Appl. Phys.* **42**, 3313–3315 (1971)
23. A.D. Mulliken, M.C. Boyce, Mechanics of the rate-dependent elastic-plastic deformation of glassy polymers from low to high strain rates. *Int. J. Solids Struct.* **43**, 1331–1356 (2006)
24. B. Nedjar, Frameworks for finite strain viscoelastic-plasticity based on multiplicative decompositions. part I: continuum formulations. *Comput. Methods Appl. Mech. Eng.* **191**, 1541–1562 (2002a)
25. B. Nedjar, Frameworks for finite strain viscoelastic-plasticity based on multiplicative decompositions. part II: computational aspects. *Comput. Methods Appl. Mech. Eng.* **191**, 1563–1593 (2002b)
26. E.A. de Neto Souza, D. Peric, D.R.J. Owen, *Computational Methods for Plasticity: Theory and Applications* (Wiley, Chichester, West Sussex, UK, 2008)
27. J. Richeton, S. Ahzi, L. Daridon, Y. Remond, A formulation of the cooperative model for the yield stress of amorphous polymers for a wide range of strain rates and temperatures. *Polymer* **46**, 6035–6043 (2005)
28. J. Richeton, S. Ahzi, K.S. Vecchio, F.C. Jiang, R.R. Adharapurapu, Influence of temperature and strain rate on the mechanical behavior of three amorphous polymers: Characterization and modeling of the compressive yield stress. *Int. J. Solids Struct.* **43**, 2318–2335 (2006)
29. J. Richeton, S. Ahzi, K.S. Vecchio, F.C. Jiang, A. Makradi, Modeling and validation of the large deformation inelastic response of amorphous polymers over a wide range of temperatures and strain rates. *Int. J. Solids Struct.* **44**, 7938–7954 (2007)
30. V. Srivastava, S.A. Chester, N.M. Ames, L. Anand, A thermo-mechanically-coupled large-deformation theory for amorphous polymers in a temperature range which spans their glass transition. *Int. J. Plast.* **26**, 1138–1182 (2010)
31. P.D. Wu, E.V.D. Giessen, Analysis of shear band propagation in amorphous glassy polymers. *Int. J. Solids Struct.* **31**, 1493–1517 (1994)
32. P.D. Wu, E.V.D. Giessen, On neck propagation in amorphous glassy polymers under plane strain tension. *Int. J. Plast.* **11**, 211–235 (1995)

Fracturing in Dry and Saturated Porous Media

Enrico Milanese, Toan Duc Cao, Luciano Simoni
and Bernhard A. Schrefler

Abstract It is now generally recognized that mode I fracturing in saturated geomaterials is a stepwise process. This is true both for mechanical loading and for pressure induced fracturing. Evidence comes from geophysics, from unconventional hydrocarbon extraction, and from experiments. Despite the evidence only very few numerical models capture this behavior. From our numerical experiments, both with a model based on Standard Galerkin Finite Elements in conjunction with a cohesive fracture model, and with a truss lattice model in combination with Monte Carlo simulations, it appears that already in dry geomaterials under mechanical loading the fracturing process is time discontinuous. In a two-phase fracture context, in case of mechanical loading, the fluid not only follows the fate of the solid phase material and gives rise to pressure peaks at the fracturing event, but it also influences this event. In case of pressure induced fracture clearly pressure peaks appear too but are of opposite sign: we observe pressure drops at fracturing. In mode II fracturing, the behavior is brittle while in mixed mode there appears a combination of pressure rises and drops.

Dedicated to Roger Owen in occasion of his 75th birthday.

L. Simoni · B.A. Schrefler (✉)
Department of Civil, Environmental and Architectural Engineering,
Via Marzolo, 9, 35131 Padua, Italy
e-mail: bernhard.schrefler@dicea.unipd.it

T.D. Cao
Center for Advanced Vehicular Systems (CAVS) and Department of Civil and Environmental
Engineering, Mississippi State University, Starkville, USA

B.A. Schrefler
Institute for Advanced Study, Technical University Munich, Munich, Germany

E. Milanese
Civil Engineering Institute, Materials Science and Engineering Institute, École Polytechnique
Fédérale de Lausanne (EPFL), Station 18, 1015 Lausanne, Switzerland

1 Introduction

Fracture advancement in saturated porous media is generally a discontinuous process both for fluid pressure induced fracture and for fracture induced by mechanical action. This is certainly true for mode I fracturing and for many situations in mixed mode fracturing. This has been observed in the field for geophysics, in hydraulic fracturing operations, and laboratory tests. As far as field observations from geophysics are concerned, see [4, 5, 11, 12, 16, 18, 48–50, 53, 62, 65]. This list contains both cases of fluid pressure induced fracture and fracture due to changes of mechanical boundary conditions. Intermittent fracture advancement is the most plausible mechanism to explain the existence of volcanic and subduction tremor. Field observations in case of non-conventional hydrocarbon extraction through hydraulic fracturing are reported by Okland et al. [51], Soliman et al. [68], and de Pater [19]. Laboratory tests evidencing the stepwise advancement have been carried out for hydraulic fracturing by Black et al. [6], Lhomme et al. [39] and Lhomme [38]. See for instance Fig. 1 from Lhomme et al. [39]. There are also tests which do not evidence the phenomenon, apart from the tests with a high viscosity fluid and low flow rate of [39], not deemed representative for hydraulic fracturing in the field. There are different reasons for this: sometimes test design criteria are introduced in order to obtain results that are directly comparable with the modeling [10, 35]; in other experiments the rate of fluid flow into the fracture is not constant and therefore cannot be described in terms of a single value of imposed flux [9] or time does not appear explicitly in the solution, which takes the form of a classical traveling wave-type solution and the sampling time is sometimes too large if compared to the experiment referred to [33]. On the other hand, some irregularity of the phenomenon can be seen also in these experiments, even though when modeling this is ignored.

For the case of mechanical load [54] clearly showed the stepwise behavior. Despite of the overwhelming evidence only very few numerical models and no analytical model capture the phenomenon as will be shown in the extensive literature survey of the next section.

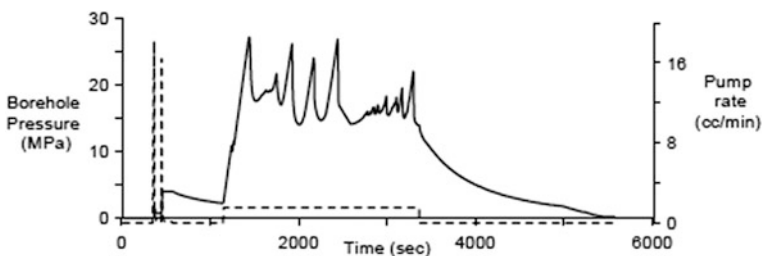


Fig. 1 Experimental pressure record and fracture inlet opening for low viscosity/high flow rate configuration. Redrawn with permission from Lhomme et al. [39]

We have investigated recently the fracturing behavior of geomaterials with both deterministic methods (Cao et al. [13]) and methods from statistical physics [43] and have found that already in dry geomaterials under mechanical loading the fracturing process is time discontinuous. In a two-phase fracture context and under mechanical loading, not only the fluid follows the fate of the solid phase and gives rise to pressure peaks at the fracturing event, but it also influences this event to a certain extent. These pressure peaks are shown in Fig. 2. In case of pressure induced fracture, pressure peaks appear too but are of opposite sign: we observe pressure drops at the fracturing event, see Fig. 3.

The following explanation has been given for this behavior, based on Biot's theory [43]: if a load, pressure, or displacement boundary condition is applied suddenly (all acting on the equilibrium of the solid–liquid mixture), then the fluid takes initially almost all the induced solicitation because its immediate response is undrained and it is much less compressible than the solid skeleton. It discharges hence the solid. Then through the coupling with the fluid through the volumetric strain, the overpressures dissipate and the solid is reloaded. Hence, we have a pressure rise upon rupture. Pressures and stresses evolve out of phase. On the contrary if flow is specified (acting on the continuity of the fluid) its effect is transmitted to the solid through the pressure coupling term in the effective stress. The solid is loaded and upon rupture produces a sudden increase of the volumetric strain. This in turn produces a drop in pressure. In this case stresses and pressures evolve in phase. In both cases the intervals between two crack tip advancements are found to be irregularly distributed. This is true even for homogeneous media.

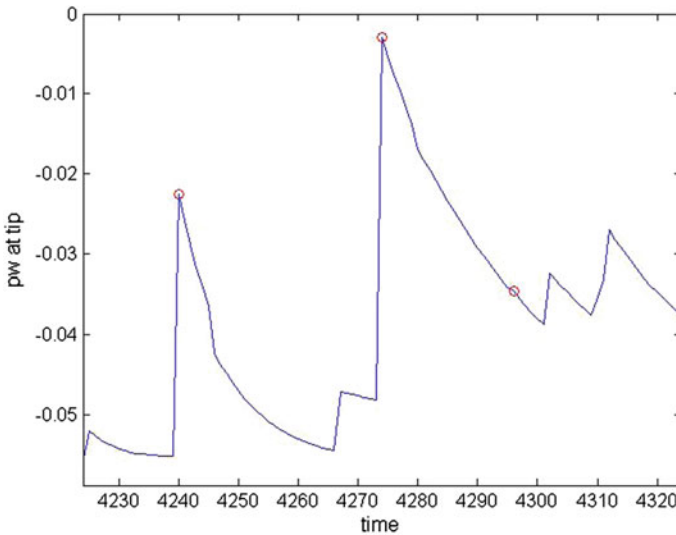


Fig. 2 Pressure rise at fracturing in case of a mechanical load. Redrawn with permission from Milanese et al. [43]

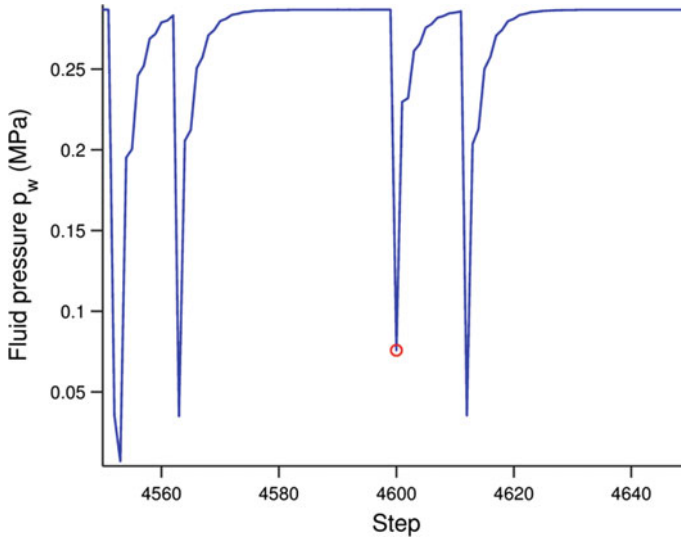


Fig. 3 Pressure drops at fracturing in case of pressure driven fracture. Redrawn with permission from Milanese et al. [43]

In mode II fracturing the behavior is brittle while in mixed mode there appears a combination of pressure rises and drops [45]. After an extensive literature survey addressing both analytical and numerical solutions the behavior under mode I fracture will be evidenced first for heterogeneous media using a lattice model and statistical analysis and then for homogeneous media by examples obtained with a lattice model, XFEM, and a model based on Standard Galerkin Finite Elements in conjunction with remeshing and cohesive fracture. Some conclusions will then be drawn.

2 Detailed Literature Review

2.1 Analytical Solutions

Contributions to the mathematical modeling of fluid-driven fractures have been made continuously since the 1960s, beginning with [17, 20, 29, 30, 52, 59]. Other papers deal with solid and fluid behavior near the crack tip (e.g. [2, 24]).

Traditional analytical solutions of hydraulic fracture problems rely on typical simplifying assumptions of asymptotic analyses that influence the real local pattern of time dependent parameters such as the tip velocity and pressure distribution near the tip. The most common ones concern fluid flow, fracture shape and velocity, leakage from the fracture, the presence of fluid lag and linear fracture mechanics for the solid. Further, uncoupled solutions are frequent, e.g. the solid/fluid interactions

are analyzed in two-step procedures in which only one field evolves in time. In more recent papers, (e.g. [1, 34]) a mixed approach is presented in which an asymptotic formulation is partially solved with numerical tools to reduce the above-mentioned simplifying assumptions, especially using finite differences in time.

Problems may arise with the assumption of linear fracture mechanics in a coupled environment. In fact, this implies a stress singularity in the tip region, hence a singularity in pressure, because of the effective stress principle. The fluid pressure consistent with the crack aperture asymptote of LEFM is weaker than $x^{(-1/2)}$ and reflects the finiteness of rate of energy dissipated by crack propagation. Consideration from lubrication theory, combined with LEFM results, implies that the fluid pressure has a logarithmic singularity. Any fluid pressure singularity is, however, precluded if the rock is permeable and diffusion of pore fluid is taking place. Indeed, a fluid pressure singularity would cause an infinite rate of energy dissipation by diffusion of fluid in the porous rock [22]. Further, LEFM is not the best model to investigate hydraulic fracturing. De Pater [19] states in fact that “carefully scaled laboratory studies have revealed that conventional models for fracture propagation which are based on LEFM cannot adequately describe propagation. Instead, propagation should at least be based on tensile failure over a cohesive zone”.

However, these analytical approaches certainly delineate the limits of the propagation regimes [25] and other important features such as the length scales. In fact, hydraulic fracturing represents a special class of cracking, due to the coupling between different processes (solid deformation, rock fracturing, fluid flow in the fracture, leak-off) taking place near the tip. As already mentioned each of these processes can be associated with a characteristic length-scale [21, 25]. Predominance amongst these length-scales determines the fracture response (the propagation regime), characterized by the order of the stress (or pressure) singularity. This yields a complex multi-scale solution for the propagation of the fracture. Even though these solutions are obtained at the scale of the near-tip region, the propagation regime of the whole fracture is determined by the tip [1]. Further, these authors remark that there is always a region immediately adjacent to the fluid front where the solution is dominated by fluid loss and most of the pressure drop occurs near the fracture tip, hence special care needs to be taken to obtain accurate results in this area.

For simple fracture geometries (radial, KGD, and PKN), the time scales can be expressed explicitly in terms of the problem parameters (fluid viscosity, rock properties, and injection rates). Recognition of the existence of multiple time scales led to the identification of particular solutions that correspond to a regime of fracture propagation dominated by one process only. For example, under conditions where the in situ stress is large enough (as is usually the case for deep stimulation treatments), two time scales characterize the evolution of a radial fracture: the first tracks the transition between a regime of propagation where most of the energy essentially is dissipated in viscous flow of the fracturing fluid, and another regime where most of the energy is used to fracture the rock; and a second time scale that

characterizes the evolution from situations where the injected fluid essentially is stored in the fracture to situations where most of the fluid has leaked into the rock. Analytical solutions are always smooth hence they do not reproduce the stepwise behavior of the tip advancement previously discussed and experimentally recorded. Further they do not represent an evolutionary problem in a domain with a real complexity, continuously changing with the evolution of the phenomenon and do not account for a material behavior more realistic than linear. Only numerical methods give the continuous alternation of the different regimes, depending on forcing functions, boundary conditions and intrinsic time scales. This fact stresses also the need of a careful time discretization of the governing equations combined with a careful choice of the crack advancement algorithm.

2.2 Numerical Simulations

From the preceding remarks, it follows clearly that a numerical solution, including coupling of fracture propagation and fluid exchange between the fracture and the formation, is the most appropriate way to simulate fracturing in fluid saturated media. We analyze briefly whether the solutions found in literature were able to evidence and model the stepwise crack advancement and pressure fluctuations experimentally observed. Given that this behavior can be properly explained by means of the generalized Biot's theory, numerical models base on fluid–solid interaction of the Biot's type should be capable of simulating the steps and pressure jumps provided that a proper crack advancement/time stepping algorithm is used. If this is not the case the respective models perturb the interactions.

The first numerical model for hydraulic fracture has been presented by Boone and Ingraffea [7]. It uses a Biot's approach coupled with linear fracture mechanics, accounts for fluid leakage in the medium surrounding the fracture and assumes a moving crack depending on the applied loads and material properties. A finite element solution for solid and finite differences for flow equation is adopted. It is assumed however that the path of the fracture is known a priori and contact elements are placed along this path. Crack length, mouth opening displacement together with mouth and fracture pressure versus time show a regular pattern.

Carter et al. [15] extended the application to a fully 3-D hydraulic fracture frame. Their model relies on hypotheses similar to [7], in particular assuming the positions where fractures initiate, but neglects the fluid continuity equation in the medium surrounding the fracture. The quasi-static solution consists of a series of snapshots in time, where the fracture geometry is fixed and the corresponding time is determined. In both cases, no care is devoted to the tip region velocity and to its regular/irregular distribution in time.

Starting from these pioneering works different numerical approaches have been presented, which are discussed next. Biot's theory in conjunction with a discrete fracture approach making use of remeshing in an unstructured mesh and automatic mesh refinement has been used by Schrefler et al. [60, 61], in a 2D setting.

An element threshold number (i.e. number of elements over the cohesive zone) was identified to obtain mesh-independent results. This approach has been extended to 3D situations by Secchi and Schrefler [63]. The last two cited papers show clearly the stepwise fracture advancement and oscillations of the crack mouth pressure. The advancement steps are irregularly distributed in time which is conjectured to be a signature that the steps are of physical nature and not numerical artifacts.

R  thor   et al. [57] proposed a two-scale model for fluid flow in a deforming, unsaturated and progressively fracturing porous medium within the realm of Biot's theory. At the microscale, the flow in the cohesive crack is modeled using Darcy's relation for fluid flow in a porous medium, considering changes in the permeability due to the progressive damage evolution inside the cohesive zone. By exploiting the partition-of-unity property of the finite element shape functions, the position and direction of the fractures are independent from the underlying discretization. A pre-notched plate is solved but the authors do not show crack advancement nor mention any fluctuations whatsoever. In our opinion two scales procedures interfere with the interacting velocities and hence affect adversely the solution.

Extended Finite Elements (XFEM) have been applied to hydraulic fracturing in a partially saturated porous medium by R  thor   et al. [58] in a 2D setting. In this case, again a two scale-model has been developed for the fluid flow. As example, rupture of a saturated square plate in plane strain conditions is investigated under a prescribed fixed vertical velocity in opposite direction at the top and bottom of the plate (tensile loading). No stepwise advancement nor pressure fluctuations are evidenced, probably because the two-step solution influences the velocity fields.

Partition of unity finite elements (PUFEM) are used for 2D mode I crack propagation in saturated porous media by Kraaijeveld and Huyghe [31] and Kraaijeveld et al. [32]. A pull test, a delamination test and an osmolarity test are simulated with rather fine regular meshes. Stepwise advancement and flow jumps were found by Kraaijeveld and Huyghe [31] with a strong and a weak discontinuity model for flow while in [30] the stepwise advancement in mode I crack propagation is difficult to see because a continuous pressure profile across the crack is used which only works for sufficiently fine meshes. In that case, the advantage of PUFEM, which allows keeping the mesh pretty rough all over the continuum, would be lost. In mode II as shown in Kraaijeveld et al. [32] a discontinuous pressure across the crack is accounted for. It is not attempted to resolve the steep pressure gradient but this gradient is reconstructed afterwards, using the Terzaghi analytical solution for pressure diffusion. This two-step procedure allows for using a rough mesh, and still handling a realistic pressure gradient. However, the resulting steps show a regular pattern and are thought to be of numerical origin, see Remij et al. [56].

Carier and Granet [14] developed a zero-thickness finite element to model hydraulic fracture in a permeable medium within the framework of Biot's theory. The fracture propagation is governed by a cohesive zone model and the flow within the fracture by the lubrication equation. The solutions are smooth. Mohammadnejad and Kohei [47] show a fully coupled numerical model for hydraulic fracture propagation in porous media using the extended finite element method in

conjunction with the cohesive crack model. The governing equations are derived within the framework of the generalized Biot's theory. The fluid flow within the fracture is modeled using Darcy's law, in which the fracture permeability follows the cubic law. Among the two examples the one related to hydraulic fracturing shows very small regular steps in the fracture advancement which according to the authors are of numerical origin and are bound to disappear with more refined meshes. The pressures are smooth.

Mohammadnejad and Kohei [46] solve the same problem as in Réthoré et al. [58], also with XFEM, using full two-phase flow throughout the region. Cavitation is found in both papers, also due to the impervious boundary conditions chosen. Here all solutions are smooth.

A two scale model is used Remij et al. [55] where the pressure approximation in the fracture is enhanced by including an additional degree of freedom. The pressure gradient due to fluid leakage near the fracture surface is reconstructed based on Terzaghi's consolidation solution. This is supposed to ensure that all fluid flow goes exclusively in the fracture and it is not necessary to use a dense mesh near the fracture to capture the pressure gradient. The spatial discretization of the balance equations is based on the partition-of-unity property of finite element shape functions. The two-step procedure, the large time step size and coarse mesh influence the resulting fluid velocities and neither fluctuation nor stepwise advancement is reported. Use of the same method but with very small elements however clearly evidences the stepwise advancement and the pressure oscillations, see Milanese et al. [44].

Phase field models for propagating fluid-filled fractures coupled to a surrounding porous medium were applied in [28, 36, 40–42, 69, 71]. The published numerical results are smooth, in line with what expected from a diffuse representation of the fracture. Only Heider and Markert [28] report some pressure oscillation.

Grassl et al. [27] use a lattice approach but fail to evidence the intermittent behavior while the lattice model of [43], discussed below, clearly evidences the phenomenon.

Numerical models not relying on Biot's theory have also been published. These usually start from the same hypotheses as the analytical approaches. For instance, Lecampion and Detournay [34] presented an implicit moving mesh algorithm for the study of the propagation of plane-strain hydraulic fracture, with the fluid front distinct from the fracture tip. In our opinion, beyond the usual restrictions of the analytic approaches, further limits of this method are evident: the problem is assumed as 1D channel (integration is performed along the linear fracture) based on a relationship between fracture opening and internal pressure valid in a very unrealistic infinite elastic medium. In addition, an impermeable surrounding medium is assumed, which hides important phenomena such as the leaching from the fracture and certainly results in a smooth solution.

From this survey, it appears that while a large majority of authors uses Biot's theory, only the Standard Galerkin Finite Element Method (SGFEM) with or without a continuous updating of the mesh [60, 61, 23], XFEM with very small elements [13, 44] and the lattice model of [43] have captured the physics of fracturing in saturated porous media.

3 Governing Equations

According to Biot’s theory of porous media the mathematical model here used is composed of an equilibrium of the overall mixture and a mass balance equation for the fluid (Lewis and Schrefler [36]). We just indicate the governing equations for sake of completeness. Considering the symbols of Fig. 4, the linear momentum balance of the mixture, discretized in space, is written as

$$\mathbf{M}\mathbf{v} + \int_{\Omega} \mathbf{B}^T \boldsymbol{\sigma}'' d\Omega - \mathbf{Q}\mathbf{p} - \mathbf{f}^{(1)} - \int_{\Gamma'} (\mathbf{N}^u)^T \mathbf{c} d\Gamma' = 0 \tag{1}$$

$$\mathbf{f}^{(1)} = \int_{\Omega} (\mathbf{N}^u)^T \rho \mathbf{b} d\Omega + \int_{\Gamma'} (\mathbf{N}^u)^T \bar{\mathbf{t}}^g d\Gamma \tag{2}$$

where Γ' is the boundary of the fracture and process zone and \mathbf{c} the cohesive traction acting in the process zone as defined e.g. in Simoni and Schrefler [67]. The cohesive traction \mathbf{c} is different from zero only if the element has a side on the lips of the fracture Γ' within the process zone. The submatrices of this and the following equations are the usual ones of soil consolidation [37], except for those specified in the sequel.

The fully saturated porous medium surrounding the fracture has constant absolute permeability and the discretized mass balance equation reads as

$$\mathbf{Q}\mathbf{u} + \mathbf{H}\mathbf{p} + \mathbf{S}\mathbf{p} - \mathbf{f}^{(2)} + \int_{\Gamma'} (\mathbf{N}^p)^T \bar{\mathbf{q}}^w d\Gamma' = 0 \tag{3}$$

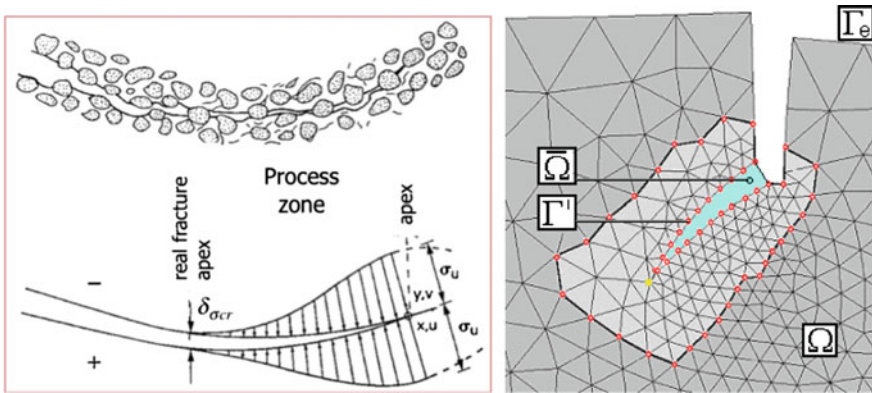


Fig. 4 Definition of cohesive crack geometry and hydraulic fracture domain. Redrawn with permission from Schrefler et al. [61]

where \bar{q}^v represents the water leakage flux along the fracture toward the surrounding medium; this term is defined along the entire fracture, i.e. the open part and the process zone. $\mathbf{f}^{(2)}$ contains the assigned flow terms. Given that the liquid phase is continuous over the whole domain, leakage flux along the opened fracture lips is accounted for through the \mathbf{H} matrix. In the present formulation, non-linear terms arise through cohesive forces in the process zone. Discretization in time is then performed with time Discontinuous Galerkin approximation following Simoni et al. [66].

We present here briefly the numerical methods used in the applications for multi-phase crack propagation.

4 Numerical Methods

4.1 *Lattice Model for Homogeneous and Heterogeneous Porous Media*

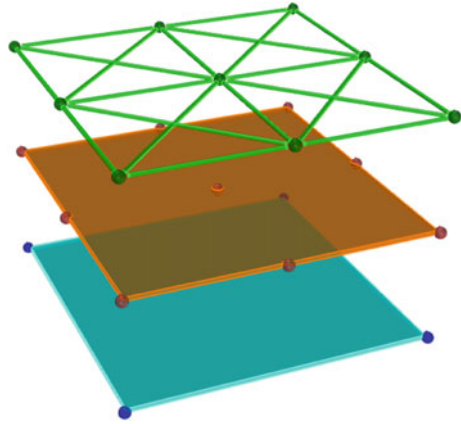
Statistical models are used to consider material disorder without the need of using averaged values of material properties, nor phenomenological models, such as cohesive ones, nor of locating geometrical singularities to trigger cracks. In Milanese et al. [43] a lattice model is used to analyse fracture propagation in a multi-phase system. The interested reader is referred to this paper for major details.

To account for material disorder, the mechanical properties of each element of the lattice are picked randomly from a statistical distribution. Because of this assumption, the exact crack path cannot be predicted and several cracks may appear at the same time within the domain. The solution of the crack problem requires several simulations run with the same boundary conditions but randomly varying material properties: a statistical analysis is then carried on the gathered data. This analysis focuses on the so-called “avalanche behaviour” of the specimen, i.e. the number of failing elements per step. It is known that in dry samples the probability distribution function of the recorded avalanches size displays power-law behaviour (see e.g. [71]). We will investigate whether adding a fluid phase changes this behaviour.

In a 2D context, the studied continuous solid domain is replaced by a lattice squared specimen with vertical, horizontal and diagonal bonds while the coupling matrix and the flow matrices are obtained by the finite element method (Fig. 5) as explained below. Random assumption of the properties of the bonds results in an isotropic macroscopic material behaviour. A central force model is locally adopted: the elements have only the axial degree of stress and strain, i.e. behave as truss elements. Linear measure of strain and constitutive equation are used.

Each bar of the lattice is provided with a stress threshold at which the bond fails. The vector of the stress thresholds of the overall bars is defined by a uniform distribution in the interval [0,1] MPa. In this way, the disorder of the medium is

Fig. 5 Representation of the overlapping three-layer unitary element of the model. From the *bottom* to the *top*: the fluid pressure 4-node plane element (*blue*), the coupling 9-node plane element (*orange*) and the solid skeleton made of 20 trusses (*green*)



represented. Each time the stress in a bond exceeds its threshold, this is updated from a new uniform distribution in the same interval.

Moreover, at the beginning of the simulation the Young's modulus is set to the same value for all the bars. During the simulation, when the stress in an element exceeds the local threshold, its elastic modulus is reduced, as $E_{new} = (1 - D)E_{old}$: where $D = 0$ means no damage and $D = 1$ means that the truss is completely broken and does not contribute anymore to the global stiffness. D is set equal to 0.1 and each truss can be damaged up to thirty times before the final failure, thus conveying an asymptotically decreasing damage rule. The model displays a clear and broad plastic phase.

Referring to the mechanical problem of Sect. 5.2.1 and to a generic load step, a uniform displacement distribution is imposed on boundary nodes. The governing equations are iteratively solved, updating the properties (elastic modulus and stress threshold) of any damaged truss, to reach an equilibrium state in which no stress threshold is exceeded in any bond. Then the successive load step is applied.

The avalanche size s is defined as the number of trusses damaged between two subsequent displacement increments.

In a two-phase plane problem, the solid field, the fluid and the coupling terms are overlapping and must be approximated: a 20-bar system, which mimics a 9-node continuous element, is assumed for the solid, a continuous 2D 4-node element is used for the fluid (matrices \mathbf{H} and \mathbf{S} in Eq. 3) and 9-node element for the coupling terms \mathbf{Q} in Eqs. 2 and 3 (Fig. 5). This results in a unitary element that builds up the lattice and can be viewed as a three-layer element with size $L_u = 2$. In this way, the Babuska-Brezzi condition is satisfied [3, 8].

According to the statistical approach, two time scales are used: one for the increments of the external loading Δt and another for the fracturing process within Biot's theory. The external loading is increased once the rearrangements are over, while a time interval for Biot's theory is fixed (in the application the value of 3000 s is assumed). The size of this interval allows to study the interaction between the two

phases. If a much smaller value is chosen, no consolidation type behavior is allowed between subsequent loading steps and damage localizes on the elements close to the border; if a much larger time increment value is chosen, consolidation type behaviour runs out before the load is increased in the following step and no interaction with the fluid phase appears. At any step n two scenarios can take place:

- (a) $t = t_n$: specified displacements are increased, Biot's coupled problem is solved and equilibrium is reached without any rearrangement (avalanche). Thus, time at step $n + 1$ equals to $t_{n+1} = t_n + \Delta t$;
- (b) $t = t_n$: specified displacements are increased, Biot's coupled problem is solved and equilibrium is not reached without rearrangements and m more sub-steps where Biot's coupled problem is solved are needed. Once the equilibrium is reached, the time for the external loading is updated. Thus, time at step $n + 1$ equals to $t_{n+1} = t_n + m \cdot \Delta t$.

4.2 SGFEM with Remeshing

In this approach, governing equations within the domain are supplemented by the fluid mass balance within the crack and a phenomenological equation for the solid behavior, i.e. the cohesive law. Two non-overlapping fluid domains are hence present (Fig. 4) and, because of their continuity, interactions such as leaching due to pressure gradients are easily accounted for. Fluid flow equation within the crack takes the following form, which highlights the different contributions and the transport law [65],

$$\mathbf{H}\mathbf{p} + \mathbf{S}\mathbf{p} + \mathbf{p} \int_{\Gamma'} (\mathbf{N}^p)^T \bar{q}^w d\Gamma' = 0 \quad (4)$$

with

$$\mathbf{H} = \int_{\bar{\Omega}} (\nabla \mathbf{N}^p)^T \frac{w^2}{12\mu_w} \nabla \mathbf{N}^p d\bar{\Omega} \quad (5)$$

$$\mathbf{S} = \int_{\bar{\Omega}} (\mathbf{N}^p)^T \frac{1}{Q^*} \mathbf{N}^p d\bar{\Omega} \quad (6)$$

In Eq. 5, w represents the fracture aperture. The last term of Eq. 4 embodies the leakage flux toward the surrounding porous medium across the fracture borders. In this formulation, this coupling term does not require special assumptions, as, e.g. in Remij et al. [55], or oversimplified assumptions that hide important phenomena taking place in the fracture domain, as e.g. in Réthoré et al. [57]. It can be

represented by means of Darcy's law using the permeability of the surrounding medium and pressure gradient generated by the application of water pressure on the fracture lips.

Because of the continuous variation of the domain due to the propagation of the cracks the domain $\bar{\Omega}$, its boundary Γ' and the related mechanical conditions change. Along the formed crack edges and in the process zone, boundary conditions are the direct result of the field equations while the mechanical parameters must be updated. The fracture path, the position of the process zone and the cohesive forces are unknown and must be regarded as products of the mechanical analysis.

The substantial improvements of SGFEM capabilities in solving hydro-mechanically coupled problems originate from the remeshing procedure. This has been discussed in detail in Schrefler et al. [61], to which the interested reader is referred. It is a common opinion that remeshing is a cumbersome, time consuming and difficult task. This is not true, if efficient mesh generators are available. For instance, to build a triangular unstructured mesh in 2D possessing optimal characteristics (i.e. all elements are almost equilateral triangles) in a very complex domain (Venice Lagoon, 550 km² with a hundred islands) using our mesh generator [63] 4.55 s are needed producing about 37,000 nodes and 67,500 elements. The advantage of this approach is to dynamically refine the mesh in areas presenting high gradients of the field variables and coarsening in others, to account for time changes of the spatial domain, with boundaries moving and singularity positions propagating in a not predictable way. Further, all equations of the mathematical model are naturally solved, without the necessity of scale length (as for instance the length of the process zone or the dimension of the area interested by the leaching from the fracture). Obviously limits exist for this approach, as in the case of micro-cracks and their coalescence, whereas nucleation and branching of macro-cracks are easily handled.

At each tip movement, the fracture domain is recognized during meshing operations, which accounts also for the process zone and fluid lag, then Eq. 4 is associated as mass balance, whereas the equilibrium equation is weakened by strongly reducing the material Young's modulus (see [65], for more details).

5 Numerical Applications

5.1 *Heterogeneous Media, Lattice Model, Statistical Analysis*

First, we show the results of a statistical analysis for heterogeneous dry and saturated media by means of the lattice model. In particular, the power law behavior and avalanche distribution versus time is addressed. With this model the cases of assigned biaxial boundary tractions, assigned pressures and assigned flow have been investigated. A square lattice of side 60 mm (mesoscopic level) is meshed

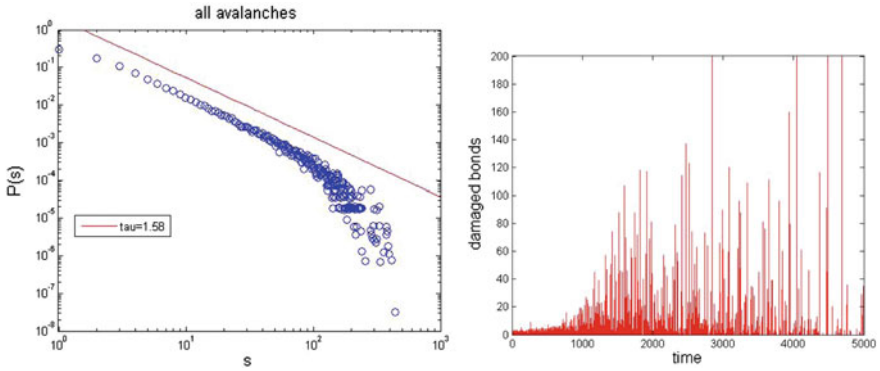


Fig. 6 Dry material square sample under boundary tractions: probability density function $P(s)$ versus avalanche size (*left*) and damaged bonds number (avalanches) versus time (*right*)

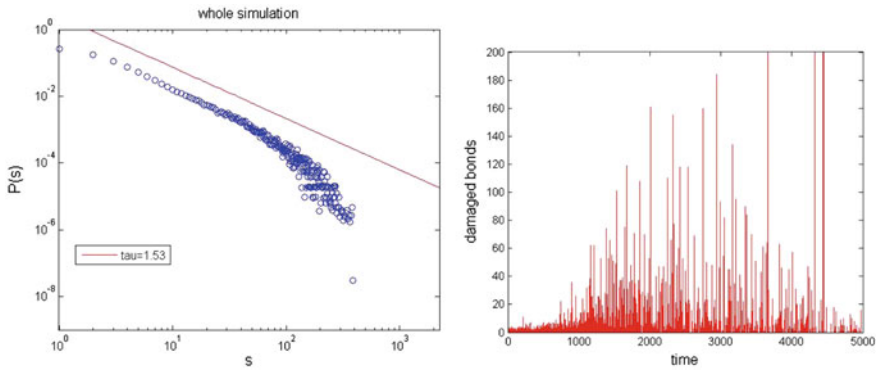


Fig. 7 Fully saturated square sample under boundary tractions: probability density function $P(s)$ versus avalanche size (*left*) and damaged bonds number (avalanches) versus time (*right*)

according to $L = 16$, where L is the number of three layer unitary elements (Fig. 5) aligned on the side direction. It has been shown in Milanese et al. [43] that, in the case of disordered media, lattices meshed with $L = 16; 32; 64$ elements per side display the same power law behavior i.e. the cut off of the avalanche size probability distribution scales with the system size and the solution is hence scale-free. This observation is confirmed in Girard et al. [26] for a mesh made of triangular elements and in Zapperi et al. [71] for a fuse model; it allows considering a sample with a smaller number of elements.

Figure 6 presents the statistical distribution of the avalanches and power law behavior obtained for a dry material. The addition of fluid to a dry sample does not change the statistical distribution of the avalanches nor the power law behavior, see Figs. 7 and 8. Imposing a pressure increase at the center of the saturated sample,

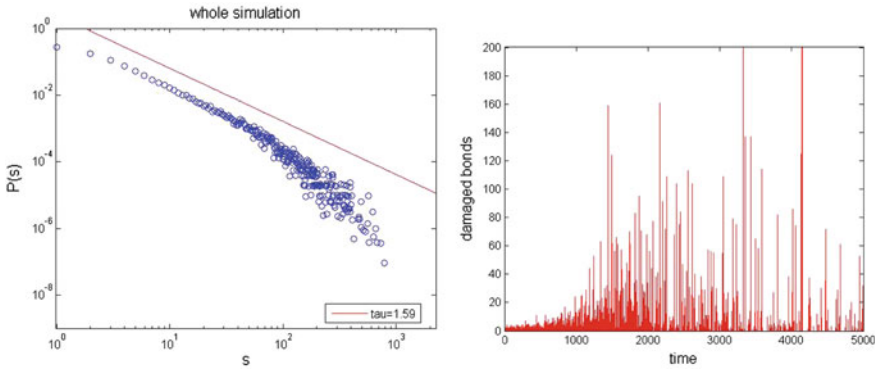


Fig. 8 Fully saturated square sample under boundary tractions and pressure increase assigned at the centre: probability density function $P(s)$ versus avalanche size (*left*) and damaged bonds number (avalanches) versus time (*right*)

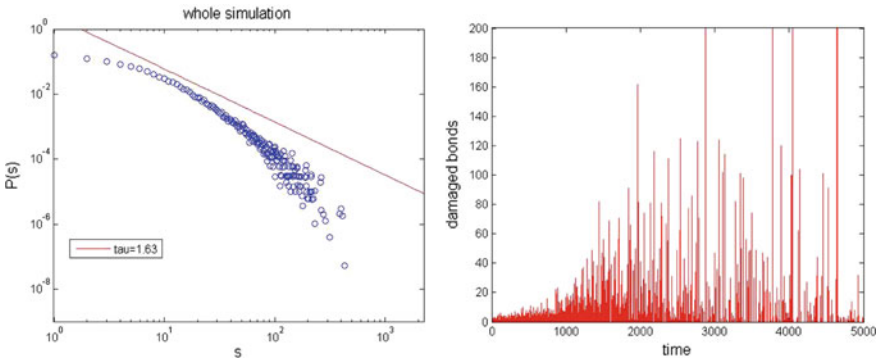


Fig. 9 Fully saturated square sample under imposed flow at the centre: probability density function $P(s)$ versus avalanche size (*left*) and damaged bonds number (avalanches) versus time (*right*)

changes the statistical behavior (bigger events are seen), not the power-law, see Fig. 8. Note that an imposed pressure is a boundary condition acting on the first of the Biot equations (equilibrium equation which is elliptic). On the contrary, by imposing fluid flow at the centre (hydraulic fracturing), the power-law does not hold anymore (see Fig. 9) except for very low flux values which are outside practical importance. Note that assigned flow acts on the second of the Biot equation, i.e. on the continuity equation which is parabolic. The results have been obtained by Monte Carlo analyses with per case some 55,000 avalanches collected on about 70 runs.

5.2 Homogeneous Media, Single Runs

Since the case of hydraulic fracturing had been extensively addressed in Milanese et al. [44], we focus here our attention on the case of fracturing under mechanical load and compare the behavior under dry and saturated conditions. For the lattice model the results of only single runs are shown.

5.2.1 Forced Displacement in a Pre-notched Plate

The first test case analyses the fracture of a square plate 0.25 m sided with an edge notch of length 0.05 m lying along its horizontal symmetry axis in plane strain conditions. The test case is the same as in Réthoré et al. [58]. The plate is loaded in tension by two uniform vertical velocities with magnitude $2.35 \times 10^{-2} \mu\text{m/s}$ applied in opposite directions to the top and bottom edges. The Young's modulus is $E = 25.85 \text{ GPa}$, fracture energy $G = 95 \text{ N/m}$ and the cohesive strength $\sigma_c = 2.7 \text{ MPa}$.

As far as the fluid field is concerned, two opposite conditions are assumed:

- The plate has permeable boundaries i.e. a drained boundary condition is enforced at all faces of the plate. The intrinsic permeability is $k = 2.78 \times 10^{-10} \text{ m}^2$ and the dynamic viscosity of the fluid (water) $\mu = 5 \times 10^{-4} \text{ Pa s}$. In these conditions the fluid does not influence the solid behavior and the problem is referred to as “dry”.
- The intrinsic permeability is $k = 2.78 \times 10^{-21} \text{ m}^2$ and the dynamic viscosity of the fluid (water) $\mu = 5 \times 10^{-4} \text{ Pa s}$. The permeability assumed is very low, lower than a high strength concrete. Therefore, no significant flow will develop. However, the impervious boundary condition imposes an isochoric constraint on the fluid which influences the process. This situation is referred to as “saturated”.

Comparison will be presented between two solution approaches discussed above, i.e. the lattice model at the mesoscale and the traditional SGFEM with remeshing (Cao et al. [13]). In the first case, a square domain of side 64 mm (mesoscopic level) is analyzed (Fig. 10): the lattice model is meshed according to $L = 30$, where L is the number of unitary overlapping elements aligned on the side direction. Recall that in case of disordered media lattices meshed with different number of elements per side display the same power law behavior, i.e. the cut off-of the avalanche size probability distribution scales with the system size. The solution is hence scale-free. Note that because of the scale-free behavior of the lattice models, the following results hold also for macroscopic scale. Time step for loading application and overall time domain discretization is 1 s.

In the SGFEM, for comparison purposes, a fixed mesh composed of 0.0025 m square elements is used, hence without accounting for the mesh refinement capabilities. Time step for overall time domain discretization is 0.125 s. The results of Fig. 13 show several advancement steps.

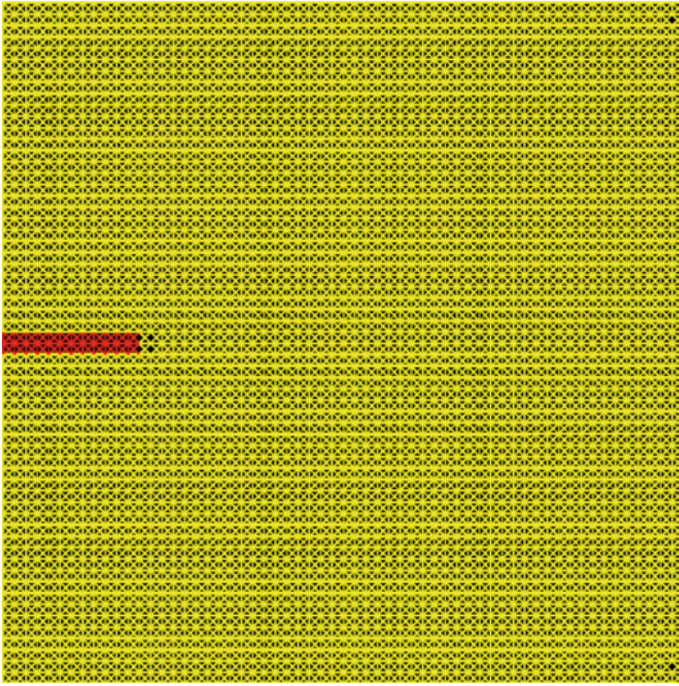


Fig. 10 Lattice model for the pre-notched plate at the beginning of the analysis: the first bars near the notch tip are breaking

The obtained results suggest some interesting remarks:

- The two approaches, very different from the theoretical point of view, give rise to consistent results;
- Breakdown is always sudden (unstable fracture propagation) and occurs first for the dry case;
- For the “dry” case (Fig. 11), the time at which the fracture is triggered is the same (nearly 560 s) in both solutions, but the complete rupture is faster in the SGFM (575 s vs. 700 s), see Fig. 13;
- Slightly higher differences arise in the “saturated” case (Fig. 12): the lattice method presents a brittle fracture at time 700 s, versus the time 575 s for the SGFM. This is because in the lattice model the external loading is increased once the rearrangements are over, i.e. overpressures completely dissipate, whereas in the SGFM there is only one time scale (the one of the external loading);
- The “dry” case shows softening behaviour, starting from the strain value 1×10^{-4} , corresponding to the cohesive strength. Whereas in the “saturated” case the behaviour is brittle, with maximum strain nearly the same as the previous case.

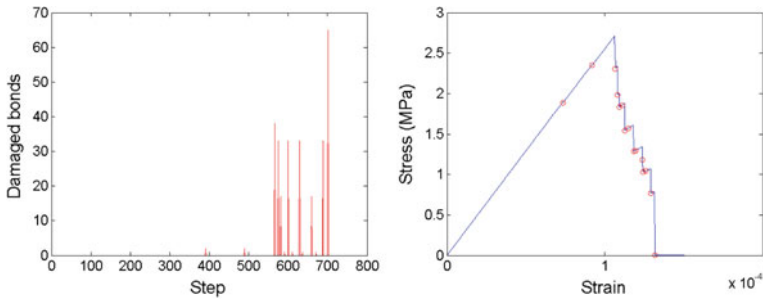


Fig. 11 Pre-notched plate test: lattice model solution for “dry” case (intrinsic permeability $2.78 \times 10^{-10} \text{ m}^2$ and drained boundary conditions)

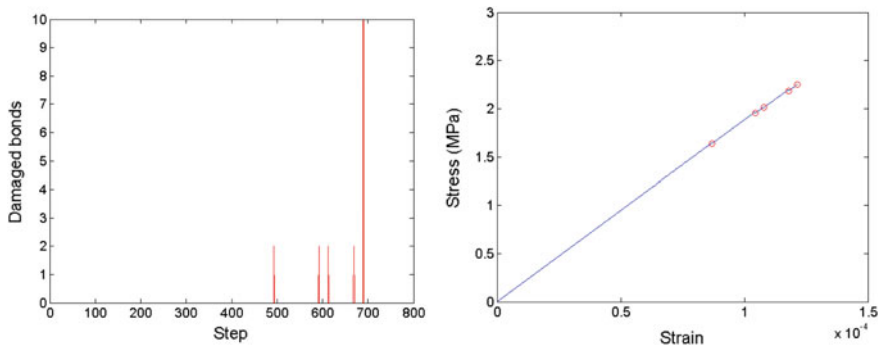


Fig. 12 Pre-notched plate test: lattice model solution for “saturated” case (intrinsic permeability $2.78 \times 10^{-21} \text{ m}^2$ and undrained boundary conditions)

- The same problem has been solved using XFEM (see Cao et al. [13]) and results are shown in Fig. 14: in all the analysed cases (dry and saturated drained/undrained conditions), intermittent movements of the fracture tip are not obtained, the cohesive zone extends over the whole sample length and the breakdown is sudden as in the “saturated” application of the lattice model (Fig. 12).

5.2.2 Peel Test of a Hydrogel Material

The second application originates from the lab experiment results shown in Pizzocolo et al. [54], where the propagation of a crack in a saturated hydrogel is studied and stepwise fracture propagation is obtained. Hydrogels are incompressible materials, hence require special care in the numerical analysis. The geometrical squared domain used in case Sect. 5.2.1 is now scaled to be representative of the

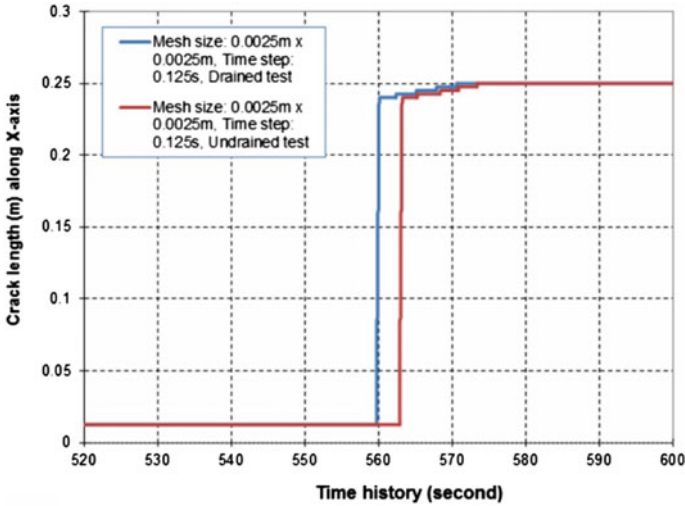
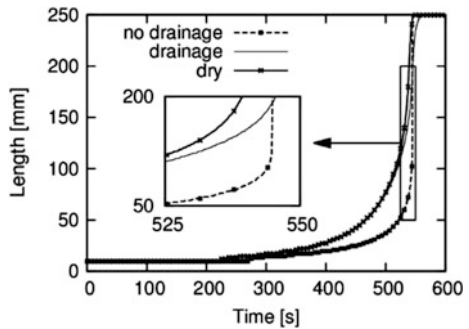


Fig. 13 Pre-notched plate test: SGFEM solutions for “saturated” undrained case (red line, intrinsic permeability $k = 2.78 \times 10^{-21} \text{ m}^2$) and “dry” drained case (blue line, intrinsic permeability $k = 2.78 \times 10^{-10} \text{ m}^2$)

Fig. 14 Pre-notched plate test: XFEM solutions for “saturated” drained/undrained case and “dry” material. Redrawn with permission from Cao et al. [13]



loaded part of the lab test sample and the Young’s modulus of each bar is selected equal to 1.924 MPa corresponding to a global modulus for the model of 0.8 MPa; the threshold of the trusses is 0.076 MPa and once exceeded the trusses are immediately removed from the lattice. Symmetry of the domain is not accounted for in the analysis, to avoid that other fracture modes could be hidden. A constant relative vertical displacement increment is applied to the left top/bottom nodes with a rate of 0.00064 mm/s.

The two limiting sets of hydraulic materials and boundary conditions, as illustrated in the previous case, are here assumed, in order to represent a “dry” and a “saturated” material.

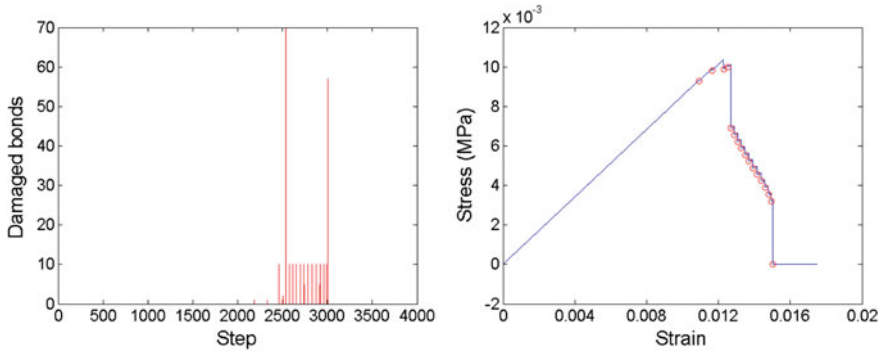


Fig. 15 Peel test: lattice model solution for “dry” case (intrinsic permeability is $k = 2.78 \times 10^{-10} \text{ m}^2$, and drained boundary conditions)

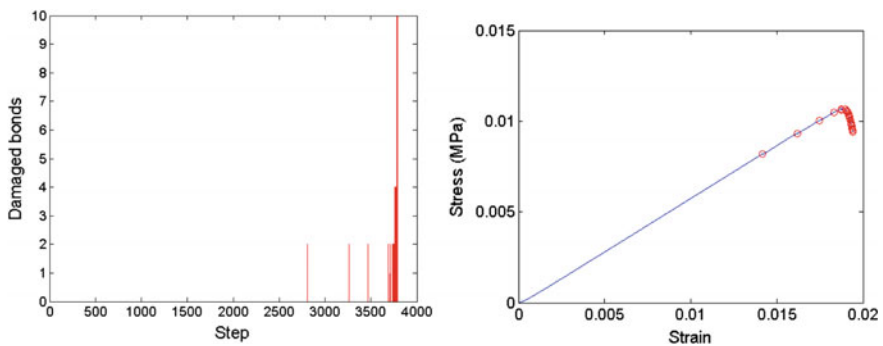


Fig. 16 Peel test: lattice model solution for “saturated” case (intrinsic permeability $k = 2.78 \times 10^{-21} \text{ m}^2$ and drained boundary conditions)

The results are displayed in Figs. 15 and 16. The number of breaking events can be seen from the stress-strain diagram. The avalanche distribution is not regular also for this homogeneous material.

Some comments can be made to the obtained results:

- in dry conditions fracture events and breakdown take place prior to those in saturated conditions; stepwise crack advancement is evident, as observed in the laboratory experiment, and, before the collapse, avalanches are of small dimensions and quite regular except for a large event near the beginning;
- maximum stress values are in accordance in the two different material cases, whereas strains are higher in saturated conditions;
- the overall behavior is plastic in dry conditions and brittle in the other.

6 Conclusions

We have analyzed fracturing in dry and saturated heterogeneous and homogeneous porous media. For the heterogeneous case a lattice model in conjunction with the Monte Carlo method has been used while for the homogeneous case the lattice model and the standard Galerkin Finite Element method have been adopted. In one case of homogeneous material also a comparison with XFEM has been shown. The results of all methods appear consistent.

From the statistical analysis for heterogeneous porous media by means of the central force (lattice) model the following conclusions can be drawn: under mechanical loading (acting on the equilibrium equations) there is no difference between dry and saturated samples: the same power law is always obtained. In the case of imposed flux (through the flow continuity equation), the picture changes: no more a power law is obtained and statistical distribution of the avalanches is different.

For homogeneous media in the case of mechanical boundary conditions, also for two very different materials, the dry sample breaks earlier. The saturated sample breaks later and the rupture is rather brittle probably due to the isochoric condition exerted by the fluid. This is somewhat similar to what happens in strain localization analysis. For the homogeneous case this conclusion has been obtained with three numerical methods, namely the Standard Galerkin FEM, the central force lattice method and a XFEM method with rather small elements. From the comparisons carried out it appears that the different methods yield qualitatively similar results but the quantitative behavior differs from method to method.

Acknowledgements B.A. Schrefler acknowledges the support of the Technische Universität München—Institute for Advanced Study, funded by the German Excellence Initiative and the European Union Seventh Framework Program under grant agreement no. 291763.

References

1. J. Adachi, E. Siebrits, A. Peirce, J. Desroches, Computer simulation of hydraulic fractures. *Int. J. Rock Mech. Min. Sci.* **44**, 739–757 (2007)
2. S.H. Advani, T.S. Lee, R.H. Dean, C.K. Pak, J.M. Avasthi, Consequences of fluid lag in three-dimensional hydraulic fracture. *Int. J. Numer. Anal. Methods Geomech.* **21**, 229–240 (1997)
3. I. Babuska, Error-bounds for finite element method. *Numer. Math.* **16**(4), 322–333 (1971)
4. G.C. Beroza, S. Ide, Deep tremors and slow quakes. *Science* **324**(5930), 1025–1026 (2009)
5. G.C. Beroza, S. Ide, Slow earthquakes and nonvolcanic tremor. *Annu. Rev. Earth Planet. Sci.* **39**, 271–296 (2011)
6. A. Black et al., DEA 13 (phase 2) Final Report (Volume 1). Investigation of Lost Circulation Problem with Oil-Base Drilling Fluids. Mar. 1988. Prepared by Drilling Research Laboratory, Inc.

7. T.J. Boone, A.R. Ingraffea, A numerical procedure for simulation of hydraulically driven fracture propagation in poroelastic media. *Int. J. Numer. Anal. Methods Geomech.* **14**, 27–47 (1990)
8. F. Brezzi, On the existence, uniqueness and approximation of saddle-point problems arising from Lagrangian multipliers, *Rev. Francaise d'autom., inform. rech. opér.: Anal. Numér.* **8** (2) 129–151 (1974)
9. A.P. Bunger, E. Gordeliy, E. Detournay, Comparison between laboratory experiments and coupled simulations of saucer-shaped hydraulic fractures in homogeneous brittle-elastic solids. *J. Mech. Phys. Solids* **61**, 1636–1654 (2013)
10. A.P. Bunger, E. Detournay, Experimental validation of the tip asymptotics for a fluid-driven crack. *J. Mech. Phys. Sol.* **56**, 3101–3115 (2008)
11. L. Burlini, G. Di Toro, P. Meredith, Seismic tremor in subduction zones: Rock physics evidence. *Geoph. Res. Lett.* **36**, L08305 (2009). doi:[10.1029/2009GL037735](https://doi.org/10.1029/2009GL037735)
12. L. Burlini, G. Di Toro, Volcanic symphony in the lab. *Science* **322**, 207–208 (2008)
13. T.D. Cao, E. Milanese, E.W. Remij, P. Rizzato, J.J.C. Remmers, L. Simoni, J.M. Huyghe, F. Hussain, B.A. Schrefler, Interaction between crack tip advancement and fluid flow in fracturing saturated porous media. *Mech. Res. Commun.* **80**, 24–37 (2017)
14. B. Carrier, S. Granet, Numerical modeling of hydraulic fracture problem in permeable medium using cohesive zone model. *Eng. Fract. Mech.* **79**, 312–328 (2012)
15. B.J. Carter, J.Desroches, A.R.Ingraffea and P.A.Wawrzynek, Simulating fully 3-D hydraulic fracturing, in *Modeling in Geomechanics*, ed. by Zaman, Booker and Gioda (Wiley, Chichester, 2000), pp. 525–567
16. B. Cesare, Synmetamorphic veining: origin of andalusite-bearing veins in the Vedrette di Ries contact aureole, Eastern Alps, Italy. *J. Metamorphic. Geol.* 643–653 (1994)
17. M.P. Cleary, Moving singularities in elasto-diffusive solids with applications to fracture propagation. *Int. J. Solids and Struct.* **14**, 81–97 (1978)
18. S.F. Cox, Faulting processes at high fluid pressures: an example of fault valve behavior from the Wattle Gully Fault, Victoria, Australia. *J. Geophys. Res.* **100**, 12841–12859 (1995)
19. C.J. de Pater, Hydraulic Fracture Containment: new insights into mapped geometry SPE, in *Hydraulic Fracturing Technology Conference* held in The Woodlands, Texas, USA, 3–5 Feb. 2015, paper SPE-173359-MS, 2015
20. E. Detournay, A.H. Cheng, Plane strain analysis of a stationary hydraulic fracture in a poroelastic medium. *Int. J. Solids Struct.* **27**, 1645–1662 (1991)
21. E. Detournay, J.I. Adachi, D.I. Garagash, Asymptotic and intermediate asymptotic behavior near the tip of a fluid-driven fracture propagating in a permeable elastic medium, in *Structural Integrity and Fracture*, ed. by Dyskin, Hu & Sahouryeh (eds.), Lisse, ISBN: 905809 5134, (2002), 9–18 Swets & Zeitlinger
22. E. Detournay, D.I. Garagash, The near-tip region for a fluid-driven fracture propagating in a permeable elastic solid. *J. Fluid Mech.* **494**, 1–32 (2003)
23. Y. Feng, K.E. Gray, Parameters controlling pressure and fracture behaviors in field injectivity tests: A numerical investigation using coupled flow and geomechanics model. *Computers and Geotechnics* **87**, 49–61 (2017)
24. D. Garagash, E. Detournay, The tip region of a fluid-driven fracture in an elastic medium. *J. Appl. Mech.* **67**, 183–192 (2000)
25. D.I. Garagash, E. Detournay, J.I. Adachi, Multiscale tip asymptotics in hydraulic fracture with leak-off. *J. Fluid Mech.* **669**, 260–297 (2011)
26. L. Girard, D. Amitrano, J. Weiss, Failure as a critical phenomenon in a progressive damage model, *J. Statistic. Mech.*, P010143 (2010)
27. P. Grassl, C. Fahy, D. Gallipoli, S.J. Wheeler, On a 2D hydro-mechanical lattice approach for modelling hydraulic fracture. *J. Mech. Phys. Solids* **75**, 104–118 (2015)
28. Y. Heider, B. Markert, A phase-field modeling approach of hydraulic fracture in saturated porous media. *Mech. Res. Commun.* **80**, 38–46 (2017)
29. N.C. Huang and S.G. Russel, Hydraulic fracturing of a saturated porous medium–I: General theory. *Theoret. Appl. Fract. Mech.* **4**, 201–213 (1985)

30. N.C. Huang and S.G. Russel, Hydraulic fracturing of a saturated porous medium—II: Special cases. *Theoret. Appl. Fract. Mech.* **4**, 215–222 (1985)
31. F. Kraaijeveld, J.M.R.J. Huyghe, Propagating cracks in saturated ionized porous media in *Multiscale Methods in Computational Mechanics*. (Springer Netherlands, 2011), pp. 425–442
32. F. Kraaijeveld, J.M.R.J. Huyghe, J.J.C. Remmers, R. de Borst, 2-D mode one crack propagation in saturated ionized porous media using partition of unity finite elements, Olivier Coussy Memorial issue. *J. Applied Mech. Trans. ASME* **80**(2), 020907 (2013)
33. C.Y. Lai, Z. Zheng, E. Dressaire, J.S. Wexler, and H. A. Stone. Experimental study on penny-shaped fluid-driven cracks in an elastic matrix. in *Proc. R. Soc. A*, 471 (2015), page 2015025. The Royal Society
34. B. Lecampion, E. Detournay, An implicit algorithm for the propagation of a hydraulic fracture with a fluid lag. *Comp. Methods Appl. Mech. Eng.* **196**(49–52), 4863–4880 (2007)
35. B. Lecampion, A. Bungler, J. Kear, D. Quesada, Interface debonding driven by fluid injection in a cased and cemented wellbore: modeling and experiments. *Int. J. Greenhouse Gas Control* **18**, 208–223 (2013). doi:[10.1016/j.ijggc.2013.07.012](https://doi.org/10.1016/j.ijggc.2013.07.012)
36. S. Lee, M.F. Wheeler, T. Wick, S. Srinivasan, Initialization of phase-field fracture propagation in porous media using probability maps of fracture networks. *Mech. Res. Commun.* **80**, 16–23 (2017)
37. R.W. Lewis, B.A. Schrefler, *The Finite Element Method in the Static and Dynamic Deformation and Consolidation of Porous Media* (Wiley, Chichester, 1998)
38. T.P.Y. Lhomme, *Initiation of Hydraulic Fractures in Natural Sandstones* (Delft University of Technology, TU Delft, 2005)
39. T.P.Y. Lhomme, C.J. de Pater, P.H. Helderich, Experimental study of hydraulic fracture initiation in Colton Sandstone, SPE/ISRM 78187, SPE/ISRM Rock Mechanics Conference, Irving, Texas, (2002)
40. S. Mauthe, C. Miehe, Hydraulic fracture in poro-hydro-elastic media. *Mech. Res. Commun.* **80**, 69–89 (2017)
41. C. Miehe, S. Mauthe, S. Teichtmeister, Minimization principles for the coupled problem of Darcy–Biot-type fluid transport in porous media linked to phase-field modeling of fracture. *J. Mech. Phys. Solids* **82**, 186–217 (2015)
42. A. Mikelic, M.F. Wheeler, T. Wick, A phase-field method for propagating fluid-filled fractures coupled to a surrounding porous medium. *SIAM Multiscale Model. Simul.* **13**(1), 367–398 (2015)
43. E. Milanese, O. Yilmaz, J.F. Molinari and B.A. Schrefler, Avalanches in dry and saturated disordered media at fracture, *Phys. Rev. E* **93**, 4, 043002, doi: [10.1103/PhysRevE.93.043002](https://doi.org/10.1103/PhysRevE.93.043002) (2016)
44. E. Milanese, P. Rizzato, F. Pesavento, S. Secchi, B.A. Schrefler, An explanation for the intermittent crack tip advancement and pressure fluctuations in hydraulic fracturing. *Hydraulic Fract. J.* **3**, 2, 30–43 (2016)
45. E. Milanese, O. Yilmaz, J.F. Molinari, B.A. Schrefler, Avalanches in dry and saturated disordered media at fracture in shear and mixed mode scenarios. *Mech. Res. Commun.* **90**, 58–68 (2017)
46. T. Mohammadnejad, A.R. Khoei, Hydromechanical modelling of cohesive crack propagation in multiphase porous media using extended finite element method. *Int. J. Numer. Anal. Methods Geomech.* **37** 1247–1279 (2013)
47. T. Mohammadnejad, A.R. Khoei, An extended finite element method for hydraulic fracture propagation in deformable porous media with the cohesive crack model. *Finite Elements Anal. Design*, **73** 77–95 (2013)
48. G. Nolet, Slabs do not go gently. *Science* **324** (5931), 1152–1153 (2009)
49. K. Obara, H. Hirose, F. Yamamizu, K. Kasahara, Episodic slow slip events accompanied by non-volcanic tremors in southwest Japan subduction zone. *Geophys. Res. Lett.* **31** (23) (2004)
50. M. Obayashi, J. Yoshimitsu, Y. Fukao, Tearing of stagnant slab. *Science* **324**(5931), 1173–1175 (2009)

51. D. Okland, G.K. Gabrielsen, J. Gjerde, S. Koen, E.L. Williams, The Importance of Extended Leak-Off Test Data for Combatting Lost Circulation. Society of Petroleum Engineers. doi:[10.2118/78219-MS](https://doi.org/10.2118/78219-MS)(2002)
52. T.K. Perkins, L.R. Kern, Widths of hydraulic fractures. *SPE J.* **222**, 937–949 (1961)
53. W.J. Phillips, Hydraulic fracturing and mineralization. *J. Geol. Soc. Lond.* **128**, 337–359 (1972)
54. F. Pizzocolo, J.M.R.J. Huyghe, K. Ito, Mode I crack propagation in hydrogels is stepwise. *Eng. Fract. Mech.* **97**, 72–79 (2013)
55. E.W. Remij, J.J.C. Remmers, J.M.R.J. Huyghe, D.M.J. Smeulders, The enhanced local pressure model for the accurate analysis of fluid pressure driven fracture in porous materials. *Comput. Methods Appl. Mech. Eng.* **286**, 293–312 (2015)
56. E.W. Remij, J.J.C. Remmers, J.M. Huyghe, D.M.J. Smeulders, An investigation of the step-wise propagation of a mode-II fracture in a poroelastic medium. *Mech. Res. Commun.* **80** 10–15 (2017)
57. J. Réthoré, R. de Borst, M.A. Abellan, A two-scale approach for fluid flow in fractured porous media. *Int. J. Numer. Meth. Eng.* **71**, 780–800 (2007)
58. J. Réthoré, R. de Borst, M.A. Abellan, A two-scale model for fluid flow in an unsaturated porous medium with cohesive cracks. *Comput. Mech.* **42**, 227–238 (2008)
59. J.R. Rice, M.P. Cleary, Some basic stress diffusion solutions for fluid saturated elastic porous media with compressible constituents. *Rev. Geophys. Space Phys.* **14**, 227–241 (1976)
60. B.A. Schrefler, S. Secchi, L. Simoni, Adaptive refinement techniques for cohesive fracture in multifield problems, Proceedings of International Conference on Adaptive Modelling and Simulation (ADMOS), Göteborg, (2003)
61. B.A. Schrefler, S. Secchi, L. Simoni, On adaptive refinement techniques in multifield problems including cohesive fracture. *Comp. Methods Appl. Mech. Eng.* **195**, 444–461 (2006)
62. S.Y. Schwartz, J.M. Rokosky, Slow slip events and seismic tremor at circum-pacific subduction zones, *Rev. Geophys.*, 45, RG3004 (2007)
63. S. Secchi, L. Simoni, An improved procedure for 2D unstructured Delaunay mesh generation. *Adv. Eng. Softw.* **34**(4), 217–234 (2003)
64. S. Secchi, B.A. Schrefler, A method for 3-D hydraulic fracturing simulation. *Int. J. Fract.* **178**, 245–258 (2012)
65. R.H. Sibson, Crustal stress, faulting and fluid flow, ed. by J. Parnell *Geofluids: Origin, Migration and Evolution of fluids in Sedimentary Basins*, Geological Soc. Special Publication, vol. 78, pp. 69–84 (1994)
66. L. Simoni, S. Secchi, Cohesive fracture mechanics for a multi-phase porous medium. *Eng. Comput.* **20**, 675–698 (2003)
67. L. Simoni, S. Secchi, · B.A. Schrefler, Numerical difficulties and computational procedures for thermo-hydro-mechanical coupled problems of saturated porous media. *Comput. Mech.* **43**, 179–189 (2008)
68. L. Simoni, B.A. Schrefler, Multi field simulation of fracture. *Adv. Appl. Mech.* **47**, 367–520 (2014)
69. M.Y. Soliman, M. Wigwe, A. Alzahabi, E. Pirayesh, N. Stegent, Analysis of fracturing pressure data in heterogeneous shale formations. *Hydraul. Fract. J.* **1**(2), 8–12 (2014)
70. M.F. Wheeler, A. Mikelic, T. Wick, A phase-field method for propagating fluid-filled fractures coupled to a surrounding porous medium. *SIAM Multiscale Model. Simul.* **13**(1), 367–398 (2015)
71. M.F. Wheeler, T. Wick, W. Wollner, An augmented-Lagrangian method for the phase-field approach for pressurized fractures. *Comp. Methods Appl. Mech. Eng.* **271**, 69–85 (2014)
72. S. Zapperi, A. Vespignani, H.E. Stanley, Plasticity and avalanche behavior in microfracturing phenomena. *Nature* **388**, 658–660 (1997)

On Multi-scale Computational Design of Structural Materials Using the Topological Derivative

J. Oliver, A. Ferrer, J.C. Cante, S.M. Giusti and O. Lloberas-Valls

Abstract This work deals on the optimization and computational material design using the topological derivative concept. The necessary details to obtain the anisotropic topological derivative are first presented. In the context of multi-scale topology optimization, it is crucial since the homogenization of the constitutive tensor of a micro-structure confers in general an anisotropic response. In addition, this work addresses the multi-scale material design problem in which the goal is then to minimize the structural (macro-scale) compliance by appropriately designing the material distribution (micro-structure) at a lower scale (micro-scale). To overcome the exorbitant computational cost, a consultation during the iterative process of a discrete material catalog (computed off-line) of micro-scale optimized topologies (Computational Vademecum) is proposed in this work. This results into a large diminution of the resulting computational costs, which make affordable the proposed methodology for multi-scale computational material design. Some representative examples assess the performance of the considered approach.

J. Oliver (✉) · A. Ferrer · J.C. Cante · O. Lloberas-Valls
CIMNE -International Center for Numerical Methods in Engineering,
Campus Nord UPC, Edifici C-1, c/Jordi Girona 1-3, 08034 Barcelona, Spain
e-mail: oliver@cimne.upc.edu

J. Oliver · O. Lloberas-Valls
E.T.S. d'Enginyers de Camins, Canals i Ports, Technical University of Catalonia,
Campus Nord UPC, Edifici C-1, c/Jordi Girona 1-3, 08034 Barcelona, Spain

A. Ferrer · J.C. Cante
Aeroespacial i Audiovisual de Terrassa, Escola Superior d'Enginyeries Industrial,
Campus de Terrassa, Edifici TR45. C. Colom, 11, 08222 Terrassa, Spain

S.M. Giusti
Regional Faculty of Córdoba (UTN/FRC - CONICET), National Technological
University, Maestro M. López esq. Cruz Roja Argentina, X5016ZAA - Córdoba,
Buenos Aires, Argentina

1 Introduction

In the last decades, topological structural optimization has gained considerable relevance in the Computational Mechanics field. In consequence, is presently applied in the aeronautical, automotive and civil engineering industries.

From the work in [16], the topological derivative mathematical concept has been recently applied to the structural topology optimization. Its success is due to the analytical expressions that measure a specific shape functional sensitivity when an inclusion is introduced into a fixed domain. Although the topological derivative concept, as a closed form mathematical expression, has been developed for a wide range of physical phenomena, most of them are restricted to homogeneous parts and isotropic constitutive elastic materials. In fact, only few works dealing with heterogeneous and anisotropic material behavior can be found in the literature, and, in general, the derived formulas are given in an abstract form (see, for instance, [6]).

In this work, we apply the closed form of the topological derivative to the total potential energy in structural materials, i.e., the compliance, associated to an anisotropic and heterogeneous elasticity problem. Full details are described in [12]. Additionally, and following the approach in [4], a level set algorithm that considers the topological derivative as a gradient in a kind of steepest descent algorithm is used.

The heterogeneous anisotropic topological derivative concept, can be applied in advanced technological areas such as topology and structural optimization when they are simultaneously combined with material-design. In fact, in multi-scale modeling settings, the homogenized constitutive response for a given micro-structure is, in general, anisotropic. In addition, since in each macroscopical structural point a different micro-structure is normally obtained, the constitutive homogenized response at the macro-scale varies from point to point and, consequently, it is heterogeneous. Therefore, for a correct evaluation of the topological sensitivity in a structural optimization problem, the topological derivative for anisotropic and heterogeneous constitutive materials is needed.

The power of the topological derivative as a sensitivity tool can be extended from structural optimization to multiscale material design. Computational multi-scale approaches providing an appropriate framework to link the material at different scales [8] have been extensively used in the recent years. Besides in [3], other works (cf. [14, 17]) have recently considered topological optimization in a multi-scale context. One of the found bottlenecks is the computational cost of the resulting multi-scale problem to be faced. Therefore, in order to restrict the resulting computational cost, either the micro-structure topology is generally kept constant over the whole domain or very coarse discretizations of this micro-structure are used.

In this work, an alternate direction algorithm is proposed as in [1] for solving the multi-scale material design problem. Then, and inspired in the *Computational Vademecum* concept [7], the computationally expensive construction of a catalog of optimal material designs is face off-line, so that only a trivial selection of the optimal micro-structure is necessary in an on-line process. As in PGD [7], or POD strategies

[13], a considerable reduction on the computational cost is obtained. To validate this approach, some numerical examples are also presented.

The paper is organized as follows: first, in Sect. 2, the topological derivative concept and the microscopic material design problem is presented. In Sect. 3, the structural design problem of anisotropic materials is tackled, presenting the topological derivative expressions and showing some optimal designs of structures with anisotropic materials. In Sect. 4, the multi-scale material design problem is formulated. Then, the Computational Vademecum is computed and some examples are shown. In addition, the homogenized constitutive tensor distribution is represented and an alternate directions algorithm is conceptually described and validated by some numerical examples. Conclusions and future perspectives are summarized in Sect. 5.

2 Background

2.1 Topological Derivative Concept

Let us consider an open and bounded domain $\Omega \subset \mathbb{R}^2$, see Fig. 1, which is subject to a non-smooth perturbation confined in a small region $\omega_\epsilon(\hat{x}) = \hat{x} + \epsilon\omega$ of size ϵ . Here, \hat{x} is an arbitrary point of Ω and ω is a fixed domain of \mathbb{R}^2 . Then, we assume that a given shape functional $J_\epsilon(\Omega)$, associated to the topologically perturbed domain, admits the following asymptotic expansion [15]

$$J_\epsilon(\Omega) = J(\Omega) + f(\epsilon)D_T J(\hat{x}) + o(f(\epsilon)), \tag{1}$$

where $J(\Omega)$ is the shape functional associated to the unperturbed domain and $f(\epsilon)$ is a positive function such that $f(\epsilon) \rightarrow 0$ when $\epsilon \rightarrow 0^+$. The function $\hat{x} \mapsto D_T J(\hat{x})$ is termed the topological derivative of J at \hat{x} . Therefore, the term $f(\epsilon)D_T J(\hat{x})$ represents a first order correction of $J(\Omega)$ to approximate $J_\epsilon(\Omega)$ in \hat{x} . In this work, the singular perturbation is characterized by a circular disc, denoted B_ϵ , with boundary ∂B_ϵ and different constitutive properties, see Fig. 1.

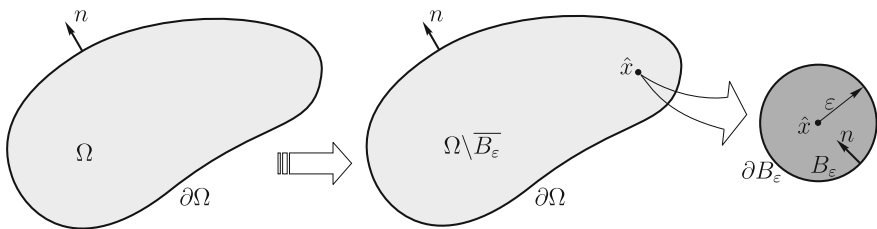


Fig. 1 Topological derivative concept

From (1), we obtain the standard definition of the topological derivative by passing to the limit $\epsilon \rightarrow 0^+$:

$$D_T \mathcal{J}(\hat{x}) = \lim_{\epsilon \rightarrow 0^+} \frac{\mathcal{J}_\epsilon(\Omega) - \mathcal{J}(\Omega)}{f(\epsilon)}. \tag{2}$$

In the case of the total potential energy defined by

$$\mathcal{J}(\Omega) = \frac{1}{2} \int_{\Omega} \sigma(u) \cdot \nabla^s u + \int_{\Gamma_N} \bar{t} \cdot u, \tag{3}$$

the difference of the shape functional can be written as [2, 15]

$$\mathcal{J}_\epsilon(\Omega) - \mathcal{J}(\Omega) = \pi \epsilon^2 \mathbb{P} \sigma(u)(\hat{x}) \cdot \nabla^s u(\hat{x}) + o(\epsilon^2), \tag{4}$$

where \mathbb{P} stands for the polarization tensor defined as

$$\mathbb{P} = \frac{1}{2} \Delta C(\hat{x}) [(C(\hat{x}))^{-1} + (C^*)^{-1} \mathbb{T}]. \tag{5}$$

where $\Delta C := C^* - C$, C is the constitutive tensor defined in $\Omega \setminus \overline{B_\epsilon}$ (matrix), C^* is the constitutive tensor defined in B_ϵ (inclusion) and \mathbb{T} is the fourth order tensor to be defined later. Thus, replacing (4) into (2) and considering $f(\epsilon) = \pi \epsilon^2$, the topological derivative yields

$$D_T \mathcal{J}(\hat{x}) = \mathbb{P} \sigma(u)(\hat{x}) \cdot \nabla^s u(\hat{x}) \quad \forall \hat{x} \in \Omega. \tag{6}$$

2.2 Microscopic Material Design Problem

The microscopic structural compliance is aimed at being minimized through the following minimization problem (see [3]):

$$\begin{aligned} & \underset{\chi_\mu}{\text{minimize}} && \alpha : \mathbb{C}_h^{-1}(\chi_\mu) : \alpha \\ & \text{subjected to:} && \int_{\Omega_\mu} \chi_\mu = V_\mu \end{aligned} \tag{7}$$

where V_μ is the solid-volume of the RVE (micro-structure domain), α stands for the, unit norm, macroscopic stress tensor here considered the driving force for the homogenization problem, and \mathbb{C}_h is the homogenized constitutive tensor.

Following the work in [9, 11] an augmented Lagrangian version of the slerp algorithm [4] is used to solve problem (7) in an unconstrained fashion. Uni-axial horizontal stress-state ($\alpha = [1 \ 0 \ 0]$), shear stress-state ($\alpha = [0 \ 0 \ 1]$) and bulk stress-state ($\alpha = \frac{1}{\sqrt{2}} [1 \ 1 \ 0]$) are considered. The obtained optimal topologies are presented in Fig. 2.



Fig. 2 Horizontal, shear and bulk stress-state optimal RVE topologies

3 Structural Design of Anisotropic Materials

Since the microscopic topology optimization problem leads, in general, to an anisotropic response in the macro-structure, to tackle multi-scale topology optimization problems (in which the macroscopic topology is also optimized) the anisotropic topological derivative expression is necessary (see [12] for full details).

3.1 Anisotropic Topological Derivative Expression

The fourth order tensor \mathbb{T} is defined as

$$\mathbb{T} = A_i \mathbb{S} \tag{8}$$

where \mathbb{S} is the following fourth order tensor

$$\mathbb{S} := \mathbb{I} - \mathbb{C}^* \mathbb{C}^{-1}. \tag{9}$$

In order to find matrix A_i , an exterior problem must be solved using complex variable (see [12]). The final expression of matrix A_i is obtained as

$$A_i = I_2 (K_G^l)^{-1} K_G^m I_2^T \tag{10}$$

where the logical matrices I_1, I_2, I_3 and I_S are defined by

$$I_1 = \begin{bmatrix} 1 & 0 & 0 \\ 0 & 0 & 0 \\ 0 & 0 & 1 \\ 0 & 1 & 0 \end{bmatrix} \quad I_2 = \begin{bmatrix} 1 & 0 & 0 & 0 \\ 0 & 1 & 0 & 0 \\ 0 & 0 & 1 & 0 \\ 0 & 0 & 1 & 0 \end{bmatrix} \quad I_3 = \begin{bmatrix} 0 & 0 & 0 & 0 \\ 0 & 0 & 0 & 1 \\ 0 & 0 & 0 & -1 \\ 0 & 0 & 0 & 0 \end{bmatrix} \quad I_S = \begin{bmatrix} 0 & 1 & 0 & 0 \\ -1 & 0 & 0 & 0 \\ 0 & 0 & 0 & 1 \\ 0 & 0 & -1 & 0 \end{bmatrix} \tag{11}$$

and the complex matrices K_G^l and K_G^m are

$$K_G^l = K_u K_\sigma^{-1} M_\sigma - M_u (\tilde{\alpha}_I + I_3) \quad \text{and} \quad K_G^m = K_u K_\sigma^{-1} M_\sigma.$$

In addition, the modified inverse constitutive matrix $\tilde{\alpha}_I$ is defined as

$$\tilde{\alpha}_I = I_1 \alpha_I I_2 \tag{12}$$

where the inverse constitutive tensor of the inclusion α_I is expressed as

$$\alpha_I = \begin{bmatrix} \alpha_{11}^I & \alpha_{12}^I & \alpha_{13}^I \\ \alpha_{12}^I & \alpha_{22}^I & \alpha_{23}^I \\ \alpha_{13}^I & \alpha_{23}^I & \alpha_{33}^I \end{bmatrix}. \tag{13}$$

The values α_{ij}^I , with $(i, j) = 1..3$, are the components of $(C^*)^{-1}$ (in matrix notation). The real matrices M_u and M_σ take the following expressions

$$M_u = \begin{bmatrix} a & 0 & 0 & 0 \\ 0 & b & 0 & 0 \\ 0 & 0 & a & 0 \\ 0 & 0 & 0 & b \end{bmatrix} \quad M_\sigma = \begin{bmatrix} 0 & a & 0 & 0 \\ 0 & 0 & -b & 0 \\ 0 & 0 & -a & 0 \\ b & 0 & 0 & 0 \end{bmatrix} \tag{14}$$

where a and b are the semi-axes of the elliptic inclusion. Since we are interested in circular inclusions, values $a = b = 1$ are considered.

The product of the complex matrices $K_u K_\sigma^{-1}$ deserves special attention. Due to some complex properties (see [10]), it can be written as

$$K_u K_\sigma^{-1} = \Re(K_{u_0} K_{\sigma_0}^{-1}) - \Im(K_{u_0} K_{\sigma_0}^{-1}) I_S \tag{15}$$

where \Re and \Im take the real and imaginary part of the complex matrix $K_{u_0} K_{\sigma_0}^{-1}$ which reads as

$$K_{u_0} K_{\sigma_0}^{-1} = \begin{bmatrix} \lambda & 0 & -\kappa & 0 \\ 0 & \lambda & 0 & -\kappa \\ \rho & 0 & -\gamma & 0 \\ 0 & \rho & 0 & -\gamma \end{bmatrix} \tag{16}$$

and the complex numbers λ , κ , ρ and γ are defined as

$$\lambda = \frac{p_1 \mu_2 - p_2 \mu_1}{\mu_1 - \mu_2} \quad \kappa = \frac{p_1 - p_2}{\mu_1 - \mu_2} \quad \rho = \frac{q_1 \mu_2 - q_2 \mu_1}{\mu_1 - \mu_2} \quad \gamma = \frac{q_1 - q_2}{\mu_1 - \mu_2}. \tag{17}$$

Finally, the complex numbers μ_1 and μ_2 are the solution of the following characteristic equation

$$\alpha_{11} \mu^4 - 2\alpha_{13} \mu^3 + (2\alpha_{12} + \alpha_{33}) \mu^2 - 2\alpha_{23} \mu + \alpha_{22} = 0, \tag{18}$$

and the complex numbers p_i and q_i are expressed as

$$\begin{aligned}
 p_i &= \alpha_{11}\mu_i^2 + \alpha_{12} - \alpha_{13}\mu_i, \\
 q_i &= \alpha_{12}\mu_i + \alpha_{22}/\mu_i - \alpha_{23}, \quad i = 1, 2.
 \end{aligned}
 \tag{19}$$

Unfortunately, the final expression of the matrix A_i and the polarization tensor \mathbb{P} are cumbersome and can not be written explicitly. However, due to symbolic algebra, they can be easily calculated and saved as a computational function, ready for its implementation in a home-made topological optimization code.

Two scenarios must be considered: the case where the inclusion is inserted by a weak material C^- on the strong one C^+ or the opposite case. Consequently, rewriting the polarization tensor as $\mathbb{P} = \mathbb{P}(C, C^*)$, both cases result to

$$\mathbb{P} = \begin{cases} \mathbb{P}^+ = \mathbb{P}(C^+, C^-) & x \in \Omega^+ \\ \mathbb{P}^- = \mathbb{P}(C^-, C^+) & x \in \Omega^- . \end{cases}
 \tag{20}$$

The analytical formula of the topological derivative presented in (6) has been numerically validated (see [12]).

3.2 Topology Optimization Examples with Anisotropic Material

In order to assess the potential application of the topological derivative for anisotropic and heterogeneous materials, some numerical examples are shown in this section. A minimum compliance objective function, subject to a certain fraction volume constraint, will be solved. To this end, the material distribution in Ω will be identified by the characteristic function χ . Thus, the objective function $J(\Omega)$ can be written as a function of χ , i.e. $J(\Omega_\chi)$, where Ω_χ stands for the geometrical dependency on the domain of the characteristic function χ . Then, the optimization problem reads:

Find the characteristic function χ such that,

$$\begin{aligned}
 \min_{\chi} \quad & J(\Omega_\chi) \\
 \text{s.t.} \quad & c(\chi) = \int_{\Omega} \chi - V = 0 ,
 \end{aligned}
 \tag{21}$$

where $J(\Omega_\chi)$ is the total potential energy of an standard elastic equilibrium problem and V the final intended volume. Note that the constitutive tensor \mathbb{C} can be heterogeneous and anisotropic. Some numerical examples with homogeneous and heterogeneous material distribution are considered. All them are solved under 2D elastic plane stress assumptions.

Fig. 3 Schematic drawing of a cantilever beam with homogeneous material distribution



3.2.1 Homogeneous Material Distribution

The constitutive behavior is considered homogeneous in the design domain. Besides, the constitutive tensor in the inclusion is defined with the contrast parameter γ as: $\mathbb{C}^- = \gamma\mathbb{C}$ with $\gamma = 10^{-4}$. The 2×1 domain is discretized with a structured mesh of 5200 P1 triangular elements. The volume fraction is taken as $V = 0.4$ and the penalty as $\rho = 0.5$. All the examples are stated to be converged when $\theta < 1^\circ$ and $|c(\psi)| < 0.001$. In the figures showing the results, the black and white colors are used to represent the part of the domain with constitutive tensor $\mathbb{C}^+ = \mathbb{C}$ and \mathbb{C}^- , respectively. The elasticity of the inclusion \mathbb{C}^- is weak enough to mimic a void.

3.2.2 Homogeneous Cantilever beam

Now a standard cantilever beam is solved. The domain is fixed at the left side and has a vertical unitary force at the middle of the right end, see Fig. 3. Some representative cases, in terms of the selected constitutive tensor, have been considered

The isotropic case is used also as a reference. Some unconventional topologies are obtained, specially in the orthotropic case (micro-structure with horizontal and vertical bars) and full anisotropic case (last row). It can be observed, that the resulting macro-structure topology, tends to arrange following the principal directions of the micro-structure topology (Fig. 4).

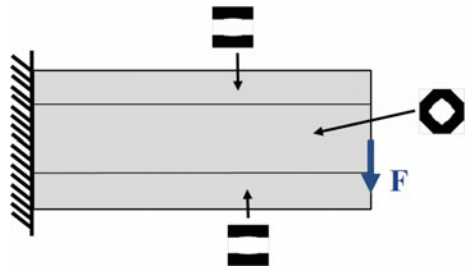
3.2.3 Heterogeneous Material Distribution

A heterogeneous distribution of material is used for a classical cantilever beam optimal design. The contrast parameter is taken $\gamma = 10^{-4}$. The 2×1 domain is discretized through a structured mesh of 6272 \mathbb{P}_1 elements. The geometry is vertically partitioned in four domains with the same width ($1/4$). The top and bottom regions are endowed with a constitutive tensor different from the center one (see Figs. 5 and 7). The intended volume fraction is $V = 0.4$ and the considered penalty value is $\rho = 0.5$. Again the iterative solution algorithm is declared converged when $\theta < 1^\circ$ and $|c(\psi)| < 0.001$.

Case	Constitutive tensor	Micro-structure	Optimal topology	Compliance
(a)	$\mathbb{C} = \begin{pmatrix} 1.0989 & 0.3297 & 0 \\ 0.3297 & 1.0989 & 0 \\ 0 & 0 & 0.3846 \end{pmatrix}$			71.392
(b)	$\mathbb{C} = \begin{pmatrix} 0.5697 & 0.0231 & 0 \\ 0.0231 & 0.0784 & 0 \\ 0 & 0 & 0.0070 \end{pmatrix}$			892.328
(c)	$\mathbb{C} = \begin{pmatrix} 0.0784 & 0.0231 & 0 \\ 0.0231 & 0.5697 & 0 \\ 0 & 0 & 0.0070 \end{pmatrix}$			1685.169
(d)	$\mathbb{C} = \begin{pmatrix} 0.2867 & 0.1900 & 0 \\ 0.1900 & 0.2867 & 0 \\ 0 & 0 & 0.1715 \end{pmatrix}$			335.980
(e)	$\mathbb{C} = \begin{pmatrix} 0.3400 & 0.1689 & 0 \\ 0.1689 & 0.3400 & 0 \\ 0 & 0 & 0.1401 \end{pmatrix}$			251.031
(f)	$\mathbb{C} = \begin{pmatrix} 0.2782 & 0.1250 & 0.0728 \\ 0.1250 & 0.2184 & 0.0120 \\ 0.0728 & 0.0120 & 0.1416 \end{pmatrix}$			224.387

Fig. 4 Representative optimal homogeneous cantilever topologies: **a** Isotropic ($E = 1$ and $\nu = 0.3$) as a reference, **b–e** Orthotropic, **f** Anisotropic. In the second column, the constitutive tensor used is shown, which is obtained by a classical homogenization procedure of the micro-structure displayed on the third column. In the fourth one and fifth column, the final optimal topology for the structure and the value of the compliance are also shown

Fig. 5 Heterogeneous cantilever beam with regions of different constitutive properties (enforced via microscopic material topology)



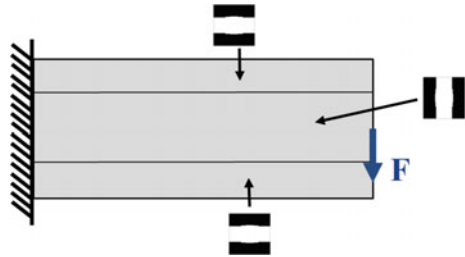
3.2.4 Case 1: Heterogeneous Cantilever Beam with Horizontal-Shear Micro-Structures

In this example, the top and bottom regions are endowed with a micro-structure topology yielding horizontally-dominant microscopic stiffness, where the center region, microscopic topology enforces shear-dominant stiffness.

Constitutive tensor	Micro-structure	Optimal topology	Compliance
$\mathbb{C} = \begin{pmatrix} 0.5697 & 0.0231 & 0 \\ 0.0231 & 0.0784 & 0 \\ 0 & 0 & 0.0070 \end{pmatrix}$			309.095
$\mathbb{C} = \begin{pmatrix} 0.2867 & 0.1900 & 0 \\ 0.1900 & 0.2867 & 0 \\ 0 & 0 & 0.1715 \end{pmatrix}$			

Fig. 6 Heterogeneous cantilever beam. Material properties and obtained results (case 1)

Fig. 7 Heterogeneous cantilever beam. Material properties and obtained results (case 2)



The material arrangement and distribution are sketched in Fig. 5. The corresponding values for the resulting homogenized constitutive properties are detailed in Fig. 6.

It is worth noting that both constitutive tensors are again anisotropic. In addition, note that the optimal topology with the anisotropic heterogeneous material distribution is quite different from the homogeneous isotropic case (first row of Fig. 4) and the homogeneous anisotropic case (last row of Fig. 4). Again, it can be observed that the macroscopic topology tends to mimic the microscopic one in the different considered regions.

3.2.5 Case 2: Heterogeneous Cantilever Beam with Horizontal-Vertical Micro-Structures

Now the top and bottom regions at the beam are endowed with a micro-structure yielding horizontally-dominant elastic stiffness, whereas the central region is endowed with a vertically-dominant one.

Figure 7 shows an schematic picture of this case. Details of the resulting homogenized elastic properties are given in Fig. 8.

In Fig. 8, the resulting (non trivial) optimal topology obtained for this case is shown.

Regarding numerical aspects, problems of convergence of the involved numerical schemes have not been found.

Besides, no substantial differences, in terms of the involved computational effort, have been found with regard to the isotropic and anisotropic cases. In all cases less than five minutes of computation are needed with a standard PC (3.40 GHz processor in a 64-bit architecture) in a Matlab[®] environment.




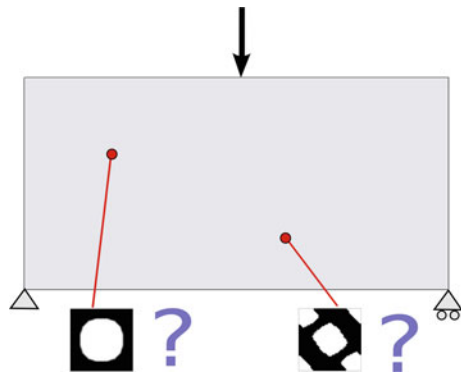
Constitutive tensor	Micro-structure	Optimal topology	Compliance
$\mathbb{C} = \begin{pmatrix} 0.5697 & 0.0231 & 0 \\ 0.0231 & 0.0784 & 0 \\ 0 & 0 & 0.0070 \end{pmatrix}$			996.863
$\mathbb{C} = \begin{pmatrix} 0.0784 & 0.0231 & 0 \\ 0.0231 & 0.5697 & 0 \\ 0 & 0 & 0.0070 \end{pmatrix}$			

Fig. 8 Optimal heterogeneous cantilever beam topology. Constitutive tensor value and its corresponding micro-structure representation are also detailed

Fig. 9 Multi-scale topology optimization problem



4 Multi-scale Material Design Problem

4.1 Formulation

The aim of the multi-scale material design problem is to determine the optimal micro-structure topology at every point of the macro-structure domain in order to achieve a functional goal at the macro-scale level, as sketched in Fig. 9.

The classical topological optimization problem in structural analysis refers to the minimum compliance (or maximum stiffness) design. Here the classical single-scale problem of determining the optimum distribution of a certain material mass at the macro-scale (or structural scale), to achieve the minimum compliance of the resulting structure [5], is reformulated as a two-scale problem in the following sense: the goal is the optimal distribution of a given material mass, *but now at the micro-scale* level for every structural point (given the shape and topology at the structural scale).

The problem is mathematically stated through:

$$\begin{aligned}
 & \underset{\sigma, \chi_\mu}{\text{minimize}} && \int_{\Omega} \sigma : \mathbb{C}_h^{-1}(\chi_\mu) : \sigma \\
 & \text{subjected to:} && \frac{\int_{\Omega_\mu} \chi_\mu}{V_\mu} - 1 \leq 0, \\
 & && \nabla \cdot \sigma = \rho b, \\
 & && + \text{Boundary conditions.}
 \end{aligned} \tag{22}$$

where the macroscopic stresses, σ that are solution of the standard equilibrium equation. In Eq. (22), $\chi_\mu \in \{0, 1\}$, refers to the characteristic function at the RVE, whose optimal spatial distribution (defining the topology of the RVE) is aimed at being obtained, and V_μ refers to the “measure” (area or volume) of the RVE. In this respect the following aspects, specific for this multi-scale problem, have to be highlighted:

1. The objective function to be minimized is highly nonlinear and defined at the macro-scale level.
2. The design variables (the values of the characteristic function χ_μ) are defined at the micro-scale.
3. The equilibrium equation couples both macro and micro levels since, although the stresses are defined macroscopically, the constitutive equation depends on the micro-structural topology.

Algorithmic separability Due to the non-linear character of the problem, different solutions, corresponding to different local minima, might be expected. Due to the multi-scale coupling character, the computational robustness of the minimization scheme can be seriously affected. As a first step, a separation of the minimization problem is introduced here to overcome those difficulties. The original problem in Eq. (23) is slightly rephrased as:

$$\begin{aligned} & \text{minimize}_{\sigma} \left\{ \begin{array}{l} \text{minimize}_{\chi_\mu} \int_{\Omega} \sigma : \mathbb{C}_h^{-1}(\chi_\mu) : \sigma \\ \text{subjected to} \quad \frac{\int_{\Omega_\mu} \chi_\mu}{V_\mu} - 1 \leq 0, \end{array} \right. \quad (23) \\ & \text{subjected to} \quad \nabla \cdot \sigma = \rho b, \\ & \quad \quad \quad + \text{Boundary conditions.} \end{aligned}$$

This subtle change could be thought as a different notation of the same problem or, even more stimulating, a way of solving the problem. Once in that stage, and inspired by the divide and conquer approach, a tentative second step seems consists of solving the minimization problem locally, i.e., rewriting Eq. (23) as,

$$\begin{aligned} & \text{minimize}_{\sigma} \int_{\Omega} \left\{ \begin{array}{l} \text{minimize}_{\chi_\mu} \sigma : \mathbb{C}_h^{-1}(\chi_\mu) : \sigma \\ \text{subjected to} \quad \frac{\int_{\Omega_\mu} \chi_\mu}{V_\mu} - 1 \leq 0, \end{array} \right. \quad (24) \\ & \text{subjected to} \quad \nabla \cdot \sigma = \rho b, \\ & \quad \quad \quad + \text{Boundary conditions.} \end{aligned}$$

where the leading change is the exchange between the minimization and the integral operator. Note that the equilibrium equation plus the boundary conditions is solved as a standard FEM equilibrium problem, that is,

$$K(\chi_\mu)u = F. \quad (25)$$

Due to the facts that all unknowns and constraints of the minimization subproblem are defined locally at Eq. (23), and also to the positive character of the integral kernel, the exchange can be done without altering the global solution. In other words, *the micro-scale topologies that provide the minimum global (structural) compliance, are those micro-structure topologies leading to minimal local compliances for every local RVE.* This fact entails a significant reduction on the computational cost.

4.2 Computational Vademecum

Multiscale problem (24) exhibits high algorithmic complexity and it becomes computationally unaffordable for real-life problems. High performance computing may alleviate the solution time but, apparently, it is not sufficient. In this context, a more efficient approach is proposed here. The main idea consists of optimizing “a priori” a very large discrete-set of micro-structures, in the set of possible macro-stresses acting on the RVE, leading to the so-called “Material Catalogue” or “Computational Vademecum” [7]. Then, when in the global (multi-scale) design problem a certain optimal micro-structure topology is requested, for a given stress-state at the macro-scale sampling point, the Vademecum is consulted and the closest optimal solution is extracted.

More specifically: given the mechanical properties of the base-material, the expensive computations requested for the Vademecum construction are done once-for-all, in an off-line process, and the Vademecum outputs (typically the tangent constitutive operator, C_h , solution of Eq. (7)), are stored in a data-base for, a sufficiently large, discrete set of entries α .

The actual multi-scale material design problem is then performed “on-line”, and it only involves a recursive equilibrium analysis at the micro-scale combined with *consultations of the Vademecum*. This translates into an impressive reduction of the computational cost of the on-line material design process. It is also highlighted that the Vademecum remains the same for a given base-material, disregard the kind of macro-scale structural problem aimed at being optimized.

4.3 Parametric Domain

The success of the proposed Vademecum-based strategy crucially relies on the appropriate determination of the Vademecum entries so that a good balance of the vademecum-error/computational-cost is achieved. Indeed, since the error is produced by the closed-entry strategy in the Vademecum consultation, the higher is the number of entries, the lower is the resulting error... but the higher is the Vademecum construction computational cost.

The parametric domain defines the range of the space of all possible macroscopic stresses σ . Inspection of Eq. (24) shows that the modulus of σ does not play any role in the determination of the optimal RVE topology. In fact, it can be readily proven that

$$\begin{aligned} \chi_\mu &= \arg \left\{ \begin{array}{l} \text{minimize } \sigma : \mathbb{C}_h^{-1}(\chi_\mu) : \sigma \\ \chi_\mu \\ \text{s.t.} \quad \int_{\Omega_\mu} \chi_\mu = V_\mu \end{array} \right\} = \\ &= \arg \left\{ \begin{array}{l} \text{minimize } \frac{\sigma}{\|\sigma\|} : \mathbb{C}_h^{-1}(\chi_\mu) : \frac{\sigma}{\|\sigma\|} \\ \chi_\mu \\ \text{s.t.} \quad \int_{\Omega_\mu} \chi_\mu = V_\mu \end{array} \right\} \end{aligned} \tag{26}$$

Therefore, $\alpha = \frac{\sigma}{\|\sigma\|}$ is the actual Vademecum entry. Hence, the parametric domain (in 2D problems) is represented by the unit radius sphere. Each point of the sphere can be seen as a micro-structure optimization case, which returns some homogenized elastic properties associated to an optimal topology (see Fig. 10).

For the subsequent examples the sphere has been discretized by means of a structured mesh of 16386 points (reduced to 2145 points because of symmetries). Some examples of this optimal RVE topologies can be seen in Fig. 11. They have been computed for the solid volume fraction at the RVE, $V_\mu = 0.6$.

It is worth mentioning that construction of such Vademecum requires a very robust methodology for the RVE topological design, so that none of the desired entry points fails to be computed. In this sense it has to be remarked that the use of the

Fig. 10 The unit-radius spherical parametric domain (Computational Vademecum)

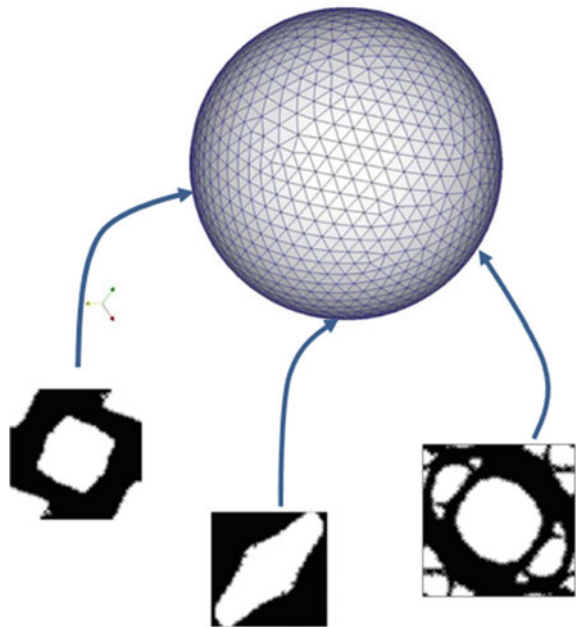




Fig. 11 Typical micro-structure topology outputs of the Computational Vademecum

isotropic topological derivative concept and its application in the slerp algorithm [4], as proposed in this work, fulfills this requirement. All cases converged for a constant value of the penalty, with a convergence tolerance $\epsilon_\theta < 1^\circ$ and a tolerance on the volume constraint $TOL < 0.001$.

The homogenized constitutive operator, C_h , constitutes the relevant “output” of the Vademecum since this is the only data retrieved from the micro-scale for the macro-scale computations (see Eq. 26). Accordingly, in Fig. 12, the Vademecum outputs for the optimal homogenized components of C_h are presented. There, the major symmetries of C^h (symmetric character of the maps of the symmetric components) as well as the rotated mirroring $C_{11} - C_{22}$ and $C_{13} - C_{23}$ can be observed.

4.4 Numerical Examples

In Algorithm 1, the numerical strategy, implemented in a Matlab code, for solving the minimization problem (24) is presented. It is based on an alternate directions algorithm, extensively used in the literature (see for example [1]).

In order to assess the proposed approach some numerical examples are presented next. In all cases the solid volume fraction at the RVE is $V_\mu = 0.6$, thus satisfying $\int_{\Omega_\mu} \chi_\mu = V_\mu = 0.6$. As start point in the iterative procedure, a micro-structure with a centered circular void fulfilling this condition is taken at all RVE’s (see Fig. 13a).

4.5 Cantilever Beam

The micro-structure topological design of the cantilever beam in Fig. 13 is considered. The problem dimensions are 2 meters length \times 1 meter height, and plane stress conditions are assumed. The beam is loaded by a unit vertical point force, at the right end center, and it is clamped at the left end.

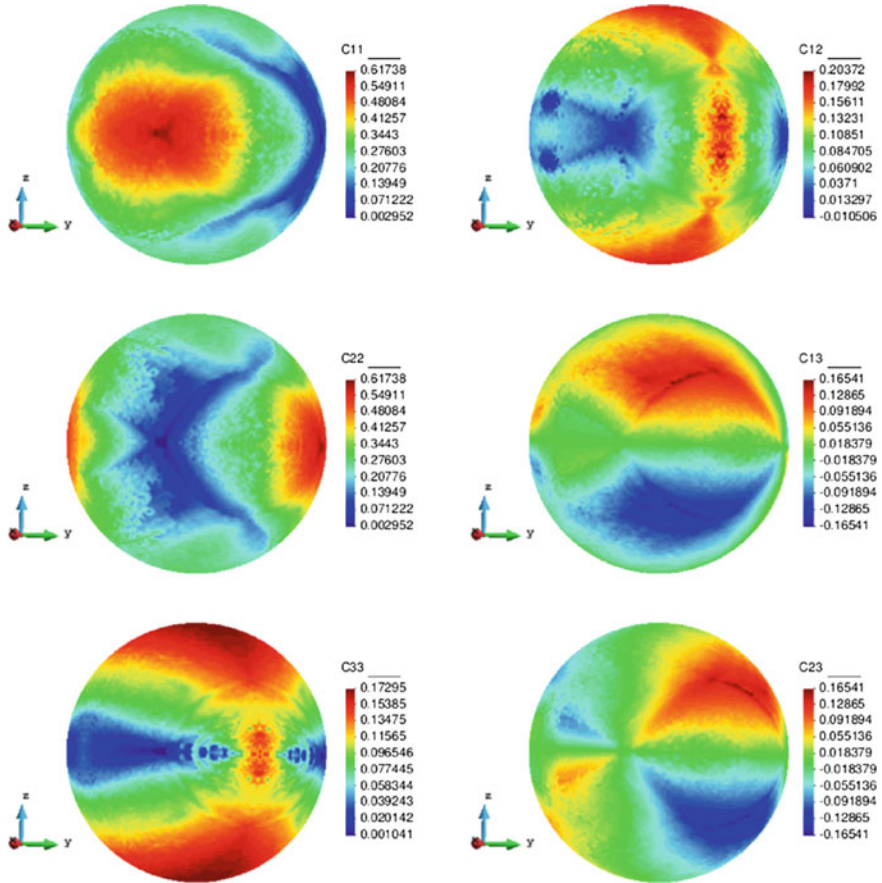


Fig. 12 Maps of the constitutive tensor components on the unit-radius spherical parametric domain

This rectangular macroscopic domain, is discretized into 2618 three-nodded triangular elements. The elastic properties of the basis material are: Young Modulus $E_\mu = 1$ and Poisson ratio $\nu_\mu = 0.3$. In Fig. 13 the evolution of the micro-structure topology, along the iterative design process are displayed.

In Fig. 14, the evolution of the global cost function (structural compliance) and of the residue of the alternate directions algorithm is depicted. As it can be checked there, four iterations suffice to achieve full convergence with a 30% reduction of the original compliance. The convergence ratio of the iterative process is linear, as expected from the used alternate directions algorithm.

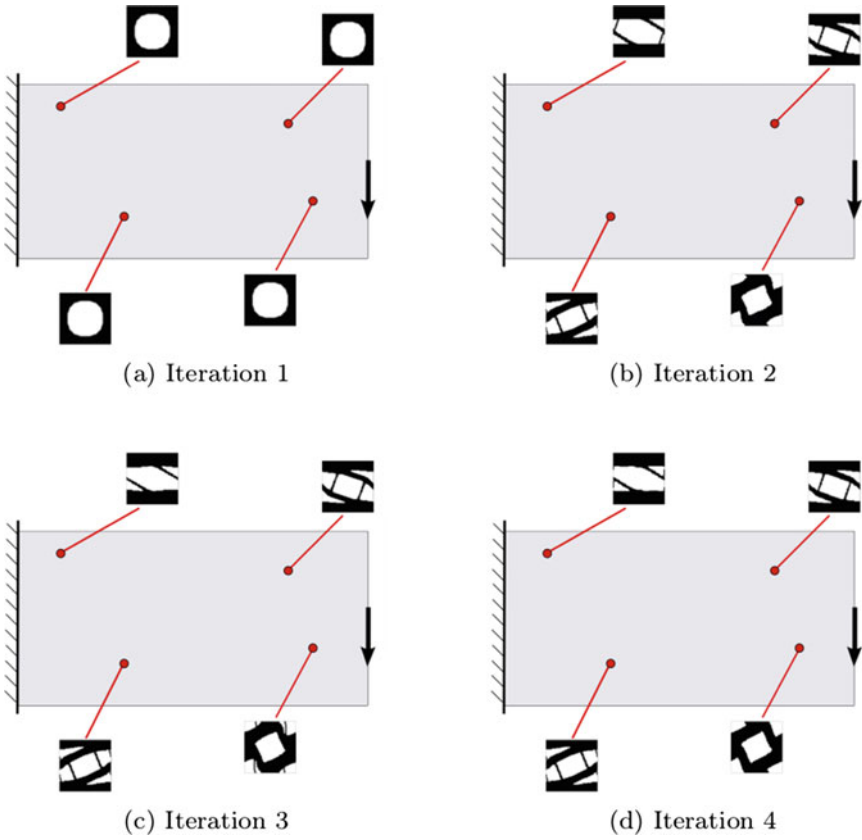


Fig. 13 Cantilever Beam microstructure design: RVE topology distribution along the iterative design process

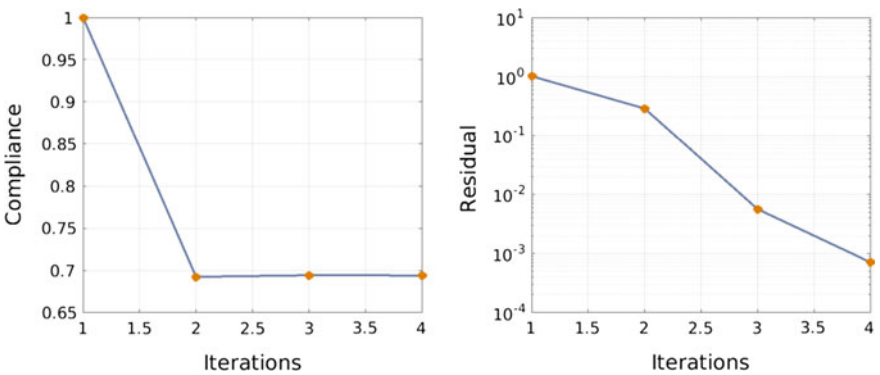


Fig. 14 Cantilever Beam microstructure design: compliance and residue evolutions for the alternate directions algorithm

Algorithm 1 Alternate directions algorithm

Input: Set an initial micro-structure topology distribution χ_μ^0 for an equilibrated structure with σ_0 stresses.

while $\epsilon^k > TOL$ **do**

- Selecting on Computational Vademecum (the nearest point), solve

$$\chi_\mu^{k+1} = \arg \left\{ \begin{array}{l} \text{minimize } \sigma_k : C_h^{-1}(\chi_\mu) : \sigma_k \\ \chi_\mu \\ \text{s.t.} \quad \int_{\Omega_\mu} \chi_\mu = V_\mu \end{array} \right\}$$
- Solve an standard equilibrium equation (u_{k+1}, σ_{k+1}) with χ_μ^{k+1} in (25)
- Update stopping criteria $\epsilon_k = \frac{\|u_{k+1} - u_k\|}{\|u_0\|}$
- Increase iteration $k = k + 1$

end while

5 Conclusions

The anisotropic topological derivative is presented in this work. The derived formula is general, i.e. for any kind of anisotropy, in two dimensional problems, and orthotropy and isotropy (of the background material or the inclusion or a combination of both) can be derived as particular cases.

The presented numerical simulation show that the selected material properties heavily affect the optimal topology in an standard topology optimization problem. In addition, influence of the microscopic topology on the optimal macroscopic topology is observed which, in some cases, becomes very relevant. Since real applications involve non homogeneous isotropic material, the obtained closed formula of the topological derivative for heterogeneous anisotropic materials generalizes the concept of topology optimization for any kind of material properties and distribution. This is a breakthrough in solving the challenging problem of two-scales topology optimization.

Additionally, a new approach to computational material design has been presented and applied to multi-scale topological design of structural materials. A computational homogenization scheme for two scales (FE2) has been considered to account for the repercussion of the material distribution at the lower scale on the global structural properties.

To overcome the large computational cost typical of brute-force FE2 homogenization methods, and taking advantage of the macro/micro separability properties of the stated problem, a Vademecum-based strategy has been devised. It consists of the, off-line, construction of a discrete material catalog, containing an appropriate large set of optimal RVE designs, each one corresponding to a single macroscopic

stress state. The topological derivative mathematical tool, jointly with a level-set algorithm on the slerp algorithm, have proved robust enough to provide the optimal RVE designs necessary for the Vademecum construction (more than 2000 for the presented examples).

In this framework a global optimization algorithm, based on consultation of the Vademecum in combination with the equilibrium solution of the macroscopic structural problem results into a highly non-linear problem that, however, can be robustly solved by means of a fixed point (or alternate directions) algorithm.

The resulting strategy becomes both robust and computationally efficient for tackling the micro-structure computational design problem in structural materials. Some representative examples illustrate the proposed methodology, and show that large reductions of the structural compliance (up to 40%) can be achieved by using the proposed “local” topology design strategy, in front of the alternative “homogeneous” material distribution.

Acknowledgements The research leading to these results has received funding from the European Research Council under the European Union’s Seventh Framework Program (FP/2007–2013)/ERC Grant Agreement n. 320815, Advanced Grant Project COMP-DES-MAT.

References

1. G. Allaire, *Shape Optimization by the Homogenization Method*, vol. 146 (Springer Science & Business Media, 2012)
2. H. Ammari, H. Kang, Polarization and moment tensors with applications to inverse problems and effective medium theory. *Applied Mathematical Sciences*, vol. 162 (Springer, New York, 2007)
3. S. Amstutz, S.M. Giusti, A.A. Novotny, E.A. De Souza Neto, Topological derivative for multi-scale linear elasticity models applied to the synthesis of microstructures. *Int. J. Numer. Methods Eng.* **84**(6), 733–756 (2010)
4. S. Amstutz, H. Andrä, A new algorithm for topology optimization using a level-set method. *J. Comput. Phys.* **216**(2), 573–588 (2006)
5. M.P. Bendsoe, N. Kikuchi, Generating optimal topologies in structural design using a homogenization method. *Comput. Methods Appl. Mech. Eng.* **71**(2), 197–224 (1988)
6. G. Cardone, S.A. Nazarov, J. Sokolowski, Asymptotic analysis, polarization matrices, and topological derivatives for piezoelectric materials with small voids. *SIAM J. Control Optim.* **48**(6), 3925–3961 (2010)
7. F. Chinesta, A. Leygue, F. Bordeu, J.V. Aguado, E. Cueto, D. Gonzalez, I. Alfaro, A. Ammar, A. Huerta, PGD-Based computational vademecum for efficient design, optimization and control. *Arch. Comput. Methods Eng.* **20**(1), 31–59 (2013)
8. E.A. De Souza Neto, R.A. Feijóo, Variational foundations of large strain multiscale solid constitutive models: kinematical formulation. *Advanced Computational Materials Modeling: From Classical to Multi-Scale Techniques-Scale Techniques*, pp. 341–378, 2010
9. D. Esteves Campeão, S. Miguel Giusti, A. Antonio Novotny, Topology design of plates considering different volume control methods. *Eng. Comput.* **31**(5), 826–842 (2014)
10. A. Ferrer, *Multi-scale topological design of structural materials: an integrated approach*. Ph.D. thesis, Universitat Politècnica de Catalunya, 2017
11. S.M. Giusti, L.A.M. Mello, E.C.N. Silva, Piezoresistive device optimization using topological derivative concepts. *Struct. Multidiscip. Optim.* **50**(3), 453–464 (2014)

12. S.M. Giusti, A. Ferrer, J. Oliver, Topological sensitivity analysis in heterogeneous anisotropic elasticity problem. Theoretical and computational aspects. *Comput. Methods Appl. Mech. Eng.* **311**, 134–150 (2016)
13. J.A. Hernandez, J. Oliver, A.E. Huespe, M.A. Caicedo, J.C. Cante, High-performance model reduction techniques in computational multiscale homogenization. *Comput. Methods Appl. Mech. Eng.* **276**, 149–189 (2014)
14. J. Kato, D. Yachi, K. Terada, T. Kyoya, Topology optimization of micro-structure for composites applying a decoupling multi-scale analysis. *Struct. Multidiscip. Optim.* **49**(4), 595–608 (2014)
15. A.A. Novotny, J. Sokolowski, Topological derivatives in shape optimization. *Interaction of Mechanics and Mathematics* (Springer, Berlin, 2013)
16. J. Sokolowski, A. Zochowski, The topological derivative method in shape optimization. *SIAM J. Control Optim.* **37**(4), 1251–1272 (1999)
17. L. Xia, P. Breitkopf, Concurrent topology optimization design of material and structure within FE2 nonlinear multiscale analysis framework. *Comput. Methods Appl. Mech. Eng.* **278**, 524–542 (2014)

Advances in the DEM and Coupled DEM and FEM Techniques in Non Linear Solid Mechanics

Eugenio Oñate, Francisco Zárate, Miguel A. Celigueta,
José M. González, Juan Miquel, Josep M. Carbonell, Ferran
Arrufat, Salvador Latorre and Miquel Santasusana

Abstract In this chapter we present recent advances on the Discrete Element Method (DEM) and on the coupling of the DEM with the Finite Element Method (FEM) for solving a variety of problems in non linear solid mechanics involving damage, plasticity and multifracture situations.

1 Introduction

The Discrete Element Method (DEM) is a popular technique for analysis of the mechanics of granular matter, as well as for modeling multifracture situations in frictional materials such as concrete and geomaterials.

The Finite Element Method (FEM), on the other hand, is a standard numerical technique for linear and non linear analysis of structures. Differently from the DEM, the FEM has difficulties for reproducing multifracture situations in solids. The combination of FEM and DEM procedures seems therefore a win-win situation for modeling and simulation of a wider range of problems in non linear solid mechanics, than using any of the two methods separately.

In this chapter we present first recent advances in the DEM for non linear analysis of cohesive and non cohesive materials. Then a method for coupling the DEM and FEM procedures and for studying the interaction of physical particles and deformable solids is explained. In the last part of the chapter we present an approach for modeling multifracture situations in a solid by starting with the FEM analysis of the continuum domain in the standard manner. Discrete elements at the element

Dedicated to professor Roger Owen on his 75th birthday.

E. Oñate (✉) · F. Zárate · M.A. Celigueta · J.M. González · J. Miquel ·
J.M. Carbonell
Centre Internacional de Mètodes Numèrics a l'Enginyeria (CIMNE),
Universitat Politècnica de Catalunya (UPC), Barcelona, Spain
e-mail: onate@cimne.upc.edu

F. Arrufat · S. Latorre · M. Santasusana
Centre Internacional de Mètodes Numèrics a l'Enginyeria (CIMNE), Barcelona, Spain

© Springer International Publishing AG 2018

E. Oñate et al. (eds.), *Advances in Computational Plasticity*, Computational
Methods in Applied Sciences 46, DOI 10.1007/978-3-319-60885-3_15

nodes are progressively introduced as damage on the center of the element sides exceeds a given value. Examples of this FEM-DEM technique are presented for a number of structural problems involving single fracture and multifracture situations such as the failure analysis of concrete samples and beams under external loads, fracture of a shale rock domain under a pulse load and multifracture situations due to a blasting load in a tunnel front and a granite rock specimen.

2 A Local DEM Model

2.1 DEM Model Overview

The DEM was initially developed by Cundall et al. [5] in the 1970s. It is based on the interaction of discrete elements (also called particles)—typically cylinders (in 2D) and spheres (in 3D)—to simulate the behavior of continuum and discontinuum domains [2, 3, 6, 7, 12, 14, 15, 21, 24, 26, 31]. This interaction is governed by a set of kinematic equations involving the forces acting over the discrete elements and the displacements, velocities and accelerations of the particles. The forces acting over a discrete element are related to the stresses and strains according to a constitutive model. In our work we use the local constitutive model for the DEM for cohesive and non-cohesive materials proposed by Oñate et al. [21]. In the following a brief description of this model is presented.

2.1.1 Kinematic Equations and Integration Scheme

The translation and rotation of the particles in the DEM is governed by the standard dynamics equations for rigid bodies,

$$m_i \ddot{\mathbf{u}}_i = \mathbf{F}_i \quad , \quad \mathbf{I}_i \dot{\omega}_i = \mathbf{T}_i \quad (1)$$

where \mathbf{u}_i and ω_i are the i -th particle displacement and the angular velocity respectively, m_i and \mathbf{I}_i are the mass and the inertia tensor of the particle, and \mathbf{F}_i and \mathbf{T}_i are vectors containing the forces and torques due to the interaction of a particle with its neighbors (Fig. 1). The set of forces applied on a particle include external forces (\mathbf{F}_i^{ext}), damping forces (\mathbf{F}_i^{damp}) and interaction forces between neighbor particles (\mathbf{F}^{ij}) (Fig. 2)

$$\mathbf{F}_i = \mathbf{F}_i^{ext} + \mathbf{F}_i^{damp} + \sum_{j=1}^{n_i} \mathbf{F}^{ij} \quad (2)$$

where n is the number of particles adjacent to the i th particle.

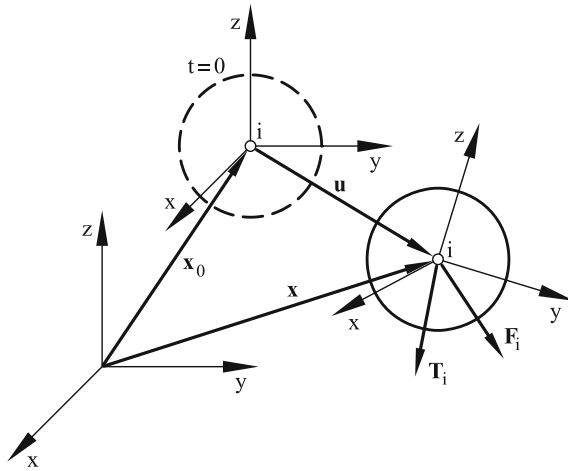


Fig. 1 Motion of a rigid particle

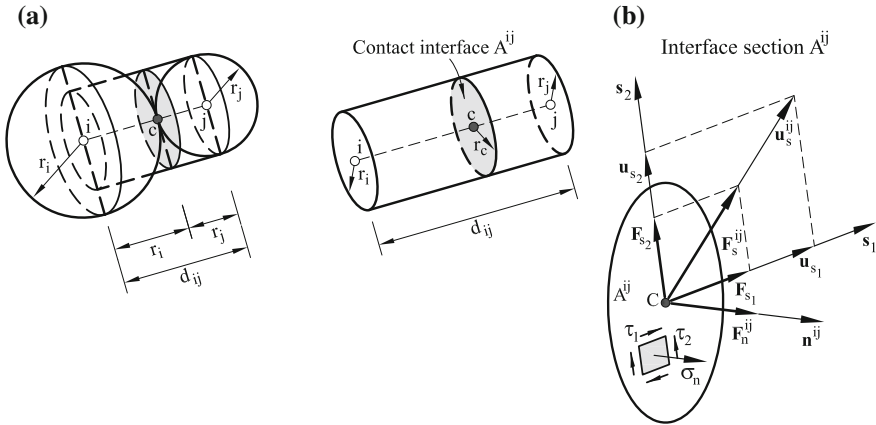


Fig. 2 **a** Definition of contact interface between two discrete particles. **b** Forces acting along the normal and shear directions on a contact interface section A^{ij}

The expression for the torques can be derived from Eq. (2) [22]. The dynamic set of equations (Eq. (1)) are integrated in time using an explicit scheme as expressed in (3) for the translation motion,

$$\ddot{\mathbf{u}}_i^n = \frac{\mathbf{F}_i^n}{m_i} \quad , \quad \dot{\mathbf{u}}_i^{n+1/2} = \dot{\mathbf{u}}_i^{n-1/2} + \ddot{\mathbf{u}}_i^n \Delta t \quad , \quad \mathbf{u}_i^{n+1} = \mathbf{u}_i^n + \dot{\mathbf{u}}_i^{n+1/2} \Delta t \quad (3)$$

The explicit time integration scheme is chosen due to the high computational cost of the DEM solution for large problems. However, the stability of the scheme

is conditioned to the time step value. The critical time step is related to the high frequency of the problem, (ω^{max}), i.e.

$$\Delta t \leq \Delta t_{cr} = \frac{2}{\omega^{max}} \left(\sqrt{1 + \xi^2} - \xi \right) \quad (4)$$

where ξ is a fraction of the critical damping [5, 22].

2.1.2 Forces Acting Over the Discrete Element

The interaction forces at the contact interface between two particles i and j (\mathbf{F}^{ij}) are obtained from the normal (\mathbf{F}_n^{ij}) and tangential (\mathbf{F}_s^{ij}) components (Fig. 2b).

The normal component of the interaction forces is calculated as,

$$F_n^{ij} = \sigma_n \alpha_{ij} A^{ij} \quad \text{with } A^{ij} = \pi r_c^2 \quad (5)$$

where σ_n is the normal stress at the contact interface, r_c is the minimum radius of the two interacting particles (Fig. 2a) and α_{ij} is a parameter that depends on the number of contacts and the packing of the particles [21]. In our work we have used a global definition of $\alpha_{ij} = \alpha = 40 \frac{P}{N_c}$ where N_c and P are respectively the average number of contacts per sphere and the average porosity for the whole particle assembly [21]. The normal stress σ_n is calculated from the strain ξ_n and the strain rate $\dot{\xi}_n$ along the normal direction as,

$$\sigma_n = E \xi_n + c \dot{\xi}_n \quad (6)$$

where E is the Young modulus and c is a local damping parameter calculated as

$$c = 2 \frac{\xi}{r_c} \sqrt{m_{ij} K_n^{ij}} \quad \text{with } m_{ij} = \frac{m_i m_j}{m_i + m_j} \quad (7)$$

where K_n^{ij} is the normal stiffness parameter (see Eq. 10).

The normal strain and strain rate values are computed from the kinematic variables as,

$$\epsilon_n = \frac{u_n}{d_{ij}} \quad \dot{\epsilon}_n = \frac{\dot{u}_n}{d_{ij}} \quad (8)$$

where u_n and \dot{u}_n are the relative displacements and the relative velocity between two particles along the normal direction at the contact interface and d_{ij} is the distance between the centroids of the two particles (Fig. 2b).

Equations (5)–(8) lead to a general relation between for the normal force and the kinematic variables as

$$F_n^{ij} = \frac{\alpha_{ij} A^{ij}}{d_{ij}} \left[E u_n + 2 \frac{\xi}{r_c} \sqrt{m_{ij} K_n^{ij}} \dot{u}_n \right] = K_n^{ij} u_n + C_n^{ij} \dot{u}_n \quad (9)$$

where K_n^{ij} and C_n^{ij} are the normal stiffness and the normal viscous damping parameters at the contact interface between particles i and j that can be deduced from Eq. (9) as

$$K_n^{ij} = \frac{\alpha_{ij} A^{ij}}{d_{ij}} E \quad , \quad C_n^{ij} = \frac{2\alpha_{ij} A^{ij} \xi}{d_{ij} r_c} \sqrt{m_{ij} K_n} \quad (10)$$

A similar approach leads to the constitutive expression for the shear forces in the two tangential directions as [21]

$$\mathbf{F}_s^{ij} = K_s^{ij} \mathbf{u}_s^{ij} \quad (11)$$

where vector \mathbf{u}_s^{ij} is the shear component of the relative displacements between particles, calculated as,

$$\mathbf{u}_s^{ij} = \mathbf{u}^{ij} - (\mathbf{u}^{ij} \cdot \mathbf{n}^{ij}) \mathbf{n}^{ij} \quad (12)$$

In Eq. (11) K_s^{ij} is the shear stiffness parameter at the contact interface (assumed to be the same for both shear directions), given by

$$K_s^{ij} = \frac{K_n^{ij}}{2(1 + \nu)} \quad (13)$$

where ν is the Poisson's ratio of the material.

The damping forces are computed from the application of a global damping over the set of particles. This damping component is characterized by translation (α^t) and rotation (α^r) damping parameters defined as a fraction of the stiffness parameters. In this work we have taken $\alpha^r = \alpha^t = 0, 10$. The damping forces act in opposite direction to the motion of the particles according to the following expressions:

$$\mathbf{F}_i^{damp} = -\alpha^t \left| \mathbf{F}_i^{ext} + \mathbf{F}^{ij} \right| \frac{\dot{\mathbf{u}}_i}{|\dot{\mathbf{u}}_i|} \quad (14a)$$

$$\mathbf{T}_i^{damp} = -\alpha^r \left| \mathbf{T}_i \right| \frac{\dot{\omega}_i}{|\dot{\omega}_i|} \quad (14b)$$

The local DEM constitutive model described above holds for cohesive and non-cohesive materials, this latter as a particular case of the former, when the bonds between the particles are assumed to be initially broken. More details can be found in [21].

2.2 Normal and Shear Failure

Cohesive bonds at a contact interface are assumed to start breaking when the interface strength is exceeded either in the normal direction by the tensile contact force, or in the tangential direction by the shear force. The *uncoupled* failure (decohesion) criterion for the normal and tangential directions at the contact interface between particles i and j is written as

$$F_{n_i} \geq \mathcal{F}_{n_i} \quad , \quad F_s \geq \mathcal{F}_s \quad (15)$$

where \mathcal{F}_{n_i} and \mathcal{F}_s are the interface strengths for pure tension and shear-compression conditions, respectively, F_{n_i} is the normal tensile force and F_s is the modulus of the shear force vector \mathbf{F}_s^{ij} (Fig. 2 and Eq. 11).

The interface strengths are defined as

$$\mathcal{F}_{n_i} = \sigma_t^f \bar{A}^{ij} \quad , \quad \mathcal{F}_s = \tau^f \bar{A}^{ij} + \mu_1 |F_{n_c}| \quad (16)$$

where $\bar{A}^{ij} = \alpha_{ij} A_{ij}$, σ_t^f and τ^f are the tensile and shear strengths respectively, F_{n_c} is the compressive normal force at the contact interface and $\mu_1 = \tan \phi_1$ is a (static) friction parameter, where ϕ_1 is an internal friction angle. These values are assumed to be an intrinsic property of the material and are determined experimentally. In our work σ_t^f is taken as the tensile strength of the material measured in a bending-tensile (BT) or a Brazilian tensile strength test [21].

As for the shear strength τ^f we have estimated its value as a percentage of the maximum compressive stress in a uniaxial compression strength (UCS) test, $(\sigma_{n_c}^f)_{UCS}$, as

$$\tau^f = \beta (\sigma_{n_c}^f)_{UCS} \quad (17)$$

where β is a parameter that is calibrated in numerical experiments via shear and UCS tests. Typically $\beta \simeq 0.5$ [21].

Following tension failure, the constitutive behavior in the shear direction is governed by the standard Coulomb law

$$\mathbf{F}_s = \mu_2 |F_{n_c}| \frac{\mathbf{u}_s}{|\mathbf{u}_s|} \quad \text{with} \quad \mu_2 = \tan \phi_2 \quad (18)$$

where μ_2 is a dynamic Coulomb friction coefficient and ϕ_2 is the post-failure internal friction angle. Both parameters are determined from experimental tests.

Figure 3a shows the graphical representation of the failure criterium described by Eqs. (15), (16) and (18). This criterium assumes that the tension and shear forces contribute to the failure of the contact interface in a decoupled manner. On the other hand, shear failure under normal compressive forces follows a failure line that is a function of the shear failure stress, the compression force and the internal friction angle.

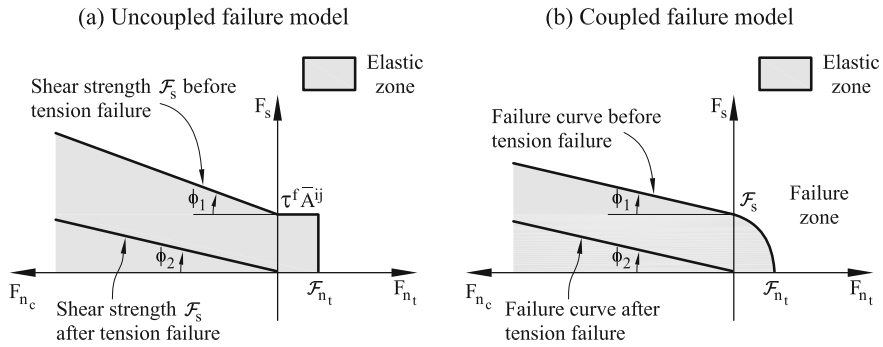


Fig. 3 Failure line in terms of normal and shear forces. **a** Uncoupled failure model. **b** Coupled failure model

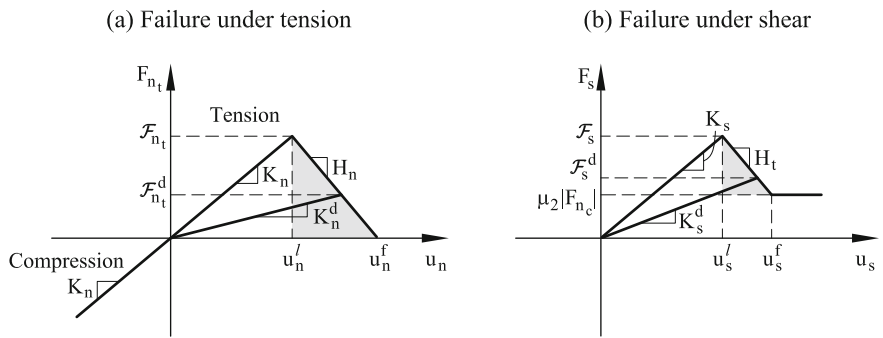


Fig. 4 Undamaged and damaged elastic moduli under tension **a** and shear **b** forces

Indeed, a coupled failure model in the tension-shear zone can also be used, as described in [21] (see Fig. 3b). For the numerical tests presented in this work the uncoupled model has been used.

Figure 4 shows the evolution of the normal tension force F_{n_t} and the shear force modulus F_s at a contact interface until failure in terms of the relative normal and tangential displacement increments. Elastic damage under tensile and shear conditions has been taken into account in this work by assuming a linear softening behaviour defined by the softening moduli H_n and H_t introduced into the force-displacement relationships in the normal (tensile) and shear directions, respectively (Fig. 4). For details see [21].

2.3 Elasto-Plastic Model for Compression Forces

The compressive stress-strain behaviour in the normal direction at the contact interface for frictional cohesive materials, such as cement, rock and concrete, is typically

governed by an initial elastic law followed by a non-linear constitutive equation that varies for each material. The compressive normal stress increases under linear elastic conditions until it reaches the limit normal compressive stress $\sigma_{n_c}^l$. This is defined as the axial stress level where the experimental curve relating the axial stress and the axial strain starts to deviate from the linear elastic behaviour. After this point the material is assumed to yield under *elastic-plastic* conditions.

The *elasto-plastic relationships* in the normal compressive direction are defined as

Loading path

$$dF_{n_c} = K_{T_n} du_n \quad (19a)$$

Unloading path

$$dF_{n_c} = K_{n_0} du_n \quad (19b)$$

In Eq. (19) dF_{n_c} and du_n are respectively the variation of the normal compressive force and the normal (relative) displacement, K_{n_0} is the initial (elastic) compressive stiffness for a value of $E = E_0$ (Fig. 5), and K_{T_n} is the tangent compressive stiffness given by

$$K_{T_n} = \frac{E_T}{E_0} K_{n_0} \quad (20)$$

where E_T is the slope of the normal stress-strain curve in the elastoplastic branch (i.e. $E_T = E_1, E_2, E_3$ in Fig. 5).

Plasticity effects in the normal compressive direction affect the evolution of the tangential forces at the interface, as the interface shear strength is related to the normal compression force by Eq. (16).

Figure 5 shows the diagram relating the compressive axial stress and the compressive axial strain used for modelling the elasto-plastic constitutive behaviour at the contact interfaces. The form of each diagram is obtained from experimental tests [8].

Figures 6 and 7 show an example of the DEM to the analysis of application of a UCS test and a BST of a cylindrical specimen for a cement material. The material parameters are shown in Table 1.

2.4 Enhanced Local Constitutive Model for the DEM that Accurately Reproduces the Elastic Behavior of a Continuum

The standard DEM technique is known to suffer from sensitivity to the packaging pattern and density of the particles when applied to the linear elastic analysis of a continuum. Standard features of an elastic continuum domain, such as the Poisson's ratio effect, are difficult to predict with the DEM in a consistent manner.

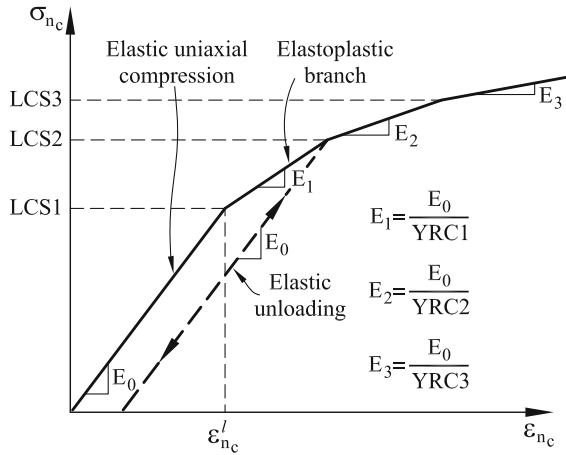


Fig. 5 Compressive axial stress-compressive axial strain diagram for elastoplastic material. LCS1 is the limit compressive stress (σ_{nc}^l) defining the onset of elastoplastic behaviour at the contact interface

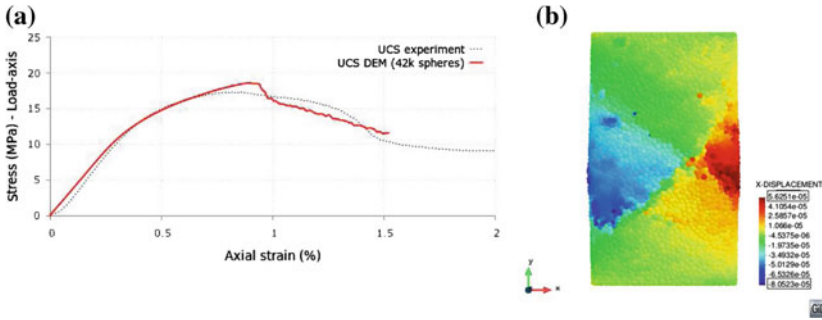


Fig. 6 DEM and experimental results for UCS test in a cement sample using 42000 spherical particles. **a** Axial stress-axial strain curve. **b** Contour of the horizontal displacement at the failure load

Celigueta et al. [2] have presented a procedure for correcting the local constitutive equations at a contact interface in the DEM, so that it can be accurately applied for predicting the elastic behavior of a continuum.

The enhanced local constitutive model for the DEM is based on a modified expression of the force-displacement relationships at the contact interface between particles i and j (Eqs. 9 and 11) as follows

$$F_n^{ij} = K_n^{ij} u_n^{ij} + A^{ij} v(\sigma_{s_1}^{ij} + \sigma_{s_2}^{ij}) \tag{21}$$

$$F_{s_k}^{ij} = K_s^{ij} u_{s_k}^{ij} + GA^{ij} \left(\frac{\partial u_n}{\partial s_k} \right)^{ij}, \quad k = 1, 2 \tag{22}$$

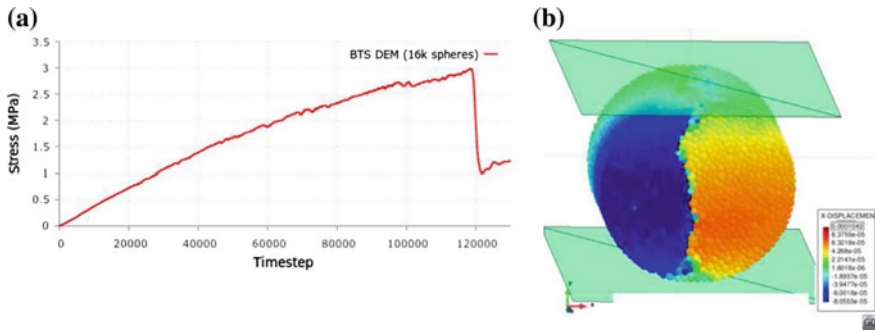


Fig. 7 DEM results for BTS test in cement sample using 16000 spheres. **a** Time evolution of the stress at the center point. **b** Contour of horizontal displacement at the failure load. The experimental failure stress is 3 MPa

Table 1 DEM constitutive parameters for analysis of UCS and BTS tests on a cement sample

ρ (g/cc)	μ_1	μ_2	E_0 (GPa)	ν	σ'_t (MPa)	τ_f (MPa)
1.70	0.30	0.40	3.80	0.20	4.80	8.50
LCS1 (MPa)	LCS2 (MPa)	LCS3 (MPa)	YRC1	YRC2	YRC3	α
8.5	9.0	11	3	9	24	1.0

where K_n^{ij} and K_s^{ij} are the normal and tangential stiffness parameters associated to the contact interface given by Eqs. (10) and (12), respectively and u_{s_k} is the relative displacement in the k th tangential direction (Fig. 2).

The underlined terms in Eqs. (21) and (22) introduce the effect of the *average stress field at the contact interface* on the normal and tangential forces at the interface. Details of the computation of these terms is given in [2].

The stresses σ_{s_1} and σ_{s_2} in Eq. (21) are obtained by projecting the average stress tensor $[\sigma]^i$ for the i th particle into the local coordinate system (s_1, s_2, \mathbf{n}) (Fig. 2b). Tensor $[\sigma]^i$ is computed as

$$[\sigma]^i = \frac{1}{V_i} \sum_{i=1}^{n_i} \mathbf{l}_i \otimes \mathbf{F}_i \quad (23)$$

where n_i is the number of contact points for the i th particle, \mathbf{l}_i is the vector connecting the center of the particle to the i th contact point, \mathbf{F}_i is the force vector at the i th contact point and V_i is a volume associated to the particle used to average the stresses.

A good estimation of V_i is essential for the success of this approach. In our work we have estimated V_i using the areas of the contact interfaces associated to each particle as

$$V_i = \sum_{j=1}^{n_i} \frac{1}{3} \hat{A}^{ij} \|\mathbf{I}_i\| \tag{24}$$

where \hat{A}^{ij} is an enhanced value of the area of the contact interface between particles i and j . The value of \hat{A}^{ij} is computed as

$$\hat{A}^{ij} = A^{ij} \frac{4\pi\alpha_i r_i^2}{A_i^T} \tag{25}$$

where A^{ij} is the area of the j th contact interface computed by Eq. (5), r_i is the radius of the i th particle, A_i^T is the sum of the contact interface areas $\left(A_i^T = \sum_{j=1}^{n_i} A^{ij} \right)$ and α_i is a parameter that depends on the number of neighboring particles to the i th particle and on the uniformity of the contact areas due to a random distribution of the particle sizes. More details are given in [2].

The non-local terms in Eqs. (21) and (22) have proven to be essential for accurately predicting the elastic and non-linear response of samples of cohesive material using the DEM.

As an example Table 2 shows the expected and computed values for the Young modulus and the Poisson’s ratio for a prismatic sample of elastic material modelled with cartesian, staggered and random distribution of spheres. Note the large errors for the values of E and ν using the standard DEM for staggered and random packings. The errors are negligible when the enhanced local constitutive model for the DEM presented in the previous lines is used.

The enhanced local constitutive model for the DEM has also shown an excellent behavior for accurately predicting the non-linear response and cracking pattern of geomaterials and concrete using a simple Rankine failure model at the contact interface.

Table 2 Prediction of E and ν in a sample using the normal and tangential contact forces

Input parameters: $E = 1.0e9$, $\nu = 0.35$

Error in computed values	Cartesian packing		Staggered packing		Random packing	
	Standard DEM	Improved DEM	Standard DEM	Improved DEM	Standard DEM	Improved DEM
Poisson’s ratio E	-0.6%	-0.6%	-23.0%	0.7%	-28.0%	-0.2
Poisson’s ratio ν	-100.0%	0.22%	-64.0%	-2.9%	-62.0%	-3.5

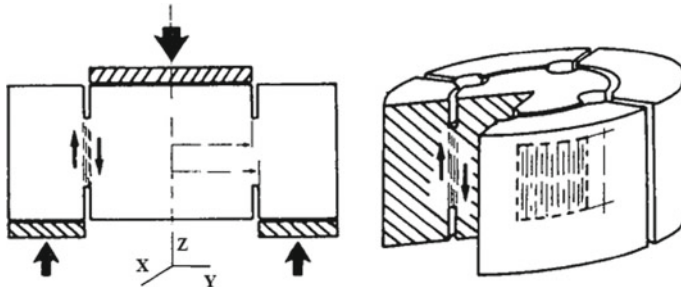


Fig. 8 Shear test in notched concrete specimen

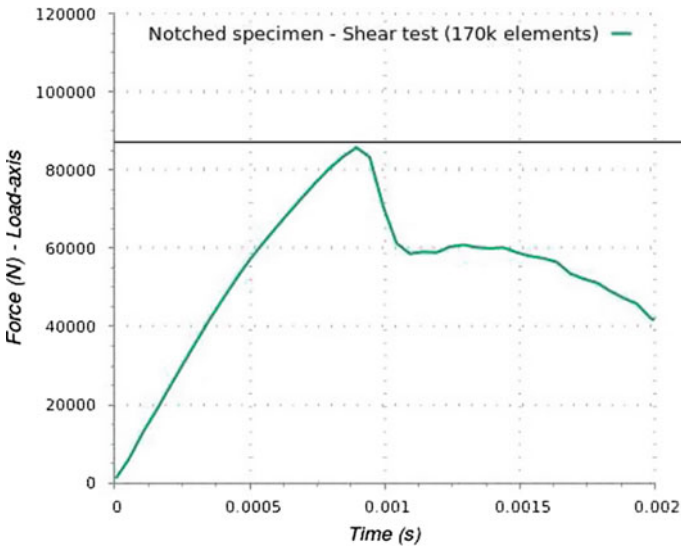


Fig. 9 Shear test in notched concrete specimen. Load-displacement curve obtained with the DEM. Experimental failure load = 82,3 kN

We present an application of the enhanced local constitutive model for the DEM to the analysis of a shear test [16] in a cylindrical notched specimen of concrete material. The definition of the test is shown in Fig. 8. More details of this particular test can be found in [8].

The material properties for the DEM analysis are $E = 35.5$ GPa, $\nu = 0,20$, $\mu_1 = 0,1$ and $\sigma_t^f = 4,5$ MPa. The analysis was carried out using 170k spherical particles. Figure 9 shows the load vertical displacement curve obtained with the DEM. Good agreement of the maximum load compared to the experimental value of 82,3 kN is obtained. Figure 10a show the multifracture pattern on the cylindrical sample at failure. The experimental results are displayed in Fig. 10b.

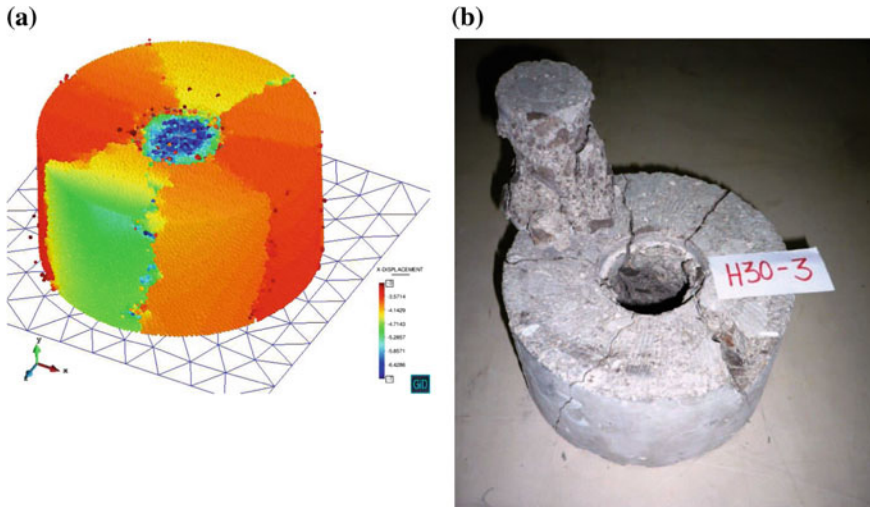


Fig. 10 Shear test in concrete specimen. **a** DEM results. **b** Experimental results

The enhanced local DEM constitutive model can be used in conjunction with any constitutive law in solid mechanics for predicting the linear and non linear behavior of a solid. This opens the door for predicting with the DEM the linear and non linear response of solids and structures of any material (including metallic materials) [3], which is unusual for standard DEM models.

3 Interaction of Discrete Particles and Solids Modelled with the FEM

The interaction of discrete particles and solids can be studied by coupling the potential of the DEM and FEM approaches. Isolated particles can be modeled with the DEM, while solids are better modeled using the FEM. Indeed, complex objects can also be modeled using a collection of DEM particles, which allows one to use the standard frictional contact algorithms between particles and rigid/deformable objects developed for the DEM. Clearly, for rigid objects only the DEM particles discretizing the boundary of the object need to be accounted for.

The author's group has developed an innovative algorithms for modeling contact situations between discrete particles and solids modeled with the DEM [28]. The so-called Double Hierarchy Method (termed in short H^2) is a simple contact algorithm specially designed to resolve efficiently the intersection of spheres with triangles and planar quadrilaterals but it can also work well with any other higher order planar convex polyhedra [28, 29]. A two layer the hierarchy is applied upgrading the classical the hierarchy method presented by Horner et al. [12], namely hierarchy on type of

contact followed by hierarchy on distance. The first hierarchy classifies the type of contact (facet, edge or vertex) for every contacting neighbour in a hierarchical way, while the distance-based hierarchy determines which of the contacts found are valid or relevant and which ones have to be removed.

The H^2 algorithm has been developed taking into account its implementation in a parallel computing environment. This is particularly important for industrial problems involving a large number of particles interacting with a fine FEM mesh.

Summarizing, the H^2 contact search satisfies the following requirements:

- Includes poly-disperse elements for both the FEM and the DEM.
- Allows different FE geometries and primitives (triangle, quadrilateral, polygon).
- Ensures contact continuity in non-smooth regions (edges and vertices).
- Resolve multiple contacts and contact with different entities simultaneously.
- Low memory storage.
- Simple, fast and accurate need.
- Fully parallelizable.

A simple particle-structure interaction example is presented next in order to assess the DEM-FEM coupling procedure. The example consists on a spherical particle colliding a simply supported beam (Fig. 11). Two different cases are reproduced. The reference solution to this problem, taken from linear modal dynamics was proposed by Timoshenko [30] and is reviewed in [17].

The two examples are reproduced with the same DEM and FEM parameters. In the first one the particle radius is 0.01 m and the length of the beam is 15.35 m, while in the second one the particle radius is 0.02 m and the beam length is 30.70 m. The material properties and the simulation parameters are summarized in Table 3.

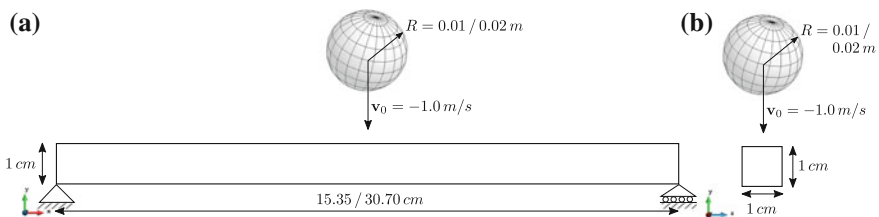


Fig. 11 Simply supported beam hit vertically at its centre by a sphere. **a** Front view. **b** Side view

Table 3 Simple supported beam hit by a sphere. Simulation parameters

Material properties	DEM	Analysis parameters	
Sphere radius (m)	0.01/0.02		
Density (kg/m ³)	7960		
Young's modulus (GPa)	215.82	Initial velocity of sphere (m/s)	[0.0, -0.01, 0.0]
Poisson's ratio	0.289	Gravity (m/s ²)	[0.0, 0.0, 0.0]
Friction parameter	0.0	Neighbour search freq.	50

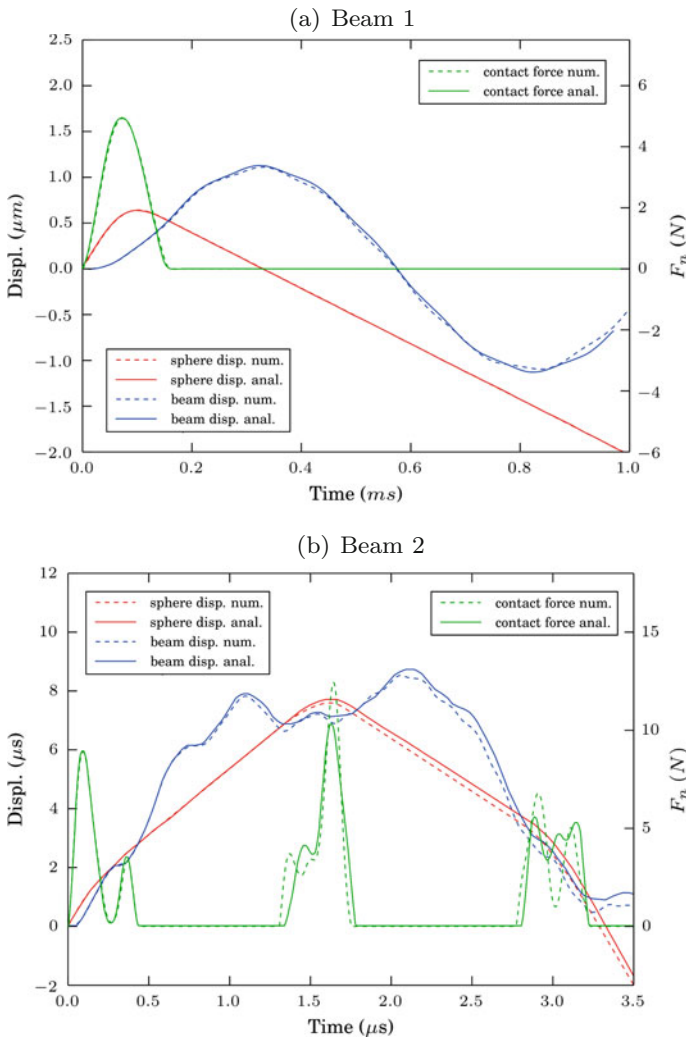


Fig. 12 Lateral impact of a sphere on a simply supported beam. Results for the deflection of the beam center, the sphere displacement and the contact force. **a** Analytical solution *versus* DEM-FEM numerical solution for the beam 1. **b** Analytical solution *versus* DEM-FEM numerical solution for the beam 2

The first case produces a single impact while the second yields three particle/beam impacts. The FEM meshes used are $60 \times 4 \times 3$ 8-nodded hexahedral elements respectively for the beam length, height and depth, respectively in the first example and $120 \times 4 \times 3$ hexahedra in the second example.

The results shown in Figs. 11 and 12 are quite satisfactory and the H^2 model reproduces well the displacements selected and the contact forces. Once the contact ends, the beam oscillates in a combination of different excited modes. The largest frequency mode, which can be easily identified in the figures, corresponds to the

natural frequency of the beam and it is perfectly matched. The higher vibration modes however, are not correctly captured by the linear hexahedral elements, as they are not the best suited elements to simulate flexural modes. Consequently, there is a deviation on the second and third contact events in the second example (Fig. 12b).

More details of this example and the H^2 procedure can be found in [28, 29].

3.1 A FEM-DEM Procedure for Multifracture Analysis of Solids

The DEM is a flexible method to simulate granular and non-continuum media, in particular the propagation of initial cracks. On the other hand, these contact properties are defined at the micro scale, while the material properties usually refer to experimental results at the macro scale. The step between both scales is not easy and requires a calibration task. The FEM otherwise is based in a continuum formulation involving the macro properties of the material. The FEM allows one to establish failure criteria compatible with the equilibrium equations in continuum mechanics, which makes it consistent and easy to apply for different materials.

The distance between DEM and FEM approaches is wide. Extensive research has been carried out in last years to combine FEM and DEM procedures, taking advantage of the merits of both numerical methods. Combination of the FEM with the standard DEM using circular and spherical particles are reported in [13, 20, 22, 27]. A combined finite-discrete element method based on the splitting of the finite elements into discrete elements of polygonal shape is presented in [10, 11, 18–20, 23]. Zárate and Oñate [32, 35] have recently presented a coupled FEM-DEM formulation for the numerical simulation of cracks starting from a finite element discretization of the domain.

The FEM-DEM formulation presented in [32, 35] discretizes the continuum using linear 3-noded triangles (in 2D) and 4-noded tetrahedra (in 3D) whose nodes define the position of a (virtual) discrete element. These discrete elements are introduced in the simulation process when cracks appear. The normal contact forces between discrete elements are calculated by integrating the stiffness matrix of the linear triangle along its sides that connect the discrete particles as shown in Fig. 13 [32]. The mechanical problem in the crack-free region is solved using the standard FEM and an appropriate damage model. In the examples shown in this chapter, damage onset and evolution of damage are governed by a Mohr-Coulomb failure criteria.

Onset of a crack at the center of an element side depends on the damage level at that point. The stresses over the edge are computed as the mean of the stresses in the elements sharing that side.

Once the damage limit is reached, a stiffness loss is induced in the triangle. The stiffness loss is associated to the area determined by the centroid of the triangle and the damaged side as shown in Fig. 14.

The stiffness matrix of a damaged element is recalculated at every time step as follows

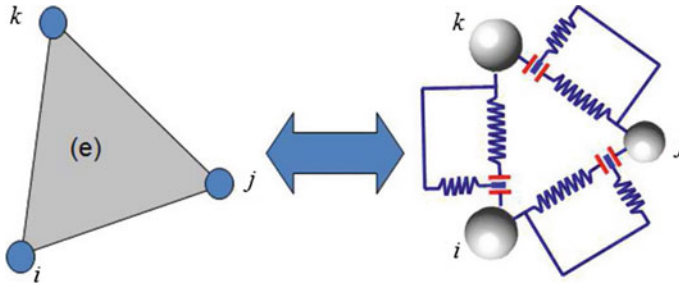


Fig. 13 Equivalence between stiffness matrix (FEM) and cohesive link (DEM)

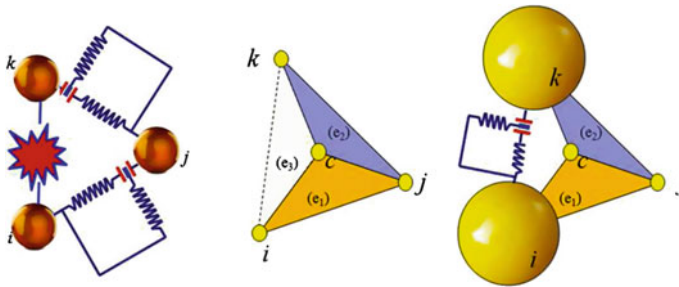
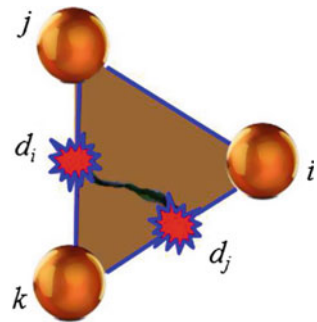


Fig. 14 Equivalence between stiffness matrix (FEM) and cohesive link (DEM) with a damaged edge

Fig. 15 Three-noded triangle with two sides damaged



$$\mathbf{K}^{(e)} = \left[1 - \frac{d_i + d_j}{2} \right] \mathbf{K}_0^{(e)} \tag{26}$$

where \mathbf{K}_0 is the initial stiffness matrix of the undamaged element and d_i and d_j are to the two maximum values of the damage parameters for the three element sides (Fig. 15).

When a cohesive bond is removed the side nodes of the element are disconnected and two discrete particles are introduced at the same nodal positions. Their radii and

masses are defined as the maximum ones to guarantee contact without overlapping other discrete elements in order to avoid spurious contact forces [14].

Once the discrete elements are created their interaction is governed according to contact and friction laws, as in the general DEM formulation described in a previous section.

A relevant point in the FEM-DEM approach described is its computational cost. Most of the cost in a DEM simulation is due to the contact searching algorithms. In the FEM-DEM technique presented the number of discrete particles is in general much lower than the number of nodes in the FEM mesh because the fractured area is typically smaller than the whole calculation domain. Hence, the computational time consumed by the contact searching algorithms is much lower than in a standard DEM solution.

3.2 Examples of Application of the FEM-DEM Procedure

3.2.1 Four-Point Bending Beam

The 2D version of the FEM-DEM technique is applied to the study of the failure of a double notch concrete beam analyzed under plane stress conditions. The beam is supported at two points and deforms in a bending mode by imposing the displacements at the two points depicted in Fig. 16 where the beam dimensions are also shown.

Figure 17 shows the crack path obtained with the 2D FEM-DEM approach for the three meshes analysed which coincide with the numerical results of Cervera et al. [4]. The mix-mode fracture is clearly seen. Figure 18 shows the plots of the vertical reaction at any of the two points where the displacement is imposed depicted in Fig. 16. The graphs are in good agreement with the results reported in [4]. We note the insensitivity of the load-displacement curve to the mesh size.

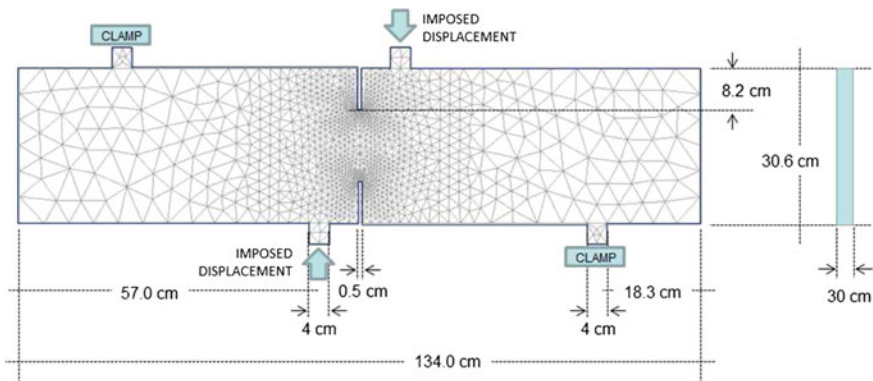


Fig. 16 Double notched concrete beam. Dimensions and boundary conditions

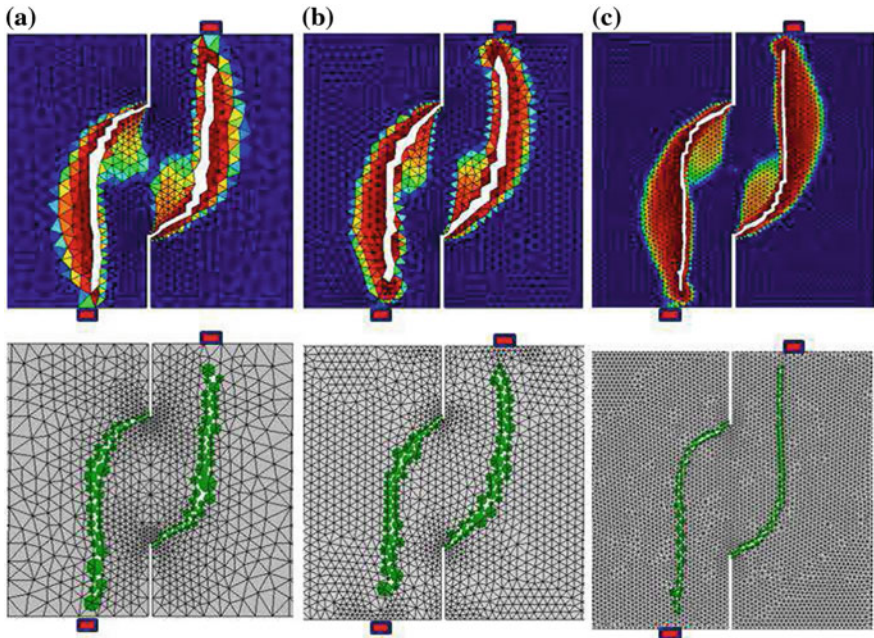


Fig. 17 Double notched concrete beam. Displacement contours and crack path at the two notches regions using three different meshes of 3-noded triangles. **a** Coarse mesh (2202 triangles). **b** Intermediate mesh (3480 triangles). **c** Fine mesh (11206 triangles). Discrete elements generated at the cracks using the FEM-DEM technique

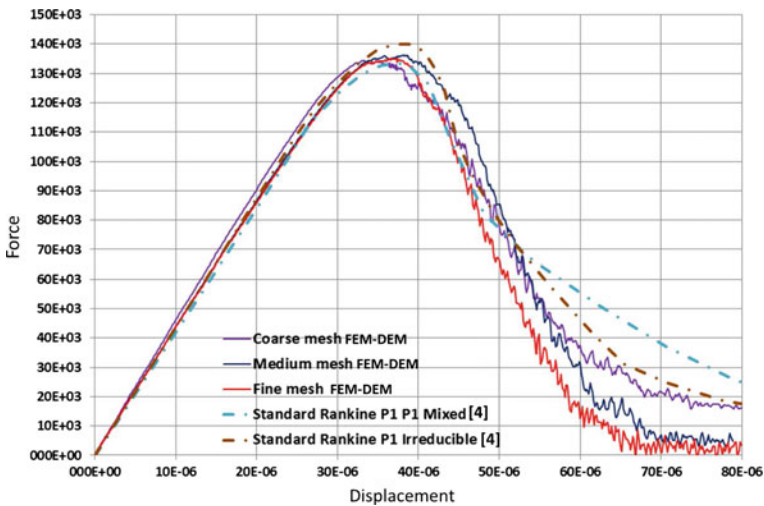


Fig. 18 Double notched concrete beam. Relationship between the reaction force and the imposed displacement at any of the two points depicted in Fig. 16. 3D FEM-DEM results are compared with those given in [4]

3.2.2 Brazilian Tensile Strength (BTS) Test

We have applied the 3D FEM-DEM procedure [35] to the simulation of a BTS test on a cylindrical concrete sample of diameter $D = 0.2$ m and 0.1 m thickness (t). The tensile strength value is computed by [1]:

$$f_t = \frac{2P}{\pi t D} \quad (27)$$

where P is the applied load.

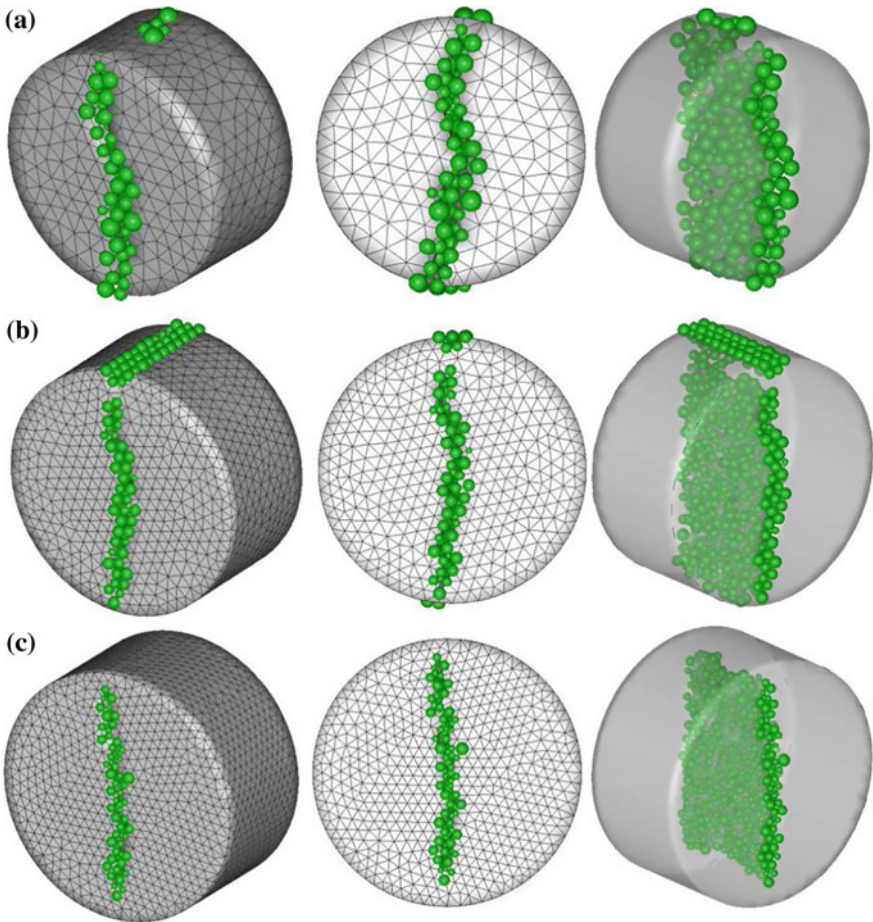


Fig. 19 3D FEM-DEM analysis of BTS test on a concrete specimen. Damage zone and discrete elements generated. **a** Coarse mesh. **b** intermediate mesh. **c** Fine mesh

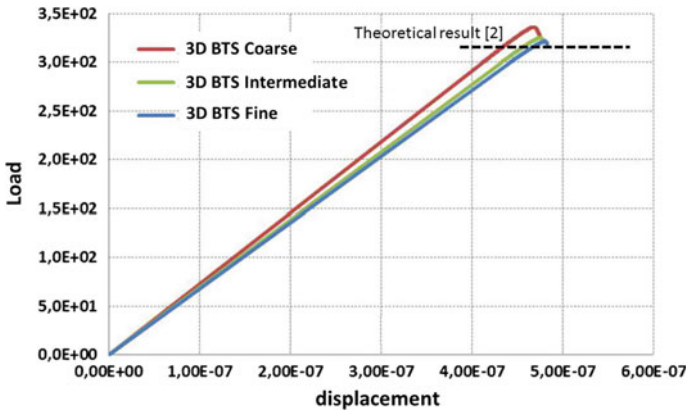


Fig. 20 3D FEM-DEM analysis of BTS test on a concrete specimen. Force-displacement relationship for the three meshes used

The material properties are $E_o = 21 \text{ GPa}$, $\nu = 0.2$, $\gamma = 7.8 \times 10^3 \text{ N/m}^3$, $f_t = 10 \text{ KPa}$ and $G_f = 1 \times 10^{-3} \text{ J/m}^2$. Using Eq. (27) this corresponds to a failure load of $P = 314.16 \text{ N}$.

Three finite element meshes were used for the analysis with 9338, 31455 and 61623 4-noded linear tetrahedra, respectively. The crack patterns obtained for each mesh are depicted in Fig. 19. The numerical results for the load-displacement curve are presented in Fig. 20. The numerical values obtained for the tensile strength were (coarse to fine mesh) 10693 Pa, 10351 Pa and 10 235 Pa which yielded a range of 6% to 2% error versus the expected value of $f_t = 10 \text{ kPa}$. Again the load-displacement curves were quite insensitive to the mesh size.

3.2.3 Fracture of Shale Rock Under a Pulse Load

The FEM-DEM procedure has been applied to the study of the fracture of a rock mass under a pulse load [9]. This is a usual procedure in the so-called fracking technique used in the oil and gas industry.

Figure 21 shows the geometry of the domain analyzed and the loads acting at the boundary. These loads are computed in terms of the depth of the rock mass analyzed. The evolution of the pulse load acting at central hole is shown in Fig. 21. Figure 22 depicts the finite element mesh of 3-noded triangles used for the analysis. The fracture pattern in the rock obtained with the FEM-DEM technique for a depth of 500 ft are shown in Fig. 23. The length of the vertical crack obtained is 36 ft which compares well with the length of 40 ft using the DEM [9] and also with an alternative FEM formulation [25].

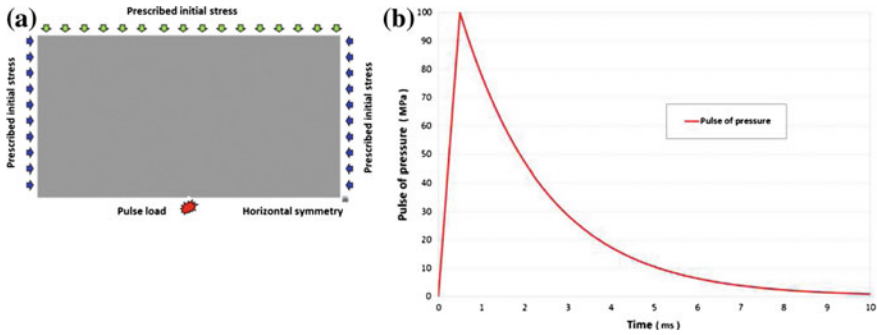


Fig. 21 Fracture of shale rock. a Analysis domain and applied loads. b Pulse pressure function

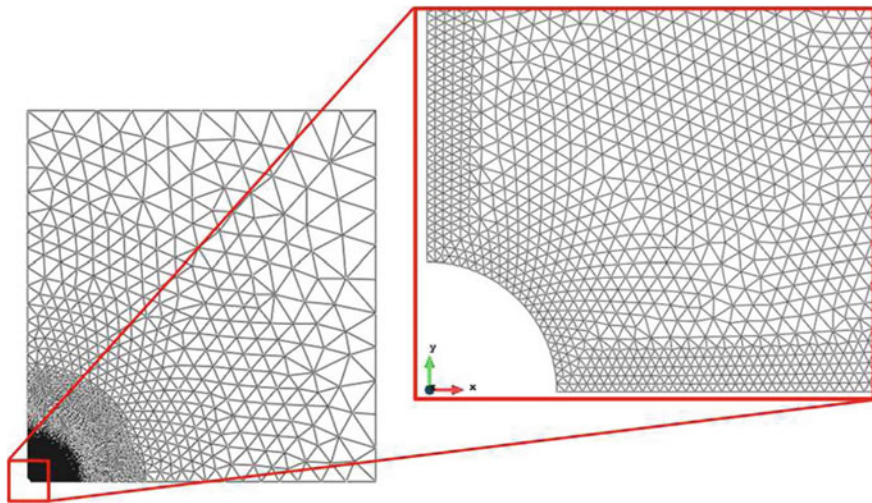


Fig. 22 Shale rock domain under pulse load. Mesh of 3-noded triangles for FEM-DEM analysis

3.2.4 Multifracture of a Tunnel Front Induced by a Blast Load

This example shows the capability of the FEM-DEM approach for simulating the evolution of multiple cracks in a tunnel front induced by a blast load.

Figure 24 shows the geometry of the front of the Bekkelaget tunnel in Norway, including the distribution of blast holes and the mesh of 38000 3-noded triangles discretizing the tunnel front. Details of the material properties, the blasting sequence and the computational features of this problem can be found in [34].

Figure 25 shows the evolution of cracks at the front induced by a particular blasting sequence. The results demonstrate the usefulness of the FEM-DEM technique for simulating this complex multifracturing problem.

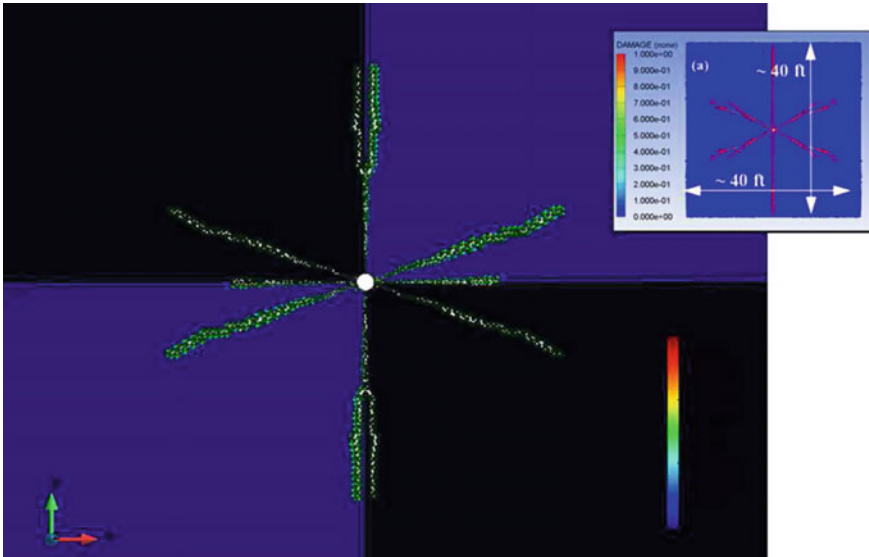


Fig. 23 Crack simulation with FEM-DEM model. Depth 500 ft. FEM results in box from [25]

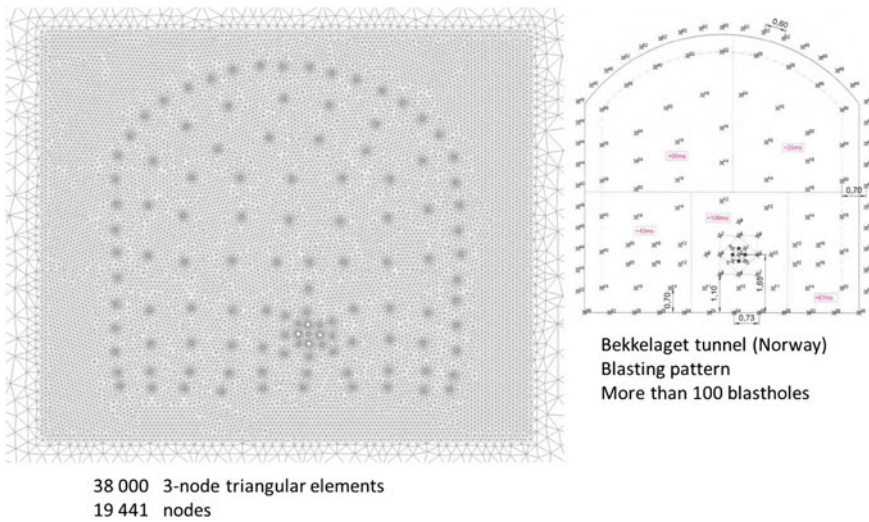


Fig. 24 Distribution of blast holes at the front of the Bekkelaget tunnel (Norway) and finite element method for FEM-DEM simulation of the cracking pattern

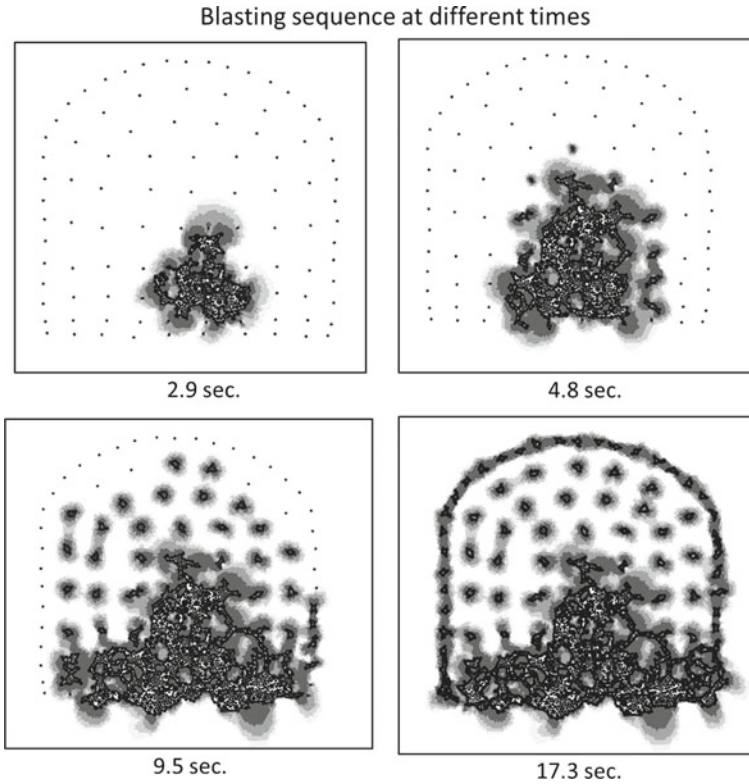


Fig. 25 Evolution of cracking at the front of the Bekkelaget tunnel induced by a blasting sequence. FEM-DEM results

3.2.5 Fracture Pattern in a Granite Rock Specimen Under Pulse Load Accounting for the Gas Pressure

Figure 26 shows the fracture pattern in a cylindrical specimen of granite rock under a pulse load acting at the central hole. The effect of the gas filling the cracks has been taken into account by coupling the FEM-DEM procedure described earlier with a compressible flow FEM solver using an embedded solution technique. The coupling strategy solves the equations for the compressible gas flow in the finite element mesh that fills the spaces created by the cracks. Figure 26 shows a snapshot of the pressure field in the gas domain between the cracks at a certain instant. More information of this coupled gas-structure solution can be found in [33].

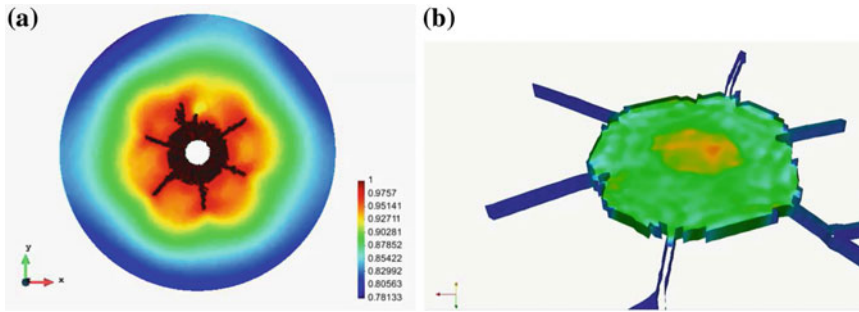


Fig. 26 Fracture pattern in a cylindrical specimen of granite rock under an internal pulse load. FEM-DEM solution accounting for the effect of the gas filling the crackings. **a** Cracking pattern. **b** Pressure field in the gas domain within the cracks [33]

4 Concluding Remarks

This chapter has shown the possibility of the DEM for linear and non linear analysis of cohesive materials and structures, as well as the advantages of coupling the FEM and DEM techniques for studying the interaction of particles with structures and the prediction of complex multifracture situations in solids.

Acknowledgements This research was partially funded by the ICEBREAKER project of the European Research Council. Support for this work was also provided from the Office for Naval Research Global (ONRG) of the US Navy through the NICE-SHIP project. We also acknowledge the financial support of the CERCA programme of the Generalitat de Catalunya.

References

1. F.L.L.B. Carneiro, A new method to determine the tensile strength of concrete, in *Proceedings of the 5th Meeting of the Brazilian Association for Technical Rules 126–129*, (In Portuguese), 1943
2. M.A. Celigueta, S. Latorre, F. Arrufat, E. Oñate, Accurate modelling of the elastic behavior of a continuum with the Discrete Element Method. Submitted to *Comput. Part. Mech.* (2017)
3. M.A. Celigueta, F. Arrufat, E. Oñate, Non linear analysis of solids accounting for damage, plasticity and fracture with the Discrete Finite Element. *Comput. Mech.* (Submitted) (2017)
4. M. Cervera, M. Chiumenti, R. Codina, Mesh objective modelling of cracks using continuous linear strain and displacements interpolations. *Int. J. Numer. Methods Eng.* **87**, 962–987 (2011)
5. P.A. Cundall, O.D.L. Strack, A discrete numerical model for granular assemblies. *Geotechnique* **29**(1), 47–65 (1979)
6. F. Donzé, F. Richefeu, S. Magnier, Advances in Discrete Element Method applied to soil, rock and concrete mechanics. *Electron. J. Geotechnol. Eng.* **8**, 144 (2009)
7. Y.T. Feng, K. Han, D.R.J. Owen, Discrete element simulation of the dynamics of high energy planetary ball milling processes. *Mater. Sci. Eng. A* **375**, 815–819 (2004)

8. T. Garcia, C. Hurtado, J. Cabrerizo, R. Mc-Aloon, Experimental tests for H30 and H50 concrete samples (in Spanish). Laboratorio de Tecnología de Estructuras. Universitat Politècnica de Catalunya, LTE/TGV/0415-24, Barcelona (2015)
9. J.M. González, E. Oñate, F. Zarate, Pulse fracture simulation in shale rock reservoirs. DEM and FEM-DEM approaches. *Comput. Part. Mech.* March (Submitted) (2017)
10. K. Han, D. Peric, D.R.J. Owen, J. Yu, A combined finite/discrete element simulation of shot peening processes Part II: 3D interaction laws. *Eng. Comput.* **17**(6), 680–702 (2000)
11. K. Han, D.R.J. Owen, D. Peric, Combined finite/discrete element and explicit/implicit simulations of peen forming process. *Eng. Computat.* **19**(1), 92–118 (2002)
12. D.A. Horner, F.J. Peters, A. Carrillo, Large scale discrete element modeling of vehicle-soil interaction. *J. Eng. Mech.* **127**(10), 1027–1032 (2001)
13. S. Katagiri, S. Takada, Development of fem-dem combined method for fracture analysis of a continuous media. *Memoirs of the Graduate School of Science and Technology*, vol. 20A (Kobe University Japan, 2003), pp. 65–79
14. C. Labra, E. Oñate, High-density sphere packing for discrete element method simulations. *Commun. Numer. Methods Eng.* **25**(7), 837–849 (2009)
15. C. Labra, J. Rojek, E. Oñate, F. Zárate, Advances in discrete element modelling of underground excavations. *Acta Geotechnica* **3**(4), 317–322 (2008)
16. M.P. Luong, Tensile and shear strengths of concrete and rock. *Eng. Fract. Mech.* **35**, 127–135 (1990)
17. J. Meijaard, Lateral impacts on flexible beams in multibody dynamics simulations. *IUTAM Symposium on Multiscale Problems in Multibody System Contacts*, vol. 1 (Springer, Netherlands, 2007), p. 173182
18. S. Moharnmadi, D.R.J. Owen, D. Peric, A combined finite/discrete element algorithm for delamination analysis of composites. *Finite Elem. Anal. Des.* **28**(4), 321–336 (1998)
19. A. Munjiza, D.R.J. Owen, N. Bicanic, A combined finite-discrete element method in transient dynamics of fracturing solids. *Eng. Comput.* **12**(2), 145–174 (1995)
20. A. Munjiza, *The Combined Finite-Discrete Element Method* (Wiley, 2004). ISBN: 0-470-84199-0
21. E. Oñate, F. Zárate, J. Miquel, M. Santasusana, M.A. Celiueta, F. Arrufat, R. Gandijota, K. Valiullin, L. Ring, A local constitutive model for the discrete element method. Application to geomaterials and concrete. *Comput. Part. Mech.* **2**, 139–160 (2015)
22. E. Oñate, J. Rojek, Combination of discrete element and finite element methods for dynamic analysis of geomechanics problems. *Comput. Methods Appl. Mech. Eng.* **193**, 3087–3128 (2004)
23. D.R.J. Owen, Y.T. Feng, Parallelised finite/discrete element simulation of multi-fracturing solids and discrete systems. *Eng. Comput.* **18**(3–4), 557–576 (2001)
24. D. Potyondy, P. Cundall, A bonded-particle model for rock. *Int. J. Rock Mech. Min. Sci.* **41**(8), 1329–1364 (2004)
25. M. Reza Safari, R. Gandikota, U. Mutlu, M. Ji, J. Glanville, H. Abass, Pulsed fracturing in shale reservoirs: geomechanical aspects, ductile-brittle transition and field implications, in *Presented at the Unconventional Resources Technology Conference*, Denver, Colorado, USA, Aug 2013, pp. 12–14
26. J. Rojek, C. Labra, O. Su, E. Oñate, Comparative study of different discrete element models and evaluation of equivalent micromechanical parameters. *Int. J. Solids Struct.* **49**, 1497–1517 (2012)
27. J. Rojek, E. Oñate, Multiscale analysis using a coupled discrete/finite element method. *Interact. Multiscale Mech.: Int. J. (IMMIJ)* **1**(1), 1–31 (2007)
28. M. Santasusana, J. Irazábal, E. Oñate, J.M. Carbonell, The Double Hierarchy Method. A parallel 3D contact method for the interaction of spherical particles with rigid FE boundaries using the DEM. *Comput. Part. Mech.* **3**(3), 407–428 (2016)
29. M. Santasusana, Numerical techniques for non-linear analysis of structures combining discrete element and finite element methods. Ph.D. Thesis, Barcelona, Dec 2016
30. S. Timoshenko, *Goodier JN Theory of Elasticity* (McGraw-Hill, Print, 1951)

31. V.T. Tran, F.-V. Donzé, P. Marin, A discrete element model of concrete under high triaxial loading. *Cem. Concr. Compos.* **33**(9), 936948 (2011)
32. F. Zárate, E. Oñate, A simple FEM-DEM technique for fracture prediction in materials and structures. *Comput. Part. Mech.* **2**(3), 301–314 (2015)
33. F. Zárate, R. Löhner, E. Oñate, Modeling of multifracture in solids induced by blast load accounting for coupled gas solid interaction effects. *Comput. Part. Mech.* (Submitted) (2017)
34. F. Zárate, J.M. Gonzalez, E. Oñate, Application of the FEM-DEM technique to the multifracture of rock under blast load. *Comput. Part. Mech.* (Submitted) (2017)
35. F. Zárate, E. Oñate, Three dimensional FEM-DEM technique for multifracture analysis of solids and structures. *Comput. Part. Mech.* (Submitted) (2017)

The Influence of the Collagen Architecture on the Mechanical Response of the Human Cornea

Anna Pandolfi

Abstract The hierarchical architecture of the stromal collagen is strictly related to the optical function of the human cornea. The basic features of the corneal collagen organization have been known for a while, but recently the advance of optical imaging has revealed changes across the thickness that might be related to particular aspects of the corneal behavior. It is worth to investigate whether the actual structure possesses some relevance in the overall mechanical behavior of the cornea and whether it should not be disregarded in computational models with predictive purposes. In this study, finite element analyses of the human cornea considering four different architectures of the collagen are presented. Results of the numerical simulations of quasistatic and dynamic tests are compared and discussed.

1 Introduction

The corneal stroma plays several pivotal roles within the eye. Optically, the cornea is the main refracting lens and thus has to combine almost perfect transmission of visible light with precise shape, in order to focus incoming light. Furthermore, the cornea has to be extremely tough mechanically in order to protect the inner contents of the eye. These functions are governed by the corneal structure at all hierarchical levels. The evolution of modern refractive surgery has focused attention on the relationship between collagen architecture and biomechanical properties of the human cornea, in particular trying to establish factors that help in maintaining the corneal shape and transparency under physiological, pathological, or surgical conditions.

The corneal stroma transparency depends particularly on the regular ordering of stromal collagen fibrils, which cause destructive interference from scattered light except in the forward direction [1]. Collagen structural protein is characterized by triple helical domains, which self-assemble into fibrils that further form fibers and more complex three-dimensional networks responsible for the architecture of organs. The structural units of the stroma are the ribbon-like fibers called lamellae which

A. Pandolfi (✉)
Politecnico di Milano, Milan, Italy
e-mail: anna.pandolfi@polimi.it

consist of aligned, evenly spaced collagen fibrils surrounded by a proteoglycan-rich matrix. Stromal lamellae run parallel to the mean surface of the cornea shell, counting approximately 300 in the central cornea and 500 close to the limbus. This hierarchical organization of collagen is crucial to the biophysical and mechanical properties of the cornea.

Qualitative observations on the variation of collagen architecture through the depth of the human corneal stroma have been documented for over 100 years [2]. Kokott studied the organization of collagen bundles in human cornea and sclera by tearing their fibrils apart [3] and concluded that the lamellae had an orthogonal arrangement in the central cornea and extended without interruption from limbus to limbus, with a circular arrangement at the limbus itself. Earlier X-ray diffraction studies showed that about 49% of the stromal lamellae are preferentially aligned orthogonally, along the vertical and horizontal meridians [4]. Advanced imaging techniques, such as optical coherence tomography (OCT) and the second-harmonic generation imaging (SHG, a particular type of non-linear optical microscopy), have now provided new insights on the in-depth organization of the stromal collagen. Although such techniques are not yet applicable in-vivo to produce reliable patient-specific models, the recent findings may be of relevance in the optical and mechanical behavior of the cornea, and the actual architecture of the collagen should be considered in a numerical model with predictive ambitions.

The importance of the stromal microstructure has been acknowledged in several numerical models of the anterior chamber of the eye built with the aim of estimating the mechanical properties of the cornea or supporting surgical interventions [5, 6]. Indeed, the opportunity of recreating the exact microstructural and morphological features of the cornea is recognized in advanced model of artificial engineered tissues planned to be used in corneal transplants [7].

Aim of this study is to introduce the multiple features of the collagen architecture that OCT and SHG have revealed into an advanced numerical model of the cornea, and to ascertain the relevance of such microstructures on the mechanical response of the anterior chamber through the simulation of in-vivo static and dynamic tests.

2 Advanced Insights in Collagen Architecture of the Human Cornea

The basic principles of corneal structure and transparency have been known for some time, but in recent years X-ray scattering and other methods have revealed that the details of this structure are far more complex than previously thought and that the intricacy of the arrangement of the collagenous lamellae provides the shape and the mechanical properties of the tissue. Light microscopy was sufficient to discover more interweaving of lamellae in the anterior layers than the posterior, characterized by thinner lamellae that weave in and out of each other with orientations that are inclined relative to the corneal surface. The development of modern imaging techniques has led to improved quantification of lamellar size and organization.

The hypothesized structure hand drawn by Kokott [3] included the presence of superior–inferior (SI) and nasal–temporal (NT) preferred directions at the center of the cornea and circumferential directions at the limbus. With X-ray diffraction experiments, Meek et al. [8] first quantified the orientation of lamellae as viewed in the plane perpendicular to the optical axis. Scanning electron microscopy (SEM) and transmission electron microscopy (TEM) measurements demonstrated that posterior lamellae are one order wider and twice as thick as anterior lamellae [9]. SEM imaging was used to show how lamellae branch and interweave, and to quantify the in-plane angles between adjacent lamellae [10]. The raw X-ray data provide scattering intensities versus orientation on a discrete grid of points over the cornea surface corresponding to the experimental measurement procedure, but do not provide information about scattering variations with depth. X-ray diffraction combined with electron microscopy have shown that collagen lamellae in the posterior cornea are generally twice as thick as those in the anterior [9, 11]. Later studies proved the presence of aligned collagen running between adjacent cardinal points forming chords across the outer cornea [12]. These additional lamellae have been supposed to contribute to peripheral corneal flattening and seem to occur only in the posterior third of the cornea.

The regional differences in lamellar orientation across and throughout the thickness of the normal human cornea were analyzed in [13]. Collagen in the central 8 mm shows a strong orthogonal alignment, along the SI and NT directions, but only in deeper stromal regions. The average percentage of total fibers exhibiting the well-known preferred azimuthal directions was 42% in the posterior third thickness, but only 22% in the anterior third. This increase in alignment toward the posterior is quite interesting because it is in clear contrast with the trend of more inclined fibers toward the anterior. Another aspect of lamellar organization believed to be of mechanical importance is the interlamellar interaction as a result of interweaving [14]. Interlamellar sliding may be important for describing changes of the mechanical behavior with aging and the development of pathological situations such as keratoconus and ectasia after surgical intervention.

In the attempt of characterizing the elastic properties of the stromal tissue, Petsche et al. [15] found that the shear modulus is two to three orders of magnitude inferior to the tensile moduli, commonly measured and reported in the literature. They observed that the transverse shear stiffness of the cornea varies with the depth, and the shear stiffness of the anterior cornea is almost one order of magnitude greater than that of the posterior cornea. It was hypothesized that the inclination of lamellae in the anterior cornea and the decreasing degree of inclination with depth must be responsible for the measured depth dependent transverse shear properties, because the density of the collagen does not vary markedly with depth.

The well-documented limbal collagen annulus circumscribing the human cornea is located in the posterior third of the limbus thickness, according to the observations documented in [13], while the arrangement becomes less unidirectional in proximity to the anterior surface of the cornea. In addition to the contribution from the

dominant direction of fibril alignment, the different mechanical properties of the peripheral cornea and limbus with respect to the central tissue are influenced by the increment in both the size of the collagen fibrils and the number of lamellae [16].

Electron microscopy and X-ray scattering patterns obtained by using synchrotron radiation source have provided very important information about the anisotropic arrangements of collagen lamellae through the whole stroma in different regions of the cornea. Nevertheless, both techniques require tissue fixation preventing any in-vivo mechanical assays. More recently, SHG microscopy has proven to be an efficient tool for obtaining *virtual biopsies* in unstained fresh corneas, and introduce the viability of constructing patient-specific models.

To date, patient-specific models of the collagen architecture of the human cornea are not available and are not used directly in clinical applications, although advanced models that account for the details of the corneal collagen architecture have been around for a while [5, 6, 17–25]. Several investigations have pointed out that any material point within the cornea will have a unique lamellar orientation distribution; precise symmetry in the distributions over corneal quadrants is not observed in general, and realistic modeling cannot assume such symmetry. This is true especially when distributions associated with pathological conditions are modelled. Petsche and Pinsky [26] introduced a corneal model where the collagen orientation was taken directly from X-ray diffraction measurements on a single, full thickness, cornea. Incorporating the X-ray diffraction data describes the anisotropy resulting from the well documented SI and NT preferred directions of lamellae in the vicinity of the corneal vertex as well as the circumferentially preferred orientations at the limbus. The model in [26] included 3D lamella orientations and inclinations in the view to explain the depth-dependent shear stiffness properties and to fully characterize the mechanics of inclined lamellae. A microstructural model proposed in Studer et al. [27] first accounted for some interlamellar effects by including, in their formulation, ad hoc cross-link fibers perpendicular to the lamellar directions but without depth dependence.

Beside exhaustive information on the geometry of eye and on the microstructure of the stroma [28], a patient-specific numerical model of the cornea requires the realistic characterization of the mechanical properties of the materials [29]. Mechanical properties cannot be simply determined through optical imaging, but it is necessary to setup a protocol of in-vivo static and dynamic tests, thought and carried on in a concerted manner, to allow the identification of the material model. Tests must be combined with identification procedures based on inverse analysis, that, simulating the experimental tests, will provide the best estimate of the sought material properties.

An important question emerging in the definition of a numerical model of the cornea—a model obviously predictive in the view of applications in surgical practice—concerns the ability of a mechanical test to spring out the micromechanical characteristics of the cornea. In spite of several studies recently published, the mechanical consequences of specific collagen architectures have not been investigated sufficiently in the literature, especially in terms of overall configurations; in general only global averaged quantities are provided. Often, comparisons with in-

vivo experiments have been limited to a component of displacement, or a displacement profile [30, 31]; with a few exceptions [20, 32], no documentation of the stress level observed in the numerical simulations is reported, thus a comparison between the performance of different models is hardly possible.

In the following, we present a numerical study conducted with the aim of comparing the mechanical response of different collagen architectures in a model of human cornea undergoing in-vivo static and dynamic tests. For the sake of simplicity, we use a model of the cornea that we have been developing in-house, and consider a patient-specific geometry acquired with a corneal topographer and already used in previous studies [28, 31, 33].

3 Material and Methods

The finite element method has been widely used for modeling the behavior of the cornea, under static and dynamic conditions [6, 17, 19, 21–23, 25]. In the last decade we have been developing an ad-hoc finite element code [6, 20, 28, 32, 34] with the following distinguished features: (i) patient-specific geometries directly derived from corneal topographies; (ii) stochastic fiber distributed material models, to describe the complex architecture of reinforcing collagen fibrils in the stromal tissue; (iii) automatic identification of the stress-free configuration of the cornea; (iv) customization of the main material parameters of the cornea on the basis of diagnostic measurements.

3.1 Geometrical and Material Model

Patient-specific geometries of the cornea, constructed using an ad hoc software from sets of anterior and posterior corneal surface coordinates supplied by ocular topographer (Sirius, CSO, Italy) [28], are automatically discretized at the desired level of refinement in standard finite elements, e.g., 8-node bricks with linear interpolation of the displacements, see Fig. 1. The knowledge of the physiologic geometry of the cornea is not sufficient to create a patient-specific numerical model. The topographer images refer to the cornea reacting to the intraocular pressure (IOP) exerted by the filling gels. A correct stress analysis requires the recovery of the stress-free configuration, corresponding to a null IOP. The automatic procedure that allows for the recovery of the stress-free configuration is described in [28].

Necessarily, the model has several limitations. It accounts only for the main central layer (stroma) of the cornea and disregards the thin anterior and posterior membranes, known to provide negligible contributions to the mechanical stiffness of the cornea. The geometrical model does not include the adjacent biological tissues, i.e., the white sclera and the iris, which are accounted for in terms of compliant boundaries at the limbus [32]. Adjacent tissues are not included because of the lack of

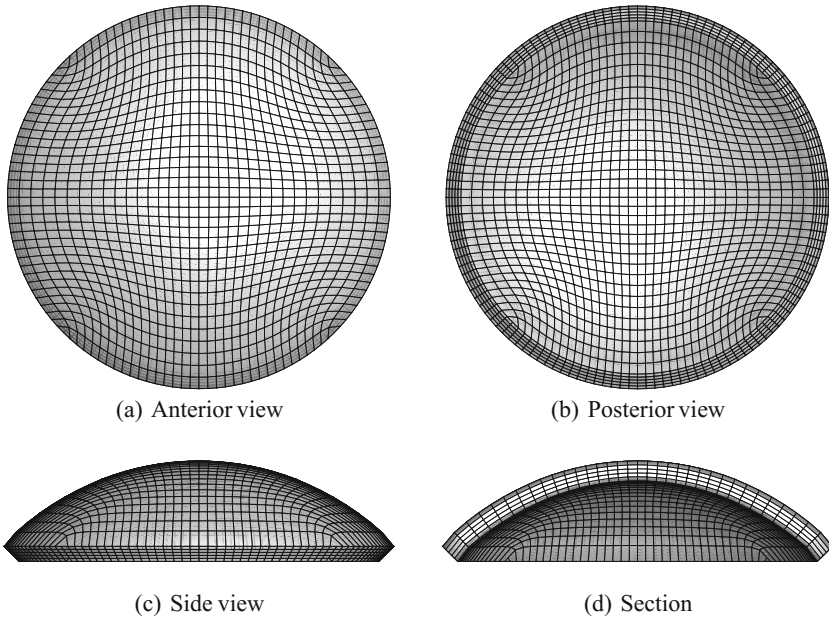


Fig. 1 Patient specific finite element model of the cornea. The mesh comprises 7,350 nodes and 5,780 8-node elements. The geometry refers to the stress-free configuration of a corneal topography already used in previous studies [28], with a finer finite element discretization

knowledge of their in-vivo mechanical characteristics, to avoid uncertainties larger than the ones introduced by the exclusion of such parts. As explained in [20], a reasonable choice of the cornea boundary conditions narrows the effects of these deficiencies. Finally, the model does not account explicitly for the interaction between the deformable cornea and the ocular fluid (aqueous humor) filling the anterior chamber. Fluids may play a role in a dynamic test, because they interact with the posterior surface of the moving cornea. While we are currently developing a numerical algorithm of fluid-solid interaction to analyze the problem with more accuracy [35], we account here for the presence of the fluid in a simplified way, by adding extra masses to the posterior nodes of the discretized cornea, cf. [33].

The material model adopted for the stroma is hyperelastic and anisotropic, accounting for statistically distributed sets of collagen fibrils with a second order approximation, and able to switch from fully 3D [36] to planar [37] von Mises type distributions of the orientation of the fibrils, described by a coefficient b . In keeping with approaches typically adopted in the modelling of biomaterials, the behavior of the proteoglycan matrix and of the reinforcing collagen fibrils is modeled separately. Thus, the strain energy density function Ψ is assumed to be the sum of three independent contributions with full separation of the arguments:

$$\Psi = \Psi_{\text{vol}}(J) + \Psi_{\text{iso}}(\bar{I}_1, \bar{I}_2) + \Psi_{\text{aniso}}(I_{4M}^*). \quad (1)$$

The term Ψ_{vol} accounts for the volumetric elastic response and depends on the Jacobian $J = \det \mathbf{F}$, where $\mathbf{F} = \partial \mathbf{x} / \partial \mathbf{X}$ is the deformation gradient. Ψ_{vol} is regarded as a penalty term to enforce the incompressibility constraint and has the operative form

$$\Psi_{\text{vol}}(J) = \frac{1}{4} K (J^2 - 1 - 2 \log J), \quad (2)$$

where K is a stiffness coefficient related to the bulk modulus. The term Ψ_{iso} describes the behavior of the isotropic components of the material, and depends on the first and second invariants, \bar{I}_1 and \bar{I}_2 (see Appendix) of the isochoric Cauchy-Green deformation tensor $\bar{\mathbf{C}} = \bar{\mathbf{F}}^T \bar{\mathbf{F}}$, with $\bar{\mathbf{F}} = J^{-1/3} \mathbf{F}$, according to Mooney-Rivlin's model

$$\Psi_{\text{iso}}(\bar{I}_1, \bar{I}_2) = \frac{1}{2} \mu_1 (\bar{I}_1 - 3) + \frac{1}{2} \mu_2 (\bar{I}_2 - 3), \quad (3)$$

where $\mu = \mu_1 + \mu_2$ is the shear modulus of the material. The term Ψ_{aniso} addresses the anisotropic contribution of two statistically dispersed families of collagen fibrils. The M fibril family is defined in terms of a unit vector field, $\mathbf{a}_M(\mathbf{x})$, that identifies the dominant orientation of the fibrils, and by a dispersion coefficient $b(\mathbf{x})$, cf. [32]. The anisotropic strain energy function Ψ_{aniso} used in the model is

$$\Psi_{\text{aniso}}(I_{4M}^*, K_M^*) = \sum_{M=1}^2 \frac{k_1}{2k_2} \exp \left[k_2 (I_{4M}^* - 1)^2 \right] \left(1 + K_M^* \sigma_{I_{4M}^*}^2 \right), \quad (4)$$

where k_1 is a stiffness parameter for fibrils in moderate extension, and k_2 is a dimensionless rigidity parameter that describes the behavior of fibrils in large extension. The expression of the variables I_{4M}^* and K_M^* in Eq. (4), that describes the dispersion of the fibrils in both 3D and planar distribution, is reported in Appendix. The material model is characterized by five parameters: the bulk modulus K , two shear moduli μ_1 and μ_2 for the Mooney-Rivlin model, the fibril stiffness k_1 , and the fibril rigidity k_2 . The set of elastic material properties calibrated for the patient group in [28] is used also in the present study, see Table 1.

Here we restrict our attention to the collagen architecture of the cornea and to the way the different features recently pointed out by the research in the field are affecting the mechanical response of the cornea. The simulations illustrated here make use of a reference model (baseline) for the internal structure of the collagen fiber distribution, describing an architecture of the fibrils which is in line with X-ray imaging on ex-vivo corneas [12, 38], presenting different levels of the dispersion parameter $b(\mathbf{x})$ in different locations of the cornea. Fibrils are strongly aligned at the center, where they follow an orthogonal organization in the NT and SI directions; at the periphery fibrils are mostly aligned to the limbus circumference, see Fig. 2, cf. [28, 32]. In the baseline model, a fully 3D dispersion model of the fibrils is considered, with no variations across the thickness.

Table 1 Material parameters used in the present study, cf. [28]

Model	K [MPa]	μ_1 [MPa]	μ_2 [MPa]	k_1 [MPa]	k_2	b	ρ [kg/m ³]
Baseline	5.5	0.06	-0.01	0.04	200	0.2–2.8 (in plane)	1,062
ST	5.5	0.06	-0.01	0.0091–0.091	36–360	0.2–2.8 (in plane)	1,062
SL	5.5	0.06	-0.01	0.0091–0.091	36–360	0.2–2.8 (in plane)	1,062
DT	5.5	0.06	-0.01	0.04	200	0.2–2.8 (thickness)	1,062

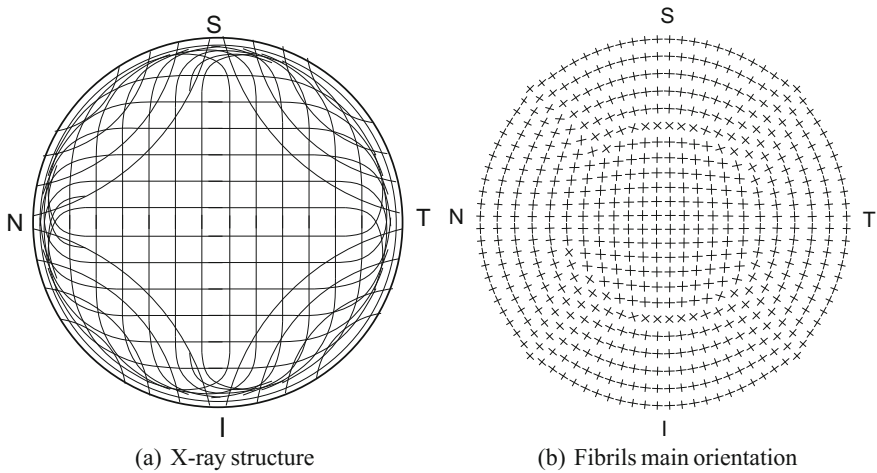


Fig. 2 **a** Structure of the fibril organization within the cornea, cf. [12, 38]. S denotes the superior point, I the inferior point, N the nasal point and T the temporal point. **b** Main orientation of the fibrils assumed in the numerical model. In the central region, the two sets of fibrils have an equivalent stiffness. In the limbal region, the two sets of fibers may have a different stiffness

In the numerical models considered in this comparative study, we preserve the orientation of the fibrils described in Fig. 2b, but include variations in the dispersion and in the stiffness of the two sets of fibers, in order to incorporate more recent findings and to evaluate their relevance on the global mechanical response of the cornea. We consider the following three alternative models:

1. Model ST. Variation of the stiffness across the thickness. The stiffness of the fibrils in the anterior stroma is set 10 times larger than the stiffness of the fibrils of the posterior stroma, according to the experimental observation reported in [15].
2. Model SL. Variation of the stiffness and of the dispersion of the fibrils at limbus. The dispersion of the fibrils at the limbus is varied from $b = 0.2$ on the anterior

surface to $b = 2.8$ in the posterior surface. Moreover, the stiffness parameters of the fibrils running circumferentially in the deepest one third of the limbal thickness are set 10 times larger than the stiffness parameters of the fibrils oriented radially, to follow the observation reported in [13].

3. Model DT. Variation of the dispersion of the fibrils across the thickness. We use a fully 3D von Mises dispersion model, assigning different values of the dispersion coefficient from the anterior ($b_{\min} = 0.2$) to the posterior ($b_{\max} = 2.8$) surface, as a simplified trial to reflect the indication reported in [39].

The range of the parameters used in the four model for the numerical analyses are listed in Table 1.

3.2 Static and Dynamic Analysis

In the view of future clinical applications, the comparison between the four different models is achieved through the simulation of two in-vivo mechanical contact and contactless tests. Mechanical tests induce an important deformation localized at the center of the cornea, without damaging its delicate tissues. Simulations require to conduct an initial static analysis, to attain a stress state corresponding to the condition of the cornea under the action of the physiological IOP, which in this calculation is set $16 \text{ mmHg} = 2.13 \text{ kPa}$. The boundary conditions imposed to the nodes at the limbus allow for the rotation of the cornea about the limbus circumference, optimizing the difference between the current model and a model that includes limbus and sclera, see [20].

Once the physiological state has been reached, the static or dynamic test begins. For the static test, we model the action of an optomechanical testing device [40] which applies a mechanical probe at the corneal apex. The loading procedure consists in advancing the mechanical probe in six steps of $100 \mu\text{m}$ into the cornea. The probe is a 0.5 mm diameter cylindrical indenter with a hemispherical tip [15]. Static analysis are conducted with an explicit solver.

For the dynamic test, we model the action of a contactless ocular tonometer (CorVis ST) that induces a motion of the cornea with a localized air jet. The sudden pulse exerted by the instrument causes the inwards motion of the cornea, which passes through an applanation, and successively snaps into a slight concavity. When the air pulse pressure decreases, the elastic corneal tissue recovers the original configuration, passing through a second applanation. Although the actual space and time profile of the air jet pressure and its maximum value are not provided by the instrument, the imprint of the air jet on the anterior corneal surface has been estimated, through preliminary parametric analyses, using an analytical expression [31]. The air jet pressure is applied over a 1.5 mm radius circular area centered at the apex of the cornea. The pressure has the functional form

$$p(t, r) = p_0 \exp \left[-64 \left(\frac{t}{T} - \frac{1}{4} \right)^2 \right] \exp(-0.44r^2) \quad (5)$$

where $p_0 = 40$ kPa is the maximum air jet pressure, $T/2 = 20$ ms the duration of the air jet, and r the distance in mm from the center of the jet of a point on the corneal surface, cf. [31]. Note that the dynamical test is not correctly modelled, since the presence of the fluids filling the anterior chamber of the eye has been disregarded for the sake of simplicity. Since the effect of the fluid-structure interaction is not accounted for, the analysis is not able to describe the final part of the test, where a delay in the motion of the cornea is observed due to the presence of the fluid. As already mentioned, this issue is currently tackled in a parallel work [35]. The dynamical analysis is conducted with a central difference time stepping algorithm.

Prior to conduct the numerical tests, the stress-free configuration for the four models case has been identified through the iterative procedure described in [32]. The stress-free geometry has been used subsequently for the quasistatic and dynamic analysis.

Before conducting the simulation of the two in-vivo mechanical tests, we simulated an ideal inflation test, where the cornea is loaded with a growing IOP from 0 to 40 mmHg.

4 Results

Figure 3 shows the results of the ideal inflation test for the four models, in terms of IOP versus the displacement of the cornea apex. The curves superpose well to the baseline curve up to the physiological IOP (16 mmHg), revealing a maximum

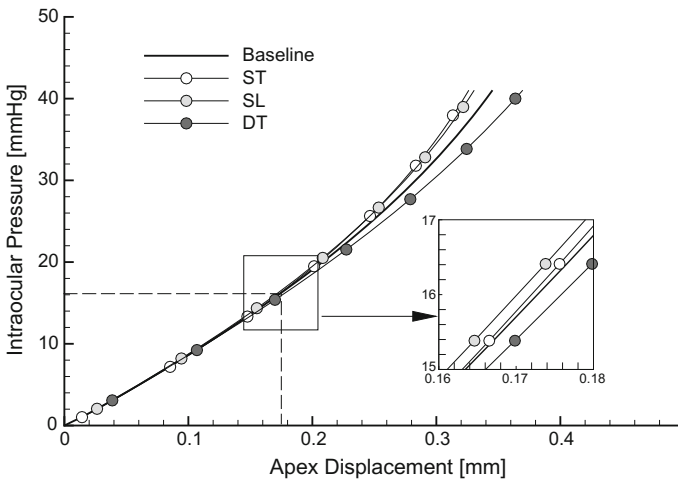


Fig. 3 Inflation test. Force applied to the probe versus apex displacement. The *thick line* represents the response of the reference model

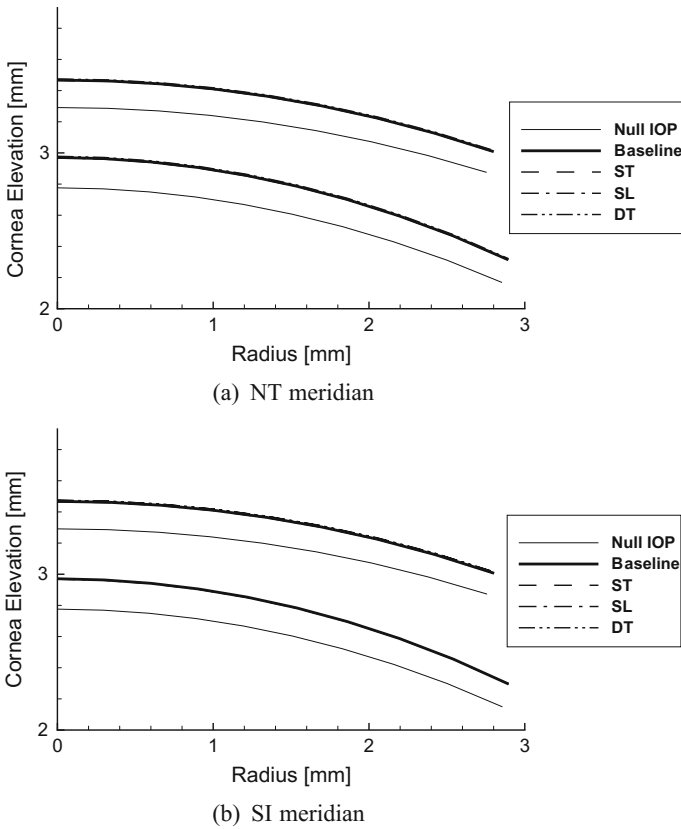
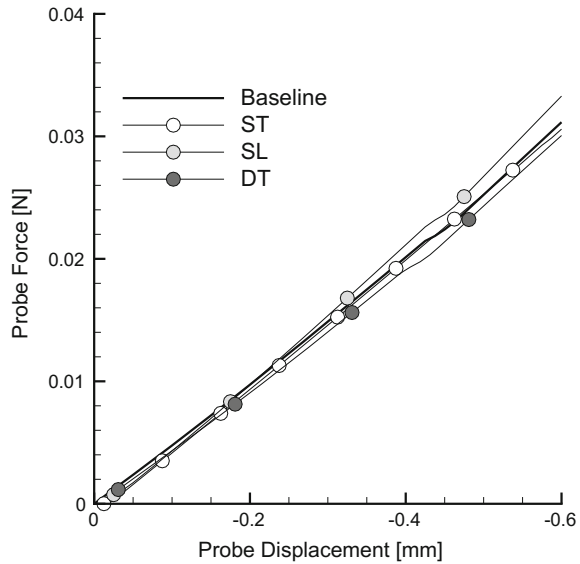


Fig. 4 Inflation test. Comparison of the anterior and posterior profiles of the cornea at the physiological IOP, along the **a** Nasal-Temporal meridian (from center to Temporal side); **b** Superior-Inferior meridian (from the center of the cornea to the superior edge). *Thin lines* denote the posterior and anterior surfaces of the cornea at zero IOP

relative displacement less than $2 \mu\text{m}$. The similarity of the response is further highlighted in Fig. 4, where the numerically computed corneal profiles along the NT and SI meridians are compared. Differences between the geometrical configurations associated to the four models cannot be appreciated. However, at higher IOP the four curves show marked differences, and are characterized by a stiffer response (ST and SL models) or a more compliant response (DT model) with respect to the baseline model, see Fig. 3.

The results of the simulations of quasistatic contact tests are shown in Figs. 5 and 6. Figure 5 compares the global mechanical response of the four models in terms of probe force versus probe displacement, which corresponds to the displacement of the corneal apex. In the whole range of the imposed displacements, the curves corresponding to the DT and SL models show a small deviation from the curve of the baseline model. In particular, the DT model reveals a more compliant behavior,

Fig. 5 Probe test. Cornea profiles at the maximum displacement of the probe, corresponding to an indentation of the cornea of 0.6 mm. The *dashed curves* represent the anterior and posterior surface of the cornea at the physiological IOP



requiring a smaller force to reach the final displacement of the probe. Contrariwise, the SL model is characterized by a stiffer behavior, with a larger force exerted by the probe. The ST model, instead, does not show marked differences with respect to the baseline model. The small differences in the mechanical response to the probe action can be appreciated in Fig. 6, where the corneal profiles along the NT and SI meridian obtained for the four models are visualized. The more compliant behavior of the DT model leads to an enhanced deformation in the peripheral zone at 2 mm from the corneal center; while the stiffer model SL shows a less marked deformation in the same area.

The results of the simulations of dynamic contactless tests are visualized in Figs. 7 and 8. Figure 7 compares the response of the four models considering the displacement of the corneal apex. Figure 7a shows the time history of the apex displacement for the four models. Figure 7b shows the mechanical response of the four models in terms of air jet pressure versus apex displacement. Unlike the other tests previously discussed, dynamical tests highlight differences between the models. Figure 8 compares the configuration of the four models in correspondence to the maximum value of the applied air jet pressure. Note that the maximum displacement is reached at different times for the four models. The DT model is confirmed as the most compliant, showing a larger displacement at all times, while SL model confirms the stiffer behavior already shown in the other tests. The ST model, instead, behaves closely to the baseline model.

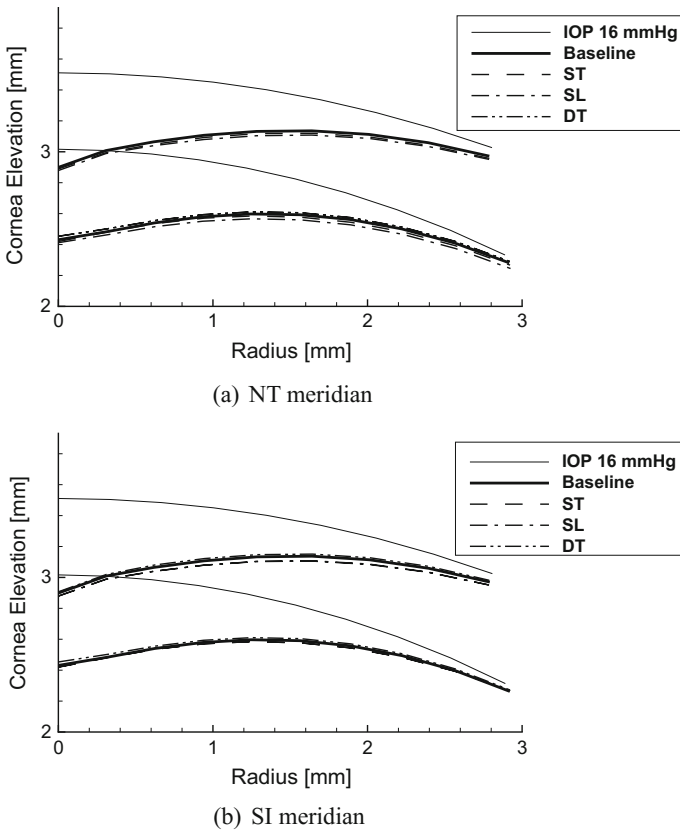


Fig. 6 Probe test. Cornea profiles at the maximum displacement of the probe, corresponding to an indentation of the cornea of 0.6 mm. The *two thin lines* describe the anterior and posterior surfaces of the cornea at the physiological IOP

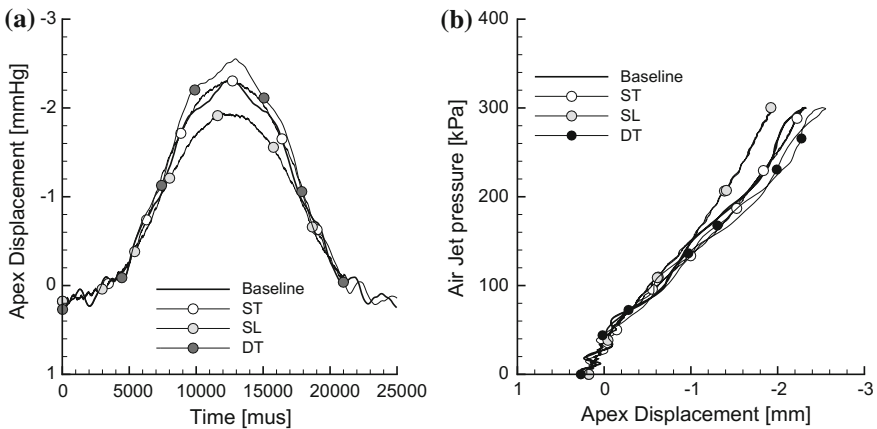


Fig. 7 Dynamic contactless test. **a** Cornea apex displacement time history. **b** Air jet pressure versus apex displacement curve. The *thick line* denotes the reference model

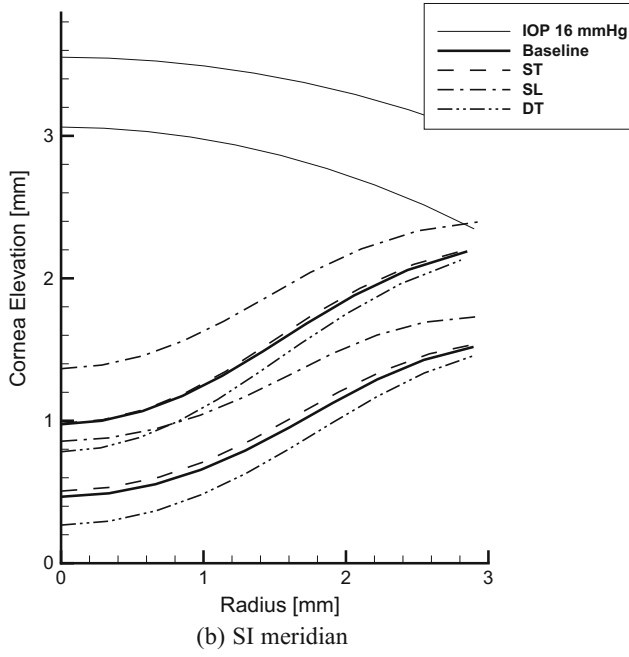
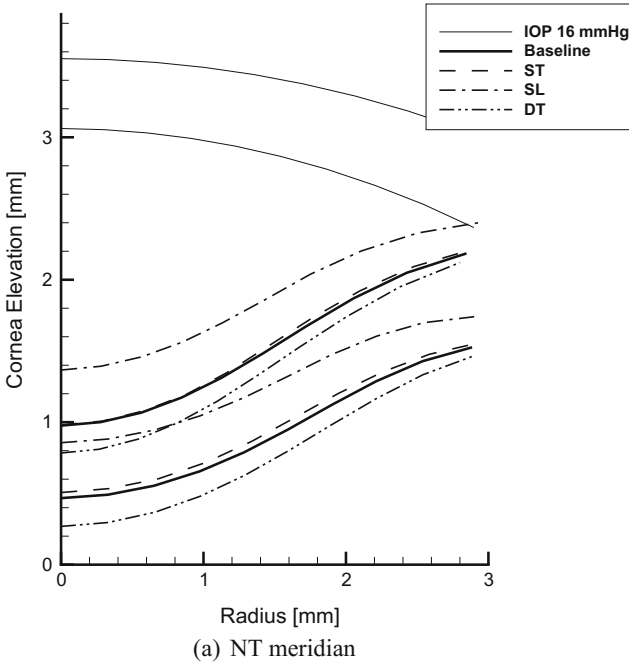


Fig. 8 Dynamic contactless test. Comparison of the cornea profiles at the maximum value of the air jet for the four models. The *two thin line curves* represent the anterior and posterior surfaces of the cornea at the physiological IOP

5 Discussion and Conclusions

The description of the collagen architecture of the stroma in numerical models that are used to predict the biomechanical behavior of the human cornea has been object of a vibrant discussion in the last years. Modern diagnostic technologies and advanced optical instruments have provided accurate information about the organization of the collagen within the stroma thickness, although a definite physical or chemical motivation of such peculiar structure has not been found yet. Recent contributions in the literature have been presenting models of the human cornea that account for the variability of the collagen structure and distribution, see, e.g. [6, 28, 31–33, 41–45].

It is a commonly well accepted and acknowledged opinion that any predictive numerical model of the cornea, to be used to anticipate the outcomes of refractive surgery, must be personalized to the particular patient under consideration. This requires the identification of geometrical and material properties of the cornea by means of inverse procedures that compare the results of in-vivo tests with the outcomes of numerical simulations. However, given the nonlinearity of the models and the large kinematics involved in the tests, the identification procedures provide different values to the mechanical parameters of the cornea, according to the different material model adopted, see, e.g., [20]. The selection of the most appropriate material model, however, is not sufficient to ascertain the correct value of the material properties, because results may vary according to the model chosen to describe the underlining collagen structure of the stroma.

For a particular advanced hyperelastic, anisotropic, fiber dispersed based material model, here we study the response of a cornea model where the collagen microstructure within the stroma is assumed to vary in different manners across the thickness and at different locations of the surface. We refer to an advanced model of the human cornea used in recent works [28, 31, 32], evolution of the original model developed in [6, 34], and consider three variants, to account for the variability of the stiffness of the stroma across the thickness (ST model) or in proximity of the limbus (SL model), and for the different level of dispersion of the collagen across the thickness (DT model).

We begin by comparing the behavior of the four models considering an ideal inflation tests, where the cornea undergoes the action of a growing IOP. The inflation test is the most common simulation conducted in order to compare different material models, but this simple loading condition is not able to point out at all the differences between the models at the physiological IOP level, see Figs. 3 and 4. Moreover, the inflation test is all non-natural, it cannot be performed in-vivo, and thus cannot be used to characterize the mechanical properties of the cornea.

Next, we simulate a quasistatic mechanical test where a rigid probe, moved in small steps, indents the center of the cornea. Such a test, although not yet used routinely in clinical investigations, can be effectively used for the calibration of the material model of the cornea. The results of the probe test are able to visualize the differences between the four models. Numerical results seem to exclude

appreciable differences in the mechanical behavior between the baseline model and the SL model; while the ST and DT models present some difference in the displacement field.

Finally, we simulate the dynamical air puff test, commonly used in the modern clinical practice. The air jet acts at the center of the cornea for a very short time, and causes the inward deflection of the cornea in the central region. The mechanical response of the cornea models is visualized in Figs. 7 and 8. The apex experiences the larger displacements during the test, thus the plots in Fig. 7 clarify sufficiently the difference between the four models. The DT and ST models confirm their higher compliance and higher stiffness, respectively, while the SL model maintains a strong resemblance with the baseline model. The maximum deflected configurations of the four models are compared in Fig. 8. The differences between the SL model and the baseline model appear only in the profile plots, and, interestingly, involve mainly the posterior surface of the cornea.

In considering the results presented here, it is clear that simple inflation tests are not able to provide sufficient information about the material parameters that characterize the collagen structure of the cornea. In fact, the particular structure of the collagen is not activated by the test and the mechanical characterization of the parameters may lead to several sets of values. Contrariwise, in-vivo contact and contactless tests are able to activate (although in a non-natural manner) the particular internal structure of the reinforcing collagen, therefore they might be used to characterize a specific material model. Moreover, between the quasistatic and the dynamic tests, the air puff tests seems to be superior, in the sense that the amplitude of the induced displacements in the cornea might be easier to be measured through optical imaging.

According to the present study, it appears that the relevance of the collagen organization at the limbus is not very important in terms of mechanical response of the corneal shell. In fact, among the four models, the SL model is the closest to the baseline model in all the numerical simulations. This observation suggests that the main biomechanical features of the cornea derive from the structure of the collagen in the optical zone.

The present research has a few drawbacks that we are trying to remove in concurrent studies. The most important drawback, that affects only the dynamical tests, is the absence of the filling fluids, which indeed play an important role in the mechanical response of the system. We are presently developing a coupled fluid-structure interaction approach, based on meshfree discretization of the fluid domain, to tackle this issue [35]. A second drawback is the missing comparison of the stress fields between the different models. The complexity of the stress fields induced by the contact and contactless tests requires a heavy manipulation of the numerical results, that are object of an additional current study.

Appendix

The first and second invariant of the isochoric Cauchy-Green deformation tensor are defined as

$$\bar{I}_1 = \text{tr } \bar{\mathbf{C}}, \quad \bar{I}_2 = \frac{1}{2} \left[(\text{tr } \bar{\mathbf{C}})^2 - \text{tr}(\bar{\mathbf{C}}^2) \right]. \quad (6)$$

The two pseudo-invariants \bar{I}_{4M}^* , $M = 1, 2$ are defined as

$$I_{4M}^* = \mathbf{H}_M : \mathbf{C}. \quad (7)$$

The structure tensor \mathbf{H}_M is defined as

$$\mathbf{H}_M = \kappa_M \mathbf{I} + (1 - 3\kappa_M) \mathbf{A}_M, \quad \mathbf{A}_M = \mathbf{a}_M \otimes \mathbf{a}_M, \quad (8)$$

\mathbf{I} being the identity tensor. The scalar parameter κ_M depends of the chosen spatial distribution of the fibrils orientation $b_M(\mathbf{x})$. For 3D distributions characterized by rotational symmetry it holds [36]

$$\kappa_M = \frac{1}{4} \int_0^\pi \rho_M(\Theta) \sin^3 \Theta d\Theta, \quad (9)$$

while for planar π -periodic distributions it holds [37]

$$\kappa_M^{\text{pl}} = \frac{1}{\pi} \int_{-\pi/2}^{\pi/2} \rho(\Theta) \sin^2 \Theta d\Theta. \quad (10)$$

The two terms

$$K_M^* = k_{2M} + 2k_{2M}^2 (I_{4M}^* - 1)^2 \quad (11)$$

and

$$\sigma_{I_{4M}^*}^2 / = \mathbf{C} : \langle \mathbf{A}_M \otimes \mathbf{A}_M \rangle : \mathbf{C} - (\mathbf{H}_M : \mathbf{C})^2, \quad (12)$$

are introduced to include the variance of the fibril orientation distribution in the material model, see [36].

References

1. A.J. Bron, The architecture of the corneal stroma. *Br. J. Ophthalmol.* **85**(4), 379–381 (2001)
2. M. Salzmann, in *The Anatomy and Histology of the Human Eyeball in the Normal State, its Development and Senescence*, (University of Chicago Press, 1912)
3. W. Kokott, über mechanisch-funktionelle strukturen des auges. *Albrecht von Graves Archiv für Ophthalmologie* **138**(4), 424–485 (1938)

4. A. Daxer, P. Pratzl, Collagen fibril orientation in the human corneal stroma and its implication in keratoconus. *Investig. Ophthalmol. Vis. Sci.* **38**, 121–129 (1997)
5. P.M. Pinsky, D. van der Heide, D. Chernyak, Computational modeling of mechanical anisotropy in the cornea and sclera. *J. Cataract Refract. Surg.* **31**(1), 136–145 (2005)
6. A. Pandolfi, F. Manganiello, A material model for the human cornea. Constitutive behavior and numerical analysis. *Biomech. Model. Mechanobiol.* **5**, 237–246 (2006)
7. C.J. Connon, Approaches to corneal tissue engineering: top-down or bottom-up? **110**, 15–20 (2015)
8. K.M. Meek, T. Blamires, G.F. Elliot, T.J. Gyi, C. Nave, The organization of collagen fibrils in the human corneal stroma: a synchrotron x-ray diffraction study. *Curr. Eye Res.* **6**, 841–846 (1987)
9. Y. Komai, T. Ushiki, The three-dimensional organization of collagen fibrils in the human cornea and sclera. *Investig. Ophthalmol. Vis. Sci.* **32**(8), 2244 (1991)
10. W. Radner, M. Zehetmayer, R. Aufreiter, R. Mallinger, Interlacing and cross-angle distribution of collagen lamellae in the human cornea. *Cornea* **17**(5), 537–543 (1998)
11. A.J. Quantock, C. Boote, R.D. Young, S. Hayes, H. Tanioka, S. Kawasaki, N. Ohta, T. Iida, N. Yagi, S. Kinoshita, K.M. Meek, Small-angle fibre diffraction studies of corneal matrix structure: a depth-profiled investigation of the human eye-bank cornea. *J. Appl. Crystallogr.* **40**(SUPPL.1), s335–s340 (2007)
12. H. Aghamohammadzadeh, R.H. Newton, K.M. Meek, X-ray scattering used to map the preferred collagen orientation in the human cornea and limbus. *Structure* **12**(2), 249–256 (2004)
13. M. Abahussin, S. Hayes, N.E.K. Cartwright, C.S. Kamma-Lorger, Y. Khan, J. Marshall, K.M. Meek, 3d collagen orientation study of the human cornea using x-ray diffraction and femtosecond laser technology. *Investig. Ophthalmol. Vis. Sci.* **50**(11), 5159–5164 (2009)
14. G. Wollensak, E. Sprl, C. Mazzotta, T. Kalinski, S. Sel, Interlamellar cohesion after corneal crosslinking using riboflavin and ultraviolet a light. *Br. J. Ophthalmol.* **95**(6), 876–880 (2011)
15. S.J. Petsche, D. Chernyak, J. Martiz, M.E. Levenston, P.M. Pinsky, Depth-dependent transverse shear properties of the human corneal stroma. *Investig. Ophthalmol. Vis. Sci.* **53**(2), 873 (2012)
16. C.S. Kamma-Lorger, C. Boote, S. Hayes, J. Moger, M. Burghammer, C. Knupp, A.J. Quantock, T. Sorensen, E. Di Cola, N. White, R.D. Young, K.M. Meek, Collagen and mature elastic fibre organisation as a function of depth in the human cornea and limbus. *J. Struct. Biol.* **169**(3), 424–430 (2010)
17. P.M. Pinsky, D. van Der Heide, D. Chernyak, Computational modeling of mechanical anisotropy in the cornea and sclera. *J. Cataract Refract. Surg.* **31**(1), 136–145 (2005)
18. D. Cabrera Fernández, A.M. Niazi, R.M. Kurtz, J.P. Djotyan, T. Juhasz, Finite element analysis applied to cornea reshaping. *J. Biomed. Opt.* **10**(6), 064018 (2005)
19. V. Alastrué, B. Calvo, E. Peña, M. Doblaré, Biomechanical modeling of refractive corneal surgery. *J. Biomech. Eng.* **128**, 150–160 (2006)
20. A. Pandolfi, G.A. Holzapfel, Three-dimensional modelling and computational analysis of the human cornea considering distributed collagen fiber orientation. *J. Biomech. Eng.* **130**, 061006 (2008)
21. E. Lanchares, B. Calvo, J.A. Cristbal, M. Doblar, Finite element simulation of arcuates for astigmatism correction. *J. Biomech.* **41**(4), 797–805 (2008)
22. A. Elsheikh, Finite element modeling of corneal biomechanical behavior. *J. Refract. Surg.* **26**(4), 289–300 (2010)
23. R. Grytz, G. Meschke, A computational remodeling approach to predict the physiological architecture of the collagen fibril network in corneo-scleral shells. *Biomech. Model. Mechanobiol.* **9**(2), 225–235 (2010)
24. A.S. Roy, W.J. Dupps, Patient-specific modeling of corneal refractive surgery outcomes and inverse estimation of elastic property changes. *J. Biomech. Eng.* **133**(1) (2010)
25. A.S. Roy, W.J. Dupps Jr., Patient-specific computational modeling of keratoconus progression and differential responses to collagen cross-linking. *Investig. Ophthalmol. Vis. Sci.* **52**(12), 9174–9187 (2011)

26. S.J. Petsche, P.M. Pinsky, The role of 3d collagen organization in stromal elasticity: a model based on x-ray diffraction data and second harmonic-generated images. *Biomech. Model. Mechanobiol.* **12**(6), 1101–1113 (2013)
27. H. Studer, X. Larrea, H. Riedwyl, P. Bchler, Biomechanical model of human cornea based on stromal microstructure. *J. Biomech.* **43**(5), 836–842 (2010)
28. I. Simonini, A. Pandolfi, Customized finite element modelling of the human cornea. *PLoS One* **10**(6), e0130426 (2015)
29. A. Sinha Roy, K.M. Rocha, J.B. Randleman, R.D. Stulting, W.J. Dupps, Inverse computational analysis of in-vivo corneal elastic modulus change after collagen crosslinking for keratoconus. *Exp. Eye Res.* **113**, 92–104 (2013)
30. M.A. Ariza-Gracia, J.F. Zurita, D.P. Piñero, J.F. Rodrigues-Matas, B. Calvo, Coupled biomechanical response of the cornea assessed by non-contact tonometry. A simulation study. *PLoS One* **10**(3), e0121486 (2015)
31. I. Simonini, M. Angelillo, A. Pandolfi, Theoretical and numerical analysis of the corneal air puff test. *J. Mech. Phys. Solid* **93**, 118–134 (2016)
32. P. Sánchez, K. Moutsouris, A. Pandolfi, Biomechanical and optical behavior of human corneas before and after photorefractive keratectomy. *J. Cataract Refract. Surg.* **40**(6), 905–917 (2014)
33. I. Simonini, A. Pandolfi, The influence of intraocular pressure and air jet pressure on corneal contactless tonometry tests. *J. Mech. Beh. Biomed. Mater.* **58**, 75–89 (2016)
34. A. Pandolfi, G. Fotia, F. Manganiello, Finite element simulations of laser refractive corneal surgery. *Eng. Comput.* **25**(1), 15–24 (2009)
35. A. Montanino, M. Angelillo, A. Pandolfi, Modeling the air puff test in the human cornea with a meshfree fluid-structure interaction approach 1–23 (2017, under review)
36. A. Pandolfi, M. Vasta, Fiber distributed hyperelastic modeling of biological tissues. *Mech. Mater.* **44**, 151–162 (2012)
37. M. Vasta, A. Gizzi, A. Pandolfi, On three- and two-dimensional fiber distributed models of biological tissues. *Probab. Eng. Mech.* **37**, 170–179 (2014)
38. K.M. Meek, C. Boote, The use of X-ray scattering techniques to quantify the orientation and distribution of collagen in the corneal stroma. *Prog. Retinal Eye Res* **28**(5), 369–392 (2009)
39. X. Cheng, P.M. Pinsky, Mechanisms of self-organization for the collagen fibril lattice in the human cornea. *J. R. Soc. Interface* **10**(87) (2013)
40. S.S. Chang, J.O. Hjortdal, D.M. Maurice, P.M. Pinsky, Corneal deformation by indentation and applanation forces. *Investig. Ophthalmol. Vis. Sci.* **34**, 1241 (1993)
41. A. Elsheikh, C. Whitford, R. Hamarashid, W. Kassem, A. Joda, P. Bchler, Stress free configuration of the human eye. *Med. Eng. Phys.* **35**(2), 211–216 (2013)
42. H.P. Studer, H. Riedwyl, C.A. Amstutz, J.V.M. Hanson, P. Bchler, Patient-specific finite-element simulation of the human cornea: a clinical validation study on cataract surgery. *J. Biomech.* **46**(4), 751–758 (2013)
43. C. Whitford, H. Studer, C. Boote, K.M. Meek, A. Elsheikh, Biomechanical model of the human cornea: considering shear stiffness and regional variation of collagen anisotropy and density. *J. Mech. Behav. Biomed. Mater.* **42**, 76–87 (2015)
44. A. Sinha Roy, M. Kurian, H. Matalia, R. Shetty, Air-puff associated quantification of non-linear biomechanical properties of the human cornea in vivo. *J. Mech. Behav. Biomed. Mater.* **48**, 173–182 (2015)
45. M.Á. Ariza-Gracia, S. Redondo, D. Piñero Llorens, B. Calvo, J.F. Rodriguez Matas, A predictive tool for determining patient-specific mechanical properties of human corneal tissue. *Comput. Method Appl. Mech. Eng.* **317**, 226–247 (2017)

History of Computational Classical Elasto-Plasticity

Erwin Stein

1 Introductory Remarks

This contribution was presented by the author at COMPLAS XII in 2013 as a plenary lecture but not published so far.

The historical presentation of physical und mathematical modeling together with the computational foundation of related FEMs seems to be of current importance, also regarding the algorithms and applications of elasto-plastic deformations based on C^1 -continuous kinematics for engineering applications, including a posteriori error analysis and adaptivity. In this context I would like to emphasize the “Opus Magnum” [1] by E. A. de Souza Neto, D. Peric and D. R. J. Owen, *Computational Methods in Plasticity*, Wiley (2008), but also the fundamental scientific achievements of J. Lemaitre and J.L. Chaboche in their book *Mechanics of solid materials with macroscopic C^1 continuous material theory of elasto-visco-plasticity with all types of hardening and softening, as well as damage and fatigue, in a thermodynamical framework* [2] (1985). Of equal importance for computational elasto-plasticity is the book by J. C. Simo and T. J. R. Hughes [3] (1998). The mathematical treatment of classical elasto-plasticity [4] by W. Han and B. D. Reddy in the book *Plasticity*, Springer (2013) is also of major importance for computational methods, concerning the derivation of proper admissible test and trial spaces, existence and convergence properties as well as a priori and a posteriori error estimates. I would like to thank Professor J. S. Chen and Professor B. D. Reddy for their discussions in preparing the COMPLAS lecture in 2013.

It is my great pleasure and honor to contribute to the high international scientific reputation of my distinguished colleague and friend Professor Roger Owen.

E. Stein (✉)

Institute of Mechanics and Computational Mechanics, Leibniz Universität Hannover,
Appelstrasse 9A, D-30167 Hannover, Germany
e-mail: stein@ibnm.uni-hannover.de

© Springer International Publishing AG 2018

E. Oñate et al. (eds.), *Advances in Computational Plasticity*, Computational Methods in Applied Sciences 46, DOI 10.1007/978-3-319-60885-3_17

357

2 Milestones of Yield Conditions, Flow Rules, Incremental Deformation Theory and Finite Element Approximations for Elasto-Plastic Deformations of Ductile Crystalline Materials

The yielding of ductile materials—predominantly in metal alloys—does not occur as homogenous inelastic deformation, but predominantly due to energetically pronounced defects of the mono- or polycrystalline structure, such as dislocations, phase limits and amorphous inclusions. The origins of classical phenomenological theory of elasto-plastic deformations of ductile continua are mostly applied to metal alloys, using yield conditions and plastic flow rules. They are treated in the survey article by O. T. Bruhns [5] (2014). The main discoveries and contributions are as follows (Fig. 1):

$$\Phi(\sigma_{dev}) = |\tau|_{max} = \frac{1}{2}(\sigma_I - \sigma_{III}); \text{ y.c.: } \Phi = \kappa. \tag{1}$$

2.1 Tresca

Tresca [6], published 1864 a yield condition for the application to extrusion of metals. It states that yielding takes place if the maximum shear stress takes the critical value of $|\tau|_{max}$, according to the yield condition.

2.2 Barret de Saint Venant

Barret de Saint Venant [7], published in 1871 a constitutive equation for inelastic strains of an elastically rigid, perfectly plastifying solid material in plane stress state with the hypothesis of isotropic deformations, stating that the main axes of strain coincide with the main axes of stress. In this publication five equations for hydro-

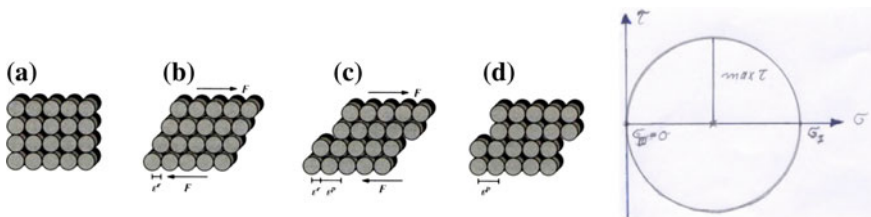


Fig. 1 Dislocations due to shear stress in regular monocrystalline material; stress circle for pure shear with the main stress $\sigma_I = 2\tau_{max}$

stereo dynamics were presented for plane state of strain. The major question remains whether a plastifying body behaves more like a solid or a fluid.

Levy, [8], published in 1871 a theory for rigid, perfectly plastic ductile materials using C^1 kinematics with coinciding main axes of strain and stress of elastic and inelastic isotropic deformations. He also presented a comparison of elastic bodies and viscous fluids. His constitutive equation reads

$$\sigma = pI + 2\mu_{vis}[d - 1/3tr(d)I]; \sigma_{dev} = \sigma - 1/3tr(\sigma)I. \tag{2}$$

2.3 Bauschinger

Bauschinger [9], published in 1886 his model for kinematic hardening as an important property of ductile materials for alternating tension and compression, Figs. 2, 3. After the yield limit for tension, a smaller yield limit takes place for following unloading and compression due to the crystal property of kinematic hardening, called Bauschinger Effect. The absolute value of the yield limit σ_y remains constant, and only the midpoint of the yield locus, the backstress α , is changing. The yield stress has to be replaced by the reduced stress in the flow rule $s = \sigma_y - \alpha$, i.e. elastic unloading and subsequent compression until yielding takes the double value of the initial yield stress in tension, being valid for small plastic deformations.

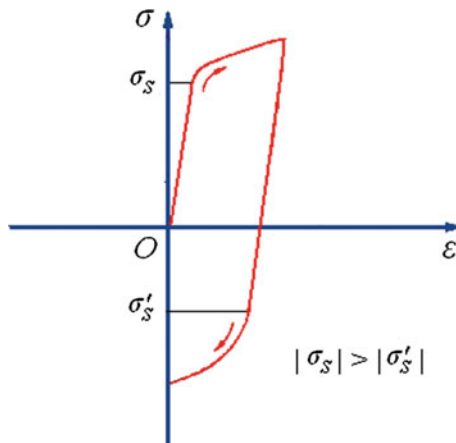


Fig. 2 Kinematic hardening of a 1D Specimen due to cyclic tension and compression

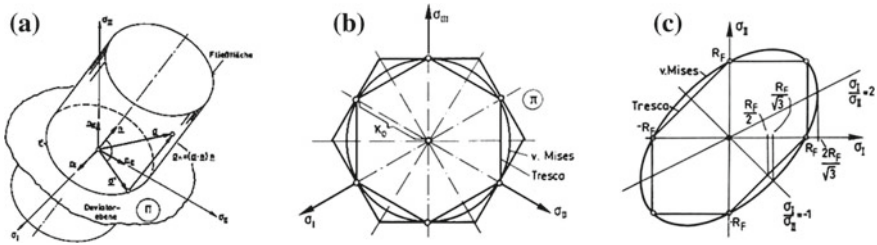


Fig. 3 a yield cylinder in main stress space, Π the deviatoric plane; b yield curves in the deviatoric plane; c yield loci for plane states of stress in main stress

2.4 Huber

Huber [10], published in 1904 a yield criterion, depending on the critical value of 2nd invariant J_2 of the deviatoric stress tensor, according to his experimental observations and measurements.

2.5 von Mises

von Mises [11], published in 1913 independently the J_2 yield condition, Fig. 3.

$$\Phi(\sigma_{ij}) = J_2(\sigma_{ij,dev}) = \kappa_0^2. \tag{3}$$

This pressure-insensitive yield criterion reads for octahedral shear stress

$$J_2 = \frac{1}{2} \text{tr}(\sigma_{dev})^2 = \kappa_0^2 > 0; J_1 = 0; J_3 = \det \sigma_{dev}, \sum_{i=1}^3 (\sigma_{dev,i})^2 = 2\kappa_0^2, \tag{4}$$

the related inelastic constitutive equation reads

$$\mathbf{d} - \frac{1}{3} \text{tr}(\mathbf{d})\mathbf{I} = c \sigma_{dev}. \tag{5}$$

2.6 Hencky

Hencky [12], proposed the above introduced deviatoric yield condition (5) in 1923 with the geometrical interpretation of the Tresca- and von Mises yield conditions by convex yield surfaces in the 3D-space of main stresses for 3D-states of stress. The following Figs. 4, 5 show graphic illustrations.

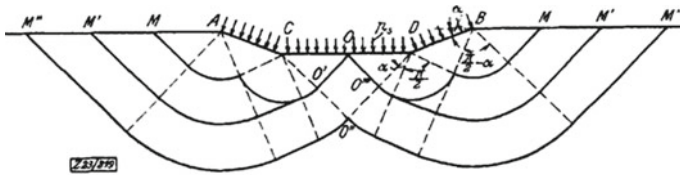


Abb. 3

Fig. 4 Patterns of orthogonal slip lines in the half plane with application to plastic gliding of soil due to static loading

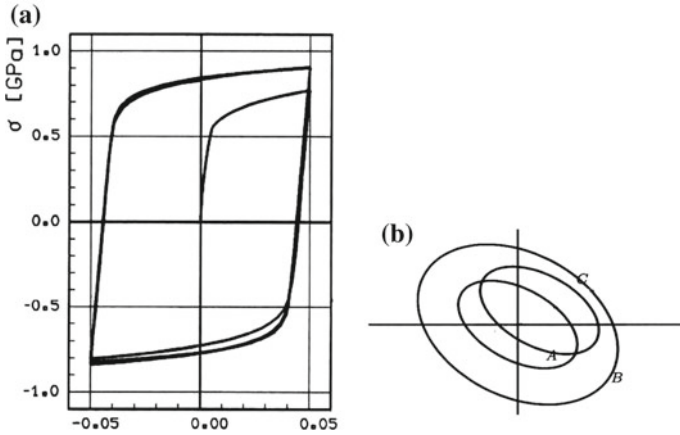


Fig. 5 Combined isotropic and kinematic hardening, (a) of a 1D tension test and (b) evolution of yield curves for 2D-states of stress

2.7 Hencky

Hencky [13], also presented a simple but practically very important slip line theory for metal forming with applications to metals and soils.

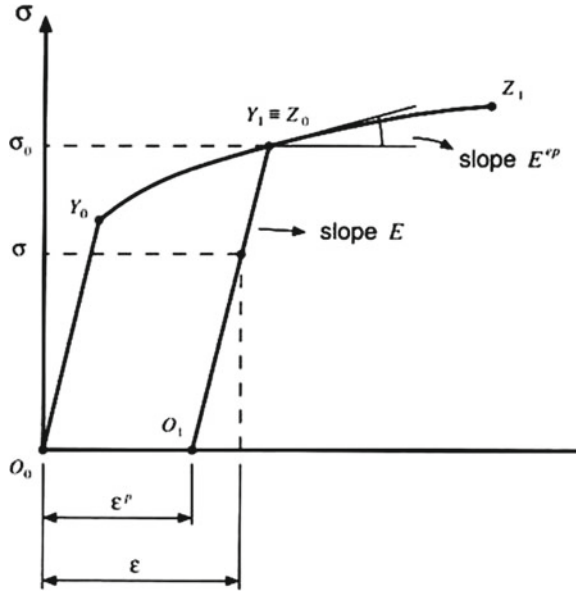
2.8 Chaboche and Rouçhellier

Chaboche and Rouçhellier [14], combined isotropic and kinematic hardening with internal variables which are not directly measurable but derivable, requiring the identification from measurable quantities and their evolution (Fig. 4).

$$\Phi(\sigma_{dev}, A(\epsilon)_{dev}^p) = \bar{\Phi}(\sigma_{dev} - A_{dev}) = k^2(\epsilon_{com}^p), \tag{6}$$

$$\kappa(\epsilon_{com}^p) = k_\infty + (k_0 - k_\infty)e^{-b\epsilon_{com}^A}. \tag{7}$$

Fig. 6 Uni-axial tension test with loading, unloading and reloading



The evolution equation for isotropic hardening is (Fig. 5)

$$\dot{\kappa}(e_{com}^p) = b(\kappa_\infty - \kappa(e_{com}^p))\dot{e}_{com}^p; \mathbf{A} = \sum_{i=1}^3 \mathbf{A}_i. \tag{8}$$

2.9 Clausius and Duhem

Clausius [15] and Duhem [16], introduced a free energy function Ψ and an internal variable tensor α for the thermodynamical theory of plastic yielding, using internal variables, $S(\mathbf{X}) = \hat{S}(\mathbf{F}(\mathbf{X}), [\Theta], \alpha); \alpha = \{\alpha_k\}$. The Clausius-Duhem inequality reads

$$\sigma : d - \rho(\dot{\Psi} + s\dot{\theta}) - \frac{1}{\theta} \mathbf{q} \cdot \mathbf{g} \geq 0, \mathbf{g} = \nabla_x \theta. \tag{9}$$

The 2nd law of thermodynamics with the maximum dissipation principle is $D_{pl} = \sigma : \dot{e}_{pl} - \beta \dot{\alpha} \geq 0$.

With this, the governing equations for yielding and hardening of isothermal linear elasto-plasticity follow for 1D-stress states as (Fig. 6):

$$(1) \textit{ Additive split} : \epsilon_{pl} := \epsilon_{geo} - \epsilon_{el}; \sigma = E\epsilon_{el} \quad (10)$$

$$(2) \textit{ Yield function} : \Phi(\sigma, \sigma_y) = |\sigma| - \sigma_y; \text{el. dom. } |\sigma| < \sigma_y \quad (11)$$

$$(3) \textit{ Plastic flow rule} : \epsilon_{pl} = \dot{\gamma} \text{sign}(\sigma) \quad (12)$$

$$(4) \textit{ Hardening law} : \sigma_y = \hat{\sigma}(\epsilon_{pl}) \quad (13)$$

$$(5) \textit{ Hard. par.} : \dot{\gamma} = \dot{\epsilon}_{pl} \quad (14)$$

$$(6) \textit{ Kuhn – Tucker conditions} : \Phi < 0, \dot{\gamma} \geq 0, \gamma\Phi = 0. \quad (15)$$

$$\text{Determination of } \dot{\gamma}: \dot{\Phi} = \text{sign}(\sigma)\dot{\sigma} - H\dot{\epsilon}_{pl}; \text{hardening modulus } H = \frac{d\sigma_y}{d\epsilon_{pl}},$$

$$\text{stress rate: } \text{sign}(\sigma)\dot{\sigma} = H\dot{\epsilon}_{pl}; \text{plastic multiplier: } \dot{\gamma} = \frac{E}{H + E}|\dot{\epsilon}|. \quad (16)$$

2.10 Prandtl (1924) and Reuss (1930)

Ludwig Prandtl [17] (1924) and Endre Reuss [18] (1930), published in 1924 and 1930 the elastoplastic tangent operator for 1D states of stress. This tangent operator reads for 3D states of stress with the associated plastic flow function $\Phi = \Psi$ for linear isothermal deformations:

$$(1) \textit{ Additive split of strain tensor} : \epsilon_{pl} := \epsilon_{geo} - \epsilon_{el}; \sigma = E\epsilon_{el} \quad (17)$$

$$(2) \textit{ Free energy function} : \Psi = \hat{\Psi}(\epsilon_{el}, \alpha) \quad (18)$$

$$(3) \textit{ Constitutive equations} : \sigma = \frac{\partial\Psi}{\partial\epsilon}; \textit{ thermodynamic force } \mathbf{A} = \frac{\partial\Psi}{\partial\alpha} \quad (19)$$

$$(4) \textit{ Yield function} : \Phi = \hat{\Phi}(\sigma, \mathbf{A}), \quad (20)$$

$$\textit{ associated flow rule} : \Psi = \Phi = \hat{\Psi}(\sigma, \mathbf{A}) \quad (21)$$

$$(5) \textit{ Plastic flow rule and hardening law derived from a flow potential} :$$

$$\dot{\epsilon}_{pl} = \dot{\gamma}N(\sigma, \mathbf{A}), N = \frac{\partial\Psi}{\partial\sigma}; \dot{\alpha} = \dot{\gamma}H(\sigma, \mathbf{A}), H = \frac{\partial\Psi}{\partial\mathbf{A}} \quad (22)$$

N flow velocity tensor, H hardening tensor

$$(6) \textit{ Loading/Unloading criterion} : \Phi \leq 0, \dot{\gamma} \geq 0, \dot{\gamma}\Phi = 0 \quad (23)$$

Optimality conditions for max. dissipation principle, Lueneberger (1973)

$$(7) \textit{ Determination of the plastic multiplier } \dot{\gamma}, \textit{ with} :$$

$$\dot{\sigma} = \mathbf{D}_{el} : (\dot{\epsilon}_{geo} - \dot{\gamma}N); \mathbf{A} = \rho \partial\Psi_{pl}/\partial\alpha; \sigma = \rho \partial\Psi_{el}/\partial\epsilon_{el}; \dot{\gamma} = \frac{\dots}{\dots}. \quad (24)$$

2.11 Consistent Numerical Elastoplastic Tangent Operator for Linearized Strains

According to E. Reuss and C. Nagtegaal, J.C. Simo and R.L. Taylor [19] (1985), derived the consistent elastoplastic tangents.

$$\mathbf{C}_{el-pl} = \frac{\partial \boldsymbol{\sigma}_{n+1}}{\partial \boldsymbol{\epsilon}_{n+1}} = \frac{\partial \hat{\boldsymbol{\sigma}}}{\partial \boldsymbol{\epsilon}_{n+1}} \Big|_{\boldsymbol{\alpha}_n}. \quad (25)$$

Consistent tangent operator for v.Mises y.c. and isotropic hardening:

$$\mathbf{C}_{el-pl} = \frac{\partial \boldsymbol{\sigma}_{n+1}}{\partial \boldsymbol{\epsilon}_{el,n+1}^{trial}}, \quad (26)$$

$$\mathbf{C}_{el-pl} = \mathbf{C}_{el} - \frac{(\mathbf{C}_{el} : \mathbf{N}) \otimes (\mathbf{C}_{el} : \mathbf{N})}{\mathbf{N} : \mathbf{C}_{el} : \mathbf{N} + \mathbf{H}}; \quad \mathbf{N} = \frac{\partial \Phi}{\partial \boldsymbol{\sigma}}; \quad \mathbf{H} = \frac{\partial^2 \Psi_{pl}}{\partial \bar{\epsilon}_{pl}^2} = \frac{\partial \kappa}{\partial \epsilon_{pl}}. \quad (27)$$

2.12 A Short Extension to Finite Strain Elastoplasticity and Consistent Numerical Tangent

Incremental finite strain elastoplasticity for stable states of equilibrium and the coercivity of internal energy is presented by using multiplicative decomposition of strain, Frechet-derivatives and the chain rule, yielding corresponding consistent tangent operators with the same formal structure as for linearized strains, published by Simo [20] (1988).

The implicit exponential map of the plastic flow equation fulfilling incompressibility condition reads

$$\mathbf{F}_{pl,n+1} = \exp(\Delta \gamma \mathbf{R}_{el,n+1}^T \cdot \frac{\partial \Psi}{\partial \boldsymbol{\tau}} \Big|_{n+1} \mathbf{R}_{el,n+1}) \cdot \mathbf{F}_{pl,n}. \quad (28)$$

The system of algebraic equations for incremental finite deformation with prescribed incremental deformation gradient \mathbf{F}_Δ is

$$\begin{aligned} \mathbf{F}_{el,n+1} &= \mathbf{F}_\Delta \cdot \mathbf{F}_{el,n} \cdot \mathbf{R}_{el,n+1}^T \exp(-\Delta \gamma \frac{\partial \Psi}{\partial \boldsymbol{\tau}} \Big|_{n+1}) \cdot \mathbf{R}_{el,n+1}, \\ \boldsymbol{\alpha}_{n+1} &= \boldsymbol{\alpha}_n + \Delta \gamma \mathbf{H}_{n+1}. \end{aligned} \quad (29)$$

The elastic predictor-return mapping algorithm follows as

$$\mathbf{F}_{el,n+1}^{trial} = \mathbf{F}_\Delta \cdot \mathbf{F}_{el,n}; \quad \boldsymbol{\alpha}_{n+1}^{trial} = \boldsymbol{\alpha}_n, \quad (30)$$

with the plastic admissibility condition $\Phi(\boldsymbol{\tau}_{n+1}^{trial}, \mathbf{A}_{n+1}^{trial}) \leq 0$.

The approximate update has the same format as for linear strain $\boldsymbol{\epsilon}_{el,n+1} = \boldsymbol{\epsilon}_{el,n+1}^{trial} - \Delta\gamma \mathbf{N}_{n+1}$.

The incremental constitutive equation reads

$$\boldsymbol{\tau} = \hat{\boldsymbol{\tau}}(\boldsymbol{\alpha}_n, \mathbf{F}_{n+1}) = \tilde{\boldsymbol{\tau}}\{\boldsymbol{\alpha}_n, \boldsymbol{\epsilon}_{el,n+1}^{trial}[\mathbf{B}_{el,n+1}^{trial}(\mathbf{F}_{pl,n}, \mathbf{F}_{n+1})]\}. \quad (31)$$

The elastoplastic consistent tangent of stress is gained with the chain rule

$$\frac{\partial \hat{\boldsymbol{\tau}}}{\partial \mathbf{F}_{n+1}} = \frac{\partial \tilde{\boldsymbol{\tau}}}{\partial \boldsymbol{\epsilon}_{el,n+1}^{trial}} : \frac{\partial \boldsymbol{\epsilon}_{el,n+1}^{trial}}{\partial \mathbf{B}_{el,n+1}^{trial}} : \frac{\partial \mathbf{B}_{el,n+1}^{trial}}{\partial \mathbf{F}_{n+1}}, \quad (32)$$

with the tangent operator $\mathbf{D}_{el,pl} = \frac{\partial \boldsymbol{\tau}}{\partial \boldsymbol{\epsilon}_{el,n+1}^{trial}}$.

3 Shakedown Theory and Finite Element Analysis

3.1 Modeling of Shakedown Without Damage Evolution

The survey article [21] by Dieter Weichert and Alan Ponter (2014) provides an historical overview. Non-smooth yield functions and associated analysis of standard generalized materials at corners are approximated by a finite number of normal vectors $\mathbf{N} = \sum_{i=1}^n c_i \mathbf{N}_i$, with the flow rule $\dot{\boldsymbol{\epsilon}}_{pl} = \sum_{i=1}^n \dot{\gamma}_i \mathbf{N}_i$; $\dot{\gamma}_i \geq 0$.

Generalized multi-surface models were published by J. König, G. Maier [22] (1981), G. Maier [23] (1988), D. Weichert [24] (1986) and E. Stein, G. Zhang and J.A. König [25] (1992).

The elastic domain is bounded by a set of non-smooth yield surfaces in stress space with yield functions Φ_i , $i = 1, \dots, n$, each with a bounding convex yield surface $\Phi_i(\boldsymbol{\sigma}, \mathbf{A}) = 0$, and the elastic domain $\mathcal{E} = \{\boldsymbol{\sigma} | \Phi_i(\boldsymbol{\sigma}, \mathbf{A}) < 0, i = 1, \dots, n$.

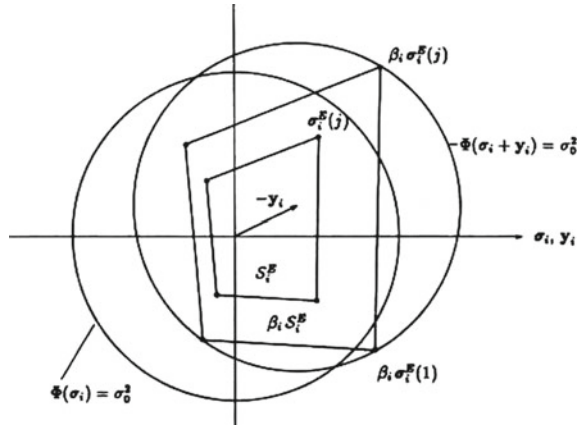
The yield surface (boundary of ϵ) is a set of all stresses with $\Phi_i(\boldsymbol{\sigma}, \mathbf{A}) = 0$ for at least one i and $\Phi_j(\boldsymbol{\sigma}, \mathbf{A}) < 0, \forall j \neq i$.

For associative flow rules, i.e. $\Psi_i = \Phi_i$, (where the subgradient is a linear combination of a finite number of normals), the normal plastic flow vectors are $\mathbf{N}_i = \frac{\partial \Phi_i}{\partial \boldsymbol{\sigma}}$, with the loading/unloading conditions $\Phi_i \leq 0, \dot{\gamma}_i \geq 0, \Phi_i \dot{\gamma}_i = 0$.

3.2 Approximation of Largest Possible Load Space Diameter Max β via Reduced Basis Technique

E. Stein et. al. [25] (1992) analyzed the maximum load space diameter $\max \beta$ with reduced basis technique (Fig. 7):

Fig. 7 Evolution of diameter β of local shakedown problem



Theorem: The conditions $\Phi(m\bar{\alpha}(x) \leq [K(x) - k_0(x)]^2$, $m > 1$ for a time-independent macro eigenstress field $\bar{\rho}(x)$ and a backstress field $\bar{\alpha}(x)$, with the yield function $\Phi\{m[\sigma_{el}(x, t) + \bar{\rho}(x) - \bar{\alpha}(x)]\} \leq k_0(x)^2$ are necessary and sufficient for shakedown within a n-dimensional load space with diameter $\max \beta$.

The adaptively controlled optimization algorithm with subspace iteration reads (Fig. 7)

$$\beta \rightarrow \max \text{ for } \sum_{i=1}^{NG} C_i \rho_i = C \rho = \mathbf{0},$$

$$\Phi(\beta \sigma_i(j) + \rho_i - \alpha_i) \leq \sigma_0^2 \quad \forall (i, j) \in I, J, \quad \Phi(\alpha_i) \leq (\sigma_y - \sigma_0)^2. \quad (33)$$

The reduction factor of the computational effort for reduced base technique is about 100.

3.3 Example of Experimental and Numerical Elastoplastic Ultimate Loads and Shakedown Loads for Steel Girders with Cutouts at the Supports

The maximum number of load cycles for cyclic loading experiments of two girders (1 and 2) before failure are (Figs. 8, 9):

for girder 1: first observed crack of 1 mm length at cycle no. 180; failure load at cycle no. 371;

for girder 2: first crack at cycle no. 145; failure load at cycle no. 372.

Fig. 8 Steel girder TPE 500, St.52-3 with cutouts at the supports and different rounding diameters and drill holes at the in-jumping corners

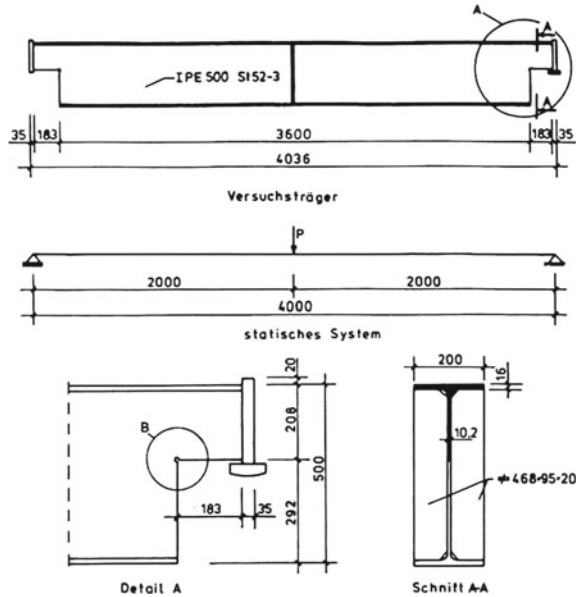
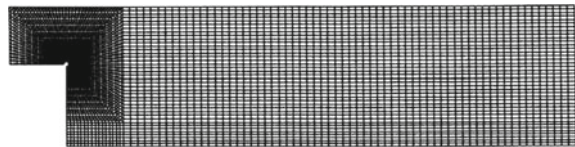


Fig. 9 2D-discretization with DKT- and Q1 finite elements



The numerical ultimate load and the maximum shakedown load, both for linear elastic, ideally plastic deformation, are $F_{ult.}^{id.pl.} = 633,2 \text{ kN}$ and $F_{sh.d.}^{id.pl.} = 164,2 \text{ kN}$. For kinematically hardening plastic deformations the corresponding results are: $F_{ult.}^{kin.hard.} = 878,0 \text{ kN}$ and $F_{sh.d.}^{kin.hard.} = 164,2 \text{ kN}$ (Figs. 8, 9).

4 A Posteriori Error Estimation for Primal FEM with h-Adaptivity

4.1 Governing Equations

This analysis is based on the following set of equations, F.-J. Barthold, M. Schmidt and E. Stein [26] (1998); E. Stein and M. Schmidt [27] (2003):

1. Kinematic linearization $\boldsymbol{\epsilon} := \boldsymbol{\epsilon}^p + \boldsymbol{\epsilon}^e$
2. Free elastic energy $\Psi = \hat{\Psi}(\boldsymbol{\epsilon}, \boldsymbol{\epsilon}^p, \alpha)$
3. Macro – stresses $\boldsymbol{\sigma} = \partial_{\boldsymbol{\epsilon}} \hat{\Psi}(\boldsymbol{\epsilon}, \boldsymbol{\epsilon}^p, \alpha)$
4. Micro – stresses $\boldsymbol{\beta} = \partial_{\alpha} \hat{\Psi}(\boldsymbol{\epsilon}, \boldsymbol{\epsilon}^p, \alpha)$
5. Dissipation and 2nd law of thermodynamics $\mathcal{D}^p = \boldsymbol{\sigma} : \dot{\boldsymbol{\epsilon}}^p - \beta \dot{\alpha} \geq 0$
6. von Mises yield condition $\Phi = \hat{\Phi}(\boldsymbol{\sigma}, \alpha) = \|\text{dev} \boldsymbol{\sigma}\| - \sqrt{\frac{2}{3}}(\sigma_0 + h(\alpha))$
7. Hardening rule $h(\alpha) = \sigma_0 + (\sigma_{\infty} - \sigma_0)(1 - e^{-\omega\alpha}) + \alpha H$
8. Flow rule, load factor γ $\dot{\boldsymbol{\epsilon}}^p = \gamma \partial_{\boldsymbol{\sigma}} \hat{\Phi}(\boldsymbol{\sigma}, \beta) = \gamma \mathbf{n}$, $\mathbf{n} := \frac{\text{dev} \boldsymbol{\sigma}}{\|\text{dev} \boldsymbol{\sigma}\|}$
9. Evolution $-\dot{\alpha} = \gamma \partial_{\beta} \hat{\Phi}(\boldsymbol{\sigma}, \beta)$
10. Kuhn – Tucker conditions $\gamma \geq 0$, $\Phi \leq 0$, $\gamma \Phi = 0$ (34)

The volume-specific stored energy rate at all points $\mathbf{x} \in \Omega \subset \mathbb{R}^3$ reads

$$\dot{\hat{\mathcal{P}}} := \underbrace{\boldsymbol{\sigma} : \dot{\boldsymbol{\epsilon}}}_{\stackrel{!}{=} 0} + \underbrace{\dot{\gamma} \Phi}_{\Psi} = \underbrace{\boldsymbol{\sigma} : \dot{\boldsymbol{\epsilon}}^{el} + \dot{\beta} \alpha}_{\Psi} + \underbrace{\boldsymbol{\sigma} : \dot{\boldsymbol{\epsilon}}^{pl} - \dot{\beta} \alpha}_{\mathcal{D}^{pl}} + \dot{\gamma} \Phi. \quad (35)$$

Parametric time integration for strain-controlled load steps $\Delta\gamma$ at time increment $\Delta t = t_{n+1} - t_n$ yields

$$\int_{t_n}^{t_{n+1}} \dot{\hat{\mathcal{P}}} dt = \int_{t_n}^{t_{n+1}} (\dot{\Psi} + \mathcal{D}^{pl} + \dot{\gamma} \Phi) dt = \Psi_{n+1} + \int_{t_n}^{t_{n+1}} (\mathcal{D}^{pl} + \dot{\gamma} \Phi) dt, \quad (36)$$

with $\dot{\hat{\mathcal{P}}} \rightarrow \dot{\Psi}$ for $\dot{\boldsymbol{\epsilon}}^{pl} \rightarrow 0$.

4.2 Spatial a Posteriori Discretization Errors in Adequate Norms

Only spatial discretization errors are analyzed in this section, whereas the error due to the choice of usually equal incremental time (load) steps is not considered herein, but will be treated in Sect. 5.

The incremental spatial discretization error $\boldsymbol{e}(X) := \boldsymbol{u}(X) - \boldsymbol{u}_h(X)$ at time t_{n+1} has three components, presented with the relevant norms for:

(i) Residual error of equilibrium

$$|||e_{eq,n+1}|||_{\Omega}^2 = \int_{\Omega,t_{n+1}} (\epsilon^{el} - \epsilon_h^{el}) : \mathbb{C} : (\epsilon^{el} - \epsilon_h^{el}) dV + \int_{\Omega,t_{n+1}} (\alpha - \alpha_h) H (\alpha - \alpha_h) dV, \quad (37)$$

(ii) Error of plastic strain rate

$$||e_{diss,n+1}||_{L_2(\Omega)}^2 = \int_{\Omega,t_{n+1}} \sigma : (\dot{\epsilon}^{pl} - \dot{\epsilon}_h^{pl}) dV + \int_{\Omega,t_{n+1}} \beta (\dot{\alpha} - \dot{\alpha}_h) dV, \quad (38)$$

(iii) Incremental error of the Kuhn-Tucker conditions for yielding, loading and unloading

$$||e_{KT,n+1}||_{L_2(\Omega)}^2 = \int_{\Omega,t_{n+1}} \dot{\gamma}_h \Phi_h dV. \quad (39)$$

Using Q1P0 quadrilateral 2D elements for numerically stable plane strain analysis of non-linear hardening mild steel, the explicit spatial residual error indicator of equilibrium reads, E. Stein and M. Schmidt [27] (2003):

$$(i) \quad \eta_{eq,res}^2 = \sum_e [h_e^2 \int_{\Omega_e} \mathbf{R}_h^2 dV + h_e \int_{\Gamma_e} \mathbf{J}_e^2 dA], \quad [\eta_{eq}] = \sqrt{Nm}, \quad (40)$$

and with gradient-smoothed C^0 continuous stresses $\sigma_*(x)$

$$\eta_{eq,smo}^2 = \sum_e \left[\int_{\Omega_e} (\sigma_* - \sigma_h) : \mathbb{C}^{-1} : (\sigma_* - \sigma_h) dV \right]. \quad (41)$$

The spatial incremental error indicator of plastic strain evolution reads

$$(ii) \quad \eta_{\dot{\epsilon}^p}^2 = ||\sigma_* : (\dot{\epsilon}_*^p - \dot{\epsilon}_h^p)||_{L_2(\Omega)}^2 + ||\beta_* \cdot (\dot{\alpha}_* - \dot{\alpha}_h)||_{L_2(\Omega)}^2, \quad [\eta_{eq}] = \sqrt{Nm}, \quad (42)$$

with gradient-smoothed stresses σ_* and β_* and plastic strain rates $\dot{\epsilon}_*^p$ and $\dot{\alpha}_*$. The related error indicator by Peric and D.R.J. Owen [28] (1994) is

$$(iii) \quad \eta_{PO} = ||(\sigma_* - \sigma_h) : (\dot{\epsilon}_*^p - \dot{\epsilon}_h^p)||_{L_2(\Omega)}, \quad (43)$$

yielding similar numerical results as ours. A relation of this indicator to the constitutive equation error estimator by P. Ladeveze (1991) can be shown.

The spatial error indicator for the Kuhn-Tucker conditions $\dot{\gamma} \geq 0$, $\Phi \leq 0$, $\dot{\gamma}\Phi = 0$ is derived by using higher order polynomials, yielding

$$(iv) \quad \eta_{KT}^2 = ||\dot{\gamma}\Phi - \dot{\gamma}_h\Phi_h||_{L_2(\Omega)}^2 = ||\dot{\gamma}_h\Phi_h||_{L_2(\Omega)}^2, \quad [\eta_{eq}] = \sqrt{Nm}. \quad (44)$$

Remark: a discontinuity of discrete solutions occurs at the transition from elastic to plastic deformation. This has to be reduced by small time (loading) steps.

The total incremental spatial error indicator for equilibrium, plastic strain evolution and the Kuhn-Tucker conditions then results in

$$\eta_{all} := (\eta_{eq}^2 + \eta_{\epsilon^p}^2 + \eta_{KT}^2)^{1/2}. \tag{45}$$

These error indicators and related adaptive meshes were calculated for the example of an aluminium plate in plane strain state with a central hole, Fig. 10.

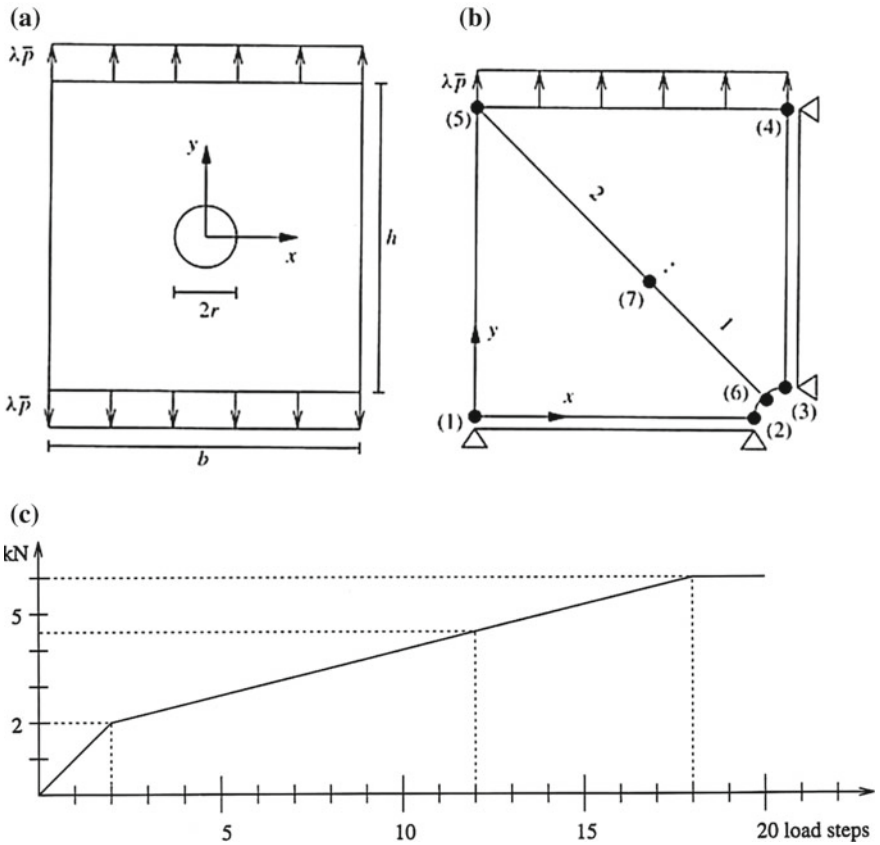


Fig. 10 **a** Stretched rectangular aluminium plate in plane strain state with a hole, **b** points for which data were collected, **c** incremental strain controlled static loading steps. The total load $\lambda \bar{t}$ is acting within 18 load steps

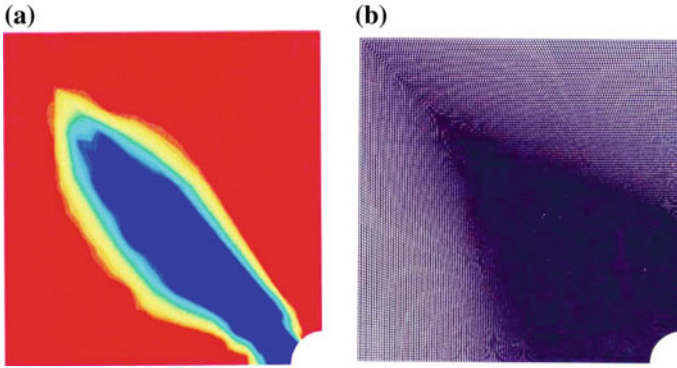


Fig. 11 **a** Plastic zone at static load factor $\lambda = 4, 60$, shortly before failure, **b** graded FE-mesh with 24200 Q1P0 finite elements, 24642 nodes and 49062 DOFs

The material data are:

Young's modulus	$E = 206899.94 \text{ MPa}$
Poisson's ratio	$\nu = 0.29$
Compr. modulus	$K = 164206 \text{ MPa}$
Initial yield stress	$y_0 = 450 \text{ MPa}$
Saturation stress	$y_\infty = 750 \text{ MPa}$
Linear hardening	$h = 129 \text{ MPa}$
Hardening exponent	$\omega = 16.93$.

Numerical Results

Plastic Zone shortly before Static Failure

Figure 11 shows the plastic zone for the load factor $\lambda = 4, 60$ which is 99% of the critical load $\lambda_{ult} = 4, 66$. The computation is started with a graded mesh, according to the analytical form of the decaying singularity from the edge of the central hole. Graded meshes are efficient as starting meshes before remeshing from a regular starting grid according to a posteriori error distribution.

Error Indicator η_{eq} for Equilibrium

Figure 12 shows the distribution of the error indicator η_{eq} at load factor $\lambda = 4, 5$ and the final adaptive FE-mesh according to the tolerance of the error indicator η_{eq} .

Error Indicator η_{ϵ^P} for Plastic Strain Rate $\dot{\epsilon}^P$

Figure 13a and b display the error indicator η_{ϵ^P} for load factor $\lambda = 4, 5$ and the related adaptive FE-mesh at the prescribed error tolerance. The error is restricted to the edge of the progressing plastic zone. Figure 13c and d shows the corresponding results for the related error indicator by Perić and Owen with about the same number of equations for the shown refined meshes.

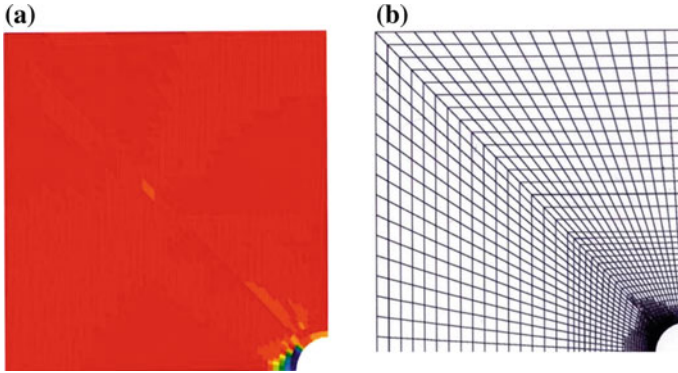


Fig. 12 **a** Error indicator η_{eq} for load factor $\lambda = 4, 5$, **b** adaptive FE-mesh according to η_{eq}

Error Indicator for the Kuhn-Tucker Conditions

In Fig. 14a the error indicator of the Kuhn-Tucker conditions is depicted, which is concentrated at the edge of the progressing yield zone. Figure 14b exhibits the related adaptively defined FE-mesh at the prescribed error tolerance.

Total spatial error indicator for the three partial error indicators $\eta_{eq}, \eta_{\dot{\epsilon}^p}, \eta_{KT}$ at load factor $\lambda = 4.5$, is presented in Fig. 15.

It can be seen from Fig. 15a and b that the dominating part of the total error indicator results from the error of equilibrium. Of course, weighting factors can be introduced to emphasize certain partial indicators.

5 Interactive a Posteriori Error Estimator in Time and Space

A rigorous coupled error estimation in time and space is only successful with a mixed approximation, useful with the discontinuous Galerkin weak form.

Using here an operator split, FDM is applied in time and FEM in space. The parametric load steps in time are chosen globally, either fixed or adaptive.

The total error in time and space can be deduced from the stress power of stored elastic energy and plastic dissipation energy, equations (35) and (36), as

$$\dot{\mathcal{P}} = \sigma : \dot{\epsilon} = \sigma : (\dot{\epsilon}^e + \dot{\epsilon}^p) = \underbrace{\sigma : \dot{\epsilon}^e}_{\dot{\Psi}} + \underbrace{\sigma : \dot{\epsilon}^p}_{\dot{D}^p}. \tag{46}$$

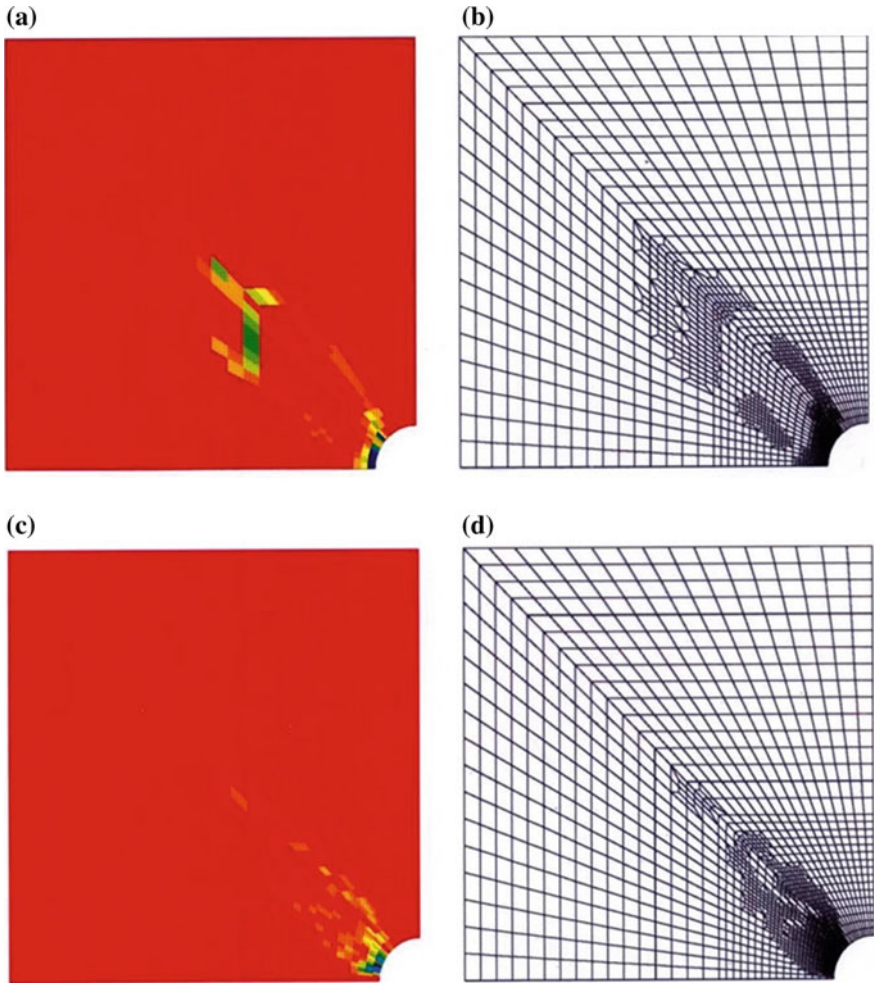


Fig. 13 **a** Error indicator η_{ϵ^p} by Stein/Schmidt for load factor $\lambda = 4, 5$ and **b** with related adaptive FE-mesh at error tolerance; **c** error indicator η_{ϵ^p} according to Perić/Owen and **d** with the adaptive FE-mesh at error tolerance

Time integration yields

$$\int_0^t \dot{\tilde{P}} dt = \int_0^t \dot{\psi} dt + \int_0^t \sigma : \dot{\epsilon}^p dt = \psi + \int_0^t \dot{D}^p dt. \tag{47}$$

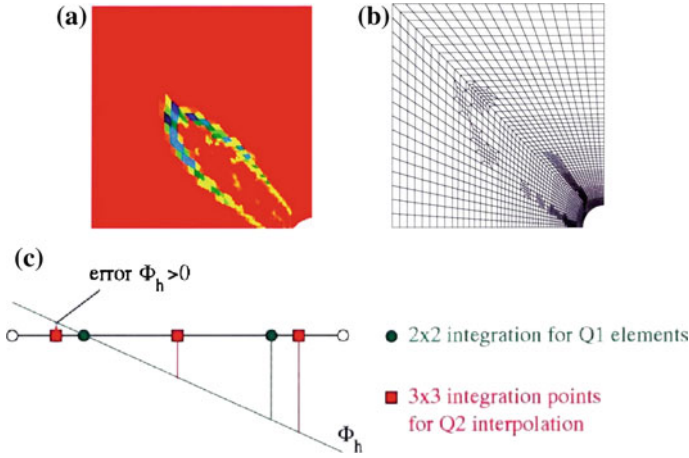


Fig. 14 a Error indicator η_{KT} at load $\lambda = 4.5$, and b adapted FE-mesh at error tolerance; c yield function Φ_h and integration points for 2×2 integration in case of $Q1$ elements as well as 3×3 integration points for $Q2$ elements

The global error reads

$$e^2 = \|\sigma - \sigma_h\|_{E(\Omega,t)}^2 + \int_0^t \|\dot{D}^p - \dot{D}_h^p\|_{D(\Omega,t)} dt. \tag{48}$$

The total error indicator is gained by recovered gradients yielding C^0 continuous, smoothed stresses σ_* improving stresses, yielding

$$\eta_{total}^2 = \frac{1}{2} \int_0^t \int_{\Omega_t} (\sigma_* - \sigma_h) : \mathbb{C}^{-1} : (\sigma_* - \sigma_h) dV dt + \int_0^t \int_{\Omega_t} (\sigma_* - \sigma_h) : (\dot{\epsilon}_*^p - \dot{\epsilon}_h^p) dV dt. \tag{49}$$

With the check $\psi > \int_0^t \dot{D}^p d\tau \rightsquigarrow$ adaptivity in space, else \rightsquigarrow adaptivity in time, adaptivity in space is activated, otherwise activity in time. The error indicator for the time increment $\Delta t = t_{n+1} - t_n$ reads

$$\eta_{\Delta t} = \|\sigma_h\|_{L_2(\Omega_n)} \left\| \int_{t_n}^{t_{n+1}} \dot{\epsilon}^p d\tau - \Delta \epsilon_h^p \right\|_{L_2(\Omega_n)}; \Delta \epsilon_h^p = \epsilon_{h,n+1}^p - \epsilon_{h,n}^p. \tag{50}$$

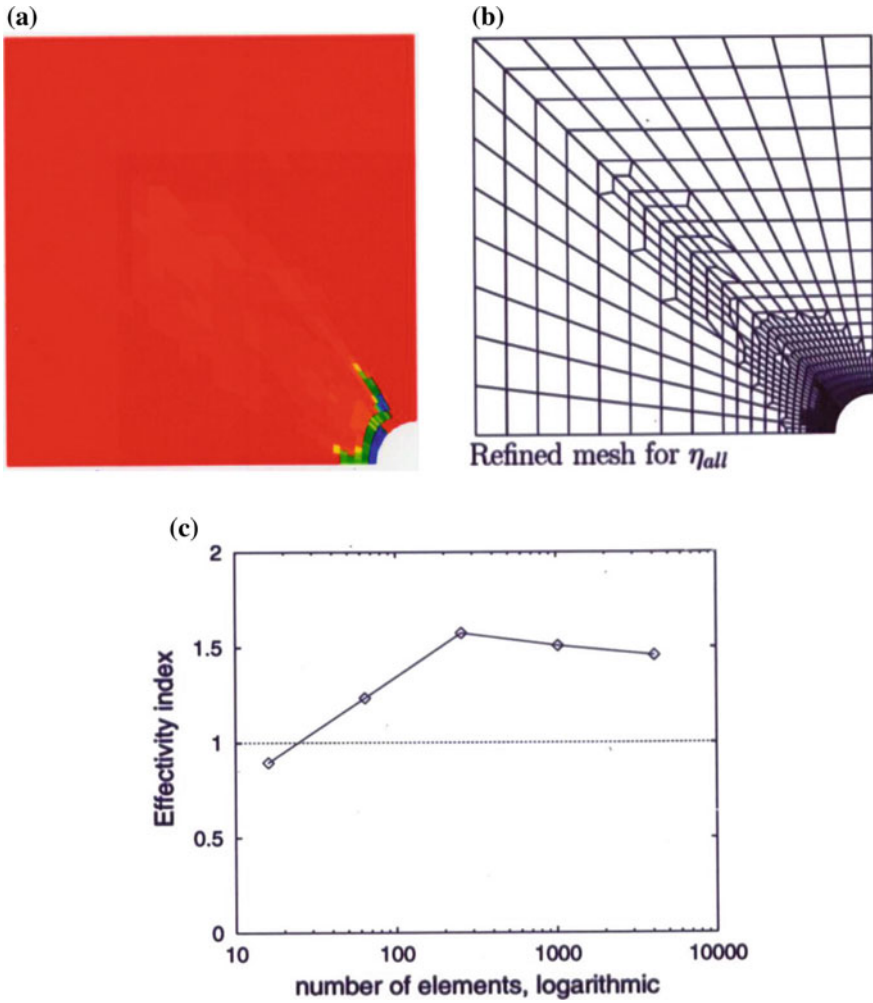


Fig. 15 **a** Error indicator η_{all} for load factor $\lambda = 4.5$, **b** adaptive FE-mesh for the prescribed error tolerance, and **c** effectivity index with respect to the number of unknown nodal displacements in logarithmic scale

The integral in equation (50) must be computed for every load step; the prefactor of this equation (50) is a weighting term for getting the overall dimension of an energy; the second term results in

$$\left\| \int_{t_n}^{t_{n+1}} \dot{\epsilon}^p \, d\tau - \Delta \epsilon_h^p \right\|_{L_2(\Omega_t)} = \left\| \int_{t_n}^{t_{n+1}} \dot{\gamma}(t) \mathbf{n}(t) \, d\tau - \Delta t \gamma_{n+1} \mathbf{n}_{n+1} \right\|_{L_2(\Omega_t)}$$

$$\begin{aligned}
 &= \left\| \int_{t_n}^{t_{n+1}} [\dot{\gamma}(t)\mathbf{n}(t) - \gamma_{n+1}\mathbf{n}_{n+1}] \, d\tau \right\|_{L_2(\Omega_t)} \\
 &\leq \int_{t_n}^{t_{n+1}} \|\dot{\gamma}(t)\mathbf{n}(t) - \gamma_{n+1}\mathbf{n}_{n+1}\|_{L_2(\Omega_t)} \, d\tau \\
 &\leq \Delta t \max_{t \in [t_n, t_{n+1}]} \|\dot{\gamma}(t)\mathbf{n}(t) - \gamma_{n+1}\mathbf{n}_{n+1}\|_{L_2(\Omega_t)}. \tag{51}
 \end{aligned}$$

We assume the worst case that the largest difference $\mathbf{n}(t) - \mathbf{n}_{n+1}$ occurs at $t = t_n$, and choosing $\gamma(t) = \gamma_{n+1}$ yields

$$\gamma_{\Delta t} \leq \gamma_{n+1} \|\mathbf{n}_n - \mathbf{n}_{n+1}\|_{L_2(\Omega_t)} \Delta t \tag{52}$$

As $\mathbf{n}_n = \mathbf{n}_{n+1}$ holds for Hencky plasticity, $\eta_{\Delta t}$ is also a measure for the difference between the Prandtl-Reuss and the Hencky plasticity theory. For $\dot{\gamma} = 0$ we get $\eta_{\Delta t} = 0$, i.e. elastic deformation does not influence $\eta_{\Delta t}$, resulting in

$$\eta_{\Delta t}^2 = \|\sigma_*\|_{L_2(\Omega, t_n)} \cdot \gamma_{\Delta t}. \tag{53}$$

The combined total error indicator in space and time (load) at time t results in

$$\eta_{total}^2 = \|\sigma_* - \sigma_h\|_{E(\Omega_t)}^2 + \int_0^t \|\dot{D}_*^p - \dot{D}_h^p\|_{D(\Omega_t)} \, d\tau, \tag{54}$$

yielding the error indicators in time and space

$$\eta_{\Delta t} \leq \|\sigma_{h,t}\|_{L_2(\Omega_t)} \|\mathbf{n}_{n+1} - \mathbf{n}_n\|_{L_2(\Omega_t)} \Delta t, \tag{55}$$

$$\eta_{space} = \|\sigma_{*,t} - \sigma_{h,t}\|_{E^*(\Omega_t)}. \tag{56}$$

This coupled error estimation requires the consistent transfer of internal variables and computed nodal data, realized by using the transfer errors of the projected material parameters via monomials of higher p-order, M. Ortiz, J.C. Simo [29] (1986) (Fig. 16).

Figure 17 exhibits the error indicators in time and space, (50) and (52), applied to incremental adaptivity of time (load)-steps $\Delta \lambda$ and the FE-mesh with Q1P0 quadrilateral elements of the stretched aluminium plate with a central hole, Fig. 10, E. Stein, S. Ohnibus and M. Rüter [30] (2001).

Remark: our coupled adaptive strategy yields the expected upper bound property for discretization errors in space and time, realized with relatively small CPU-times in total.

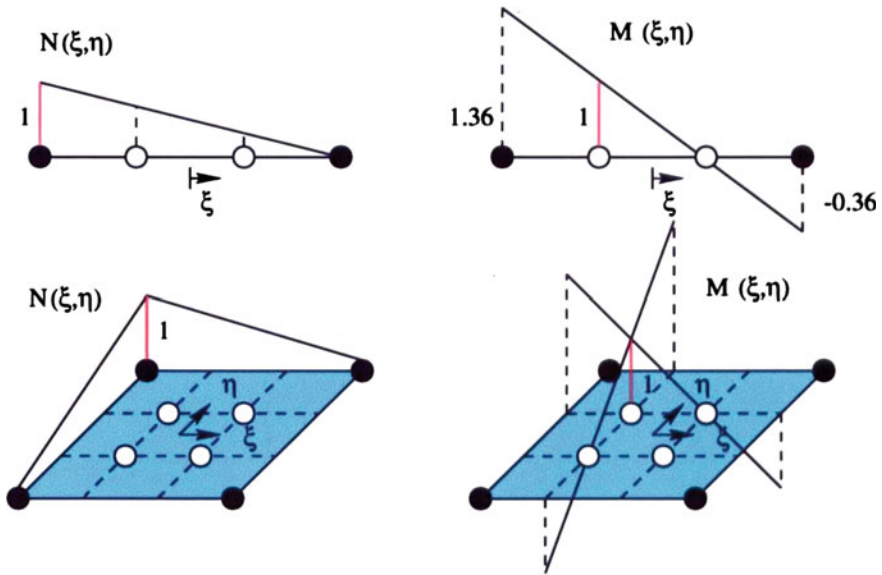


Fig. 16 Transfer errors due to projections, using Gauss-point based shape functions $M(\epsilon, n)$ by Ortiz/Quigley; with element nodes at \bullet and Gausspoints at \circ ; There are two methods, A: First interpolation from father Gausspoints to element nodes, secondly, interpolation from nodes to child Gausspoints, and B direct interpolation from parent Gausspoints to child Gausspoints, requiring only one interpolation, i.e. faster and more accurate

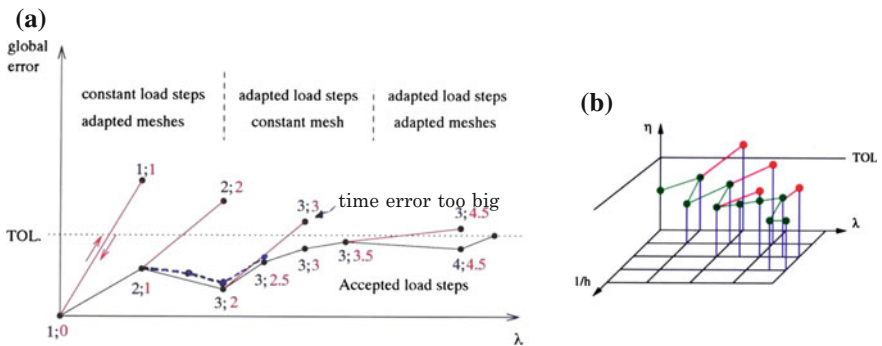


Fig. 17 a A posteriori error estimation in space and time (load) after each load step and new computation with FE-remeshing and smaller/or equal load steps for $\eta_{total} > TOL$; **b** staggered scheme for transfer of internal variables, with meshes 1, 2, 3, 4 and load increments $\Delta\lambda$, $\lambda = 0; 1; 2; 2, 5; 3; 3, 5; 4, 5; 4, 6$

Another straight-forward—but much more CPU-time consuming—strategy was published by L. Gallimard, P. Ladevèze, J.P. Pelle [31] (1997) with local error-based adaptivity in space and globally refined equal time steps, repeating the full load history for all chosen time steps.

6 Conclusion

A condensed synopsis of the history of experimental observations and classical mathematical modeling with C^1 kinematics of elastoplastically deforming polycrystalline materials is presented, combined mesh-based FEM with adaptive h-refinements. A posteriori error analysis and adaptivity in space as well as in space and parametric time is derived and applied to the example of a stretched aluminium plate with a central hole. Furthermore, adaptive shakedown analysis for kinematically hardening materials is presented with an example. In total, the main goal of this contribution is the presentation of experimentally based sound mathematical models with the challenge of verification the finite element approximations by given tolerances of related bounded error norms.

References

1. E.A. de Souza Neto, D. Peric, D.R.J. Owen, *Computational Methods in Plasticity* (Wiley, 2008)
2. J. Lemaitre, J.-L. Chaboche, *Mechanics of Solid Materials* (Cambridge University Press, 1985 (French), 1990 (English))
3. J.C. Simo, T.J.R. Hughes, *Computational Inelasticity*, Revised 2nd ed. 2006 (Springer Science & Business Media, 1998)
4. W. Han, B.D. Reddy, *Plasticity* (Springer, 2013)
5. O.T. Bruhns, *On the history of plasticity—Heinrich Hencky, a pioneer of the early years, in the history of theoretical, material and computational mechanics—mathematics meets mechanics and engineering*, ed. by E. Stein (Springer 2014), pp. 133–152
6. H.E. Tresca, Mémoire sûr l'écoulement soumis à des corps solides. Mémoire Présentée par Divers Savants, Academy des Science, Paris **59**, 754–758 (1864)
7. J. Barré de Saint Venant, *Mémoire sûr l'établissement des equations différentielles des mouvements intérieurs opérés dans les corps solides ductiles différentielles*. J. Math. Pures et Appl. **16**, 308–316 (1871)
8. M. Levy, Extrait de mémoire sûr les equations generales des mouvements interieurs des corps solides ductiles au dela des limites ou l'estacite pourrait les ramener a leur premier etat. J. Math. Pures Appl. **16**, 369–372 (1871)
9. J. Bauschinger, Jahresreport, *Mitt Mech. Lab*, München (1886)
10. T.M. Huber, *Właściwa praca odkształcenia jako miara wyczerpania materialu*. Czasopismo Techniczne **22**, 34–40, 49–50, 61–62, 80–81
11. R.E. von Mises, *Mechanik der festen Körper im plastisch deformablen Zustand* (Göttingen, Mathematisch-Physikalische Klasse, Nachrichten der Gesellschaft der Wissenschaften, 1913), pp. 582–592.
12. H. Hencky, Über einige statisch bestimmte Fälle des Gleichgewichts in plastischen Körpern. ZAMM **3**, 241–251 (1913)
13. H. Hencky, Die Bewegungsgleichungen beim nichtstationären Fließen plastischer Massen. ZAMM **5**, 144–175 (1925)
14. J.-L. Chaboche, G. Rouçhellier, On the plastic and viscoplastic constitutive equations, part I: rules developed with internal variable concept. J. Press. Vess. Tech. **105**, 153–164 (1983)
15. R. Clausius, Über eine veränderte Form des 2. Hauptsatzes der mechanischen Wärmetheorie. Ann. Physik **93**, 461–506 (1854); Abhandl. **1**, 126–154
16. P. Duhem, *Traité d'énergétique*, vol. 2 (Gautier-Villars, Paris, 1911)
17. L. Prandtl, *Spannungsverteilung in plastischen Körpern*. Proc. First Int. Congr. Appl. Mech., Delft, pp. 43–54 (1924)

18. E. Reuss, Berücksichtigung der elastischen Formänderung in der Plastizitätstheorie. *Z. angew. Math. Mech.* **10**(3), 266–274 (1930)
19. J.C. Simo, R.L. Taylor, Consistent tangent operators for rate independent plasticity. *Comp. Meths. Appl. Mech. Engg.* **48**, 101–118 (1985)
20. J.C. Simo, A framework for finite strain elasto-plasticity based on maximum plastic dissipation and multiplicative decomposition: part I. Continuum formulation. *Comput. Methods Appl. Mech. Eng.* **66**, 199–219 (1988)
21. D. Weichert, A. Ponter, *A historical view on shakedown theory, in the history of theoretical, material and computational mechanics—mathematics meets mechanics and engineering*, ed. by E. Stein. Lecture Notes in Applied Mathematics and Mechanics 1 (Springer, 2014), pp. 169–194
22. J.A. König, G. Maier, Shakedown analysis of elastoplastic structures, a review of recent developments. *Nucl. Eng. Des.* **66**, 81–85 (1981)
23. G. Maier, *A generalization to nonlinear hardening of the first shakedown theorem for discrete elastic-plastic structures* (Serie Ottava, Rendic. Acc. Naz. dei Lincei, 1988), pp. 161–174
24. D. Weichert, On the influence of geometrical nonlinearities on the shakedown of elastic-plastic structures. *Int. J. Plast.* **2**, 135–148 (1986)
25. E. Stein, G. Zhang, J.A. König, Shakedown with nonlinear strain hardening including structural computations using finite element method. *Int. J. Plast.* **8**, 1–31 (1992)
26. F.-J. Barthold, M. Schmidt, E. Stein, Error indicators and mesh refinements for finite element computations of elastoplastic deformations. *Int. J. Comput. Mech.* **22**, 225–238 (1998)
27. E. Stein, M. Schmidt, Adaptive FEM for elasto-plastic deformations, in *Error-controlled Adaptive Finite Elements in Solid Mechanics*, ed. by E. Stein (Wiley, 2003), pp. 53–108
28. D. Peric, J. Yu, D.R.J. Owen, Error estimates and adaptivity in elastoplastic solids. *Int. J. Num. Meth. Eng.* **37**, 1351–1379 (1994)
29. M. Ortiz, J.C. Simo, An analysis of a new class of integration algorithms for elastoplastic constitutive relations. *Int. J. Num. Meth. Eng.* **23**, 353–366 (1986)
30. E. Stein, S. Ohnibus, M. Rüter, *Hierarchical model- and discretization-error estimation in elastoplastic structures*, in: H. Aref and J.W. Philips (eds.): *Mechanics of a new Millenium, Proceedings 20th Internat. Congress on Thoretical and Applied Mechanics (IUTAM)*, Chicago, USA, Kluwer Academic Publishers, 40, 2001, 373–388
31. L. Gallimard, P. Ladevèze, J.P. Pelle, Error estimation and time-space parameters optimization for FEM non-linear computation. *Comput. Struct.* **64**, 145–156 (1997)

VEM for Inelastic Solids

R.L. Taylor and E. Artioli

1 Introduction

The virtual element method (VEM) is a generalization of the finite element method recently introduced in [1–5]. It is capable to deal with general polygonal/polyhedral meshes and to easily implement highly regular discrete spaces (see for instance [3]). The VEM approach has experienced an increasing interest in the scientific community, both from a mathematical and an engineering point of view.

By making use of non-polynomial shape functions, the VEM can easily handle general polygons/polyhedrons without effort in integration at the element level. Polytope meshes can be very useful in several instances, such as domains with cracks, inclusions, and for the automatic use of hanging nodes, moving boundaries, and adaptivity.

In addition to approaches cited above recent works on this topic have been applied to many areas of scientific interest, including [6–15] to name a few. In the more specific framework of structural mechanics, VEM has been introduced in [2] for two dimensional linear elasticity at general “polynomial” order, in [11] for three dimensional linear elasticity at the lowest order, in [6] for general two dimensional elastic and inelastic problems in small deformation (lowest order), in [14] for contact problems and in [16, 17] for applications to two-dimensional problems with elastic and inelastic behavior.

Dedicated to Roger Owen on the occasion of his 75th birthday.

R.L. Taylor (✉)

Department of Civil and Environmental Engineering, University of California,
Berkeley, USA
e-mail: rlt@ce.berkeley.edu

E. Artioli

Department of Civil Engineering and Computer Science, University of Rome
‘Tor Vergata’, Rome, Italy
e-mail: artioli@ing.uniroma2.it

The present contribution applies the VEM to the case of arbitrary order of accuracy in a general computational framework using the Finite Element Analysis Program (FEAP) [18]. The goal is hence to develop a numerical tool that retains the many features of an existing finite element platform for use in many problems with existing algorithms for arbitrary order of accuracy. The key idea of the method is to use a projection of the unknown field and relative gradient on a suitable polynomial space base and to treat such an approximation as it would be done for standard isoparametric finite element technology. In particular, the aim of the paper is to show that VEM structure can fit a general finite element coding setting and make use of the many available features of a general purpose FEM platform, for arbitrary “polynomial” order. Starting from this key point leads to use of classical tools of linear/nonlinear finite element analysis as shown by representative benchmarks presented in the numerical test section of the work.

2 Theory for C^0 Elements

For the two-dimensional theory, we consider a general polygon with n_e sides and vertices. In addition we assume each of the sides may have a k -order interpolation using nodes placed along the individual segments. For example for a quadratic order we use the two vertices and one mid-side node to define the behavior of the edge; for a cubic order we use the two end nodes and two nodes placed along the interior of the edge. Accordingly, each i -edge may be interpolated between vertex i and vertex $i + 1$ (assuming a numbering proceeding counter-clockwise around the element boundary) as¹:

$$\mathbf{X} = N_a^{(1)}(\xi) \tilde{\mathbf{X}}_a ; a = i, i + 1, c1, c2, \dots \quad (1)$$

where $N_a^{(1)}$ are one-dimensional Lagrange interpolation functions expressed in terms of the parent coordinate: $-1 \leq \xi \leq 1$ [19]. The interpolations are based on spacing of the nodal parent coordinates on the edge. These may be equally spaced, as is common for traditional isoparametric elements, or at the Gauss-Lobatto points as described in much of the VEM literature (e.g., the hitchhiker’s guide [4]).

The application of VEM is most easily implemented in existing finite element programs (e.g., *FEAP* [18]) by using a shape function form [19]. This allows for reuse of much of the theory in finite element references [19–21] and existing program modules for element residual and tangent operators without significant programming effort. In the classical finite element method we express the interpolations over the area (or volume) of an element in terms of two-dimensional shape functions which may be defined as

¹In this work the superscript on shape functions denotes the spatial dimension of the interpolation.

$$v(\mathbf{X}, t) = \varphi_a(\mathbf{X}) \tilde{v}_a(t) \tag{2}$$

where the *shape functions* $\varphi_a(\mathbf{X})$ satisfy the Kronecker property [19]

$$\varphi_a(\tilde{\mathbf{X}}_b) = \begin{cases} 1; & \text{if } a = b \\ 0; & \text{if } a \neq b \end{cases} \tag{3}$$

For general polygonal shaped elements, however, it is difficult to find closed form expressions for these shape functions. Instead in the VEM the displacement field is expressed by an approximation which we denote as ²

$$v(\mathbf{X}, t) \approx N_a^{(2)}(\mathbf{X}) \tilde{v}_a \tag{4}$$

which we assume also satisfy the Kronecker property. The above form is described by a projection of the classical functions onto the space of VEM functions. In addition, in VEM approximations to derivatives of the shape functions ϕ_a are obtained by a separate projection operation, that is

$$\frac{\partial v}{\partial X_j} = \frac{\partial \phi_a}{\partial X_j} \tilde{v}_a \approx \frac{\partial N_a^{(2)}}{\partial X_j} \tilde{v}_a \tag{5}$$

3 The Local Virtual Element Space

Consider a two dimension domain $\Omega \subset \mathbb{R}^2$ partitioned into a collection \mathcal{P}_h of non-overlapping polygons E , not necessarily convex: $\Omega = \cup_{E \in \mathcal{P}_h} E$.

For each polygon E , we will denote by V_i ($i = 1, \dots, n_e$) its vertices counterclockwise ordered, and by e_i the edge connecting V_i to V_{i+1} . For each polygon E we define a local finite element space $V_k(E)$. The local virtual element space $V_k(E)$ contains all polynomials of degree k plus other functions whose restriction on each edge is a polynomial of degree k . Any function $v_h \in V_k(E)$ satisfies the following properties:

- v_h is a polynomial of degree k on each edge e of E , i.e., $v_h|_e \in \mathcal{P}_k(e)$;
- v_h on ∂E is globally continuous, i.e., $v_h|_{\partial E} \in C^0(\partial E)$;
- Δv_h is a polynomial of degree $k - 2$ in E , i.e., $\Delta v_h \in \mathcal{P}_{k-2}(E)$.

It is proved [4] that $V_k(E)$ admits the following degrees of freedom:

- the value of v_h at the vertices of E ;
- the value of v_h at $k - 1$ internal points on each edge e [viz. Eq. (1)];
- the moments of v_h in E up to order $k - 2$:

$$\frac{1}{|E|} \int_E v_h m_\alpha, \quad \alpha = 1, \dots, n_{k-2}$$

²The superscript on shape functions denotes the spatial dimension of the interpolation.

where the scaled monomials m_α are defined in (8a) and $n_{k-2} = \dim \mathcal{P}_{k-2}(E)$.

As a consequence, the dimension of $V_k(E)$ is

$$\dim V_k(E) = n_e + n_e(k - 1) + n_{k-2} = n_e k + \frac{(k - 1)k}{2}.$$

4 Shape Function Approximation

We denote the approximate k -order shape functions of parameters in the VEM as

$$N_a^{(2)} = m_i^{(k)}(\hat{X}_j) P_{ia}^0 \tag{6a}$$

and those for the derivatives as

$$\frac{\partial N_a^{(2)}}{\partial X_j} = m_i^{(k-1)} P_{ija}^d \tag{6b}$$

In this regard, we again note that VEM differs from the usual isoparametric approach where the derivatives are deduced directly from the shape functions by appropriate use of the chain rule.

In the above we follow the practice of using scaled parameters to define the complete set of k -order polynomials for $m_i^{(k)}$. Accordingly, we let

$$\hat{X}_j = \frac{X_j - X_j^c}{h_d} \tag{7}$$

where X_j^c is a suitably chosen point in the interior and h_d is a measure of the diameter of the VEM. In the present work X_j^c is located at the centroid of the VEM element which simplifies some of the expressions. Thus, for a k order VEM in two-dimensions we use the set

$$\mathbf{m}^{(k)} = \left[1 \ \hat{X}_1 \ \hat{X}_2 \ \hat{X}_1^2 \ \hat{X}_1 \hat{X}_2 \ \hat{X}_2^2 \ \dots \ \hat{X}_2^k \right] \tag{8a}$$

for shape functions and for the derivatives the $k - 1$ set

$$\mathbf{m}^{(k-1)} = \left[1 \ \hat{X}_1 \ \hat{X}_2 \ \dots \ \hat{X}_2^{k-1} \right] \tag{8b}$$

4.1 Projector Development

A projection operator is introduced as follows:

$$P_{E,k}^0 : V_k(E) \longrightarrow \mathcal{P}_k(E)$$

For the sake of simplicity, the subscripts E and/or k will be omitted when no confusion can arise.

The operator P^0 is defined for every $v_h \in V_k(E)$ (up to a constant) by the following orthogonality condition:

$$\int_E \nabla p_k \cdot \nabla (P^0 v_h - v_h) = 0 \quad \text{for all } p_k \in \mathcal{P}_k(E). \tag{9}$$

For the projectors we follow the developments presented in the hitchhiker’s guide [4] and in Artioli et al. [16, 17]. We consider a VEM with n_e vertices and boundary segments.

The displacement projector, P_{ia}^0 , may be computed from

$$P_{ia}^0 = H_{il}^{-1} B_{la} \tag{10}$$

where

$$H_{1l} = \frac{1}{V_e} \sum_{a=1}^{n_e} m_l^k(\widehat{\mathbf{X}}_a) ; \quad k = 1$$

$$H_{1l} = \frac{1}{V_e} \int_{V_e} m_l^k d ; \quad k > 1 \tag{11a}$$

and

$$H_{il} = \int_{V_e} \frac{\partial m_i^k}{\partial \widehat{\mathbf{X}}_j} \frac{\partial m_l^k}{\partial \widehat{\mathbf{X}}_j} dV \tag{11b}$$

and

$$B_{1a} = \frac{1}{n_e} ; \quad a = 1, 2, 3 \quad ; \quad k = 1$$

$$B_{1a} = \begin{cases} 0 & ; a = 1, 2, \dots, \\ 1 & ; a = (k+1)(k+2)/2 \end{cases} \quad ; \quad k > 1 \tag{12}$$

$$B_{la} = \int_{V_e} \frac{\partial m_l^k}{\partial \widehat{\mathbf{X}}_j} m_i^k P_{ija}^d dV$$

Again details for the computation may be found in [4, 16].

Since neither the function v_h nor its gradient are explicitly computable in the element interior points, the method proceeds by introducing a projection operator $P_{E,k}^d$,

representing the approximated spatial gradient associated with the virtual displacement, defined as:

$$P^d_{E,k} : V_k(E) \longrightarrow \mathcal{P}_{k-1}(E) \tag{13}$$

Given $v_h \in V_k(E)$, such an operator P^d is defined as the unique function $P^d(v_h) \in \mathcal{P}_{k-1}(E)^2$ that satisfies the condition:

$$\int_E P^d(v_h) \cdot p_{k-1} = \int_E \nabla(v_h) \cdot p_{k-1}, \quad \forall p_{k-1} \in \mathcal{P}_{k-1}(E)^2. \tag{14}$$

This operator represents the best approximation of the spatial gradient (in the square integral norm) in the space of piecewise polynomials of degree $(k - 1)$. Although the functions in $V_k(E)$ are virtual, the right hand side in (14) (and thus the operator Π) turns out to be computable with simple calculations [16, 17].

The result for the derivative projector, P^d_{ija} , may be expressed by

$$P^d_{ija} = G_{il} P^s_{lja} \tag{15}$$

where

$$G_{ij} = \int_{V_e} m_i^{k-1} m_j^{k-1} dV \tag{16}$$

and for the boundary nodes

$$P^s_{lja} = \sum_{ne} \int_{\partial V_{ne}} m_l^{k-1} n_j N_a^{(1)}(\xi) dS \tag{17}$$

where n_j are components of the outward normal to the boundary and $N_a^{(1)}$ are one-dimensional shape functions that interpolate the boundary segment nodal vertex and (for $k > 1$) mid-edge parameters. In addition for $k > 1$ there are internal parameters required for these are computed as described in references [4, 16].

5 Quadratic VEM with Curved Edges

The use of VEM with interpolation along the edge permits the description of elements with curved sides. For example if we consider a quadratic VEM in two-dimensions the edges between two adjacent vertices will have 3-nodes: 2-vertex nodes and 1-node placed at the mid-side. The hexagonal VEM shown in Fig. 1a can have the top edge curved as shown in Fig. 1b. The integration of (17) may be conveniently carried out using a one-dimensional isoparametric interpolation of the edge using a Gauss quadrature [19].

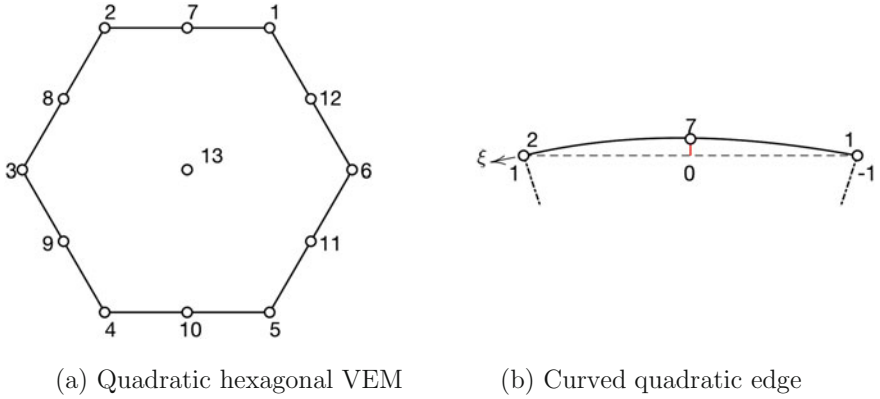


Fig. 1 Quadratic VEM with *curved* edges

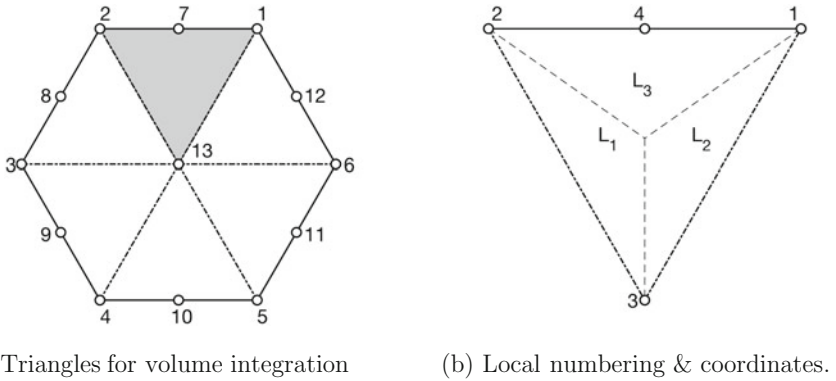


Fig. 2 Volume integration of a VEM

Volume integrations of a VEM is often computed by dividing the element into sub-triangles about a common node in the interior (viz. Fig. 2a) and using quadrature in terms of barycentric coordinates. If the barycentric coordinates on the triangle are denoted as L_a (Fig. 2b) and we let the position for L_3 be \mathbf{X}_3 (local numbering) then the interpolation for coordinates in the triangle may be described by

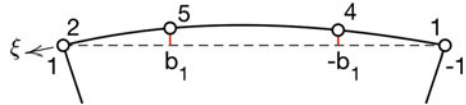
$$\mathbf{X} = N_1(L_a) \tilde{\mathbf{X}}_1 + N_2(L_a) \tilde{\mathbf{X}}_2 + L_3 \tilde{\mathbf{X}}_3 + N_4(L_a) \tilde{\mathbf{X}}_4 \tag{18a}$$

where

$$N_4(L_a) = 4 L_2 L_3 \tag{19}$$

and the shape functions for the vertex nodes are given by

Fig. 3 Curved edge boundary interpolation for cubic VEM



$$\begin{aligned}
 N_1(L_a) &= L_1 - \frac{1}{2} N_4(L_a) \\
 N_2(L_a) &= L_2 - \frac{1}{2} N_4(L_a) \\
 N_3(L_a) &= L_3
 \end{aligned}
 \tag{20}$$

Grouping the terms together gives the interpolation

$$\mathbf{X} = L_1 \tilde{\mathbf{X}}_1 + L_2 \tilde{\mathbf{X}}_2 + L_3 \tilde{\mathbf{X}}_3 + N_4(L_a) \left[\tilde{\mathbf{X}}_4 - \frac{1}{2} \tilde{\mathbf{X}}_1 - \frac{1}{2} \tilde{\mathbf{X}}_2 \right]
 \tag{21}$$

A similar process may be used to define higher order VEMs with curved edges. Figure 3 shows a cubic edge where the placements for the b_1 may be at either equal spaces as usually used in isoparametric finite element analysis or at Gauss-Lobatto points as in some previous VEM presentations. Currently, curved edges are used only at problem boundaries.

5.1 Element Development

The presentation of the shape functions in the previous sections and the procedure to integrate over element volumes using regular subregions, allows for a straight forward development of elements for small deformation problems in solid mechanics. In this case we can define the strains in terms of the approximate shape function derivatives given in (6b) as

$$\boldsymbol{\epsilon} = \begin{Bmatrix} \epsilon_{11} \\ \epsilon_{22} \\ 2\epsilon_{12} \end{Bmatrix} = \begin{bmatrix} \frac{\partial N_a^{(2)}}{\partial X_1} & 0 \\ 0 & \frac{\partial N_a^{(2)}}{\partial X_2} \\ \frac{\partial N_a^{(2)}}{\partial X_2} & \frac{\partial N_a^{(2)}}{\partial X_1} \end{bmatrix} \begin{Bmatrix} \tilde{u}_a \\ \tilde{v}_a \end{Bmatrix}
 \tag{22}$$

To account for near-incompressible constraints the three field mixed \mathbf{u} - p - θ approach may be used. [19, 20] For small strain problems in Cartesian coordinates (e.g., plane strain and plane stress) the VEM and mixed strain are of identical order and, consequently, no differences result between standard displacement and the mixed approach can be appreciated.

If we consider problems with an axisymmetric geometry the strains are given by

$$\boldsymbol{\varepsilon} = \begin{Bmatrix} \varepsilon_{rr} \\ \varepsilon_{zz} \\ \varepsilon_{\theta\theta} \\ 2\varepsilon_{rz} \end{Bmatrix} = \begin{bmatrix} \frac{\partial N_a^{(2)}}{\partial r} & 0 \\ 0 & \frac{\partial N_a^{(2)}}{\partial z} \\ \frac{N_a^{(2)}}{a} & 0 \\ \frac{r}{\partial z} & \frac{\partial N_a^{(2)}}{\partial r} \end{bmatrix} \begin{Bmatrix} \tilde{u}_a \\ \tilde{v}_a \end{Bmatrix} \tag{23}$$

where \tilde{u}_a and \tilde{v}_a are nodal displacements in the radial and axial direction, respectively. In this case we also need a projection for the shape functions $N_a^{(2)}$. For near incompressible behavior, a \mathbf{u} - p - θ mixed form may be introduced to retain constant volumetric behavior over each element. This may be introduced in the usual way as

$$\Pi_v = \int_E \hat{p} [\hat{\varepsilon}_v - \varepsilon_{ii}] r dr dz \tag{24}$$

in which we use

$$\begin{aligned} \hat{p} &= m_i^{(k)} \tilde{p}_a \\ \hat{\varepsilon}_v &= m_i^{(k)} \tilde{\varepsilon}_a \end{aligned} \tag{25}$$

Introducing the above into the weak form of a solid mechanics problem leads to the residual and tangent matrix for *the consistent part of the formulation*. In this form of the formulation we may introduce whatever constitution we want in the formulation and in the present work we utilize the material library from *FEAP* [18]. Note, however, that both consistency and stability are required for convergence of any formulation.

5.2 Stabilization

Except for simplex elements the above development for a VEM results in rank deficient tangent matrices and it is necessary to introduce proper stabilization terms. Here we use the approach described by Artioli et al. [16] where the stabilization tangent matrix for each component is given by

$$\mathbf{K}_{ab} = \tau \left[\delta_{ab} - D_{ai} d_{ij}^{-1} D_{bj} \right] \tag{26a}$$

where

$$d_{ij} = D_{ai} D_{aj} \tag{26b}$$

and τ is a parameter dependent on the consistent tangent matrix part. The basic stabilization matrix is for boundary nodes is given by

$$D_{ia} = m_i(\hat{X}_a) \quad (27a)$$

and for the internal node by

$$D_{ia} = \int_{V_e} m_i(\hat{X}) dV \quad (27b)$$

In previous presentations on elasticity the parameter τ is recommended to be selected a one-half the trace of the consistent tangent matrix. In the present work, the choice of the τ parameter for problems which may have near incompressible behavior is computed from the trace of the consistent part of the stiffness scaled by the ratio of the shear modulus to the bulk modulus of an isotropic material. Accordingly, we use

$$\tau = \frac{3}{4} \text{tr}(\mathbf{K}) \frac{1 - 2\nu}{1 + \nu} \quad (28)$$

For inelastic material we replace the trace of the stiffness by that from the previous time step to ensure that quadratic convergence occurs in our Newton algorithm.

6 Examples

The formulation for k order 1 and 2 VEM elements has been implemented as a module in the general purpose finite element program *FEAP* [18]. Element formulations for displacement and mixed \mathbf{u} - p - θ (viz. Zienkiewicz et al. [20]) are considered. The implementation has access to the material library which permits the consideration of elastic, visco-elastic and elasto-plastic models. All solution and graphics features are also available so that mesh, displacement and stress contours may be displayed.

6.1 Example: Tension Strip with Slot

Stabilization Parameter Verification

To verify the selection of our scaling of the stabilization parameter τ we consider an axisymmetric behavior for the tension strips shown in Fig. 4 with all straight edges of the slotted tensions strip quadrant restrained in the normal direction. The top edge is then subjected to a displacement of 0.002 and the total reaction force measured. The linear elastic properties of the material are selected to give a shear modulus (μ) equal to 1000 and different Poisson ratios between 0.45 and 0.4999995 are considered. Table 1 presents the results for the two stabilizing criteria for a $k = 1$ VEM and compare results to a mixed Q1P0 finite element solution. All subsequent VEM analyses use the scaled Poisson ratio value.

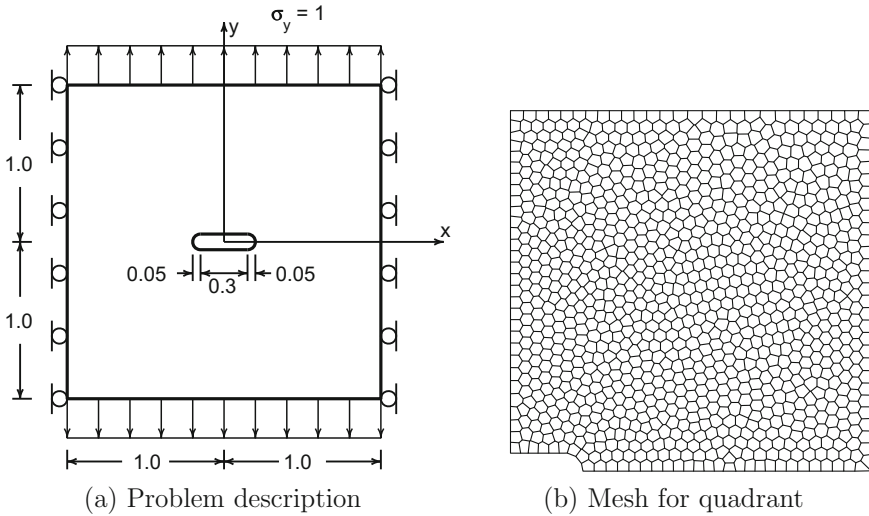


Fig. 4 Region and mesh used for slotted tension strip

Table 1 Verification on choice of stabilization parameter

ν	Total Load		
	$\frac{1}{2} \text{tr}(\mathbf{K})$	$\frac{3(1-2\nu)}{4(1+\nu)} \text{tr}(\mathbf{K})$	Q1P0
0.4500000	1.0766E + 01	1.0733E + 01	1.0740E + 01
0.4950000	9.0359E + 01	8.2794E + 01	8.3322E + 01
0.4995000	7.6399E + 02	3.1542E + 02	3.2342E + 02
0.4999500	7.1749E + 03	4.4037E + 02	4.5616E + 02
0.4999950	7.1128E + 04	4.5855E + 02	4.7570E + 02
0.4999995	7.1058E + 05	4.6064E + 02	4.7775E + 02

Elasto-plastic Tension Strip

As a second example we consider the solution of the tension strip shown in Fig. 4 for both plane and axisymmetric models that employ an elasto-plastic material model with isotropic linear hardening. For this analysis we set the properties to: $E = 2500$, $\nu = 0.25$, $\sigma_y = 5$, $H_{iso} = 5$. The load-displacement curve for the two cases is shown in Fig. 5a, b. Results were also verified by comparison with a solution using Q1P0 elements. Contours for the Mises stress are shown in Fig. 5c–f for the four cases considered. The stress contours for the VEM elements are computed using a local least squares averaging scheme [22]. For the $k = 1$ models the stress over each element is projected onto constants and averaged at the nodes. For the $k = 2$ elements the stress over each sub-triangle of the element is assumed linear and these are averaged at the nodes. As observed in Fig. 5 the results for the different schemes are smooth considering the coarse nature of the mesh around the slot.

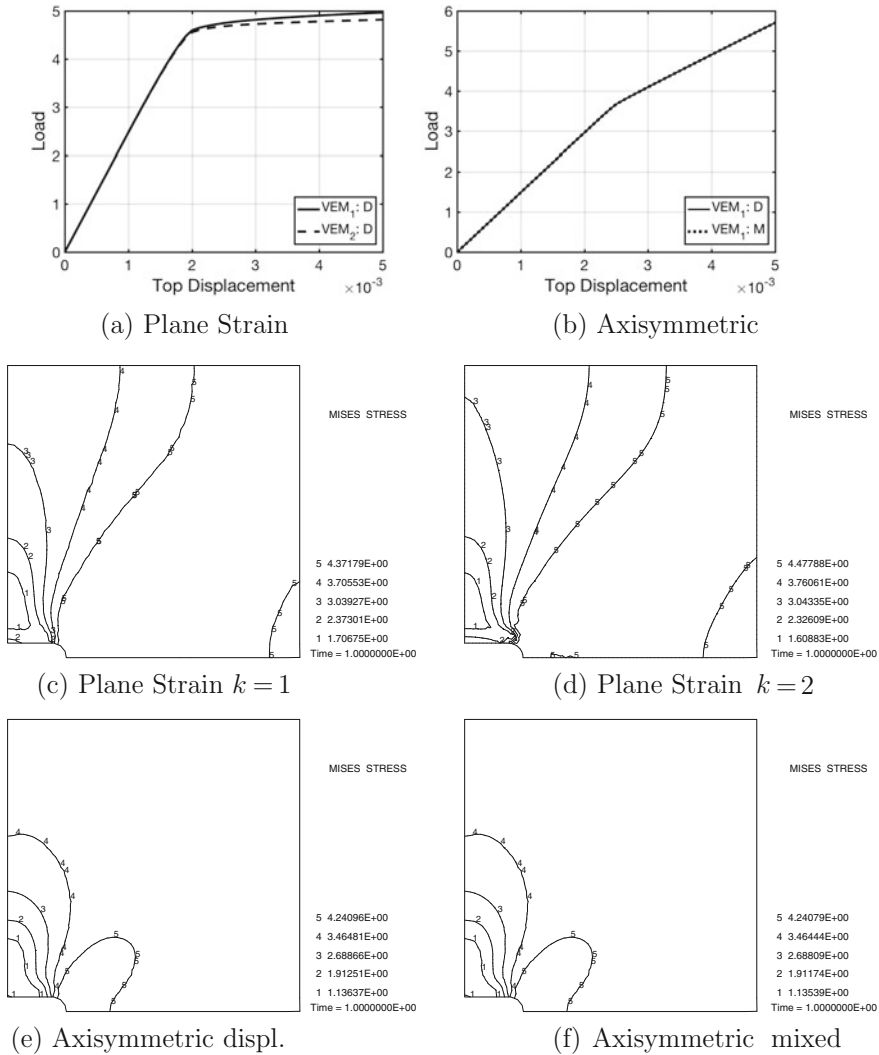
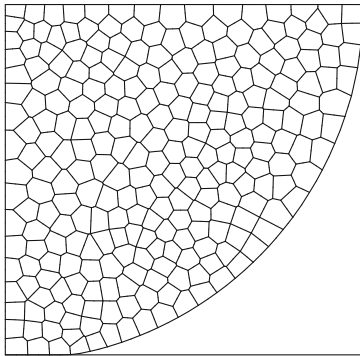


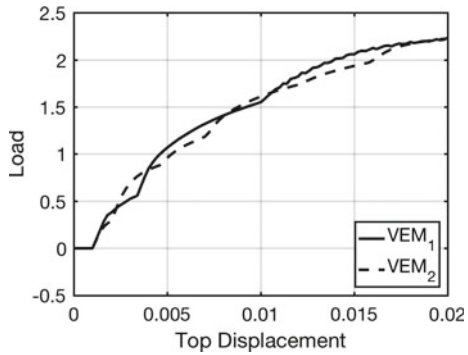
Fig. 5 a–b Load-displacement response for plane strain and axisymmetric, elasto-plastic strip with a slot. c–f Mises stress contours

6.2 Contact of a Circular Disk on a Rigid Surface

As a last example we consider the behavior of $k = 1$ and $k = 2$ VEM formulations for a circular disk with unit radius that is pressed into a rigid surface. One quadrant of the disk is meshed for $k = 1$ and $k = 2$ VEM elements and has an initial gap of 0.002 units. The material properties are elasto-plastic with the same values as for the slotted strip. A uniform displacement at the top of the disk quadrant is applied in



(a) Deformed mesh for quadrant



(b) Load-Displacement

Fig. 6 Region and mesh used for slotted tension strip

equal steps to a maximum value of 0.1 units. The final deformed mesh for the $k = 2$ discretization is shown in Fig. 6a and the load-displacement result for both cases in Fig. 6b. The contact constraint is enforced at each node using a Lagrange multiplier approach (this solution method is valid since the master contact surface is rigid). The use of quadratic elements smooths the result, primarily due to the added number of nodes on the boundary but also due to curvature of the edge which gives a more accurate modeling of the approach.

7 Closure

In this presentation we have formulated the two-dimensional virtual element method in terms of shape functions that permit the straight forward coding of the consistent part stiffness and residual for small strain inelastic behavior. The approach also allows for curved edges on elements with quadratic and higher order forms. The approach has been implemented in the general purpose finite element analysis system *FEAP* and allows for solution of both steady state and transient analyses. The methodology has been demonstrated for elasto-plastic behavior of plane strain and axisymmetric problems including a simple case of contact on a rigid surface. With a shape function approach it is possible to easily extend the solution to problems in other areas, including for example thermal, seepage, and fluid forms which utilize C^0 interpolations.

References

1. L. Beirão da Veiga, F. Brezzi, A. Cangiani, G. Manzini, L.D. Marini, A. Russo, Basic principles of virtual element methods. *Math. Models Methods Appl. Sci.* **23**(1), 199–214 (2013)
2. L. Beirão da Veiga, F. Brezzi, L.D. Marini, Virtual elements for linear elasticity problems. *SIAM J. Numer. Anal.* **51**(2), 794–812 (2013)
3. F. Brezzi, L.D. Marini, Virtual element methods for plate bending problems. *Comput. Methods Appl. Mech. Eng.* **253**, 455–462 (2013)
4. L. Beirão da Veiga, F. Brezzi, L.D. Marini, A. Russo, The hitchhiker’s guide to the virtual element method. *Math. Models Methods Appl. Sci.* **24**(8), 1541–1573 (2014)
5. B. Ahmad, A. Alsaedi, F. Brezzi, L.D. Marini, A. Russo, Equivalent projectors for virtual element methods. *Comput. Math. Appl.* **66**, 376–391 (2013)
6. L. Beirão da Veiga, C. Lovadina, D. Mora, A virtual element method for elastic and inelastic problems on polytope meshes. *Comput. Methods Appl. Mech. Eng.* **295**, 327–346 (2015)
7. L. Beirão da Veiga, F. Brezzi, L.D. Marini, A. Russo, Virtual element method for general second-order elliptic problems on polygonal meshes. *Math. Models Methods Appl. Sci.* **24**(4), 729–750 (2016)
8. M.F. Benedetto, S. Berrone, S. Pieraccini, S. Scialò, The virtual element method for discrete fracture network simulations. *Comput. Methods Appl. Mech. Eng.* **280**, 135–156 (2014)
9. M.F. Benedetto, S. Berrone, A. Borio, S. Pieraccini, S. Scialò, A hybrid mortar virtual element method for discrete fracture network simulations. *J. Comput. Phys.* **306**, 148–166 (2016)
10. F. Brezzi, R.S. Falk, L.D. Marini, Basic principles of mixed virtual element methods. *ESAIM. Math. Model. Numer. Anal.* **48**, 1227–1240 (2014)
11. A.L. Gain, C. Talischi, G.H. Paulino, The virtual element method for three-dimensional linear elasticity problems on arbitrary polyhedral meshes. *Comput. Methods Appl. Mech. Eng.* **282**, 132–160 (2014)
12. D. Mora, G. Rivera, R. Rodríguez, A virtual element method for the Steklov eigenvalue problem. *Math. Models Methods Appl. Sci.* **25**(8), 1421–1445 (2015)
13. I. Perugia, P. Pietra, A. Russo, A plane wave virtual element method for the helmholtz problem. *ESAIM. Math. Modell. Numer. Anal.* **50**, 783–808 (2016)
14. P. Wriggers, W.T. Rust, B.D. Reddy, A virtual element method for contact. *Comput. Mech.* **58**, 1039–1050 (2017)
15. G. Vacca, L. Beirão da Veiga, Virtual element methods for parabolic problems on polygonal meshes. *Numer. Methods Partial Differ. Equ.* **31**, (2015). doi:[10.1002/num.21982](https://doi.org/10.1002/num.21982)
16. E. Artioli, L. Beirão da Veiga, C. Lovadina, E. Sacco, Arbitrary order 2D virtual elements for polygonal meshes: Part I, elastic problem. *Comput. Mech.* (2017). doi:[10.1007/s00466-017-1404-5](https://doi.org/10.1007/s00466-017-1404-5)
17. E. Artioli, L. Beirão da Veiga, C. Lovadina, E. Sacco, Arbitrary order 2D virtual elements for polygonal meshes: Part II, inelastic problem. *Comput. Mech.* (2017). doi:[10.1007/s00466-017-1429-9](https://doi.org/10.1007/s00466-017-1429-9)
18. R.L. Taylor, *FEAP - A Finite Element Analysis Program, User Manual*(University of California, Berkeley), <http://projects.ce.berkeley.edu/feap/>
19. O.C. Zienkiewicz, R.L. Taylor, J.Z. Zhu, *The Finite Element Method: Its Basis and Fundamentals*, 7th edn. (Elsevier, Oxford, 2013)
20. O.C. Zienkiewicz, R.L. Taylor, D. Fox, *The Finite Element Method for Solid and Structural Mechanics*, 7th edn. (Elsevier, Oxford, 2013)
21. O.C. Zienkiewicz, R.L. Taylor, P. Nithiarasu, *The Finite Element Method for Fluid Dynamics*, 7th edn. (Elsevier, Oxford, 2014)
22. S. Govindjee, J. Strain, T.J. Mitchell, R.L. Taylor, Convergence of an efficient local least-squares fitting method for bases with compact support. *Comput. Methods Appl. Mech. Eng.* **213–216**, 84–92 (2012). doi:[10.1016/j.cma.2011.11.017](https://doi.org/10.1016/j.cma.2011.11.017)

Improved Contact Stress Recovery for Mortar-Based Contact Formulations

Christoph Wilking, Manfred Bischoff and Ekkehard Ramm

1 Introduction

In a variety of engineering applications knowledge of accurate contact stress is of great importance. The contact stress dependency of the wear depth in wear problems is a typical example. A second example are thermomechanical problems, where the contact heat transfer coefficient depends on the contact stress. In the present contribution the contact stress calculation for dual mortar formulations is addressed in a large deformation setting. Lagrange multipliers are used to enforce the contact constraints and appear as additional unknowns in the formulation. If the Lagrange multipliers are discretised by so-called dual shape functions they can be condensed from the global system of equations. This aspect makes dual mortar methods more efficient than standard mortar formulation without using dual shape functions. Originally the dual shape functions were presented in the context of mortar methods by Wohlmuth [21]. Applications to contact problems can be found for example in [1, 10, 13, 18]. An overview on dual mortar methods for contact is given in [16]. Since the Lagrange multiplier is identified as the negative contact stress, the choice of its shape functions affects the contact stress approximation. Linear dual shape functions yield discontinuous contact stresses which are physically not meaningful. In Hüeber et al. [8] an additional post-processing is suggested leading to a continuous contact stress. It can be shown that the corresponding contact stress is less accurate than the one resulting from a standard mortar formulation. In this

C. Wilking (✉) · M. Bischoff · E. Ramm
Institut für Baustatik und Baudynamik, Pfaffenwaldring 7,
70550 Stuttgart, Germany
e-mail: wilking@ibb.uni-stuttgart.de

M. Bischoff
e-mail: bischoff@ibb.uni-stuttgart.de

E. Ramm
e-mail: ramm@ibb.uni-stuttgart.de

contribution a new post-processing procedure is presented to get more accurate contact stresses for a dual mortar formulation. A variety of numerical examples demonstrate the advantage of this new approach.

2 Problem Description

This section provides the main equations for tied contact problems and unilateral contact problems between two solid bodies in 2d and 3d. The two bodies are described in the reference and current configuration by the open sets $\Omega^{(\alpha)}$ and $\Omega_t^{(\alpha)}$, where the superscript $\alpha = 1, 2$ identifies the involved bodies. The boundaries $\partial\Omega^{(\alpha)}$ of the bodies in the reference configuration are divided into three non-overlapping sets: the boundaries $\Gamma_N^{(\alpha)}$ and $\Gamma_D^{(\alpha)}$ with prescribed Neumann and Dirichlet boundary conditions, respectively, and the potential contact boundaries $\Gamma_c^{(\alpha)}$. The corresponding boundaries in the current configuration are denoted by $\gamma_N^{(\alpha)}$, $\gamma_D^{(\alpha)}$ and $\gamma_c^{(\alpha)}$, respectively. As common in the contact literature $\Gamma_c^{(1)}$, $\gamma_c^{(1)}$ are termed slave surfaces and $\Gamma_c^{(2)}$, $\gamma_c^{(2)}$ master surfaces. The current position $\mathbf{x}^{(\alpha)}$ of a material point of domain $\Omega_t^{(\alpha)}$ is expressed by the position $\mathbf{X}^{(\alpha)}$ of the material point in the reference configuration and its displacement $\mathbf{u}^{(\alpha)}$:

$$\mathbf{x}^{(\alpha)}(\mathbf{X}^{(\alpha)}, t) = \mathbf{X}^{(\alpha)} + \mathbf{u}^{(\alpha)}(\mathbf{X}^{(\alpha)}, t). \quad (1)$$

The gap g_n between each point $\mathbf{x}^{(1)}$ of $\gamma_c^{(1)}$ and the master surface in the direction of the surface normal \mathbf{n}_c at $\mathbf{x}^{(1)}$ is given by

$$g_n(\mathbf{x}^{(1)}) = -\mathbf{n}_c(\mathbf{x}^{(1)}) \cdot (\mathbf{x}^{(1)} - \bar{\mathbf{x}}^{(2)}(\mathbf{x}^{(1)})). \quad (2)$$

Herein, $\bar{\mathbf{x}}^{(2)}(\mathbf{x}^{(1)})$ is the point on the master surface which is found from the projection of $\mathbf{x}^{(1)}$ onto $\gamma_c^{(2)}$ in the direction of \mathbf{n}_c . If the gap is zero at one point the bodies are in contact leading to a contact stress $\mathbf{t}_c^{(1)}$, which is decomposed into its components in normal and tangential direction:

$$\mathbf{t}_c^{(1)} = t_n \mathbf{n}_c + \mathbf{t}_\tau, \quad t_n = \mathbf{t}_c^{(1)} \cdot \mathbf{n}_c. \quad (3)$$

The tangential contact stress \mathbf{t}_τ is zero for unilateral contact, since frictionless contact is assumed in this contribution. Equilibrium in the contact zone renders $\mathbf{t}_c^{(2)} = -\mathbf{t}_c^{(1)}$. From (2) and (3) the Hertz-Signorini-Moreau conditions for frictionless unilateral contact are given by

$$g_n \geq 0, \quad t_n \leq 0, \quad g_n t_n = 0. \quad (4)$$

For tied contact problems the contact condition is

$$\mathbf{g} = \mathbf{0}, \quad \text{with} \quad \mathbf{g} = (\mathbf{x}^{(1)} - \bar{\mathbf{x}}^{(2)}(\mathbf{x}^{(1)})). \quad (5)$$

Since only quasi-static problems are analysed in this contribution, the boundary value problem for each body reads

$$\begin{aligned} \text{Div } \mathbf{P}^{(\alpha)} + \rho_0^{(\alpha)} \mathbf{b}^{(\alpha)} &= \mathbf{0} && \text{in } \Omega^{(\alpha)}, \\ \mathbf{u}^{(\alpha)} &= \hat{\mathbf{u}}^{(\alpha)} && \text{on } \Gamma_{\text{D}}^{(\alpha)}, \\ \mathbf{P}^{(\alpha)} \mathbf{N}^{(\alpha)} &= \hat{\mathbf{t}}^{(\alpha)} && \text{on } \Gamma_{\text{N}}^{(\alpha)}, \\ \mathbf{P}^{(\alpha)} \mathbf{N}^{(\alpha)} &= \mathbf{t}_c^{(\alpha)} && \text{on } \Gamma_c^{(\alpha)}, \end{aligned} \quad (6)$$

where ρ_0 is the density in the reference configuration, \mathbf{b} is the body load, \mathbf{N} is the normal on $\Gamma_{\text{N}/c}$ and $\hat{\mathbf{T}}$ and $\hat{\mathbf{u}}$ are the prescribed traction and displacement, respectively. \mathbf{P} is the first Piola-Kirchhoff stress tensor, which is related to the second Piola-Kirchhoff stress tensor \mathbf{S} and the deformation gradient \mathbf{F} by $\mathbf{P} = \mathbf{F}\mathbf{S}$. For the St. Venant-Kirchhoff material used in this contribution via $\mathbf{S} = \mathbb{C} : \mathbf{E}$ the second Piola-Kirchhoff stress tensor \mathbf{S} is related to Green-Lagrange strain \mathbf{E} and the fourth-order elasticity tensor \mathbb{C} .

Here, the Lagrange multiplier method is used to enforce the unilateral contact constraints (4) and the tied contact constraints (5). The additional unknown Lagrange multiplier λ can be identified as the negative contact stress of the slave surface, thus

$$\mathbf{t}_c^{(1)} = -\lambda. \quad (7)$$

With this relation the virtual work principle is formulated as basis for the finite element formulation. Using admissible spaces for the unknown displacement field and the Lagrange multiplier field and their variations the virtual work principle is defined as

$$\delta \Pi = \sum_{\alpha=1}^2 \left(\delta \Pi_{\text{int}}^{(\alpha)} - \delta \Pi_{\text{ext}}^{(\alpha)} \right) + \underbrace{\int_{\gamma_c^{(1)}} \lambda \cdot (\delta \mathbf{u}^{(1)} - \delta \bar{\mathbf{u}}^{(2)}) \, da}_{\delta \Pi_c} = 0. \quad (8)$$

Equation (8) is the weak formulation of the strong boundary value problem given in (6). The first part of (8) represents the common internal and external virtual work of both bodies. With $\delta \Pi_c$ the virtual contact work is introduced which can be written as a single integral over the slave surface due to $\mathbf{t}_c^{(2)} = -\mathbf{t}_c^{(1)}$. The bar shown in $\delta \bar{\mathbf{u}}^{(2)}$ indicates the necessity of a projection for quantities defined on the master surface.

The solution of (8) for admissible \mathbf{u} and λ has to be found on condition that the constraints are satisfied. The constraints (4) for unilateral contact can be stated as variational inequality, see [7], and are given weakly as

$$\int_{\gamma_c^{(1)}} g_n (\delta \lambda_n - \lambda_n) \, da \geq 0. \quad (9)$$

The normal components $\delta\lambda_n$ and λ_n in (9) are derived analogously to (3). For tied contact the weak form of constraint (5) is defined as

$$\int_{\gamma_c^{(1)}} \delta\lambda \cdot (\mathbf{u}^{(1)} - \mathbf{u}^{(2)}) \, da = 0. \quad (10)$$

3 Spatial Finite Element Discretisation

The weak formulation of the contact problem (8)–(10) is now used to derive the mortar finite element formulation of the problem. For this the geometry, the displacement field and the virtual displacement field are discretised with standard C^0 -continuous Lagrange shape functions N_I :

$$\begin{aligned} \mathbf{X} &\approx \mathbf{X}^h(\boldsymbol{\xi}) = \sum_{I=1}^{n_{\text{nd}}} N_I(\boldsymbol{\xi}) \mathbf{X}_I, & \mathbf{u} &\approx \mathbf{u}^h(\boldsymbol{\xi}) = \sum_{I=1}^{n_{\text{nd}}} N_I(\boldsymbol{\xi}) \mathbf{d}_I. \\ \delta\mathbf{u} &\approx \delta\mathbf{u}^h(\boldsymbol{\xi}) = \sum_{I=1}^{n_{\text{nd}}} N_I(\boldsymbol{\xi}) \delta\mathbf{d}_I. \end{aligned} \quad (11)$$

Herein, n_{nd} is the number of finite element nodes, $\boldsymbol{\xi}$ are the natural coordinates of the elements, \mathbf{d}_I is the vector of discrete displacements of node I and $\delta\mathbf{d}_I$ the virtual counterpart. In this contribution solely linear approximation spaces are considered, thus bi-linear quadrilateral elements for 2d problems and tri-linear hexahedral elements for 3d problems are used.

With the quantities of (11) the discretised internal and external virtual work can be given concisely by

$$\delta\Pi_{\text{int}} = \sum_{\alpha=1}^2 \delta\Pi_{\text{int}}^{(\alpha)} \approx \delta\mathbf{d}^T \mathbf{f}_{\text{int}}(\mathbf{d}), \quad \delta\Pi_{\text{ext}} = \sum_{\alpha=1}^2 \delta\Pi_{\text{ext}}^{(\alpha)} \approx \delta\mathbf{d}^T \mathbf{f}_{\text{ext}}. \quad (12)$$

$\mathbf{f}_{\text{int}}(\mathbf{d})$ is the global vector of non-linear internal forces and \mathbf{f}_{ext} is the global vector of external forces, which is assumed to be independent of \mathbf{d} .

Similarly the unknown Lagrange multiplier field and its virtual counterpart are discretised using a Bubnov-Galerkin method:

$$\lambda \approx \lambda^h(\boldsymbol{\xi}) = \sum_{I=1}^{n_s} \Xi_I^{(1)}(\boldsymbol{\xi}) \mathbf{z}_I, \quad \delta\lambda \approx \delta\lambda^h(\boldsymbol{\xi}) = \sum_{I=1}^{n_s} \Xi_I^{(1)}(\boldsymbol{\xi}) \delta\mathbf{z}_I, \quad (13)$$

where n_s is the number of slave nodes, \mathbf{z} the global vector of nodal Lagrange multiplier values and Ξ are the shape functions for the Lagrange multiplier field. The latter will be specified in Sects. 3.1.1 and 3.1.2. Inserting (11) and (13) into $\delta\Pi_c$ yields the discretised virtual contact work:

$$\delta \Pi_c^h = \sum_{l=1}^{n_s} \sum_{K=1}^{n_s} \mathbf{z}_l \cdot \underbrace{\int_{\gamma_c^h} \Xi_I^{(1)} N_K^{(1)} da}_{D_{IK}} \delta \mathbf{d}_K^{(1)} - \sum_{l=1}^{n_s} \sum_{L=1}^{n_m} \mathbf{z}_l \cdot \underbrace{\int_{\gamma_c^h} \Xi_I^{(1)} \bar{N}_L^{(2)} da}_{M_{IL}} \delta \mathbf{d}_L^{(2)}. \quad (14)$$

Herein, n_m and n_s are the number of master and slave nodes, γ_c^h is the discrete representation of $\gamma_c^{(1)}$. D_{IK} as well as M_{IL} are so-called mortar integrals. The evaluation of the mortar integrals is a crucial step of mortar methods and described in detail in [3, 19]. The mortar integrals are elements of the mortar matrices \mathbf{D} and \mathbf{M} , which can be given as nodal blocks:

$$\mathbf{D}[I, K] = D_{IK} \mathbf{I}_{n_d}, \quad \mathbf{M}[I, L] = M_{IL} \mathbf{I}_{n_d}, \quad (I, K) = 1, \dots, n_s, \quad L = 1, \dots, n_m. \quad (15)$$

For a concise notation of the discrete virtual contact work three main sets of nodes are established: set \mathcal{N} contains all nodes which are not part of the slave or master contact boundary, set \mathcal{M} contains all nodes of the master side and set \mathcal{S} contains all nodes of the slave side. The latter is further subdivided into \mathcal{A} , including all active slave nodes, and the set \mathcal{I} of all remaining slave nodes. With this subdivision the global vectors \mathbf{d} and $\delta \mathbf{d}$ read

$$\mathbf{d} = [\mathbf{d}_{\mathcal{N}} \quad \mathbf{d}_{\mathcal{M}} \quad \mathbf{d}_{\mathcal{S}}]^T, \quad \delta \mathbf{d} = [\delta \mathbf{d}_{\mathcal{N}} \quad \delta \mathbf{d}_{\mathcal{M}} \quad \delta \mathbf{d}_{\mathcal{S}}]^T \quad (16)$$

and the discrete virtual contact work can be written concisely:

$$\delta \Pi_c^h = \delta \mathbf{d}_{\mathcal{S}}^T \mathbf{D}^T \mathbf{z} - \delta \mathbf{d}_{\mathcal{S}}^T \mathbf{M}^T \mathbf{z} = \delta \mathbf{d}^T \underbrace{\begin{bmatrix} \mathbf{0} \\ -\mathbf{M}^T \\ \mathbf{D}^T \end{bmatrix}}_{\mathbf{B}_c^T} \mathbf{z} = \delta \mathbf{d}^T \mathbf{f}_c(\mathbf{d}, \mathbf{z}). \quad (17)$$

With \mathbf{f}_c being the vector of discrete contact forces.

Using the discretised quantities from (12) and (17) to discretise the entire virtual work $\delta \Pi$ from Eq. (8) the equilibrium equation can be written as

$$\mathbf{r}(\mathbf{d}, \mathbf{z}) = \mathbf{f}_{\text{int}}(\mathbf{d}) - \mathbf{f}_{\text{ext}} + \mathbf{f}_c(\mathbf{d}, \mathbf{z}). \quad (18)$$

For tied contact problems \mathbf{f}_c is independent of the displacement and the entire non-linear system of equation is

$$\mathbf{r}(\mathbf{d}, \mathbf{z}) = \mathbf{f}_{\text{int}}(\mathbf{d}) - \mathbf{f}_{\text{ext}} + \mathbf{f}_c(\mathbf{z}) = \mathbf{0}, \quad \mathbf{B}_c \mathbf{d} = \mathbf{0}, \quad (19)$$

where the second equation represents the discrete contact constraints for tied contact problems, see e.g. [12].

To formulate the non-linear system of equations for unilateral contact, firstly the discrete weighted gap

$$\tilde{g}_I = \int_{\gamma_c^h} \Xi_I g_n^h da \quad (20)$$

is introduced. In (20) g_n^h is the discretisation of the gap defined in (2) and Ξ_I are the shape functions of the Lagrange multiplier. With the discrete weighted gap \tilde{g}_I the non-linear system of equations for unilateral contact reads

$$\mathbf{r}(\mathbf{d}, \mathbf{z}) = \mathbf{f}_{\text{int}}(\mathbf{d}) - \mathbf{f}_{\text{ext}} + \mathbf{f}_c(\mathbf{d}, \mathbf{z}) = \mathbf{0}, \quad (21)$$

$$\tilde{g}_I \geq 0, \quad z_{nI} \geq 0, \quad z_{nI} \tilde{g}_I = 0, \quad (22)$$

$$\mathbf{z}_\tau = \mathbf{0}. \quad (23)$$

Herein, \mathbf{z} is decomposed into z_n and \mathbf{z}_τ analogously to (3). Equation (22) are a point-wise representation of the weak contact constraints for frictionless unilateral contact from (9). The equivalence of the weak contact constraints and the pointwise constraints is shown in detail in [7].

The tied contact problem (19) is solved by Newton's method. One way to solve the non-linear inequalities of the unilateral contact problem given in (21)–(23) is by using a non-smooth variant of Newton's method, see e.g. [14] for a comprehensive explanation.

3.1 Discretisation of the Lagrange Multiplier Field

So far the discretisation space of the Lagrange multiplier field is not specified. Within this section two different shape functions Ξ for the approximations in (13) are considered and thereby two different mortar methods are introduced: the standard mortar method and the dual mortar method.

3.1.1 Standard Lagrange Shape Functions

In this contribution it is referred to as a standard mortar method if $\Xi = N$, i.e. if standard linear Lagrange shape functions are used for the discretisation of the Lagrange multiplier field. Thus, the Lagrange multiplier field is approximated by the same shape functions as the displacement field and the geometry. For 2d problems the shape functions used for the 2-node slave elements are

$$N_1^{(1)}(\xi) = \frac{1}{2}(1 - \xi), \quad N_2^{(1)}(\xi) = \frac{1}{2}(1 + \xi). \quad (24)$$

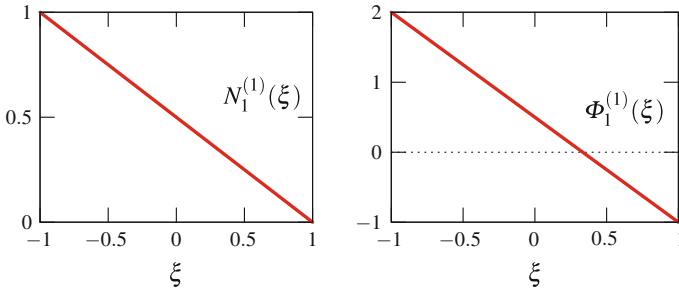


Fig. 1 Standard shape function (*left*) and dual shape function (*right*) in natural coordinates shown for node 1 of a slave element

$N_1^{(1)}(\xi)$ is shown to the left in Fig. 1. In 3d the slave elements are 4-node quadrilaterals. The well-known definition of their shape functions is skipped here for the sake of brevity.

3.1.2 Dual Shape Functions

Alternatively so-called dual shape functions Φ can be used to discretise the Lagrange multiplier field. In the framework of mortar methods dual shape functions were applied for the first time in [21]. Early applications to mortar methods for unilateral contact can be found in [9, 10]. The underlying mortar method is called dual mortar method in this contribution whenever dual shape functions are used to discretise the Lagrange multipliers, thus $\Xi = \Phi$.

Dual shape functions have some advantages compared to standard shape functions which emanate from their fulfilment of the biorthogonality relation

$$\int_{\gamma_{c,e}^{(1)}} \Phi_I(\xi) N_K(\xi) da = \delta_{IK} \int_{\gamma_{c,e}^{(1)}} N_K(\xi) da, \quad \delta_{IK} = \begin{cases} 1 & \text{for } I = K, \\ 0 & \text{for } I \neq K. \end{cases} \quad (25)$$

As a result the mortar integral D_{IK} , defined in (14), simplifies to $D_{KK} = \int_{\gamma_c^h} N_K^{(1)} da$, i.e. the mortar matrix \mathbf{D} , given in (15), becomes a diagonal matrix. As a consequence the contact constraints can be locally satisfied, allowing an efficient condensation of the Lagrange multiplier from the global system of equations, see [20] for details. Thus the formulation has only as many degrees of freedom as if contact would not be present, making the dual mortar method more efficient than the standard mortar method.

The condensation of the Lagrange multiplier can easily be shown by investigating the structure of the linearisation of (21)–(23):

$$\begin{bmatrix}
\mathbf{K}_{\mathcal{N}\mathcal{N}} & \mathbf{K}_{\mathcal{N}\mathcal{M}} & \mathbf{K}_{\mathcal{N}\mathcal{I}} & \mathbf{K}_{\mathcal{N}\mathcal{A}} & \mathbf{0} & \mathbf{0} \\
\mathbf{K}_{\mathcal{M}\mathcal{N}} & \tilde{\mathbf{K}}_{\mathcal{M}\mathcal{M}} & \tilde{\mathbf{K}}_{\mathcal{M}\mathcal{I}} & \tilde{\mathbf{K}}_{\mathcal{M}\mathcal{A}} & -\mathbf{M}_{\mathcal{I}}^T & -\mathbf{M}_{\mathcal{A}}^T \\
\mathbf{K}_{\mathcal{I}\mathcal{N}} & \tilde{\mathbf{K}}_{\mathcal{I}\mathcal{M}} & \tilde{\mathbf{K}}_{\mathcal{I}\mathcal{I}} & \tilde{\mathbf{K}}_{\mathcal{I}\mathcal{A}} & \mathbf{D}_{\mathcal{I}\mathcal{I}}^T & \mathbf{0} \\
\mathbf{K}_{\mathcal{A}\mathcal{N}} & \tilde{\mathbf{K}}_{\mathcal{A}\mathcal{M}} & \tilde{\mathbf{K}}_{\mathcal{A}\mathcal{I}} & \tilde{\mathbf{K}}_{\mathcal{A}\mathcal{A}} & \mathbf{0} & \mathbf{D}_{\mathcal{A}\mathcal{A}}^T \\
\mathbf{0} & \mathbf{0} & \mathbf{0} & \mathbf{0} & \mathbf{I}_{\mathcal{I}} & \mathbf{0} \\
\mathbf{0} & \mathbf{G}_{\mathcal{M}} & \mathbf{G}_{\mathcal{I}} & \mathbf{G}_{\mathcal{A}} & \mathbf{0} & \mathbf{0} \\
\mathbf{0} & \mathbf{0} & \mathbf{L}_{\mathcal{I}} & \mathbf{L}_{\mathcal{A}} & \mathbf{0} & \mathbf{T}_{\mathcal{A}}
\end{bmatrix}
\begin{bmatrix}
\Delta \mathbf{d}_{\mathcal{N}} \\
\Delta \mathbf{d}_{\mathcal{M}} \\
\Delta \mathbf{d}_{\mathcal{I}} \\
\Delta \mathbf{d}_{\mathcal{A}} \\
\mathbf{z}_{\mathcal{I}} \\
\mathbf{z}_{\mathcal{A}}
\end{bmatrix}
= -
\begin{bmatrix}
\mathbf{r}_{\mathcal{N}} \\
\tilde{\mathbf{r}}_{\mathcal{M}} \\
\tilde{\mathbf{r}}_{\mathcal{I}} \\
\tilde{\mathbf{r}}_{\mathcal{A}} \\
\mathbf{0} \\
\tilde{\mathbf{g}}_{\mathcal{A}} \\
\mathbf{0}
\end{bmatrix}. \quad (26)$$

For a detailed derivation of the linearisation and an explanation of each entity it is referred to [14]. Here, it should only be emphasized that from line four in (26) the Lagrange multiplier can efficiently be eliminated by condensation:

$$\mathbf{z}_{\mathcal{A}} = \mathbf{D}_{\mathcal{A}\mathcal{A}}^{-T} \left(-\tilde{\mathbf{r}}_{\mathcal{A}} - \mathbf{K}_{\mathcal{A}\mathcal{N}} \Delta \mathbf{d}_{\mathcal{N}} - \tilde{\mathbf{K}}_{\mathcal{A}\mathcal{M}} \Delta \mathbf{d}_{\mathcal{M}} - \tilde{\mathbf{K}}_{\mathcal{A}\mathcal{I}} \Delta \mathbf{d}_{\mathcal{I}} - \tilde{\mathbf{K}}_{\mathcal{A}\mathcal{A}} \Delta \mathbf{d}_{\mathcal{A}} \right). \quad (27)$$

The computational cost of the condensation is very low, since the calculation of inverse $\mathbf{D}_{\mathcal{A}\mathcal{A}}^{-T}$ is trivial due the fact of $\mathbf{D}_{\mathcal{A}\mathcal{A}}$ being diagonal. With the condensation (27) a system of equations can be formulated, which only has displacement degrees of freedom and which size is independent of the size of the active contact zone. The values for the Lagrange multipliers are calculated in a post-processing step with (27).

Several dual shape functions exist satisfying the biorthogonality relation. Here, only linear ones are considered, e.g. for 2d problems:

$$\Phi_1^{(1)}(\xi) = \frac{1}{2}(1 - 3\xi), \quad \Phi_2^{(1)}(\xi) = \frac{1}{2}(1 + 3\xi). \quad (28)$$

Dual shape function $\Phi_1^{(1)}(\xi)$ is shown to the right of Fig. 1. For 3d problems the dual shape functions depend on the geometry of the slave element and thus cannot be given a priori, see [4–6] for details relating the calculation of the dual shape functions and [1, 15] for their consistent treatment on so-called boundary elements.

The remainder of this sections focuses upon the completeness of the dual shape functions because this property is important for Sect. 4. The linear dual shape functions described before are complete up to order zero only and thus unable to represent linear functions exactly. In contrast, standard linear shape functions are 1-complete. The compatibility between interconnected elements also differs for both shape functions. The standard linear shape functions are C^0 -continuous, whereas the dual counterparts are only C^{-1} -continuous. Since the variational index of the Lagrange multiplier is $m = 0$ for the considered tied as well as the unilateral contact problem, consistency is ensured even for the dual mortar method. But it is shown in the following section that the lower continuity negatively effects the physical interpretation of the Lagrange multiplier field.

4 Contact Stress Recovery from Lagrange Multipliers

In this section the accuracy of the contact stress is investigated for the standard and the dual mortar method. The contact stress can be obtained from the finite element solution in two ways. The first one derives the stress at the contact interface from the stress field σ of the bodies in contact. In the considered case of a displacement based finite element formulation the stress field is calculated from the derivatives of the displacement field and thus it is not very accurate. Here, the second possibility is considered, which uses of the relation between the contact stress and the Lagrange multiplier from (7). In this case no derivatives are involved and therefore the contact stress is more accurate.

For the standard mortar method the approximation of the contact stress $\mathbf{t}_c^{(1)} = -\lambda$ is found from (13) using $\Xi = N$. Due to the compatibility and completeness properties of N resulting contact stresses are continuous. This is not the case for dual mortar formulation, where the contact stress is discontinuous and thereby unphysical [8]. The discontinuity originates from the zero completeness and the C^{-1} -continuity of the dual shape functions.

4.1 Continuous Contact Stress for the Dual Mortar Method

In order to obtain physically meaningful continuous contact stresses for dual mortar formulations in [8] a linear interpolation of nodal values $\tilde{\mathbf{z}}_I$ by standard Lagrange shape functions N_I is suggested. For linear shape functions the nodal values $\tilde{\mathbf{z}}_I$ correspond to \mathbf{z}_I from (27) and therefore the linear interpolation reads

$$\tilde{t}_{cx}^h = - \sum_{I=1}^{n_s} z_{Ix}^d N_I^{(1)}. \tag{29}$$

The additional superscript d point out to the discrete Lagrange multipliers of a dual mortar method. The interpolation given for the x -component of $\tilde{\mathbf{t}}_c$ can be extended accordingly to all other components. With the following illustrative example the accuracy of this contact stress representation is compared to those of the contact stress for the standard mortar method and of the discontinuous contact stress for the dual mortar method. The considered contact stress representations are abbreviated as follows:

- std m** standard mortar method, using standard Lagrange shape functions to interpolate the contact stress, continuous contact stress,
- dual m** dual mortar method, using dual shape functions to interpolate the contact stress, discontinuous contact stress,
- dual m, $\Pi^h \tilde{\mathbf{t}}_c$** dual mortar method, using standard Lagrange shape functions to interpolate the contact stress, see [8], continuous contact stress.

4.2 Illustrative Example with Linear Contact Pressure

The problem setting of the 2d example is given in the left part of Fig. 2. It consists of two separate bodies $\Omega^{(1)}$ and $\Omega^{(2)}$ which are subjected to a constant volume load in global y -direction. Due to Poisson’s ratio $\nu = 0.2$ both bodies press against each other at the contact interface γ_c , so that a linear contact pressure can be expected from theory of linear elasticity. Here, we use a geometrically non-linear setting described in Sects. 2 and 3 to solve the problem. In order to evaluate the contact pressure different mesh sizes are investigated. The coarsest mesh is illustrated in Fig. 2 and referred to as mesh level 0. Finer levels are obtained by replacing each quadrilateral element by four quads. As shown in Fig. 2 the meshes of the bodies do not coincide at the contact interface. In this example a finer mesh is used for body $\Omega^{(2)}$ than for body $\Omega^{(1)}$. The ratio of the elements on slave side to the elements on the master side is $s : m = 2 : 3$.

Since friction is neglected in this contribution, the contact stress is entirely represented by the contact pressure which acts in normal direction to the contact interface. At each slave node discrete Lagrange multiplier values \mathbf{z}_l are calculated from (27), in case of the dual mortar method, or by solving (21)–(23) in case of the standard mortar method. The distribution of the contact stresses is obtained by relations (13) and (7). For mesh level 2 the contact pressure for the different methods are given in Fig. 2. The contact pressure of the standard mortar method is almost linear and continuous. If dual shape functions are used to approximate the Lagrange multiplier field the contact pressure is discontinuous. With the linear interpolation described in Sect. 4.1 an almost linear and continuous contact pressure can be recovered from the dual mortar formulation.

To quantify the accuracy of the different contact pressure representations their error is investigated. Here, the mesh dependent \mathcal{L}^2 -error norm

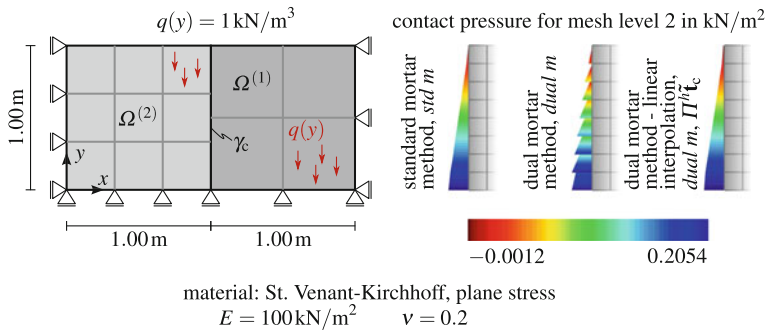
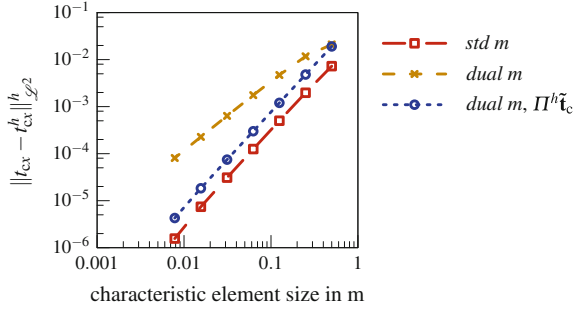


Fig. 2 Linear contact pressure—problem description, mesh shown for level 0, contact pressures for different mortar methods and interpolations

Fig. 3 Linear contact pressure—error of t_{cx} in mesh dependent \mathcal{L}^2 -norm



$$\|t_{cx} - t_{cx}^h\|_{\mathcal{L}^2}^h = \sqrt{\sum_{e=0}^{n_{se}} h_e \|t_{cx} - t_{cx}^h\|_{\mathcal{L}^2,e}^2} \tag{30}$$

is used for this purpose, compare [8]. In (30) n_{se} is the number of slave-elements, h_e is the characteristic length of the e -th slave element and

$$\|t_{cx} - t_{cx}^h\|_{\mathcal{L}^2,e}^2 = \int_{\gamma_{c:e}^{(1),h}} (t_{cx} - t_{cx}^h)^2 da \tag{31}$$

is the absolute \mathcal{L}^2 -error of the contact stress within the e -th slave element. For the problem shown in Fig. 2 the errors of mesh levels 0–6 are given in Fig. 3. As reference solution the contact pressure is calculated with mesh level 7 by a standard mortar formulation. Linear interpolation $dual\ m, \Pi^h \tilde{t}_c$ substantially reduces the error compared to the error of the originally discontinuous contact stress of the dual mortar method. But the error is slightly larger than the one resulting from the standard mortar method showing the same convergence rate compared to the standard mortar method though.

4.3 \mathcal{L}^2 -Projection of the Contact Stress of Dual Mortar Methods

The observed inaccuracy of the contact stress from dual mortar formulations compared to the contact stress of standard mortar formulation motivates the investigation of an alternative approach to obtain continuous contact stresses for dual mortar methods. The idea of the approach is illustrated in Fig. 4. The discontinuous contact stress from the dual mortar calculation is treated like an external load on the contact boundary. For this “load” consistent nodal forces b_l are calculated. In a next step a matching stress distribution has to be found for the consistent nodal forces. Generally, this procedure is not unique. But, on condition that the stress is continuous

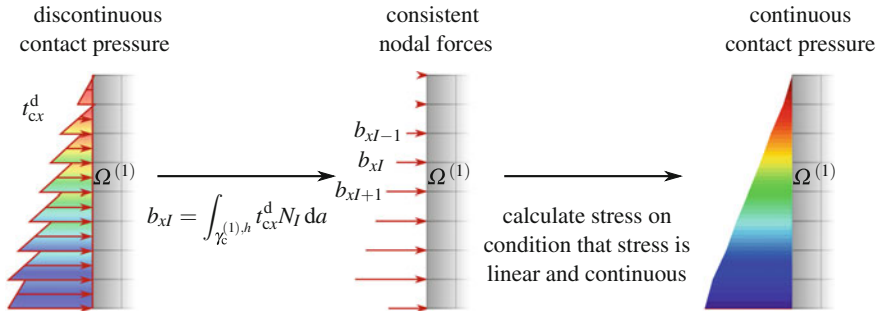


Fig. 4 Main steps of the calculation of continuous contact pressures via consistent nodal forces

and linear the problem becomes unique. Mathematically this procedure represents a piecewise linear \mathcal{L}^2 -projection of the discontinuous contact stress

$$\mathbf{t}_{cx}^d = - \sum_{I=1}^{n_s} \Phi_I \mathbf{z}_{Ix}. \tag{32}$$

The main equations to get the \mathcal{L}^2 -projection $P^h \mathbf{t}_c^d$ of \mathbf{t}_c^d are given in the following. For further details it is referred to [11]. The consistent nodal forces

$$b_{Ix} = \int_{\gamma_c^{(1),h}} t_{cx}^d N_I da \quad \forall I \in \mathcal{I} \tag{33}$$

are elements of vector \mathbf{b} , which can be used together with the analogue consistent mass matrix

$$\mathbf{M}^{\mathcal{L}^2} = [m_{IJ}^{\mathcal{L}^2}] \in \mathbb{R}^{n_s \times n_s}, \quad m_{IJ}^{\mathcal{L}^2} = \int_{\gamma_c^{(1),h}} N_I N_J da \quad \forall I, J \in \mathcal{I} \tag{34}$$

to set up the linear system

$$\mathbf{M}^{\mathcal{L}^2} \bar{\mathbf{t}}_{cx} = \mathbf{b}_x. \tag{35}$$

This linear system can be solved for vector $\bar{\mathbf{t}}_{cx}$, which contains the new nodal contact stress values. The \mathcal{L}^2 -projection is then calculated via

$$t_{cx}^{\mathcal{L}^2} = P^h t_{cx}^d = \sum_{I=0}^{n_s} N_I \bar{t}_{Ix}. \tag{36}$$

Previous equations solely consider contact stresses in x -direction, all other directions can be treated equivalently, which corresponds to solving (35) simultaneously for

Fig. 5 Linear contact pressure—error of t_{cx}^h in mesh dependent \mathcal{L}^2 -norm

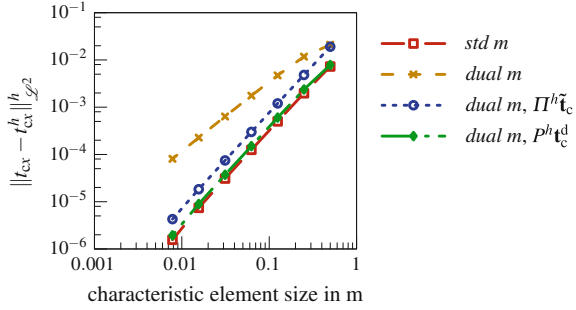
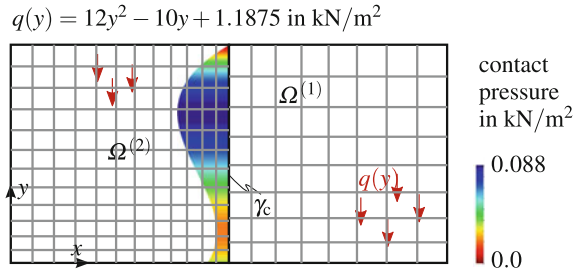


Fig. 6 Cubic Contact Pressure—load, mesh of mesh level 2 with $s : m = 2 : 3$ and concentration of mesh density to point $(1/0)$, the contact pressure of numerical reference solution



multiple vectors **b**. In the following the presented \mathcal{L}^2 -projection is abbreviated as follows:

dual m, $P^h t_c^d$ dual mortar method, using a consistent \mathcal{L}^2 -projection to get continuous contact stresses from the discontinuous ones.

The method to get continuous contact stresses presented in [8] (*dual m, $\Pi^h \tilde{t}_c$*) corresponds to a \mathcal{L}^2 -projection using a lumped mass matrix in (35).

In a first step *dual m, $P^h t_c^d$* is applied to the previously considered problem shown in Fig. 2, the error is plotted in Fig. 5. With the proposed \mathcal{L}^2 -projection the error of the contact pressure stemming from a dual mortar formulation is practically as small as that of the standard mortar method. In order to make this numerical example more challenging it is considered again with modified parameters. Instead of a constant volume load a quadratic load is applied according to Fig. 6. Due to this loading linear elasticity leads to a cubic contact pressure. The contact pressure is illustrated in Fig. 6, taken from the numerical reference solution for this load, which is calculated with a mesh discretising both bodies by 350×350 elements. Geometry and material data are kept the same. The mesh levels are generated as described above but here the mesh density increases to point $(1/0)$. Since the mesh size varies and only the nodes on the ends of the contact boundary γ_c coincide on the slave and master line. The mesh of mesh level 2 is illustrated in Fig. 6. The errors of all considered methods are given for ratios $s : m = 2 : 3$ and $s : m = 3 : 2$ in Fig. 7. Similar observations as for the linear contact pressure can be made. With *dual m, $P^h t_c^d$* the contact pressure of dual mortar formulations is considerably improved compared to

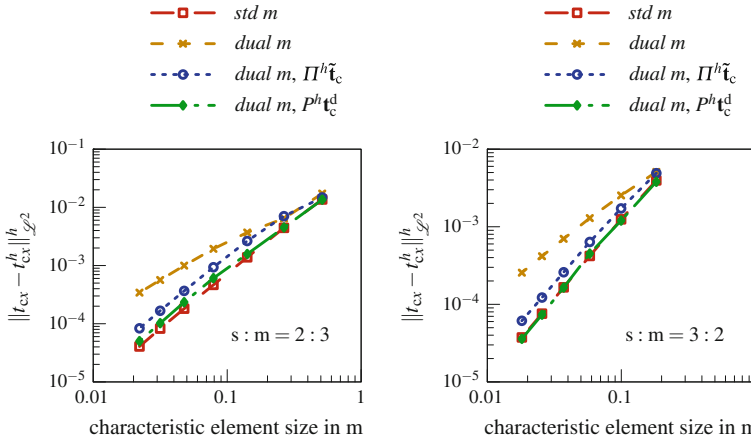


Fig. 7 Cubic Contact Pressure—error of contact stress t_{cx} for meshes with increased density to point (1/0)

dual m and *dual m, $\Pi^h \tilde{t}_c$* . The contact stress is practically as accurate as the one of the standard mortar method.

5 Numerical Examples

To confirm the observations from the previous section all mentioned methods are applied to further numerical examples. For all problems the error of the contact stress is calculated for different meshes. The mesh of level 0 is always shown in the figure describing the problem. Subsequent levels are gained by replacing each quadrilateral finite element by 4 quadrilateral finite elements. For 3d problems each cubic element is replaced by 8 hexahedrons.

5.1 Infinite Plate With Circular Hole

The first linear example is an infinite plate with a circular hole under constant in-plane tension at infinity, for which an analytical solution exists. The tied contact problem was similarly investigated in [2, 17]. The part of the analysed problem is shown in Fig. 8. The exact prescribed traction \hat{t} can be calculated from the analytical solution given in [2]. Following [17] the plate is divided into two domains with noncoinciding meshes at the contact interface.

In a first step it is shown that the error of the dual mortar method and the standard mortar method in the domain is almost identical. For this the displacement field u_y as

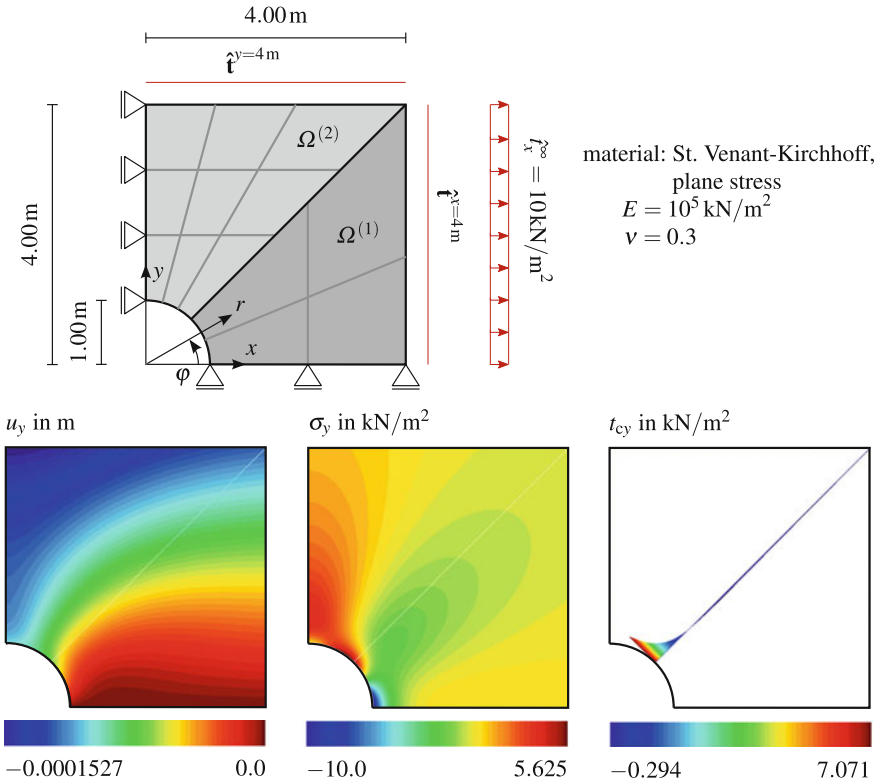


Fig. 8 Infinite Plate With Circular Hole—problem description, mesh shown for level 0, analytical solutions of u_y , σ_y and t_{cy}

well as the stress field σ_y are exemplarily investigated. Both solutions are illustrated in Fig. 8. The \mathcal{L}^2 -errors are given in Fig. 9 for both mortar methods with a mesh ratio of $s : m = 2 : 3$ and for a finite element solution fe without contact, i.e. with a mesh ratio of $s : m = 1 : 1$. Both mortar methods as well as the finite element solution show the optimal convergence rate of $O(h^2)$ and $O(h)$, respectively. Furthermore both mortar methods have almost identical errors. The error of the finite element solution is slightly larger compared to the mortar methods. This is due to the fact that different meshes are used and that the characteristic element length is taken to be the largest element diagonal. The size of the finite elements is almost identical in the entire domain. The meshes of the mortar methods have smaller elements on $\Omega^{(2)}$ leading to a higher accuracy in this domain. Since $dual\ m, \Pi^h \tilde{t}_c$ and $dual\ m, P^h \tilde{t}_c^d$ do not effect the solution in the domain their results are not shown here and can be considered identical to $dual\ m$. This investigation shows that the difference of the contact stress observed in Sect. 4 does not result from an inaccuracy of the displacement field \mathbf{u}^h .

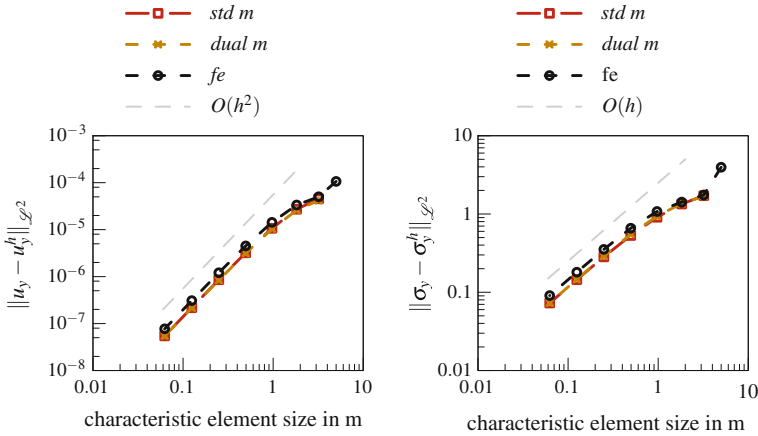
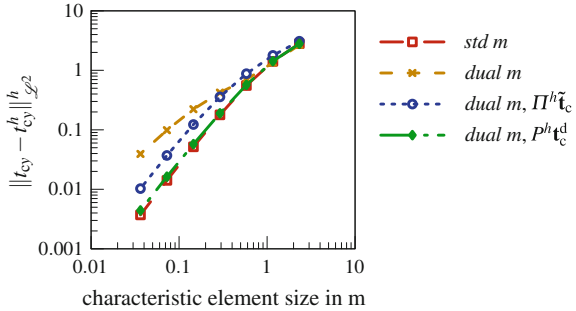


Fig. 9 Infinite Plate With Circular Hole—absolute error of u_y and σ_y

Fig. 10 Infinite Plate With Circular Hole—absolute error of t_{cy}



Now the focus is again turned to the contact stress, in particular to the y-component of \mathbf{t}_c . The expected contact stress distribution is given in Fig. 8. The errors of t_{cy} for all considered methods are given in Fig. 10. Similar to the results of the previous section, the accuracy of the standard mortar method is better than that for the dual mortar method $dual\ m$. With the two methods to recover continuous stresses $dual\ m, \Pi^h \tilde{\mathbf{t}}_c$ and $dual\ m, P^h \mathbf{t}_c^d$ for the dual mortar formulation the stress accuracy can be improved, in case of $dual\ m, P^h \mathbf{t}_c^d$ the accuracy is comparable with the standard mortar method.

5.2 Singular Contact Pressure

The second numerical example of this section is adopted from [8]. Two squares are loaded such that a singular contact stress occurs. The problem setting with the data of geometry and material, as well as the deformed bodies are given in Fig. 11. The

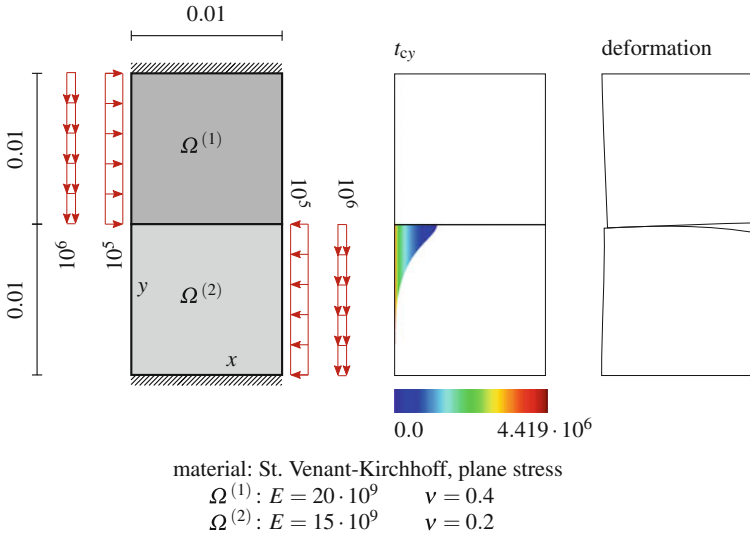
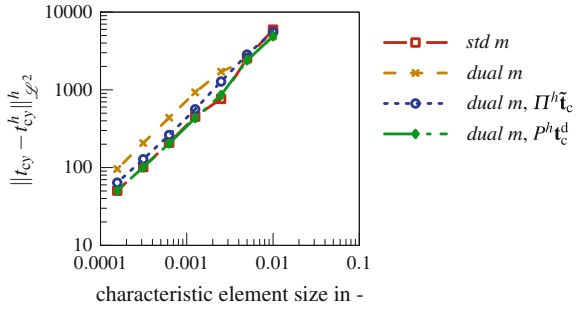


Fig. 11 Singular Contact Pressure—problem description, contact pressure, deformed configuration (shown for mesh level 8, deformation is scaled by factor 400)

Fig. 12 Singular Contact Pressure—absolute error of t_{cy}



problem is calculated considering a non-linear behaviour and unilateral contact conditions. The finite element meshes of both bodies conform on the contact boundary in the reference configuration but are non-conforming as soon as the load is applied. The coarsest mesh represents each square by one element. The contact stress t_{cy} is analysed, the stress distribution is given in Fig. 11. The contact stress distribution is taken from the numerical reference solution, which is calculated with the standard mortar method using mesh level 8. The error of t_{cy} is shown in Fig. 12. For this problem all considered methods have the same convergence rate. With $dual\ m, P^h t_c^d$ the error is as low as that of the standard mortar method.

5.3 Hertzian Contact Problem

The problem shown in Fig. 13 is similar to the classical Hertzian contact problem, but considered to be non-linear. Thus, the analytical solution of the Hertzian contact problem is not applicable. Instead the solution of the standard mortar method with mesh level 7 is taken as the numerical reference solution for comparing the contact pressure t_{cn} .

The left diagram of Fig. 14 shows the contact pressure t_{cn} for mesh level 3. If dual shape functions are used to approximate the contact pressure, large oscillations are visible and tensile contact pressures occur. Both can be avoided when standard Lagrange shape functions are used to interpolate the discrete contact pressure values. Applying the presented \mathcal{L}^2 -projection also yields a continuous contact pressure but slight tensile contact pressures occur at the end of the contact zone. The contact pressure of the standard mortar method is also slightly oscillating.

The error of t_{cn} is shown in the right diagram of Fig. 14. For this problem the error of *std m* is still smaller than the one of *dual m* but for most mesh levels the error is larger than the one of *dual m*, $\Pi^h \tilde{t}_c$ or *dual m*, $P^h t_c^d$. This was not the case in the previous examples. This irregularity is probably due to the slightly oscillating contact pressure of *std m* close to the end of the contact zone. A similar behaviour was also observed in [17]. The authors of [17] venture the guess that the reason for the oscillation results from the inappropriate application of the decoupled contact constraints (22) for standard mortar methods. Strictly speaking, the decoupled constraints are only applicable for dual mortar formulations, see [7, 12].

For this example the *dual m*, $P^h t_c^d$ leads to the smallest error for nearly all mesh levels. The convergence rates of all considered methods is similar.

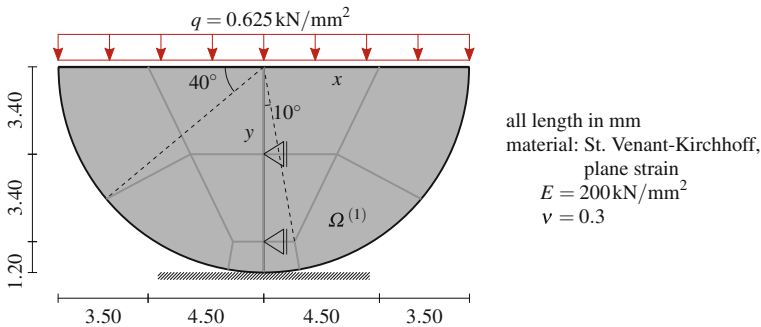


Fig. 13 Hertzian Contact Problem—problem description, mesh shown for level 0

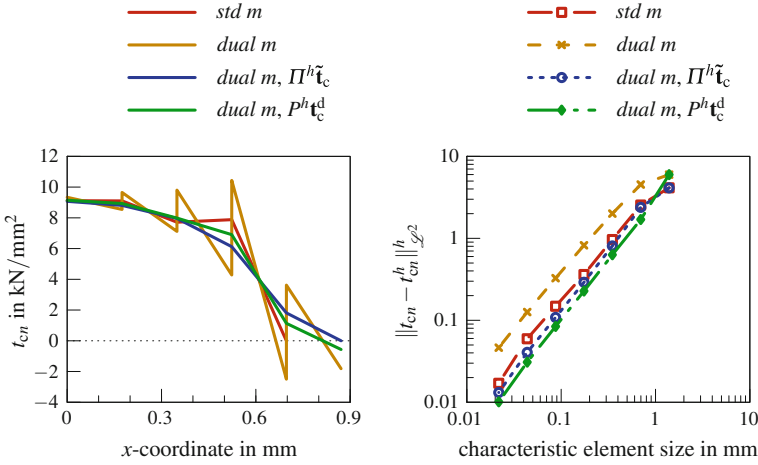


Fig. 14 Hertzian Contact Problem—contact stress t_{cn} distribution for mesh level 3 and absolute error of t_{cn}

5.4 3d Tied Contact Problem with Curved Contact Interface

The last numerical example is a 3d linear tied contact problem with a curved contact interface. The problem setting and the material data are shown in Fig. 15. The union of both bodies represents a cube. Body $\Omega^{(1)}$ is one eighth of a sphere. The face of the cube whose outward normal points in positive x -direction is fixed against displacements in x -direction. Rigid body motions are prevented by statically determinate support conditions. The constant pressure load q_x is applied to the face of the cube which lies in the global y - z -plane. Due to the loading a constant stress σ_x can be expected. Here, the component in x -direction of the contact stress vector \mathbf{t}_c is investigated, which analytically is given by

$$t_{cx} = -\cos \varphi \sin \theta \text{ kN/mm}^2. \tag{37}$$

The errors of t_{cx} for different mesh sizes are given in Fig. 16. For this 3d problem the characteristic element size is the largest diagonal of the quadrilateral slave elements. The contact stress of the standard mortar method is again the most accurate. With the presented \mathcal{L}^2 -projection the error of the dual mortar method is decreased to the error of the standard mortar method.

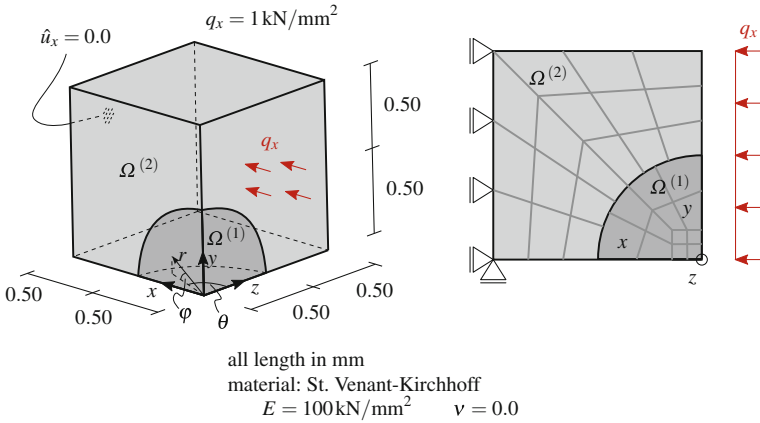
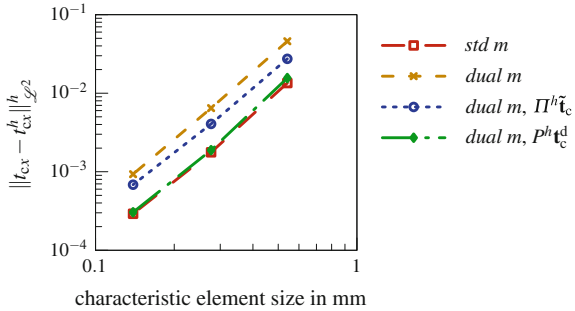


Fig. 15 3d Tied Contact Problem with Curved Contact Interface—problem description, mesh shown for level 0

Fig. 16 3d Tied Contact Problem with Curved Contact Interface—absolute error of t_{cx}



6 Conclusion

The contact stress of linear dual mortar methods is approximated by the same shape functions as the Lagrange multiplier. These C^{-1} -continuous shape functions yield discontinuous contact stresses. However, interpolating the discrete values with standard Lagrange shape functions the resulting contact stresses are continuous. But the error of the contact stress is larger than that for standard mortar formulations. As a remedy a \mathcal{L}^2 -projection of the discontinuous contact stresses is presented yielding continuous contact stresses. The error of the contact stress and its convergence rate was investigated for tied contact and unilateral contact problems. For the given numerical examples the \mathcal{L}^2 -projection leads to comparable results of the standard mortar method, they are better than known contact stress representations for dual mortar methods. So far this method has been checked only for simple contact problems and needs to be investigated in more detail.

References

1. T. Cichosz, M. Bischoff, Consistent treatment of boundaries with mortar contact formulations using dual Lagrange multipliers. *Comput. Methods Appl. Mech. Eng.* **200**, 1317–1332 (2011)
2. J.A. Cottrell, T.J.R. Hughes, Y. Bazilevs, *Isogeometric Analysis: Toward Integration of CAD and FEA* (Wiley, Chichester, 2009)
3. P. Farah, A. Popp, W.A. Wall, Segment-based vs. element-based integration for mortar methods in computational contact mechanics. *Comput. Mech.* **55**, 209–228 (2014)
4. B. Flemisch, B.I. Wohlmuth, Stable Lagrange multipliers for quadrilateral meshes of curved interfaces in 3D. *Comput. Methods. Appl. Mech. Eng.* **196**, 1589–1602 (2007)
5. S. Hartmann, Kontaktanalyse dünnwandiger Strukturen bei groen Deformationen. Dissertation, Universität Stuttgart (2007)
6. S. Hartmann, S. Brunssen, E. Ramm, B.I. Wohlmuth, Unilateral non-linear dynamic contact of thin-walled structures using a primal-dual active set strategy. *Int. J. Numer. Methods Eng.* **70**, 883–912 (2007)
7. S. Hüeber, Discretization techniques and efficient algorithms for contact problems. Dissertation, Universität Stuttgart (2008)
8. S. Hüeber, M. Mair, B.I. Wohlmuth, A priori error estimates and an inexact primal-dual active set strategy for linear and quadratic finite elements applied to multibody contact problems. *Appl. Numer. Math.* **54**, 555–576 (2005)
9. R.H. Krause, B.I. Wohlmuth, Nonconforming decomposition methods: Techniques for linear elasticity. *East-West J. Numer. Math.* **8**, 177–206 (2000)
10. R.H. Krause, B.I. Wohlmuth, A Dirichlet-Neumann type algorithm for contact problems with friction. *Comput. Vis. Sci.* **5**, 139–148 (2002)
11. M.G. Larson, F. Bengzon, *The Finite Element Method: Theory, Implementation, and Applications* (Springer, Berlin Heidelberg, 2013)
12. A. Popp, Mortar methods for computational contact mechanics and general interface problems. Dissertation, Technische Universität München (2012)
13. A. Popp, M.W. Gee, W.A. Wall, A finite deformation mortar contact formulation using a primal-dual active set strategy. *Int. J. Numer. Methods Eng.* **79**, 1354–1391 (2009)
14. A. Popp, M. Gitterle, M.W. Gee, W.A. Wall, A dual mortar approach for 3D finite deformation contact with consistent linearization. *Int. J. Numer. Methods Eng.* **83**, 1428–1465 (2010)
15. A. Popp, A. Seitz, M.W. Gee, W.A. Wall, Improved robustness and consistency of 3D contact algorithms based on a dual mortar approach. *Comput. Methods Appl. Mech. Eng.* **264**, 67–80 (2013)
16. A. Popp, W.A. Wall, Dual mortar methods for computational contact mechanics overview and recent developments. *GAMM-Mitteilungen.* **37**, 66–84 (2014)
17. A. Seitz, P. Farah, J. Kremheller, B.I. Wohlmuth, W.A. Wall, A. Popp, Isogeometric dual mortar methods for computational contact mechanics. *Comput. Methods Appl. Mech. Eng.* **301**, 259–280 (2016)
18. S. Sitzmann, K. Willner, B.I. Wohlmuth, Variationally consistent quadratic finite element contact formulations for finite deformation contact problems on rough surfaces. *Finite Elem. Anal. Des.* **109**, 37–53 (2016)
19. C. Wilking, M. Bischoff, Alternative integration algorithms for three-dimensional mortar contact. *Comput. Mech.* **59**, 203–218 (2017)
20. B.I. Wohlmuth, *Discretization Methods and Iterative Solvers Based on Domain Decomposition* (Springer, Berlin, 2001)
21. B.I. Wohlmuth, A mortar finite element method using dual spaces for the lagrange multiplier. *SIAM J. Numer. Anal.* **38**, 989–1012 (2000)

Efficient Low Order Virtual Elements for Anisotropic Materials at Finite Strains

P. Wriggers, B. Hudobivnik and J. Korelc

Abstract Virtual elements were introduced in the last decade and applied to problems in solid mechanics. The success of this methodology when applied to linear problems asks for an extension to the nonlinear regime. This work is concerned with the numerical simulation of structures made of anisotropic material undergoing large deformations. Especially problems with hyperelastic matrix materials and transversely isotropic behaviour will be investigated. The virtual element formulation is based on a low-order formulations for problems in two dimensions. The elements can be arbitrary polygons. The formulation considered relies on minimization of energy, with a novel construction of the stabilization energy and a mixed approximation for the fibers describing the anisotropic behaviour. The formulation is investigated through a several numerical examples, which demonstrate their efficiency, robustness, convergence properties, and locking-free behaviour.

1 Introduction

Boundary value problems can be solved with the established finite element method which can handle problems in nonlinear solid mechanics, (see for example the texts by Bathe [1], Belytschko et al. [7] and Wriggers [35]). However in recent years different methods like the isogeometric analysis, see e.g. Cottrell [15] and the virtual element method were introduced as tools that bring some new features to numerical solution schemes in solid mechanics. Virtual element methods, see Beirão da Veiga et al. [2], allow to explore features like flexibility with regard to mesh generation and choice of element shapes. There are other element formulations like the polygonal

P. Wriggers (✉) · B. Hudobivnik
Leibniz Universität Hannover, Hannover, Germany
e-mail: wriggers@ikm.uni-hannover.de

B. Hudobivnik
e-mail: hudobivnik@ikm.uni-hannover.de

J. Korelc
University of Ljubljana, Ljubljana, Slovenia
e-mail: Joze.Korelc@fgg.uni-lj.si

or polyhedral elements which also allow for complex element shapes. Some representative works in this regard are those by Sukumar [32] and Sukumar and Malsch [33]; for finite deformation problems including contact, see Biabanaki and Khoei [9], Biabanaki et al. [10] and Chi et al. [14]. In this paper we like to focus on the virtual element methodology.

The virtual element method (VEM) is a relatively recent extension of the classical Galerkin finite element method. The method permits the use of polygonal element for problems in two dimensions where there is no need for a restriction to convex elements, nor is it necessary to avoid degeneracies such as element sides having an interior angle close to π radians. Thus the method permits the direct use of Voronoi meshers, hence crystals in a polycrystalline material can be represented by single elements. The method was introduced and discussed in the works by Beirão da Veiga et al. [2, 4] and, for problems in elasticity, Beirão da Veiga et al. [3] and Gain et al. [17]). Stabilization procedures for the virtual element method that are using hourglass stabilization, well known from the work of Belytschko et al. [8], are described in Cangiani et al. [12] for linear Poisson problems. The use of VEM for nonlinear problems has been discussed recently in Beirão da Veiga et al. [5] and Chi et al. [13] for inelastic materials at small strains and hyperelastic materials at finite deformations.

Within the VEM a variable φ_h in the weak formulation or energy functional is replaced by its projection $\Pi\varphi_h$ onto a polynomial space. This results in a rank-deficient structure, so that it is necessary to add a stabilization term to the formulation. There are different possibilities to formulate the stabilization. One relies on the introduction of the difference $\varphi_h - \Pi\varphi_h$ between the original variable and its projection. In order to adhere to a fundamental aspect of VEM in which all integrations take place on element boundaries, the stabilization term proposed, for example, in Beirão da Veiga et al. [2, 3] takes the form of a sum of a function of nodal variables. This is the approach adopted in the recent nonlinear investigation by Chi et al. [13], with the scalar stabilization parameter of the linear case being replaced by one that depends on the fourth-order elasticity tensor (that is, the derivative of the relevant stress measure with respect to the deformation). This leads to a formulation that works very well when smaller load-steps are applied since the stabilization parameter is always related to the deformation of the last converged load step. Another approach was introduced lately in Wriggers et al. [36] which relies on the addition of a positive-definite energy $\hat{\Psi}(\varphi_h)$ to the positive semidefinite mean strain energy $\Psi(\Pi\varphi_h)$. The energy $\hat{\Psi}(\varphi_h)$ is evaluated using full quadrature, and for consistency subtraction of a term involving $\hat{\Psi}(\Pi\varphi_h)$ as a function of the mean strain. This formulation can be consistently linearized and leads to a Newton scheme with quadratic convergence properties independent of load steps. This stabilization technique was first described in Nadler and Rubin [26], generalized in Boerner et al. [11] and simplified in Krysl [21] in the context of stabilization procedures for the mean-strain hexahedron.

The method is extended here to materials that are transversely anisotropic. For this we will formulate a constraint form to introduce the stiffening related to fibers. This will be based on a perturbed Lagrangian formulation which is added to the

neo-Hookian strain energy functions describing the matrix material. A special ansatz for the Lagrangian multiplier associated with the fiber stiffness yields locking-free behaviour. The formulation performs extremely well in benchmark tests involving regular, distorted and Voronoi meshes.

The structure of the rest of this work is as follows. The governing equations for nonlinear elasticity are presented in Sect. 2. Section 3 is devoted to a presentation of the VEM, including the formulation for anisotropic materials. Section 3.2.2 summarizes the stabilization term. Some numerical examples are presented and discussed in Sect. 4.

2 Governing Equations for Finite Elasticity with Anisotropic Material Behaviour

Consider an elastic body that occupies the bounded domain $\Omega \subset \mathbb{R}^2$. The body Ω has a boundary Γ which comprises non-overlapping sections Γ_D and Γ_N such that $\Gamma_D \cup \Gamma_N = \Gamma$, see Fig. 1.

The position \mathbf{x} of a material point initially at \mathbf{X} is given by the motion

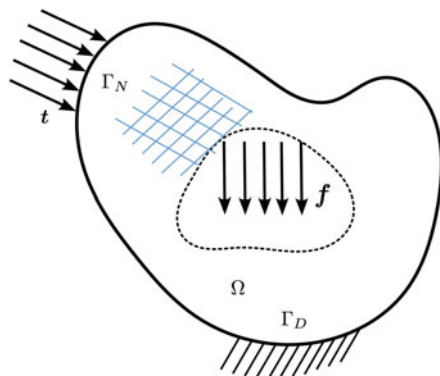
$$\mathbf{x} = \varphi(\mathbf{X}, t) = \mathbf{X} + \mathbf{u}(\mathbf{X}, t)$$

where \mathbf{u} is the displacement. We define the deformation gradient \mathbf{F} by

$$\mathbf{F} = \text{Grad } \varphi \tag{1}$$

where the gradient has to be evaluated with respect to \mathbf{X} . The right Cauchy-Green tensor $\mathbf{C}(\mathbf{u})$ is defined as $\mathbf{C} = \mathbf{F}^T \mathbf{F}$ will be introduced as strain measure and the Jacobian $J(\mathbf{u})$ of the deformation is given as $J = \det \mathbf{F}$.

Fig. 1 Anisotropic solid with boundary conditions



The body satisfies, on Ω the equation of equilibrium

$$-\text{Div } \mathbf{P} = \mathbf{f}, \quad (2)$$

with the body force \mathbf{f} and the first Piola-Kirchhoff stress \mathbf{P} .

The Dirichlet and Neumann boundary conditions are respectively

$$\mathbf{u} = \bar{\mathbf{u}} \quad \text{on } \Gamma_D, \quad (3)$$

$$\mathbf{P}\mathbf{N} = \mathbf{t} \quad \text{on } \Gamma_N. \quad (4)$$

with \mathbf{N} the outward unit normal vector, $\bar{\mathbf{u}}$ the prescribed displacement, and \mathbf{t} the surface traction on Γ_N .

For the description of anisotropic materials two directions of fibers are introduced by the vectors \mathbf{a}_1 and \mathbf{a}_2 which can shown in arbitrary directions as denoted by the blue grid in Fig. 1. The strain in fiber direction can be computed from

$$\varepsilon_a = \frac{1}{2}(\text{tr}[\mathbf{C}\mathbf{M}_a] - 1) \quad (5)$$

with the structure tensor $\mathbf{M}_a = \mathbf{a}_a \otimes \mathbf{a}_a$ and $a = 1, 2$.

For a homogeneous compressible isotropic hyperelastic material we adopt the neo-Hookean strain energy function

$$\Psi^i(\mathbf{u}) = \frac{\lambda}{4}(J(\mathbf{u})^2 - 1 - 2 \ln J(\mathbf{u})) + \frac{\mu}{2}(\text{tr } \mathbf{C}(\mathbf{u}) - 3 - 2 \ln J(\mathbf{u})) \quad (6)$$

in which λ and μ are the Lamé constants. This strain energy is known as Neo-Hookean model.

For anisotropic materials the strain energy can be based on an extension of (6). For high differences in the material parameters of the matrix and the fibers materials a constraint formulation is advantageous. This leads with (5) to the strain energy

$$\Psi^a(\mathbf{u}) = \Psi^i(\mathbf{u}) + \sum_{a=1}^2 \left(\lambda_a 2\varepsilon_a - \frac{1}{2C_{ca}} \lambda_a^2 \right). \quad (7)$$

The anisotropic part is now formulated using a perturbed Lagrangian functional which relaxes the constraint $2\varepsilon_a = 0$, $a = 1, 2$, by a penalty parameter C_{ca} , see Wriggers et al. [38]. The parameters C_{ca} can be interpreted as fiber stiffnesses and the parameters λ_a are the Lagrange parameter related to the stress in direction \mathbf{a}_a .

The development of a hyperelastic virtual element can start from the potential energy function directly instead of using a weak form. For the isotropic case the potential energy can be written with (6) as

$$U^i(\mathbf{u}) = \int_{\Omega} [\Psi^i(\mathbf{u}) - \mathbf{f} \cdot \mathbf{u}] \, d\Omega - \int_{\Gamma_N} \mathbf{t} \cdot \mathbf{u} \, d\Gamma \tag{8}$$

For anisotropic materials the potential energy is extended by

$$U^a(\mathbf{u}) = U^i(\mathbf{u}) + \sum_{a=1}^2 \int_{\Omega} \left(\lambda_a 2\varepsilon_a - \frac{1}{2C_{ca}} \lambda_a^2 \right) \, d\Omega. \tag{9}$$

where in the latter the constraint due to the stiff fibers is added via the perturbed Lagrangian formulations and the parameter λ_a can be interpreted as the fiber stress. Within this paper we will use (9) to demonstrate that the virtual element method is able to treat anisotropic materials at finite strains. Further formulations and discretizations of problems including anisotropy can be found in [30] and [31].

3 Formulation of the Virtual Element Projection

The main idea of the virtual element method (VEM) is a Galerkin projection of the deformation onto a specific ansatz space. The domain Ω is partitioned into non-overlapping polygonal elements which need not be convex. Here a low-order approach is adopted, using linear ansatz functions where nodes are placed only at the vertices of the polygonal elements. Furthermore, the restriction of the element shape functions to the element boundaries are linear function, see Fig. 2.

3.1 Ansatz Functions for VEM

The virtual element method relies on the split of the ansatz space into a part $\Pi \mathbf{u}_h$ and a remainder

$$\mathbf{u}_h = \Pi \mathbf{u}_h + (\mathbf{u}_h - \Pi \mathbf{u}_h) \tag{10}$$

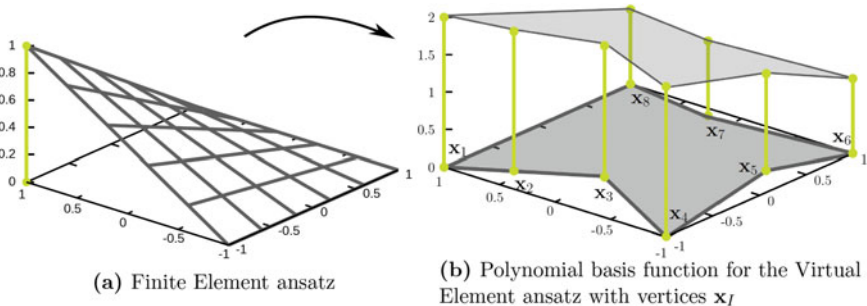


Fig. 2 Comparison of the ansatz functions for FEM and VEM formulations

The projection Π is defined at element level by a linear function

$$\Pi \mathbf{u}_h = \mathbf{H} \mathbf{a} = \begin{bmatrix} 1 & 0 & x & 0 & y & 0 \\ 0 & 1 & 0 & x & 0 & y \end{bmatrix} \begin{Bmatrix} a_1 \\ a_2 \\ \dots \\ a_6 \end{Bmatrix} \quad (11)$$

Additionally a linear ansatz for the deformation along the element edge is selected for a boundary segment k of the virtual element, defined by the local nodes (1)–(2), see right side of Fig. 3,

$$(\mathbf{u}_h)_k = (1 - \xi_k) \mathbf{u}_1 + \xi_k \mathbf{u}_2 = M_{k1} \mathbf{u}_1 + M_{k2} \mathbf{u}_2 \quad \text{with } \xi_k = \frac{x_k}{L_k}. \quad (12)$$

Here, for example, M_{k1} is the ansatz function along a segment k related to node (1), ξ_k is the local dimensionless coordinate and \mathbf{u}_1 is the nodal value at that node, see Fig. 3.

The projection Π is defined such that it satisfies, see Beirão da Veiga et al. [5],

$$\nabla \Pi \mathbf{u}_h|_e = \frac{1}{\Omega_e} \int_{\Omega_e} \text{Grad } \mathbf{u}_h \, d\Omega = \frac{1}{\Omega_e} \int_{\Gamma_e} \mathbf{u}_h \otimes \mathbf{N} \, d\Gamma \quad (13)$$

where \mathbf{N} is the normal at the boundary Γ_e of the domain Ω_e . From (11), the gradient of the projection is constant at element level

$$\nabla \Pi \mathbf{u}_h|_e = \begin{bmatrix} a_3 & a_5 \\ a_4 & a_6 \end{bmatrix}. \quad (14)$$

The right hand side of (13) yields with (12)

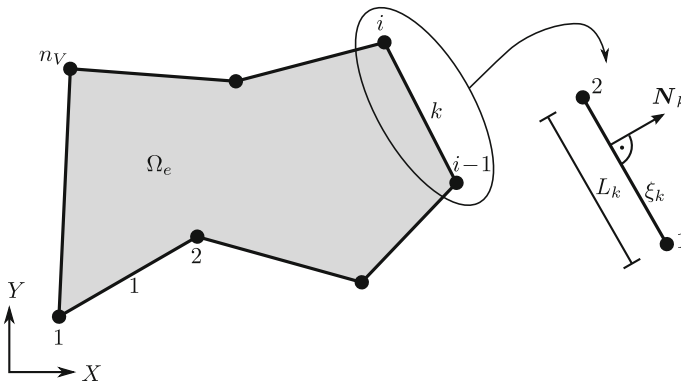


Fig. 3 Virtual element with n_V nodes and local boundary segment of the element

$$\frac{1}{\Omega_e} \int_{\Gamma_e} \mathbf{u}_h \otimes \mathbf{N} \, d\Gamma = \frac{1}{\Omega_e} \sum_{k=1}^{n_V} \int_{\Gamma_k} \begin{bmatrix} u_x(\mathbf{x}_k) N_x & u_x(\mathbf{x}_k) N_y \\ u_y(\mathbf{x}_k) N_x & u_y(\mathbf{x}_k) N_y \end{bmatrix} L_k \, d\Gamma \quad (15)$$

where we have used $\mathbf{N} = \{N_x, N_y\}^T$ and $\mathbf{u} = \{u_x, u_y\}^T$, and n_V are the number of segments of the element. Note that the normal vector \mathbf{N} changes from segment to segment. All quantities are related to the undeformed or initial configuration. Furthermore we have used a form of \mathbf{N}_k that is not normalized since the length L_k cancels out when the integral in (15) is evaluated over the edges. The integral in (15) can be evaluated for the ansatz functions (12) exactly by using the trapezoidal or Gauss-Lobatto rule, see Wriggers et al. [36].

This projection determines the ansatz $\Pi \mathbf{u}_h$ on (11) within an element only up to a translation. It has to be supplemented by a further condition to ensure uniqueness. For this purpose we adopt the condition that the sum of the nodal values of \mathbf{u}_h and of its projection $\Pi \mathbf{u}_h$ are equal. This yields for each element Ω_e

$$\frac{1}{n_V} \sum_{I=1}^{n_V} \Pi \mathbf{u}_h(\mathbf{x}_I) = \frac{1}{n_V} \sum_{I=1}^{n_V} \mathbf{u}_h(\mathbf{x}_I), \quad (16)$$

where \mathbf{x}_I are the coordinates of the nodal point I and the sum includes all boundary nodes. Note that the constant gradient $\nabla \Pi \mathbf{u}_h|_e$ can be computed directly using (14) and (15). Thus for the computation of the strain energy it is not necessary to evaluate Eq. (16).

3.2 Construction of the Virtual Element

A virtual element based only on the projection $\Pi \mathbf{u}_h$ would lead to a rank deficient element once the number of vertices is greater than 3. Thus the formulation has to be stabilized like the classical one-point integrated elements developed by Flanagan and Belytschko [16], Belytschko and Bindeman [6], Reese et al. [28], Reese and Wriggers [29], Reese [27], Mueller-Hoeppe et al. [25], Korelc et al. [19], Krysl [22]. In the following we will first discuss the formulation of the element part that stems from the projection, see last section, for the isotropic and anisotropic cases. Furthermore, different possibilities for stabilizing the virtual element method will be considered.

The development of the virtual element starts from the hyperelastic potential function (8). By summing up all element contributions for the n_e virtual elements we obtain

$$U(\mathbf{u}) = \sum_{e=1}^{n_e} [U_c(\Pi \mathbf{u}_h|_e) + U_{stab}(\mathbf{u}_h|_e - \Pi \mathbf{u}_h|_e)]. \quad (17)$$

3.2.1 Constant Part Due to Projection

The simplest possible formulation for a finite deformation virtual element is a split into a constant part of the deformation gradient and an associated stabilization term. This was performed for the linear case in Beirão da Veiga et al. [3] and also in Wriggers et al. [37] where the focus was on contact mechanics. The same approach can be found in the work of Beirão da Veiga et al. [5], Chi et al. [13] and Wriggers et al. [36] for the nonlinear case.

Isotropic case. The first part in Eq. (17) can be computed by using the results obtained in the last section. This yields

$$U_c^i(\Pi \mathbf{u}_h|_e) = \int_{\Omega_e} [\Psi(\Pi \mathbf{u}_h|_e) - \mathbf{f} \cdot \Pi \mathbf{u}_h|_e] d\Omega - \int_{\Gamma_e^\sigma} \mathbf{t} \cdot \Pi \mathbf{u}_h|_e d\Gamma. \quad (18)$$

It is clear from the expression

$$\Psi(\Pi \mathbf{u}_h|_e) = \frac{\lambda}{4}(J(\Pi \mathbf{u}_h|_e))^2 - 1 - 2 \ln J(\Pi \mathbf{u}_h|_e) + \frac{\mu}{2}(\text{tr} \mathbf{C}(\Pi \mathbf{u}_h|_e) - 3 - 2 \ln J(\Pi \mathbf{u}_h|_e)) \quad (19)$$

that the strain energy depends on functions that are constant in each element Ω_e since the deformation gradient, see (14), is constant: $\mathbf{F}_e = \mathbf{1} + \nabla \Pi \mathbf{u}_h|_e$. Thus

$$\int_{\Omega_e} [\Psi(\Pi \mathbf{u}_h|_e)] d\Omega = \Psi(\Pi \mathbf{u}_h|_e) \Omega_e \quad (20)$$

where Ω_e is the area of the virtual element. However the strain energy $\Psi(\Pi \mathbf{u}_h|_e)$ is still a nonlinear function with respect to the displacement nodal degrees of freedom.

Now the strain energy function in (18) can be evaluated using the approximation at element level of the deformation gradient \mathbf{F}_e , see (14), which depends on the nodal degrees of freedom. Likewise, the Jacobian $J_e = \det \mathbf{F}_e$ and the right Cauchy–Green tensor $\mathbf{C}_e = \mathbf{F}_e^T \mathbf{F}_e$ can be evaluated simply. All derivations leading to the residual vector \mathbf{R}_e^c and the tangent matrix \mathbf{K}_{Te}^c were performed with the symbolic tool ACE-GEN, see Korelc and Wriggers [20]. This yields for (18)

$$\mathbf{R}_e^c = \frac{\partial U_c^i(\Pi \mathbf{u}_h|_e)}{\partial \mathbf{u}_e} \quad \text{and} \quad \mathbf{K}_{Te}^c = \frac{\partial \mathbf{R}_e^c(\mathbf{u}_e)}{\partial \mathbf{u}_e} \quad (21)$$

where \mathbf{u}_e are the nodal displacements of the virtual element Ω_e .

Anisotropic case. The same procedure can be used to include anisotropic materials. For this the anisotropic part of the functional in (9) will be used to introduce the discretization.

$$U^a(\Pi \mathbf{u}_h|_e, \bar{p}_a) = U^i(\Pi \mathbf{u}_h|_e) + \sum_{a=1}^2 \int_{\Omega_e} \left(\bar{p}_a (\text{tr}[\mathbf{C}(\Pi \mathbf{u}_h|_e) \mathbf{M}_a] - 1) - \frac{1}{2C_{ca}} \bar{p}_a^2 \right) d\Omega_e. \quad (22)$$

where the fiber stresses p_a are assumed to be constant at element level $p_a = \bar{p}_a$. The structural tensor \mathbf{M} is defined as $\mathbf{M}_a = \mathbf{a}_a \otimes \mathbf{a}_a$, see also (5).

Since \bar{p}_a , \mathbf{M} and $\mathbf{C}(\Pi \mathbf{u}_h|_e)$ are constant in the virtual element Ω_e the integration of the last two terms is trivial, leading to

$$U^a(\Pi \mathbf{u}_h|_e, \bar{p}_a) = U^i(\Pi \mathbf{u}_h|_e) + \sum_{a=1}^2 \left(\bar{p}_a (\text{tr}[\mathbf{C}(\Pi \mathbf{u}_h|_e) \mathbf{M}_a] - 1) - \frac{1}{2C_{ca}} \bar{p}_a^2 \right) \Omega_e. \quad (23)$$

Note that the anisotropic part will be only introduced in the constant part U_c since no stabilization is needed for the anisotropic part. This formulation introduces two additional variables p_a which can however be eliminated at element level.

The perturbed Lagrangian formulation in (23) is a regularized method for enforcing the constraint of rigid fibers where the parameter C_c is a penalty parameter that can be interpreted as stiffness of the fibers. Thus this formulation can also be used for numerical simulation of anisotropic materials with a given fiber stiffness that allows for deformation of the fibers.

All derivations with respect to the unknown displacements leading to the residual vector \mathbf{R}_e^c and the tangent matrix \mathbf{K}_{Te}^c were performed with the symbolic tool ACEGEN, see Korelc and Wriggers [20]. This yields for (18)

$$\mathbf{R}_e^c = \frac{\partial U_c^a(\Pi \mathbf{u}_h|_e)}{\partial \mathbf{u}_e} \quad \text{and} \quad \mathbf{K}_{Te}^c = \frac{\partial \mathbf{R}_e^c(\mathbf{u}_e)}{\partial \mathbf{u}_e} \quad (24)$$

where \mathbf{u}_e now includes nodal displacements and additional variables of the virtual element Ω_e . The residual and tangent for the incompressible case are evaluated similarly.

3.2.2 Nonlinear Stabilization

We use here a novel stabilization approach for virtual elements which was presented in Wriggers et al. [36]. This stabilization is based on a scheme proposed in Krysl [21]. The essence of the approach is to introduce a new, positive definite strain energy $\hat{\Psi}$ and to define the stabilization contribution to the strain energy by

$$U_{stab}(\mathbf{u}_h|_e - \Pi \mathbf{u}_h|_e) = \hat{U}(\mathbf{u}_h|_e) - \hat{U}(\Pi \mathbf{u}_h|_e). \quad (25)$$

The second term on the right side ensures the consistency of the total potential energy. In other words, once the element size is very small, a constant strain will occur in each virtual element. In that case $\hat{U}(\mathbf{u}_h)$ will approach $\hat{U}(\Pi \mathbf{u}_h)$ and thus not influence the final result. The total potential energy is now given by

$$U(\mathbf{u}_h) = U(\Pi \mathbf{u}_h) + \hat{U}(\mathbf{u}_h) - \hat{U}(\Pi \mathbf{u}_h), \tag{26}$$

and in which

$$\hat{U}(\mathbf{u}_h) = \sum_{e=1}^{n_e} \int_{\Omega_e} \hat{\Psi}(\mathbf{u}_h|_e) d\Omega. \tag{27}$$

represents an isotropic strain energy analogous to (6). The terms involving $\Pi \mathbf{u}_h$ can be integrated as (18). It remains to devise a procedure for computing the term involving the displacement $\mathbf{u}_h|_e$.

In Wriggers et al. [36] the displacement field $\mathbf{u}_h|_e$ in (10) was approximated by an inscribed triangular finite element mesh, see Fig. 4. This mesh can then be used to compute the stabilization energy. The specific choice of the mesh using n_{int} linear three-noded triangles that are connected to the nodes of the virtual element does not introduce extra degrees of freedom.

Following the approach advocated in Krysl [21], we propose the stabilization strain energy

$$\hat{U}(\mathbf{u}_h|_e) = \sum_{m=1}^{n_{int}} \int_{\Omega_m^i} \left[\frac{\hat{\lambda}}{2} (J_m - 1)^2 + \frac{\hat{\mu}}{2} (\text{tr } \mathbf{C}_m - 3 - 2 \ln J_m) \right] d\Omega. \tag{28}$$

Once an ansatz is formulated for the approximation within each triangle Ω_m^i of the inscribed mesh for the displacement field, here denoted by \mathbf{u}_m the deformation measures J_m and \mathbf{C}_m can be easily computed in the standard way, either by using an isoparametric formulation for the three noded triangle or by direct evaluation of the ansatz functions.

The gradient $\text{Grad } \mathbf{u}_m$ is constant over each inscribed element. Hence the deformation gradient $\mathbf{F}_m^i = \mathbf{I} + \text{Grad } \mathbf{u}_m$ within each element Ω_m^i is constant as well. With this the potential (28) can be computed which is a nonlinear function of the nodal displacements related to the interior triangular mesh. All further derivations leading to the residual vector \mathbf{R}_e and the tangent matrix \mathbf{K}_{Te} were performed with the symbolic tool ACEGEN, see Korelc and Wriggers [20]. This yields for (25)

Fig. 4 Internal triangular mesh

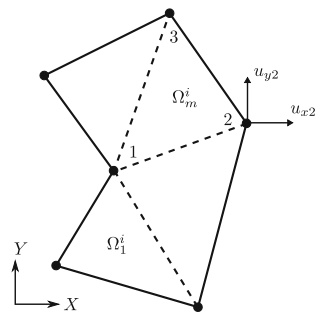
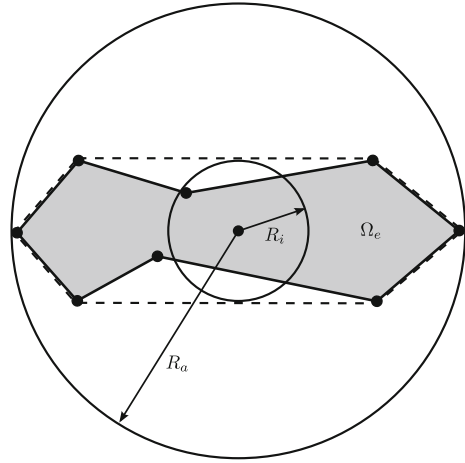


Fig. 5 Inner and outer radius of a virtual element



$$\mathbf{R}_e^s = \frac{\partial U_{stab}(\mathbf{u}_e)}{\partial \mathbf{u}_e} \quad \text{and} \quad \mathbf{K}_{Te}^s = \frac{\partial \mathbf{R}_e^s(\mathbf{u}_e)}{\partial \mathbf{u}_e}. \tag{29}$$

Thus the total residual and tangent matrix of the virtual element are given by the sum of expressions (24) and (29): $\mathbf{R}_e = \mathbf{R}_e^c + \mathbf{R}_e^s$ and $\mathbf{K}_{Te} = \mathbf{K}_{Te}^c + \mathbf{K}_{Te}^s$.

The values of the Lamé parameters in the strain energy (28) have to be selected in a proper way. Here the same procedure as in Wriggers et al. [36] is chosen that takes into account the element distortion to compute the Lamé parameters $\hat{\lambda}$ and $\hat{\mu}$. It is based on the geometry of a virtual element, see Fig. 5. The algorithm to determine the material parameters for the stabilization energy is as follows, see Krysl [23] and Wriggers et al. [36]:

1. Convert the Lamé parameters, related to the problem, to Young’s modulus and Poisson ratio.
2. Compute a geometry parameter by using the inner and outer radii, R_i^2, R_a^2 respectively, see Fig. 5, to obtain

$$\beta = 2\sqrt{2}(1 + \nu) \frac{R_i^2}{R_a^2 - R_i^2}. \tag{30}$$

The inner radius is computed by using the distance from the geometrical centre to the convex hull of the virtual element while the outer radius is defined by the maximum distance of nodes related to the virtual element, see Fig. 5.

3. By comparing the bending energy of a rectangular block with that of a beam in order to enhance the bending behaviour of the element, see Krysl [23], the correction

$$\hat{E} = E \frac{\beta}{1 + \beta} \quad \hat{\nu} = 0.3. \tag{31}$$

for the Young's modulus and the Poisson ratio of a related brick element can be computed. Note that $\bar{\nu}$ is kept constants since the Poisson ratio does not influence the convergence behaviour of the element and avoids locking in the stabilization term for incompressible problems. A similar procedure was used in the work of Nadler and Rubin [26] who stabilized their Cosserat brick element using 18 deformation modes for bending and torsion and matched the stiffness of these modes by comparisons with linear elastic solutions. Extensions for non-rectangular elements were provided in Loehnert et al. [24] and Boerner et al. [11].

4. The Lamé parameters for the stabilization energy are finally obtained from

$$\hat{\lambda} = \frac{\hat{E} \hat{\nu}}{(1 + \hat{\nu})(1 - 2\hat{\nu})} \quad \hat{\mu} = \frac{\hat{E}}{2(1 + \hat{\nu})} \quad (32)$$

4 Numerical Examples

In this section we will apply the new virtual element formulation to some problems involving anisotropic material behaviour. The examples are selected such that the applied loads lead to finite deformation strain states.

All computations are performed by using a Newton-Rapson algorithm with load stepping when necessary. Due to the fact that all formulations are linearized in a consistent manner, using ACEGEN, quadratic convergence is achieved.

4.1 Beam Under End Load

When a beam that is clamped at one end is subjected to an end load then the beam will usually bend in the direction of the loading. Here we will investigate the case of a special anisotropic constraint that allows no deformation in horizontal direction. In case that the axial movement is constraint the beam can only undergo shear deformations. The beam has a length of $L = 2$, a height of $H = 0.5$ and a thickness $T = 1$ (in dimensionless coordinates), see Fig. 6. The constitutive data are provided for the Lamé constants: $\mu = 40$ and $\lambda = 100$. The direction of anisotropy is given by $\mathbf{a} = \{1, 0\}$ which enforces the constraint in horizontal x - direction by using a penalty parameter of $C_c = 10^8$. The beam is clamped at the left end using the boundary conditions: $u_x = u_y = 0$ for all nodes at $x = 0$. The beam is loaded by a constant load of $p_y = 1$ at the right end.

The loading is such that a moderate strain state occurs for pure shear. This leads to a deformed state that is reported in Fig. 7. Here the deformation is scaled by a factor of 5. The displacement at the right side of the beam is $u_y = 0.0531$. This result can approximately be checked using the classical beam theory. Here the shear deformation at the end of the beam is

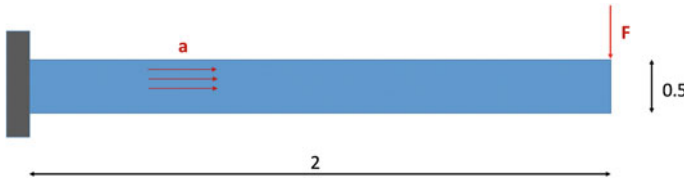


Fig. 6 Beam under end load

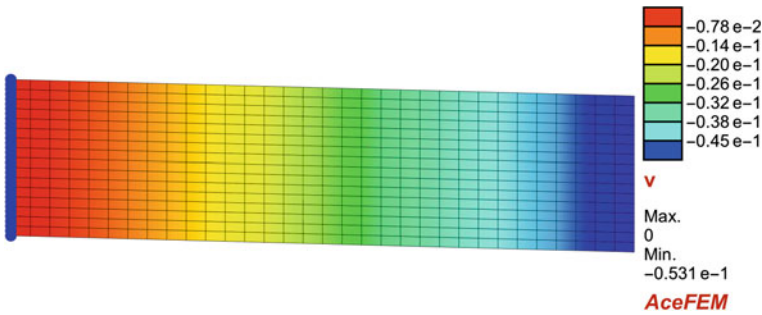


Fig. 7 Pure shear deformation of the beam for a mesh with 32×16 elements

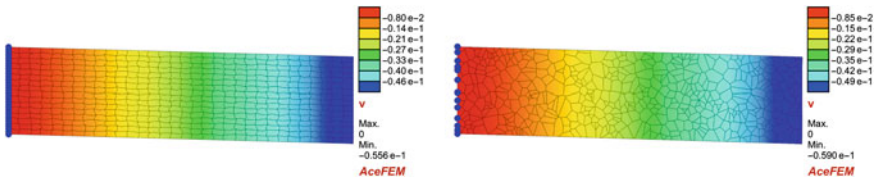


Fig. 8 Pure shear deformation two distorted meshes with 32×16 elements

$$u_{yB} = \frac{QL}{\mu A}$$

with $A = 0.5$, $Q = p_y A = 0.5$ and it follows $u_{yB} = 0,05$. A convergence study shows that the solution converges to $u_y = 0.05$ for a high density mesh with 512×256 virtual elements. Figure 9 depicts the convergence behaviour of different meshes. Here a regular mesh with 8-node virtual elements (VEM-8), a distorted mesh with 8-node elements (VEM-8-D) is used as well as a Voronoi mesh (VEM-VO). The deformed shapes for the distorted meshes can be found in Fig. 8. All meshes converge to the correct solution.

The relatively slow convergence for this simple problem stems from the fact that the anisotropic constraint in the virtual element formulation is fulfilled as mean value for an element Ω_e . This is somehow equivalent to a fulfillment at mid point and actually leads for only one element to pure bending since at a beam axis the constraint is fulfilled exactly in bending. Thus if we use a special mesh where a very thin upper

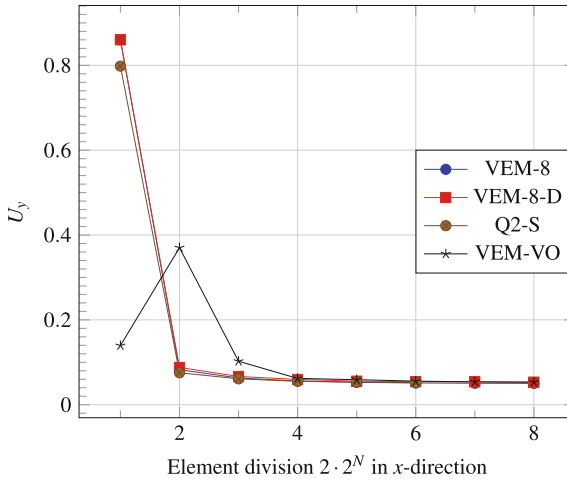


Fig. 9 Convergence study for the shear beam: VEM-T1- and Q2S-element

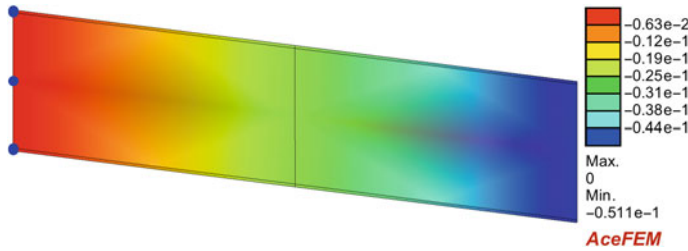


Fig. 10 Pure shear deformation of the beam for a mesh with 2×3 virtual elements, scaled by a factor of 5

and lower layer is introduced then the constraint is enforced at the upper and lower side of the beam and thus the pure shear mode is recovered, see Fig. 10. The solution is with $u_y = 0.0511$ very close to the converged solution despite the very coarse mesh with only six virtual elements. Also note that in this example the very thin upper and lower elements with an element ratio of $1/100$ do not lead to locking.

Hence we can conclude that the shear deformation pattern can be computed for different mesh types when using the virtual element method. The results clearly show that the constraint due to anisotropic behaviour can be reproduced.

4.2 Bias-Extension Test

A problem where tension locking for anisotropy can occur is the tensile test where fibers are oriented in $\pm 45^\circ$ in the initial configuration. This bias-extension test was

used in Thjie and Akkerman [34] and Hamila and Boisse [18] to investigate behaviour of standard finite element formulations and special interpolation techniques to avoid locking. The test is performed on a rectangular specimen, see Fig. 11. The length of the specimen is $L = 300$, its width is $H = 100$ and the thickness of the specimen is $T = 1$. The specimen is clamped at both ends and pulled using a constant displacement $\bar{u}_x = 65$. The specimen consists of a very soft matrix material in which the fibers are embedded under the angle of $\pm 45^\circ$. The material properties of the matrix material are described by the Lamé constants $\lambda = 1$ and $\mu = 1$. The stiffness for both fibers is $C_{c1} = C_{c2} = 4000$.

Several meshes were used to obtain the numerical solution of the bias-extension test. The load was applied in one step and Newton’s method was used to obtain the solution of this nonlinear problem. One can see the large deformation state of the specimen after loading in Fig. 12 which depicts the deformed configuration of the specimen for the applied displacement.

Next a convergence study for different meshes is performed. Again a virtual element formulation with 8-noded regular quads (VEM-8) and 8-noded non-convex quads (VEM-8-D) meshes as well as Voronoi (VEM-VO) meshes are compared to solution obtained with Q1 and Q2S elements. It can be observed that the Q1 element is not able to represent the solution while the other elements work fine. The relatively bad result for a Voronoi mesh with 8×4 elements is related to the fact that the nonuniformity in element size due to the random mesh generator of the Voronoi cells for such coarse mesh influences the results very much (Fig. 13).

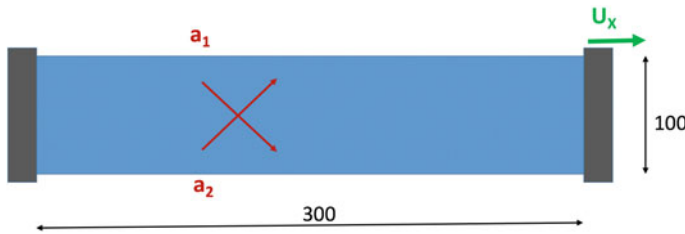


Fig. 11 Bias extension test of a woven composite

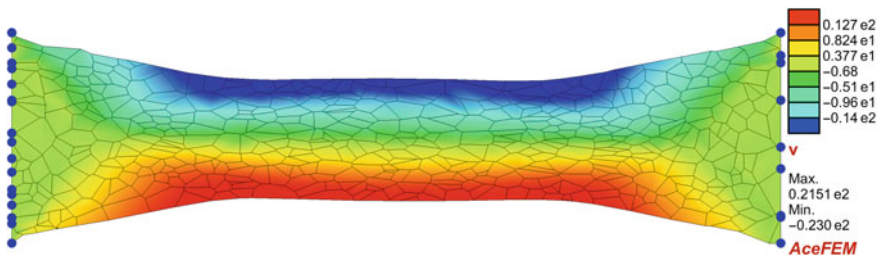
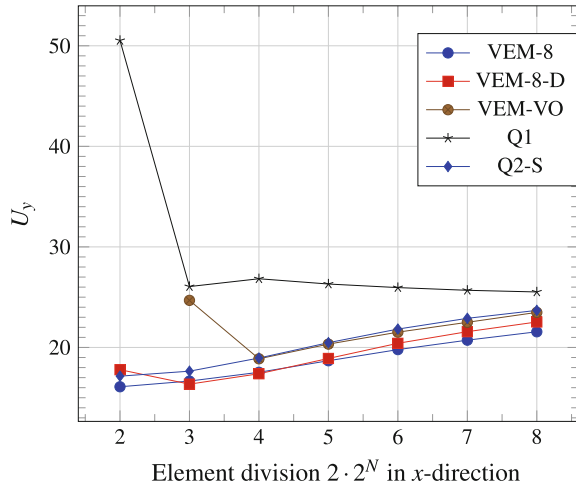


Fig. 12 Bias-extension: deformed configuration computed with a Voronoi mesh

Fig. 13 Convergence study for the bias-test: VEM-T1-, Q1-, Q2S-element



Generally it can be concluded that the new virtual element formulation for anisotropic materials is locking free and thus can be applied to problems with finite deformations.

Acknowledgements The paper is a contribution to honor Professor Roger Owen on behalf of his 75th birthday. The authors like to thank Roger Owen for his continuous support and friendship throughout the last four decades of research on finite element methods. The first author would like to thank for the support of the DFG within the priority program SPP 1748 1748 ‘Reliable simulation techniques in solid mechanics: Development of non-standard discretization methods, mechanical and mathematical analysis’ under the project WR 19/50-1.

References

1. K.J. Bathe, *Finite Element Procedures* (Prentice-Hall, Englewood Cliffs, New Jersey, 1996)
2. L. Beirão da Veiga, F. Brezzi, A. Cangiani, G. Manzini, L. Marini, A. Russo, Basic principles of virtual element methods. *Math. Models Methods Appl. Sci.* **23**(01), 199–214 (2013)
3. L. Beirão da Veiga, F. Brezzi, L. Marini, Virtual Elements for linear elasticity problems. *SIAM J. Numer. Anal.* **51**(2), 794–812 (2013)
4. L. Beirão da Veiga, F. Brezzi, L.D. Marini, A. Russo, The Hitchhiker’s guide to the virtual element method. *Math. Models Methods Appl. Sci.* **24**(08), 1541–1573 (2014)
5. L. Beirão da Veiga, C. Lovadina, D. Mora, A virtual element method for elastic and inelastic problems on polytope meshes. *Comput. Methods Appl. Mech. Eng.* **295**, 327–346 (2015)
6. T. Belytschko, L.P. Bindeman, Assumed strain stabilization of the 4-node quadrilateral with 1-point quadrature for nonlinear problems. *Comput. Methods Appl. Mech. Eng.* **88**(3), 311–340 (1991)
7. T. Belytschko, W.K. Liu, B. Moran, *Nonlinear Finite Elements for Continua and Structures* (Wiley, Chichester, 2000)
8. T. Belytschko, J.S.J. Ong, W.K. Liu, J.M. Kennedy, Hourglass control in linear and nonlinear problems. *Comput. Methods Appl. Mech. Eng.* **43**, 251–276 (1984)

9. S. Biabanaki, A. Khoei, A polygonal finite element method for modeling arbitrary interfaces in large deformation problems. *Comput. Mech.* **50**, 19–33 (2012)
10. S.O.R. Biabanaki, A.R. Khoei, P. Wriggers, Polygonal finite element methods for contact-impact problems on non-conformal meshes. *Comput. Methods Appl. Mech. Eng.* **269**, 198–221 (2014)
11. E. Boerner, S. Loehnert, P. Wriggers, A new finite element based on the theory of a Cosserat point—extension to initially distorted elements for 2D plane strains. *Int. J. Numer. Methods Eng.* **71**, 454–472 (2007)
12. A. Cangiani, G. Manzini, A. Russo, N. Sukumar, Hourglass stabilization and the virtual element method. *Int. J. Numer. Methods Eng.* **102**, 404–436 (2015)
13. H. Chi, L. Beirão da Veiga, G. Paulino, Some basic formulations of the virtual element method (VEM) for finite deformations. *Comput. Methods Appl. Mech. Eng.* (2016). doi:[10.1016/j.cma.2016.12.020](https://doi.org/10.1016/j.cma.2016.12.020)
14. H. Chi, C. Talischi, O. Lopez-Pamies, G.H. Paulino, Polygonal finite elements for finite elasticity. *Int. J. Numer. Methods Eng.* **101**(4), 305–328 (2015)
15. J.A. Cottrell, T.J.R. Hughes, Y. Bazilevs, *Isogeometric Analysis: Toward Integration of CAD and FEA* (Wiley, 2009)
16. D. Flanagan, T. Belytschko, A uniform strain hexahedron and quadrilateral with orthogonal hour-glass control. *Int. J. Numer. Methods Eng.* **17**, 679–706 (1981)
17. A.L. Gain, C. Talischi, G.H. Paulino, On the virtual element method for three-dimensional linear elasticity problems on arbitrary polyhedral meshes. *Comput. Methods Appl. Mech. Eng.* **282**, 132–160 (2014)
18. N. Hamila, P. Boisse, Locking in simulation of composite reinforcement deformations. analysis and treatment. *Composites: Part A* 109–117 (2013)
19. J. Korelc, U. Solinc, P. Wriggers, An improved EAS brick element for finite deformation. *Comput. Mech.* **46**, 641–659 (2010)
20. J. Korelc, P. Wriggers, *Automation of Finite Element Methods* (Springer, Berlin, 2016)
21. P. Krysl, Mean-strain eight-node hexahedron with optimized energy-sampling stabilization for large-strain deformation. *Int. J. Numer. Methods Eng.* **103**, 650–670 (2015a)
22. P. Krysl, Mean-strain eight-node hexahedron with stabilization by energy sampling stabilization. *Int. J. Numer. Methods Eng.* **103**, 437–449 (2015b)
23. P. Krysl, Mean-strain 8-node hexahedron with optimized energy-sampling stabilization. *Finite Elements Anal. Des.* **108**, 41–53 (2016)
24. S. Loehnert, E. Boerner, M. Rubin, P. Wriggers, Response of a nonlinear elastic general Cosserat brick element in simulations typically exhibiting locking and hourglassing. *Comput. Mech.* **36**, 255–265 (2005)
25. D.S. Mueller-Hoeppe, S. Loehnert, P. Wriggers, A finite deformation brick element with inhomogeneous mode enhancement. *Int. J. Numer. Methods Eng.* **78**, 1164–1187 (2009)
26. B. Nadler, M. Rubin, A new 3-D finite element for nonlinear elasticity using the theory of a cosserat point. *Int. J. Solids Struct.* **40**, 4585–4614 (2003)
27. S. Reese, On a consistent hourglass stabilization technique to treat large inelastic deformations and thermo-mechanical coupling in plane strain problems. *Int. J. Numer. Methods Eng.* **57**, 1095–1127 (2003)
28. S. Reese, M. Kuessner, B.D. Reddy, A new stabilization technique to avoid hourglassing in finite elasticity. *Int. J. Numer. Methods Eng.* **44**, 1617–1652 (1999)
29. S. Reese, P. Wriggers, A new stabilization concept for finite elements in large deformation problems. *Int. J. Numer. Methods Eng.* **48**, 79–110 (2000)
30. J. Schröder, Anisotropic polyconvex energies, in *Polyconvex Analysis*, vol. 62, ed. by J. Schröder (CISM, Springer, Wien, 2009), pp. 1–53
31. J. Schröder, P. Wriggers, D. Balzani, A new mixed finite element based on different approximations of the minors of deformation tensors. *Comput. Methods Appl. Mech. Eng.* **200**, 3583–3600 (2011)
32. N. Sukumar, Construction of polygonal interpolants: a maximum entropy approach. *Int. J. Numer. Methods Eng.* **61**, 2159–2181 (2004)

33. N. Sukumar, E.A. Malsch, Recent advances in the construction of polygonal finite element interpolants. *Arch. Comput. Methods Eng.* **13**, 129–163 (2006)
34. R.H.W. ten Thije, R. Akkerman, Solutions to intra-ply shear locking in finite element analyses of fibre reinforced materials. *Composites: Part A* 1167–1176 (2008)
35. P. Wriggers, *Nonlinear Finite Elements* (Springer, Berlin, Heidelberg, New York, 2008)
36. P. Wriggers, B.D. Reddy, W. Rust, B. Hudobivnic, Efficient virtual element formulations for compressible and incompressible finite deformations. *Comput. Mech.* (accepted) (2017)
37. P. Wriggers, W. Rust, B.D. Reddy, A virtual element method for contact. *Comput. Mech.* **58**, 1039–1050 (2016a)
38. P. Wriggers, J. Schröder, F. Auricchio, Finite element formulations for large strain anisotropic materials. *Int. J. Adv. Model. Simul. Eng. Sci.* **3**(25), 1–18 (2016b)